Modeling, Assessment, and Optimization of the Indirectly Heated Carbonate Looping Process for CO_2 Capture from Lime Plants

Martin Nicolas Greco Coppi

Cuvillier Verlag Göttingen
Internationaler wissenschaftlicher Fachverlag

Modeling, Assessment, and Optimization of the Indirectly Heated Carbonate Looping Process for CO_2 Capture from Lime Plants

Modeling, Assessment, and Optimization of the Indirectly Heated Carbonate Looping Process for CO_2 Capture from Lime Plants

Technical University of Darmstadt,
Department of Mechanical Engineering,
Institute for Energy Systems and Technology

Accepted cumulative dissertation of

Martin Nicolas Greco Coppi, M.Sc.

from Buenos Aires

submitted in fulfillment of the requirements for the
degree of *Doktoringenieur* (Dr.-Ing.)

First referee: Prof. Dr.-Ing. Bernd Epple
Co-referee: Prof. Dr.-Ing. Jürgen Karl

Submission date: December 3, 2024
Disputation date: January 28, 2025

Darmstadt 2025

Bibliographical information held by the German National Library

The German National Library has listed this book in the *Deutsche Nationalbibliografie* (German national bibliography); detailed bibliographic information is available online at http://dnb.d-nb.de.
1st edition - Göttingen: Cuvillier, 2025

The doctoral dissertation *Modeling, Assessment, and Optimization of the Indirectly Heated Carbonate Looping Process for CO_2 Capture from Lime Plants* by Martin Nicolas Greco Coppi has been conducted under the supervision of Prof. Dr.-Ing. Bernd Epple at the Institute for Energy Systems and Technology (EST), Department of Mechanical Engineering, Technical University of Darmstadt, in Darmstadt, Germany, since October 2019.
Disputation date: January 28, 2025

© CUVILLIER VERLAG, Göttingen, Germany 2025

Nonnenstieg 8, 37075 Göttingen, Germany
Telephone: +49 (0)551-54724-0
Telefax: +49 (0)551-54724-21
www.cuvillier.de

This work is licensed under the Creative Commons Attribution 4.0 International License (CC BY 4.0). You are free to share and adapt the material, even for commercial purposes, provided that appropriate credit is given. You must also provide a link to the license and indicate if changes were made. All rights reserved for any content not covered by this license. License details: https://creativecommons.org/licenses/by/4.0/

“Research Paper I” is included with permission from the original rights holder. This material is not covered by the CC BY 4.0 International License applied to the rest of this publication. All rights to “Research Paper I” remain with its original author(s) and/or publisher.

Cover image "Roasting rotary furnace with pipe at manufacturing plant" by *nordroden*. This material is not covered by the CC BY 4.0 International License applied to the rest of this publication. Image rights acquired by Cuvillier Verlag. Used under Adobe Stock license terms.

1st edition, 2025
This publication is printed on acid-free paper.

ISBN 978-3-68952-845-4
eISBN 978-3-68952-846-1
ORCID 0000-0002-0374-3673
ISNI 0000 0005 2425 7326
DOI 10.61061/ISBN_9783689528454

Foreword

The past two decades have seen a growing demand for advanced processes capable of replacing fossil-based products. The success of these processes not only requires the effective avoidance of greenhouse gas emissions, but also depends on their energy efficiency and cost-effectiveness. Only those solutions combining outstanding environmental performance, high resource utilization, and low costs will be implemented at commercial scale. Moreover, a broad portfolio of advanced processes is needed to meet the specific requirements of each application.

The Institute for Energy Systems and Technology (EST) at the Technical University of Darmstadt has been addressing these challenges for over two decades by developing innovative CO_2 capture, energy supply, and energy conversion processes. Since the year 2010, the EST institute investigates the Indirectly Heated Carbonate Looping (IHCaL) process, which offers a groundbreaking approach to capturing CO_2 from carbon-intensive industrial plants and power stations. The first IHCaL pilot tests at the EST institute were conducted within the EU-RFCS CARINA project (07/2010–09/2013). In the ACT ANICA project (10/2019–09/2023), the IHCaL process was investigated for its integration into lime and cement plants, including experiments at the one-of-a-kind 300-kW_{th} semi-industrial plant at the EST institute.

Lime plays a crucial role in modern industry—essential in steelmaking, construction, agriculture, and chemical manufacturing. However, its production is inherently carbon intensive. To drastically reduce CO_2 emissions, efficient carbon capture solutions are needed. The IHCaL process can efficiently capture CO_2 from lime and cement production. By leveraging synergies with existing industrial processes, IHCaL technology minimizes energy penalties and economic costs. Yet, until now, key integration challenges and modeling gaps have remained unaddressed.

To fill this research gap, this doctoral dissertation presents innovative IHCaL process integration approaches for efficient CO_2 capture; advanced reactor models based on experimental data; strategies for heat recovery, power generation, and fuel optimization; and insights on CO_2 capture and economics based on process simulations. All of this is complemented by practical design guidelines for scaling up IHCaL technology.

In this work, Martin Greco-Coppi provides essential tools for effectively implementing the IHCaL process in lime production, from conceptual integration to detailed process simulations and reactor modeling. The excellence of this work is reflected in the publications in top-tier journals, notably two scientific articles in the *Chemical Engineering Journal*—one of the most prestigious journals in the field, renowned for its rigorous peer-review process. Furthermore, this exceptionally comprehensive dissertation features a well-structured synopsis with clear graphs and accessible explanations. Overall, this dissertation is a key reference for advancing IHCaL technology toward commercialization and accelerating the decarbonization of lime production.

I believe that Mr. Greco-Coppi's exemplary work will interest a broad audience, including researchers and engineers working on industrial decarbonization, professionals in the cement and lime industries, policymakers and experts shaping the future of low-carbon manufacturing, as well as students in engineering and natural sciences. In summary, this dissertation is an invaluable reference for anyone interested in the challenges and innovations driving the transition to a low-carbon economy.

Prof. Dr.-Ing. Bernd Epple
Professor of Mechanical Engineering
Head of the Institute for Energy Systems and Technology
Technical University of Darmstadt

Darmstadt, May 2025

“The beginning of wisdom is the most sincere desire for instruction,
and concern for instruction is love of her,
and love of her is the keeping of her laws,
and giving heed to her laws is assurance of immortality,
and immortality brings one near to God;
so the desire for wisdom leads to a kingdom.”

Book of Wisdom 6:17–20

Abstract

Lime is an essential raw material for iron and steel production, in construction and agriculture, in civil engineering, in environmental protection, and in manifold chemical manufacturing processes. To solve the problem of unavoidable process CO_2 emissions associated with the production of lime, efficient and affordable capture technologies need to be developed and implemented. The indirectly heated carbonate looping (IHCaL) process is a promising technology for capturing CO_2 from lime and cement production. This process can exploit synergies with these industries, achieving low penalties in terms of economics and energy utilization. However, this requires integration measures that have not been undertaken until now. Furthermore, experimental efforts to develop IHCaL technology have not been matched by modeling work. Yet, accurate models are crucial for interpreting experiments and scaling up this technology for commercial operation.

In this study, we introduce concepts for efficiently integrating the IHCaL process into lime production. The main configurations are a tail-end solution suitable for retrofitting lime plants and a fully integrated configuration for greenfield projects. Furthermore, we present different fueling and heat integration strategies. We assessed these concepts in terms of energy efficiency, net CO_2 emissions, and CO_2 avoidance costs (*CAC*). The processes were simulated with Aspen Plus, including customized reactor models. EBSILON professional was used to model the steam cycles for heat recovery and power generation, and ECLIPSE was used for the economic analysis. The results show a considerable increase in fuel consumption, but approximately 30 % of the entire heat input can be converted into electric power via heat recovery steam generation. The critical parameters influencing the process efficiency are the preheating temperature of the combustion air, the sorbent temperature at calciner inlet, and the sorbent circulation rate. Utilizing the sorbent purge as lime product is necessary for the feasibility of the proposed concepts. The heat recovery strategy can be optimized to achieve tailored outcomes, such as reduced fuel requirement or increased power production. Net-negative CO_2 emissions higher than $-1.8\ t_{CO2}/t_{CaO}$ can be obtained when firing waste-derived fuels. Fuels with a high biogenic fraction and low specific CO_2 emissions, such as solid recovered fuels (SRFs) with a high calorific value, perform remarkably well in terms of energy utilization ($SPECCA < 1.5\ MJ_{LHV}/kg_{CO2,av}$) and cost efficiency ($CAC < 20$ €/$t_{CO2,av}$).

We present a novel carbonator model for CO_2 capture using IHCaL technology. Our model is based on a systematic literature review, and experimental results from pilot tests and thermogravimetric analysis (TGA). The model features a reactor sub-model to simulate flow patterns and gas-solid contact, and a particle sub-model to deal with sorbent deactivation and reaction kinetics. We follow an original approach to non-ideal calcination and introduce a new calculation methodology for sorbent aging that considers fluctuations in sorbent circulation and make-up rates. We highlight that modeling assumptions commonly found in the literature can result in a significant overestimation of the carbonator performance. Additionally, we offer guidelines for the appropriate selection of these assumptions.

Finally, we introduce a novel calciner model by combining a particle sub-model with a one-dimensional reactor sub-model. The model was validated with results from experimental campaigns conducted at two different pilot plants (300-kW_{th} and 1-MW_{th}). The predictions of the model were interpreted using a stochastic methodology and novel dimensionless numbers. Based on the model, we introduce a three-step approach to designing calciners for CO_2 capture. Calciners with oxy-fuel combustion should be operated at 930–965 °C to achieve sufficient sorbent regeneration. For indirectly heated calciners, an operating temperature of 950 °C is necessary for high performance, but lower temperatures (e.g., 900 °C) are also possible using steam for fluidization. Considerations regarding particle residence time are also discussed. Our guidelines are straightforward and enable the design of a calciner with simple calculations.

Overall, our study provides valuable information on the potential of IHCaL technology for reducing CO_2 emissions in the lime industry and demonstrates how process configurations, fuel properties, operating parameters, and components can be optimized to exploit this potential. Our results reduce design uncertainties, avoidance costs, and energy penalties, thereby bringing this technology closer to commercialization.

Kurzfassung

Kalk ist ein essenzielles Rohmaterial für die Eisen- und Stahlproduktion, im Bauwesen und in der Landwirtschaft, im Tiefbau, im Umweltschutz und in zahlreichen chemischen Herstellungsprozessen. Um das Problem der unvermeidbaren Prozess-CO_2-Emissionen, die mit der Kalkproduktion verbunden sind, zu lösen, müssen effiziente und kostengünstige CO_2-Abscheidungstechnologien entwickelt und implementiert werden. Der indirekt beheizte Carbonte-Looping Verfahren (IHCaL) ist eine vielversprechende Technologie zur CO_2-Abscheidung in der Kalk- und Zementproduktion. Dieser Prozess kann Synergien mit diesen Industrien nutzen und dabei geringe wirtschaftliche und energetische Einbußen erreichen. Dies erfordert jedoch Integrationsmaßnahmen, die bisher nicht umgesetzt wurden. Darüber hinaus wurde die IHCaL-Technologie bislang nicht ausreichend modelliert. Genaue Modelle sind jedoch entscheidend, um Experimente zu interpretieren und die IHCaL-Technologie hochzuskalieren.

In dieser Dissertation werden Konzepte für die effiziente Integration des IHCaL-Prozesses in die Kalkproduktion vorgestellt. Die Hauptkonfigurationen sind eine Tail-End-Lösung, die für die Nachrüstung von Kalkwerken geeignet ist, und eine voll integrierte Konfiguration für Greenfield-Projekte. Es werden verschiedene Strategien zur Brennstoff- und Wärmeintegration vorgestellt. Diese Konzepte wurden im Hinblick auf Energieeffizienz, Netto-CO_2-Emissionen und Vermeidungskosten (*CAC*) bewertet. Die Prozesse wurden mit Aspen Plus simuliert. Für die Modellierung der Dampfkreisläufe zur Wärmerückgewinnung und Stromerzeugung wurde EBSILON professional verwendet, und für die wirtschaftliche Analyse wurde ECLIPSE eingesetzt. Die Ergebnisse zeigen einen erheblichen Anstieg des Brennstoffverbrauchs, aber ca. 30 % der gesamten Wärmezufuhr kann über die Dampferzeugung mit Wärmerückgewinnung in elektrischen Strom umgewandelt werden. Die kritischen Parameter, die die die Prozesseffizienz beeinflussen, sind die Vorwärmtemperatur der Verbrennungsluft, die Sorbenttemperatur am Einlass des Kalzinators und die Sorptionsmittelumlaufrate. Die Nutzung des Sorbentpurges als Kalkprodukt ist für die Durchführbarkeit der vorgeschlagenen Konzepte erforderlich. Die Wärmerückgewinnungsstrategie kann optimiert werden, um maßgeschneiderte Ergebnisse zu erzielen, z. B. einen geringeren Brennstoffbedarf oder eine höhere Stromerzeugung. Negative CO_2-Emissionen von mehr als $-1{,}8\ t_{CO2}/t_{CaO}$ können durch die Verbrennung von abfallbasierten Brennstoffen erreicht werden. Brennstoffe mit hohem biogenem Anteil und niedrigen spezifischen CO_2-Emissionen, wie Ersatzbrenstoffe mit hohem Heizwert, zeichnen sich besonders durch eine hohe Energie- ($SPECCA < 1{,}5\ MJ_{LHV}/kg_{CO_2,av}$) und Kosteneffizienz ($CAC < 20$ €/$t_{CO_2,av}$) aus.

Ein neues IHCaL-Karbonatormodell wurde entwickelt und validiert. Das Modell enthält ein Reaktormodell zur Simulation von Gas-Feststoff-Kontakt sowie ein Partikelmodell zur Behandlung der Sorbent-Deaktivierung und der Reaktionskinetik. Ein neuer Ansatz für die nicht-ideale Kalzinierung wurde verfolgt, und eine neue Berechnungsmethodik für die Alterung des Sorbents wurde eingeführt, die Schwankungen in der Sorbent-Zirkulation und der Make-up-Rate berücksichtigte. Diese Arbeit bietet Richtlinien für die angemessene Auswahl dieser Annahmen.

Abschließend entwickeln wir ein neues Kalzinatormodell, indem wir ein Partikelmodell mit einem eindimensionalen Reaktormodell kombinieren. Das Modell wird mit Ergebnissen aus experimentellen Kampagnen in zwei verschiedenen Pilotanlagen validiert. Die Vorhersagen des Modells werden mit stochastischen Methoden und neuartigen dimensionslosen Zahlen interpretiert. Darüber hinaus stellen wir einen Ansatz für die Gestaltung von Kalzinatoren zur CO_2-Abscheidung vor. Oxyfuel-Kalzinatoren sollten bei 930–965 °C betrieben werden. Für IHCaL-Kalzinatoren ist eine Betriebstemperatur von 950 °C notwendig, um eine ausreichende Kalzinierung zu erzielen, aber auch niedrigere Temperaturen (z. B. 900 °C) sind möglich, wenn Dampf für die Fluidisierung verwendet wird. Unsere Richtlinien sind einfach und ermöglichen die Gestaltung eines Kalzinators mit einfachen Berechnungen.

Diese Dissertation liefert wertvolle Informationen über das Potenzial der IHCaL-Technologie zur Verringerung der CO_2-Emissionen in der Kalkindustrie und zeigt, wie Prozesskonfigurationen, Brennstoffeigenschaften, Betriebsparameter und Komponenten optimiert werden können, um dieses Potenzial zu nutzen. Unsere Ergebnisse verringern Unsicherheiten, Kosten und Energieverluste und bringen die Technologie näher an die Kommerzialisierung.

Acknowledgements

I would like to thank Prof. Dr.-Ing. Epple for giving me the opportunity to work at the institute for Energy Systems and Technology (EST) and conduct the research that led to this dissertation. His trust and support over these past five years have been invaluable to me.

I gratefully acknowledge Prof. Dr.-Ing. Jürgen Karl for agreeing to be the co-referee for my dissertation.

Dr.-Ing. Jochen Ströhle was always willing to give advice and support my investigations with suggestions regarding technical and methodological issues. For this, I am very grateful.

I had the privilege of attending lectures and working under the supervision of brilliant professors during my studies in Argentina. I would like to thank all my teachers at the Buenos Aires Institute of Technology (ITBA), especially Prof. Dr. Sebastián D'hers, Prof. Dr. Cecilia Smoglie, Prof. Hernán Baranda, Prof. Dr. Roberto Vieytes, and Prof. Vicente Celani.

My time at the EST institute was enriched by my teammates. Many of them participated in the ANICA pilot tests, which was an important contribution to the work presented here. I would like to thank all the EST research scientists for their collaboration and the good working atmosphere. In particular, I extend my gratitude to the CaL team: Dr.-Ing. Carina Hofmann, Dr.-Ing. Martin Haaf, Matti Löhden, and Robin Suardi.

The pilot-scale experiments of the IHCaL process would not have been possible without the support of the technical workshop. Special thanks go to Christof Bonk, Pascal Reinig, Joachim Wagner, Fabian Buchman, and Alexander Hoch.

Many scientists and engineers outside our institute supported my research through discussions, comments, and suggestions. These include project partners, reviewers, and peers, many of whom are acknowledged in the publications within this cumulative dissertation. I am deeply grateful to all of them. In particular, I would like to highlight the support from Dr.-Ing. Diethelm Walter, Prof. Dr. Juan Carlos Abanades, and Dr. José Ramón Fernández, the latter of whom also provided invaluable recommendations to improve the dissertation synopsis.

Throughout this journey, I had the help of many friends that became like family. Prof. Dr. Ferran Jarabo Carbonell, you are a spiritual father for me. The Minati family, Tomás M. Guisado, Mariano Francioni, Evangelino Garrido, and Hugo Giménez. To all of you, thank you.

The help of many students during their bachelor's and master's theses under my supervision and supporting my research activities as *HiWi* research assistants is greatly acknowledged.

To my family in Argentina: Thank you! The encouragement of my parents, Marcelo A. Greco and Alicia E. Coppi, was key for the success of this journey. My siblings, Sofía B. Greco-Coppi, Agustín T. Greco-Coppi, and Juan Pablo Greco-Coppi were always there to share the good and the "not-so-good".

I would like to thank my beloved wife and *adequate helper*, Alina M. Greco-Coppi. Without your countless proofreads, your suggestions, your support, and—most of all—your great patience, none of this would have been possible. I love you and always will: *all the days of my life*.

My daughters, Chiara Sofia, and Lucy Marie, always remind me of the purpose of life and give me perspective for my research activities. Every day next to you is a taste of heaven. Thank you.

This journey of science and engineering was enriched by the teachings and intercession of St. John Paul II, which were a constant motivation in the unavoidable search for truth. With him, I want to also thank the Virgin Mary, *Seat of Wisdom*, and St. Joseph, *model of workers*.

This dissertation was submitted on December 3, 2024, the feast day of Saint Fracis Xavier, and defended on January 28, 2025, the feast day of Saint Thomas Aquinas. To these two exemplary and dearest friends, who have assumed the patronage of the present work, I offer my sincerest thanks.

Finally, I thank God, with all His angels and saints, for the many graces I have received, especially during my years as a doctoral candidate. This dissertation, like every achievement and my life itself, is a gift from You that I offer back to You, as it belongs to You.

Table of contents

Abstract i
Kurzfassung ii
Acknowledgements iii
Table of contents v
Index of author's publications vii
List of research papers in this dissertation xi
Declaration of own contribution to the research papers xiii
Declaration of authorship xv
Nomenclature xvii

Part one: Synopsis 1
1 Introduction 3
  1.1 Research background 3
  1.2 State of the art 11
  1.3 Research questions 14
  1.4 Approach of the dissertation 15
2 Synthesis 21
  2.1 Process development, simulation, and assessment 21
  2.2 Carbonator modeling and design 30
  2.3 Calciner modeling and design 36
  2.4 Conclusion 39
  2.5 Outlook 41
References 43

Part two: Research papers 57
Research Paper I 61
Research Paper II 75
Research Paper III 111
Research Paper IV 133
Research Paper V 163
Research Paper VI 195

Index of author's publications

In this section we report the works published by the author of this cumulative dissertation, including publications in peer-reviewed journals, theses and reports, patents, and presentations in international conferences.

Publications in peer-reviewed journals

Research papers in this dissertation

Greco-Coppi, M; Ströhle, J; Epple, B (2025). Modeling and design of a calciner for commercial-scale CO_2 capture using stochastic methods and results from pilot tests. In *Fuel* 388. https://doi.org/10.1016/j.fuel.2024.133931

Greco-Coppi, M; Ströhle, J; Epple, B (2024). A carbonator model for CO_2 capture based on results from pilot tests. Part II: Deactivation and reaction model. In *Chemical Engineering Journal* 508. https://doi.org/10.1016/j.cej.2024.159041

Greco-Coppi, M; Ströhle, J; Epple, B (2024). A carbonator model for CO_2 capture based on results from pilot tests. Part I: Hydrodynamics and reactor model. In *Chemical Engineering Journal* 500. https://doi.org/10.1016/j.cej.2024.155119.

Greco-Coppi, M; Seufert, PM; Hofmann, C; Rolfe, A; Huang, Y; Rezvani, S; Ströhle, J; Epple, B (2024). Efficient CO_2 capture from lime plants: Techno-economic assessment of integrated concepts using indirectly heated carbonate looping technology. In *Carbon Capture Science & Technology* 11. https://doi.org/10.1016/j.ccst.2023.100187.

Greco-Coppi, M; Hofmann, C; Walter, D; Ströhle, J; Epple, B (2023). Negative CO_2 emissions in the lime production using an indirectly heated carbonate looping process. In *Mitigation and Adaption Strategies for Global Change* 28 (6). https://doi.org/10.1007/s11027-023-10064-7.

Greco-Coppi, M; Hofmann, C; Ströhle, J; Walter, D; Epple, B (2021). Efficient CO_2 capture from lime production by an indirectly heated carbonate looping process. In *International Journal of Greenhouse Gas Control* 112. https://doi.org/10.1016/j.ijggc.2021.103430.

Other publications in peer-reviewed journals

Hofmann, C; Greco-Coppi, M; Ströhle, J; Epple, B (2024). Enhancement of a 300 kW_{th} pilot plant for testing the indirectly heated carbonate looping process for CO_2 capture from lime and cement industry. In *Experimental Thermal and Fluid Science* 151. https://doi.org/10.1016/j.expthermflusci.2023.111091.

Theses and reports

Greco-Coppi, M; Hofmann, C; Ströhle, J (2024). Advanced indirectly heated carbonate looping process (ANICA) – Final report. Accelerating CCS Technologies (ACT). https://doi.org/10.26083/tuprints-00026729.

Greco-Coppi, M (2019). Wind energy in Argentine Patagonia: shortening the distance between the source and the consumers. Karlsruhe Institute of Technology. Master's thesis for obtaining the Master of Science degree in Energy Technologies.

Greco-Coppi, M (2015). Development of a torque anchor for progressing cavity pump systems. Buenos Aires Institute of Technology. Final project report for obtaining the Engineer's Degree in Mechanical Engineering.

Presentations in international conferences

Contributions as presenting author

Greco-Coppi, M; Eisenbach, N., Kurkunc, M.D.; Sattler, M.; Roloff, N; Ströhle, J; Epple, B (2024). Carbon-neutral polygeneration in waste-to-energy plants: Techno-economic study using carbon capture and utilization. In: proceedings of the *17th International Conference on Greenhouse Gas Control Technologies*, Calgary, Canada, October 20–24, 2024. https://dx.doi.org/10.2139/ssrn.5069382

Greco-Coppi, M; Dinkova, A; Hofmann, C; Walter, D; Böge, K; Ströhle, J; Epple, B (2023). Design of a 2 MW_{th} Indirectly Heated Carbonate Looping Demonstration Facility at a Lime Plant in Germany. IEAGHG, *7th Post Combustion Capture Conference*, Pittsburgh, Pennsylvania, September 25–27, 2023. https://doi.org/10.26083/tuprints-00026537.

Greco-Coppi, M; Seufert, PM; Hofmann, C; Rolfe, A; Huang, Y; Rezvani, S; Walter, D; Ströhle, J; Epple, B (2023). Efficient CO_2 capture from lime plants: Techno-economic assessment of integrated concepts using indirectly heated carbonate looping technology. The *12th Trondheim Conference on CO_2 Capture, Transport and Storage,* June 19–21, 2023.

Greco-Coppi, M; Hofmann, C; Ströhle, J; Epple, B (2022). Negative CO_2 Emissions in the Lime Production Using an Indirectly Heated Carbonate Looping Process. Darmstadt, IEA Bioenergy, *2nd International Conference on Negative CO_2 Emissions*, Chalmers University of Technology, Gothenburg, Sweden, June 14–17, 2022. https://doi.org/10.26083/tuprints-00026539.

Greco-Coppi, M; Hofmann, C; Ströhle, J; Walter, D; Epple, B (2021). Efficient CO_2 Capture from Lime Production by an Indirectly Heated Carbonate Looping Process. In: proceedings of the *15th International Conference on Greenhouse Gas Control Technologies*, Abu Dhabi UAE, March 15–18, 2021, https://doi.org/10.2139/ssrn.3817331.

Contributions as co-author

Hofmann, C; Greco-Coppi, M; Ströhle, J; Epple, B (2023). Performance of a limestone-based coupled fluidized bed reactor system aiming CO_2 capture in a 300 kW_{th} pilot plant. *Fluidization XVII*, Edinburgh, Scotland, May 21–25, 2023. https://doi.org/10.26083/tuprints-00028046

Hofmann, C; Greco-Coppi, M; Walter, D; Ströhle, J; Epple, B (2023). Pilot testing of the indirectly heated carbonate looping process for lime plants. *9th High Temperature Solid Cycles Network Meeting*, Piacenza, Italy, March 14–15, 2023. https://doi.org/10.26083/tuprints-00028047

Hofmann, C; Greco-Coppi, M; Ströhle, J; Epple, B (2023). Pilot testing of the indirectly heated carbonate looping process for CO_2 capture from lime industry. *12th Mediterranean Combustion Symposium*, Luxor, Egypt, January 23– 26, 2023. https://doi.org/10.26083/tuprints-00028048

Hofmann, C; Greco-Coppi, M; Ströhle, J; Epple, B (2022). Pilot testing of the indirectly heated carbonate looping process for cement and lime pants. In: proceedings of the *16th Greenhouse Gas Control Technologies Conference*, Lyon, France, October 23–24, 2022. https://doi.org/10.2139/ssrn.4278810.

Hofmann, C; Greco-Coppi, M; Ströhle, J; Epple, B (2022). Operation of a 300 kW_{th} indirectly heated carbonate looping plant for CO_2 capture from lime industry. *24th Fluidized Bed Conference*, Gothenburg, Sweden, May 08–11, 2022. https://doi.org/10.26083/tuprints-00026550.

Hofmann, C; Greco-Coppi, M; Ströhle, J; Epple, B (2022). Adaption of a 300 kW_{th} pilot plant for testing the indirectly heated carbonate looping process for CO_2 capture from lime and cement industry. *13th European Conference on Industrial Furnaces and Boilers*, Algarve, Portugal, April 19–22, 2022. https://doi.org/10.26083/tuprints-00028045

Ströhle, J; Hofmann, C; Greco-Coppi, M; Epple, B (2021). CO_2 Capture from Lime and Cement Plants using an Indirectly Heated Carbonate Looping Process – The ANICA Project. In: TCCS-11 – *Trondheim Conference on CO_2 Capture, Transport and Storage*: June 21–23, 2021, pp. 529–535, Trondheim, Norway, ISBN 978-82-536-1714-5.

Patents

Greco-Coppi, M; Ströhle, J; Epple, B (2024). *Verfahren zur Kohlendioxidabscheidung für eine Müllverbrennungsanlage* (CO_2 capture process for a waste incineration plant). Pending to the Technical University of Darmstadt at the Deutsche Patent- und Markenamt (no. 10 2024 130 087.6).

Greco-Coppi, M; Ströhle, J; Epple, B (2024). *Vorrichtung und Verfahren zum Herstellen von Kalk und Zement* (Apparatus and method for producing lime and cement). Pending to the Technical University of Darmstadt at the Deutsche Patent- und Markenamt (no. 10 2024 109 181.9).

Greco-Coppi, M; Hofmann, C; Ströhle, J; Epple, B; Walter, D (2023). *Vorrichtung und Verfahren zum Herstellen von Kalk* (Apparatus and method for producing lime). Pending to the Technical University of Darmstadt and Rheinkalk GmbH (Lhoist) at the Deutsche Patent- und Markenamt (no. 10 2023 114 354.9).

List of research papers in this dissertation

This cumulative dissertation consists of six research papers (RP), which are included in the second part of this work. In this section, we report the main bibliographic information of the research papers.

Research Paper I

Title: Efficient CO_2 capture from lime production by an indirectly heated carbonate looping process
Authors: Martin Greco Coppi, Carina Hofmann, Jochen Ströhle, Diethelm Walter, Bernd Epple
Journal: International Journal of Greenhouse Gas Control (Elsevier)
DOI: https://doi.org/10.1016/j.ijggc.2021.103430

Research Paper II

Title: Negative CO_2 emissions in the lime production using an indirectly heated carbonate looping process
Authors: Martin Greco Coppi, Carina Hofmann, Diethelm Walter, Jochen Ströhle, Bernd Epple
Journal: Mitigation and Adaptation Strategies for Global Change (Springer)
DOI: https://doi.org/10.1007/s11027-023-10064-7

Research Paper III

Title: Efficient CO_2 capture from lime plants: Techno-economic assessment of integrated concepts using indirectly heated carbonate looping technology
Authors: Martin Greco Coppi, Peter Seufert, Carina Hofmann, Angela Rolfe, Ye Huang, Sina Rezvani, Jochen Ströhle, Bernd Epple
Journal: Carbon Capture Science & Technology (Elsevier)
DOI: https://doi.org/10.1016/j.ccst.2023.100187

Research Paper IV

Title: A carbonator model for CO_2 capture based on results from pilot tests. Part I: Hydrodynamics and reactor model
Authors: Martin Greco Coppi, Jochen Ströhle, Bernd Epple
Journal: Chemical Engineering Journal (Elsevier)
DOI: https://doi.org/10.1016/j.cej.2024.155119

Research Paper V

Title: A carbonator model for CO_2 capture based on results from pilot tests. Part II: Deactivation and reaction model
Authors: Martin Greco Coppi, Jochen Ströhle, Bernd Epple
Journal: Chemical Engineering Journal (Elsevier)
DOI: https://doi.org/10.1016/j.cej.2024.159041

Research Paper VI

Title: Modeling and design of a calciner for commercial-scale CO_2 capture using stochastic methods and results from pilot tests
Authors: Martin Greco Coppi, Jochen Ströhle, Bernd Epple
Journal: Fuel (Elsevier)
DOI: https://doi.org/10.1016/j.fuel.2024.133931

Declaration of own contribution to the research papers

The nine researchers (1–9) listed below have contributed to the research papers of this dissertation:

1) Martin Greco Coppi (MG) – Technical University of Darmstadt
2) Carina Hofmann (CH) – Technical University of Darmstadt
3) Peter Seufert (PS) – Technical University of Darmstadt
4) Angela Rolfe (AR) – University of Ulster
5) Ye Huang (YH) – University of Ulster
6) Sina Rezvani (SR) – ESTRA–Energy Technology Strategies Ltd.
7) Diethelm Walter (DW) – Lhoist Germany Rheinkalk GmbH
8) Jochen Ströhle (JS) – Technical University of Darmstadt
9) Bernd Epple (BE) – Technical University of Darmstadt

For each of these papers, the author contributions are defined within the paper itself and are listed below. For term explanation, please refer to the *CRediT taxonomy*. These research papers are not part of any other cumulative dissertation, whether past or planned.

Research Paper I. MG: conceptualization, methodology, software, visualization, and writing (original draft). CH: conceptualization and methodology. JS: conceptualization, writing (review & editing), project administration, and funding acquisition. DW: conceptualization, methodology, and writing (review & editing). BE: supervision, and funding acquisition.

Research Paper II. MG: conceptualization, methodology, software, visualization, and writing (original draft). CH: writing (review & editing). DW: writing (review & editing). JS: writing (review & editing), supervision, project administration, and funding acquisition. BE: supervision and funding acquisition.

Research Paper III. MG: conceptualization, methodology, software (Aspen Plus, EBSILON Professional), visualization, writing (original draft, lead), and writing (review & editing, lead). PS: writing (original draft, supporting), and software (Aspen Plus, EBSILON Professional). C.H.: writing (review & editing). AR: methodology, writing (original draft, economic assessment), and writing (review & editing, economic assessment). YH: software (ECLIPSE). SR: writing (review & editing). JS: writing (review & editing), supervision, project administration, and funding acquisition. BE: supervision and funding acquisition.

Research Paper IV. MG: conceptualization, methodology, software (MATLAB), validation, investigation, data curation, visualization, writing (original draft), and writing (review & editing). JS: writing (review & editing), supervision, project administration, and funding acquisition. BE: supervision.

Research Paper V. MG: conceptualization, methodology, software (MATLAB), validation, investigation, data curation, visualization, writing (original draft), and writing (review & editing). JS: writing (review & editing), supervision, project administration, and funding acquisition. BE: supervision.

Research Paper VI. MG: conceptualization, methodology, software (MATLAB), validation, formal analysis, investigation, data curation, visualization, writing (original draft), and writing (review & editing). JS: writing (review & editing), supervision, project administration, and funding acquisition. BE: supervision.

Declaration of authorship

I hereby declare that I have completed this dissertation independently and only with the aids indicated. The first-person plural (*pluralis modestiae*) is utilized for stylistic purposes only. I am the sole author of this work.

Martin N. Greco Coppi

Nomenclature

Latin symbols

Ar	Archimedes number (-)
$BESP$; $BESP_{\mathrm{CC}}$; $BESP_{\mathrm{ref}}$	Break-even selling price of lime; for the plant with CO_2 capture; without CO_2 capture (€/t_{CaO})
$\mathfrak{C}^*$	Equivalent driving force (mol/m^3)
CAC	CO_2 avoidance costs (€/$t_{\mathrm{CO2,av}}$)
DF	Driving force (-)
d_p^*	Dimensionless particle diameter (-)
e_{CO2}; $e_{\mathrm{CO2,CC}}$; $e_{\mathrm{CO2,ref}}$	Equivalent CO_2 emissions per unit product; for the plant with CO_2 capture; for the reference plant ($kgCO_2/kg_{\mathrm{CaO}}$)
$e_{\mathrm{CO2,d}}$; $e_{\mathrm{CO2,i}}$	Direct CO_2 emissions per unit product; indirect CO_2 emissions per unit product (kg_{CO2}/ kg_{CaO})
$e_{\mathrm{CO2,fuel}}$	Fuel specific CO_2 emissions ($g_{\mathrm{CO2}}/MJ_{\mathrm{LHV}}$)
$e_{\mathrm{ref,el}}$	CO_2 emissions factor of the electricity mix (g_{CO2}/MJ)
E	Overall CO_2 capture efficiency (%)
E_{calc}	Calciner efficiency (%)
E_{carb}; E_{PM}; E_{RM}	Carbonator efficiency; calculated with the particle sub-model; with the reactor sub-model (%)
F_0	Molar flow rate of make-up (mol_{CaCO3}/s)
F_{CO2}; $F_{\mathrm{CO2,carb}}$; $F_{\mathrm{CO2,calc}}$; F_{inert}	Molar flow rate of CO_2 entering the carbonator; exiting the carbonator; exiting the calciner; molar flow rate of inert fluidization gases (mol/s)
F_R; $F_{\mathrm{R+0}}$	Molar sorbent circulation rate; total active flow into the calciner (mol_{Ca}/s); $F_{\mathrm{R+0}} \equiv F_R + F_0$
HR; HR_a	Heat ratio; absolute heat ratio (-)
k_c	Particle kinetic rate (1/s)
$k_{\mathrm{c\text{-}w}}$	Specific core-wall exchange coefficient (m/s)
K_r	Global reaction rate (various)
LHV	Lower heating value of the fuel (MJ/kg)
$\dot{m}_{\mathrm{CaO}}$; $\dot{m}_{\mathrm{CaO,CC}}$; $\dot{m}_{\mathrm{CaO,ref}}$	Lime production; in the lime plant w/CO_2 capture; w/o CO_2 capture (kg/s)
$\dot{m}_{\mathrm{CO2,capt}}$; $\dot{m}_{\mathrm{CO2,foss}}$	CO_2 capture rate; generation rate of fossil CO_2 (kg/s)
$\dot{m}_{\mathrm{fuel}}$	Fuel consumption rate (kg/s)
N	Number of carbonation-calcination cycles (-)
p; p_{CO2}; $p_{\mathrm{CO2,eq}}$; $p^*_{\mathrm{CO2,out}}$	Pressure; CO_2 partial pressure; for equilibrium conditions; at the calciner outlet corresponding to full calcination (Pa)
P_{el}	Net power consumption (MW_{el})
PR	Product ratio (-)
q; q_{CC}; q_{ref}	Equivalent specific primary energy consumption per unit of product; for the plant with CO_2 capture; for the reference plant ($MJ_{\mathrm{LHV}}/kg_{\mathrm{CaO}}$)
Re_{p}	Particle Reynolds number (-)
RMSE	Root mean square error (various)
$SPECCA$	Specific primary energy consumption per CO_2 avoided ($MJ_{\mathrm{LHV}}/kg_{\mathrm{CO2,av}}$)
SR	Steam ratio ($kg_{\mathrm{H2O}}/kg_{\mathrm{CO2}}$)
t; t_c	Time, calcination time (s)
T; T_{preheat}; $T_{\mathrm{sorb,calc,in}}$	Temperature; preheating temperature of the combustion air; solids temperature at the calciner inlet (°C)
u_0^*	Dimensionless superficial gas velocity (-)
X; X_{carb}; X_{calc}; $\bar{X}_{\mathrm{carb}}$	Carbonation degree; at the carbonator outlet; at the carbonator inlet/at the calciner outlet; average at the calciner inlet ($mol_{\mathrm{CaCO3}}/mol_{\mathrm{Ca}}$); $\bar{X}_{\mathrm{carb}} \equiv \left(X_{\mathrm{carb}}F_R + F_0\right)/\left(F_R + F_0\right)$
X_N; $\bar{X}_N$; $\bar{X}_{N+1}$	Sorbent activity; average sorbent activity; average sorbent activity after one additional calcination-carbonation cycle ($mol_{\mathrm{CaCO3}}/mol_{\mathrm{Ca}}$)
z	Height (m)

Greek symbols

α	Conversion/reaction progress (-)
γ	Overall system age number (-)
ε_s	Solid volume fraction (-)
$\eta_{\text{ref,el}}$	Reference electric efficiency of the grid (-)
λ	Air-fuel equivalence ratio (-)
Λ	Make-up ratio ($\text{mol}_{\text{CaCO3}}/\text{mol}_{\text{CO2}}$)
Φ	Sorbent circulation ratio ($\text{mol}_{\text{Ca}}/\text{mol}_{\text{CO2}}$)
τ	Mean particle residence time (s)
τ^*_{act}	Dimensionless active time (-)

Abbreviations

1-D; 3-D	One-dimensional; three-dimensional
ASU	Air separation unit
BAU	Business as usual (reference)
BECCS	Bioenergy with CCS
BFB	Bubbling fluidized bed
CaL	Carbonate looping
CCS; CCU; CCUS	Carbon capture and storage; carbon capture and utilization; carbon capture, utilization, and storage
CDR	Carbon dioxide removal
CFB	Circulating fluidized bed
CFD	Computational fluid dynamics
CGSM	Changing Grain Size Model
CSTR	Continuous stirred-tank reactor
DDPM	Dense Discrete Phase Model
EGR	Exhaust gas recirculation
EOR	Enhanced oil recovery
FEED	Front-end engineering design
GHG	Greenhouse gas
IGCC	Integrated gasification combined cycle
IHCaL	Indirectly heated carbonate looping
IPCC	Intergovernmental Panel on Climate Change
KL	Kunii and Levenspiel (model)
LCA	Life cycle assessment
Lhoist	Lhoist Germany Rheinkalk GmbH
PRK	Preheated rotary kiln
R3	Volumetric (model)
RP	Research paper
RTD	Residence time distribution
TFM	Two Fluid Model
TGA	Thermogravimetric analysis
TU	Technical University (of Darmstadt)

Subscripts and superscripts

calc	Calciner (outlet)
capt	Captured CO_2
carb	Carbonator (outlet)
CC	CO_2 capture/plant with CO_2 capture
d	Direct
el	Electric
eq	Equilibrium conditions
foss	Fossil
fuel	Fuel
i	Indirect
in	Inlet
p	Particle
preheat	Combustion air preheating
ref	Reference/plant without CO_2 capture
sorb	Sorbent
th	Thermal

Part one: Synopsis

1 Introduction

1.1 Research background

CO_2 emissions in the production of lime

Lime (CaO) is an important product used in construction and building, iron and steelmaking, treatment of water and gaseous effluents, agriculture, the food industry, and the chemical industry [1,2]. It is produced through the calcination of limestone (mainly $CaCO_3$) at temperatures between 900 and 1200 °C. This process is highly endothermic and requires the combustion of fuels such as gas oil, coal, coke, or some types of secondary fuels (e.g. oil, plastics, paper) [3]. CO_2 emissions from combustion, known as *combustion CO_2 emissions*, can be reduced by replacing fossil fuels with renewable fuels such as biomass. *Process CO_2 emissions*, resulting from the decomposition of $CaCO_3$, account for approximately 65% of total CO_2 emissions and can only be avoided using CO_2 capture [4]. Overall, the total CO_2 emissions per ton of burnt lime vary between 1 to 2 t_{CO2}/t_{lime} [3]. Due to the nature and high level of CO_2 emissions, CO_2 capture, utilization, and storage (CCUS) is fundamental to decarbonize the lime production [5].

Only a few studies have analyzed CO_2 capture technologies specifically for the lime industry [6–9], whereas many works have been published recently that consider carbon capture for the cement industry (e.g., [10–12]). There are similarities between both industries, like the calcination of $CaCO_3$, which is the main process in terms of energy consumption [3]. Moreover, CO_2 capture from cement and lime plants have many common features. In both production processes, most of the CO_2 emissions come from the raw material, and the specific CO_2 emissions per unit of product are approximately the same. The other components of the flue gas (e.g., HCl, SO_2, moisture, NO_x and N_2, and residual dust) are also comparable if the same fuels are used [3]. A robust process is needed in both cases to capture the CO_2 from the flue gases. Even though this work focuses on the CO_2 capture from a lime plant, reference studies on carbon capture from cement kilns are used for comparison purposes. The production of lime and cement is responsible for around 8 % of global anthropogenic CO_2 emissions [13].

The entire carbon capture and storage (CCS) value chain for preventing CO_2 from being emitted into the atmosphere consists of separation, purification, transport, and geological storage of CO_2. Alternatively, CO_2 can be captured and utilized (CCU), e.g., to produce chemicals. CO_2 utilization has been proposed as an alternative to permanent storage. However, utilizing CO_2 is likely to serve as a minor complement. The scale of emissions reduction needed to decarbonize the industry is expected to rely mainly on CCS [14].

There are many means to transport CO_2, such as rail tankers and trucks [15]. For large-scale transportation, pipelines are the best option, but more research is required to better understand the impact of impurities (e.g., H_2O, O_2, H_2S) and mature this technology. The lowest costs are achieved when CO_2 is transported in pipelines as a dense-phase fluid, i.e., above the critical pressure and below the critical temperature [16], typically at 100 bar and ambient temperature [17]. Ships have been used for over 30 years to transport CO_2 and are a good alternative for large distances. The optimal condition for CO_2 transportation via ships is cryo-compressed at 15 bar and −30 °C [18].

CO_2 can be sequestered through mineral, oceanic, or geological storage [15]. The latter is the most proven sequestration method. Among the several options of geological CO_2 storage, enhanced oil recovery (EOR), and injection into saline formations [19] are the most mature. Currently, tens of facilities store CO_2 via EOR [20]. Recent commercial-scale projects such as Gorgon CO_2 Injection (Australia) and Quest CCS (Canada) store CO_2 in saline formations [16].

The latest report of the Intergovernmental Panel on Climate Change (IPCC) states that net-negative CO_2 emissions are required to achieve net zero greenhouse gas (GHG) emissions [21] and cap global warming to 1.5 °C with no or limited overshoot [22]. This strategy, known as *carbon dioxide removal* (CDR), is a “key element” to limit global warming because it is the only means to counterbalance the so- called “residual emissions”, i.e., uneconomical to abate anthropogenic GHG emissions [23]. Emission scenarios compatible with the 1.5 °C limit (67 % probability) require huge amounts of CDR on top of deep emissions reductions; namely, 730 Gt_{CO2} on average [22,24]. One of the most promising ways to achieve net-negative CO_2 emissions is the implementation of CCS into industrial processes that emit high amounts of biogenic CO_2. This approach is called bioenergy with carbon capture and storage (BECCS) [23,25]. BEECS can help decarbonize the production of lime and cement and deliver negative CO_2 emissions at competitive costs [26].

The capture process is the most energetically demanding step of the entire CCS chain, accounting for about 70–80 % of the total costs [27,28]. The main research projects on CO_2 capture from lime and cement industries of the last years were the LEILAC project, the CEMCAP project, the CLEANKER project, and the ANICA project [29–31]. Many more research projects to advance CO_2 capture technologies for lime and cement plants are currently running [14], while several industrial-scale capture projects for cement plants have been announced [26]. Since this dissertation focuses on CO_2 capture, we provide a more detailed discussion of this step below.

CO_2 capture technologies

Different classifications for CO_2 capture technologies have been proposed [32,33]. In this dissertation, we adopt the following classification, according to the overarching separation approach [15]: (i) pre-combustion, (ii) oxy-fuel combustion, (iii) post-combustion, and (iv) integrated industrial separation. Most studies agree on the first three. Approaches (i) to (iii) are suitable for capturing CO_2 from power plants [34]. Capturing CO_2 from industrial production, such as cement and lime plants, can be performed using oxy-fuel combustion (ii), post-combustion capture (iii), or fully integrated capture technologies, such as those relying on indirect calcination (iv). A special approach, known as direct air capture (DAC), involves extracting CO_2 directly from the atmosphere [35]. It is a flexible technology capable of achieving net-negative CO_2 emissions [36]. However, it comes with significantly higher costs compared to other capture methods, due to the much lower CO_2 concentration in the gas phase from which CO_2 is extracted (i.e., the atmosphere).

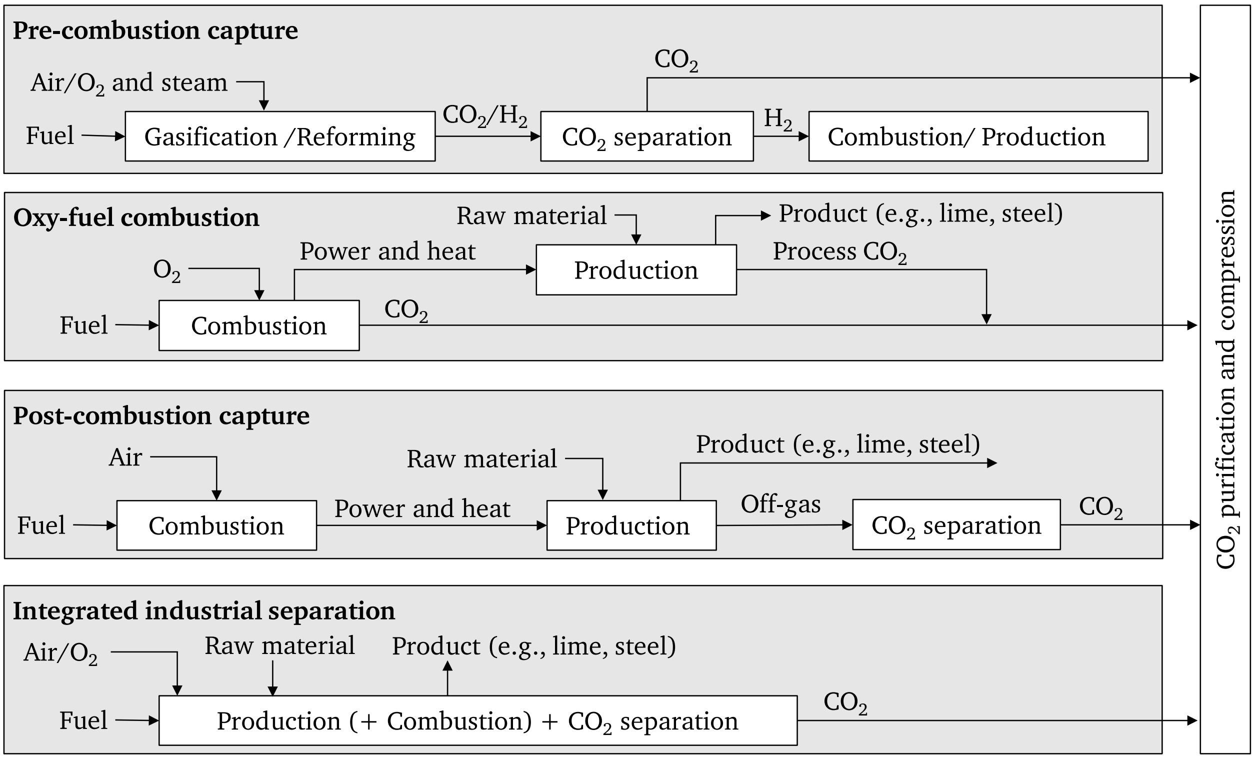
Pre-combustion capture
Air/O2 and steam
Fuel
Gasification /Reforming
CO2/H2
CO2 separation
CO2
H2
Combustion/ Production
Oxy-fuel combustion
Raw material
Product (e.g., lime, steel)
Power and heat
Production
Process CO2
O2
Fuel
Combustion
CO2
Post-combustion capture
Air
Raw material
Product (e.g., lime, steel)
Fuel
Combustion
Power and heat
Production
Off-gas
CO2 separation
CO2
Integrated industrial separation
Air/O2
Raw material
Product (e.g., lime, steel)
Fuel
Production (+ Combustion) + CO2 separation
CO2
CO2 purification and compression

Figure 1. CO_2 capture technologies categorized according to the overarching separation approach, adapted from [15,37].

Figure 1 illustrates the four overarching approaches to capture CO_2 from industrial sources. After the separation, further processing, including compression, dehydration, and purification is usually required to comply with the requirements of transport and storage, or utilization [38,39].

Pre-combustion CO_2 capture consists in converting coal, natural gas, heavy oil fractions, biomass, or waste-derived fuels into a gaseous mixture composed mainly by CO and H_2 (synthesis gas) [33]. The main routes to produce synthesis gas are the gasification of solid or liquid fuels, and the reforming/partial oxidation of gaseous fuels [40]. The yield of H_2 can be increased by reacting CO with steam in a water-gas-shift reactor. If the CO_2 is separated and permanently stored, the synthesis gas is a carbon-free energy carrier. The separation can be performed using either physical or chemical absorption processes, cryogenic separation, or solid physical adsorption (pressure swing and temperature swing). Physical absorption methods, such as Rectisol®, are viable for pre-combustion capture due to the relatively high CO_2 concentrations (15–60 vol%) before the separation step, which also helps reduce equipment costs [28]. Pre-combustion CO_2 capture has been proposed for power generation in a combined cycle. This approach is known as integrated gasification combined cycle (IGCC) technology. Using pre-combustion CO_2 capture technologies in industrial production can only avoid fuel-related CO_2 emissions, but not process CO_2 emissions [26]. This is why, in practice, this approach is not applicable to lime and cement industries.

The Quest CCS facility is a commercial example of pre-combustion CO_2 separation, which currently captures and stores approximately one million tonnes of CO_2 per year in Canada. Commissioned in 2015, this facility uses a pre-combustion process to separate ca. 50 % of the CO_2 generated during hydrogen production.

Oxy-combustion technology is based on the combustion of fuels using pure oxygen instead of air to avoid diluting the CO_2 of the flue gases with N_2 [33]. It allows to obtain highly concentrated CO_2 streams (> 80 vol%$_{wb}$). This approach, which was originally proposed for combustion systems, is also suitable for capturing CO_2 from industrial processes (industrial separation), such as cement plants [41].

Eriksson et al. [6] studied oxy-fuel combustion in a lime rotary kiln. They found that with this system, the total CO_2 emissions may be reduced, but pointed out technical challenges to control the temperature and, in this way, comply with the high-quality standards of rotary-kiln lime products. The high environmental and economic potential of oxy-fuel combustion for cement production has been highlighted by different authors [42,43]. Carrasco et al. [44] investigated oxy-fuel carbon capture from cement production in a 500 kW$_{th}$ testing facility. This technology has good energy performance and high potential for low CO_2 avoidance costs, which have been calculated at approximately 42 €/t$_{CO2,av}$ for cement production [45]. However, significant retrofitting challenges may hinder its economic feasibility [46].

Within the *GeZero* project, an oxy-fuel cement kiln will be built in at a Heidelberg Materials facility in Geseke, making it the first commercial cement plant in Germany with full-scale CO_2 carbon capture and storage [26]. The objective of this project is to capture 700 kt$_{CO2}$/y starting in 2029. Additionally, an oxy-fuel pilot plant is being constructed in Mergelstetten, Germany, as part of the *catch4climate* project [47]. This semi-industrial plant will use an oxy-fuel process developed by thyssenkrupp Polysius. Commissioning is scheduled for the beginning of 2025.

Post-combustion systems separate CO_2 from flue gases downstream of combustion [33]. The CO_2 concentration in the combustion gases is generally 3–15 vol% but higher concentrations are possible in off-gases of industrial processes. Different separation techniques can be deployed in post-combustion CO_2 capture, such as absorption in liquid sorbents, membrane separation, adsorption-desorption processes, and cryogenic capture [15]. However, the majority of them have high thermodynamic and economic penalties [46,48–50].

Absorption technologies are well-established but require considerable heat for sorbent regeneration and the used sorbents have potential negative effects on the environment [51]. Among them, amine-based CO_2 capture technologies are more suitable for retrofitting than oxy-combustion and have high technology-readiness levels [46]. However, most amine absorption technologies have very high energy requirements, which increases the costs of CO_2 capture and significantly reduces system efficiency [52]. Gardarsdottir et al. [45] evaluated different post-combustion carbon capture processes for cement production. They calculated that monoethanolamine (MEA) absorption, the reference post-combustion carbon capture technology, has a specific primary energy consumption for CO_2 avoided (*SPECCA*) of 7.0 $\mathrm{MJ/kg_{CO2,av}}$ and a cost of CO_2 avoided of 80 $€/\mathrm{t_{CO2,av}}$. Barker et al. [43] calculated CO_2 avoidance costs exceeding 100 $€/\mathrm{t_{CO2,av}}$ for retrofitting a 1-Mt/y cement plant in Northeast Scotland with a solvent-based post-combustion capture unit. Membrane separation offers high market accessibility but presents operational challenges such as fouling, and significant expenses when high capture efficiencies are needed [51]. Membrane separation technology is sometimes regarded as a competitive alternative to decarbonize the lime and cement industries, but it is still costly (> 80 $€/\mathrm{t_{CO2,av}}$) if capture rates of more than 80 % are to be achieved [45,53,54]. Adsorption processes face significant energy penalties associated with the desorption step required to regenerate the adsorbent. While cryogenic separation has extensive operational experience, it is only economically viable for high CO_2 concentrations, due to the substantial energy costs associated with cooling. The carbonate looping (CaL) process, which is the predecessor of the capture process analyzed in this dissertation, is a promising post-combustion CO_2 capture technology that can be deployed in the lime industry [55]. It is discussed in the following subsection.

The Petra Nova CCS plant captures approximately 90 % of the CO_2 emissions from a coal-fired power plant in Texas (USA). The CO_2 is separated from the rest of the flue gas with the KM CDR post-combustion process from Mitsubishi Heavy Industries, which employs a proprietary amine developed by the company. The CO_2 is compressed, transported, and utilized for enhanced oil recovery (EOR), permanently sequestering it underground. This project was commissioned in the year 2017. After a 3-year shutdown, the plant has been operational since September 2023.

Currently, a capture facility using an amine-based capture process developed by Aker Carbon Capture is being built at a cement plant in Brevik, Norway [56]. The heat for regenerating the sorbent will be obtained from electrical power and waste heat recovery from the cement process and the CO_2 compression. After separation, the CO_2 will be liquefied and transported via ships to the storage location in the North Sea. It will be the first industrial-scale CO_2 capture plant in the cement industry worldwide, with an annual capture rate of 400 $\mathrm{kt_{CO2}/y}$. Commissioning is planned for 2025.

After Brevik, the Edmonton CCUS project represents the most advanced development in carbon capture within the cement industry, aiming to avoid 1 $\mathrm{Mt_{CO2}/y}$ [57]. This project involves retrofitting a post-combustion amine capture system and a combined heat and power plant into a cement production facility operated by Heidelberg Materials in Canada. The combined heat and power plant is crucial to the project's economic viability. The final investment decision is anticipated by early 2025.

The project CalCC, which started in 2023, aims to construct the first CO_2 capture facility at a commercial lime plant [58]. The Lhoist Group's Réty lime plant in France will be retrofitted with a Cryocap FG unit, from Air Liquide. The Cryocap technology captures CO_2 at very high purity using cryogenic temperatures. The captured CO_2 will be transported via an 80-km pipeline, shared with other industrial streams, to the Port of Dunkirk. The CO_2 will then be liquefied and shipped to a location in the North Sea for permanent geological storage.

Integrated industrial separation technologies use indirect heating or electrification to capture CO_2 from hard-to-abate industries. One promising integrated technology to decarbonize the lime industry is the direct separation of the LEILAC project (low emissions intensity lime and cement), which uses an indirectly heated vertical tube for the calcination [59]. This technology has been demonstrated at a scale of 240 t/d of raw meal, separating 85 t/d of CO_2. A scale-up of this technology will take place within the LEILAC-2 project, aiming to capture 100 kt of CO_2 per year [60]. Direct separation enables the capture of all process emissions at a low cost [61], but it cannot separate the CO_2 produced by combustion. The fully integrated indirectly heated carbonate looping process [62], which is analyzed in this dissertation, is another example of integrated industrial separation.

Carbonate looping technology

One of the most promising CO_2 capture technologies for lime and cement plants is the *carbonate looping* (CaL) process [63], which operates based on the reversible carbonation-calcination reaction of CaO [64,65]. CO_2 is captured through the carbonation of CaO in a *carbonator* operating at ca. 650 °C—see Eq. (1). Since the carbonation is an exothermic reaction, the reactor needs to be cooled and the reaction heat can be recovered, e.g., in a steam cycle.

$$\mathrm{CaO\,(s)} + \mathrm{CO_2\,(g)} \rightarrow \mathrm{CaCO_3\,(s)};\ \ \Delta H_{298\mathrm{K}} = -180\ \mathrm{kJ/mol} \tag{1}$$

The sorbent is regenerated through calcination in a *calciner* operating at higher temperatures (ca. 900 °C)—see Eq. (2). Heat needs to be provided to the calciner because of the endothermic nature of the reaction.

$$\mathrm{CaCO_3\,(s)} \rightarrow \mathrm{CaO\,(s)} + \mathrm{CO_2\,(g)};\ \ \Delta H_{298\mathrm{K}} = +180\ \mathrm{kJ/mol} \tag{2}$$

Due to the different reactor temperatures, the equilibrium CO_2 partial pressure ($p_{\mathrm{CO2,eq}}$) changes, enabling carbonation in the carbonator, and calcination in the calciner. Figure 2 illustrates the variation of $p_{\mathrm{CO2,eq}}$ with the operating temperature (T), highlighting the regions corresponding to carbonation (lower T) and calcination (higher T). For operating conditions relevant to the CaL process, $p_{\mathrm{CO2,eq}}$ is generally calculated with Eq. (3), which was obtained by García-Labiano et al. [66] based on thermodynamical data from Barin [67]. This correlation agrees remarkably well with those reported in previous empirical studies [68].

$$p_{\mathrm{CO2,eq}} = 4.137\,10^{12}\ \exp\frac{-20474}{T+273.15} \qquad [\mathrm{Pa}] \tag{3}$$

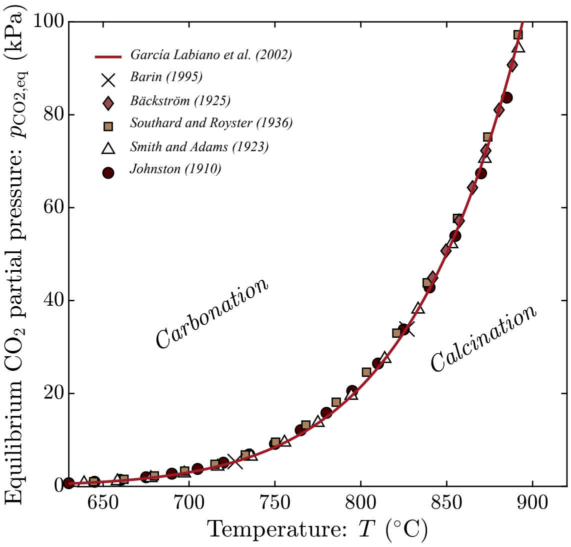

Figure 2. Equilibrium CO_2 partial pressure for carbonation-calcination calculated using the correlation from García Labiano et al. [66]. Results from historical correlations [68] derived from empirical data are plotted with markers only for their range of validity. Values calculated using thermodynamical data from Barin (1995) [67] are indicated with a cross (×). Adapted from RP VI.

On account of its high operating temperatures, the CaL process allows for various efficient heat integration strategies, including power generation through heat recovery. Additionally, the raw materials used in cement and lime production can function as sorbents in the CaL process, while spent sorbents can be recycled as feedstocks for lime and cement plants. These advantages significantly enhance the energy utilization of the process, enabling efficient CO_2 capture without incurring high costs [69,70].

Figure 3 illustrates the CaL process schematically. The solid sorbent, lime (mainly CaO), circulates between the carbonator and the calciner, both operating as fluidized bed reactors [71–73]. Concepts involving entrained flow reactors have also been proposed [74,75]. In the carbonator, CO_2 from off- gas reacts with the sorbent to form $CaCO_3$—see Eq.(1). The carbonated sorbent is regenerated in the calciner and CO_2 is released in a high purity stream—see Eq. (2). In the standard configuration, the heat for the calcination is provided via oxy-fuel combustion, directly in the calciner, using pure oxygen and fuel (see [76]). A fraction of the captured CO_2 is recirculated back into the calciner to achieve optimal fluidization velocities and control the reactor temperature. The sorbent's capacity to capture CO_2 declines rapidly during the initial calcination-carbonation cycles [77], due to loss of porosity caused by sintering [78]. To sustain sorbent activity at acceptable levels, fresh limestone (make-up) is introduced into the system, while spent material is removed (purge).

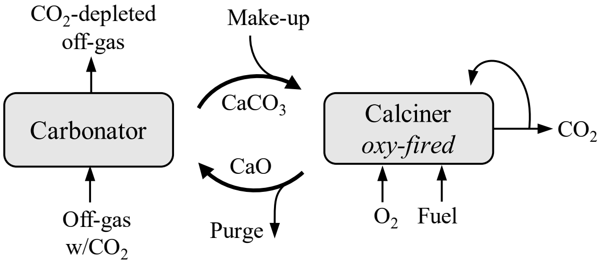

Figure 3. Scheme of the oxy-fired carbonate looping (CaL) process.

One significant drawback of standard CaL technology is the requirement of pure oxygen, which is obtained with an energy-intensive air separation unit (ASU). The installation of an ASU entails significant investment. De Lena et al. [69] calculated that the ASU accounts for around 15 % of the total plant cost for an integrated CaL system for CO_2 capture from a cement plant. A similar result was obtained by Fu et al. [79] for the implementation of the CaL process in natural gas combined cycle plants. Additionally, the electric power required to operate the ASU can exceed 40 % of the total electricity demand of the CaL system, including compression and purification [69,80].

For power plants, the CaL process has the potential to achieve high CO_2 capture rates with low energy penalties. Lasheras et al. [81] estimated that a full-scale power plant could be retrofitted with CaL to capture 88 % of the total CO_2 formed, with an energy penalty of less than 2.9 %. Astolfi et al. [82] calculated that a specific primary energy consumption for CO_2 avoided (*SPECCA*) of 2.2 $MJ_{LHV}/kg_{CO2,av}$ could be achieved by the integration of the CaL process into power plants with thermochemical energy storage, and Haaf et al. [80] estimated a *SPECCA* of 5.7 $MJ_{LHV}/kg_{CO2,av}$ for the integration into waste-to-energy plants. De Lena et al. [69] investigated the application of different CaL configurations in the cement industry. They reported *SPECCA* values between 2.8–3.0 $MJ_{LHV}/kg_{CO2,av}$ for systems utilizing pure limestone as sorbent, and between 3.5–4.6 $MJ_{LHV}/kg_{CO2,av}$ for systems that utilize cement raw meal.

Santos and Hanak [83] reviewed the available techno-economic analysis studies on carbon capture for industrial processes of the last ten years. They concluded that CaL is superior to other CO_2 capture technologies for this kind of application. According to their estimations, CaL technology has average CO_2 avoidance costs of 33 to 43 €/$t_{CO2,av}$ and an equivalent energy requirement between 2.0 and 3.7 $MJ_{th}/kg_{CO2,av}$. De Lena et al. [84] analyzed carbonate looping technology for cement plants and obtained slightly higher costs (52–59 €/$t_{CO2,av}$) for their scenarios. Romano et al. [85] presented an integrated concept for cement production and power generation that would be profitable even for low carbon taxes, starting at 27 €/t_{CO2}.

CaL technology has been demonstrated up to the pilot scale for manifold operating conditions [86], including firing with waste-derived fuels [87]. CO_2 capture rates higher than 99 % in CaL operations have been reported [88]. Since the beginning of the last decade, extensive experimental work has been conducted in semi-industrial facilities [86]. The oxy-fired CaL process has been demonstrated in many pilot tests. The major test facilities are located in Stuttgart (200 kW_{th}) [89–91] and Darmstadt (1 MW_{th}) [92,93], Germany; La Pereda, Spain [94,95]; and Heping, Taiwan

(1.9 MW_{th}) [96]. Firing various types of fuels in a CaL calciner was successfully demonstrated, including hard coal and lignite [97], solid recovered fuels [98], and biomass pellets [88]. Recently, Magli et al. [99] achieved over 90 % capture efficiency at a pilot facility built *in situ* at a cement plant in Vernasca, Italy, which features a 105-meter entrained-flow carbonator [100].

The indirectly heated carbonate looping process

The efficiency penalty of the CaL process can be further reduced by eliminating the need for oxygen in the calciner [101]. This can be achieved by using steam [102–104] or solar energy [105,106] for sorbent regeneration, or by electrifying the calciner, employing plasma burners, electrical resistance, or induction [107–109]. Another alternative is to indirectly heat the calciner by combustion of fuels in an external *combustor*. This promising approach is known as the *indirectly heated carbonate looping* (IHCaL) process (see Figure 4). Heat can be transferred into the calciner by means of metallic walls [59,110], by solids circulation [111,112], or via heat pipes [101,113]. Heat pipes offer an excellent heat transfer performance based on evaporation and condensation of a liquid, i.e., sodium for temperatures > 800 °C, inside a closed pipe [114].

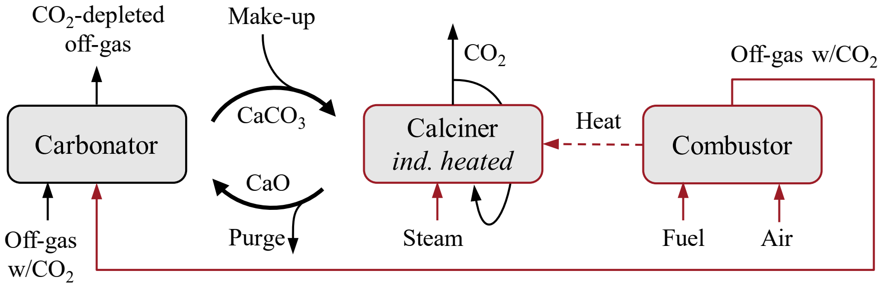

Figure 4. Scheme of the indirectly heated carbonate looping process (IHCaL). Differences with the CaL process are highlighted with red borders.

Figure 4 illustrates the IHCaL process with heat pipes. The operating principle is analogous to that of the oxy-fired CaL process (see Figure 3), with solid sorbent (CaO) circulating between a carbonator and a calciner to separate CO_2 into a high-purity stream. Heat from an external combustor is transferred to the calciner via heat pipes. For the fluidization of the calciner, steam, recirculated CO_2, or a mixture of both may be used (cf. [115]). The flue gas from the external combustor is directed to the carbonator, where most of the CO_2 is captured by carbonation. To ensure efficient heat transfer, the calciner and the combustor operate as bubbling bed reactors, with heat pipes immersed in the fluidized beds.

The main advantages of the IHCaL process compared to the standard CaL process are summarized as follows [62,116]:

- No air separation unit is needed to produce pure oxygen, which leads to lower investment costs and lower energy consumption.
- Fewer impurities (sulfur, ash) from a supplementary firing are brought into the Ca-loop, so that spent sorbent will be of higher purity and therefore be better suited for further utilization.
- Lower CaO deactivation rates are expected due to “mild” calcination around the heat pipe surfaces compared to rather harsh conditions in an oxy-fired calciner so that sorbent remains more reactive.
- Lower attrition rates are expected due to a low fluidization velocity in the calciner, which improves the operability of the fluidized bed system.
- An almost pure CO_2 stream leaves the calciner, which allows for technically easy and cost-effective CO_2 purification for storage/utilization of CO_2.

The IHCaL concept using heat pipes has previously been evaluated for CO_2 capture from coal-fired power plants [114]. CO_2 avoidance costs have been calculated at 23 €/t_{CO2} [116], excluding

CO_2 transport and storage. Until the start of the work leading to this dissertation, the IHCaL process had only been considered for power plant applications [114,116] but not for lime or cement plants. The CaL and the IHCaL processes can be integrated into the lime industry using waste-derived fuels or biomass, thus enabling negative CO_2 emissions (CDR) through bioenergy with carbon capture and storage (BECCS) (e.g., [117]).

Pilot testing of the IHCaL process

To date, the only pilot tests of the IHCaL process using a heat-pipes heat exchanger [114] were performed in a 300-kW_{th} pilot facility at the Technical University of Darmstadt, Germany [118]. This pilot facility, commissioned in 2015, is illustrated in Figure 5. It is composed of three reactors: a carbonator for CO_2 capture, a calciner for sorbent regeneration, and a combustor for heat generation. The carbonator is an eight-meter-high circulating fluidized bed (CFB) with an internal diameter of 250 mm. It is fluidized using a synthetic flue gas composed of air, CO_2, SO_2, and H_2O. The calciner is a bubbling bed (BFB) fluidized with air, featuring a mean particle residence time of ca. 20 min. The height of the bed is determined by the solid outlet, which is located 1.9 m from the bottom of the reactor. The external combustor is a BFB operating with sand. Heat is transferred from the combustor into the calciner via 72 heat pipes. A *cone valve* is located downstream of the carbonator to control the sorbent circulation rate. Solid sorbent can be extracted discontinuously from the cone-valve arrangement for sampling. A detailed explanation of the experimental setup can be found in previous publications [119–122]. Recently, this plant has been expanded with a gas tract to feed the combustor's flue gas into the carbonator and capture its CO_2 [121].

Several test campaigns have been conducted at this pilot facility, totaling ca. 700 hours of operation [123]. The tests included operating conditions relevant to power plants [120], and lime and cement plants [119]. Recently, Hofmann et al. [121] operated the IHCaL facility by co-firing propane with both dried lignite and refuse-derived fuel.

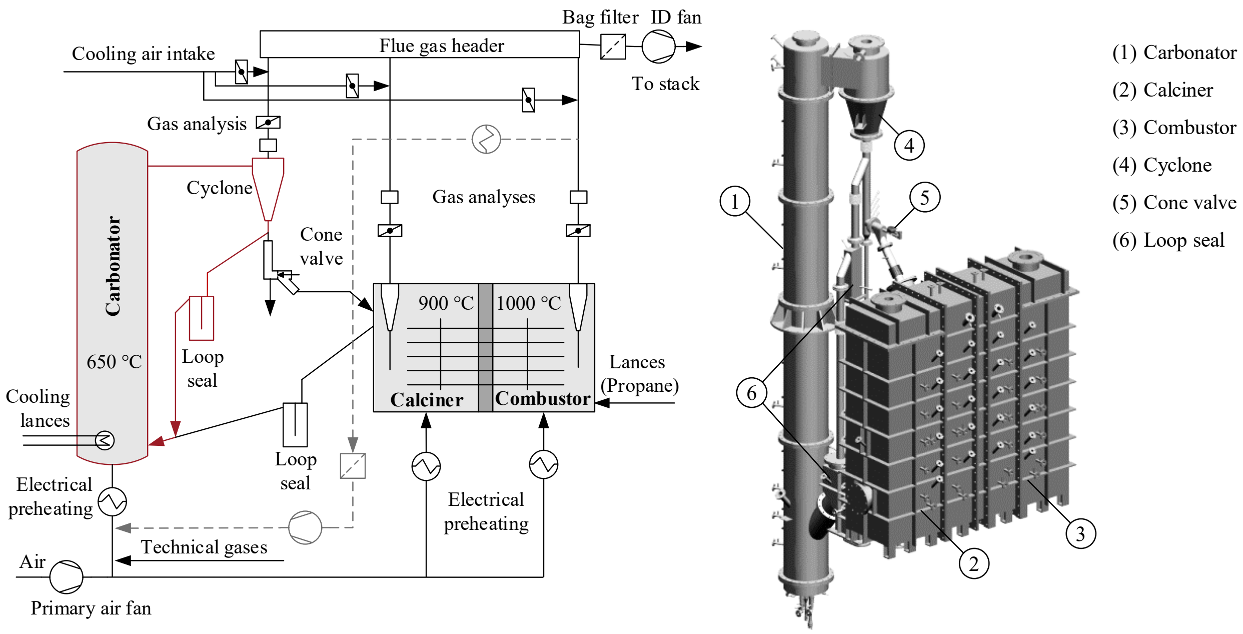
Bag filter
ID fan
Cooling air intake
Flue gas header
To stack
Gas analysis
Cyclone
Gas analyses
Carbonator
Cone valve
900 °C
1000 °C
650 °C
Loop seal
Lances (Propane)
Calciner
Combustor
Cooling lances
Loop seal
Electrical preheating
Electrical preheating
Technical gases
Air
Primary air fan
1
2
3
4
5
6
(1) Carbonator
(2) Calciner
(3) Combustor
(4) Cyclone
(5) Cone valve
(6) Loop seal

Figure 5. Pilot plant at the Technical University of Darmstadt for testing the indirectly heated carbonate looping (IHCaL) process at the 300-kW_{th} scale. The left subfigure is a process flow diagram adapted from RP IV. The main reactors are shaded in gray. The new flue-gas tract commissioned in 2022 are indicated with light-gray broken lines. The carbonator with its internal circulation is indicated with red borders. The figure on the right is a render of the CAD model illustrating the reactors and the components for solid circulation (adapted from [120]).

1.2 State of the art

Until the start of this dissertation, experimental efforts to develop IHCaL technology have been unparalleled by modeling work. However, alongside reliable empirical results from semi-industrial facilities, accurate models are essential for interpreting experiments and scaling up IHCaL technology for commercial application. This section reviews the current state of IHCaL development for lime plants, focusing on the aspects most relevant to this dissertation: process integration and modeling. Based on the limitations of previous studies, we identify the key research needs that led to the research questions outlined in Section 1.3.

Integration of IHCaL technology in the lime production

There are many potential synergies between the IHCaL process and the production of lime and cement. Cement raw meal and limestone, the primary materials in cement and lime production, can serve as sorbents for the IHCaL process, and spent sorbents can be repurposed as raw materials to produce cement and lime. Additionally, the heat and electrical energy demands of cement and lime plants offer opportunities for heat recovery. Moreover, the common practice of using waste-derived fuels in the cement industry, when combined with IHCaL technology, can enable net-negative CO_2 emissions.

Given the large quantity of CO_2 emissions associated with the lime and cement production (see Section 1.1), large-scale capture plants are necessary. This scale is attractive for IHCaL technology, which is CAPEX-driven and therefore benefits considerably from economies of scale. The CO_2 concentration in off-gases from lime plants is generally higher than the CO_2 concentration in flue gases from power plants, which affects the process by influencing reactor performance and energy requirements.

Despite the high potential of IHCaL technology for capturing CO_2 in the lime and cement industries, no integration concepts had been developed prior to this cumulative dissertation. Integrating the IHCaL process into cement and lime production plants was one of the goals of the ACT ANICA Project [124]. Integrating it into cement production was carried out by a project partner (cf. [125]), while we focused on the integration into lime production, a primary topic of this dissertation. Many of the methods developed and conclusions drawn from our study on lime plants may also be applicable to integrating the IHCaL process into cement plants.

Modeling of the IHCaL process

Accurate reactor models are essential for assessing sorbent performance, interpreting experimental findings, designing optimized reactors, and safely scaling up IHCaL and CaL technology for commercial applications [126]. Carbonator and calciner models include considerations on reactor behavior (reactor sub-model), as well as sorbent kinetics and deactivation (particle sub-model). Complete process simulations are commonly performed using Aspen Plus [127] (e.g., [81,128]). Some of the reactor models can be integrated into Aspen Plus process models using customized FORTRAN routines (e.g., [81]), which considerably enhances the reliability of the process simulations. The steam cycles may be modeled with EBSILON professional [129] (e.g., [130]).

Carbonator reactor sub-models are abundant in the literature [126]. Most of them simulate circulating fluidized bed carbonators, which are the most established reactor type for the CaL and IHCaL processes. Some models assume continuous stirred-tank reactor (CSTR) operation [73,131,132]. They have the advantage of being easy to calculate but do not account for the influence of reactor hydrodynamics on the capture process, which leads to high uncertainties (cf. [133]). Other models are based on three-dimensional CFD simulations [134–136], which can predict empirical data well, but require considerable computational resources, which makes them impractical for many applications, especially modeling of big reactors. One useful modeling approach is the so-called *Kunii and Levenspiel* (KL) reactor model for fluidized beds [137], which considers two phases (gas and solid) for the simulations and uses semi-empirical equations to model the solids distribution and the gas-solid contact behavior [138]. KL models provide good results with less computational effort than three-dimensional CFD models [126] (cf. [134]). Therefore, they can be easily integrated into global models of CaL systems. There are many KL-type carbonator models in the literature. Lasheras et al. [81] developed a model based on semi-empirical equations from Kunii and Levenspiel [139] and particle models from previous works [72,140]. They assumed that the sorbent entering the carbonator was fully calcined. Their model overpredicted empirical data for some operating conditions of the 1-MW$_{th}$ CaL pilot plant at the TU Darmstadt [93]. Romano [141] developed a carbonator model considering a particle *residence time distribution* (RTD) for the calculation of sorbent deactivation and carbonation reaction rates. Although his results presented reasonable agreement with experimental data, he reported a systematic overestimation of the capture efficiency. Ylätalo et al. [142] used a one-dimensional model to evaluate the performance of a carbonator, considering an axial temperature gradient across the height of the reactor. The results they obtained were consistent with experimental results from a CaL laboratory test rig (30 kW$_{th}$) during steady-state operation. Their model relied on a *back-flow ratio*, which was not disclosed. It is uncertain whether their accurate predictions are based on a fitting process specific to the laboratory operating conditions. Recently, Tizfahm et al. [143] developed a model that considers reaction kinetics and reactor hydrodynamics. However, they only validated the kinetic sub-model with experimental data, not the KL reactor model. Most KL carbonator models lack a comprehensive discussion of their methodology. Furthermore, new models often build upon old ones without scrutinizing underlying assumptions. For instance, solids distribution profiles are usually adopted from previous works without analyzing the fluidization regimes for which they are valid. Something similar occurs with the constants for the calculation of core-wall gas interchange and the equations to obtain the reactor gas-particle contact efficiencies.

There are still issues that need to be investigated to enable the commercialization of CaL and IHCaL. One of the unanswered questions is how fluidization regimes influence carbonator behavior. Charitos et al. [73] compared two CaL test rigs and reported high CO_2 capture rates for facilities operating in different fluidization regimes. However, they pointed out that the reactors operating in the turbulent fluidization regime presented better gas-solid contact. Recently, Diego and Arias [144] reported experimental results from a 1.7-MW$_{th}$ CaL pilot facility showing that the carbonator performance was better for lower gas velocities. Still, there has been no investigation of the fluidization regimes of CaL carbonators using appropriate explanatory models.

Carbonator particle sub-models are essential for linking sorbent kinetics and carrying capacity to reactor behavior, which are heavily influenced by sorbent make-up and circulation rates. These factors play a critical role in determining capture efficiency, as widely recognized in the literature [126,145,146]. However, experimental and modeling results often exhibit contradictions across different studies. Furthermore, previous assumptions are generally incorporated into new models without critically assessing the studies on which they are based. This issue is not consistently addressed when incorporating particle sub-models into carbonator models.

Considering the interconnectedness of the carbonator and the calciner is essential for developing a comprehensive CaL model. High calcination temperatures should be avoided to prevent damage to the heat pipes and minimize energy penalties. Conversely, excessively low temperatures can result in poor calciner performance, thereby compromising CO_2 capture efficiency. Therefore, a precise model of the calciner's influence on carbonator operation is crucial.

Numerous studies have identified difficulties in attaining high calciner performance. Rodríguez et al. [147] highlighted low calcination efficiency as a potential cause of reduced carbonator performance in a 30-kW$_{th}$ CaL test facility. Haaf et al. [98] reported a reduction in calciner efficiency associated with low calcination temperatures in a 1-MW$_{th}$ CaL pilot plant using waste-derived fuels and oxygen to fire the calciner. Reitz et al. [120] disclosed difficulties in achieving high calcination efficiencies in a 300-kW$_{th}$ indirectly heated test rig. Recently, Hofmann [148] identified poor calcination performance as a critical factor contributing to low capture efficiency in the IHCaL plant at the TU Darmstadt. Despite reported challenges in achieving high calcination efficiency across various operating conditions, the impact of calcination degree on carbonator performance is still not fully understood.

Rodríguez et al. [149] used a simplified CaL process model to explain that lower calcination efficiencies affect carbonator performance by reducing the amount of CaO available for CO_2 capture. Martínez et al. [128] integrated Rodríguez et al.'s model into a CaL process model in AspenHysys and adjusted operating conditions to achieve 95 % calcination efficiency. The deviation from ideal calcination resulted in a slight improvement in sorbent activity, which seems to contradict the system behavior observed during pilot tests. Atsonios et al. [134] investigated the influence of calcination efficiency on the carbonator under a specific set of operating conditions. For this, they used a CFD model coupled with an Aspen Plus routine. They observed a significant decline in the CO_2 capture rate when the $CaCO_3$ content upstream from the carbonator exceeded 4 mol%. However, they did not discuss how varying the operating parameters, such as the sorbent circulation rate, affects the carbonator's sensitivity to calciner performance.

Sorbent deactivation increases the required make-up and circulation rates, which affects fuel requirements and component dimensions [77,150,151]. Sorbent activity decreases rapidly throughout the first calcination-carbonation cycles and stabilizes slowly towards a residual value that is normally smaller than 0.1. The cause of the deactivation is thought to be the sintering of the sorbents and the associated loss of porosity, which is enhanced by higher calcination temperatures [77,78,152–155]. Consequently, it is advantageous to operate the calciner at low temperatures (< 900 °C), which may affect the calcination efficiency. The overwhelming majority of sorbent deactivation models applied to CaL rely on the assumption of stable operation over long periods of time (e.g., [149]). However, this is usually not the case in pilot plant operation, which poses challenges for the application and validation of these models.

Calciner models for CaL are scarce in the open literature, in contrast to the numerous studies on carbonator modeling [126]. Ylätalo et al. [156] studied a 1.7-MW_{th} oxy-fired pilot calciner. They used a steady-state, three-dimensional (3-D) calciner model and a steady-state, one-dimensional (1-D) process model. Their 3-D model solves the fundamental balance equations of fluidized bed operation using the control volume method. They also included semi-empirical equations to describe solid entrainment, chemical reactions, and heat transfer, thus reducing computational effort. Both the 1-D and 3-D approaches yielded similar results. However, they did not validate their models with experimental data. Kanellis et al. [157,158] developed two 3-D CFD models capable of predicting empirical results from a single operating point of the IHCaL pilot plant at the TU Darmstadt [120], namely the pressure profile, the CO_2 concentration at the calciner exit, and the CO_2 production rate. They used two different modeling strategies, obtaining similar results: their first model uses an Eulerian-Eulerian approach (Two Fluid Model [159], TFM), and their second model uses an Eulerian-Lagrangian framework (Dense Discrete Phase Model [160], DDPM). In both models, the drag coefficient is calculated with a sub-grid energy minimization multiscale (EMMS) scheme, and the calcination kinetics are described with the Changing Grain Size Model (CGSM) developed by García-Labiano et al. [66]. Höftberger et al. [114] modeled the heat transfer with heat pipes in a bench test rig using semi-empirical equations for heat transfer between fluidized beds and immersed heating surfaces [161]. Martínez et al. [162] developed a simple calciner model using a basic description of the fluid dynamics and a grain model for the calcination [163]. While useful for preliminary calculations, it does not account for the effect of CO_2 concentration gradients in the calciner. A recent study [148] concluded that this model does not accurately predict the performance of the calciner at the IHCaL pilot plant at the TU Darmstadt.

Despite commendable efforts in calciner modeling, the available numerical studies are not sufficiently supported by empirical data from relevant pilot tests. Moreover, existing detailed models are often too complex, allowing for the computation of only a limited number of operating points within a reasonable timeframe. Poor calciner performance limits CO_2 removal efficiency by reducing the sorbent’s capacity to capture CO_2 [149,164]. The commercialization of carbonate looping technology requires simple yet precise design guidelines for calciners, which still need to be developed.

1.3 Research questions

From the discussion above, the indirectly heated carbonate looping process (IHCaL) appears to have significant potential for reducing CO_2 emissions in the lime industry. However, this potential has not yet been fully assessed. Furthermore, it remains uncertain how process integration, fuel selection, operating parameters, and reactor configurations should be designed to maximize efficiency and reduce capture costs. In summary, the following overarching research question needs to be answered:

> *What is the potential of indirectly heated carbonate looping technology for reducing CO_2 emissions in the lime industry, and how can the process configurations, fuel properties, operating parameters, and components be optimized to fully exploit this potential?*

The overarching research question has been broken down into seven sub-questions. Below, we introduce each research sub-question by a description of the research gap. In Section 1.4, we explain how each sub-question is addressed within this dissertation.

Until now, no concepts have been proposed to exploit the potential synergies in capturing CO_2 from lime plants using the IHCaL process. Previous studies [101,114] analyzed the energy requirements for IHCaL plants. However, these studies are not specific for lime applications, thus excluding energetic advantages that can be achieved through efficient integration. Furthermore, a deeper understanding of the impact of operating parameters on the energy requirements of the IHCaL process is needed for assessing viability and improving the energy efficiency of integrated configurations. This leads to the following research sub-question:

> *(i) What are the key integration parameters influencing heat requirements and energy efficiency in lime plants with CO_2 capture using IHCaL technology?*

The European lime producers strive to achieve net-negative CO_2 emissions by 2050 [14]. The IHCaL process may play an important role in attaining this objective by enabling net-negative CO_2 emissions in lime plants through BECCS. This leads to the following research sub-question:

> *(ii) What is the potential for achieving net-negative CO_2 emissions using IHCaL technology in the lime production, and how can this potential be exploited?*

The IHCaL combustor is a bubbling fluidized bed compatible with different fuel options, such as dried lignite and waste-derived fuels [121]. On top of the advantages in terms of costs, waste-derived fuels have a fraction of biogenic carbon, which can be captured to permanently remove CO_2 through BECCS. However, the properties of these fuels such as lower heating value and moisture content are different to those of dried lignite. This leads to the following research sub-question:

> *(iii) How do fuel type and properties influence the economic and energy performance of the integrated IHCaL process in the lime production?*

Economic competitiveness is crucial for the viability of CO_2 capture processes, which are responsible for the largest costs of the entire CCS value chain [27,28]. Previous studies have reported significantly low costs associated with the IHCaL processes [116,165]. However, no economic results are available for the IHCaL process integrated into lime production or any other industrial process. This leads to the following research sub-question:

> *(iv) What is the cost-reduction potential of the IHCaL process for CO_2 capture from the lime production?*

Experimental results from IHCaL and CaL operation indicate that the carbonator flow regime has a significant impact on performance [144]. Furthermore, it is well known that reactor model predictions heavily depend on the accurate description of gas-solid contacting patterns [133]. However, most studies on carbonator modeling rely on previous models without discussing fluidization regimes or validating assumptions with empirical data. This leads to the following research sub-question:

(v) *What is the influence of carbonator hydrodynamics on the CO_2 capture efficiency of an IHCaL system?*

A recent study reported that poor calciner performance reduces the carbonator efficiency in an IHCaL pilot plant [148]. However, there is currently insufficient understanding of the interconnectedness between carbonator and calcination performance. Additionally, existing sorbent deactivation models are limited to constant make-up and circulation rates, which do not correspond to pilot operating conditions [122]. This leads to the following research sub-question:

(vi) *How do operating parameters and calciner performance affect sorbent activity in an IHCaL system, and how does sorbent activity, in turn, impact the overall performance of the process?*

Previous studies have reported poor calciner performance in IHCaL pilot tests but were unable to explain the underlying causes [120,121]. Furthermore, previous calciner models are either too computationally intensive or fail to predict empirical data [148]. This leads to the following research sub-question:

(vii) *How can the operating conditions of an IHCaL calciner be optimized to reduce the energy penalty of the process without compromising CO_2 capture efficiency?*

1.4 Approach of the dissertation

In this section, we present the approach of this dissertation to answering the research questions and advancing IHCaL technology for commercial application in lime production. First, we explain the contributions of this dissertation to the development of IHCaL processes for lime plants and their interrelation with previous and future research tasks. To do so, we contextualize our work within the entire design process required to bring IHCaL technology for lime plants to commercial maturity. Second, we explain the approaches and contributions of each research papers in addressing the research questions.

Contributions to the engineering design process

This section outlines the design process required to commercialize IHCaL technology for lime plants, following the structure proposed by Towler and Sinnott [166]. This structure has been adapted to account for the research-driven nature of the design process, as there is no prior experience with developing and constructing full-scale plants using the same technology (cf. [167]). Figure 6 illustrates the design process for integrating IHCaL technology in lime plants, from the determination of the customer needs to the beginning of operations in a first-of-a-kind commercial plant. The arrows using broken lines indicate future activities that are necessary to achieve commercialization. The steps of the design process addressed in this dissertation, highlighted with background shading in Figure 6, are generating design concepts, building performance models, predicting fitness for service, conducting economic evaluations, and performing optimization. The overarching tasks associated with these steps, as well as the scope of each research paper, are explained in the following section.

The design problem and research questions of this dissertation are part of the ACT ANICA project [125] (ACT Project no. 299653), which was conducted between October 2019 and September 2023. The ACT ANICA project received funding through the ACT program (Accelerating CCS Technologies, Horizon 2020 Project no. 691712) and financial contributions were made by the German Federal Ministry for Economic Affairs and Climate Action (BMWK Project no. 03EE5025). The scope of this project within the design process is indicated with a rectangle on the background in Figure 6. In this dissertation, we focus on the integration of the IHCaL process in the lime production, especially on the aspects of process development, assessment, and modeling. More information on the scope and results of the ACT ANICA project, including the integration of the IHCaL process into cement plants can be found in the project final report [124].

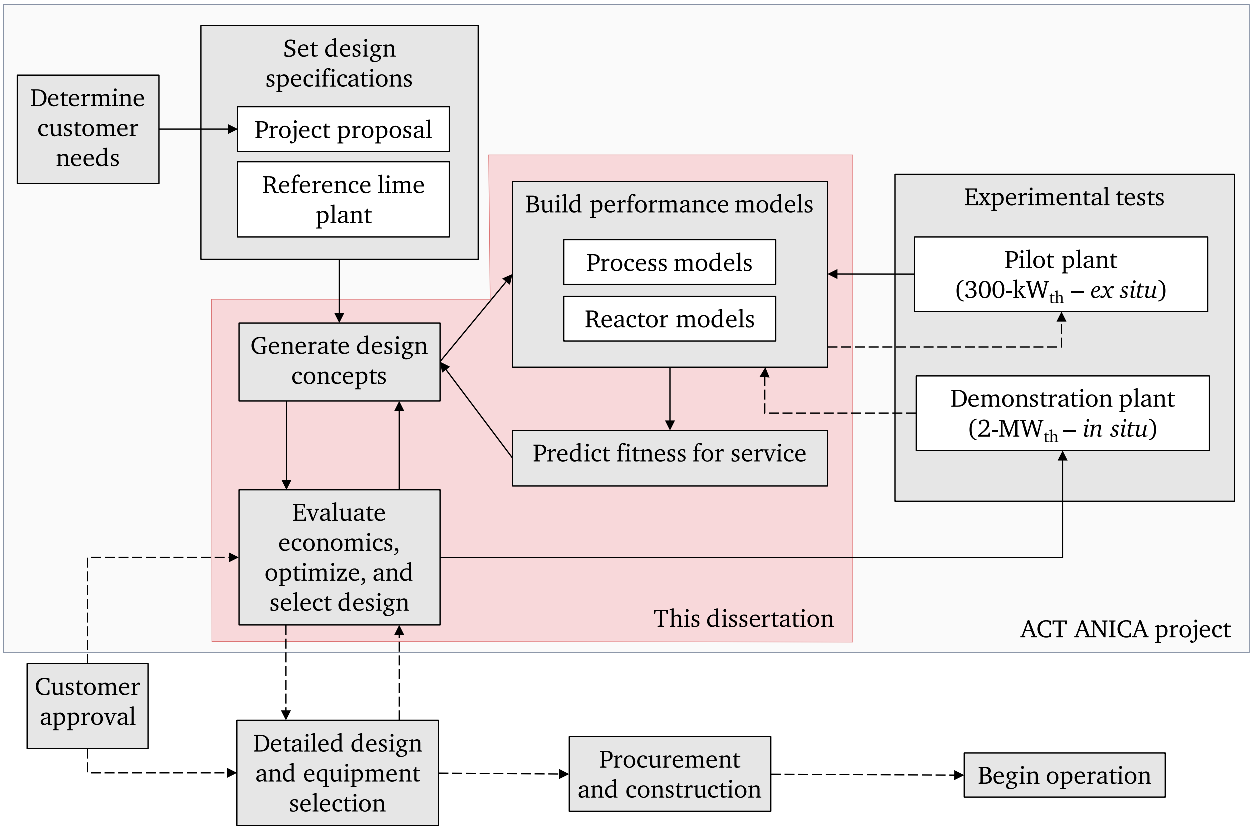
Determine customer needs
Set design specifications
Project proposal
Reference lime plant
Build performance models
Process models
Reactor models
Experimental tests
Pilot plant (300-kW$_{th}$ – *ex situ*)
Demonstration plant (2-MW$_{th}$ – *in situ*)
Generate design concepts
Predict fitness for service
Evaluate economics, optimize, and select design
This dissertation
ACT ANICA project
Customer approval
Detailed design and equipment selection
Procurement and construction
Begin operation

Figure 6. The design process in chemical engineering, adapted from Towler and Sinnot [166] to the design of the IHCaL process for CO_2 capture in lime plants. Arrows using broken lines indicate future activities toward commercialization. Background shading highlights the scopes of this dissertation and the ACT ANICA project.

Every design process in engineering starts with the identification of the customer needs and the design specifications. In commercial processes, the customers may be internal (e.g., production department of the same company), or external (e.g., for contractors or consultants). In our work, the customer needs are the requirements of lime producers—and, more broadly, society—for cost-efficient solutions to the problem of CO_2 emissions in the lime industry, explained in Section 1.1. The overall specifications for the CO_2 capture plants using IHCaL technology were established in the proposal of the scientific research project [124]. These can be summarized as follows:

- Achieving CO_2 capture efficiency higher than 90 %
- Separating CO_2 into a high purity stream with a concentration higher than 95 %
- Enabling net-negative CO_2 emissions by utilizing waste-derived fuels
- Recovering heat in the IHCaL facility with net electrical efficiencies higher than 45 %
- Decreasing CO_2 capture costs below 25 €/t_{CO2}

Apart from these specifications, it was necessary to select a reference lime plant for the integration of the IHCaL proceses. This was one of the first tasks of the ACT ANICA project, which was performed in collaboration with Lhoist Germany Rheinkalk GmbH (Lhoist). The selected lime plant is a German facility operated by this company. It is located in Hönnetal and features a preheated rotary kiln (PRK) calciner that produces over 600 tonnes of lime per day. This plant was considered as the reference for the process development, as the host plant for the design of an *in-situ* demonstration plant, and as the candidate for a first-of-a-kind commercial IHCaL facility.

Generating design concepts was an extensive task within the research project. Different extraction points from the off gas of the PRK were considered and the most suitable was selected, as explained in RP I. Two integration strategies were developed (see Section 2.1), process flow diagrams were generated, and a patent was filed in collaboration with Lhoist [168]. Furthermore, different fuel strategies were proposed (see RP II) and heat recovery steam cycles were designed to generate electrical power from waste heat (see RP III).

We developed performance models with commercial software, which were used to simulate the different designs (see Section 2.1). The process simulations considered the host lime plant, the IHCaL processes, the steam cycles, and the compression train. The simulations of the host plant were validated using operational data provided by Lhoist. Furthermore, advanced one-dimensional reactor models were developed based on empirical data from thermogravimetric analysis (TGA) and pilot tests at the 300-kW_{th} IHCaL plant (see Section 2.2).

The performance models were used to predict the compliance with the design specifications, optimize the concepts, and select appropriate designs. This step, which is closely related to answering the research questions, is broken down in the following section, considering the scope of each research paper. The developed designs allow achieving most of the objectives established by the research project, including high capture efficiency (see RP I and RP IV), net-negative CO_2 emissions (see RP II), and low CO_2 avoidance costs (see RP III). However, net electrical efficiencies higher than 45 % require steam cycle optimizations that are not justified by the economy of scale. Net electrical efficiencies close to 43 % give a good balance between energy utilization and investment costs (see RP III).

Within the ANICA ACT project, the 300-kW_{th} pilot plant at the TU Darmstadt [118] was upgraded and two pilot campaigns were performed. The results were published in a peer-reviewed publication that is not part of this dissertation [121]. A recent doctoral dissertation reported and discussed the plant upgrades and campaign results in detail [148].

For the development and validation of the models included in this dissertation, results from earlier pilot tests in the same pilot plant conducted in 2016 were used [120,122]. The reasons for using the 2016 test results were the significantly higher availability of sorbent samples and the better performance compared to the tests conducted in 2022. However, the 2022 pilot campaigns, conducted within the ANICA ACT project, presented performance issues that stimulated improvements in the reactor models (see Sections 2.2 and 2.3). As an example, Hofmann [148] observed low calciner efficiencies in these campaigns and reported that a previous calciner model [162] failed to predict empirical data from the pilot plant. This motivated the development of an improved calciner model to explain the performance issues observed during the pilot tests. For future tests campaigns at the IHCaL pilot plant, our models should be used to optimize the operating conditions and achieve better performance.

The performance models were used to design a demonstration plant for *in-situ* CO_2 capture at the host lime plant in Hönnetal. The design was performed by thyssenkrupp Polysius GmbH with the collaboration of the Institute for Energy Systems and Technology (TU Darmstadt) [169]. This plant could be built as part of a follow-up research project. The results from the operation of the demonstration plant would be useful for refining the models. A subsequent upscaling (e.g., up to 20 MW_{th}) may be required before commercialization can be realized.

The developed concepts were assessed with the aid of the performance models. Apart from the results presented in this dissertation (see Section 2.1), the University of Ulster performed economic analysis and life cycle assessments (LCA), and Energy Technology Strategies Ltd executed a risk assessment with the assistance of the TU Darmstadt and Lhoist [125].

Figure 6 illustrates the future activities toward the commercialization of the IHCaL process in the lime production, indicated by broken-line arrows. Once a sufficient technology readiness is achieved— e.g., after successfully finalizing a follow-up project—the customer approval is required to proceed with the detailed design and construction of a full-scale IHCaL plant. In this case, the potential customers are the lime producers seeking to reduce the CO_2 emissions of their lime plants. Additionally, public institutions may support the deployment of IHCaL technology by granting funding or tax exemptions. After customer approval, the detailed plant design, equipment selection, and assessment in the form of a front-end engineering design (FEED) should be completed before a final decision of investment can be made, allowing the project to advance to procurement and construction. The final step is commissioning the plant to initiate commercial operation.

Addressing the research questions

In this section, we explain the approach of this dissertation to addressing the research questions from Section 1.3 and clarify the scope and contributions of each research paper (RP). Considering the complexity of the overarching research question—manifested in the numerous sub-questions—the work was divided into the following tasks, which were addressed by the six research papers constituting this dissertation: (i) process development, simulation, and assessment (Section 2.1); (ii) carbonator modeling and design (Section 2.2); and (iii) calciner modeling and design (Section 2.3).

The tasks performed within this cumulative dissertation are shown schematically in Figure 7. RP I–III address process development, simulation, and assessment. RP IV–V focus on carbonator modeling and design, while RP VI focuses on calciner modeling and design.

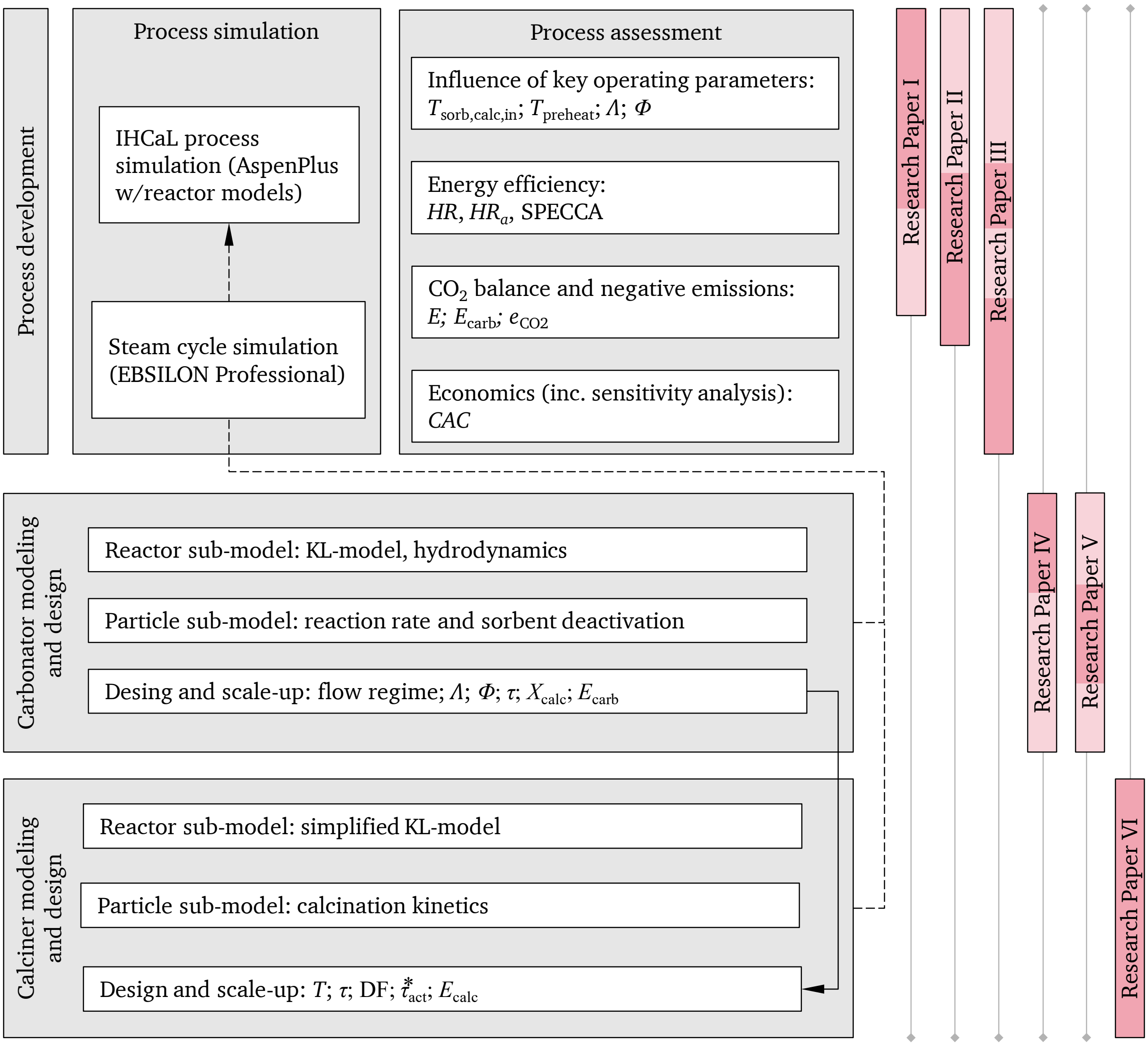
Process development
Process simulation
IHCaL process simulation (AspenPlus w/reactor models)
Steam cycle simulation (EBSILON Professional)
Process assessment
Influence of key operating parameters: $T_{\mathrm{sorb,calc,in}}$; T_{preheat}; Λ; Φ
Energy efficiency: HR, HR_a, SPECCA
CO_2 balance and negative emissions: E; E_{carb}; e_{CO2}
Economics (inc. sensitivity analysis): CAC
Carbonator modeling and design
Reactor sub-model: KL-model, hydrodynamics
Particle sub-model: reaction rate and sorbent deactivation
Desing and scale-up: flow regime; Λ; Φ; τ; X_{calc}; E_{carb}
Calciner modeling and design
Reactor sub-model: simplified KL-model
Particle sub-model: calcination kinetics
Design and scale-up: T; τ; DF; τ^*_{act}; E_{calc}
Research Paper I
Research Paper II
Research Paper III
Research Paper IV
Research Paper V
Research Paper VI

Figure 7. Scheme of this cumulative dissertation. The bars on the right illustrate the scope of each research paper, indicating the main tasks with a darker shading.

Process development consists in generating design concepts and evaluating them for fitness to capture CO_2 and comply with the design specifications. Two integration approaches were developed. One consists in a tail-end retrofitting concept. The other is a fully integrated new facility for lime production and CO_2 capture. The two concepts are explained in detail in RP I, fueling strategies are discussed mainly in RP II, and the design of the heat recovery steam cycle is addressed in RP III.

Process simulations were performed in RP I–III. The developed processes were simulated using Aspen Plus for the CO_2 capture process, including the reference lime plant, the capture island, and the compression train. The software EBSILON Professional was used to simulate the steam cycles. The IHCaL process simulations used reactor models from previous studies. The integration of the carbonator and calciner models developed within this dissertation should be performed in future studies to validate the conclusions and improve simulation results. This is indicated with a broken-line arrow in Figure 7.

Process assessment was performed based on the simulation results. The assessment considered four aspects: influence of key operating parameters, energy efficiency, CO_2 balance, and economics. Based on the assessment, the processes were improved and recalculated until the resulting configurations were suitable in terms of energy performance and CO_2 capture rate. The influence of key operating parameters was analyzed by performing a parametric study with the Aspen Plus process models in RP I. To assess energy efficiency, the following key performance indicators were calculated: the heat ratio (*HR*, Eq. (10)), the absolute heat ratio (HR_a, Eq. (9)), and the specific primary energy consumption per CO_2 avoided (*SPECCA*, Eq. (12)). The economic analysis was part of RP III. The main indicator of economic performance is the CO_2 avoidance cost (*CAC*, Eq.(16)). The analysis of the CO_2 emissions considered the emissions from fuel combustion, as well as the indirect emissions associated with electricity. The biogenic carbon content of the fuels was taken into account to assess the potential for achieving net-negative CO_2 emissions. The main performance indicators for the CO_2 balance were the overall capture efficiency (E), the carbonator efficiency (E_{carb}), and the equivalent specific CO_2 emissions (e_{CO2}). The overall capture efficiency is the molar ratio of captured CO_2 to the total CO_2. It is calculated using the following equation:

$$E = \frac{F_{\text{CO2,calc}}}{F_{\text{CO2,carb}} + F_{\text{CO2,calc}}} \tag{4}$$

Here, $F_{\text{CO2,carb}}$ and $F_{\text{CO2,calc}}$ are the molar flow rates of CO_2 leaving the carbonator and the calciner, respectively. The carbonator efficiency, E_{carb}, represents the CO_2 capture rate in the carbonator, which is obtained with Eq. (5), where F_{CO2} is the molar flow rate of CO_2 entering the carbonator. Corresponding to the project proposal, the efficiency target was $E > 90\ \%$ [124].

$$E_{\text{carb}} = 1 - \frac{F_{\text{CO2,carb}}}{F_{\text{CO2}}} \tag{5}$$

The calciner efficiency (E_{calc}) reflects the performance of the calciner [162]. It is defined as the ratio of moles of $CaCO_3$ calcined to the total moles of $CaCO_3$ introduced into the reactor—see Eq. (6). This important parameter must be considered in the design of calciners, as it affects the entire CaL systems, particularly the carbonator performance.

$$E_{\text{calc}} = \frac{\text{moles of CaCO}_3\text{ calcined}}{\text{moles of CaCO}_3\text{ introduced}} \tag{6}$$

Research sub-question (i) was addressed with the assessment of the influence of key operating conditions, which was the focus of RP I. The heat recovery strategies were investigated in RP III, obtaining complementary information regarding the influence of the steam cycle on the energy utilization of the IHCaL process.

To address *research sub-question (ii)*, integrated IHCaL configurations were assessed in RP II, considering different fuel options: dried lignite (benchmark), solid recovered fuel, refuse-derived fuel, and municipal solid waste. The results were analyzed in terms of CO_2 emissions and energy efficiency. The net-negative CO_2 emissions were quantified and broken down into categories (fossil, biogenic, indirect).

The impact of fuel type on energy performance indicators in the IHCaL process for lime production with CO_2 capture was investigated in RP II and RP III to address *research sub-question (iii)*. The economic implications of choosing solid recovered fuel over dried lignite in various integrated configurations were assessed in RP III. A sensitivity analysis was included to address the uncertainty and variability in fuel costs.

Research sub-question (iv) was addressed in RP III through techno-economic assessment of different IHCaL configurations for lime production. Various fuel types, as well as different steam cycle configurations, were considered. The CO_2 avoidance costs (*CAC*) were calculated for ten scenarios and compared with costs reported in the literature for other CO_2 capture processes.

Carbonator modeling and design were studied in RP IV and RP V. We developed an improved carbonator model consisting of a reactor sub-model and a particle sub-model. The reactor sub-model, developed as part of RP IV, accounts for the fluidization regime and enables the calculation of the solids concentration and CO_2 partial pressure along the carbonator. The particle sub-model includes considerations on reaction rate and sorbent deactivation. It has been developed within RP V. The carbonator model, including the reactor and particle sub-models, was validated with empirical data from thermogravimetric analysis (TGA) and pilot tests at the 300-kW_{th} scale [120]. The carbonator model was used to derive guidelines for simulating and designing carbonators. *Research sub-question (v)* is primarily addressed with the reactor sub-model in RP IV, while *research sub-question (vi)* is mostly addressed with the particle sub-model in RP V.

Lastly, RP VI addresses *research sub-question (vii)* through calciner modeling and design. A numerical calciner model for accurate calciner design and analysis was developed in RP VI. The new model is based on laboratory (TGA) experiments and pilot tests at the Technical University of Darmstadt [120]. It features a reactor sub-model to account for the CO_2 partial pressure distribution along the reactor and a particle sub-model to describe the reaction kinetics. In Figure 7, the continuous-line arrow indicates that the carbonator design determines the required calcination performance, which is an input for the calciner design. The new calciner model was used along with a stochastic methodology to derive guidelines for designing and upscaling IHCaL and CaL calciners.

In summary, this cumulative dissertation addresses the overarching research question and the research sub-questions by developing IHCaL process concepts and specifications, performing process simulations, assessing the developed processes, and advancing reactor models for accurate simulation and robust design. The results of the research papers are summarized in the Synthesis (Section 2), including a concise presentation of the applied methods. We utilize scientifically derived color maps [170] to enhance the accuracy of figure representation and ensure clarity for readers with color vision deficiencies, as well as for grayscale print [171].

2 Synthesis

2.1 Process development, simulation, and assessment

Research Paper I (RP I) studies the key integration parameters for implementing IHCaL technology in lime production, with a focus on minimizing heat consumption. Its objective is to reduce fuel requirements, enabling more compact facilities and lowering both investment and operating costs. The study uses the heat ratio (*HR*) as its key performance indicator, defined as the ratio of specific heat requirement of a lime plant with CO_2 capture to that of the reference lime plant without capture. The goal of RP I is to minimize *HR*.

Two novel concepts for integrating the IHCaL process into lime plants were developed, with a patent currently pending [168]: a tail-end and a fully integrated solution. The tail-end concept (Figure 8) is suitable for retrofitting existing lime plants by placing an IHCaL capture facility after the lime kiln. In the fully integrated process, the lime production and the carbon capture are realized within a single IHCaL facility. The application of these concepts is studied using an existing lime plant featuring a preheated rotary kiln (PRK) as the reference industrial plant (see Section 1.4). The same reference plant is used for all the research papers in this dissertation dealing with process development, simulation, and assessment (RP I–III). Heat and mass balances are computed using Aspen Plus [127], and a sensitivity analysis (see, e.g., Figure 9) is performed to assess the impact of the key parameters on the energy requirements.

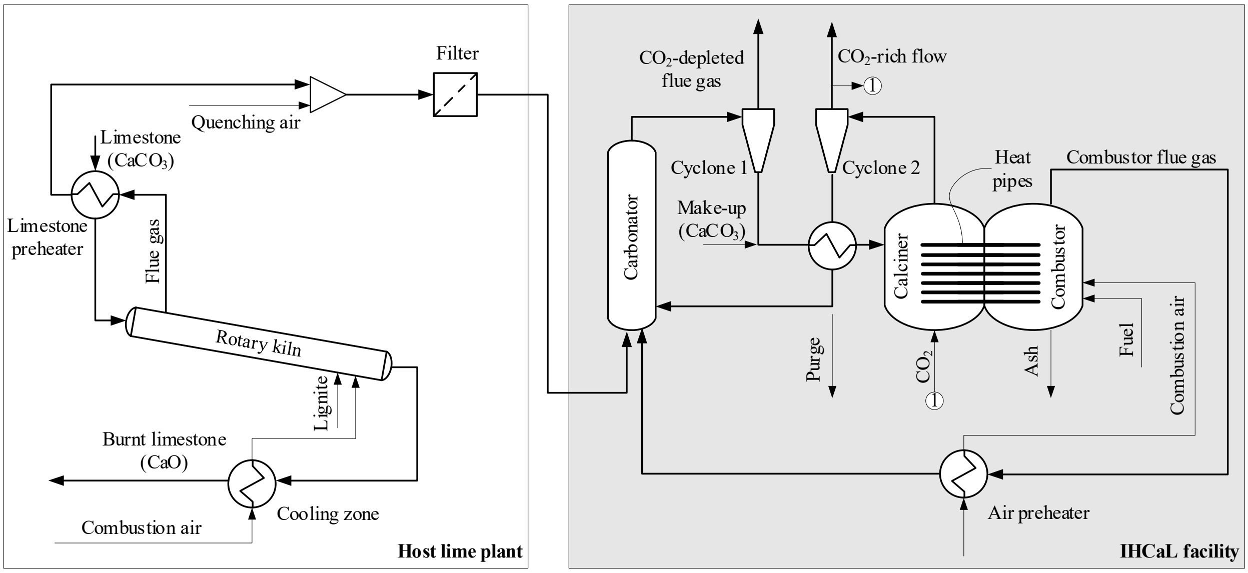
Filter
Quenching air
Limestone
(CaCO₃)
Limestone preheater
Flue gas
Rotary kiln
Lignite
Burnt limestone
(CaO)
Cooling zone
Combustion air
Host lime plant
CO₂-depleted flue gas
CO₂-rich flow
①
Cyclone 1
Cyclone 2
Carbonator
Make-up
(CaCO₃)
Heat pipes
Combustor flue gas
Calciner
Combustor
Purge
CO₂
①
Ash
Fuel
Combustion air
Air preheater
IHCaL facility

Figure 8. Tail-end IHCaL process to produce lime with CO_2 capture (adapted from RP III).

The first concept considered is the tail-end solution. It entails a low degree of integration and is therefore suitable for retrofitting. The IHCaL facility is located downstream at the end of the lime production facility, as shown schematically in Figure 8. The original PRK facility is depicted on the left side of Figure 8. The raw material (limestone) is fed into the rotary kiln through a preheater. The limestone is calcined in the PRK, and the burnt lime exits the PRK through a cooling zone. After cooling, the product (lime) is processed for commercialization. Sensible heat is recovered from the burnt lime by preheating of the combustion air. The flue gases from the kiln are used to preheat the limestone in the limestone preheater. Afterwards, they are cooled in a quench, filtered, and transferred to the IHCaL facility using a blower (not shown). The flue gases enter the carbonator, where the CO_2 reacts with CaO to form $CaCO_3$. Downstream of the carbonator, the CO_2-depleted gases are separated from the solids in the first cyclone. The solid particles enter the calciner where the sorbent regeneration takes place. After leaving the calciner, the solids are separated from the gases in the second cyclone. A high-purity CO_2 stream exits the calciner and the solids (mainly CaO) are transferred back to the carbonator to close the loop. For the fluidization of the calciner, a fraction of the high purity CO_2 stream is recirculated. Fuel is burned in the combustor to obtain the heat for the calcination. The same lignite that is being used to fire the PRK is fed into the combustor, but other fuels such as refused-derived fuels could also be used for this purpose (see RP II). Heat is transferred to the calciner via heat-pipes [114]. Downstream of cyclone 2, there is a sorbent extraction point to extract the purge stream. This purge stream consists of highly concentrated CaO that is considered as lime product. Thus, the implementation of the IHCaL expands the lime production capacity while allowing for CO_2 capture.

To reduce fuel consumption, the combustion air is preheated with the flue gases from the combustor. Moreover, a solid-solid heat exchanger is installed to transfer heat between the circulating sorbent streams, reducing the energy requirements in the calciner. The heat from the CO_2-depleated flue gases, the CO_2-rich flow, and the cooling of the carbonator are used to generate power through a heat recovery steam cycle [81,172]. To ensure high CO_2 capture rates, it is necessary to maintain a high activity of the sorbent inventory. This is realized by continuously removing a fraction of the solid inventory and replacing it with make-up (i.e., fresh limestone). The purge is extracted after the calciner so that it can be sold as high-purity lime.

The second integration concept is the fully integrated configuration, in which the reference plant is replaced by a new facility. The new IHCaL facility, which is similar to the one illustrated in Figure 8 (right), operates as a calcination unit with inherent CO_2 capture. In this configuration, the calcination plays an important role in producing lime apart from regenerating the carbonated sorbent. Around 5–10 % of the recirculated lime is removed from the system to be processed and sold. Since all the limestone is calcined by indirect heating, all the CO_2 from the limestone calcination is released in the calciner. As a result, the need for a downstream separation of process CO_2 is avoided and only the CO_2 emissions from the combustor need to be captured. For this reason, the fully integrated scheme has much lower heat requirements and sorbent circulation rates than the tail-end configuration. Regarding heat integration, the same strategies for heat recovery as in the tail-end concept are applied, along with the additional strategy of using the CO_2-depleated stream exiting cyclone 1 to preheat limestone.

The software Aspen Plus was used to solve the mass and energy balances of the IHCaL process. Aspen Plus is a steady-state process simulation software, which has a powerful database of properties for various substances [173]. The programming was performed graphically, including custom routines in FORTRAN language. Steady-state operation was assumed, and cyclone separation was considered ideal. The Redlich-Kwong-Soave model was used for the calculation of the properties of the gases [174]. For the solids, the properties were calculated with polynomial functions, which are already programmed in Aspen Plus. In particular, the energy, enthalpy, entropy, and heat capacity were calculated with the Barin equations [175]. The APV110 database, from Aspen Technology Inc., was used as input for the property calculations. The PRK was modeled using three reactor blocks, according to the work of Zhang et al. [173]. For all the combustion processes, an air-fuel equivalence ratio (λ) of 1.2 was assumed according to the operating experience from the host plant. The temperature of the IHCaL combustor was set to 1000 °C to maintain a 100 °C temperature difference with the calciner according to Reitz et al. [118,120].

The key operating parameters are the temperature of the solids stream entering the calciner ($T_{\text{sorb,calc,in}}$), the temperature of the preheated air entering the IHCaL combustor (T_{preheat}), the make-up ratio ($\mathit{\Lambda}$), and the sorbent circulation ratio ($\mathit{\Phi}$). The make-up ratio is defined as [176]:

$$\mathit{\Lambda} = F_0 / F_{\text{CO2}} \tag{7}$$

Here, F_0 is the molar flow rate of make-up (fresh limestone) into the system and F_{CO2} is the molar flow rate of CO_2 into the carbonator. Usually, $\mathit{\Lambda}$ is in the order of ~ 0.05 but higher values are also typical for integrated concepts for lime and cement production. The circulation ratio is defined in Eq. (8) based on the molar circulation rate of sorbent (F_R) [176]. It generally ranges between 5 and 20.

$$\mathit{\Phi} = F_R / F_{\text{CO2}} \tag{8}$$

The key performance indicators for energy efficiency are the absolute heat ratio (HR_a), the specific heat ratio (HR), and the specific primary energy consumption per CO_2 avoided ($SPECCA$). The indicators HR_a and HR are defined in Eqs. (9) and (10), respectively.

$$HR_a = \dot{Q}_{\text{in,CC}} / \dot{Q}_{\text{in,ref}} \tag{9}$$

$$HR = HR_a / PR; \qquad PR = \dot{m}_{\mathrm{CaO,CC}} / \dot{m}_{\mathrm{CaO,ref}} \tag{10}$$

Here, $\dot{Q}_{\mathrm{in,CC}}$ and $\dot{Q}_{\mathrm{in,ref}}$ represent the total heat requirement in the CO_2 capture scenario and the reference (BAU) scenario, respectively; and *PR* is the product ratio that relates the lime production in the lime plant with CO_2 capture ($\dot{m}_{\mathrm{CaO,CC}}$) to that of the reference plant without CO_2 capture ($\dot{m}_{\mathrm{CaO,ref}}$). The ratios HR_a and *HR* are typically higher than 1 due to the increased heat requirements to regenerate the sorbent in the calciner. For the retrofitted IHCaL process, the spent sorbent is considered as product, resulting in $PR > 1$.

With the objective of minimizing *HR* and reducing facility size, a sensitivity analysis was conducted. The results for the fully integrated concept are summarized in Figure 9. Figure 9.a shows the variation of *HR* with the main temperatures involved in heat integration: the temperature of the sorbent at the calciner inlet ($T_{\mathrm{sorb,calc,in}}$) and the temperature of preheated combustion air (T_{preheat}). A decrease in T_{preheat} and $T_{\mathrm{sorb,calc,in}}$ requires additional energy in the calciner to heat the incoming gases and solids, respectively. This increased energy demand leads to higher fuel consumption in the combustor, generating additional CO_2 that must be captured in the carbonator. Consequently, more energy is required for sorbent regeneration, resulting in a higher *HR*. This process creates a positive feed-back mechanism, causing an exponential-like increase of *HR* as T_{preheat} and $T_{\mathrm{sorb,calc,in}}$ decrease, a trend visible in Figure 9.a.

The *HR* values exhibit the same tendency for both the tail-end concept (see RP I, Figure 3) and the fully integrated concept (see Figure 9.a): higher T_{preheat} and $T_{\mathrm{sorb,calc,in}}$ result in lower *HR* due to reduced energy requirements for heating the solids and gases entering the calciner. However, for the same set of temperatures, the *HR* of the fully integrated solution is lower. This is because only the CO_2 emissions from the combustor need to be captured, leading to lower energy demand, as previously explained. Toward the limit of maximum theoretical integration (highest temperatures), *HR* approaches ≈ 1 for the fully integrated concept. The minimum achievable *HR* for the tail-end solution is approximately 2.

(a) Influence of the sorbent temperature and the air preheating

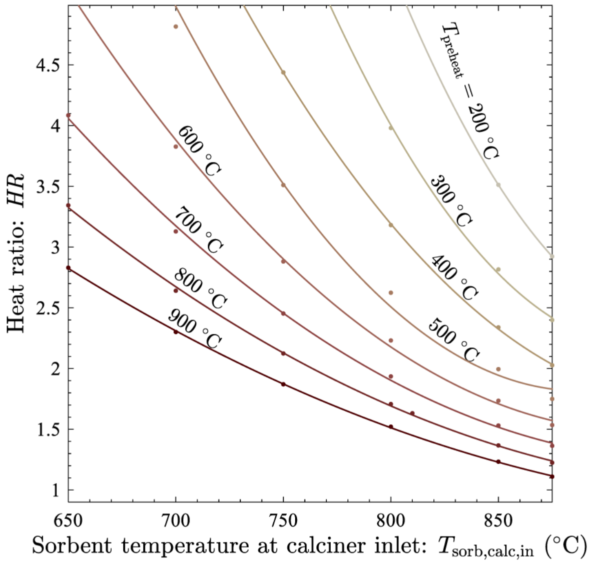

(b) Influence of the sorbent circulation rate

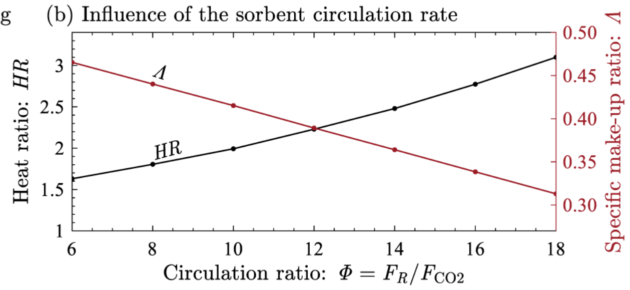

(c) Influence of the carbon capture efficiency

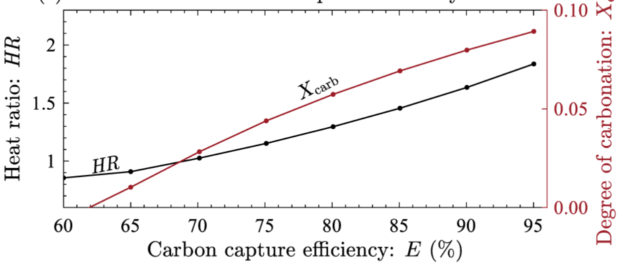

Figure 9. Sensitivity analysis for the fully integrated concept. In (a), the influence of the sorbent temperature at the calciner inlet and the air preheating temperature (T_{preheat}) on the heat ratio (*HR*) is depicted. Graph (b) shows the variation of the heat ratio (HR) and the specific make-up ratio (*Λ*) with the specific circulation ratio (*Φ*). Finally, the influence of the carbon capture efficiency (*E*) on the heat ratio (*HR*) and on the required degree of carbonation (X_{carb}) is presented in graph (c). Adapted from RP I.

The influence of the specific circulation ratio (*Φ*) is illustrated in Figure 9.b. Increasing *Φ* results in higher *HR*, as additional energy is required to heat the larger stream of solids entering the calciner. The variation of *HR* with *Φ* for the fully integrated solution closely resembles that of the tail-end configuration (see RP I, Figure 3.b). Regarding the specific make-up ratio (*Λ*), an increase in the sorbent circulation rate between the reactors (higher *Φ*) raises *HR* due to the additional energy required to heat more incoming solids. As a result, more CO_2 is generated from the increased fuel consumption (higher F_{CO2}), leading to lower values of Λ for a constant make-up rate (F_0)—see Eq.(7). Despite this reduction in the specific make-up, Λ remains high for CaL operation, well above the typical values (usually less than 0.2) [176,177], resulting in elevated levels of sorbent activity (see [149,178]).

The influence of the carbon capture efficiency (E) is shown in Figure 9 (c). Higher capture rates require higher carbonation degrees in the carbonator (X_{carb}), which increases the energy needed to regenerate the sorbent. For values below 62 %, no conversion occurs in the carbonator (i.e., $X_{\mathrm{carb}} = 0$). This means that, since most of the CO_2 is produced in the calciner, $E = 62\,\%$ can be achieved without capturing the CO_2 from the combustor's flue gases.

Overall, our results show that combustion air preheating, the performance of the solid-solid heat exchanger, and the sorbent circulation rate are critical factors to efficiently capture CO_2 in the lime production using IHCaL technology. These findings partially answer *research sub-question (i)*. Preheating combustion air is a well-established strategy for reducing fuel requirements. However, preheating to high temperatures (>500°C) and transferring heat between the circulating streams is technically challenging and may involve high investment costs. For the implementation of the solid-solid heat exchanger, different designs are possible: (i) a concept with molten salt and a regenerative heating/cooling of a solid, (ii) a concept with heat pipes, and (iii) a concept with two concentric L-valves [125,179]. The construction and validation of a solid-solid heat exchanger for IHCaL processes have yet to be performed. Regarding utilization of spent sorbent, we assumed that the purge (lime) is suitable for substituting the product from conventional lime plants, which is an important assumption for the viability of the developed processes. Some previous studies provide evidence to support this assumption [180–183]. However, this issue necessitates further investigations (cf. [125]).

Recently, He et al. [184] analyzed three different CaL configurations using Aspen Plus simulations, each with a distinct heat supply strategy for the calciner. They reported that the sorbent make-up ratio and the average CaO conversion—closely related to the sorbent circulation ratio—significantly impact the energy performance of the indirectly heated CaL process. Their findings support our conclusions.

Research Paper II (RP II) studies the net removal of CO_2 from the atmosphere using tail-end IHCaL configurations in lime production. Its objective is to determine the potential of the IHCaL process to achieve net-negative CO_2 emissions, focusing on the influence of fuel type on process performance, particularly in terms of energy utilization and emissions reduction.

Different fueling scenarios were simulated using an Aspen Plus V12 model, following a methodology similar to that used in RP I. The carbonator efficiency (E_{carb}, Eq. (5)) was calculated using the carbonator model developed by Lasheras et al. (2011) [81], which considers: (i) the CFB hydrodynamics model from Kunii and Levenspiel [139], (ii) the carbonation reaction model from Abanades et al. [72]; and (iii) the sorbent deactivation model from Abanades et al. [185]. The make-up ratio was set to $\Lambda = 0.1$, and Φ was adjusted to achieve a CO_2 capture efficiency of $E = 90\,\%$. Key performance indicators were calculated and compared to those from other CO_2 capture methods. The calculation of the electric power in the reference facility was based on the data from Schorcht et al. [3]. The compression takes place in a 5-stage CO_2 compressor, which was also simulated in Aspen Plus, based on the methodology from Posch and Haider [186]. The power requirements for the blowers were calculated from the pressure drop across the reactors and the auxiliary components (i.e., nozzle grids, cyclones, heat exchangers, filters, and ducts), using experimental data from our research group [120]. The isentropic and mechanical efficiencies of the blowers were set to 0.65 and 0.9, respectively [187]. The power generation was calculated using steam cycle simulations with the software EBSILON Professional [129]. The main assumptions for the calculations were: (i) superheating of steam up to 565 °C and 130 bar; (ii) preheating of feedwater with steam extractions; (iii) isentropic turbine efficiency equal to 85 %. The calculated heat-to-power efficiency (η_{h2p}) is 42.4 %, which corresponds to an equivalent net electrical efficiency of approximately 38 % for a thermal power plant (e.g., pulverized coal), consistent with values from the literature [188].

Four fuels were considered in the analysis: (i) dried lignite from the reference process in the host plant in Germany [62]; (ii) RDF pellets, which were used in pilot test campaigns at the Technical University of Darmstadt [30]; (iii) a Class 3 SRF, according to EN ISO 21640:2021-11, that was successfully utilized in the 1-MW_{th} pilot plant at the Technical University of Darmstadt for CaL operation [98]; and (iv) municipal solid waste (MSW) with the composition and properties reported in [80]. Dried lignite was maintained as the fuel of the reference plant for all cases, and only the fuel for the IHCaL combustor was varied. The carbon content of lignite was considered of 100 % fossil origin. The rest of the fuels had a biogenic fraction of ca. 50 %. The fuel properties including composition, lower heating value, biogenic fraction, particle size, and moisture, are available in RP II.

One useful parameter to analyze the influence of type of fuel in the IHCaL process is the *fuel CO_2 emissions index* [189,190], also known as the *fuel specific CO_2 emissions* ($e_{CO2,fuel}$). This parameter indicates the mass of CO_2 produced per unit of energy obtained from fuel combustion. It is calculated using Eq. (11), where $w_{C,wet}$ is the wet-basis mass fraction of carbon in the fuel, *LHV* is the lower heating value of the fuel on a wet basis, M_{CO2} is the molar mass of CO_2, and M_C is the molar mass of carbon.

$$e_{CO2,fuel} = \frac{w_{C,wet}\left(M_{CO2}/M_C\right)}{LHV} \tag{11}$$

The simulation results show that the combustor has the greatest influence on the direct formation of CO_2. The direct CO_2 formation is minimized by fuels with a lower CO_2 emissions index ($e_{CO2,fuel}$)—see Eq. (11). Moreover, the use of dried lignite doubles the total direct fossil CO_2 formation. This means that the additional fossil CO_2 associated with carbon capture is approximately equal to the CO_2 emissions of the reference plant. Given this, it seems more reasonable to use waste-derived fuels—or biomass—for the tail-end IHCaL, whereby the increase in total direct fossil CO_2 formation linked to the capture is relatively low (approximately 30 %).

The increase in specific heat requirements due to the carbon capture ranges from 201 % to 271 %, with respect to the reference case. This result is highly dependent on the make-up ratio Λ. The CO_2 formation in the combustor increases with $e_{CO2,fuel}$; thus, increasing the total captured CO_2. Due to the more demanding capture requirement, more heat is needed in the calciner, and *HR* becomes higher. The direct fuel consumption, *q*, and the direct CO_2 emissions, $e_{CO2,d}$, increase with *HR*.

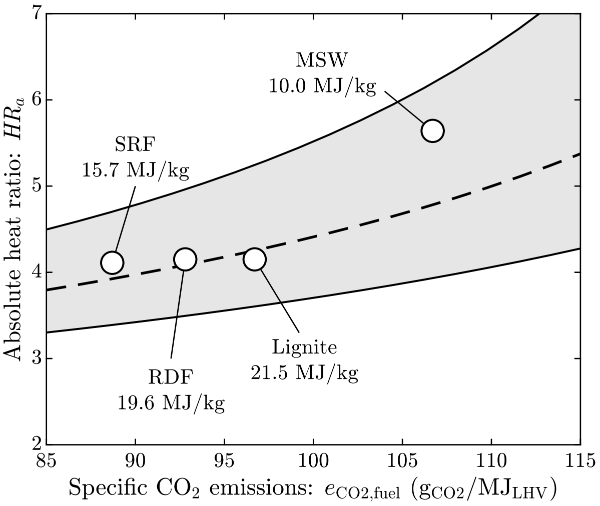

Figure 10. Absolute heat ratio and specific CO_2 emissions for each fuel. The markers indicate the results of the simulations with Aspen Plus. The gray area represents the calculated increase of the heat requirement for a wide range of fuels.

Figure 10 illustrates the relationship between the absolute heat rate (HR_a, see Eq.(9)) and the CO_2 specific emissions for each fuel considered in this study. The HR_a increases with the CO_2 emissions index ($e_{CO2,fuel}$), due to the higher CO_2 formation in the combustor. Other parameters, such as the lower heating value (*LHV*) and the amount of hydrogen in the elemental composition of fuels, also influence the variation in heat requirements. Higher *LHV* and lower $e_{\mathrm{CO2,fuel}}$ minimize HR_a in the combustor, as shown in Figure 10. Here, the gray area indicates the variation of HR_a for different operating parameters and a wide range of fuels.

Figure 11 shows the breakdown of the specific CO_2 emissions per tonne of burnt lime (e_{CO2})—see Eq. (14). The emissions are divided into three categories: (i) direct fossil emissions, (ii) direct biogenic emissions, and (iii) indirect emissions associated with the electric power. The direct biogenic emissions are negative for waste-derived fuels, indicating a net-negative contribution to the carbon balance due to the capture of biogenic CO_2. The sum of all the emissions in the three categories gives the equivalent CO_2 emissions (e_{CO2}). The results are presented for the reference plant (business as usual, BAU), and the cases with CO_2 capture using different fuels. Four energy-mix scenarios were considered for the calculations: Coal state-of-the-art power plant, European energy mix (2015), Renewables, and Nuclear. The indirect and equivalent CO_2 emissions depend on the reference efficiency of the energy scenario ($e_{\mathrm{ref,el}}$)—see Eq. (14). The results are identical for the renewable and the nuclear energy scenarios because they both have $e_{\mathrm{ref,el}} = 0$. The reference case, without carbon capture, presents the highest emissions level. The major contribution comes from the direct fossil emissions corresponding to the calcination and combustion in the lime kiln. The indirect emissions are almost negligible. The results are similar for all the energy scenarios. For the carbon capture scenarios, net-negative equivalent CO_2 emissions are achieved in every case, except when fueling lignite for the renewables and nuclear energy scenarios. If waste-derived fuels are used, the highest contribution to the negative emissions corresponds to the captured biogenic CO_2, which is independent of the energy scenario. The indirect emissions are strongly dependent on $e_{\mathrm{ref,el}}$ because of the significant power generation in the retrofitted plants (42–63 MW_{el}). The negative values result from electricity generation exceeding the own demand. With waste-derived fuels, negative emissions as high as -1805 $\mathrm{kg_{CO2}/t_{CaO}}$ can be achieved. This corresponds to an equivalent CO_2 avoidance of over 230 %.

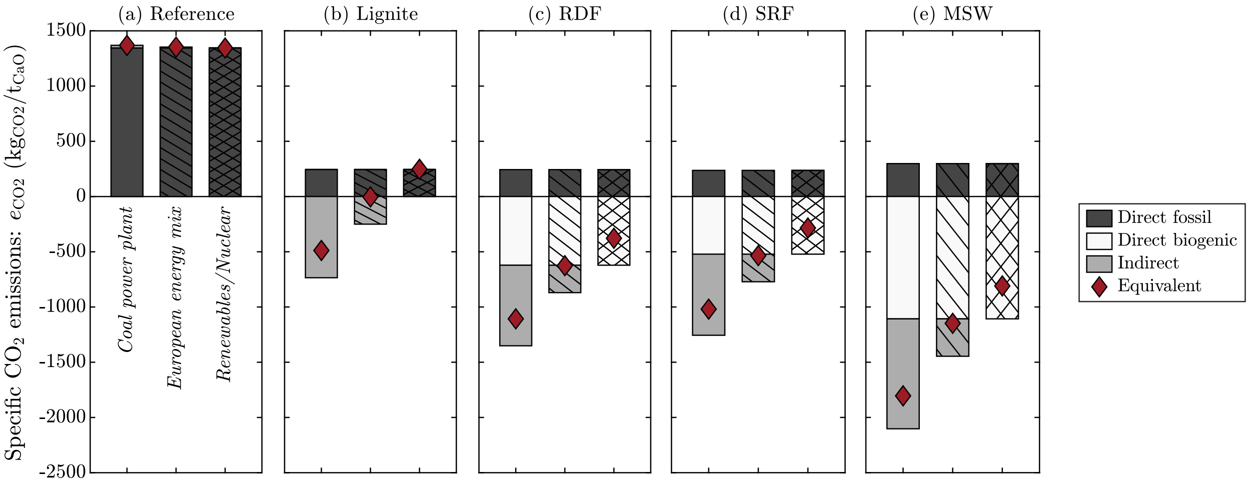

Figure 11. Specific CO_2 emissions for (a) the reference facility without CO_2 capture; and the scenarios with CO_2 capture using different fuels: (b) dried lignite, (c) refuse-derived fuel (RDF), (d) solid recovered fuel (SRF), and (e) municipal solid waste (MSW). The breakdown of the CO_2 emissions is depicted with bars. The energy-mix scenarios are indicated with the filling type: coal power plant (solid), European energy mix (hatched), and Renewables/Nuclear (crossed). The equivalent specific CO_2 emissions ($e_{\mathrm{CO2,eq}}$) are indicated with a diamond (◊).

The specific primary energy consumption per CO_2 avoided (*SPECCA*) is a key indicator of the process performance in terms of energy utilization, calculated using Eq. (12).

$$SPECCA = \frac{q_{\mathrm{CC}} - q_{\mathrm{ref}}}{e_{\mathrm{CO2,ref}} - e_{\mathrm{CO2,CC}}} \tag{12}$$

Here q_{CC} and q_{ref} represent the equivalent specific primary energy consumption (q) for the plant with CO_2 capture and without CO_2 capture, respectively. In turn, $e_{\mathrm{CO2,CC}}$ and $e_{\mathrm{CO2,ref}}$ are the equivalent specific CO_2 emissions of the plant (e_{CO2}) with CO_2 capture and without CO_2 capture, respectively.

The calculation of q considers the direct primary energy consumption from the fuel input and the indirect primary energy consumption related to the net power requirement (P_{el}), according to Eq.(13).

$$q = \frac{\dot{m}_{\mathrm{fuel}}\, LHV + P_{\mathrm{el}} / \eta_{\mathrm{ref,el}}}{\dot{m}_{\mathrm{CaO}}} \tag{13}$$

Here, $\dot{m}_{\mathrm{fuel}}$ is the fuel mass flow rate into the system, LHV is the lower heating value of the fuel, P_{el} is the net electric power consumption, $\eta_{\mathrm{ref,el}}$ is the reference electric efficiency of the grid, and $\dot{m}_{\mathrm{CaO}}$ is the lime production rate. To compute the equivalent specific CO_2 emissions (e_{CO2}), the direct CO_2 emissions from combustion and calcination ($e_{\mathrm{CO2,d}}$) and the indirect CO_2 emissions ($e_{\mathrm{CO2,i}}$) associated with the electric power (P_{el}) are considered. Eq. (14) is used to calculate e_{CO2}, where $e_{ref,el}$ represents the CO_2 emissions factor of the electricity mix.

$$e_{\mathrm{CO2}} = e_{\mathrm{CO2,d}} + e_{\mathrm{CO2,i}}; \qquad e_{\mathrm{CO2,i}} = P_{\mathrm{el}}\, e_{\mathrm{ref,el}} \big/ \dot{m}_{\mathrm{CaO}} \tag{14}$$

Lastly, $e_{\mathrm{CO2,d}}$ is calculated by considering the fossil CO_2 generation rate ($\dot{m}_{\mathrm{CO2,foss}}$) and the CO_2 capture rate ($\dot{m}_{\mathrm{CO2,capt}}$), using Eq. (15).

$$e_{\mathrm{CO2,d}} = \frac{\dot{m}_{\mathrm{CO2,foss}} - \dot{m}_{\mathrm{CO2,capt}}}{\dot{m}_{\mathrm{CaO}}} \tag{15}$$

Our study showed that very low *SPECCA*, from 0.50 to 2.79 $\mathrm{MJ_{LHV}/kg_{CO2,av}}$, can be achieved for three of the simulated scenarios: Coal, European energy mix (2015), and Nuclear. In particular, *SPECCA* values between 0.50 and 1.98 $\mathrm{MJ_{LHV}/kg_{CO2,av}}$ were achieved for the scenarios utilizing waste-derived fuels in the combustor. The *SPECCA* values are lower than those reported for other capture technologies for cement plants, such as monoethanolamine (MEA) scrubbing, and the chilled ammonia process (CAP) [46,69,84,191,192], indicating that the IHCaL process is highly efficient in terms of energy utilization. Because of its low primary energy requirements, the IHCaL technology is very promising for carbon capture from lime plants. It has a high potential for deployment in contexts where the energy mix is characterized by high specific CO_2 emissions or high carbon intensity, making the power generation benefits of the IHCaL process particularly advantageous.

The results from RP II effectively address *research sub-question (ii)*, demonstrating that negative CO_2 emissions can be realized by using waste-derived fuels, while also achieving efficient energy utilization. Our calculations excluded CO_2 emissions from transportation, storage, and facility construction and disposal. On the other hand, the CO_2 absorbed by utilization of lime was not considered in the balance (cf. [193]). These factors should be taken into account in future work to refine our conclusions.

Research Paper III (RP III) investigates heat recovery from IHCaL plants, focusing on energy utilization and economic performance. Its objective was to optimize the IHCaL process for lime plants, taking into account both economic and energy-efficiency indicators, primarily the CO_2 avoidance costs (*CAC*) and specific primary energy consumption per CO_2 avoided (*SPECCA*). Within this work, ten scenarios using IHCaL technology to capture CO_2 from a lime plant were simulated considering different process configurations, heat recovery strategies, and fueling options. The calculated mass and energy flows were used for analyzing each configuration's efficiency and conducting a techno-economic assessment.

The heat recovery strategy plays a crucial role in the integration due to the substantial amount of heat available at high temperatures (> 650 °C). Figure 12 illustrates the integration strategies analyzed in RP III, which feature different approaches for recovering heat from the combustor flue gas. The first strategy (I) consists in only recovering heat through preheating of the combustor air. This increases the thermal efficiency of the IHCaL process but requires a gas-gas heat exchanger operating at high temperatures—up to 1000°C on the hot side, and up to 800°C on the cold side. Another possibility is to utilize this heat in a steam cycle with a heat exchanger after (strategy II) or before the air preheater (strategy III). However, the operating temperatures of the heat exchangers need to be carefully considered to prevent corrosion when using waste-derived fuels.

The processes were modeled based on the methodology of RP II. The Aspen Plus simulations were performed using available material property data (ASPEN APV120 database) and property methods [175]. Each heat recovery strategy was modeled in Aspen Plus. The steam cycles were designed and simulated with EBSILON Professional [129] considering the amount and quality of the heat available for each scenario.

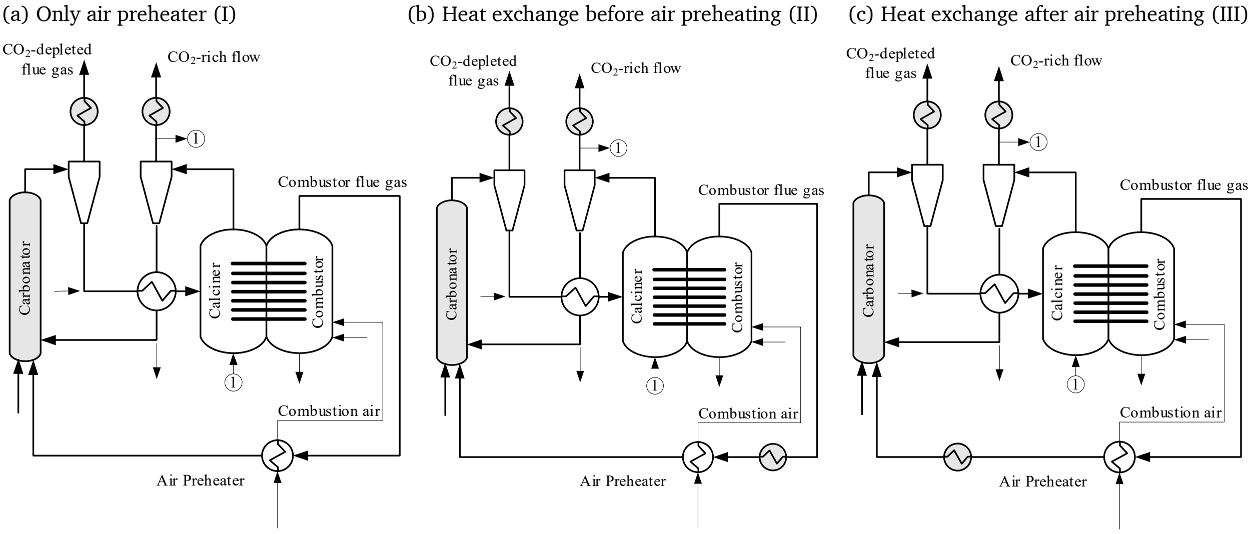
(a) Only air preheater (I)
(b) Heat exchange before air preheating (II)
(c) Heat exchange after air preheating (III)

Figure 12. Heat recovery strategies: only air preheater (I), heat exchange before air preheating, and (III) heat exchange after air preheating. Adapted from RP III.

The economic analysis was performed by the University of Ulster, with the collaboration of the TU Darmstadt, using the in-house ECLIPSE modeling and simulation software [194,195]. For each scenario, the process flow diagrams and technical data were input into ECLIPSE. The mass and energy balances were calculated using ECLIPSE and validated with results from Aspen Plus and EBSILON Professional simulations. The mass and energy flows, along with user-input utilities data and database information, were used to determine the utilities usage (e.g., electricity, water) for each process. The data on utilities usage was then applied to the costs estimation, incorporating engineering data and information from the cost database. Finally, the economic analysis was completed using the previously determined capital and operating costs. The Chemical Engineering Plant Cost Index (CEPCI) was used to normalize the data and results to the year 2020 [196,197].

The calculated primary energy consumption (*SPECCA*) of the different scenarios is displayed in Figure 13 (left). Since there is considerable power generation in all IHCaL configurations, there is high variability with the energy-mix scenarios, which affects the calculation of indirect energy requirements and indirect emissions according to Eqs. (13) and (14). The mean *SPECCA* values for IHCaL technology—especially those for the fully integrated concept—are low compared to the *SPECCA* values for other CO_2 capture processes. Overall, the results indicate that IHCaL technology is more attractive in energy scenarios with low renewable share and high CO_2 emissions associated with the power generation (high $e_{\mathrm{ref,el}}$). Depending on the electric grid and anticipated changes in the energy mix over the project's lifetime, a facility can be optimized either for power production (heat recovery strategy II) or for minimizing fuel consumption (heat recovery strategy I). In terms of *SPECCA*, heat recovery strategy (II) exhibits inferior performance compared to the other two strategies, as it lowers the combustion gas temperature before the air preheater. This limitation hinders effective air preheating, a critical integration strategy, as demonstrated in RP I. Heat recovery strategies I and III have similar *SPECCA*, with the latter performing slightly better due its combination of high-temperature preheated combustion air and increased heat recovery in the steam cycle through heat exchange downstream of the air preheater.

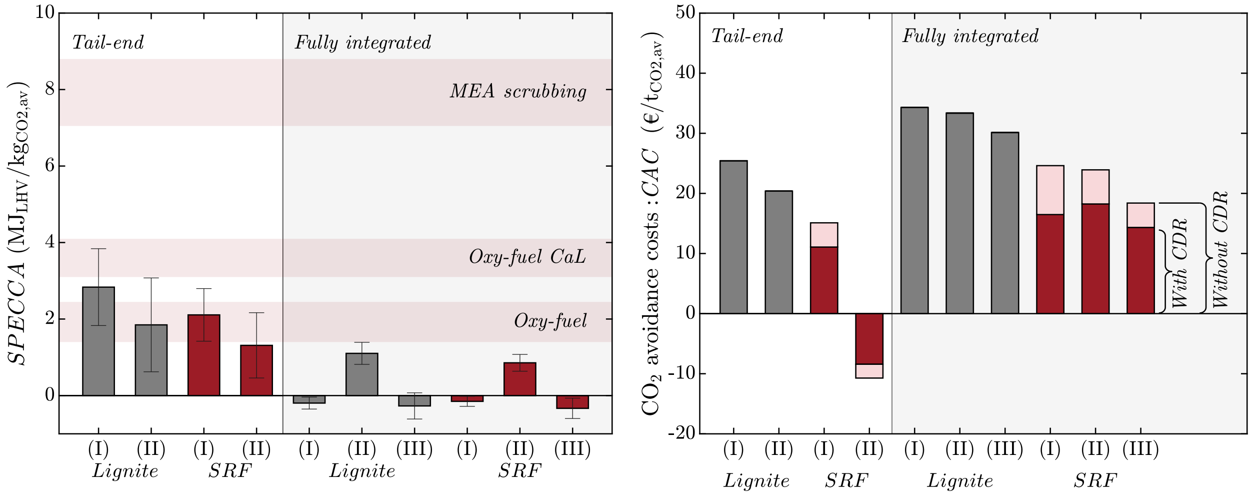

Figure 13. Specific energy consumption (*SPECCA*, left) and CO_2 avoidance costs (*CAC*, right) of the IHCaL process for decarbonization of lime plants under different integration scenarios. On the left, the bars represent mean values, with the error bands showing the variation of plus-minus one standard deviation across the energy-mix scenarios. The background shading indicates SPECCA values for other technologies, based on results from Voldsund et al. [46]. On the right, the effect of CDR on *CAC* is shown by the shading of the bars for the SRF scenarios. Adapted from RP III.

To assess the impact of CO_2 capture on the plant economics, the CO_2 avoidance costs (*CAC*) are calculated using Eq. (16), which consider the reduction of CO_2 emissions per unit of the net product produced [198,199].

$$CAC = \frac{BESP_{\mathrm{CC}} - BESP_{\mathrm{ref}}}{e_{\mathrm{CO2,ref}} - e_{\mathrm{CO2,CC}}} \tag{16}$$

Here, $BESP_{\mathrm{CC}}$ and $BESP_{\mathrm{ref}}$ are the break-even selling prices (BESP) of lime for the plant with CO_2 capture and without CO_2 capture, respectively. The economic benefit of CDR is considered in the calculation of *CAC* by treating the captured biogenic CO_2 emissions as negative (see Figure 13, right). Costs for CO_2 transport and storage were excluded from the calculations. These typically range from 4 to 40 €/t_{CO2}, depending on factors such as transport distance, amount of CO_2, and reservoir geology [200].

The CO_2 avoidance costs (*CAC*) for the IHCaL process are reported in Figure 13 (right). Our results align with literature values [201]. Electricity export significantly impacts the avoidance costs. For plants using lignite, *CAC* ranges from 20.4 to 34.3 €/$t_{\mathrm{CO2,av}}$, with the tail-end (II) case having the lowest costs due to substantial power generation. Conversely, the fully integrated (I) plant has the lowest electricity export, resulting in the highest costs, despite having the lowest fuel consumption.

For the SRF plants, the maximum and minimum values correspond to the tail-end SRF (I) case and the fully integrated SRF (I) case, respectively. Apart from the income from electricity export, the SRF plants attain additional revenue from utilizing this kind of fuel. As the tail-end SRF (II) plant consumes the largest amount of SRF, it receives a higher value from this revenue stream, which explains the negative costs (i.e., net earnings before adding the benefits of CO_2 certificates).

The influence of capturing biogenic CO_2 emissions (carbon dioxide removal, CDR) is illustrated in Figure 13 with darker bands. If negative CO_2 emissions are computed for the captured biogenic CO_2, net-negative emissions are achieved in all the scenarios using SRF as fuel for the IHCaL (cf. RP II), and *CAC* is reduced due to the higher amount of CO_2 avoided (except for negative *CAC*). If the economic benefit of CDR is considered, the avoidance costs are lower than 19 €/$t_{\mathrm{CO2,av}}$ for all the analyzed scenarios.

The results from RP III primarily address *research sub-question (iii)* by demonstrating that significantly low *CAC* values are achievable using IHCaL technology in lime production. The values shown in Figure 13 are competitive with those reported for other CO_2 capture technologies in similar applications ($>$ 30 €/$t_{\mathrm{CO2,av}}$) [83,84].

2.2 Carbonator modeling and design

Research Paper IV (RP IV) and **Research Paper V** (RP V) focus on carbonator modeling and design. The objective of these research papers was to develop an improved carbonator model to analyze reactor performance in a semi-industrial CO_2 capture facility and facilitate the effective scaling-up of the carbonator for commercial IHCaL and CaL applications. This goal was achieved by creating a new model based on insights from a systematic literature review and results from pilot tests.

Figure 14 summarizes the main features and improvements of our carbonator model. In RP IV, we discuss the *reactor sub-model*, which is used to calculate the gas-solid contact efficiency and obtain the CO_2 concentration along the carbonator. The *particle sub-model*, which is essential to calculate the reaction rate and the sorbent deactivation, is thoroughly discussed in RP V. The main output of the carbonator model is the carbonator efficiency (E_{carb})—see Eq. (5). The model was validated using data from pilot tests on the 300-kW$_{th}$ scale [120] (see Figure 5). Using the carbonator model, we derived conclusions concerning design and scale-up.

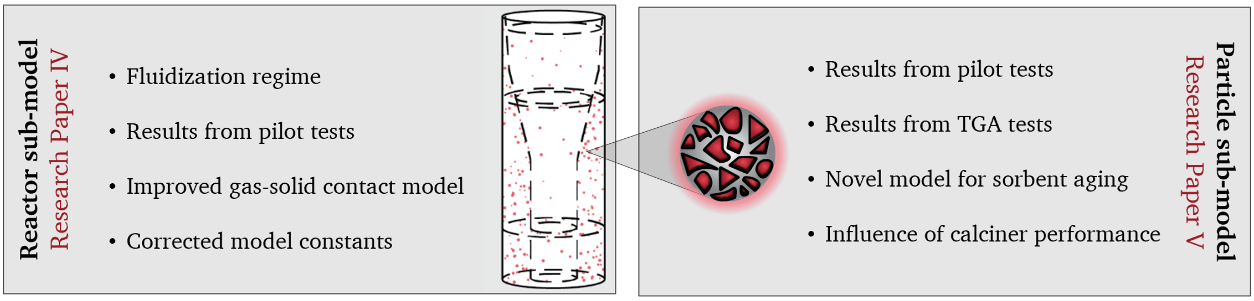
Reactor sub-model
Research Paper IV
• Fluidization regime
• Results from pilot tests
• Improved gas-solid contact model
• Corrected model constants
• Results from pilot tests
• Results from TGA tests
• Novel model for sorbent aging
• Influence of calciner performance
Particle sub-model
Research Paper V

Figure 14. Illustration of the carbonator model. The carbonator model is composed of a reactor and hydrodynamics sub-model (left, RP IV) and a particle sub-model (right, RP V).

RP IV provides a thorough analysis of the fluidization regimes for carbonator operation. Additionally, it includes considerations on reactor performance and modeling assumptions. We have improved the gas-solid contact model by correcting equations from previous studies and deriving expressions that are less dependent on case-specific constants, thus broadening the range of application of the model. Furthermore, we included a review of model constants for the hydrodynamics calculations and offered recommendations to select these constants based on empirical observations.

Our reactor sub-model uses the one-dimensional KL reactor model for fluidized beds [137], which considers the gas and the solid phase and simulates the gas-solid contact efficiency using semi-empirical correlations. The reactor hydrodynamics are characterized using the Geldard diagram [202] and the Grace diagram [203]. The transition velocity into the fast-fluidization regime was calculated according to Bi et al. [204]. The solids axial distribution inside of the carbonator is computed using the exponential decay model developed by Kunii and Levenspiel [139]. The solids radial distribution is modeled with a *core*, lean in solids, and an outer *annulus* with high solids concentration [137]. The annulus is thicker in the bottom dense region and becomes thinner throughout the top lean region, as illustrated in Figure 14 (left). The governing equations to obtain the CO_2 concentration along the reactor and the carbonator efficiency are based on the work from Kunii and Levenspiel [137].

The particle sub-model has been developed and validated using results from thermogravimetric analysis (TGA), as well as experimental results from pilot campaigns at the TU Darmstadt. This sub-model features a novel approach to simulate sorbent deactivation (aging) for varying sorbent circulation and make-up rates. It also considers the influence of calciner performance, which is essential for accurately predicting the carbonator efficiency.

Our particle sub-model assumes that the following in-series steps are needed for the carbonation to occur (see [139, p.451,205,206]): (i) CO_2 mass transfer through the gas boundary layer that surrounds the sorbent particle (*external mass transfer*), (ii) internal diffusion of CO_2 inside the pores of the solid (pore diffusion), (iii) CO_2 penetration and diffusion through the solid layer of $CaCO_3$ that was formed by previous reaction events (*product diffusion*), and (iv) reaction of CO_2 with CaO (*chemical reaction*) according to Eq. (1). The first step is modeled using a gas-gas diffusion approach, but we showed that it is generally irrelevant to the carbonation kinetics in CaL systems. The second step can be neglected for typical operating conditions of CFB carbonators for particle sizes of 70–400 μm [132]. This is because of the large pores present in the deactivated sorbent, as demonstrated by Grasa and Abanades [207]. To account for the third step, we consider only the reaction kinetics in the chemically controlled *fast stage*, in which the product diffusion is irrelevant. It is well known that the reaction rate decreases significantly beyond this stage due to limiting product diffusion, resulting in the onset of a *slow stage* [64,140]. We assume that no further reaction occurs past the fast stage, which is a reasonable assumption under industrial operating conditions in CFB carbonators [141,146]. The end of the chemically controlled fast stage is marked by a specific carbonation degree, known as *sorbent activity* X_N, beyond which the product layer becomes thick enough to limit the reaction kinetics [208]. The value of X_N depends on the number of complete calcination-carbonation cycles the sorbent has undergone. The reaction kinetics are modeled based on the first-order correlation of Bhattia and Perlmutter [140] and the grain particle model from Nitsch [209]. The rate constant is calculated according to Grasa et al. [207] to account for the influence of sorbent deactivation. We adopt the model from Romano [141] with data from Grasa et al. [210] to simulate the enhancement of the deactivation due to the presence of SO_2. We assume an exponential particle residence time distribution (RTD) in the carbonator [139, p.338], consistent with complete mixing of the solids in the carbonator, including the return leg. This assumption is justified by the strong particle mixing and high rates of solid recirculation typical of circulating fluidized beds [141]. The average sorbent activity ($\overline{X}_N$) is calculated by adapting the model of Rodríguez et al. [149] to consider the variations in the sorbent circulation rate and the make-up rate.

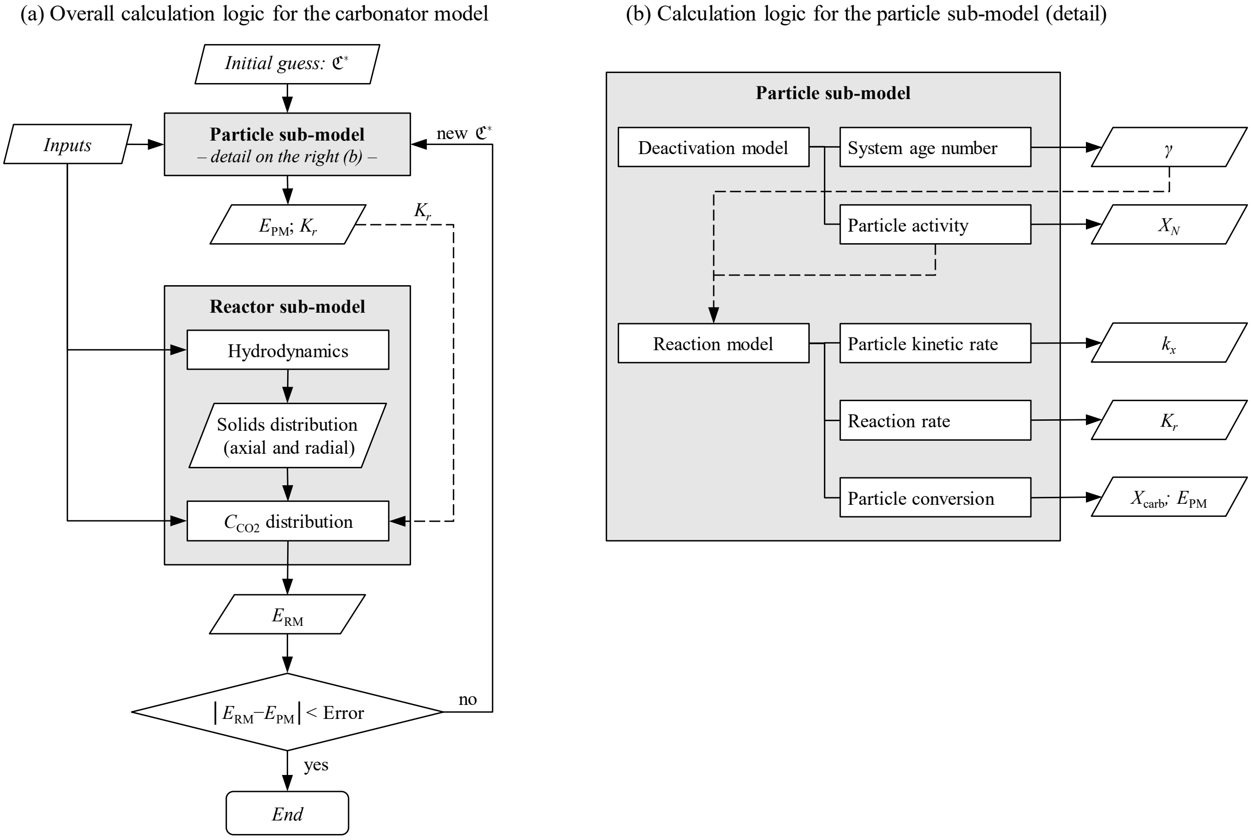
(a) Overall calculation logic for the carbonator model

(b) Calculation logic for the particle sub-model (detail)

Initial guess: $\mathfrak{C}^*$
Inputs
Particle sub-model
– detail on the right (b) –
new $\mathfrak{C}^*$
E_{PM}; K_r
K_r
Reactor sub-model
Hydrodynamics
Solids distribution (axial and radial)
C_{CO2} distribution
E_{RM}
$|E_{RM}-E_{PM}|$ < Error
no
yes
End
Particle sub-model
Deactivation model
System age number
γ
Particle activity
X_N
Reaction model
Particle kinetic rate
k_x
Reaction rate
K_r
Particle conversion
X_{carb}; E_{PM}

Figure 15. Calculation logic of the carbonator model: (a) overall calculation logic and (b) detail of the particle sub-model. Adapted from RP IV and RP V.

The calculation logic of the carbonator model is illustrated in Figure 15.a. To account for the variation of CO_2 concentration throughout the reactor we use an equivalent driving force ($\mathfrak{C}^*$) [141]. At the beginning of the calculation, an initial guess for $\mathfrak{C}^*$ is made and the inputs for the sub-models are specified. For the pilot testing, the input parameters were based on empirical data from measurements and samples. For the parametric study and sensitivity analysis, they were varied using mean operating conditions from pilot tests as the reference. The particle sub-model gives the global reaction rate (K_r), which is an input for the reactor sub-model, and the carbonation efficiency (E_{PM}). Within the reactor sub-model, the hydrodynamics calculations are used to obtain the solids distribution, which is an input to calculate the CO_2 concentration profile and the carbonator efficiency (E_{RM}). The entire carbonator model is solved iteratively using the bisection method of Bolzano [211,p.53–59]. If the predictions of the particle sub-model (E_{PM}) and the reactor sub-model (E_{RM}) coincide within a tolerable error, the calculation is terminated. Otherwise, a new value of $\mathfrak{C}^*$ is computed, and a new iteration begins.

Figure 15.b illustrates the detailed calculation logic of the particle sub-model, which is composed of a *deactivation model* and a *reaction model*. The main results from the deactivation model are the *overall system age number* (γ) and the particle activity ($\overline{X}_N$), with the latter depending on the calcination-carbonation cycles of each particle (N). The main outputs from the reaction model are the particle kinetic rate (k_x), the global reaction rate (K_r), and the particle conversion (X_{carb}). The value of X_{carb} is used to compute the carbonation efficiency of the particle sub-model (E_{PM}) based on a molar balance [212].

The validation of the carbonator model using over 60 balance points from pilot tests is illustrated in Figure 16. Figure 16 (left) compares the experimental and simulation values of the carbonator efficiency (E_{carb}), while Figure 16 (right) compares the experimental and simulation values of the carbonation degree at the carbonator outlet (X_{carb}). The simulation results agree with the time-averaged experimental data within the ± 20% relative error for most of the balance points. The main sources of error were the calculation of sorbent deactivation and the estimation of the sorbent circulation rate (F_R) from empirical data.

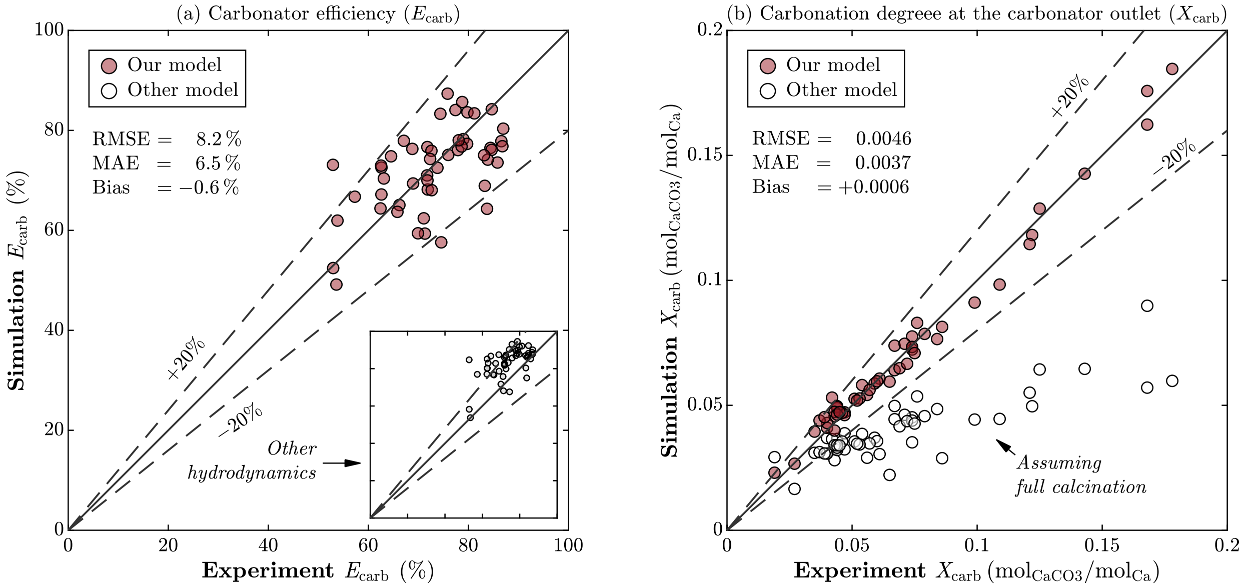

Figure 16. Validation of the carbonator model: reactor model (left, RP IV) and particle model (right, RP V).

An important finding is that the hydrodynamics are determinant for the calculation of the reactor performance. This is in line with the observation of Levenspiel [133], who stated that "often the lack of knowledge of the expected flow pattern in the reactor is the main cause of uncertainty in the design of reactors, not the kinetics." If the hydrodynamics model and constants fail to predict the carbonator's flow pattern, the prediction of E_{carb} from the carbonator model will be inaccurate. On the bottom-right corner of Figure 16 (left), we included the model's predictions assuming the set of assumptions for hydrodynamics from previous studies [141]. The simulation values of E_{carb} were much higher than those calculated from the empirical data, indicating that the set of hydrodynamics assumptions typically used in the literature overpredict our experimental results. If the sorbent is not fully calcined ($X_{calc} > 0$), the remaining $CaCO_3$ after the calciner—i.e., at the carbonator inlet—reduces the sorbent's CO_2 capture capacity [148]. However, previous studies have assumed that the sorbent entering the carbonator is fully calcined. Our model results indicate that this assumption introduces inaccuracies in predicting the performance of the IHCaL pilot plant (see Figure 16, right).

During pilot tests, we obtained higher capture rates operating in the turbulent fluidization regime (Figure 17). For higher velocities, beyond the onset of fast fluidization, it was not possible to achieve more than 75 % capture efficiency (see Figure 17, right). Our model predicts the capture efficiency in this region with acceptable accuracy but shows a slight positive bias. This may be caused by the loss of contact efficiency due to the transition into the fast fluidization regime. The lower performance cannot be explained form changes in the inventory.

Charitos et al. [73] compared two CaL test rigs. One of them was operated in the turbulent fluidization regime (INCAR-CSIC), whereas the other was operated in the fast fluidization regime (IFK). They concluded that the operation in both regimes is possible but reported that the gas-solid contact efficiency of the turbulent bed was 62 % higher than that of the fast-fluidized reactor. Our results point in the same direction. Recently, Diego and Arias [144] reported better carbonator performance for lower gas velocities, based on experimental results from a 1.7-$\mathrm{MW_{th}}$ CaL pilot facility. They explained that the inventory reduction due to increased entrainment was the cause of performance loss at higher velocities. Nevertheless, with appropriate reactor design and coupling devices (taller reactor, efficient cyclones, etc.) the high entrainment can be compensated for. Our observation of a shift in the fluidization regime gives a plausible explanation for the significant entrainment increase and the impaired reactor performance.

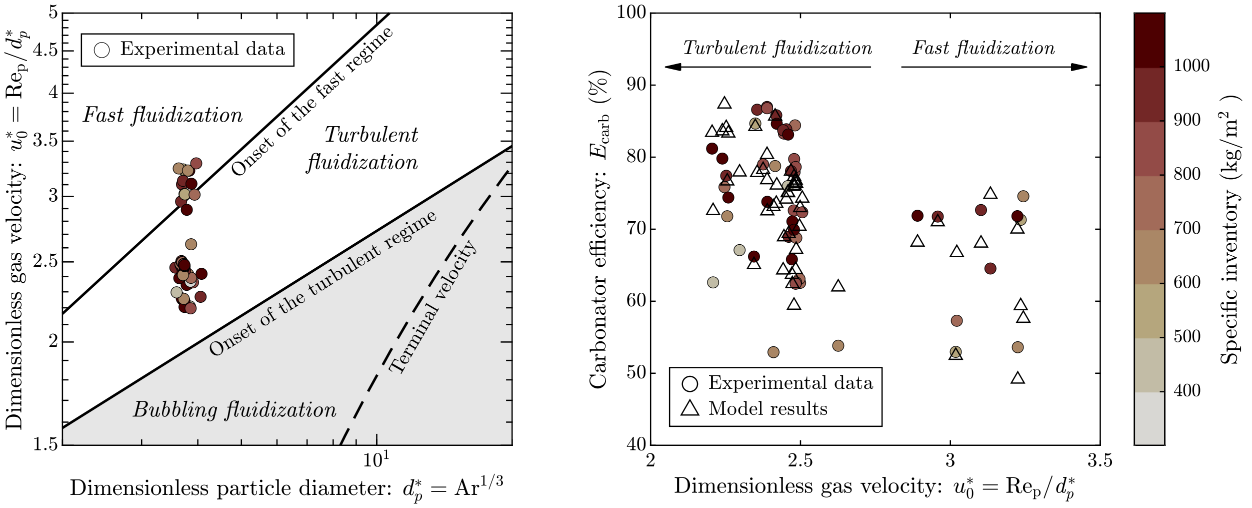

Figure 17. Carbonator performance and fluidization regime. The carbonator efficiency is higher for lower velocities corresponding with the turbulent regime. On the other hand, the influence of the inventory is low. Adapted from RP IV.

Regarding the influence of the inventory on the carbonator efficiency (E_{carb}), it is generally reported that high inventories increase CO_2 capture rates. We found this to be true up to a minimum threshold, after which E_{carb} is almost independent of the amount of sorbent in the reactor. This is explained by the low contact efficiency in the dense region or bed. As long as there is a minimum amount of material to maintain a dense bed at the bottom of the reactor, the lean region remains almost unaffected by the additional inventory. Our observations from the reactor sub-model match the experimental data well, which do not indicate any influence of the inventory in the reactor performance beyond a specific inventory of approximately 400 kg/m^2. A similar behavior has been reported in previous experimental studies. Diego et al. [144] observed a sharp decrease of CO_2 capture capacity below the 400-kg/m^2 threshold based on experimental data from a 1.7-$\mathrm{MW_{th}}$ plant. Haaf et al. [87] indicated a good carbonator performance for inventories between 400 and 500 kg/m^2 in a 1-$\mathrm{MW_{th}}$ CaL pilot plant.

The carbonator hydrodynamics for the pilot tests at the 300-$\mathrm{kW_{th}}$ pilot plant are illustrated in Figure 18. Figure 18.a displays the pressure distribution along the carbonator for four different operating conditions: low speed ($u_0^* < 2.6$) and high speed ($u_0^* > 2.6$), corresponding to turbulent and fast fluidization, and high inventory (> 45 kg) and low inventory (< 45 kg). The solid volume fraction (ε_s) was obtained by considering the weight of the particles as equal to the drag force generated by the upward-moving gas [139] and differentiating the pressure data numerically using a central-difference scheme [211]. The calculated solids distribution is illustrated in Figure 18.b for the balance points corresponding to the data of Figure 18.a. For all the balance points, a dense bed can be distinguished, which agrees with our modeling approach (see Figure 14, left). In Figure 18.b, our model predictions (indicated in red) are compared to those of previous studies (indicated in black) [141]. The main difference of our model is that we corrected the solid volume fraction (ε_s) in the dense region (bottom section of the reactor) and the decay ratio shaping the exponential curve in the lean region (top section of the reactor). This figure highlights that using model constants from previous studies can lead to significant inaccuracies in predicting the solids distribution. A similar finding had already been reported by Junk [213, p.113] when analyzing data from a 1-MW$_{\text{th}}$ CaL facility. He obtained higher values of ε_s in the dense region than those recommended in the literature for carbonator modeling. His hydrodynamics model was only able to predict the experimental results after adjusting this input. Accurately modeling carbonator hydrodynamics is crucial for achieving precise prediction of the carbonator efficiency. If the solids distribution is not properly modeled considering riser characteristics and operating conditions, the carbonator model may fail to predict the reactor behavior accurately.

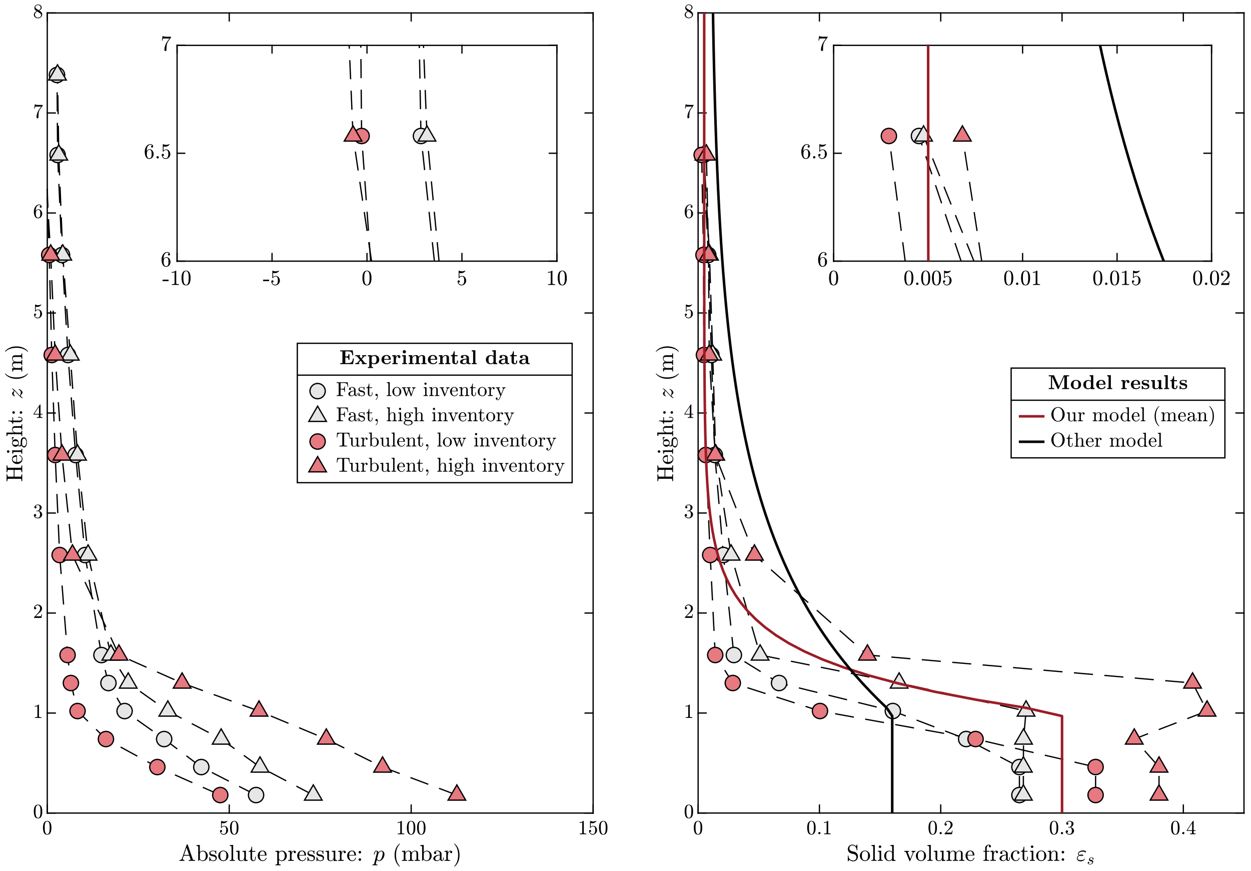

Figure 18. Hydrodynamics of the pilot plant: pressure experimental data (left), and solid volume fraction from experimental data compared with our model (mean values) and other model based on typical assumptions from the literature (right). Adapted from RP IV.

The model predictions indicate better performance for taller reactors and smaller cross sections. Other parameters influencing E_{carb} are the particle diameter (d_p^*) and the specific core-wall exchange coefficient ($k_{\text{c-w}}$). This indicates that reactor geometry, particle characteristics, and the operating regime have a significant impact on performance. These factors should be considered when scaling up the carbonator. This can be done by using our carbonator model and following the recommendations of RP IV and RP V.

The validation of the particle sub-model was performed using experimental data from pilot tests at the 300-kW$_{\text{th}}$ scale and TGA analysis from our experiments and from the open literature [140,207]. We considered three aspects for the validation: (i) validation of the reaction kinetics using TGA data; (ii) validation of the sorbent deactivation using results from pilot plant operation, which is independent of the reactor sub-model (see Figure 19); and (iii) validation of the entire model using pilot test results (see Figure 16, right). For the last aspect (iii), the overall model including the particle sub-model and the reactor sub-model is validated using the particle carbonation degree after the carbonator (X_{carb}).

The validation of the deactivation model is illustrated in Figure 19. The discrete results, represented by circles and triangles, were obtained from solid samples extracted from the 300-kW$_{\mathrm{th}}$ pilot plant during the 2016 test campaigns (see Section 1.4). To obtain the mean sorbent activities, the solid samples were fully calcined and recarbonized [122]. Since this methodology imposed an additional calcination-carbonation cycle, the activity from sorbent samples is denoted as $\bar{X}_{N+1}$. The mean sorbent activity ($\bar{X}_N$) of the model was obtained using the calculated values of γ based on the sorbent circulation and make-up rates from the pilot tests. The model results are indicated with a red continuous line. The same calculation was performed by starting the series at $N = 2$ (corresponding to $N+1$), yielding the model values of $\bar{X}_{N+1}$ for comparison with the results from solid samples. In Figure 19, these model results are displayed with a black continuous line. The calculated $\bar{X}_N$ is slightly higher than the values of X_{carb} determined from solid samples. This shows that the model's prediction is accurate, since $\bar{X}_N$ represents the maximum possible value of X_{carb}. The model results of $\bar{X}_{\mathrm{N+1}}$ fit the empirical data reasonably well. The deviations can be explained by the uncertainties in calculating the circulation and make-up rates, as well as the variability in the performance of the carbonator and the calciner. Overall, our deactivation model predicts the empirical data with reasonable accuracy, despite significant variations in make-up and circulation rates. An alternative calculation of $\bar{X}_{\mathrm{N+1}}$ using the deactivation model from Abanades et al. [185] resulted in a considerable overprediction of sorbent activity due to neglecting the particle age distribution.

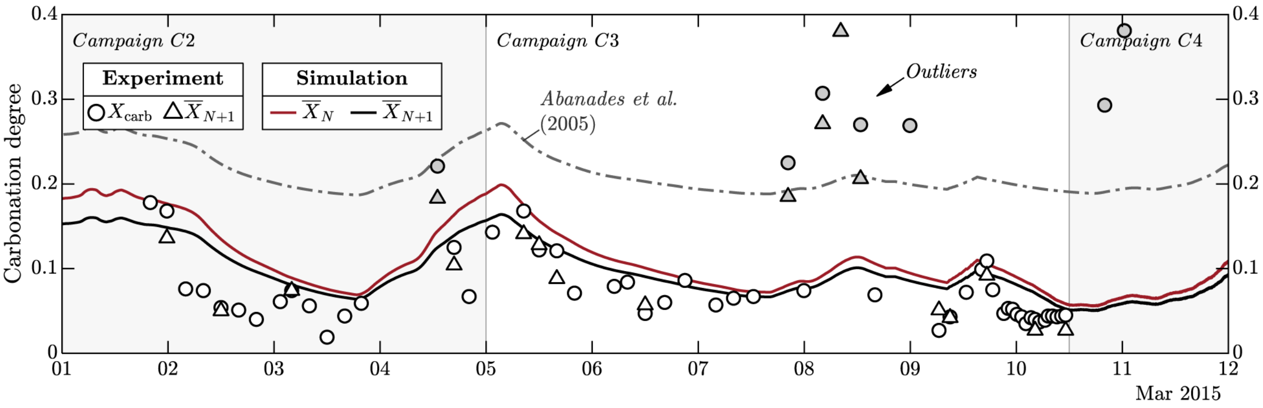

Figure 19. Sorbent behavior throughout the pilot tests: sorbent activity ($\bar{X}_N$), sorbent conversion (X_{carb}), and validation of the deactivation model. The markers represent discrete data from sorbent samples taken during the pilot tests. The gray markers correspond to outliers. Simulation results are indicated with lines. Adapted from RP V.

At the end of March 9, SO_2 was added to the gas entering the carbonator to evaluate the influence of this contaminant in the capture capacity. At around this time, many sorbent samples were taken. There is some overprediction of the sorbent activity, which may indicate that the deactivation due to the formation of $CaSO_4$ was higher than the one calculated with our model.

Overall, the carbonation degree of the particles at the carbonator outlet (X_{carb}) was relatively low. This may be due to prolonged periods with little or no make-up material added. Another possible reason is that the calciner was operated near equilibrium, which likely caused multiple recarbonation and calcination cycles within the reactor, accelerating particle deactivation. During some periods of low X_{carb}, high carbonation efficiency (E_{carb}) could still be achieved due to the high circulation rates.

Using our carbonator model, we estimated the influence of the calciner performance on E_{carb}. Previous works had done this, but only for a narrow set of operating conditions. In contrast, we evaluate the influence of the overall system age number ($\gamma \simeq F_R/F_0$) and the circulation rate (F_R/F_{CO2}) on the sensitivity to the degree of carbonation at the carbonator inlet (X_{calc}), which depends on E_{calc}—see Eq. (6). The result of this analysis is summarized in Figure 20. Atsonios et al. [134] used an Aspen Plus Gibbs reactor to take the calcination into account for their CaL CFD simulations. Assuming $F_R/F_{CO2} = 14$, they observed a drop in CO_2 capture efficiency for $X_{calc} > 0.04$. Our results confirm their observations for the case $\gamma = 50$ (see Figure 20.a).

If the sorbent circulation rate (F_R) is kept constant, there is an improvement in the maximum sorbent activity ($\bar{X}_N$) for lower E_{calc} (i.e., higher X_{calc}) due to a reduction in the number of effective calcination-carbonation cycles of the particles. However, this comes with a decrease in the carbonator efficiency (E_{carb}) due to the influence of E_{calc} in the carbonator performance. Rodríguez et al. [149] observed that if E_{carb} is maintained constant by increasing F_R, the value of $\bar{X}_N$ decreases with lower E_{calc}. They indicated that this effect is stronger for higher sorbent make-up rates. Nevertheless, as shown in Figure 20, systems with more aged sorbent are more sensitive to E_{calc}; thus, higher make-up rates reduce the sensitivity to calciner performance. In summary, CaL systems experiencing calcination issues will benefit from additional make-up.

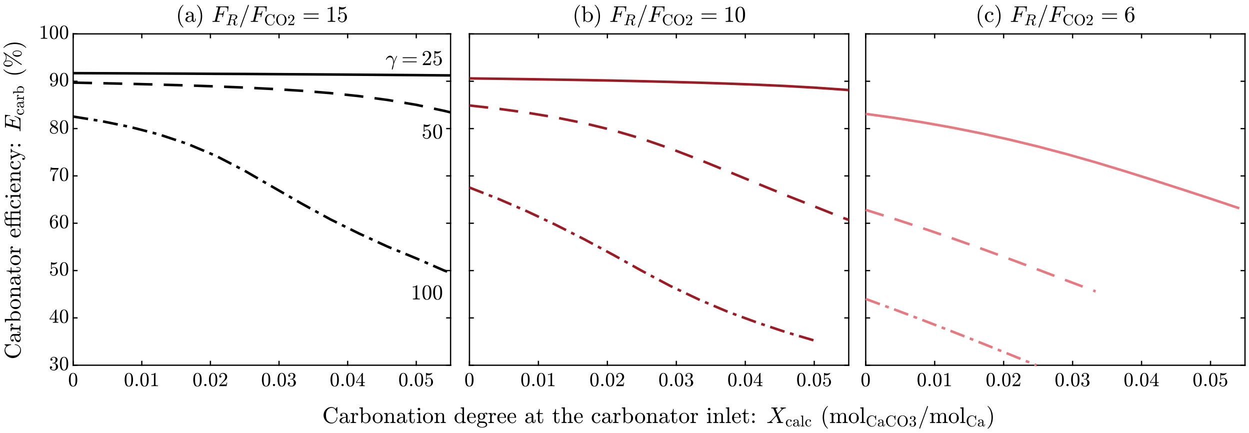
(a) $F_R/F_{CO2} = 15$
(b) $F_R/F_{CO2} = 10$
(c) $F_R/F_{CO2} = 6$

Figure 20. Variation of the carbonator efficiency (E_{carb}) with the calcination performance (characterized by X_{calc}). Results are displayed for different specific circulation rates (a–c) and different system ages (γ). Adapted from RP V.

Apart from the penalty in E_{carb}, the destination of the spent sorbent is to be considered for the design of the calciner. If the spent sorbent is to be used as quicklime or as material for the production of cement clinker, high calcination rates with mild operating conditions (e.g., low temperature) are desirable [125]. For some scenarios, it may be possible that the specifications of the spent sorbent are stricter than the process constraints.

In RP IV, we addressed *research sub-question (v)* by demonstrating that accurately modeling reactor hydrodynamics is essential for predicting carbonator performance, and by showing that turbulent fluidization offers advantages in operating carbonators for CO_2 capture. *Research sub-question (vi)* was primarily addressed in RP V, which highlighted the influence of calciner performance and sorbent activity on the carbonator efficiency, proving that calciner issues can be mitigated by increasing make-up rates.

In conclusion, many of the modeling assumptions found in the literature of carbonator models lead to overprediction of our pilot plant experimental data. RP IV and RP V present guidelines for accurate carbonator modeling, including procedures for deriving model constants from empirical data, improved gas-solid contact equations, a thorough discussion of fluidization regimes, a methodology for considering the influence of calciner performance, and a novel approach to include the effect of variations in sorbent circulation and make-up rates.

2.3 Calciner modeling and design

In **Research Paper VI** (RP VI), the CaL calciner is modeled and optimized based on results from TGA and pilot tests. The novel model consists of two sub-models: a *particle sub-model*, considering particle conversion and kinetics, and a *reactor sub-model* for the simulation of the gas conversion and the calculation of the CO_2 concentration throughout the reactor height.

The particle sub-model consists of a volumetric (R3) shrinking model using the dependency on the CO_2 partial pressure (p_{CO2}) from García-Labiano et al. [66]. Other models, such a shrinking surface model (see [214]), were also considered, but the R3 mechanism provided the best fit. An

Arrhenius-type dependency is assumed to include the effect of temperature on the reaction rate. To obtain the main kinetic parameters, thermogravimetric analyses (TGA) were performed using an STA 449 *F3 Jupiter* TGA from the company Netzsch [215]. The analyzed samples consisted of 3 mg of the sorbent used in the pilot tests, specifically Messinghausen limestone (98.3 wt.% CaO). For the TGA tests, the particle size of the samples was 106–200 μm. The temperatures varied between 850 °C and 875 °C, and the CO_2 partial pressure was in the range 10–70 kPa. Figure 21 illustrates the results of the TGA tests as well as the fitting exercise with the R3 model. The model predicts all test points with a root mean square error (RMSE) lower than 3 %.

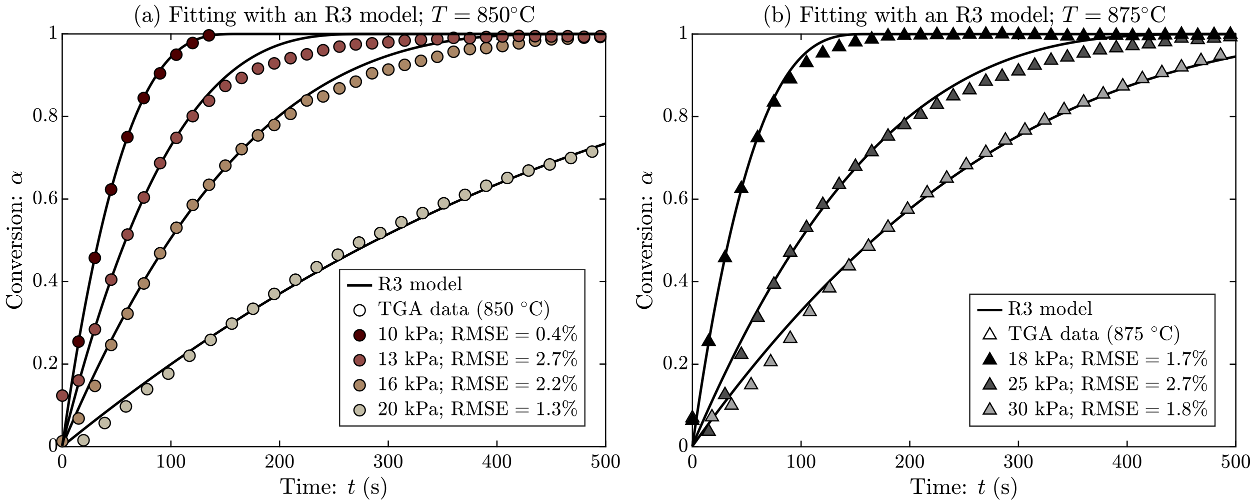

Figure 21. Data from TGA fitted with a volumetric shrinking model (R3) for different temperature and partial pressures. The best fit was achieved with the R3 model, which was used for the calculations in the calciner model. Adapted from RP VI.

The total calcination at the calciner outlet is calculated using a residence time distribution (RTD) to account for the contributions of each particle. We assume perfect mixing of the particles in the calciner, following previous studies on modeling of fluidized beds [63,146,162]. We derived the following expression for the calcination efficiency dependent only on the calcination time (t_c), i.e., the time to achieve full calcination, and the mean particle residence time in the calciner (τ):

$$E_{\text{calc}} = \left[1 - \exp\left(-t_c / \tau\right)\right] 6\left(\tau / t_c\right)^3 - 6\left(\tau / t_c\right)^2 + 3\left(\tau / t_c\right) \tag{17}$$

The calcination time (t_c) is obtained using the particle sub-model. Since this parameter depends on p_{CO2}, which varies along the reactor, t_c is calculated using an equivalent CO_2 partial pressure (p^*_{CO2}), which is obtained iteratively with the reactor sub-model. To achieve an efficiency of 90% in the calciner, a mean residence time of $\tau \approx 2\ t_c$ is required.

An important novelty of our calciner model is the calculation of the CO_2 concentration throughout the reactor height using a Kunii and Levenspiel (K-L) reactor sub-model [137]. This approach enables accurate predictions for both the oxy-fired and indirectly heated calciners, without requiring significant computational effort. The model was implemented in MATLAB R2023b. For the computation of the entire model, we followed a similar approach to that used in previous works on reactor modeling (mainly [141,212]). This approach involves solving the particle and reactor sub-models iteratively until an equivalent CO_2 partial pressure (p^*_{CO2}) that satisfies the mass balance is obtained.

In RP VI, we introduce two dimensionless parameters to enable generalized predictions of calciner performance, and to support effective calciner assessment and design across a wide range of operating conditions: the *driving force* (DF) and the *dimensionless active time* (τ^*_{act}). The driving force, DF, is the ratio of the equilibrium CO_2 partial pressure ($p_{CO2,\text{eq}}$) to the maximum achievable CO_2 partial pressure at the calciner outlet corresponding to full calcination ($p^*_{CO2,\text{out}}$):

$$\text{DF} = p_{CO2,\text{eq}} \Big/ p^*_{CO2,\text{out}}; \qquad p^*_{CO2,\text{out}} = \frac{p}{1 + \left[\overline{X}_{\text{carb}}\, F_{R+0} \Big/ F_{\text{inert}} - \left(1 - p / p_{CO2,\text{in}}\right)^{-1}\right]^{-1}} \tag{18}$$

In Eq. (18), $p_{CO2,eq}$ is the equilibrium CO_2 partial pressure from Eq. (3), p is the reactor pressure (typically atmospheric), $\overline{X}_{carb}$ F_R is the molar flow rate of carbonate into the calciner, F_{inert} is the molar flow rate of inert fluidization gases (e.g., N_2, H_2O), and $p_{CO2,in}$ is the CO_2 partial pressure at the calciner inlet. The term $\overline{X}_{carb}\, F_R / F_{inert}$ represents the influence of the CO_2 generated through calcination on p_{CO2}. Increasing this term or the inlet CO_2 partial pressure ($p_{CO2,in}$) reduces DF, making it more challenging to obtain high levels of calcination. The definition of DF is based on the premise that the ratio $p_{CO2,eq}/p_{CO2}$ is the primary driver of calcination, which strongly aligns with empirical observations [66]. Eq. (18) was obtained by performing a molar balance in the calciner. Figure 22 (left) illustrates the influence of DF on the calciner efficiency using both experimental and modeling results.

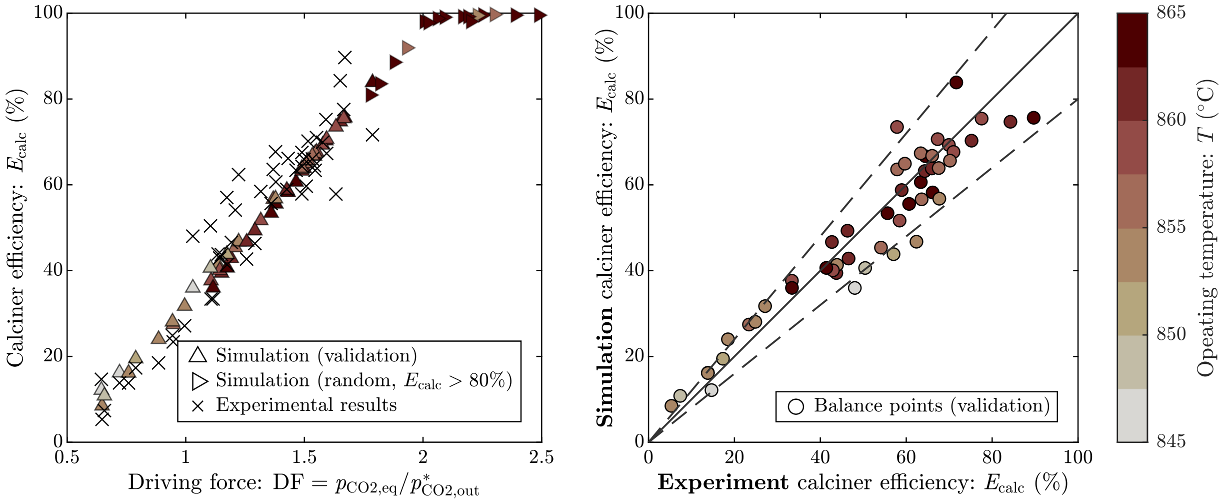

Figure 22. Validation of the calciner model with results from pilot tests at the 300-kW$_{th}$ pilot plant. The dependence of the calciner efficiency on the driving force DF (left) and the parity plot (right) show agreement between the model and the empirical results. The broken lines in the party plot (right) indicate a 20 % deviation from the experimental values. Adapted from RP VI.

The *dimensionless active time* (τ^*_{act}) is used to assess the influence of the particle residence time on the calciner efficiency. This parameter is derived from the ratio of mean particle residence time (τ) to calcination time (t_c), which governs calciner performance (see Eq. (17)). Using our particle model, we obtain the following definition of τ^*_{act}:

$$\tau^*_{act} = \frac{\tau}{3\overline{X}_{carb}/k_c} \tag{19}$$

Here, k_c is the particle kinetic rate obtained with the particle model and data from TGA tests. The denominator ($3\ \overline{X}_{carb}/k_c$) corresponds to the calcination time (t_c) without the function that accounts for the influence of the CO_2 partial pressure, as this effect is already incorporated into DF. The factor 3 depends on the influence of the particle conversion on the calcination rate and should be adjusted if a different particle model is used. Since the dimensionless active time (τ^*_{act}) depends on the specific kinetics of the sorbent, it can be used to derive general results, applicable across a wide range of operating conditions, including different sorbents. We recommend using τ^*_{act} only in conjunction with DF.

Our calciner model was validated with experimental data from two different pilot tests at the TU Darmstadt: the 300-kW$_{th}$ IHCaL pilot plant with a heat-pipes heat exchanger, featuring a bubbling fluidized bed (BFB) calciner [118,120]; and the 1-MW$_{th}$ oxy-fired CaL plant with a circulating fluidized bed (CFB) calciner [177,216]. The validation using results from IHCaL pilot tests is illustrated in Figure 22. In Figure 22 (right), each marker represents a balance point in which sorbent samples were taken. For each balance point, two-hour average values were calculated and used as inputs for the calciner model. The simulation results align with the empirical values. The validation results are also included in Figure 22 (left) to demonstrate that the simulation and experimental results exhibit similar variations with DF. To illustrate the influence of higher driving forces (DF), we ran our calciner model using random input parameters representative of the IHCaL pilot plant, following the methodology explained in RP VI. The results shown in Figure 22 (left) correspond to cases where $E_{\mathrm{calc}} > 80$ %.

In RP VI, we use our calciner model to derive generalized predictions of calciner performance using a stochastic methodology. To do this, we ran our model 5,000 times with randomly generated inputs corresponding to commercial IHCaL and oxy-combustion CaL facilities. To interpret the results, we use the dimensionless numbers DF and τ^{*}_{act}. Figure 23 illustrates the influence of DF and τ^{*}_{act} on the calciner efficiency (E_{calc}). For calciners with high specific inventories ($\tau^{*}_{\mathrm{act}} > 100$), DF = 2 delivers optimal performance. For lower specific inventories, $\tau^{*}_{\mathrm{act}} = 15$ is effective with DF = 3. However, additional optimal combinations are possible (see Figure 23, right). In general, the lower the τ^{*}_{act}, the higher the DF required to achieve high calciner efficiency.

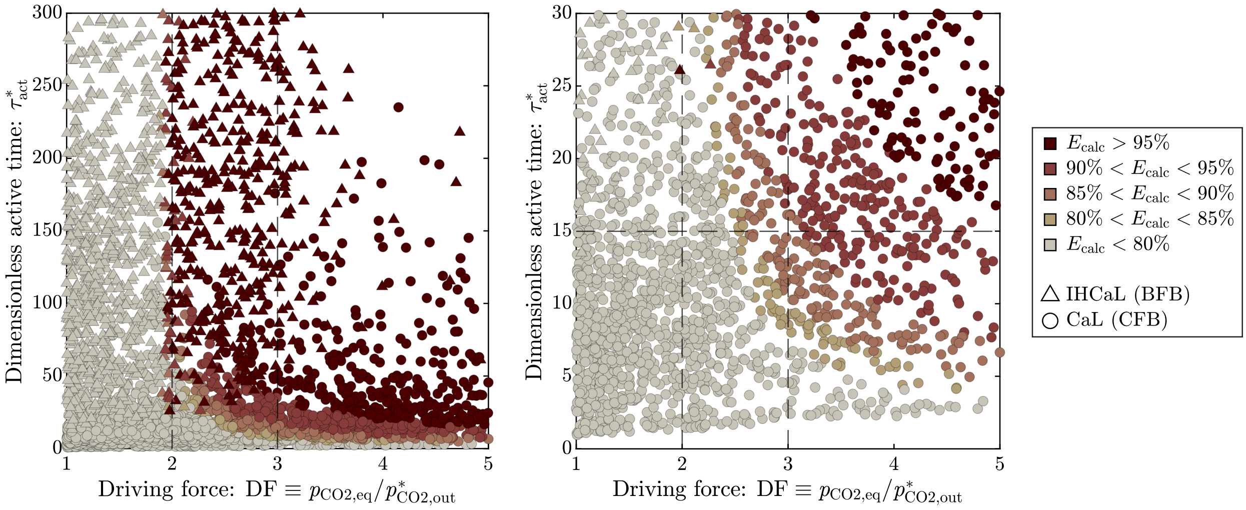

Figure 23. Calciner performance (E_{calc}) for varying DF and τ^{*}_{act}, using our calciner model and the operating conditions corresponding to IHCaL (BFB) and oxy-fuel CaL (CFB) operation. The two sub-figures show the same results but use different scales for τ^{*}_{act}. No. of model runs: 5,000. Adapted from RP VI.

Using the results from our study, we developed a simple methodology for optimizing the calciner design. For oxy-fired calciners, the condition $\tau^{*}_{\mathrm{act}} \geq 15$ should be verified and the calciner operating temperature (T) is obtained by setting DF = 3 in Eq.(18). For realistic operating conditions, T will be in the range 930–965 °C. For indirectly heated calciners (IHCaL) we set $T = 950$ °C unless steam is used to lower the operating temperature. Some possible set points are $T = 900$ °C with a steam ratio (SR) of $SR = 0.4\ \mathrm{kg_{H2O}/kg_{CO2}}$, and $T = 925$ °C with $SR = 0.2\ \mathrm{kg_{H2O}/kg_{CO2}}$.

In conclusion, RP VI addressed *research sub-question (vi)* by developing a calciner model capable of accurately predicting calciner operation for IHCaL and CaL systems. The model was validated with data from tests performed at different facilities, which indicates its wide range of application. The guidelines derived using the calciner model and a stochastic methodology allow minimizing energy penalties without compromising CO_2 capture efficiency.

2.4 Conclusion

This dissertation brings IHCaL CO_2 capture technology for lime plants closer to commercialization by developing novel integration concepts, enhancing the understanding of this technology through new reactor models, and demonstrating the competitiveness of the analyzed configurations via techno-economic analysis. Our study provides valuable information on the potential of indirectly heated carbonate looping technology (IHCaL) for reducing CO_2 emissions in the lime industry. Furthermore, it demonstrates how process configurations, fuel properties, operating parameters, and components can be optimized to exploit this potential. The results from this cumulative dissertation led to the following answers to the research sub-questions:

i) What are the key integration parameters influencing heat requirements and energy efficiency in lime plants with CO_2 capture using IHCaL technology?

The critical integration parameters are the preheating temperature of the combustion air, the temperature of the sorbent stream at the calciner inlet, and the circulation ratio. Additionally, the utilization of the sorbent purge as lime product is required for the feasibility of the integrated concepts. For a highly integrated IHCaL configuration, there is an increase of 63 % in the direct fuel requirement, but almost 30 % of the entire heat input can be converted into electric power via heat recovery steam generation. Lastly, we found that heat recovery in IHCaL processes can be tailored to achieve desired outcomes such as reduced fuel consumption or enhanced power generation.

ii) What is the potential for achieving net-negative CO_2 emissions using IHCaL technology in the lime production, and how can this potential be exploited?

Negative CO_2 emissions are achievable using waste-derived fuels. Using IHCaL technology, we attained emission reductions exceeding 200 % of the CO_2 emissions of the reference lime plant without CO_2 capture.

iii) How do fuel type and properties influence the economic and energy performance of the integrated IHCaL capture process in the lime production?

Efficient primary energy utilization is achieved by firing fuels with high biogenic fraction and low specific CO_2 emissions, such as high-calorific solid recovered fuels (SRFs). The evaluated waste-derived fuels generate a significant reduction in CO_2 avoidance costs, compared to using dried lignite to fire the combustor. The reason for this is the lower fuel cost and the additional revenue associated with capturing the biogenic CO_2.

iv) What is the cost-reduction potential of the IHCaL process for CO_2 capture from the lime production?

We obtained CO_2 avoidance costs lower than 20 €/$t_{CO2,av}$ using solid-recovered fuel (SRF). The developed IHCaL concepts are competitive with alternative CO_2 capture technologies for the lime production, which have avoidance costs of at least 30 €/$t_{CO2,av}$.

v) What is the influence of carbonator hydrodynamics on the CO_2 capture efficiency of an IHCaL system?

Inaccurate hydrodynamics models lead to significant overestimation of the CO_2 capture efficiency in carbonator models. The newly developed carbonator model, which successfully predicts empirical data of the 300-kW_{th} IHCaL pilot plant, indicates that operating in the turbulent fluidization regime is advantageous in terms of reactor performance. Based on this model, we provided guidelines for selecting model assumptions and designing carbonators for efficient CO_2 capture.

vi) How do operating parameters and calciner performance affect sorbent activity in an IHCaL system, and how does sorbent activity, in turn, impact the overall performance of the process?

The assessment performed with the carbonator model showed that the calcination efficiency influences the carbonator performance differently depending on operating conditions. The sensitivity to calcination efficiency is highly influenced by the sorbent circulation rate and the sorbent activity. Poor calciner performance in CaL and IHCaL systems can be compensated for by increasing sorbent make-up rates. Our results show that previous models fail to accurately predict the capture efficiency of the IHCaL pilot plant due to the assumption of ideal calcination.

vii) How can the operating conditions of an IHCaL calciner be optimized to reduce the energy penalty of the process without compromising CO_2 capture efficiency?

We developed a new calciner model that predicts the calcination efficiency of an IHCaL and a CaL pilot plant accurately. Modeling the CO_2 concentration distribution in the calciner is crucial for predicting the performance of the indirectly heated calciner. Our model was used to derive optimization guidelines for the design of calciners. Calciners with oxy-fuel combustion should be operated at 930–965 °C to accomplish sufficient sorbent regeneration. For indirectly heated calciners, an operating temperature of 950 °C is required to achieve high performance. Lower temperatures (e.g., 900 °C) are also possible if steam is used for fluidization.

2.5 Outlook

Despite the contributions of this dissertation to advancing IHCaL and CaL technology, significant research efforts are still required for commercialization. In this section, we outline key contributions that need to be made in terms of process development, reactor modeling, and experimental research.

Process development

The reactor models (RP IV–VI) were developed after the process assessment was finalized (RP I–III). For this reason, previous models from the literature were used in the process assessment. These previous models have some limitations, which were pointed out throughout this dissertation. Studies following up on our work should reassess our conclusions from process modeling considering our improved reactor models and our observations from IHCaL pilot operation. Furthermore, the methodology developed and the results obtained in this dissertation provide a valuable foundation for integrating the IHCaL process into other industrial applications, such as cement production and steelmaking—an area that remains insufficiently explored.

For the commercialization of IHCaL technology, the heat integration was found to be critical. Simulation results and techno-economic indicators are promising if optimistic assumptions are made regarding preheating of the combustion air and performance of the solid-solid heat exchanger. However, the technical and economic feasibility of achieving the heat transfer rates required is yet to be demonstrated. Further research should focus on developing key integration components and demonstrating them with experimental tests.

In this dissertation, we optimized the IHCaL process in a broad sense, meaning that we suggest design considerations based on model predictions, experience, and good judgement. In many cases, the best design decision was immediately obvious. However, to further advance the IHCaL process, a more rigorous optimization based on formally setting up and solving mathematical optimization problems may be useful [217]. An example of this could be a mathematical optimization based on the minimization of the CO_2 avoidance costs. Considering the many parameters influencing the reactor and process models, as well as the increasing complexity required to achieve accurate simulations, artificial intelligence (AI) may be deployed to accelerate calculations without compromising accuracy [218]. The implementation of AI can bring benefit to empirical studies as well by aiding in interpreting large experimental datasets.

Reactor modeling

Although we were able to validate our carbonator model, more data is required to ensure that the model predictions are still valid up to higher scales and for a wider range of operating conditions. Additionally, the radial solids distribution was not simulated in detail in our reactor sub-model. Further work should assess whether this may affect the accuracy of our model under different operating conditions, and if so, improve the model to achieve a more detailed description of the radial solids distribution. The effect of attrition can also be incorporated [219]. Sorbent deactivation due to influence of real flue gases containing SOx, NOx, Cl, and solid particles is currently being investigated through long-term tests at CaL pilot plants. The findings from ongoing projects should be used to update our model to different operating conditions, including those relevant to CO_2 capture from lime and cement plants, waste to energy (WtE) facilities, and steel mills.

The calciner model was validated using tests data from two pilot plants, which exhibited significant differences in operating conditions, such as particle residence time in the calciner.

Further research should explore whether our model and general guidelines are also applicable to different sorbents and operating conditions. Additionally, follow-up studies should explore if even lower operating temperatures can be achieved due to the catalytic effect of steam on calcination, which was neglected in our model [220,221]. Similarly, other proposed strategies for decreasing the calciner's temperature may also be integrated in our model [164].

Experimental research

Further experimental research in pilot and demonstration plants is still needed before CaL and IHCaL technologies can be deployed on a commercial scale without incurring significant risks. The results of ongoing projects will be key to achieving commercialization in the near future.

Until now, the IHCaL process with heat pipes has only been demonstrated using air to fluidize the calciner [120,121]. However, this does not correspond to real operating conditions. Future pilot tests should demonstrate the feasibility of IHCaL technology using realistic fluidization gases for the calciner: CO_2 from EGR, steam, or a combination of both. Utilization of the spent sorbent is a *conditio sine qua non* for the industrial application of the IHCaL process. Therefore, the resulting samples from pilot operation under more realistic calcination conditions should be analyzed to validate this type of integration.

Within the ACT ANICA project and the current dissertation, a capture efficiency of 90 % and above has been considered sufficient [124]. However, higher capture efficiencies may not only viable but also advantageous [222]. Different strategies have been proposed to achieve better carbonator performance in CaL systems, such as cooling the higher regions of the carbonator [88] and injecting $Ca(OH)_2$ (slaked lime) [223]. Enhancing the carbonator efficiency under IHCaL operation should be the focus of future research and pilot tests, with the models developed in this work updated accordingly.

Other forms of calcination with CO_2 capture based in the IHCaL process may result in more efficient energy utilization and reduced costs. One of these processes is the indirect calcination process with integrated CO_2 capture developed by Greco-Coppi et al. [224]. This process is based on IHCaL technology but avoids looping the sorbent, thereby significantly reducing sorbent deactivation and energy losses associated with heating solids. Future studies should focus on validating this process through experimental tests in a semi-industrial environment.

References

[1] J.A. Oates, Lime and limestone, Wiley-VCH, Weinheim, 1998. https://doi.org/10.1002/9783527612024.

[2] M. Kenny, T. Oates, Lime and limestone, in: Ullmann's encyclopedia of industrial chemistry, 2007. https://doi.org/10.1002/14356007.a15_317.pub2.

[3] F. Schorcht, I. Kourti, B.M. Scalet, S. Roudier, L. Delgado Sancho, Best available techniques (BAT) reference document for the production of cement, lime and magnesium oxide: Industrial Emissions Directive 2010/75/EU (integrated pollution prevention and control), Publications Office, Luxembourg, 2013. https://doi.org/10.2788/12850.

[4] IEA, Energy Technology perspectives 2020 - Special report on carbon capture utilisation and storage: CCUS in clean energy transitions, OECD Publishing, Paris, 2020. https://doi.org/10.1787/208b66f4-en.

[5] Mineral Products Association (MPA) Lime, Net negative 2040 roadmap, 2023.

[6] M. Eriksson, B. Hökfors, R. Backman, Oxyfuel combustion in rotary kiln lime production, *Energy Science & Engineering* 2 (2014), pp. 204–215. https://doi.org/10.1002/ese3.40.

[7] M. Erans, D. Hanak, J. Mir, E.J. Anthony, V. Manovic, Process modelling and techno-economic analysis of natural gas combined cycle integrated with calcium looping, *Thermal Science* 20 (2016), pp. 59–67. https://doi.org/10.2298/TSCI151001209E.

[8] Y. Yang, L. Wang, D. Xia, Z. Jiang, B. Jiang, P. Zhang, Novel lime calcination system for CO_2 capture and its thermal-mass balance analysis, *ACS omega* 5 (2020), pp. 27413–27424. https://doi.org/10.1021/acsomega.0c03850.

[9] M. Jafarian, B.B. Dally, G.J. Nathan, Hydrogen peroxide for fuel oxidation to achieve CO_2 capture from lime production, *Energy Conversion and Management: X* 15 (2022) 100276. https://doi.org/10.1016/j.ecmx.2022.100276.

[10] P. Busch, A. Kendall, C.W. Murphy, S.A. Miller, Literature review on policies to mitigate GHG emissions for cement and concrete, *Resources, Conservation and Recycling* 182 (2022) 106278. https://doi.org/10.1016/j.resconrec.2022.106278.

[11] D.R. Nhuchhen, S.P. Sit, D.B. Layzell, Decarbonization of cement production in a hydrogen economy, *Applied Energy* 317 (2022) 119180. https://doi.org/10.1016/j.apenergy.2022.119180.

[12] C. Carbone, D. Ferrario, A. Lanzini, S. Stendardo, A. Agostini, Evaluating the carbon footprint of cement plants integrated with the calcium looping CO_2 capture process, *Frontiers in Sustainability* 3 (2022) 809231. https://doi.org/10.3389/frsus.2022.809231.

[13] R.M. Andrew, Global CO_2 emissions from cement production, *Earth System Science Data* 10 (2018), pp. 195–217. https://doi.org/10.5194/essd-10-195-2018.

[14] European Lime Association, A pathway to negative CO_2 emissions by 2050 (2023).

[15] B. Dziejarski, R. Krzyżyńska, K. Andersson, Current status of carbon capture, utilization, and storage technologies in the global economy: A survey of technical assessment, *Fuel* 342 (2023) 127776. https://doi.org/10.1016/j.fuel.2023.127776.

[16] Global CCS Institute, Global Status of CCS (2021).

[17] V. Becattini, P. Gabrielli, C. Antonini, J. Campos, A. Acquilino, G. Sansavini, M. Mazzotti, Carbon dioxide capture, transport and storage supply chains: Optimal economic and environmental performance of infrastructure rollout, *International Journal of Greenhouse Gas Control* 117 (2022) 103635. https://doi.org/10.1016/j.ijggc.2022.103635.

[18] Y. Seo, C. Huh, S. Lee, D. Chang, Comparison of CO_2 liquefaction pressures for ship-based carbon capture and storage (CCS) chain, *International Journal of Greenhouse Gas Control* 52 (2016), pp. 1–12. https://doi.org/10.1016/j.ijggc.2016.06.011.

[19] S. Bachu, Review of CO_2 storage efficiency in deep saline aquifers, *International Journal of Greenhouse Gas Control* 40 (2015), pp. 188–202. https://doi.org/10.1016/j.ijggc.2015.01.007.

[20] Z. Dai, R. Middleton, H. Viswanathan, J. Fessenden-Rahn, J. Bauman, R. Pawar, S.-Y. Lee, B. McPherson, An integrated framework for optimizing CO_2 sequestration and enhanced oil recovery, *Environmental Science & Technology Letters* 1 (2014), pp. 49–54. https://doi.org/10.1021/ez4001033.

[21] IPCC, Climate change 2022: Mitigation of climate change. Contribution of Working Group III to the Sixth Assessment Report of the Intergovernmental Panel on Climate Change, 2022. https://doi.org/10.1017/9781009157926.

[22] IPCC, Global warming of 1.5°C: An IPCC Special Report on the impacts of global warming of 1.5°C above pre-industrial levels and related global greenhouse gas emission pathways, in the context of strengthening the global response to the threat of climate change, 2018.

[23] M.A. Quader, S. Ahmed, Bioenergy with carbon capture and storage (BECCS), in: M.G. Rasul, A.K. Azad, S.C. Sharma (Eds.), Clean energy for sustainable development: Comparisons and contrasts of new approaches, Academic Press, Amsterdam, Boston, Heidelberg, London, New York, Oxford, Paris, San Diego, San Francisco, Singapore, Sydney, Tokyo, 2017, pp. 91–140. https://doi.org/10.1016/B978-0-12-805423-9.00004-1.

[24] C. Merk, J. Grunau, M.-C. Riekhof, W. Rickels, The need for local governance of global commons: The example of blue carbon ecosystems, *Ecological Economics* 201 (2022) 107581. https://doi.org/10.1016/j.ecolecon.2022.107581.

[25] L. Clarke, K. Jiang, K. Akimoto, M. Babiker, G. Blanford, K. Fisher-Vanden, J.C. Hourcade, V. Krey, E. Kriegler, A. Löschel, Assessing Transformation Pathways, in: O. Edenhofer (Ed.), Climate change 2014: Mitigation of climate change; Working Group III contribution to the Fifth Assessment Report of the Intergovernmental Panel on Climate Change, Cambridge Univ. Press, New York, NY, 2014, pp. 413–510. https://doi.org/10.1017/CBO9781107415416.012.

[26] M. Wilkes, S. Brown, Decarbonizing the Lime & Cement industry using BECCS: a mini-review, in: Proceedings of the 17th International Conference on Greenhouse Gas Control Technologies, 20–24 Oct, 2024. https://doi.org/10.2139/ssrn.5016506.

[27] J.G. Vitillo, B. Smit, L. Gagliardi, Introduction: Carbon capture and separation, *Chemical reviews* 117 (2017), pp. 9521–9523. https://doi.org/10.1021/acs.chemrev.7b00403.

[28] J.R. Fernández, An overview of advances in CO_2 capture technologies, *Energies* 16 (2023) 1413. https://doi.org/10.3390/en16031413.

[29] Y. Guo, L. Luo, T. Liu, L. Hao, Y. Li, P. Liu, T. Zhu, A review of low-carbon technologies and projects for the global cement industry, *Journal of Environmental Sciences* 136 (2024), pp. 682–697. https://doi.org/10.1016/j.jes.2023.01.021.

[30] J. Ströhle, C. Hofmann, M. Greco-Coppi, B. Epple, CO_2 capture from lime and cement plants using an indirectly heated carbonate looping process – The ANICA project, in: N.A. Røkke, H.K. Knuutila (Eds.), TCCS-11: CO_2 capture, transport and storage, Trondheim, 22nd-23rd June 2021: Short papers from the 11th International Trondheim CCS Conference, SINTEF Academic Press, Oslo, 2021, pp. 529–535.

[31] Lhoist, Carbon action 2030 (2021).

[32] D.Y. Leung, G. Caramanna, M.M. Maroto-Valer, An overview of current status of carbon dioxide capture and storage technologies, *Renewable and Sustainable Energy Reviews* 39 (2014), pp. 426–443. https://doi.org/10.1016/j.rser.2014.07.093.

[33] IPCC, IPCC special report on carbon dioxide capture and storage, 1st ed., Cambridge Univ. Press, Cambridge, 2005.

[34] J. Karl, *Dezentrale Energiesysteme*: *Neue Technologien im liberalisierten Energiemarkt*, 3rd ed., Oldenbourg-Verl., München, 2012.

[35] J. Young, N. McQueen, C. Charalambous, S. Foteinis, O. Hawrot, M. Ojeda, H. Pilorgé, J. Andresen, P. Psarras, P. Renforth, S. Garcia, M. van der Spek, The cost of direct air capture and storage can be reduced via strategic deployment but is unlikely to fall below stated cost targets, *One Earth* 6 (2023), pp. 899–917. https://doi.org/10.1016/j.oneear.2023.06.004.

[36] S. Rackley, Overview of negative emissions technologies, in: S. Rackley (Ed.), Negative emissions technologies for climate change mitigation, Elsevier, 2023, pp. 19–39. https://doi.org/10.1016/B978-0-12-819663-2.00001-0.

[37] H.C. Lau, S. Ramakrishna, K. Zhang, A.V. Radhamani, The role of carbon capture and storage in the energy transition, *Energy & Fuels* 35 (2021), pp. 7364–7386. https://doi.org/10.1021/acs.energyfuels.1c00032.

[38] J.O. Ejeh, A.Z. Yousef, P. Bugryniec, M.D. Wilkes, R.T.J. Porter, S. Martynov, H. Mahgerefteh, S. Brown, Perspectives on future CCUS infrastructure design, in: Proceedings of the 16th International Conference on Greenhouse Gas Control Technologies, 23–24 Oct, 2022. https://doi.org/10.2139/ssrn.4271511.

[39] Z. Abbas, T. Mezher, M.R. Abu-Zahra, CO_2 purification. Part I: Purification requirement review and the selection of impurities deep removal technologies, *International Journal of Greenhouse Gas Control* 16 (2013), pp. 324–334. https://doi.org/10.1016/j.ijggc.2013.01.053.

[40] D. Jansen, M. Gazzani, G. Manzolini, E. van Dijk, M. Carbo, Pre-combustion CO_2 capture, *International Journal of Greenhouse Gas Control* 40 (2015), pp. 167–187. https://doi.org/10.1016/j.ijggc.2015.05.028.

[41] C.-C. Cormos, Decarbonization options for cement production process: A techno-economic and environmental evaluation, *Fuel* 320 (2022) 123907. https://doi.org/10.1016/j.fuel.2022.123907.

[42] A. Rolfe, Y. Huang, M. Haaf, A. Pita, S. Rezvani, A. Dave, N.J. Hewitt, Technical and environmental study of calcium carbonate looping versus oxy-fuel options for low CO_2 emission cement plants, *International Journal of Greenhouse Gas Control* 75 (2018), pp. 85–97. https://doi.org/10.1016/j.ijggc.2018.05.020.

[43] D.J. Barker, S.A. Turner, P.A. Napier-Moore, M. Clark, J.E. Davison, CO_2 capture in the cement industry, *Energy Procedia* 1 (2009), pp. 87–94. https://doi.org/10.1016/j.egypro.2009.01.014.

[44] F. Carrasco, S. Grathwohl, J. Maier, J. Ruppert, G. Scheffknecht, Experimental investigations of oxyfuel burner for cement production application, *Fuel* 236 (2019), pp. 608–614. https://doi.org/10.1016/j.fuel.2018.08.135.

[45] S. Gardarsdottir, E. de Lena, M.C. Romano, S. Roussanaly, M. Voldsund, J.-F. Pérez-Calvo, D. Berstad, C. Fu, R. Anantharaman, D. Sutter, M. Gazzani, M. Mazzotti, G. Cinti, Comparison of technologies for CO_2 capture from cement production—Part 2: Cost analysis, *Energies* 12 (2019) 542. https://doi.org/10.3390/en12030542.

[46] M. Voldsund, S. Gardarsdottir, E. de Lena, J.-F. Pérez-Calvo, A. Jamali, D. Berstad, C. Fu, M.C. Romano, S. Roussanaly, R. Anantharaman, H. Hoppe, D. Sutter, M. Mazzotti, M. Gazzani, G. Cinti, K. Jordal, Comparison of technologies for CO_2 capture from cement production—Part 1: Technical evaluation, *Energies* 12 (2019) 559. https://doi.org/10.3390/en12030559.

[47] Schwenk, *Forschungsprojekt* „catch4climate“: *Große Fortschritte beim Bau der CO_2-Abscheide-Anlage in Mergelstetten*, 2024, https://www.schwenk.de/forschungsprojekt-catch4climate-grosse-fortschritte-beim-bau-der-co2-abscheide-anlage-in-mergelstetten/, accessed 23 November 2024.

[48] C.d.S. Cachola, M. Ciotta, A. Azevedo dos Santos, D. Peyerl, Deploying of the carbon capture technologies for CO_2 emission mitigation in the industrial sectors, *Carbon Capture Science & Technology* 7 (2023) 100102. https://doi.org/10.1016/j.ccst.2023.100102.

[49] W.Y. Hong, A techno-economic review on carbon capture, utilisation and storage systems for achieving a net-zero CO_2 emissions future, *Carbon Capture Science & Technology* 3 (2022) 100044. https://doi.org/10.1016/j.ccst.2022.100044.

[50] A. Krishnan, A. Nighojkar, B. Kandasubramanian, Emerging towards zero carbon footprint via carbon dioxide capturing and sequestration, *Carbon Capture Science & Technology* 9 (2023) 100137. https://doi.org/10.1016/j.ccst.2023.100137.

[51] A.E. Geweda, M.E. Zayed, M.Y. Khan, A.B. Alquaity, Mitigating CO_2 emissions: A review on emerging technologies/strategies for CO_2 capture, *Journal of the Energy Institute* 118 (2025) 101911. https://doi.org/10.1016/j.joei.2024.101911.

[52] M. Hanifa, R. Agarwal, U. Sharma, P.C. Thapliyal, L.P. Singh, A review on CO_2 capture and sequestration in the construction industry: Emerging approaches and commercialised technologies, *Journal of CO_2 Utilization* 67 (2023) 102292. https://doi.org/10.1016/j.jcou.2022.102292.

[53] M.-C. Ferrari, A. Amelio, G.M. Nardelli, R. Costi, Assessment on the application of facilitated transport membranes in cement plants for CO_2 capture, *Energies* 14 (2021) 4772.

[54] R.W. Baker, B. Freeman, J. Kniep, Y.I. Huang, T.C. Merkel, CO_2 capture from cement plants and steel mills using membranes, *Industrial & Engineering Chemistry Research* 57 (2018), pp. 15963–15970. https://doi.org/10.1021/acs.iecr.8b02574.

[55] J.C. Abanades, B. Arias, A. Lyngfelt, T. Mattisson, D.E. Wiley, H. Li, M.T. Ho, E. Mangano, S. Brandani, Emerging CO_2 capture systems, *International Journal of Greenhouse Gas Control* 40 (2015), pp. 126–166. https://doi.org/10.1016/j.ijggc.2015.04.018.

[56] A. Burns, Y. Davila Gomez, Lessons learned in the design and construction of the Brevik CCS facility, in: Proceedings of the 17th International Conference on Greenhouse Gas Control Technologies, 20–24 Oct, 2024. https://doi.org/10.2139/ssrn.5012849.

[57] B. Corwyn, P. Cheruvallath, W. Srisang, B. Korobanik, A. Lockwhood, Heidelberg Edmonton CCUS – Project update, in: Proceedings of the 17th International Conference on Greenhouse Gas Control Technologies, 20–24 Oct, 2024.

[58] Lhoist, CALCC – Project summary, 2024, https://www.lhoist.com/en/calcc, accessed 14 November 2024.

[59] T. Hills, M. Sceats, D. Rennie, P. Fennell, LEILAC: Low cost CO_2 capture for the cement and lime industries, *Energy Procedia* 114 (2017), pp. 6166–6170. https://doi.org/10.1016/j.egypro.2017.03.1753.

[60] European Commission, H2020, Low Emissions Intensity Lime And Cement 2: Demonstration Scale. LEILAC 2 Project (2020).

[61] J.G. Driver, T. Hills, P. Hodgson, M. Sceats, P.S. Fennell, Simulation of direct separation technology for carbon capture and storage in the cement industry, *Chemical Engineering Journal* 449 (2022) 137721. https://doi.org/10.1016/j.cej.2022.137721.

[62] M. Greco-Coppi, C. Hofmann, J. Ströhle, D. Walter, B. Epple, Efficient CO_2 capture from lime production by an indirectly heated carbonate looping process, *International Journal of Greenhouse Gas Control* 112 (2021) 103430. https://doi.org/10.1016/j.ijggc.2021.103430.

[63] T. Shimizu, T. Hirama, H. Hosoda, K. Kitano, M. Inagaki, K. Tejima, A twin fluid-bed reactor for removal of CO_2 from combustion processes, *Chemical Engineering Research and Design* 77 (1999), pp. 62–68. https://doi.org/10.1205/026387699525882.

[64] R. Barker, The reversibility of the reaction $CaCO_3 \rightleftarrows CaO+CO_2$, *Journal of Applied Chemistry and Biotechnology* 23 (1973), pp. 733–742. https://doi.org/10.1002/jctb.5020231005.

[65] B.R. Stanmore, P. Gilot, Review—calcination and carbonation of limestone during thermal cycling for CO_2 sequestration, *Fuel Processing Technology* 86 (2005), pp. 1707–1743. https://doi.org/10.1016/j.fuproc.2005.01.023.

[66] F. García-Labiano, A. Abad, L.F. de Diego, P. Gayán, J. Adánez, Calcination of calcium-based sorbents at pressure in a broad range of CO_2 concentrations, *Chemical Engineering Science* 57 (2002), pp. 2381–2393. https://doi.org/10.1016/S0009-2509(02)00137-9.

[67] I. Barin, Thermochemical data of pure substances, 3rd ed., VCH, Weinheim, 1995. https://doi.org/10.1002/9783527619825.

[68] L.E. Steiner, Introduction to chemical thermodynamics, 2nd ed., Mcgraw-hill Book Company Inc., 1948.

[69] E. De Lena, B. Arias, M.C. Romano, J.C. Abanades, Integrated calcium looping system with circulating fluidized bed reactors for low CO_2 emission cement plants, *International Journal of Greenhouse Gas Control* 114 (2022) 103555. https://doi.org/10.1016/j.ijggc.2021.103555.

[70] M. Zhao, A.I. Minett, A.T. Harris, A review of techno-economic models for the retrofitting of conventional pulverised-coal power plants for post-combustion capture (PCC) of CO_2, *Energy Environ. Sci.* 6 (2013), pp. 25–40. https://doi.org/10.1039/C2EE22890D.

[71] Y. Wang, S. Lin, Y. Suzuki, Study of limestone calcination with CO_2 capture: Decomposition behavior in a CO_2 atmosphere, *Energy & Fuels* 21 (2007), pp. 3317–3321. https://doi.org/10.1021/ef700318c.

[72] J.C. Abanades, E.J. Anthony, D.Y. Lu, C. Salvador, D. Alvarez, Capture of CO_2 from combustion gases in a fluidized bed of CaO, *AIChE Journal* 50 (2004), pp. 1614–1622. https://doi.org/10.1002/aic.10132.

[73] A. Charitos, N. Rodríguez, C. Hawthorne, M. Alonso, M. Zieba, B. Arias, G. Kopanakis, G. Scheffknecht, J.C. Abanades, Experimental validation of the calcium looping CO_2 capture process with two circulating fluidized bed carbonator reactors, *Industrial & Engineering Chemistry Research* 50 (2011), pp. 9685–9695. https://doi.org/10.1021/ie200579f.

[74] N. Mader, B. Arias, J. Maier, G. Scheffknecht, Oxy-Fuel combustion in an entrained flow reactor for regeneration of spent Calcium Looping sorbents, *Fuel* 381 (2025) 133784. https://doi.org/10.1016/j.fuel.2024.133784.

[75] M. Spinelli, I. Martínez, M.C. Romano, One-dimensional model of entrained-flow carbonator for CO_2 capture in cement kilns by Calcium looping process, *Chemical Engineering Science* 191 (2018), pp. 100–114. https://doi.org/10.1016/j.ces.2018.06.051.

[76] K. Myöhänen, T. Hyppänen, T. Pikkarainen, T. Eriksson, A. Hotta, Near zero CO_2 emissions in coal firing with oxy-fuel circulating fluidized bed boiler, *Chemical Engineering & Technology* 32 (2009), pp. 355–363. https://doi.org/10.1002/ceat.200800566.

[77] J.C. Abanades, D. Alvarez, Conversion limits in the reaction of CO_2 with lime, *Energy & Fuels* 17 (2003), pp. 308–315. https://doi.org/10.1021/ef020152a.

[78] J. Agnew, E. Hampartsoumian, J. Jones, W. Nimmo, The simultaneous calcination and sintering of calcium based sorbents under a combustion atmosphere, *Fuel* 79 (2000), pp. 1515–1523. https://doi.org/10.1016/S0016-2361(99)00287-2.

[79] C. Fu, S. Roussanaly, K. Jordal, R. Anantharaman, Techno-economic analyses of the $CaO/CaCO_3$ post-combustion CO_2 capture from NGCC power plants, *Frontiers in Chemical Engineering* 2 (2021) 596417. https://doi.org/10.3389/fceng.2020.596417.

[80] M. Haaf, R. Anantharaman, S. Roussanaly, J. Ströhle, B. Epple, CO_2 capture from waste-to-energy plants: Techno-economic assessment of novel integration concepts of calcium looping technology, *Resources, Conservation and Recycling* 162 (2020) 104973. https://doi.org/10.1016/j.resconrec.2020.104973.

[81] A. Lasheras, J. Ströhle, A. Galloy, B. Epple, Carbonate looping process simulation using a 1D fluidized bed model for the carbonator, *International Journal of Greenhouse Gas Control* 5 (2011), pp. 686–693. https://doi.org/10.1016/j.ijggc.2011.01.005.

[82] M. Astolfi, E. de Lena, M.C. Romano, Improved flexibility and economics of Calcium Looping power plants by thermochemical energy storage, *International Journal of Greenhouse Gas Control* 83 (2019), pp. 140–155. https://doi.org/10.1016/j.ijggc.2019.01.023.

[83] M.P.S. Santos, D.P. Hanak, Carbon capture for decarbonisation of energy-intensive industries: a comparative review of techno-economic feasibility of solid looping cycles, *Frontiers of Chemical Science and Engineering* 16 (2022), pp. 1291–1317. https://doi.org/10.1007/s11705-022-2151-5.

[84] E. De Lena, M. Spinelli, M. Gatti, R. Scaccabarozzi, S. Campanari, S. Consonni, G. Cinti, M.C. Romano, Techno-economic analysis of calcium looping processes for low CO_2 emission cement plants, *International Journal of Greenhouse Gas Control* 82 (2019), pp. 244–260. https://doi.org/10.1016/j.ijggc.2019.01.005.

[85] M.C. Romano, M. Spinelli, S. Campanari, S. Consonni, G. Cinti, M. Marchi, E. Borgarello, The calcium looping process for low CO_2 emission cement and power, *Energy Procedia* 37 (2013), pp. 7091–7099. https://doi.org/10.1016/j.egypro.2013.06.645.

[86] Y. Tan, W. Liu, X. Zhang, W. Wei, S. Wang, Conventional and optimized testing facilities of calcium looping process for CO_2 capture: A systematic review, *Fuel* 358 (2024) 130337. https://doi.org/10.1016/j.fuel.2023.130337.

[87] M. Haaf, J. Hilz, J. Peters, A. Unger, J. Ströhle, B. Epple, Operation of a 1 MW_{th} calcium looping pilot plant firing waste-derived fuels in the calciner, *Powder Technology* 372 (2020), pp. 267–274. https://doi.org/10.1016/j.powtec.2020.05.074.

[88] B. Arias, Y. Alvarez Criado, A. Méndez, P. Marqués, I. Finca, J.C. Abanades, Pilot testing of calcium looping at TRL7 with CO_2 capture efficiencies toward 99%, *Energy & Fuels* 38 (2024), pp. 14757–14764. https://doi.org/10.1021/acs.energyfuels.4c02472.

[89] M. Hornberger, J. Moreno, M. Schmid, G. Scheffknecht, Experimental investigation of the carbonation reactor in a tail-end Calcium Looping configuration for CO_2 capture from cement plants, *Fuel Processing Technology* 210 (2020) 106557. https://doi.org/10.1016/j.fuproc.2020.106557.

[90] C. Hawthorne, H. Dieter, A.R. Bidwe, A. Schuster, G. Scheffknecht, S. Unterberger, M. Käß, CO_2 capture with CaO in a 200 kW_{th} dual fluidized bed pilot plant, *Energy Procedia* 4 (2011), pp. 441–448. https://doi.org/10.1016/j.egypro.2011.01.073.

[91] H. Dieter, A.R. Bidwe, G. Varela-Duelli, A. Charitos, C. Hawthorne, G. Scheffknecht, Development of the calcium looping CO_2 capture technology from lab to pilot scale at IFK, University of Stuttgart, *Fuel* 127 (2014), pp. 23–37. https://doi.org/10.1016/j.fuel.2014.01.063.

[92] J. Kremer, A. Galloy, J. Ströhle, B. Epple, Continuous CO_2 capture in a 1-MW_{th} carbonate looping pilot plant, *Chemical Engineering & Technology* 36 (2013), pp. 1518–1524. https://doi.org/10.1002/ceat.201300084.

[93] J. Ströhle, M. Junk, J. Kremer, A. Galloy, B. Epple, Carbonate looping experiments in a 1MW_{th} pilot plant and model validation, *Fuel* 127 (2014), pp. 13–22. https://doi.org/10.1016/j.fuel.2013.12.043.

[94] B. Arias, M.E. Diego, J.C. Abanades, M. Lorenzo, L. Diaz, D. Martínez, J. Alvarez, A. Sanchez-Biezma, Demonstration of steady state CO_2 capture in a 1.7MW_{th} calcium looping pilot, *International Journal of Greenhouse Gas Control* 18 (2013), pp. 237–245. https://doi.org/10.1016/j.ijggc.2013.07.014.

[95] B. Arias, M.E. Diego, A. Méndez, J.C. Abanades, L. Díaz, M. Lorenzo, A. Sanchez-Biezma, Operating Experience in la Pereda 1.7 MW_{th} Calcium Looping Pilot, *Energy Procedia* 114 (2017), pp. 149–157. https://doi.org/10.1016/j.egypro.2017.03.1157.

[96] M.-H. Chang, W.-C. Chen, C.-M. Huang, W.-H. Liu, Y.-C. Chou, W.-C. Chang, W. Chen, J.-Y. Cheng, K.-E. Huang, H.-W. Hsu, Design and Experimental Testing of a 1.9MW_{th} Calcium

Looping Pilot Plant, *Energy Procedia* 63 (2014), pp. 2100–2108. https://doi.org/10.1016/j.egypro.2014.11.226.

[97] J. Hilz, M. Helbig, M. Haaf, A. Daikeler, J. Ströhle, B. Epple, Investigation of the fuel influence on the carbonate looping process in 1 MW_{th} scale, *Fuel Processing Technology* 169 (2018), pp. 170–177. https://doi.org/10.1016/j.fuproc.2017.09.016.

[98] M. Haaf, J. Peters, J. Hilz, A. Unger, J. Ströhle, B. Epple, Combustion of solid recovered fuels within the calcium looping process – Experimental demonstration at 1 MW_{th} scale, *Experimental Thermal and Fluid Science* 113 (2020) 110023. https://doi.org/10.1016/j.expthermflusci.2019.110023.

[99] F. Magli, E. De Lena, R. Cremona, M. Spinelli, M. Alonso, N. Mader, M. Lindemann Lino, M. Gatti, M.C. Romano, Cleanker pilot test results, in: Cleanker Conference, 15 Mar, 2023.

[100] M. Fantini, M. Balocco, L. Buzzi, F. Canonico, S. Consonni, R. Cremona, M. Gatti, J. Hammerich, R. Koehler, F. Magli, M.C. Romano, M. Spinelli, Calcium looping technology demonstration in industrial environment: Status of the CLEANKER pilot plant, in: Proceedings of the 15th International Conference on Greenhouse Gas Control Technologies, 25–18 Mar, 2021. https://doi.org/10.2139/ssrn.3817346.

[101] M. Junk, M. Reitz, J. Ströhle, B. Epple, Thermodynamic evaluation and cold flow model testing of an indirectly heated carbonate looping process, *Chemical Engineering & Technology* 36 (2013), pp. 1479–1487. https://doi.org/10.1002/ceat.201300019.

[102] L.-S. Fan, H. Gupta, M. Iyer, Separation of carbon dioxide from gas mixtures by calcium based reaction separation (2012).

[103] S. Ramkumar, L.-S. Fan, Thermodynamic and experimental analyses of the three-stage calcium looping process, *Industrial & Engineering Chemistry Research* 49 (2010), pp. 7563–7573. https://doi.org/10.1021/ie100846u.

[104] W. Wang, S. Ramkumar, S. Li, D. Wong, M. Iyer, B.B. Sakadjian, R.M. Statnick, L.-S. Fan, Subpilot demonstration of the carbonation−calcination reaction (CCR) process: High-temperature CO_2 and sulfur capture from coal-fired power plants, *Industrial & Engineering Chemistry Research* 49 (2010), pp. 5094–5101. https://doi.org/10.1021/ie901509k.

[105] M.I. Khan, A.S. Mishamandani, F. Asfand, S. Fadlallah, T.A. Kurniawan, Solar driven calcium-looping for thermochemical energy storage system and carbon capture in power and cement industry: A review, *Process Safety and Environmental Protection*. https://doi.org/10.1016/j.psep.2024.11.067.

[106] S.G. Spyroglou, A.A. Skaltsogiannis, S.G. Yiantsios, A.A. Lemonidou, Multiscale modeling of an entrained flow solar calciner for thermochemical energy storage via calcium looping, *Chemical Engineering Journal* 486 (2024) 150171. https://doi.org/10.1016/j.cej.2024.150171.

[107] E. Svensson, H. Wiertzema, S. Harvey, Potential for negative emissions by carbon capture and storage from a novel electric plasma calcination process for pulp and paper mills, *Frontiers in Climate* 3 (2021) 705032. https://doi.org/10.3389/fclim.2021.705032.

[108] R.M. Jacob, L.-A. Tokheim, Electrified calciner concept for CO_2 capture in pyro-processing of a dry process cement plant, *Energy* 268 (2023) 126673. https://doi.org/10.1016/j.energy.2023.126673.

[109] L.-A. Tokheim, A. Mathisen, L.E. Øi, C.K. Jayarathna, N.H. Eldrup, T. Gautestad, Combined calcination and CO_2 capture in cement clinker production by use of electrical energy., in: TCCS–10. CO_2 Capture, Transport and Storage. Trondheim 17th–19th June 2019. Selected papers from the 10th International Trondheim CCS Conference, 2019, pp. 101–109.

[110] M.G. Sceats, C.J. Horley, P. Richardson, System and method for the calcination of minerals, US08807993 (2014).

[111] H. Moon, H. Yoo, H. Seo, Y.-K. Park, H.H. Cho, Thermal design of heat-exchangeable reactors using a dry-sorbent CO_2 capture multi-step process, *Energy* 84 (2015), pp. 704–713. https://doi.org/10.1016/j.energy.2015.03.034.

[112] I. Martínez, R. Murillo, G. Grasa, N. Rodríguez, J.C. Abanades, Conceptual design of a three fluidised beds combustion system capturing CO_2 with CaO, *International Journal of Greenhouse Gas Control* 5 (2011), pp. 498–504. https://doi.org/10.1016/j.ijggc.2010.04.017.

[113] B. Epple, J. Seeber, *Verfahren und Einrichtung zur Abscheidung von CO_2 aus Abgas*, EP 2299176 B1 (2014).

[114] D. Höftberger, J. Karl, The indirectly heated carbonate looping process for CO_2 capture—A concept with heat pipe heat exchanger, *Journal of Energy Resources Technology* 138 (2016) 042211. https://doi.org/10.1115/1.4033302.

[115] D. Höftberger, J. Karl, Self-fluidization in an indirectly heated calciner, *Chemical Engineering & Technology* 36 (2013), pp. 1533–1538. https://doi.org/10.1002/ceat.201300111.

[116] M. Junk, M. Reitz, J. Ströhle, B. Epple, Technical and economical assessment of the indirectly heated carbonate looping process, *Journal of Energy Resources Technology* 138 (2016) 042210. https://doi.org/10.1115/1.4033142.

[117] D.P. Hanak, Transforming carbon-intensive coal-fired power plants into negative emission technologies via biomass-fired calcium looping retrofit, *Clean Energy* 8 (2024), pp. 263–282. https://doi.org/10.1093/ce/zkae089.

[118] M. Reitz, M. Junk, J. Ströhle, B. Epple, Design and erection of a 300 kW_{th} indirectly heated carbonate looping test facility, *Energy Procedia* 63 (2014), pp. 2170–2177. https://doi.org/10.1016/j.egypro.2014.11.236.

[119] C. Hofmann, M. Greco-Coppi, J. Ströhle, B. Epple, Pilot testing of the indirectly heated carbonate looping process for cement and lime plants, in: Proceedings of the 16th International Conference on Greenhouse Gas Control Technologies, 23–24 Oct, 2022. https://doi.org/10.2139/ssrn.4278810.

[120] M. Reitz, M. Junk, J. Ströhle, B. Epple, Design and operation of a 300 kW_{th} indirectly heated carbonate looping pilot plant, *International Journal of Greenhouse Gas Control* 54 (2016), pp. 272–281. https://doi.org/10.1016/j.ijggc.2016.09.016.

[121] C. Hofmann, M. Greco-Coppi, J. Ströhle, B. Epple, Enhancement of a 300 kW_{th} pilot plant for testing the indirectly heated carbonate looping process for CO_2 capture from lime and cement industry, *Experimental Thermal and Fluid Science* 151 (2024) 111091. https://doi.org/10.1016/j.expthermflusci.2023.111091.

[122] M. Reitz, *Experimentelle Untersuchung und Bewertung eines indirekt beheizten Carbonate-Looping-Prozesses*. Doctoral dissertation, 1st ed., Cuvillier Verlag, Göttingen, 2017.

[123] M. Greco-Coppi, C. Hofmann, D. Walter, J. Ströhle, B. Epple, Negative CO_2 emissions in the lime production using an indirectly heated carbonate looping process, *Mitigation and Adaptation Strategies for Global Change* 28 (2023). https://doi.org/10.1007/s11027-023-10064-7.

[124] ACT – Accelerating CCS technology, ANICA proposal, 2019.

[125] M. Greco-Coppi, C. Hofmann, J. Ströhle, Advanced indirectly heated carbonate looping process (ANICA) – Final report, Accelerating CCS Technologies (ACT), 2024. https://doi.org/10.26083/tuprints-00026729.

[126] I. Martínez, G. Grasa, J. Parkkinen, T. Tynjälä, T. Hyppänen, R. Murillo, M.C. Romano, Review and research needs of Ca-Looping systems modelling for post-combustion CO_2 capture applications, *International Journal of Greenhouse Gas Control* 50 (2016), pp. 271–304. https://doi.org/10.1016/j.ijggc.2016.04.002.

[127] Aspen Technology, Inc., Aspen Plus® V12 (38.0.0.380) [Computer software]. https://www.aspentech.com/en/products/engineering/aspen-plus, 2020.

[128] I. Martínez, B. Arias, G.S. Grasa, J.C. Abanades, CO_2 capture in existing power plants using second generation Ca-Looping systems firing biomass in the calciner, *Journal of Cleaner Production* 187 (2018), pp. 638–649. https://doi.org/10.1016/j.jclepro.2018.03.189.

[129] Steag Energy Services GmbH, EBSILON®*Professional* Version 16.0.0.32608 [Computer software]. https://www.ebsilon.com/de/, 2022.

[130] C. Hawthorne, M. Trossmann, P. Galindo Cifre, A. Schuster, G. Scheffknecht, Simulation of the carbonate looping power cycle, *Energy Procedia* 1 (2009), pp. 1387–1394. https://doi.org/10.1016/j.egypro.2009.01.182.

[131] C. Ortiz, R. Chacartegui, J.M. Valverde, J.A. Becerra, L.A. Perez-Maqueda, A new model of the carbonator reactor in the calcium looping technology for post-combustion CO_2 capture, *Fuel* 160 (2015), pp. 328–338. https://doi.org/10.1016/j.fuel.2015.07.095.

[132] M. Alonso, N. Rodríguez, G. Grasa, J.C. Abanades, Modelling of a fluidized bed carbonator reactor to capture CO_2 from a combustion flue gas, *Chemical Engineering Science* 64 (2009), pp. 883–891. https://doi.org/10.1016/j.ces.2008.10.044.

[133] O. Levenspiel, Chemical Reaction Engineering, *Industrial & Engineering Chemistry Research* 38 (1999), pp. 4140–4143. https://doi.org/10.1021/ie990488g.

[134] K. Atsonios, M. Zeneli, A. Nikolopoulos, N. Nikolopoulos, P. Grammelis, E. Kakaras, Calcium looping process simulation based on an advanced thermodynamic model combined with CFD analysis, *Fuel* 153 (2015), pp. 370–381. https://doi.org/10.1016/j.fuel.2015.03.014.

[135] M. Zeneli, A. Nikolopoulos, N. Nikolopoulos, P. Grammelis, E. Kakaras, Application of an advanced coupled EMMS-TFM model to a pilot scale CFB carbonator, *Chemical Engineering Science* 138 (2015), pp. 482–498. https://doi.org/10.1016/j.ces.2015.08.008.

[136] A. Stroh, F. Alobaid, J. Ströhle, J. Hilz, B. Epple, CFD simulation of 1 MW carbonator using DDPM-DEM model, in: 6th High Temperature Solid Looping Cycles Network Meeting, 2015.

[137] D. Kunii, O. Levenspiel, The K-L reactor model for circulating fluidized beds, *Chemical Engineering Science* 55 (2000), pp. 4563–4570. https://doi.org/10.1016/S0009-2509(00)00073-7.

[138] B. Epple, R. Leithner, W. Linzer, H. Walter, *Simulation von Kraftwerken und Feuerungen*, Springer Vienna, Vienna, 2012. https://doi.org/10.1007/978-3-7091-1182-6.

[139] D. Kunii, O. Levenspiel, Fluidization Engineering, 2nd ed., Elsevier, 1991. https://doi.org/10.1016/C2009-0-24190-0.

[140] S.K. Bhatia, D.D. Perlmutter, Effect of the product layer on the kinetics of the CO_2-lime reaction, *AIChE Journal* 29 (1983), pp. 79–86. https://doi.org/10.1002/aic.690290111.

[141] M.C. Romano, Modeling the carbonator of a Ca-looping process for CO_2 capture from power plant flue gas, *Chemical Engineering Science* 69 (2012), pp. 257–269. https://doi.org/10.1016/j.ces.2011.10.041.

[142] J. Ylätalo, J. Ritvanen, B. Arias, T. Tynjälä, T. Hyppänen, 1-Dimensional modelling and simulation of the calcium looping process, *International Journal of Greenhouse Gas Control* 9 (2012), pp. 130–135. https://doi.org/10.1016/j.ijggc.2012.03.008.

[143] M. Tizfahm, M. Tahmasebpoor, H.R. Behtash, M. Balsamo, F. Montagnaro, Coupled kinetic and hydrodynamic model for a carbonator reactor of calcium looping process: Sulfur dioxide effect, *Process Safety and Environmental Protection*. https://doi.org/10.1016/j.psep.2024.03.065.

[144] M.E. Diego, B. Arias, Impact of load changes on the carbonator reactor of a 1.7 MW_{th} calcium looping pilot plant, *Fuel Processing Technology* 200 (2020) 106307. https://doi.org/10.1016/j.fuproc.2019.106307.

[145] N. Afandi, M. Satgunam, S. Mahalingam, A. Manap, F. Nagi, W. Liu, R.B. Johan, A. Turan, A. Wei-Yee Tan, S. Yunus, Review on the modifications of natural and industrial waste CaO based sorbent of calcium looping with enhanced CO_2 capture capacity, *Heliyon* 10 (2024) e27119. https://doi.org/10.1016/j.heliyon.2024.e27119.

[146] J.C. Abanades, The maximum capture efficiency of CO_2 using a carbonation/calcination cycle of CaO/$CaCO_3$, *Chemical Engineering Journal* 90 (2002), pp. 303–306. https://doi.org/10.1016/S1385-8947(02)00126-2.

[147] N. Rodríguez, M. Alonso, J.C. Abanades, Experimental investigation of a circulating fluidized-bed reactor to capture CO_2 with CaO, *AIChE Journal* 57 (2011), pp. 1356–1366. https://doi.org/10.1002/aic.12337.

[148] C. Hofmann, *Bewertung und Optimierung des indirekt beheizten Carbonate-Looping-Prozesses im Pilotmaßstab für die Anwendung in der Kalkindustrie*. Doctoral dissertation, Darmstadt, Germany, 2025. https://doi.org/10.26083/tuprints-00029329.

[149] N. Rodríguez, M. Alonso, J.C. Abanades, Average activity of CaO particles in a calcium looping system, *Chemical Engineering Journal* 156 (2010), pp. 388–394. https://doi.org/10.1016/j.cej.2009.10.055.

[150] C. Zhang, Absorption principle and techno-economic analysis of CO_2 absorption technologies: A review, *IOP Conference Series: Earth and Environmental Science* 657 (2021) 012045. https://doi.org/10.1088/1755-1315/657/1/012045.

[151] B. Arias, J.C. Abanades, G.S. Grasa, An analysis of the effect of carbonation conditions on CaO deactivation curves, *Chemical Engineering Journal* 167 (2011), pp. 255–261. https://doi.org/10.1016/j.cej.2010.12.052.

[152] J. Blamey, E.J. Anthony, J. Wang, P.S. Fennell, The calcium looping cycle for large-scale CO_2 capture, *Progress in Energy and Combustion Science* 36 (2010), pp. 260–279. https://doi.org/10.1016/j.pecs.2009.10.001.

[153] A.I. Lysikov, A.N. Salanov, A.G. Okunev, Change of CO_2 carrying capacity of CaO in isothermal recarbonation−decomposition cycles, *Industrial & Engineering Chemistry Research* 46 (2007), pp. 4633–4638. https://doi.org/10.1021/ie0702328.

[154] A.A. Scaltsoyiannes, A.A. Lemonidou, On the factors affecting the deactivation of limestone under calcium looping conditions: A new comprehensive model, *Chemical Engineering Science* 243 (2021) 116797. https://doi.org/10.1016/j.ces.2021.116797.

[155] V. Manovic, J.-P. Charland, J. Blamey, P.S. Fennell, D.Y. Lu, E.J. Anthony, Influence of calcination conditions on carrying capacity of CaO-based sorbent in CO_2 looping cycles, *Fuel* 88 (2009), pp. 1893–1900. https://doi.org/10.1016/j.fuel.2009.04.012.

[156] J. Ylätalo, J. Parkkinen, J. Ritvanen, T. Tynjälä, T. Hyppänen, Modeling of the oxy-combustion calciner in the post-combustion calcium looping process, *Fuel* 113 (2013), pp. 770–779. https://doi.org/10.1016/j.fuel.2012.11.041.

[157] G. Kanellis, M. Zeneli, N. Nikolopoulos, C. Hofmann, J. Ströhle, S. Karellas, J. Konttinen, CFD modelling of an indirectly heated calciner reactor, utilized for CO_2 capture, in an Eulerian framework, *Fuel* 346 (2023) 128251. https://doi.org/10.1016/j.fuel.2023.128251.

[158] G. Kanellis, D. Stefanitsis, M. Zeneli, N. Nikolopoulos, J. Konttinen, Development and numerical investigation of a DDPM-KTGF model for modelling flow hydrodynamics and heat transfer phenomena in a bubbling calciner reactor, *Fuel* 352 (2023) 128960. https://doi.org/10.1016/j.fuel.2023.128960.

[159] J. Ding, D. Gidaspow, A bubbling fluidization model using kinetic theory of granular flow, *AIChE Journal* 36 (1990), pp. 523–538. https://doi.org/10.1002/aic.690360404.

[160] M. Adnan, J. Sun, N. Ahmad, J.J. Wei, Verification and validation of the DDPM-EMMS model for numerical simulations of bubbling, turbulent and circulating fluidized beds, *Powder Technology* 379 (2021), pp. 69–88. https://doi.org/10.1016/j.powtec.2020.10.041.

[161] W. Michel (Ed.), *Wirbelschichttechnik in der Energiewirtschaft*: Mit 16 Tabellen, 1st ed., Dt. Verl. für Grundstoffindustrie, Leipzig, 1992.

[162] I. Martínez, G. Grasa, R. Murillo, B. Arias, J.C. Abanades, Modelling the continuous calcination of $CaCO_3$ in a Ca-looping system, *Chemical Engineering Journal* 215-216 (2013), pp. 174–181. https://doi.org/10.1016/j.cej.2012.09.134.

[163] I. Martínez, G. Grasa, R. Murillo, B. Arias, J.C. Abanades, Kinetics of calcination of partially carbonated particles in a Ca-looping system for CO_2 capture, *Energy & Fuels* 26 (2012), pp. 1432–1440. https://doi.org/10.1021/ef201525k.

[164] R. Han, Y. Wang, S. Xing, C. Pang, Y. Hao, C. Song, Q. Liu, Progress in reducing calcination reaction temperature of Calcium-Looping CO_2 capture technology: A critical review, *Chemical Engineering Journal* 450 (2022) 137952. https://doi.org/10.1016/j.cej.2022.137952.

[165] B. Epple, M. Junk, J. Ströhle, M. Reitz, J. Karl, D. Höftberger, Carbon capture by means of indirectly heated carbonate looping process (CARINA): Final report, Publications Office of the European Union, Luxembourg, 2016. https://doi.org/10.2777/708428.

[166] G. Towler, R. Sinnott, Introduction to design, in: G. Towler, R.K. Sinnott (Eds.), Chemical engineering design: Principles, practice, and economics of plant and process design, Elsevier, Amsterdam, 2013, pp. 3–32. https://doi.org/10.1016/B978-0-08-096659-5.00001-8.

[167] P. Dieringer, Demonstration and optimization of the chemical looping gasification technology in 1 MW_{th} scale, 2024. https://doi.org/10.26083/tuprints-00026623.

[168] M. Greco-Coppi, C. Hofmann, J. Ströhle, B. Epple, *Vorrichtung und Verfahren zum Herstellen von Kalk* (patent pending), no. 10 2023 114 354.9, Deutsches Patent- und Markenamt (2023).

[169] M. Greco-Coppi, A. Dinkova, C. Hofmann, D. Walter, K. Böge, J. Ströhle, B. Epple, Design of a 2 MW_{th} indirectly heated carbonate looping demonstration facility at a lime plant in Germany, in: 7th Post Combustion Capture Conference, Pittsburgh, Pennsylvania, 2023. https://doi.org/10.26083/tuprints-00026537.

[170] F. Crameri, Scientific colour maps, Zenodo, 2023. https://doi.org/10.5281/zenodo.1243862.

[171] F. Crameri, G.E. Shephard, P.J. Heron, The misuse of colour in science communication, *Nature communications* 11 (2020) 5444. https://doi.org/10.1038/s41467-020-19160-7.

[172] E. De Lena, M. Spinelli, M.C. Romano, CO_2 capture in cement plants by “Tail-End” Calcium Looping process, *Energy Procedia* 148 (2018), pp. 186–193. https://doi.org/10.1016/j.egypro.2018.08.049.

[173] Y. Zhang, S.-X. Cao, S. Shao, Y. Chen, S.-L. Liu, S.-S. Zhang, Aspen Plus-based simulation of a cement calciner and optimization analysis of air pollutants emission, *Clean Technologies and Environmental Policy* 13 (2011), pp. 459–468. https://doi.org/10.1007/s10098-010-0328-y.

[174] P. Tilak, M.M. El-Halwagi, Process integration of Calcium Looping with industrial plants for monetizing CO_2 into value-added products, *Carbon Resources Conversion* 1 (2018), pp. 191–199. https://doi.org/10.1016/j.crcon.2018.07.004.

[175] Aspen Technology, Inc., Aspen physical property system: Physical property methods and models V11.1, Cambridge, 2001.

[176] M. Haaf, Utilization of waste-derived fuels in the carbonate looping process: Experimental demonstration and techno-economic assessment. Doctoral dissertation, Darmstadt, Germany, 2020.

[177] J. Ströhle, J. Hilz, B. Epple, Performance of the carbonator and calciner during long-term carbonate looping tests in a 1 MW_{th} pilot plant, *Journal of Environmental Chemical Engineering* 8 (2020) 103578. https://doi.org/10.1016/j.jece.2019.103578.

[178] M. Greco-Coppi, J. Ströhle, B. Epple, A carbonator model for CO_2 capture based on results from pilot tests. Part II: Deactivation and reaction model, *Chemical Engineering Journal* 508 (2025) 159041. https://doi.org/10.1016/j.cej.2024.159041.

[179] C. Papalexis, D. Stefanitsis, M. Zeneli, N. Nikolopoulos, P. Tzouganakis, Proof of concept of a novel solid–solid heat exchanger based on a Double L-Valve concept, *Energies* 16 (2023) 6156. https://doi.org/10.3390/en16176156.

[180] T. Hills, Investigations of the use of spent sorbent from the Ca looping process in cement manufacture and investigation of long-term CO_2 uptake in cement and concrete. Doctoral dissertation, Imperial College London, 2016. https://doi.org/10.25560/39286.

[181] C. Dean, T. Hills, N. Florin, D. Dugwell, P.S. Fennell, Integrating calcium looping CO_2 capture with the manufacture of cement, *Energy Procedia* 37 (2013), pp. 7078–7090. https://doi.org/10.1016/j.egypro.2013.06.644.

[182] D. Gastaldi, F. Canonico, V. Merlo, F. Magli, Clinker based on calcium looped meals from the Cleanker Project, *Journal of microscopy* 294 (2024), pp. 90–104. https://doi.org/10.1111/jmi.13243.

[183] N. Rong, S. Wang, C. Chu, Z. Guo, K. Liu, L. Han, L. Ge, X. Shi, G. Wang, Y. Wang, Deactivated Ca-based sorbent derived from calcium looping CO_2 capture as a partial substitute for cement to obtain low-carbon cementitious building materials, *Construction and Building Materials* 454 (2024) 139175. https://doi.org/10.1016/j.conbuildmat.2024.139175.

[184] S. He, L. Gao, Y. Zheng, J. Wang, D. Yang, X. Zeng, Thermodynamic performance comparison of calcium looping processes for post-combustion capture: influence of CO_2 enrichment routes among three heat supply methods, *Journal of the Energy Institute*. https://doi.org/10.1016/j.joei.2024.101878.

[185] J.C. Abanades, E.J. Anthony, J. Wang, J.E. Oakey, Fluidized bed combustion systems integrating CO_2 capture with CaO, *Environmental science & technology* 39 (2005), pp. 2861–2866. https://doi.org/10.1021/es0496221.

[186] S. Posch, M. Haider, Optimization of CO_2 compression and purification units (CO_2CPU) for CCS power plants, *Fuel* 101 (2012), pp. 254–263. https://doi.org/10.1016/j.fuel.2011.07.039.

[187] K.-H. Grote, J. Feldhusen (Eds.), Dubbel: *Taschenbuch für den Maschinenbau*, 22nd ed., Springer Berlin Heidelberg, Berlin, Heidelberg, 2007.

[188] IEA, Projected costs of generating electricity, Paris, 2020.

[189] P. Madejski, K. Chmiel, N. Subramanian, T. Kuś, Methods and techniques for CO_2 Capture: review of potential solutions and applications in modern energy technologies, *Energies* 15 (2022) 887. https://doi.org/10.3390/en15030887.

[190] E. Furimsky, Carbon dioxide emission index as a mean for assessing fuel quality, *Energy Sources, Part A: Recovery, Utilization, and Environmental Effects* 30 (2007), pp. 119–131. https://doi.org/10.1080/15567030600820583.

[191] E. De Lena, M. Spinelli, I. Martínez, M. Gatti, R. Scaccabarozzi, G. Cinti, M.C. Romano, Process integration study of tail-end Ca-Looping process for CO_2 capture in cement plants, *International Journal of Greenhouse Gas Control* 67 (2017), pp. 71–92. https://doi.org/10.1016/j.ijggc.2017.10.005.

[192] M. Voldsund, R. Anantharaman, D. Berstad, E. de Lena, C. Fu, S.O. Gardarsdottir, A. Jamali, J.-F. Pérez-Calvo, M.C. Romano, S. Roussanaly, J. Ruppert, O. Stallmann, D. Sutter, D4.6 CEMCAP comparative techno-economic analysis of CO_2 capture in cement plants, Zenodo, 2019. https://doi.org/10.5281/ZENODO.2597090.

[193] F.P. Campo, C. Tua, L. Biganzoli, S. Pantini, M. Grosso, Natural and enhanced carbonation of lime in its different applications: a review, *Environmental Technology Reviews* 10 (2021), pp. 224–237. https://doi.org/10.1080/21622515.2021.1982023.

[194] University of Ulster, ECLIPSE process simulator. Energy Research Centre, Coleraine, Copyright 1992 [Computer software], 1992.

[195] B.C. Williams, J.T. McMullan, Techno-economic analysis of fuel conversion and power generation systems — the development of a portable chemical process simulator with capital cost and economic performance analysis capabilities, *International Journal of Energy Research* 20 (1996), pp. 125–142. https://doi.org/10.1002/(SICI)1099-114X(199602)20:2%3C125::AID-ER239%3E3.0.CO;2-2.

[196] Chemical Engineering, The Chemical Engineering Plant Cost Index, 2024, https://www.chemengonline.com/pci-home, accessed 12 July 2024.

[197] D. Mignard, Correlating the chemical engineering plant cost index with macro-economic indicators, *Chemical Engineering Research and Design* 92 (2014), pp. 285–294. https://doi.org/10.1016/j.cherd.2013.07.022.

[198] S. Roussanaly, Calculating CO_2 avoidance costs of Carbon Capture and Storage from industry, *Carbon Management* 10 (2019), pp. 105–112. https://doi.org/10.1080/17583004.2018.1553435.

[199] D. Simbeck, D. Beecy, The CCS paradox: The much higher CO_2 avoidance costs of existing versus new fossil fuel power plants, *Energy Procedia* 4 (2011), pp. 1917–1924. https://doi.org/10.1016/j.egypro.2011.02.071.

[200] E. Smith, J. Morris, H. Kheshgi, G. Teletzke, H. Herzog, S. Paltsev, The cost of CO_2 transport and storage in global integrated assessment modeling, *International Journal of Greenhouse Gas Control* 109 (2021) 103367. https://doi.org/10.1016/j.ijggc.2021.103367.

[201] J. Yin, C. Li, G. Paicu, S. Su, Techno-economic assessment of retrofitting indirect-heated calcium looping using coal and biomass as fuels into an existing cement plant for CO_2 capture, *Gas Science and Engineering* 123 (2024) 205236. https://doi.org/10.1016/j.jgsce.2024.205236.

[202] D. Geldart, A.R. Abrahamsen, Homogeneous fluidization of fine powders using various gases and pressures, *Powder Technology* 19 (1978), pp. 133–136. https://doi.org/10.1016/0032-5910(78)80084-9.

[203] J.R. Grace, Contacting modes and behaviour classification of gas—solid and other two-phase suspensions, *Canadian Journal of Chemical Engineering* 64 (1986), pp. 353–363. https://doi.org/10.1002/cjce.5450640301.

[204] X.T. Bi, J.R. Grace, J. Zhu, Regime transitions affecting gas-solids suspensions and fluidized-beds, *Chemical engineering research & design* 73 (1995), pp. 154–161.

[205] J. Szekely, J.W. Evans, H.Y. Sohn, Gas-solid reactions, 1st ed., Academic Press, New York, 1976.

[206] Z. Li, H. Sun, N. Cai, Rate equation theory for the carbonation reaction of CaO with CO_2, *Energy & Fuels* 26 (2012), pp. 4607–4616. https://doi.org/10.1021/ef300607z.

[207] G.S. Grasa, J.C. Abanades, M. Alonso, B. González, Reactivity of highly cycled particles of CaO in a carbonation/calcination loop, *Chemical Engineering Journal* 137 (2008), pp. 561–567. https://doi.org/10.1016/j.cej.2007.05.017.

[208] D. Alvarez, J.C. Abanades, Determination of the critical product layer thickness in the reaction of CaO with CO_2, *Industrial & Engineering Chemistry Research* 44 (2005), pp. 5608–5615. https://doi.org/10.1021/ie050305s.

[209] W. Nitsch, *Über die Druckabhängigkeit der $CaCO_3$-Bildung aus dem Oxyd*, *Zeitschrift für Elektrochemie, Berichte der Bunsengesellschaft für physikalische Chemie* 66 (1962), pp. 703–708. https://doi.org/10.1002/bbpc.19620660821.

[210] G.S. Grasa, M. Alonso, J.C. Abanades, Sulfation of CaO particles in a carbonation/calcination loop to capture CO_2, *Industrial & Engineering Chemistry Research* 47 (2008), pp. 1630–1635. https://doi.org/10.1021/ie070937.

[211] J.H. Mathews, K.D. Fink, Numerical methods using MATLAB, 3rd ed., Prentice Hall, Upper Saddle River, N.J., London, 1999.

[212] M. Greco-Coppi, J. Ströhle, B. Epple, A carbonator model for CO_2 capture based on results from pilot tests. Part I: Hydrodynamics and reactor model, *Chemical Engineering Journal* 500 (2024) 155119. https://doi.org/10.1016/j.cej.2024.155119.

[213] M. Junk, Technical and economical assessment of various carbonate looping process configurations, 1st ed., Cuvillier Verlag, Göttingen, 2017.

[214] L. Fedunik-Hofman, A. Bayon, S.W. Donne, Kinetics of solid-gas reactions and their application to carbonate looping systems, *Energies* 12 (2019) 2981. https://doi.org/10.3390/en12152981.

[215] Erich Netzsch GmbH & Co. Holding KG, STA 449 F3 Jupiter, 2023, https://analyzing-testing.netzsch.com/_Resources/Persistent/4/c/b/e/4cbe0375352415b080dab9d281329c613a551c10/STA_449_F3_Jupiter_de_web.pdf, accessed 8 August 2023.

[216] A. Galloy, J. Ströhle, B. Epple, Design and operation of a 1 MW_{th} carbonate and chemical looping CCS test rig, *VGB Power Tech* (2011), pp. 64–68.

[217] G. Towler, R. Sinnott, Optimization in design, in: G. Towler, R.K. Sinnott (Eds.), Chemical engineering design: Principles, practice, and economics of plant and process design, Elsevier, Amsterdam, 2013, pp. 525–553. https://doi.org/10.1016/B978-0-08-096659-5.00012-2.

[218] A.K. Priya, B. Devarajan, A. Alagumalai, H. Song, Artificial intelligence enabled carbon capture: A review, *The Science of the total environment* 886 (2023) 163913. https://doi.org/10.1016/j.scitotenv.2023.163913.

[219] M. Haaf, A. Stroh, J. Hilz, M. Helbig, J. Ströhle, B. Epple, Process modelling of the calcium looping process and validation against 1 MW_{th} pilot testing, *Energy Procedia* 114 (2017), pp. 167–178. https://doi.org/10.1016/j.egypro.2017.03.1159.

[220] M. Silakhori, M. Jafarian, A. Chinnici, W. Saw, M. Venkataraman, W. Lipiński, G.J. Nathan, Effects of steam on the kinetics of calcium carbonate calcination, *Chemical Engineering Science* 246 (2021) 116987. https://doi.org/10.1016/j.ces.2021.116987.

[221] Y. Deng, J. Liu, S. Li, R. Dewil, H. Zhang, J. Baeyens, H. Mikulčić, The steam-assisted calcination of limestone and dolomite for energy savings and to foster solar calcination processes, *Journal of Cleaner Production* 363 (2022) 132640. https://doi.org/10.1016/j.jclepro.2022.132640.

[222] P. Brandl, M. Bui, J.P. Hallett, N. Mac Dowell, Beyond 90% capture: Possible, but at what cost?, *International Journal of Greenhouse Gas Control* 105 (2021) 103239. https://doi.org/10.1016/j.ijggc.2020.103239.

[223] M. Secomandi, M. Nikku, B. Arias, J. Ritvanen, A conceptual evaluation of the use of $Ca(OH)_2$ for attaining carbon capture rates of 99% in the calcium looping process, *International Journal of Greenhouse Gas Control* 139 (2024) 104279. https://doi.org/10.1016/j.ijggc.2024.104279.

[224] M. Greco-Coppi, J. Ströhle, B. Epple, *Vorrichtung und Verfahren zum Herstellen von Kalk und Zement* (patent pending), no. 10 2024 109 181.9, Deutsches Patent- und Markenamt (2024).

Part two: Research papers

In this section, we present the research papers in chronological order based on their submission dates, corresponding to the numbering system adopted in this dissertation (I–VI). Each paper is introduced by a short summary based on its abstract. Additionally, the graphical abstracts have been adapted from those of the corresponding research papers.

Research Paper I

Research Paper I

Title: Efficient CO_2 capture from lime production by an indirectly heated carbonate looping process
Authors: Martin Greco Coppi, Carina Hofmann, Jochen Ströhle, Diethelm Walter, Bernd Epple
Journal: International Journal of Greenhouse Gas Control (Elsevier)
Status: Published (October 31, 2021)
Volume: 112 (December 2021)
DOI: https://doi.org/10.1016/j.ijggc.2021.103430
Licensing: Elsevier Ltd. All rights reserved.

Short Summary

This study analyzes two concepts for efficiently integrating the IHCaL into lime plants using heat and mass balances and a sensitivity analysis based on process simulations using Aspen Plus. The results show an increase of 63 % in the direct fuel consumption for a highly integrated concept, but almost 30 % of the entire heat input can be converted into electric power via heat recovery steam generation. Direct CO_2 emissions are reduced by up to 87 % when coal is used as fuel in the IHCaL process. The preheating of the combustion air, the efficiency of the sorbent solid-solid heat exchanger, and the utilization of the sorbent purge as lime product are critical for the efficiency of the integration.

International Journal of Greenhouse Gas Control 112 (2021) 103430

Contents lists available at ScienceDirect

International Journal of Greenhouse Gas Control

journal homepage: www.elsevier.com/locate/ijggc

Efficient CO_2 capture from lime production by an indirectly heated carbonate looping process

Martin Greco-Coppi [a,*], Carina Hofmann [a], Jochen Ströhle [a], Diethelm Walter [b], Bernd Epple [a]

[a] Technische Universität Darmstadt, Energy Systems and Technology, Otto-Berndt-Str. 2, 64287 Darmstadt, Germany
[b] Lhoist Germany Rheinkalk GmbH, Am Kalkstein 1, 42489 Wülfrath, Germany

ARTICLE INFO

Keywords:
CO_2 capture
Lime production
Calcium looping
Indirect heating
Heat pipe
Indirectly heated carbonate looping
Process modelling

ABSTRACT

Lime production is associated with unavoidable process CO_2 emissions that can only be avoided by CO_2 capture technologies. The indirectly heated carbonate looping (IHCaL) is a promising post-combustion carbon capture technology that can be applied to lime plants with high potential for heat and mass integration. In this work, two concepts for efficiently integrating the IHCaL into lime plants are proposed and evaluated. To study and characterize these concepts, heat and mass balances were established, sensitivity analyses were performed, and key performance indicators were calculated by means of process simulations. The results show an increase of 63% in the direct fuel consumption for a highly integrated concept, but almost 30% of the entire heat input can be converted into electric power via heat recovery steam generation. Direct CO_2 emissions are reduced by up to 87% when coal is used as fuel in the IHCaL process, but net negative CO_2 emissions could be achieved when using biogenic fuels. Critical points for integration are the preheating of the combustion air, the efficiency of the sorbent solid-solid heat exchanger, and the utilization of the sorbent purge as lime product. The developed models and the obtained results will be used to further develop the integration of the IHCaL into lime plants through both experimental and numerical methods.

1. Introduction

Lime (CaO) is an important product used in different sectors of the industry as well as in agriculture. The production of lime is achieved through the calcination of limestone (mainly $CaCO_3$) at temperatures between 900 and 1200 °C. This process is highly endothermic and requires the combustion of fuels such as gas oil, coal, coke, or some types of secondary fuels (e.g. oil, plastics, paper) (Schorcht et al., 2013). CO_2 emissions from combustion can be reduced by replacing fossil fuels with renewable fuels such as biomass. Process CO_2 emissions resulting from the decomposition of $CaCO_3$ amount to around 65% of total CO_2 emissions and can only be avoided by CO_2 capture technology (IEA, 2020).

Several CO_2 capture processes are currently being developed, but most of them have the consequence of high energy consumption leading to lower plant efficiencies and increased costs (IEAGHGT, 2014). Pre-combustion capture is not suitable for lime processes since process CO_2 emissions cannot be captured (Bosoaga et al., 2009). Oxyfuel combustion can allow for CO_2 capture from both process emissions and combustion emissions, but it requires an air separation unit for supply of pure technical oxygen (Carrasco-Maldonado et al., 2016). Post-combustion capture technologies generally have the possibility to capture the major part of the total CO_2 emissions. Solvent-based technologies are highly developed, but require huge amounts of heat for sorbent regeneration (around 3.5 GJ/t_{CO2}) (Tola and Pettinau, 2014). Another concept for capturing CO_2 from cement plants is the implementation of Calix's Direct Separation Technology, in which raw meal is calcined through indirectly heating to capture the unavoidable process CO_2 emissions. This capture strategy is being developed within the LEILAC (Low Emissions Intensity Lime And Cement) project. A pilot plant capable of processing 10 tonnes of raw cement meal per hour has been built and is being used to demonstrate the technology (Hills et al., 2017; Hodgson et al., 2019). Within the CEMCAP project, four different CO_2 capture technologies for cement industry were evaluated: oxyfuel technology, chilled ammonia process (CAP), membrane- assisted CO_2 liquefaction (MAL) and carbonate looping (CaL) (Anantharaman et al., 2018; Jordal et al., 2017; Voldsund et al., 2019). The results of CEMCAP show that the lowest costs of CO_2 avoided correspond to Oxyfuel (42.4 $€/t_{CO2}$) and CaL (52.4 $€/t_{CO2}$) (Voldsund et al., 2019).

The carbonate looping (CaL) process, first proposed by Shimizu et al. (1999), has the potential to significantly reduce the efficiency loss compared to solvent-based technologies (Zhao et al., 2013). The process

---

* Corresponding author.
E-mail address: martin.greco@est.tu-darmstadt.de (M. Greco-Coppi).

https://doi.org/10.1016/j.ijggc.2021.103430
Received 10 May 2021; Received in revised form 28 July 2021; Accepted 8 August 2021
Available online 31 October 2021
1750-5836/© 2021 Elsevier Ltd. All rights reserved.

Nomenclature

CaL	Carbonate looping
Calc	Calciner
Carb	Carbonator
Cyc.	Cyclone
e_{CO2}	Direct CO_2 emissions (kg CO_2/t_{CaO})
E	Carbon capture efficiency (%)
f_{calc}	Fractional conversion (calcination) in calciner (-)
f_{carb}	Fractional conversion (carbonation) in carbonator (-)
F_0	Molar flow rate of make-up calcium species (kmol/s)
F_{CO_2}	Molar flow rate of CO_2 generated (kmol/s)
$F_{CO_2}^{calc,out}$	Molar flow rate of calciner CO_2 output (kmol/s)
$F_{CO_2}^{carb,out}$	Molar flow rate of carbonator CO_2 output (kmol/s)
F_R	Molar flow rate of calcium species at carbonator inlet (kmol/s)
HR	Heat ratio (-)
IHCaL	Indirectly heated carbonate looping process
IHCaL_{NP}	Indirectly heated carbonate looping newly built plant
$\text{IHCaL}_{\text{PRH}}$	Indirectly heated carbonate looping retrofit plant with regenerative solids/solids preheating
LHV	Lower heating value (kJ/kg)
$\dot{m}_{CaO;prod}$	Total lime production of the process (t/day)
P_{el}	Power generation through heat recovery in the IHCaL (MW_{el})
PR	Product ratio (-)
Prod	Lime product (CaO)
PRK	Preheated rotary kiln
Ref	Reference lime production facility
q	Direct fuel consumption (MJ/t_{CaO})
Q_{in}	Total heat consumption of the process (MW_{th})
$Q_{out,IHCaL}$	Total heat extracted from the IHCaL to produce electricity (MW_{th})
$T_{preheat}$	Combustor preheated air temperature (°C)
$T_{sorb,calc,in}$	Sorbent temperature at calciner inlet (°C)
η_{h2p}	Heat-to-power efficiency
Λ	Specific make-up ratio (mol_{CaCO3}/mol_{CO2})
Φ	Specific sorbent circulation rate (mol_{Ca}/mol_{CO2})

operates at high temperatures, which allows for the utilization of heat for power production in a steam cycle (Martínez et al., 2011; Lena et al., 2017). Furthermore, the CaL process offers synergies with the lime industry since the sorbent is the raw material of the process. To supply the heat for the calcination into the calciner, the most straightforward strategy is the direct combustion of fuel with oxygen in the calciner (Shimizu et al., 1999). This oxy-fired CaL process has been successfully tested in several pilot plants up to 1 MW_{th} scale at the Technical University of Darmstadt (Hilz et al., 2017) and up to 1.7 MW_{th} scale in la Pereda (Spain) (Arias et al., 2013). The integration of the CaL process into the cement production using entrained flow reactors is being evaluated within the CLEANKER project (Magli et al., 2021; Fantini et al., 2021). With the objective of setting the basis for an industrial application, a demonstrator at TRL7 has been erected at a cement plant in Vernasca, Italy, and various test campaigns will be carried out during 2021 (Fantini et al., 2021).

The efficiency penalty of the CaL process can be further decreased when the need for oxygen in the plant can be avoided (Junk et al., 2013). This can be achieved by using steam for the regeneration of the sorbent, as proposed by Fan et al. (Fan, 2012; Ramkumar and Fan, 2010; Wang et al., 2010; Jordal et al., 2017). Another alternative is the indirect heating of the calciner, e.g. through metallic walls (Martínez et al., 2011; Abanades et al., 2007), by solids circulation (Abanades et al., 2007; Moon et al., 2015), or via heat pipes (Junk et al., 2013; Reitz et al., 2016; Hoeftberger and Karl, 2016). Heat pipes offer an excellent heat transfer performance based on evaporation and condensation of a liquid, i.e. sodium for temperatures > 800 °C, inside a closed pipe (Hoeftberger and Karl, 2016). The flue gas of the external combustion chamber is directed to the carbonator, where most of the CO_2 contained in this flue gas is absorbed by CaO.

The main advantages of this indirectly heated carbonate looping process (IHCaL) compared to the standard CaL process are summarized as follows (Junk et al., 2016):

- No air separation unit is needed to produce pure oxygen, which leads to lower investment costs and to a lower energy consumption.
- Fewer impurities (sulphur, ash) from a supplementary firing are brought into the Ca-loop, so that spent sorbent will be of higher purity and therefore be better suited for further utilization.
- Lower CaO deactivation rates are expected due to “mild” calcination around the heat pipe surfaces compared to rather harsh conditions in an oxy-fired calciner, so that sorbent remains more reactive.
- Lower attrition rates are expected due to a low fluidization velocity in the calciner, which improves the operability of the fluidized bed system.
- An almost pure CO_2 stream leaves the calciner, which allows for technically easy and cost-effective CO_2 purification process for compression and storage/utilization of CO_2.

The IHCaL concept with heat pipes was previously evaluated with respect to CO_2 capture from coal-fired power plants (Hoeftberger and Karl, 2016). CO_2 avoidance costs have been calculated to 22.6 €/t_{CO2} (Junk et al., 2016) excluding CO_2 storage. A 300 kW_{th} pilot plant for investigation of indirect calcination via heat pipes was successfully operated for more than 400 h, with stable CO_2 capture at a temperature difference between combustor and calciner of around 100 K (Reitz et al., 2016).

Until now, the IHCaL process has only been considered for power plant applications (Hoeftberger and Karl, 2016; Junk et al., 2016), but not for lime or cement plants. This paper presents two novel concepts for integrating the IHCaL process into an existing lime plant in Germany (host plant), which have been developed within the ANICA project (AdvaNced Indirectly heated CArbonate looping process). The host lime plant uses a preheated rotary kiln (PRK) to burn limestone. With the PRK, more than 600 tons of lime are produced per day in normal operating conditions. One concept is a tail-end solution in an existing lime plant placed after the kiln and capturing the CO_2 of the flue gas. The other is an integrated solution in which the lime production and the carbon capture are realized within the IHCaL facility. The concepts were studied numerically and the corresponding results are presented in this paper. For the experimental validation, three test campaigns in the pilot scale (300 kW_{th}) are foreseen within the ANICA project (Ströhle et al., 2021).

2. Process concepts

2.1. Tail-end integration concept

The first concept considered in the analysis is the tail-end integration solution, also known as the indirectly heated carbonate looping retrofit with regenerative solids/solids preheating ($\text{IHCaL}_{\text{PHR}}$) (Junk et al., 2013). It entails a low amount of integration and is therefore suitable for retrofitting. The IHCaL facility is located downstream at the end of the lime production facility, as shown schematically in Fig. 1. Its main

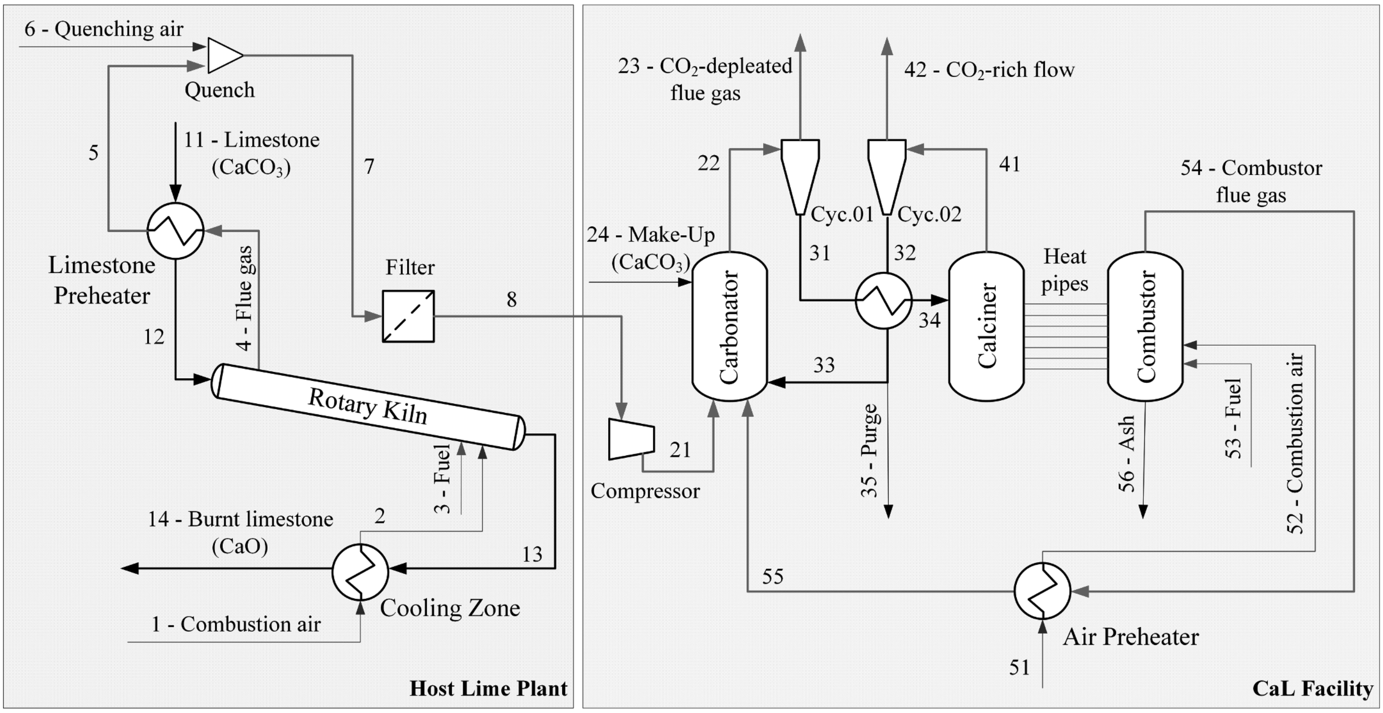

Fig. 1. Process diagram of the tail-end integration of the IHCaL into a lime plant in Germany.

components are the three reactors: the carbonator that operates as a circulating fluidized bed (CFB) as well as the calciner and combustor operating as bubbling fluidized bed reactors (BFB).

The original PRK facility is depicted on the left side of Fig. 1. The raw material, i.e. limestone, is fed to the rotary kiln through a preheater (11 and 12). The limestone is calcined in the kiln and the burnt lime exits the kiln (13). Afterwards, it is cooled down and processed for commercialization (14). The heat of the burnt lime is recovered by preheating the combustion air (1 and 2). The flue gases from the kiln (4) are used to preheat the limestone (11) in the preheater. They are then cooled in a quench (5 and 7), filtered (7 and 8), and driven to the IHCaL facility with a compressor (8 and 21). The flue gases enter the carbonator (21) where the CO_2 reacts with CaO to form $CaCO_3$. Downstream of the carbonator, the CO_2-depleted gases are separated from the solids in the first cyclone (Cyc.01, 22, 23, and 31). The solid particles enter the calciner (34) where the calcination takes place. After leaving the reactor, the solids are separated from the gases in the second cyclone (Cyc.02, 41, 42, and 32). The CO_2 exits in a high purity stream (42), and the solids, composed mainly by CaO, are transferred back to the carbonator to restart the loop (33). For the fluidization of the solid particles in the calciner, a part of the high purity CO_2 stream (42) is recirculated (not displayed). Fuel (53) is burned in the combustor to generate the heat for the calcination. The same lignite that is being used to fire the PRK (3) is fed into the combustor (53), but other fuels such as refused-derived fuels could also be used for this purpose. The heat is transferred to the calciner via heat-pipes (Hoeftberger and Karl, 2016). Downstream of Cyc.02, there is a sorbent extraction point to extract the purge stream (35). This purge stream consists of highly concentrated CaO that can be considered as lime product output. Thus, the implementation of the IHCaL expands the lime production capacity while allowing for CO_2 capture.

In the tail end configuration, the IHCaL facility could be placed at two different locations of the existing lime plant. The first one is the location right downstream of the limestone preheater (5). This location has the advantage of a high CO_2 concentration, i.e. 31.0 vol-% (wet-based). However, it has two disadvantages, i.e. high temperature (≈ 370 °C) and high solid particle concentration. This would enforce the addition of a heat exchanger and a high temperature filter before the IHCaL facility, which would increase the CAPEX and maintenance costs considerably. The second location is right after the main flue gas filter (7). Upstream of this point, the flue gas has been quenched with air (6), thus, the CO_2 is diluted to a concentration of 18.1 vol-% (wet-based). This concentration is slightly higher than typical concentrations for power plants (Haaf, 2020; Junk, 2017). The previous pilot tests at TUDA used a CO_2 concentration of 14 vol-% (dry-based) corresponding to a reference power plant (Reitz et al., 2016). The low temperatures at this location make the integration of an IHCaL facility a straightforward task, without the necessity of adding preparation equipment such as filters or heat exchangers. From the economic point of view, this solution was therefore chosen for this study.

In order to reduce the fuel consumption in the combustor (53), the combustion air (51 and 52) is preheated with the flue gases from the combustor (54). Moreover, a solid-solid heat exchanger is installed to transfer heat between the circulating sorbent streams (31 and 32), reducing the energy requirement in the calciner to heat up the entering solids (34). The heat from the CO_2-depleated flue gases (23), the CO_2-rich flow (42), and the cooling of the carbonator is used to generate power through a heat recovery steam cycle (De Lena et al., 2018; Lasheras et al., 2011). In order to maintain a high CO_2 capture rate, it is necessary to maintain a high activity of the sorbent inventory. This is realized by removing a fraction of the solid inventory (35) and replacing it with fresh limestone (24). In the tail-end solution, the purge is extracted after the calciner (35), so that it can be sold as lime product of high purity.

2.2. *Fully integrated concept*

The second integration concept is a full integration, in which the reference plant is completely replaced by a new facility. This concept is referred to as IHCaL newly built plant ($IHCaL_{NP}$) (Junk et al., 2013). The IHCaL facility serves as calcination unit with inherent CO_2 capture. In the analysis of this solution, the same operation parameters as used in the tail-end solution were adopted.

An overview of the fully integrated concept is presented in Fig. 2. The raw material (11), limestone, is directly fed to the carbonator (12),

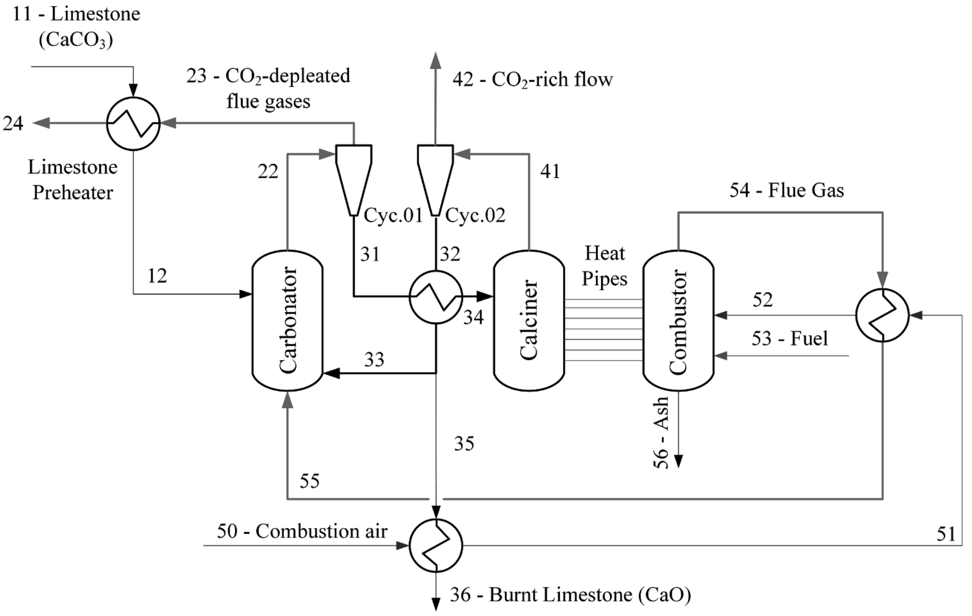

Fig. 2. Process diagram of the fully integrated concept of an IHCaL for lime production and carbon capture.

where it is mixed with the circulating solid inventory. In the carbonator, the CO_2 contained in the flue gas from the combustor reacts with the lime to form $CaCO_3$. The solids and the gases exiting the carbonator (22) are separated by Cyc.01.

The solids enter the calciner (34) where the calcination takes place. In this model, the calcination plays an important role in the production of lime from limestone, apart from regeneration of the sorbent. Downstream of the calciner, the high-purity CO_2 stream is separated from the solids, composed mainly by lime (32, 41, and 42). The lime is then recirculated to the carbonator to close the loop (33). Around 5-10% of the recirculated lime is removed from the system to be processed and sold (35 and 36).

The particularity of this solution is that all the limestone is calcined by indirect heating, and therefore the CO_2 from the limestone calcination is produced entirely in the calciner. Thus, the need for a downstream separation of process CO_2 is avoided. As a result, the only CO_2 emissions that need to be captured in the carbonator are the ones generated by burning the fuel in the combustor to generate the heat for the calciner. This poses a huge advantage over the tail-end scheme, i.e. much lower heat requirements and lower recirculation rates for the same conditions.

Regarding the heat integration, the CO_2-depleated stream coming from Cyc.01 (23) is used to preheat the limestone (11). Furthermore, the combustion air (50) is preheated with the burnt limestone (35) and the flue gases coming from the combustor (54). Additionally, a solid-solid heat exchanger is included to transfer heat between the two loop-streams (31 and 32). Lastly, power is generated by recovering the heat from the two flue gas streams (23 and 42) and the cooling of the carbonator.

3. Methods

3.1. Process modelling

The software ASPEN PLUS™, version V11, was used to solve the mass and energy balances. ASPEN PLUS™ is a steady-state process simulation software, which has a powerful data base of properties for various substances (Zhang et al., 2011). The programming in ASPEN PLUS™ was carried out graphically, and some custom routines in FORTRAN language were added. Furthermore, the software allows for conducting sensitivity analyses in an efficient way. This feature was integrated in this work.

For the simulations, the process was modelled in steady state conditions, and the solid-gas separation in the cyclones was considered ideal. The system pressure was set to 1.013 bar, and the pressure drops were neglected. The solids were considered inert with respect to the phase equilibrium, i.e. no dissolution or vaporization was allowed for solids. The Redlich-Kwong-Soave model was used for the calculation of the properties of the gases (Tilak and El-Halwagi, 2018). For the solids, the properties were calculated with polynomial functions, which are already programmed in ASPEN PLUS™. In particular, the energy, enthalpy, entropy and heat capacity were calculated with the Barin equations (Aspen Technology, Inc. 2001). The APV110 database, from Aspen Technology Inc., was used as input for the property calculations. The rotary kiln was modelled using three reactor blocks, according to the work of Zhang et al. (2011). To model coal combustion, the fuel was first inserted into a yield reactor that decomposes it into the elementary molecules and heat. Afterwards, the resulting stream was burned with the combustion air in a Gibbs reactor, which minimizes the Gibbs' free energy in order to calculate the heat production and the products yield. Finally, the heat, the combustion products, and the lime were inserted into a conversion reactor, where the calcination takes place. The degree of calcination of $CaCO_3$, in this reactor, was set to 99%, according to available empirical data from the host plant. The combustor of the IHCaL process was modelled analogously. For all the combustion processes, an air-fuel equivalence ratio (λ) of 1.2 was considered according to the host plant. The temperature of the IHCaL combustor was set to 1000 °C to allow for 100 K temperature difference to the calciner, according to (Reitz et al., 2016, 2014). The calcination and carbonation reactions in the IHCaL reactors were modelled with conversion reactor blocks, where the reactions take place at specified molar fractional conversions (f). The fractional conversions are the degree of carbonation (f_{carb}) for the carbonator, and the degree of calcination (f_{calc}), for the calciner. f_{calc} was set to 0.99, according to previous models of the research group (Junk et al., 2013; Haaf, 2020; Haaf et al., 2017), and f_{carb} was varied relative to the capture efficiency set point. The heat exchangers were modelled considering the temperature variation as input (see Table 3) to obtain the heat flows as a result.

The fuel and raw material compositions (shown in Tables 1 and Table 2, respectively) were defined according to the reference plant. The same pre-dried lignite (LHV = 21,500 kJ/kg) used to fire the PRK was implemented as fuel for the combustor in the IHCaL. Similarly, the

Table 1
Composition of the pre-dried lignite (LHV = 21,500 kJ/kg) implemented as fuel for the PRK and the combustor of the IHCaL.

Component	Mass fraction (%)
C	56.7
H	4.3
Cl	0.2
S	0.8
O	21.5
N	0.7
H_2O (moisture)	10.3
Ash	5.5

Table 2
Composition of the limestone.

Component	Mass fraction (%)
$CaCO_3$	98.3
$MgCO_3$	0.7
SiO_2	0.7
Fe2O_3	0.1
Al2O_3	0.2
SO_3	<0.1

limestone's composition from the reference plant (98.3 wt% $CaCO_3$) was used for all the limestone inputs in the model.

3.2. Key performance indicators

In order to evaluate the solutions proposed, the following key performance indicators were considered. The CO_2 capture efficiency, *E*, is defined as the ratio of the captured CO_2 to the generated CO_2, in terms of molar flow rate. *E* is obtained by Eq. (1) considering the CO_2 leaving the calciner, $F_{CO_2}^{calc,out}$, and the CO_2 leaving the carbonator, $F_{CO_2}^{carb,out}$. In previous IHCaL pilot tests, CO_2 capture efficiencies higher than 90% were achieved (Reitz et al., 2016). A CO_2 capture efficiency of 90% was set as an input parameter because the focus of this study is on the energy and mass balances rather than the kinetic and the design of the components.

$$E = \frac{F_{CO_2}^{calc,out}}{F_{CO_2}^{calc,out} + F_{CO_2}^{carb,out}} \tag{1}$$

The product ratio, *PR*, considers the production of the entire process including the IHCaL unit, $\dot{m}_{CaO;prod}$, in relation to the production in the reference plant, $\dot{m}_{CaO;prod}^{ref}$, according to Eq. (2).

$$PR = \frac{\dot{m}_{CaO,prod}}{\dot{m}_{CaO,prod}^{ref}} \tag{2}$$

The heat ratio, *HR*, defined in Eq. (3), is used as the indicator of the heat requirement for CO_2 capture and lime production. It is calculated considering the lime produced and the heat requirement in the original process, Q_{in}^{ref}, and in the entire process including CO_2 capture, Q_{in}.

$$HR = \frac{Q_{in} \Big/ \dot{m}_{CaO,prod}}{Q_{in}^{ref} \Big/ \dot{m}_{CaO,prod}^{ref}} \tag{3}$$

For the power generation, P_{el}, from the high temperature heat of the IHCaL, $Q_{out,IHCaL}$, a heat-to-power efficiency, η_{h2p}, of 45% is assumed in this work (see Eq. (4)). This value of η_{h2p}corresponds to a net electrical efficiency of around 40%, in the case of a thermal power plant, which is in agreement with reference values from the literature (IEA, 2020). A detailed concept for heat recovery of a similar system can be found in the work of (Lena et al., 2017).

$$P_{el} = \eta_{h2p} \cdot Q_{out,IHCaL} \tag{4}$$

For the CO_2 balance, the specific direct CO_2 emissions, e_{CO2}, are calculated as the amount of CO_2 directly emitted into the atmosphere from the complete process per unit of lime produced. The specific direct fuel consumption, *q*, is defined as the direct primary energy consumption in the entire facility per unit of product (i.e. CaO).

3.3. IHCaL operation parameters and sensitivity analysis

The results from former experimental and numerical work of the group (Hilz et al., 2017; Reitz et al., 2016; Haaf, 2020) were used to define the fractional conversion in the reactors and the main operation parameters. With respect to the boundary conditions, the operating temperature of the calciner is set at 900 °C to enable a full calcination at nearly pure CO_2 atmosphere, according to the models of Baker and García (Baker, 1962). The operation temperature of the carbonator is set to 650 °C, according to Junk (2017), in order to achieve a maximum capture efficiency of around 90%.

The make-up flow, which is needed to avoid the build-up of inert species and to maintain the proper activity of the sorbent (De Lena et al., 2018), is characterized with the make-up ratio, Λ, i.e. the ratio of the molar flow rate of make-up calcium species to the total molar flow rate of CO_2 according to Eq. (5). For the base-case simulations, the make-up ratio was set to 0.2, considering Hilz et al (2017).

$$\Lambda = \frac{F_0}{F_{CO_2}} \tag{5}$$

Another important dimensionless parameter is the specific sorbent circulation rate, Φ, which considers the molar flow rate of calcium species that are fed to the carbonator, F_R, as defined in Eq. (6). The specific sorbent circulation rate was varied between 6 and 24 (Haaf, 2020) in the simulations. The optimal design point depends on the make-up ratio, the set point of the capture efficiency, the deactivation of the sorbent, and techno-economic considerations.

$$\Phi = \frac{F_R}{F_{CO_2}} \tag{6}$$

For the sensitivity analysis, five parameters were considered—three key performance indicators and two temperatures, namely, the sorbent temperature at the calciner inlet ($T_{sorb,calc,in}$) and the temperature of the preheated combustor air ($T_{preheat}$). A base case was defined and each parameter was then varied leaving the others constant. The values in the base case as well as the range of variation are shown in Table 3. The operation parameters are summarized in Table 4.

4. Results and discussion

4.1. Results of the base case

The heat and mass balances of the reference PRK facility were calculated with less than 1% deviation from the reference values provided by the operator. The output parameters considered for the validations are the flue gas molar flow after the preheater, the CO_2 concentration of that facility, and the production in tones per hour of lime.

Table 3
Base case and range of variation for each parameter in the sensitivity analysis.

	Base case	Range
Carbon capture efficiency (*E*)	0.9	0.4 - 0.95
Specific make-up ratio (Λ)	0.2	0.05 - 0.40
Specific sorbent circulation rate (Φ)	6	6 - 30
Combustion air temperature (combustor) ($T_{preheat}$) [°C]	800	200 - 900
Sorbent temperature at calciner inlet ($T_{sorb,calc,in}$) [°C]	810	650 - 875

Table 4
Summary of the operating parameters assumed for the modelling of the base case.

Main IHCaL Parameters	
CO_2 capture efficiency (E)	90%
Specific sorbent circulation rate (Φ)	6
Specific make-up ratio* (Λ)	0.20
f_{calc}	0.99
Operation Temperatures	
Carbonator operating temperature [°C]	650
Calciner operating temperature [°C]	900
Sorbent temperature at calciner inlet [°C]	810
Combustor operating Temperature [°C]	1000

* Λ is an output for the $IHCaL_{NP}$.

Table 5
Results summary and main operation parameters.

	$IHCaL_{PRH}$	$IHCaL_{NP}$
Heat ratio (*HR*)	2.54	1.63
Product ratio (*PR*)	2.26	1.01
Specific make-up ratio (Λ)	0.20*	0.47
Carbonator		
Flue gas temperature at carbonator inlet [°C]	338	574
Sorbent temperature at carbonator inlet [°C]	664	656
Flue gas from lime plant [kmol/s]	1.13	-
Flue gas from IHCaL combustion [kmol/s]	2.53	0.88
Total flue gas flow to the carbonator [kmol/s]	3.66	0.88
Total CO_2 molar concentration in the flue gas [mol/mol]	0.164	0.157
Molar conversion of the sorbent exiting the carbonator [mol_{CaCO3}/mol_{Ca}]	0.148	0.154
Calciner		
Sorbent mole flow at calciner inlet [kmol/s]	4.63	1.52
Purge CaO flow [t/day]	718	582
Calciner heat input [MW_{th}]	141	49.1
Combustor		
Fuel Consumption IHCaL [kg/s]	8.38	2.93
Combustor heat input [MW_{th}]	180	62.9

* Λ is an input for the $IHCaL_{PRH}$.

The lime extracted from the purges of the IHCaL shows a high purity (97.5 wt% CaO). Consequently, it can be sold as product of the lime production, which makes the IHCaL process especially suitable for the application to lime plants. For the base case defined in Table 3, the main results are shown in Tables 5 and Table 6.

The direct fuel consumption of the reference PRK (5090 MJ/t_{CaO}) is in the lower limit for this kind of kilns, according to the BREF values (Schorcht et al., 2013). The tail-end solution ($IHCaL_{PRH}$) leads to a 154% increase of the direct fuel consumption (12900 MJ/t_{CaO}) and a 70.5% reduction of the direct CO_2 emissions with respect to the reference plant. For the fully integrated case ($IHCaL_{NP}$), the increase in fuel consumption is only 63% (8300 MJ/t_{CaO}), and the reduction in direct CO_2 emissions is 87.4%. For this case, the electricity generated through heat recovery amounts to 29.6% of the total thermal energy input. This implies a further reduction in the net CO_2 emissions, considering the avoidance of the CO_2 from the grid's power generation. Furthermore, the combustor can be adapted to burn refuse-derived fuels with high biogenic content, which would allow for negative CO_2 emissions.

In the tail-end concept, the product ratio is as high as 2.26, which means that more lime is being produced in the IHCaL facility than in the PRK. The production of the $IHCaL_{NP}$ is very similar to the reference plant ($PR = 1.01$) because the raw material input is the same for both. The specific make-up ratio is set to 0.2 for the tail-end concept. This parameter controls the production from the IHCaL facility in the case of the $IHCaL_{PRH}$. While it may be more reasonable to keep this production low, it is necessary to maintain a certain make-up as explained in Section 3.3. For the fully integrated solution, the make-up ratio is an output variable. This is because the raw material input is considered the same as for the reference plant in order to achieve the same production. Due to the high value of Λ for this integration solution, a highly reactive solid inventory can be expected. The modelling of the inventory's activity is out of the scope of this paper. It will be studied empirically during the test campaigns at the 300 kW_{th} pilot plant of the Technical University of Darmstadt (Ströhle et al., 2021).

4.2. Sensitivity analysis

The most important results of the sensitivity analysis for the tail-end concept are shown in Fig. 3. Fig. 3 (a) is a graph of the *HR* as a function of the sorbent temperature at the calciner inlet, $T_{sorb,calc,in}$, for different values of preheated air temperature, $T_{preheat}$, under the assumption of constant circulation rate and make-up ratio. For $T_{preheat} = 800$ °C, an increase of $T_{sorb,calc,in}$ from 700 °C to 800 °C generates a decrease of 0.92 points in the *HR*, in the reference lime plant.

As expected, the higher the temperatures of the combustor air and the sorbent at the calciner inlet, the lower the *HR*. This means that the heat requirement is influenced by the heat exchange at the preheater and at the solid-solid heat exchanger. In particular, the high influence of solids preheating is remarkable, considering that a variation of 100 K modifies the *HR* in as much as 0.9 points. Since the heat integration affects the CO_2 production and the sorbent flows should be adjusted to comply with the CO_2 molar flow rate, there is an indirect influence of the temperatures $T_{sorb,calc,in}$ and $T_{preheat}$ on the product ratio, *PR*, as shown in Fig. 3 (b). It is observed that the better the heat integration, the smaller the production. An increase of the production could be a disadvantage if there were limitations in space and capacity at the specific site. For example, in the base case ($T_{preheat} = 800$ °C and $T_{sorb,calc,in} = 810$ °C), it would be necessary to double the production ($PR = 2.26$) for the new concept in order to capture the CO_2 of the rotary kiln.

Fig. 3 (c) shows that an increase in the make-up, and thus the production, lowers the *HR* of the entire facility. This is because the CO_2 emissions of the limestone calcined in the IHCaL calciner do not need to be captured downstream, as it is the case of the emissions of the PRK. Furthermore, as the production of the IHCaL facility is increased, the tail-end solution becomes more similar to the fully integrated concept. In this last concept, the heat penalty for carbon capture is smaller than for the tail-end solution.

The results of the sensitivity analysis for the fully integrated concept

Table 6
Model results: CO_2 and energy balances.

	Reference plant	$IHCaL_{PRH}$	$IHCaL_{NP}$
CO_2 balance			
Molar flow rate of CO_2 from kiln [kmol/h]	735	735	-
Molar flow rate of CO_2 from IHCaL combustor [kmol/h]	-	1428	497
Molar flow rate of CO_2 from calcined make-up in IHCaL [kmol/h]	-	544	437
Total CO_2 output [kmol/h]	735	2706	934
Specific direct CO_2 emissions (e_{CO2}) [kg CO_2/t_{CaO}]	1345	221	169
Energy balance			
Total heat input [MW_{th}]	38.2	218	62.9
Power generation (P_{el}) [MW_{el}]	-	70.6	18.6
Specific direct fuel consumption (q) [GJ/t_{CaO}]	5.7	14.6	9.3

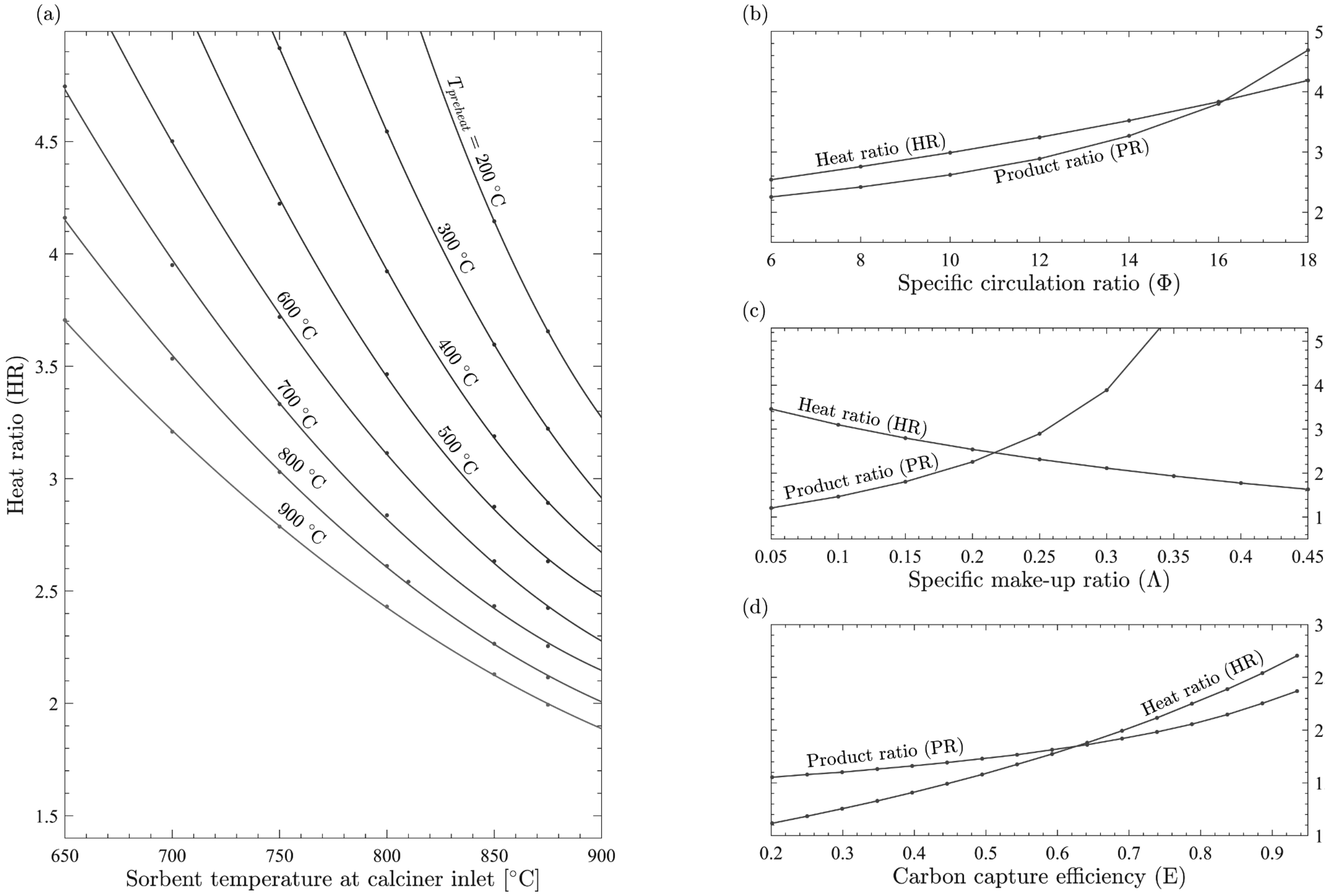

Fig. 3. Sensitivity analysis for the tail-end integration concept. In (a), the influence of $T_{sorb,calc,in}$ and $T_{preheat}$ on the heat ratio (*HR*) is depicted. Furthermore, the variation of the heat ratio (*HR*) and the product ratio (*PR)* with the specific circulation ratio (Φ) (b), the specific make-up ratio (Λ) (c), and the carbon capture efficiency (*E)* (d) is depicted.

are summarized in Fig. 4. Fig. 4 (a) shows the variation of the heat ratio with the main temperatures for the heat integration, $T_{sorb,calc,in}$ and $T_{preheat}$. It is remarkable that, compared with the results from the tail-end solution, the values of *HR* are much lower for the same temperature values. Furthermore, it can be noticed that towards the limit of the maximum theoretical integration, the *HR* tends towards 1; whereas in the tail-end solution, the minimum achievable *HR* is around 2. For the base case, there is a reduction of the *HR* by 36% in the full integration concept with respect to the tail-end configuration.

The influence of the specific circulation ratio, Φ, is shown in Fig. 4 (b). The variation of the *HR* with Φ is very similar to the one of the tail-end configuration shown in Fig. 3 (b). The main difference is that the values of *HR* in the integrated solution are smaller, because the heat requirement associated with capturing the process CO_2 emissions is avoided. Regarding the specific make-up rate, Λ, with increasing Φ, the carbon capture becomes less efficient and therefore more CO_2 is produced by the increased fuel consumption. Even though this reduces the value of Λ, it remains within the accepted range for IHCaL operation (Haaf, 2020).

The influence of the carbon capture efficiency (*E*) for the $IHCaL_{NP}$ is shown in Fig. 4 (c). For values below 62%, there is no conversion in the carbonator. This means that, because the majority of CO_2 is produced in the calciner, 62% efficiency can be achieved without the need to capture the CO_2 from the flue gases of the combustor. With this idea, a fully integrated concept without recirculation of the flue gases from the combustor into the carbonator would be possible if low carbon capture efficiencies were admitted. This might be accepted if renewable fuels are used in the combustor.

5. Conclusions

Two concepts for the integration of the IHCaL into the lime production have been presented. Based on the heat and mass balances and a sensitivity analysis, the following conclusions can be drawn.

In the tail-end solution, i.e. an end-of-pipe configuration that is suitable for retrofitting existing lime plants, the direct CO_2 emissions were reduced to 29.5% of the reference value with an increase of 154% in the direct fuel consumption. Such concepts might be applicable to existing lime plants, especially when combining them with the use of secondary fuels. The required amount of make-up to avoid the deactivation of the sorbent is an important parameter that governs the lime output mass flow. Because this concept allows for an increase in the production, it may be a good option for lime plants that are looking to capture CO_2, and, at the same time, want to expand their productive capacity.

In the fully integrated configuration, corresponding to a newly built plant with 100% of the lime production integrated into the IHCaL calcination process, a higher energy efficiency and less CO_2 emissions can be achieved. The direct CO_2 emissions are reduced to 12.6% of the reference value with a 63% increase in the direct fuel consumption.

The sensitivity analysis shows that it is very important to maximize the preheating temperature of the combustion air and to achieve the best possible heat exchange in the solid-solid heat exchanger, in order to cap the energy requirements of the capture process. Due to the relatively high mass flow from the purge, i.e. 126 % of the kiln production in the base case $IHCaL_{PRH}$, the utilization of this material as product is crucial for the viability of the tail-end solutions.

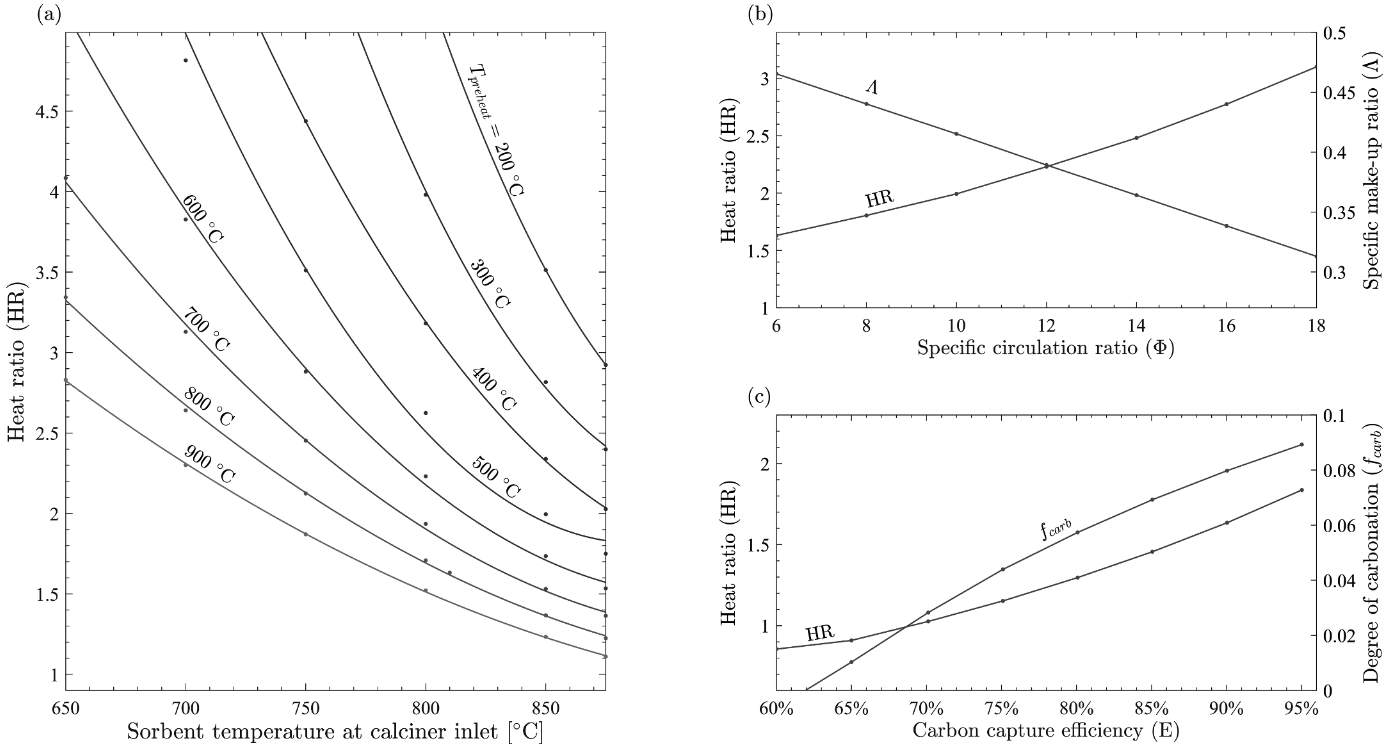

Fig. 4. Sensitivity analysis for the fully integrated concept. In (a), the influence of $T_{sorb,calc,in}$ and $T_{preheat}$ on the heat ratio (*HR*) is depicted. Graph (b) shows the variation of the heat ratio (*HR*) and the specific make-up ratio (Λ) with the specific circulation ratio (Φ). Finally, the influence of the carbon capture efficiency (*E*) on the heat ratio (*HR*) and on the degree of carbonation (f_{carb}) is presented in graph (c).

For both configurations, it was assumed that the purge (lime) is suitable to substitute the product of the rotary kiln. Some previous studies on the effect of looping CaO in a CaL process provide some evidence to support this assumption (Hills, 2016; Dean et al., 2013). Nevertheless, the validity of this assumption will be verified by testing the purge material from the upcoming test campaigns at the 300 kW_{th} pilot plant at the Technical University of Darmstadt (Ströhle et al., 2021).

For the implementation of the solid-solid heat exchanger, different designs are being evaluated within the ANICA project. Potential configurations are (i) a concept with molten salt and a regenerative heating/cooling of a solid, (ii) a concept with heat pipes, and (iii) a concept with two concentric L-valves. The sensitivity analysis of $T_{sorb,calc,in}$, presented in this paper, will be used to evaluate and dimension the different designs, and then select the most suitable configuration for this application.

The use of waste fuels with high biogenic content instead of coal and power generation through heat recovery enable these concepts to further reduce the net CO_2 emissions and even reach negative values. The developed models and the results will be further used to establish boundary conditions for the planned test campaigns at the 300 kW_{th}-scale, under lime plant conditions (Ströhle et al., 2021), as well as to execute economic, environmental, and risk analyses on the integration of the IHCaL into the lime production process.

CRediT author statement

Martin Greco-Coppi: Conceptualization, Methodology, Software, Visualization, and Writing (Original Draft). Carina Hofmann: Conceptualization and Methodology; Jochen Ströhle: Conceptualization, Writing (Review & Editing), Project administration, and Funding acquisition; Diethelm Walter: Conceptualization, Methodology, and Writing (Review & Editing); Bernd Epple: Supervision, and Funding acquisition.

Funding

The work leading to these results have received funding through the ACT program (Accelerating CCS Technologies, Horizon 2020 Project N° 294766) within the ANICA project. Financial contributions were made from the German Federal Ministry of Economic Affairs and Energy, the Department for Business, Energy an Industrial Strategy of the United Kingdom, and the Greek General Secretariat for Research and Technology.

Declaration of Competing Interest

The authors declare that they have no known competing financial interests or personal relationships that could have appeared to influence the work reported in this paper.

Supplementary materials

Supplementary material associated with this article can be found, in the online version, at doi:10.1016/j.ijggc.2021.103430.

References

Abanades, J.C., Grasa, G., Alonso, M., Rodriguez, N., Anthony, E.J., Romeo, LM., 2007. Cost structure of a postcombustion CO2 capture system using CaO. Environ. Sci. Technol. 41 (15), 5523–5527. https://doi.org/10.1021/es070099a.

Anantharaman, R., Berstad, D., Cinti, G., de Lena, E., Gatti, M., Hoppe, H., et al., 2018. Cemcap framework for comparative techno-economic analysis of Co2 capture from cement plants - D3.2. Zenodo.

Arias, B., Diego, M.E., Abanades, J.C., Lorenzo, M., Diaz, L., Martínez, D., et al., 2013. Demonstration of steady state CO2 capture in a 1.7MWth calcium looping pilot. Int. J. Greenh. Gas Control 18, 237–245. https://doi.org/10.1016/j.ijggc.2013.07.014.

Aspen Technology, Inc. Aspen physical property system: physical property methods and models V11.1. Cambridge; 2001.

Baker, EH., 1962. The calcium oxide–carbon dioxide system in the pressure range 1—300 atmospheres. J. Chem. Soc. 464–470. https://doi.org/10.1039/JR9620000464, 0(0).

Bosoaga, A., Masek, O., Oakey, J.E., 2009. CO2 capture technologies for cement industry. Energy Procedia 1 (1), 133–140. https://doi.org/10.1016/j.egypro.2009.01.020.

Carrasco-Maldonado, F., Spörl, R., Fleiger, K., Hoenig, V., Maier, J., Scheffknecht, G., 2016. Oxy-fuel combustion technology for cement production – State of the art research and technology development. Int. J. Greenh. Gas Control 45, 189–199. https://doi.org/10.1016/j.ijggc.2015.12.014.

De Lena, E., Spinelli, M., Romano, M.C., 2018. CO2 capture in cement plants by "Tail-End" Calcium Looping process. Energy Procedia 148, 186–193. https://doi.org/10.1016/j.egypro.2018.08.049.

Dean, C., Hills, T., Florin, N., Dugwell, D., Fennell, P.S., 2013. Integrating calcium looping CO2 capture with the manufacture of cement. Energy Procedia 37 (6), 7078–7090. https://doi.org/10.1016/j.egypro.2013.06.644.

Fan L.-S. Separation of carbon dioxide from gas mixtures by calcium based reaction separation; 2012; Available from: https://patents.google.com/patent/us8226917/en.

Fantini, M., Balocco, M., Buzzi, L., Canonico, F., Consonni, S., Cremona, R., et al., 2021. Calcium looping technology demonstration in industrial environment: status of the CLEANKER pilot plant. SSRN J. https://doi.org/10.2139/ssrn.3817346.

Haaf, M., Stroh, A., Hilz, J., Helbig, M., Ströhle, J., Epple, B., 2017. Process modelling of the calcium looping process and validation against 1 MWth pilot testing. Energy Procedia 114, 167–178. https://doi.org/10.1016/j.egypro.2017.03.1159.

Haaf, M., 2020. Utilization of Waste-Derived Fuels in the Calcium Looping Process: Experimental Demonstration and Techno-Economic Assessment. Technische Universität Darmstadt, Darmstadt, Germany [Doctoral Dissertation].

Hills, T.P., 2016. Investigations of the Use of Spent Sorbent from the Ca Looping Process in Cement Manufacture and Investigation of Long-Term CO2 Uptake in Cement and Concrete [PhD Thesis]. Imperial College London of Science, Technology and Medicine.

Hills, T.P., Sceats, M., Rennie, D., Fennell, P., 2017. LEILAC: low cost CO2 capture for the cement and lime industries. Energy Procedia 114, 6166–6170. https://doi.org/10.1016/j.egypro.2017.03.1753.

Hilz, J., Helbig, M., Haaf, M., Daikeler, A., Ströhle, J., Epple, B., 2017. Long-term pilot testing of the carbonate looping process in 1 MWth scale. Fuel 210 (Part 1), 892–899. https://doi.org/10.1016/j.fuel.2017.08.105.

Hodgson, P., Sceats, M., Vincent, A., Rennie, D., Fennell, P., Hills, T., 2019. Direct separation calcination technology for carbon capture: demonstrating a low cost solution for the lime and cement industries in the LEILAC project. SSRN Electron. J. https://doi.org/10.2139/ssrn.3365844.

Hoeftberger, D., Karl, J., 2016. The indirectly heated carbonate looping process for CO2 capture—a concept with heat pipe heat exchanger. J. Energy Res. Technol. 138 (4), 148A. https://doi.org/10.1115/1.4033302.

IEA, 2020. Energy Technology Perspectives 2020 - Special Report on Carbon Capture Utilisation and Storage. OECD.

IEAGHGT, 2014. CO2 Capture at Coal Based Power and Hydrogen Plants.

IEA. Projected costs of generating electricity. Paris; 2020.

Jordal, K, Voldsund, M, Størset, S, Fleiger, K, Ruppert, J, Spörl, R, et al., 2017. CEMCAP – Making CO2 Capture Retrofittable to Cement Plants. Energy Procedia 114, 6175–6180. https://doi.org/10.1016/j.egypro.2017.03.1755.

Jordal, K., Voldsund, M., Størset, S., Fleiger, K., Ruppert, J., Spörl, R., et al., 2017. CEMCAP – Making CO2 capture retrofittable to cement plants. Energy Procedia 114, 6175–6180. https://doi.org/10.1016/j.egypro.2017.03.1755.

Junk, M., Reitz, M., Ströhle, J., Epple, B., 2016. Technical and economical assessment of the indirectly heated carbonate looping process. J. Energy Res. Technol. 138 (4) https://doi.org/10.1115/1.4033142.

Junk M., Reitz M., Ströhle J., Epple B. Technical and economical assessment of the indirectly heated carbonate looping process. undefined 2016.

Junk, M., Reitz, M., Ströhle, J., Epple, B., 2013. Thermodynamic evaluation and cold flow model testing of an indirectly heated carbonate looping process. Chem. Eng. Technol. 36 (9), 1479–1487. https://doi.org/10.1002/ceat.201300019.

Junk, M., 2017. Technical and Economical Assessment of Various Carbonate Looping Process Configurations, 1st ed. Cuvillier Verlag, Göttingen.

Lasheras, A., Ströhle, J., Galloy, A., Epple, B., 2011. Carbonate looping process simulation using a 1D fluidized bed model for the carbonator. Int. J. Greenh. Gas Control 5 (4), 686–693. https://doi.org/10.1016/j.ijggc.2011.01.005.

Lena, E., Spinelli, M., Martínez, I., Gatti, M., Scaccabarozzi, R., Cinti, G., et al., 2017. Process integration study of tail-end Ca-looping process for CO2 capture in cement plants. Int. J. Greenh. Gas Control 67, 71–92. https://doi.org/10.1016/j.ijggc.2017.10.005.

Martínez, I., Murillo, R., Grasa, G., Rodríguez, N., Abanades, J.C., 2011. Conceptual design of a three fluidised beds combustion system capturing CO2 with CaO. Int. J. Greenh. Gas Control 5 (3), 498–504. https://doi.org/10.1016/j.ijggc.2010.04.017.

Magli, F., Spinelli, M., Fantini, M., Romano, M.C., Gatti, M., 2021. Techno-economic and off-design analysis of two CO2 purification units for low-carbon cement plants with oxy-fuel calcination. SSRN J. https://doi.org/10.2139/ssrn.3821716.

Moon, H., Yoo, H., Seo, H., Park, Y.-.K., Cho, HH., 2015. Thermal design of heat-exchangeable reactors using a dry-sorbent CO2 capture multi-step process. Energy 84, 704–713. https://doi.org/10.1016/j.energy.2015.03.034.

Ramkumar, S., Fan, L.-S., 2010. Thermodynamic and experimental analyses of the three-stage calcium looping process. Ind. Eng. Chem. Res. 49 (16), 7563–7573. https://doi.org/10.1021/ie100846u.

Reitz, M., Junk, M., Ströhle, J., Epple, B., 2014. Design and erection of a 300 kWth indirectly heated carbonate looping test facility. Energy Procedia 63, 2170–2177. https://doi.org/10.1016/j.egypro.2014.11.236.

Reitz, M., Junk, M., Ströhle, J., Epple, B., 2016. Design and operation of a 300kWth indirectly heated carbonate looping pilot plant. Int. J. Greenh. Gas Control 54, 272–281. https://doi.org/10.1016/j.ijggc.2016.09.016.

Schorcht, F., Kourti, I., Scalet, B.M., Roudier, S., Delgado Sancho, L., 2013. Best available techniques (BAT) reference document for the production of cement, lime and magnesium oxide: Industrial Emissions Directive 2010/75/EU (integrated pollution prevention and control). Publications Office, Luxembourg.

Shimizu, T., Hirama, T., Hosoda, H., Kitano, K., Inagaki, M., Tejima, K., 1999. A twin fluid-bed reactor for removal of CO2 from combustion processes. Chem. Eng. Res. Des. 77 (1), 62–68. https://doi.org/10.1205/026387699525882.

Ströhle, J., Hofmann, C., Greco-Coppi, M., Epple, B., 2021. CO2 Capture from Lime and Cement Plants Using an Indirectly Heated Carbonate Looping Process - The ANICA Project. Short Papers from the 11th International Trondheim CCS Conference 529–535. In press.

Tilak, P., El-Halwagi, M.M., 2018. Process integration of Calcium Looping with industrial plants for monetizing CO2 into value-added products. Carbon Resourc. Convers. 1 (2), 191–199. https://doi.org/10.1016/j.crcon.2018.07.004.

Tola, V., Pettinau, A., 2014. Power generation plants with carbon capture and storage: a techno-economic comparison between coal combustion and gasification technologies. Appl. Energy 113, 1461–1474. https://doi.org/10.1016/j.apenergy.2013.09.007.

Voldsund, M., Anantharaman, R., Berstad, D., de Lena, E., Fu, C., Gardarsdottir, S.O., et al., 2019. D4.6 CEMCAP comparative techno-economic analysis of CO2 capture in cement plants. Zenodo.

Wang, W., Ramkumar, S., Li, S., Wong, D., Iyer, M., Sakadjian, B.B., et al., 2010. Subpilot demonstration of the carbonation−calcination reaction (CCR) process: high-temperature CO 2 and sulfur capture from coal-fired power plants. Ind. Eng. Chem. Res. 49 (11), 5094–5101. https://doi.org/10.1021/ie901509k.

Zhao, M., Minett, A.I., Harris, A.T., 2013. A review of techno-economic models for the retrofitting of conventional pulverised-coal power plants for post-combustion capture (PCC) of CO 2. Energy Environ. Sci. 6 (1), 25–40. https://doi.org/10.1039/C2EE22890D.

Zhang, Y., Cao, S.-.X., Shao, S., Chen, Y., Liu, S.-L., Zhang, S.-S., 2011. Aspen Plus-based simulation of a cement calciner and optimization analysis of air pollutants emission. Clean Techn. Environ. Policy 13 (3), 459–468. https://doi.org/10.1007/s10098-010-0328-y.

Research Paper II

Research Paper II

Title: Negative CO_2 emissions in the lime production using an indirectly heated carbonate looping process

Authors: Martin Greco Coppi, Carina Hofmann, Diethelm Walter, Jochen Ströhle, Bernd Epple

Journal: Mitigation and Adaptation Strategies for Global Change (Springer)

Status: Published (June 12, 2023)

Volume: 28 (2023)

DOI: https://doi.org/10.1007/s11027-023-10064-7

Licensing: The authors. CC BY 4.0

Short Summary

In this work, a retrofit configuration of the IHCaL process is presented and analyzed for net-negative CO_2 emissions. Four scenarios using different fuels are simulated with an Aspen Plus model, key performance indicators are calculated, and the results are compared with those from previous studies using other CO_2 capture methods. Net-negative CO_2 emissions as high as −1.8 t_{CO2}/t_{CaO} are obtained. This represents an equivalent CO_2 avoidance of more than 230 % with respect to the reference plant without capture (1.4 t_{CO2}/t_{CaO}). For some scenarios, the specific primary energy consumption for CO_2 avoided (*SPECCA*) was lower than 1.5 $MJ_{LHV}/kg_{CO2,av}$. Particularly promising results can be accomplished when applying fuels with high biogenic fraction and low specific CO_2 emissions, such as solid recovered fuels (SRFs) with a high calorific value.

Mitig Adapt Strateg Glob Change (2023) 28:30
https://doi.org/10.1007/s11027-023-10064-7

ORIGINAL ARTICLE

Negative CO_2 emissions in the lime production using an indirectly heated carbonate looping process

Martin Greco-Coppi[1] · Carina Hofmann[1] · Diethelm Walter[2] · Jochen Ströhle[1] · Bernd Epple[1]

Received: 4 October 2022 / Accepted: 29 April 2023 / Published online: 12 June 2023
© The Author(s) 2023

Abstract

Lime is an essential raw material for iron and steel production, in construction and agriculture, in civil engineering, in environmental protection, and in manifold chemical manufacturing processes. To address the problem of unavoidable process CO_2 emissions associated with the production of lime, efficient capture technologies need to be developed and implemented. The indirectly heated carbonate looping (IHCaL) process is an efficient candidate for this application because it utilizes lime as the sorbent for the CO_2 capture. In this work, a retrofit configuration of this process is presented and analyzed for net negative CO_2 emissions. This is done considering different fuels that provide the heat required for the regeneration of the sorbent. The different scenarios were simulated with an AspenPlus® model, key performance indicators were calculated, and the process was compared with other post-combustion capture methods. The results show that net negative CO_2 emissions as high as $-1805\ \mathrm{kg_{CO2}/t_{CaO}}$, calculated with a state-of-the-art coal power plant energy scenario ($\eta_e = 44.2$ %; $e_{ref,el} = 770\ \mathrm{kg_{CO2}/MWh_{el}}$), can be obtained. This represents an equivalent CO_2 avoidance of more than 230% with respect to the reference plant without capture ($1368\ \mathrm{kg_{CO2}/t_{CaO}}$). A specific primary energy consumption for CO_2 avoided (*SPECCA*) lower than $1.5\ \mathrm{MJ_{LHV}/kg_{CO2,av}}$ was achieved for the same energy scenario. Particularly promising results can be accomplished when applying fuels with high biogenic fraction and low specific CO_2 emissions, such as solid recovered fuels (SRFs) with a high calorific value.

Keywords Negative CO_2 emissions · Carbonate looping · Indirectly heated · Carbon dioxide removal · Refuse-derived fuels · Solid recovered fuels · Lime production

Nomenclature

AFR	Air-fuel ratio ($\mathrm{kg_{air}/kg_{fuel}}$)
c_p	Specific heat capacity (massic) ($\mathrm{J\ kg^{-1}\ K^{-1}}$)
$\overline{c}_p$	Specific heat capacity (molar) ($\mathrm{J\ mol^{-1}\ K^{-1}}$)
e_{CO2}	CO_2 emissions (direct) ($\mathrm{kg_{CO2}/t_{CaO}}$)
$e_{CO2,fuel}$	Specific CO_2 emissions of the fuel ($\mathrm{g_{CO2}/MJ_{LHV}}$)
$e_{ref,el}$	Reference CO_2 emissions for power production ($\mathrm{kg_{CO2}/MW_{el}}$)
E	Carbon capture efficiency (%)

Extended author information available on the last page of the article

E_{calc}	Calciner efficiency (%)
E_{carb}	Carbonator efficiency (%)
F_0	Molar flow rate of make-up calcium species (kmol/s)
F_{CO2}	Molar flow rate of CO_2 at carbonator inlet (kmol/s)
F_{CO2}^{calc}	Molar flow rate of CO_2 at calciner outlet (kmol/s)
F_{CO2}^{carb}	Molar flow rate of CO_2 at carbonator outlet (kmol/s)
F_R	Molar flow rate of calcium species at carbonator inlet (kmol/s)
h	Height (m)
HHV	Higher heating value (kJ/kg)
HR	Specific heat ratio (-)
HR_a	Absolute heat ratio (-)
LHV	Lower heating value (kJ/kg)
M	Molar mass, atomic mass (kg/kmol)
$\dot{m}_{CaO,prod}$	Total lime production (t/day)
P_{el}	Net power consumption of the entire facility (MW_{el})
PR	Product ratio (-)
q	Fuel consumption (direct) (MJ/t_{CaO})
$\dot{Q}$	Heat flow (MW_{th})
$SPECCA$	Specific primary energy consumption for CO_2 avoided ($MJ_{LHV}/kg_{CO2,av}$)
$T_{preheat}$	Combustor preheated air temperature (°C)
$T_{sorb,calc,in}$	Sorbent temperature at calciner inlet (°C)
x_{bio}	Biogenic carbon fraction in the fuel (%)
X_{bN}	Maximum CaO conversion in the kinetic region after N cycles (mol_{CaCO3}/mol_{Ca})
X_{carb}	Fraction of $CaCO_3$ in the solid stream leaving the carbonator (mol_{CaCO3}/mol_{Ca})
X_{calc}	Fraction of $CaCO_3$ in the solid stream leaving the calciner (mol_{CaCO3}/mol_{Ca})

Greek symbols

Δp	Pressure drop in reactor and auxiliary components (mbar)
η_{h2p}	Heat-to-power efficiency (%)
$\eta_{ref,el}$	Reference electrical efficiency (%)
λ	Air-fuel equivalence rate (-)
Λ	Specific make-up rate (mol_{CaCO3}/mol_{CO2})
τ	Mean residence time or space time (s)
Φ	Specific sorbent circulation rate (mol_{Ca}/mol_{CO2})

Subscripts and superscripts

av	Avoided
bio	Biogenic
calc	Calciner
carb	Carbonator
capt	Captured CO_2
CC	Retrofitted case with carbon capture
comb	Combustor
dry	Dry basis

el	Electric
eq	Equivalent
equil	Equilibrium
FA	Fluidization agent
foss	Fossil
i	Indirect
in	Input, requirement
out	Output, generation
preheat	Combustor preheated air
plant	Reference plant, upstream from capture facility
ref	Reference plant without carbon capture
sorb	Sorbent (CaO and $CaCO_3$)
th	Thermal
wet	Wet basis

Abbreviations

BECCS	Bioenergy with carbon capture and storage
BFB	Bubbling fluidized bed
CaL	Carbonate looping
CCS	Carbon capture and storage
CDR	Carbon dioxide removal
CEN	European Committee of Standardization
CFB	Circulating fluidized bed
CPU	CO_2 compression and purification unit
Cyc.	Cyclone
GHG	Greenhouse gas
HX	Heat exchanger
IHCaL	Indirectly heated carbonate looping
IPCC	Intergovernmental panel on climate change
KPI	Key performance indicator
MSW	Municipal solid waste
PRK	Preheated rotary kiln
RDF	Refuse-derived fuel
Ref	Reference lime production facility without carbon capture
SRF	Solid recovered fuel

1 Introduction

The latest report of the Intergovernmental Panel on Climate Change (IPCC) stated that carbon dioxide removal (CDR) needs to be deployed to achieve net zero greenhouse gas (GHG) emissions (IPCC, 2022). Furthermore, CDR is required in order to cap the global warming to 1.5 °C with no or limited overshoot (IPCC, 2018). CDR is a “key element” to limit global warming because it is the only means to counterbalance the so-called “residual emissions,” i.e., uneconomical to abate anthropogenic GHG emissions (Quader and Ahmed, 2017). Emission scenarios compatible with the 1.5 °C limit (67% probability) require huge amounts of CDR on top of deep emissions reductions; namely, 730 Gt_{CO2} on average (IPCC, 2018; Merk et al., 2022). One of the most promising ways to achieve net negative CO_2 emissions, i.e., CDR, is the implementation of carbon capture and storage (CCS) into industrial processes which emit high amounts of biogenic CO_2 (Clarke et al., 2014; Fuss et al., 2018; Fuss et al., 2014; Quader and Ahmed, 2017). This approach is called bioenergy with carbon capture and storage (BECCS).

Waste-derived fuels have the potential to allow for more economical carbon capture systems due to their lower costs and at the same time enable CDR through BECCS (Haaf et al., 2020c). Refuse-derived fuels (RDFs) and solid recovered fuels (SRFs) are obtained by factions of municipal solid waste (MSW) that cannot be recycled. SRFs are fuels obtained from MSW, which comply with standards from the European Committee for Standardization (CEN) (Gerassimidou et al., 2020), e.g., DIN EN ISO (2021). The term RDF normally refers to waste-derived combustibles of high heating value[1], obtained through the selection of high-quality waste fractions (e.g., paper, wood, plastic, cardboard), which are not defined by CEN standards (Velis et al., 2010). Depending on the quality, consumers may have to pay for these fuels. For low-quality RDF/SRF, suppliers pay the consumers (Sarc and Lorber, 2013).

Lime plants are responsible for the production of raw materials that are widely used in agriculture and the industrial sector. Lime-related products are obtained from the calcination of limestone —mainly calcium carbonate ($CaCO_3$)— at high temperature (900–1200 °C). The calcination reaction is highly endothermic; thus, a heat input is required, e.g., from the combustion of fuels such as coal, coke, and secondary fuels. Carbon dioxide is emitted as a result of the combustion. Additional CO_2 is produced due to the chemical conversion of $CaCO_3$ into calcium oxide (CaO) during the calcination. This so-called "process CO_2," which can only be avoided through CO_2 capture, represents approximately 65 % of the total CO_2 emissions (IEA, 2020a). Overall, the total CO_2 emissions per ton of burnt lime vary between 1 to 2 t_{CO2}/t_{lime} (Schorcht et al., 2013).

In order to capture the process and fuel CO_2 emissions, two groups of carbon capture technologies can be deployed, namely, post-combustion and oxyfuel combustion technologies (Plaza et al., 2020). Only few studies have analyzed carbon capture technologies specifically for the lime industry (Erans et al., 2016; Eriksson et al., 2014; Jafarian et al., 2022; Yang et al., 2020), whereas many works have been published recently that consider carbon capture for the cement industry (e.g., Busch et al., 2022; Nhuchhen et al., 2022; Carbone et al., 2022). There are similarities between both industries, like the calcination of $CaCO_3$, which is the main process in terms of energy consumption (Schorcht et al., 2013). Moreover, CO_2 capture —in particular post-combustion capture— from cement and lime plants have many common features. In both production processes, the majority of the CO_2 emissions come from the raw material, and the specific CO_2 emissions per unit of product are approximately the same. The other components of the flue gas (e.g., HCl, SO_2, moisture, NO_x and N_2, and residual dust) are also comparable if the same fuels are used [2]. A robust process is needed in both cases to capture the CO_2 from the flue gases. Even though this work focusses on the CO_2 capture from a lime plant, reference studies on carbon capture from cement kilns are used for comparison purposes.

Eriksson et al. (2014) proposed using oxyfuel combustion directly in a lime rotary kiln. They found that, with this system, the total CO_2 emissions may be reduced, but pointed out the technical challenges to control the temperature and, in this way, comply with the high-quality standards of rotary kiln lime products. The environmental and economic potential of oxyfuel combustion for cement production was analyzed by different authors (e.g., Rolfe et al., 2018; Barker et al., 2009). Carrasco et al. (2019) investigated oxyfuel carbon capture from the cement production in a 500 kW_{th} testing facility. This technology has good energy performance, but presents significant disadvantages when it comes to retrofitability (Voldsund et al., 2019b).

---

[1] Typically, LHV_{wet} ranges from 14 to 20 MJ/kg for these fuels (Bhatt et al. 2021).

[2] Reference values can be found in Schorcht et al. (2013).

Post-combustion CO_2 capture technologies have a high CO_2 abatement potential and are more suitable for retrofitting compared to oxyfuel combustion (Voldsund et al., 2019b). Nonetheless, the majority of these technologies have very high energy requirements, which increase the costs of the final products and reduce the efficiency of the entire system considerably. Gardarsdottir et al. (2019) evaluated different post-combustion carbon capture processes for the cement production. They calculated that monoethanolamine-based absorption, the reference post-combustion carbon capture technology, has a specific primary energy consumption for CO_2 avoided (*SPECCA*) of 7.02 $MJ/kg_{CO2,av}$ and a cost of CO_2 avoided of 80.2 $€/t_{CO2,av}$. Barker et al. (2009) estimated that the cost of CO_2 avoided would be higher than 100 $€/t_{CO2,av}$ to retrofit a 1 Mt_{cement}/y cement plant located in North East Scotland with a solvent-based post-combustion capture unit.

One noteworthy post-combustion carbon capture technology is the carbonate looping (CaL) process (Shimizu et al., 1999), whereby the CO_2 capture is achieved by utilizing limestone as a sorbent, i.e., the raw material of the lime production facility. The sorbent binds CO_2 from the kiln flue gases in a carbonator and is regenerated through a temperature increase in a calciner, according to the reaction in Eq. (1) (Anantharaman et al., 2018).

$$CaCO_{3(s)} \rightleftharpoons CO_{2(g)} + CaO_{(s)};\Delta H_{298K} = \pm 1,780\mathrm{kJ/kg} \tag{1}$$

For the regeneration of the sorbent in the standard CaL process, fuel is burnt directly in the calciner. For this, technically pure oxygen is used, which requires an air separation unit (ASU) (Carrasco-Maldonado et al., 2016). CaL technology has the potential to efficiently capture CO_2 from lime plants by exploiting the synergies of the calcination.

The CaL process has been successfully operated up to the pilot scale in Stuttgart, Germany (200 MW_{th}) (Charitos et al., 2011; Dieter et al., 2014; Hornberger et al., 2021, 2020), in Darmstadt, Germany (1 MW_{th}) (Haaf et al., 2020b; Hilz et al., 2018, 2017; Kremer et al., 2013; Ströhle et al., 2020; Ströhle et al., 2014), and in La Pereda, Spain (1.7 MW_{th}) (Arias et al., 2017b; Arias et al., 2013; Diego et al., 2020; Diego et al., 2016b). For power plants, the CaL process has the potential to achieve high CO_2 capture rates with low energy penalties. Lasheras et al. (2011) estimated that a full-scale power plant could be retrofitted with CaL to capture 88% of the total CO_2 formed, with an energy penalty of less than 2.9%. Astolfi et al. (2019) calculated that a *SPECCA* of 2.16 $MJ_{LHV}/kg_{CO2,av}$ could be achieved by the integration of the CaL process into power plants with thermochemical energy storage, and Haaf et al. (2020a) estimated a *SPECCA* of 5.72 $MJ_{LHV}/kg_{CO2,av}$ for the integration into waste-to-energy plants.

Experimental investigations are being carried out to apply CaL technology into the cement industry. Arias et al. (2017a) achieved more than 90% CO_2 capture in a CaL 30 kW_{th} test facility at relevant conditions for cement plants. Within the CLEANKER project, a demonstrator CaL unit has been erected to capture CO_2 from an operating cement plant that produces 1.3 Mt_{cement}/y in Vernasca, Italy (Fantini et al., 2021). De Lena et al. (2022) investigated the application of different CaL configurations into the cement industry and reported *SPECCA* values between 2.8 and 3.0 $MJ_{LHV}/kg_{CO2,av}$ for systems utilizing pure limestone as sorbent, and between 3.5 and 4.6 $MJ_{LHV}/kg_{CO2,av}$ for systems that utilize cement raw meal.

The ASU in the CaL process increases the *SPECCA* by approximately 1 $MJ_{LHV}/kg_{CO2,av}$ (De Lena et al., 2022). The requirement for technically pure O_2 can be avoided by indirectly heating the calciner, e.g., through solid looping (Diego et al., 2016a), and thus the energy penalty is reduced (Martínez et al., 2016). One excellent means to achieve this is through heat pipes (Hoeftberger and Karl, 2016), which transfer heat from an external combustor into the calciner via evaporation and condensation of a fluid. This indirectly heated carbonate looping (IHCaL) process (Epple, 2009) presents several advantages compared to the oxy-fired CaL process: reduced energy requirement, improved sorbent activity, lower sorbent attrition rates, and high purity of the captured CO_2. It has the potential to enable carbon capture with very low CO_2 avoidance costs[3] (Junk et al., 2016).

The IHCaL process has been successfully operated for 400 h at the 300 kW_{th} facility of the Technical University of Darmstadt (Reitz et al., 2016) in operating conditions corresponding to CO_2 capture from coal-fired power plants. Additional test campaigns in Darmstadt were carried out during 2022 to prove the operability of the IHCaL process under lime plant conditions at the pilot scale with solid fuel feedstock (Hofmann et al., 2022a, 2022b; Ströhle et al., 2021). The facility was operated for more than 300 additional hours during the year 2022.

Furthermore, the utilization of secondary fuels has been successfully demonstrated up to the pilot scale (1 MW_{th}) for CaL operation (Haaf et al., 2020d; Haaf et al., 2020b). Regarding the IHCaL process, different solid fuels were fueled in the 300 kW_{th} heat pipe IHCaL testing facility of the Technical University of Darmstadt (Hofmann et al., 2022a, 2022b). The combustor was operated around 20 h with lignite and around 20 h with RDF pellets, with the compositions and heating values displayed in Table 5.

At the Technical University of Darmstadt, novel concepts for the integration of the IHCaL process into the lime production were developed and evaluated through process simulation (Greco-Coppi et al., 2021). The published results show that the direct CO_2 emissions can be reduced by up to 87% by utilizing dried lignite as fuel for both the lime kiln and the IHCaL combustor. Nevertheless, the application of waste-derived fuels into these concepts to enable CDR has not been discussed yet.

This work investigates the influence of four different fuels on the CO_2 emissions and energy requirements of a tail-end IHCaL process integrated into a lime plant. The objective of this paper is to unravel the potential of the IHCaL process to achieve net negative CO_2 emissions, thus enabling CDR. Furthermore, it aims to assess the energy performance of the IHCaL process, compared to other carbon capture technologies that are being considered for deployment in the cement and lime industries.

2 Methodology

2.1 Process integration

The IHCaL concept considered in this paper is referred to as the tail-end or retrofit configuration in previous works reported in the literature (Greco-Coppi et al., 2021; Junk et al.,

---

[3] Junk et al. (2016) reported 22.6 €/$t_{CO2,av}$ for an IHCaL process (without compression) integrated into a 1052 MW_{el} hard-coal-fired power plant.

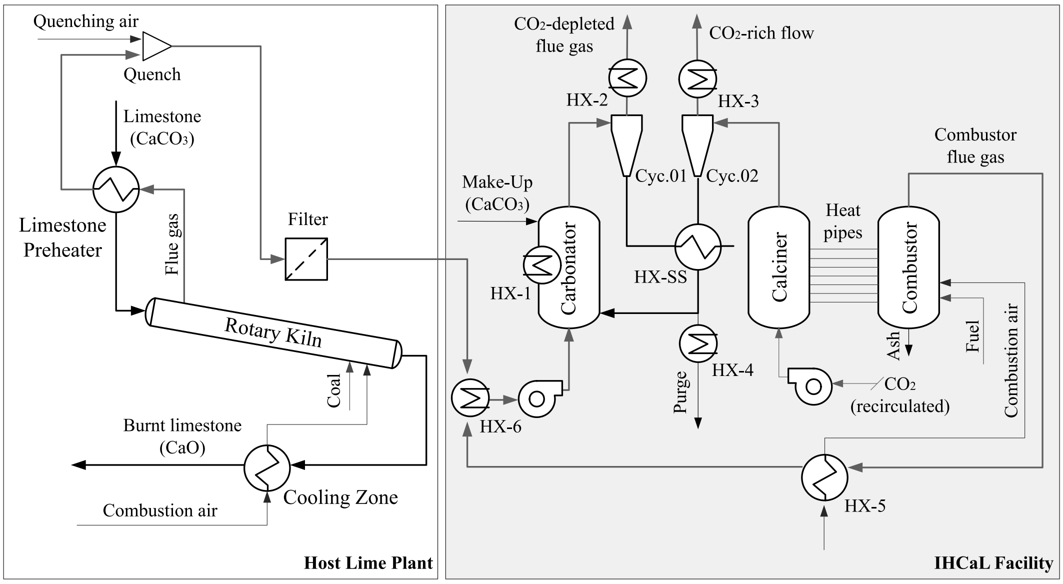
Quenching air
Quench
Limestone (CaCO3)
Limestone Preheater
Flue gas
Filter
Rotary Kiln
Coal
Burnt limestone (CaO)
Cooling Zone
Combustion air
Host Lime Plant
CO2-depleted flue gas
CO2-rich flow
HX-2
HX-3
Cyc.01
Cyc.02
Make-Up (CaCO3)
Carbonator
HX-1
HX-SS
Calciner
Heat pipes
Combustor
Combustor flue gas
Ash
Fuel
Combustion air
Purge
HX-4
CO2 (recirculated)
HX-6
HX-5
IHCaL Facility

Fig. 1 Tail-end concept for the integration of the IHCaL CO_2 capture process into an existing lime plant, introduced by Greco-Coppi et al. (2021)

2013). This process is suitable for capturing CO_2 from operating lime plants[4]. The configuration is shown schematically in Fig. 1. It consists of a host lime plant (left side) and an IHCaL facility (right side). In Europe, this configuration has the potential to decarbonize existing facilities with more than one kiln. The IHCaL facility replaces one kiln and, at the same time, captures the CO_2 of the remaining kilns.

The host facility for this work is the lime production line located in Germany described by Greco-Coppi et al. (2021). The rotary kiln is equipped with a limestone preheater (PRK) and is fueled with dried lignite ($LHV = 21500$ kJ/kg$_{\mathrm{wet}}$). The burnt lime (mainly CaO) is cooled downstream of the kiln with the combustion air. The kiln flue gases are used to preheat the raw material. An air quench is used to reduce the temperature before the filter and the blower. The flue gases exit the host plant at 236 °C and high[5] CO_2 concentrations (19.0 vol%$_{\mathrm{dry}}$).

The IHCaL facility allows for the capture of CO_2 utilizing CaO as sorbent and increases the total production of the plant through the calcination of the make-up stream ($CaCO_3$). There are three main reactors: (i) a carbonator operating as a circulating fluidized bed (CFB) for the absorption of CO_2, (ii) a calciner operating in a bubbling bed regime (BFB) for the sorbent regeneration, and (iii) a BFB combustor providing the energy required to regenerate the sorbent.

The flue gases from the kiln and the combustor are cooled at HX-6 to reduce the propelling energy requirements. Afterwards, they enter the carbonator from the bottom by means of a blower. The same flue gas is the fluidizing agent that allows for the CFB operation. In the carbonator, the CO_2 from the flue gas is absorbed by the circulating sorbent (CaO) to form $CaCO_3$. The CO_2-depleted flue gas exits the IHCaL facility through the cyclone 1, and the $CaCO_3$ enters the calciner. In the calciner, the sorbent is regenerated, and the CO_2 is released in a high concentration (> 95 $\text{vol\%}_{\text{dry}}$) stream. This CO_2 is then conditioned for transport and storage. The main assumptions for the downstream conditioning facility are presented in Section 2.3. The solids leaving the calciner enter the carbonator; thus, the calcium loop is established. Heat is supplied into the calciner from the combustor via heat pipes (Hoeftberger and Karl, 2016). The combustor can be fueled with lignite or waste-derived fuels, as explained in Section 2.5.

---

[4] Greco-Coppi et al. (2021) showed that the fully integrated IHCaL process would be more suitable for newly built CO_2 lime plants, compared to the tail-end concept, when utilizing dried lignite to fuel the combustor.

[5] Previous pilot tests on the 300 kW$_{\mathrm{th}}$ IHCaL pilot facility in Darmstadt demonstrated the feasibility to capture CO_2 from more diluted flue gas (14 vol%$_{\mathrm{dry}}$), corresponding to typical power plant flue gases (Reitz et al. (2014); Reitz et al. (2016)).

As a result of the deactivation of the sorbent, a constant make-up is required to maintain a high carbon capture rate (Grasa and Abanades, 2006). Make-up can be added into the process directly into the carbonator or the calciner or into the connecting elements (e.g., loop seals). The used sorbent (CaO) is removed from the system downstream of the calciner and may be sold as burnt lime[6]. The limestone composition from the host lime plant (see Table 1) is considered in this work. It is assumed that this limestone is used, not only for the rotary kiln, but also as make-up and sorbent for the IHCaL process.

2.2 Process model

The heat and mass balances were calculated with the software AspenPlus®, version V12. Custom routines in FORTRAN code were included. Steady-state conditions were assumed, and the cyclone separation was considered ideal. The ambient pressure and temperature were set to 1.013 bar and 15 °C, respectively, and a plant capacity factor of 91.3% was assumed in accordance with Voldsund et al. (2019a). The calculation of the material properties and the balances in the reactors was performed as explained by Greco-Coppi et al. (2021). For the combustor, an air-fuel equivalence ratio (λ) of 1.2 was specified.

The temperatures of the reactors and the main operating parameters for the calculations are displayed in Table 2. It was assumed that the reactors, heat exchangers, and ducts are adequately insulated, and thus the thermal losses are negligible. Accordingly, these components were modeled adiabatic (Chen et al., 2020).

In this work, the make-up solid stream (F_0) and the circulating solid stream (F_R) are calculated from defined ratios (Λ, Φ) and the total CO_2 molar flow rate entering the carbonator (F_{CO2}), according to Eq. (2).

$$F_0 = \Lambda \cdot F_{CO2};\ F_R = \Phi \cdot F_{CO2} \tag{2}$$

The CO_2 capture efficiency (E, see Eq. 7), is given as an input: $E = 90\%$. The required carbonator efficiency (E_{carb}) is calculated with Eq. (3), from the molar flow rates of CO_2 entering (F_{CO2}) and leaving (F_{CO2}^{carb}) the carbonator.

---

[6] The suitability of the spent sorbent to be sold as burnt lime is still being investigated. Some previous studies (Dean et al. 2013; Hills 2016) suggest that this is possible. Within the ANICA project, the spent sorbent of the pilot testing campaigns at the Technical University of Darmstadt will be tested to verify its quality compared to the rotary kiln product (Ströhle et al. 2021).

Table 1 Composition of the limestone used in the reference plant and in the IHCaL carbon capture facility (Greco-Coppi et al., 2021)

Component	Mass fraction
$CaCO_3$	98.3%
$MgCO_3$	0.7%
SiO_2	0.7%
Fe_2O_3	0.1%
Al_2O_3	0.2%
SO_3	< 0.1%

Table 2 Main operating parameters of the IHCaL process

Parameter	Value
Main IHCaL parameters	
CO_2 capture efficiency (E)	90%
Calciner efficiency (E_{calc})	99%
Specific sorbent circulation rate (Φ)	(variable)
Specific make-up rate (Λ)	$0.10\ mol_{CaCO3}/mol_{CO2}$
Operating temperatures	
Carbonator (T_{carb})	650 °C
Calciner (T_{calc})	900 °C
Combustor (T_{comb})	1000 °C
Combustion air preheating, after HX-5 ($T_{preheat}$)	800 °C
Sorbent at calciner inlet, after HX-SS ($T_{sorb,calc,in}$)	810 °C

$$E_{carb} = 1 - \frac{F_{CO2}^{carb}}{F_{CO2}} \tag{3}$$

The calciner efficiency is an input for the model and is defined as:

$$E_{calc} \equiv \frac{X_{carb} - X_{calc}}{X_{carb}} \tag{4}$$

Here, X_{calc} and X_{carb} are the fractions of $CaCO_3$ in the calcium (Ca) stream leaving the calciner and the carbonator, respectively. The composition of Table 1 was used to model the limestone streams. This includes the make-up stream and the raw material input into the rotary kiln.

The carbonator efficiency (E_{carb}) is calculated with the carbonator reactor model developed by Lasheras et al. (2011) that considers: (i) circulating fluidized bed hydrodynamics according to Kunii and Levenspiel (1991); (ii) the carbonation reaction model from Abanades et al. (2004); and (iii) sorbent deactivation as modeled by Abanades et al. (2005). The make-up rate was set to $\Lambda = 0.1$, and Φ was varied to achieve the necessary CO_2 capture efficiency of $E = 90\%$. The carbonator reactor model assumptions and results are included in Appendix 1 and Appendix 2, respectively.

2.3 Power requirements

In this work, the battery limits for the analysis are the input of the flue gases from the reference facility before the stack and the exit from the CO_2 compression unit. The CO_2 emissions and primary energy consumption related with the transport and storage of CO_2, transport and pre-treatment of raw materials and fuels (e.g., fractioning), and the erection of the carbon capture facility are out of the scope of this paper[7]. The main assumptions and input parameters for the analysis are summarized in Table 3.

For the calculation of the electric power in the reference facility, the data from the best available technique reference document for cement, lime, and magnesium oxide (Schorcht et al., 2013) was considered: 17–45 kWh/t_{lime} for a lime rotary kiln. The mean value was used for the calculations: 31 kWh/t_{lime}. The power demand from the IHCaL facility and the downstream conditioning are used to obtain the net power generation (P_{el}) for the calculation of the indirect CO_2 emissions (Eq. 12) and indirect primary energy consumption (Eq. 10).

After a post-combustion carbon capture facility, downstream conditioning of the captured CO_2 is necessary. For oxy-fired CaL, purification is required due to the presence of combustion gases other than CO_2 (mainly O_2). Furthermore, the CO_2 stream is to be compressed up to a suitable temperature for transportation of around 110 bar. Such CO_2 compression and purification units (CPUs) have relatively high energy requirements that range from 80 to 120 kWh_e/t_{CO2} (De Lena et al., 2018; Garðarsdóttir et al., 2018; Jackson and Brodal, 2019; Magli et al., 2022; Svensson et al., 2021). In the IHCaL process presented in this work, the combustion to generate the heat for the regeneration takes place in an external combustor, and thus the CO_2 stream after the calciner is almost pure. The only conditioning required is the cooling and the filtering, after which, the stream is ready for compression. The compression takes place in a 5-stage CO_2 compressor. The compression was simulated in Aspen Plus, based on the method reported by Posch and Haider (2012). The assumptions for the compression unit are reported in Table 3.

The power requirement of the blowers depends on the pressure drop (Δp) in the reactors and the auxiliary components, i.e., the nozzle grid, cyclone, cooler, filter, and ducts. The following values were assumed according to the experimental data of the research group: 100 mbar for the carbonator, 130 mbar for the calciner, and 150 mbar for the combustor (Reitz et al., 2016). For the blowers, the isentropic and mechanical efficiencies were set to 0.65 and 0.9, respectively (Grote and Feldhusen, 2007). It was assumed that the flue gases entering the carbonator and the combustion air act as fluidization agents for the corresponding reactors. For the calciner, the fluidization agent[8] is a fraction of the pure CO_2 flow stream that is recirculated to allow for BFB operation. To calculate the amount of recirculation required, the following assumptions were made: (i) superficial velocity for the

---

[7] Carbone et al. (2022) performed a carbon footprint evaluation on a similar process, namely, an oxy-fired CaL process for cement plants. Their results suggest that the specific CO_2 emissions associated with the infrastructure are similar in plants without carbon capture and with downstream CaL. Furthermore, the contribution of GHG emissions in the supply of the raw meal (sorbent) was almost negligible.

[8] In this work, it is assumed that an external fluidization agent, i.e., recirculated CO_2, is required for the fluidization of the calciner. Hoeftberger and Karl (2013) demonstrated the so-called self-fluidization of the IHCaL calciner experimentally. In the self-fluidization regime, no external fluidization agent is required, because the amount of CO_2 released during the calcination is enough to maintain the fluidization of the BFB. If the calciner were operated without an external fluidization agent, the power requirements would be reduced.

Table 3 Main assumptions and general input parameters for the calculation of power requirements

Parameter	Unit	Value
CO_2 Compression		
Number of stages[a]	-	5
Temperature after intercooler	°C	25
Pressure drop intercooler	mbar	100
Polytropic efficiency	%	80
Mechanical efficiency	%	95
Discharge temperature	°C	25
Discharge pressure	bar_a	110
Inlet temperature	°C	25
Inlet pressure	bar_a	1.013
Blowers of the IHCaL facility		
Mechanical efficiency	%	90
Isentropic efficiency	%	65
Δp_{carb}	mbar	100
Δp_{calc}	mbar	130
Δp_{comb}	mbar	150
$u_{0,calc}$	m/s	0.25
F_{calc}	Nm^3/h	9700
$T_{FA,carb}$	°C	250
$T_{FA,calc}$	°C	450

[a] Equal pressure ratio

fluidization agent at inlet $u_{0,calc} = 0.25$; (ii) heat pipe properties as reported by Höftberger et al. (2016), namely, 3 m calciner width (i.e., 6 m heat pipes), 7.2 m calciner length/50 MW_{th}; (iii) and calciner heat input equal to 100 MW_{th}. Finally, the temperature of the fluidization agent (T_{FA}) before the blowers is defined. The air for the combustor is compressed from ambient temperature. The flue gases entering the carbonator are cooled down to 250 °C before the compression, and the recirculated gases for the fluidization in the calciner are cooled down to 450 °C.

2.4 Heat integration and power generation

The configuration displayed in Fig. 1 allows for efficient heat utilization. The combustion air for the combustor is preheated ($T_{preheat}$), and heat is exchanged between the solid streams to increase the temperature of the solids entering the calciner ($T_{sorb,calc,in}$). These design specifications minimize the total heat requirement, as shown by Greco-Coppi et al. (2021).

To achieve a high $T_{sorb,calc,in}$, a solid-solid heat exchanger (HX-SS) is required. Different configurations are possible for the design of this heat exchanger: (i) a concept that utilizes molten salt circulating inside of metal tubes; (ii) a concept with heat-pipes, similar to those presented by Hoeftberger and Karl (2016) to transfer heat into the calciner; (iii) a concept with high surface area metal walls separating the solid flows; and (iv) a concept consisting of two concentric L-valves (Greco-Coppi et al., 2021). For the considered inputs (see Table 2), a counter-current configuration of this heat exchanger yields a logarithmic mean temperature difference of around 90 °C.

The high operating temperatures (650–900 °C) make the IHCaL process particularly suitable for power generation through a heat recovery steam cycle (De Lena et al., 2018; Lasheras et al., 2011). Steam can be produced from the cooling of the carbonator and from the gas streams exiting the carbonator (650 °C), the calciner (900 °C), and the combustor (1000 °C). For the calculation of the power generation through a heat recovery steam cycle, the recovered heat is obtained from the AspenPlus® simulations. The temperatures assumed for this purpose are displayed in Table 4.

For the calculation of the power generation, the steam cycle was simulated with the software EBSILON Professional^{TM}. The main assumptions for the calculations were: (i) superheating of steam up to 565 °C and 130 bar; (ii) preheating of feed-water with steam extractions; (iii) isentropic turbine efficiency equal to 85%. The calculated heat-to-power efficiency (η_{h2p}) was 42.4%. This value corresponds to an equivalent net electrical efficiency of around 38% for a thermal power plant (e.g., pulverized coal), which is in agreement with values from the literature (IEA, 2020b). The total power generation from the IHCaL facility can be calculated with Eq. (5). Here, $\dot{Q}_{IHCaL,HRSG}$ is the recovered heat from the IHCaL unit.

$$P_{el,out} = \eta_{h2p} \cdot \dot{Q}_{IHCaL,HRSG} \tag{5}$$

2.5 Fuels and CO_2 emissions

The focus of this work lies on the investigation of the effect of implementing different fuels in the IHCaL process. The biogenic CO_2 capture and associated negative emissions are of special interest. Four fuels were selected for the analysis: (i) dried lignite from the reference process in the host plant in Germany (Greco-Coppi et al., 2021); (ii) RDF pellets, which are used in pilot test campaigns at the Technical University of Darmstadt (Ströhle et al., 2021); (iii) a class 3 SRF, according to EN ISO 21640:2021-11 (2021), that was successfully utilized in the 1 MW_{th} pilot plant at the Technical University of Darmstadt for CaL operation (Haaf et al., 2020d); and (iv) municipal solid waste (MSW), with the composition from the CaL techno-economic analysis from Haaf et al. (2020a). Dried lignite was maintained as the fuel of the reference plant for all cases, and only the fuel for the IHCaL combustor was varied.

The fuel CO_2 emissions index (Furimsky, 2007; Madejski et al., 2022) is also known as the fuel-specific CO_2 emissions, $e_{CO2,fuel}$ (g_{CO2}/MJ_{LHV}). It indicates the mass of CO_2 produced by the combustion of fuel per unit of energy obtained. The Eq. (6) can be used to calculate it. Here, $w_{c,wet}$

Table 4 Operating temperatures for the heat exchangers (HX), flue gas side

Operating temperatures in heat exchangers (°C)	Upstream	Downstream
HX-1: carbonator[a]	650	-
HX-2: carbonator flue gas	650	250
HX-3: calciner flue gas	900	250
HX-4: purge (for air preheating)[b]	900	40
HX-5: preheater[c]	1000	(Variable)
HX-6: flue gases before carbonator	350	250

[a] No temperature change on the flue gas side due to the carbonation heat of the reaction

[b] Solid stream side

[c] The design temperature is the downstream temperature on the air side ($T_{preheat}$)

is the wet-basis mass fraction of carbon in the fuel, LHV_{wet} is the fuel lower heating value in wet basis, M_{CO2} is the molar mass of CO_2, M_c is the molar mass of carbon. The input parameters of the fuels considered in this analysis, including the CO_2 emissions index, are presented in Table 5.

$$e_{CO2,fuel} = \frac{w_{c,wet}}{LHV_{wet}} \cdot \frac{M_{CO2}}{M_C} \tag{6}$$

For the calculation of the negative CO_2 emissions, the biogenic and fossil emissions are distinguished. CO_2 emissions from pre-dried lignite are considered 100% fossil, as well as the emissions from limestone calcination. For the fuels burnt in the combustor, the biogenic carbon fractions (x_{bio}) are defined. According to Moora et al. (2017), x_{bio} varies considerably depending on the waste selection process and the region-dependent source segregation. The determination of the x_{bio} of the RDF pellets was performed according to the German standard DIN EN 15440:2011 (2011). For the other fuels, x_{bio} was assumed considering values from the literature (Astrup et al., 2009; Haaf et al., 2020a; Mohn et al., 2012; Mohn et al., 2008; Obermoser et al., 2009). Astrup et al. (2009) reported a range of 45–85% for MSW and explained that the biogenic carbon content of SRF is normally low, compared to MSW, because of the selective fractioning. The values of x_{bio} used in this work are displayed in Table 5.

2.6 Key performance indicators

Key performance indicators (KPIs) of the IHCaL process are the carbon capture efficiency (E), the heat ratios (HR_a, HR), and the product ratio (PR). The carbon capture efficiency of the IHCaL process (E) is defined as the ratio of CO_2 captured to total CO_2 generated. It can be calculated as follows:

$$E = \left(1 + \frac{F_{CO2}^{carb}}{F_{CO2}^{calc}}\right)^{-1} \tag{7}$$

Table 5 Input parameters of the fuels used in this analysis

Parameter	Unit	Dried lignite[a]	RDF pellets[b]	SRF[c]	MSW[d]
LHV	MJ/kg_{wet}	21.5	19.6	15.7	10.0
x_{bio}	%	0	51	45	60
$e_{CO2,fuel}$	g_{CO2}/MJ_{LHV}	96.7	92.8	88.7	106.0
Particle size	mm	0–4	ø 5	$d_{95} < 50$	$d_{95} < 100$[e]
C	$wt.\%_{wet}$	56.7	49.6	38.0	28.9
H	$wt.\%_{wet}$	4.3	6.43	5.2	3.2
N	$wt.\%_{wet}$	0.7	0.27	1.0	0.5
S	$wt.\%_{wet}$	0.8	0.43	0.3	0.1
O	$wt.\%_{wet}$	21.5	24.1	19.9	23.1
Cl	$wt.\%_{wet}$	0.2	0.47	0.7	0.4
H_2O	$wt.\%_{wet}$	10.3	8.1	19.4	25.0
Ash	$wt.\%_{wet}$	5.5	11.1	15.4	18.8

[a]Greco-Coppi et al. (2021); [b]Ströhle et al. (2021); [c]Haaf et al. (2020d); [d]Haaf et al. (2020a); [e]Typical limit for waste incinerators according to Velis et al. (2010)

Where $F_{CO_2}^{calc}$ and $F_{CO_2}^{carb}$ are the molar flow rates of the captured CO_2 leaving the calciner and the CO_2 leaving the carbonator, respectively. In this work, E was set as an input, and the required E_{carb} to achieve this efficiency was calculated.

The heat and product ratios are calculated with Eq. (8), where $\dot{m}_{CaO;prod}$ is the total lime production, $\dot{Q}_{in}$ is the total heat input from the fuel combustion, and the superscript ref indicates the lime production plant without carbon capture. PR is the product ratio, HR_a is the absolute heat ratio, and HR is the specific heat ratio that indicates the increase in heat input per unit of lime produced.

$$PR \equiv \frac{\dot{m}_{CaO,prod}}{\dot{m}_{CaO,prod}^{ref}}; \quad HR_a \equiv \frac{\dot{Q}_{in}}{\dot{Q}_{in}^{ref}}; \quad HR \equiv \frac{HR_a}{PR} \tag{8}$$

The KPIs introduced above are specific of the IHCaL process. Other important KPIs, which allow to compare with other carbon capture technologies, are introduced hereunder. They were selected considering relevant work in post-combustion carbon capture from cement and lime plants (De Lena et al., 2017; Ströhle et al., 2021; Voldsund et al., 2019a), especially the work within the CEMCAP project, which established a framework for comparative analysis of CO_2 capture processes for cement plants (Anantharaman et al., 2018).

For the calculation of the specific primary energy consumption for CO_2 avoided (*SPECCA*), a procedure similar to the one considered by Haaf et al. (2020a) was adopted. The following power generation scenarios are taken into account: (i) the state-of-the-art for coal power plants (abbreviated "coal," in this work) (De Lena et al., 2018; European Union, 2015), (ii) the European energy mix (abbreviated "energy mix," in this work) calculated and used in CEMCAP (Anantharaman et al., 2018; De Lena et al., 2018), (iii) the renewable (Anantharaman et al., 2018), and (iii) the nuclear (Anantharaman et al., 2018). For each of them, a reference electrical efficiency ($\eta_{ref,el}$) and a reference CO_2 emissions factor for power production ($e_{ref,el}$) are defined (see Table 6). For the scenarios (i) and (ii), these parameters are within the range of the values used normally in the literature[9]. The scenarios (iii) and (iv) are zero-CO_2-emission with $\eta_{ref,el} = 100\%$ and $\eta_{ref,el} = 33\%$, respectively. They were chosen to study the sensitivity of the results to $\eta_{ref,el}$.

The equivalent fuel consumption (q_{eq}) and the equivalent CO_2 emissions ($e_{CO2,eq}$) for the different cases can be calculated with Eq. (9).

$$q_{eq} = q + q_i; \; e_{CO2,eq} = e_{CO2} + e_{CO2,i} \tag{9}$$

The direct fuel consumption (q) is the primary energy entering the system through the combustion of the fuels in the rotary kiln and the combustor. The indirect fuel consumption (q_i) is the primary energy consumption related to the net electric generation (or consumption) in the entire facility (P_{el}). It depends on the reference electrical efficiency $\eta_{ref,el}$:

$$q_i = \frac{P_{el}}{\eta_{ref,el}} \tag{10}$$

---

[9] $\eta_{ref,el} = 40\%–60\%$; and $e_{ref,el} = 260–760\ \mathrm{kg_{CO2}/MWh_{el}}$; e.g. Bonalumi et al. (2016), De Lena et al. (2018), Martínez et al. (2018), Spinelli et al. (2018).

Table 6 Main results and KPIs for the different fuels

Parameter	Unit	Ref.	Dried lignite	RDF pellets	SRF	MSW
HR	-	1.00	3.01	3.03	3.02	3.71
HR_a	-	1.00	4.15	4.15	4.11	5.64
PR	-	1.00	1.38	1.37	1.36	1.52
E	%	-	90	90	90	90
Direct fuel consumption (q)	$\mathrm{MJ_{LHV}/kg_{CaO}}$	5.7	17.2	17.3	17.3	21.3
Direct CO_2 emissions ($e_{CO2,d}$)	$\mathrm{kg_{CO2}/t_{CaO}}$	1344	247	−378	−285	−810
State-of-the-art coal power plant ($\eta_{ref,el}$ = 44.2 %; $e_{ref,el}$ = 770 kg_{CO2}/MWh_{el})						
Indirect fuel consumption (q_i)	$\mathrm{MJ_{LHV}/kg_{CaO}}$	0.25	−7.77	−7.71	−7.77	−10.52
Equivalent fuel consumption (q_{eq})	$\mathrm{MJ_{LHV}/kg_{CaO}}$	5.97	9.46	9.60	9.51	10.73
Indirect CO_2 emissions ($e_{CO2,i}$)	$\mathrm{kg_{CO2}/t_{CaO}}$	24	−735	−729	−734	−995
Equivalent CO_2 emissions ($e_{CO2,eq}$)	$\mathrm{kg_{CO2}/t_{CaO}}$	1368	−488	−1107	−1019	−1805
SPECCA	$\mathrm{MJ_{LHV}/kg_{CO2,av}}$	-	1.88	1.46	1.48	1.50
Energy mix (2015) EU-28 non-CHP ($\eta_{ref,el}$ = 45.9 %; $e_{ref,el}$ = 262 kg_{CO2}/MWh_{el})						
Indirect fuel consumption (q_i)	$\mathrm{MJ_{LHV}/kg_{CaO}}$	0.24	−7.49	−7.43	−7.48	−10.13
Equivalent fuel consumption (q_{eq})	$\mathrm{MJ_{LHV}/kg_{CaO}}$	5.97	9.75	9.88	9.80	11.12
Indirect CO_2 emissions ($e_{CO2,i}$)	$\mathrm{kg_{CO2}/t_{CaO}}$	8	−250	−248	−250	−339
Equivalent CO_2 emissions ($e_{CO2,eq}$)	$\mathrm{kg_{CO2}/t_{CaO}}$	1352	−3	−626	−535	−1148
SPECCA	$\mathrm{MJ_{LHV}/kg_{CO2,av}}$	-	2.79	1.98	2.03	2.06
Renewables ($\eta_{ref,el}$ = 100 %; $e_{ref,el}$ = 0 kg_{CO2}/MWh_{el})						
Indirect fuel consumption (q_i)	$\mathrm{MJ_{LHV}/kg_{CaO}}$	0.11	−3.44	−3.41	−3.43	−4.65
Equivalent fuel consumption (q_{eq})	$\mathrm{MJ_{LHV}/kg_{CaO}}$	5.83	13.80	13.90	13.85	16.61
Indirect CO_2 emissions ($e_{CO2,i}$)	$\mathrm{kg_{CO2}/t_{CaO}}$	0	0	0	0	0
Equivalent CO_2 emissions ($e_{CO2,eq}$)	$\mathrm{kg_{CO2}/t_{CaO}}$	1344	247	−378	−285	−810
SPECCA	$\mathrm{MJ_{LHV}/kg_{CO2,av}}$	-	7.26	4.69	4.92	5.00
Nuclear ($\eta_{ref,el}$ = 33%; $e_{ref,el}$ = 0 kg_{CO2}/MWh_{el})						
Indirect fuel consumption (q_i)	$\mathrm{MJ_{LHV}/kg_{CaO}}$	0.34	−10.41	−10.33	−10.40	−14.10
Equivalent fuel consumption (q_{eq})	$\mathrm{MJ_{LHV}/kg_{CaO}}$	6.06	6.83	6.98	6.88	7.16
Indirect CO_2 emissions ($e_{CO2,i}$)	$\mathrm{kg_{CO2}/t_{CaO}}$	0	0	0	0	0
Equivalent CO_2 emissions ($e_{CO2,eq}$)	$\mathrm{kg_{CO2}/t_{CaO}}$	1344	247	−378	−285	−810
SPECCA	$\mathrm{MJ_{LHV}/kg_{CO2,av}}$	-	0.70	0.53	0.50	0.51

The direct CO_2 emission (e_{CO2}) is the sum of fossil CO_2 directly emitted at the stack of the facility per unit of produced lime. The CO_2 from the calcination, i.e., process emission, is considered fossil emission. For the retrofitted case with carbon capture (CC), e_{CO2} can be calculated with Eq. (11), where $\dot{m}_{CO2,foss}$ (kg_{CO2}/h) is the total fossil CO_2 emissions generation, $\dot{m}_{CO2,capt}$ (kg_{CO2}/h) is the captured CO_2, and $\dot{m}_{CaO}$ (kg_{CaO}/h) is the total production from the retrofitted plant, including the product from the IHCaL unit.

$$e_{CO2,CC} = \frac{\dot{m}_{CO2,foss} - \dot{m}_{CO2,capt}}{\dot{m}_{CaO}} \tag{11}$$

The indirect CO_2 emissions ($e_{CO2,i}$) are those associated to P_{el}. They can be calculated with Eq. (12), considering the reference CO_2 emissions factor for power production ($e_{ref,el}$) of the corresponding reference energy scenario (see Table 6).

$$e_{CO2,i} = P_{el} \cdot e_{ref,el} \tag{12}$$

The final equation for the calculation of the *SPECCA* is:

$$SPECCA = \frac{q_{eq} - q_{eq,ref}}{e_{CO2,ref} - e_{CO2}} \tag{13}$$

3 Results and discussion

In this section, the results for the analyzed cases are presented. Firstly, the specific CO_2 formation in each component is discussed. Afterwards, the results of the main KPIs are explained. Finally, the IHCaL process is compared with other post-combustion carbon capture processes.

Figure 2 shows the specific CO_2 formation in each component of the new integrated concepts (b–e), as well as the reference pilot plant without capture (a). The gray and green bars represent the fossil and biogenic specific CO_2, respectively. Direct negative CO_2 emissions are achieved for the scenarios that utilize waste-derived fuels in the combustor (Fig. 2c–e). In these cases, the total direct negative CO_2 emissions are depicted in the figure with a pink rhombus. For the reference facility and the carbon capture scenario with dried lignite (Fig. 2a–b), the direct CO_2 emissions balance is positive. The net direct CO_2 emissions are displayed with a white rhombus. No net negative direct emissions are achieved with dried lignite, since no biogenic emissions are captured.

The total specific CO_2 formation increases with the addition of the IHCaL facility (Fig. 2b–e), compared to the reference case (Fig. 2a). This is because of the CO_2 generation associated with the additional energy requirement for the carbon capture. The additional formation correlates with the fuel CO_2 emissions index ($e_{CO2,fuel}$). For fuels with lower $e_{CO2,fuel}$, the total formation is also lower, as less amount of CO_2 is generated in the combustor to supply the heat to the calciner. For this reason, the scenario with SRF has the less total formation of all the carbon capture scenarios.

If dried lignite is burnt in the combustor (Fig. 2b), the specific direct fossil CO_2 generation is almost two times that from the reference case (Fig. 2a). This means that, for dried lignite, the direct fossil CO_2 generation associated with the carbon capture is approximately

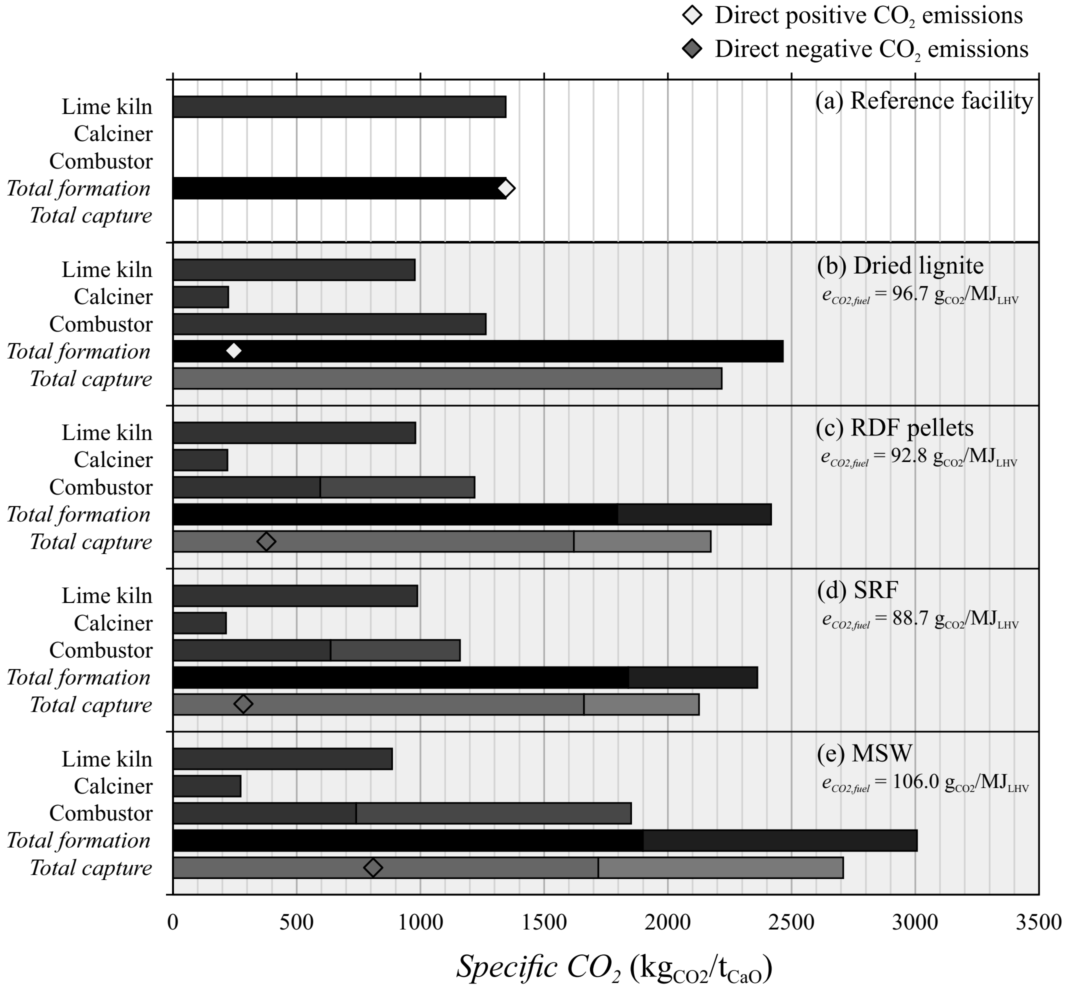

Fig. 2 Specific CO_2 formation and capture by component for all five cases considered within this study: (**a**) reference facility; and IHCaL fueled with (**b**) dried lignite, (**c**) RDF pellets, (**d**) SRF, and (**e**) MSW. The biogenic CO_2 formation is indicated with green, whereas gray represents the fossil formation. For the cases (**a**) and (**b**), the direct CO_2 balance is positive, and the total direct CO_2 emissions are displayed with a white rhombus (◇). For the remaining cases, direct negative CO_2 emissions are achieved. They are indicated with a pink rhombus (◇)

equal to the avoided CO_2. On the other hand, for the waste-derived fuels (Fig. 2c–e), the avoidance can be achieved without forming huge amounts of additional direct fossil CO_2 emissions (around 35% increase). The case with the lowest direct fossil CO_2 formation is the one of the RDF pellets (Fig. 2c), due to the combination of high x_{bio} with low $e_{CO2,fuel}$.

The highest variation of the formation with fuel type occurs in the combustor, where the fuel is burnt. The combustor is the most critical component regarding the direct formation of CO_2 in the IHCaL. Here, the formation is minimized by fuels with lower $e_{CO2,fuel}$. When dried lignite is used (Fig. 2b), the direct CO_2 formation in the IHCaL combustor is higher than the formation in the lime kiln. On the contrary, when RDF or SRF are utilized (Fig. 2c–d), the direct fossil generation in the combustor is much lower (61–65%). In the case of the MSW (Fig. 2e), the fossil emission of the combustor and the lime kiln are similar (84%).

The reduction of the specific CO_2 formation in the lime kiln with respect to the reference case is explained by the increase of the production, i.e., $PR > 1$. This reduction is stronger in the scenario with MSW (Fig. 2e), because of the higher *PR*. Nevertheless, due to the high $e_{CO2,fuel}$, more CO_2 is formed from the combustion in the IHCaL; thus, this case presents the highest total direct CO_2 formation.

Due to the high biogenic fractions of the waste-derived fuels, net negative direct CO_2 emissions can be achieved in all three cases (Fig. 2c–e). The total net direct CO_2 emissions can be read from the graph as the difference between the total capture and the total fossil formation. It is indicated with a pink rhombus. The values displayed in Fig. 2 correspond only to the direct emissions, whereas the equivalent emissions are illustrated in Fig. 4.

The main results and the KPIs of the simulated scenarios are reported in Table 6. The increase in specific heat requirement due to the carbon capture (see *HR*) ranges from 201 to 271%, with respect to the reference case. The difference results from the strong influence of the $e_{CO2,fuel}$ in the heat consumption, illustrated in Fig. 3. This result is also highly dependent on Λ, as demonstrated by Greco-Coppi et al. (2021), who presented scenarios with less than 100% specific heat requirement increase for the CO_2 capture. The CO_2 formation in the combustor increases with $e_{CO2,fuel}$; thus, increasing the total captured CO_2. Due to the more demanding capture requirement, more heat is needed in the calciner and *HR* becomes higher. The direct fuel consumption, q, and the direct CO_2 emissions, $e_{CO2,d}$, increase with *HR*.

Due to the addition of the IHCaL facility, the total production increases ($PR > 1$). The increase is almost the same for lignite, RDF, and SRF and ranges from 36 to 38%. For the MSW, the production increases more (52%) because of the additional make-up requirements associated with higher CO_2 mass flows (see Fig. 2e). The product ratio can be increased by increasing the make-up rate (i.e., higher Λ). This has the effect of augmenting the production exponentially while reducing *HR* (Greco-Coppi et al., 2021).

Figure 3 illustrates the relation between HR_a and the specific CO_2 emissions for each fuel considered in this study. The HR_a rises with increasing CO_2 emissions index ($e_{CO2,fuel}$). This is due to the additional CO_2 that has to be captured from the carbonator. Other parameters such as *LHV* and the amount of hydrogen in the fuels also play a role in the variation of the heat requirements. Higher *LHV* and lower $e_{CO2,fuel}$ minimize HR_a. The range of variation represented by the gray area was calculated with the energy balance of the calciner and the combustor (see Appendix 3).

The breakdown of specific CO_2 emissions per tonne of burnt lime (product) is displayed in Fig. 4. The emissions are separated in three categories: (i) direct fossil emissions, (ii) direct biogenic emissions, and (iii) indirect emissions. The sum of all three gives the equivalent CO_2 emissions ($e_{CO2,eq}$). The results are presented for all the calculated cases, and all the considered energy scenarios. The indirect and equivalent CO_2 emissions depend on the reference efficiency of the energy scenario ($e_{ref,el}$). The results are identical for the renewable and the nuclear energy scenarios because they both have $e_{ref,el} = 0$.

The reference case, without carbon capture, presents the highest emissions level, $e_{CO2,eq}$, of 1344–1368 $kg_{CO2/tCaO}$. The major contribution comes from the direct fossil emissions corresponding to the calcination and combustion in the lime kiln. The indirect emissions are almost negligible. The results are similar for all the energy scenarios.

For the carbon capture scenarios, net negative equivalent CO_2 emissions can be achieved in every case, except when fueling lignite, for the renewables and nuclear energy scenarios. If waste-derived fuels are used, the highest contribution to the negative emissions corresponds to the captured biogenic CO_2, which is independent from the energy scenario. The indirect emissions are strongly dependent on $e_{ref,el}$ because of the relatively high power generation in the retrofitted plants (42–63 MW_{el}). With waste-derived fuels, negative emissions as high as −1805 $kgCO_2/t_{CaO}$ can be achieved. This corresponds to an equivalent CO_2 avoidance of over 230%.

The *SPECCA* is one of the most important thermodynamic KPIs. It represents the primary energy consumption associated with the CO_2 avoidance. In Fig. 5, the

Fig. 3 Absolute heat ratio and CO_2 specific emissions for the fuels considered in this work. The circles represent the results of the simulations corresponding to each of the fuels. The gray area represents the theoretical increase of the heat requirement with the CO_2-specific emission, for a wide range of fuels

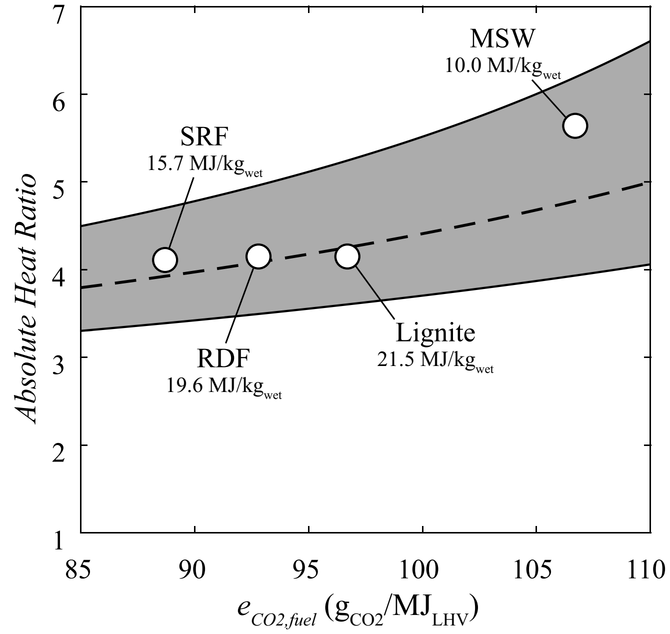

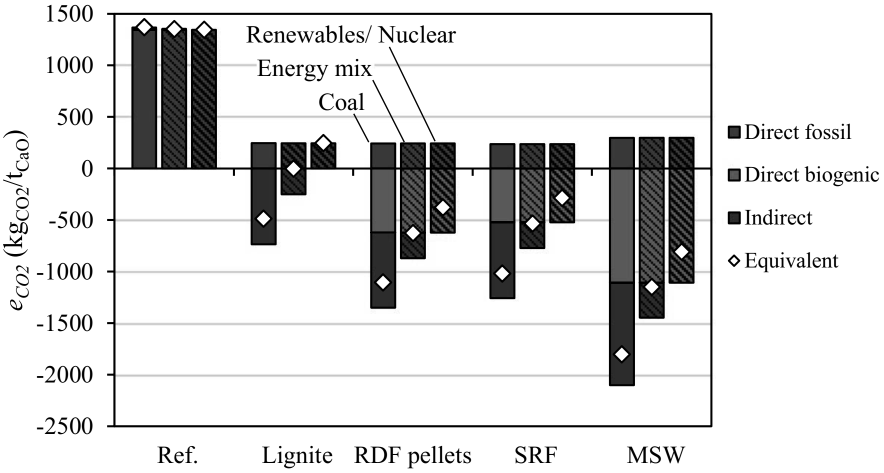

Fig. 4 Specific CO_2 emissions for the different fuels considered within this work. The breakdown of the emissions is depicted with bars. The power generation scenarios are indicted with the filling type (solid, hatched). The equivalent specific CO_2 emissions ($e_{CO2,eq}$) are displayed with a rhombus (◇)

breakdown of *SPECCA* for all the carbon capture scenarios is displayed, considering (i) the CO_2 compression power requirement, (ii) the power requirement increase (without compression), (iii) the fuel requirement increase, and (iv) the power generation. The values are presented for the energy scenarios utilized throughout this work. Because of the high power generation (light blue bar in Fig. 5), the results depend strongly on the reference power generation efficiency ($\eta_{ref,el}$). The lower the $\eta_{ref,el}$, the better the results in terms of SPECCA. The values corresponding to the European energy mix scenario are higher than for the state-of-the-art coal power plant due to the lower associated CO_2 avoided (see Fig. 4). In the same way, the *SPECCA* values

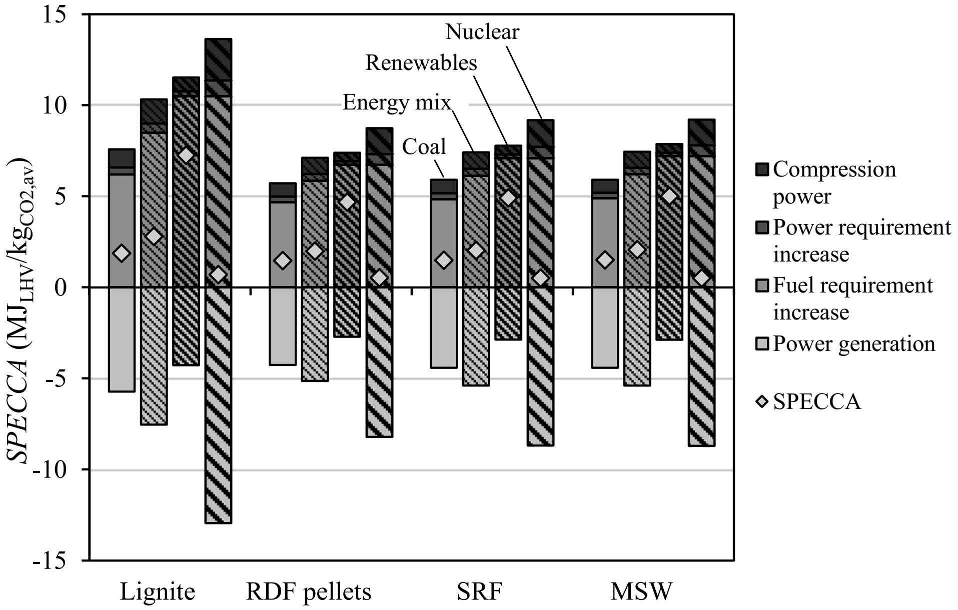

Fig. 5 *SPECCA* breakdown for all the carbon capture scenarios analyzed in this work. Each category of the breakdown is indicated with solid bars (state-of-the-art coal power plant) and hatched bars (energy mix, renewables, and nuclear). The *SPECCA* values are displayed with a rhombus (◇)

of the lignite scenario are relatively high because of the low CO_2 avoidance compared to the waste-derived fuels that allow for net negative CO_2 emissions. When compared with an oxy-fired CaL process, the *SPECCA* values presented in this work are in general much lower, mainly because of the avoided penalty of the ASU, which increases the total *SPECCA* by approximately 1 $MJ_{LHV}/kg_{CO2,av}$ in the European mix scenario (De Lena et al., 2022). Nevertheless, for the renewable scenario, relatively high values were obtained because of the high $\eta_{ref,el}$. These values are discussed hereunder.

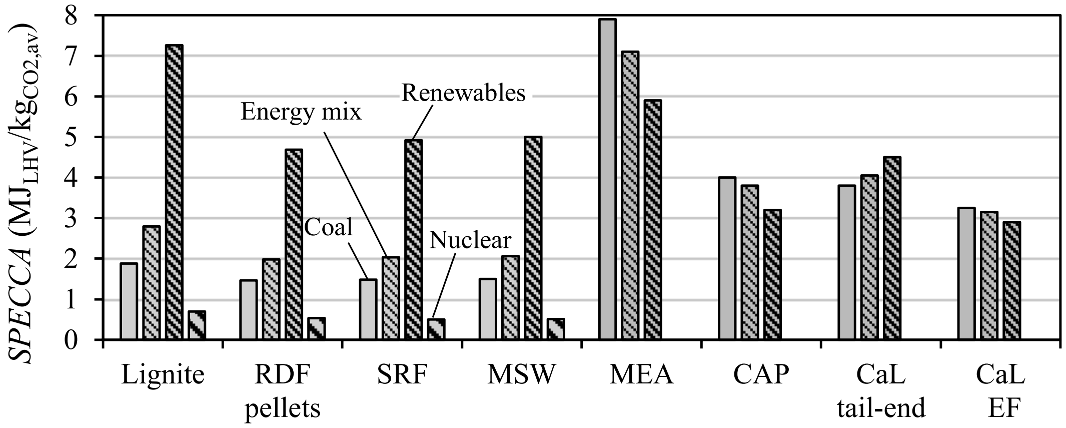

Fig. 6 *SPECCA* comparison between the different fuels considered within this work and other post-combustion carbon capture processes: monoethanolamine absorption (MEA), chilled ammonia process (CAP), tail-end directly heated carbonate looping (CaL), and entrained flow (EF) directly heated CaL. The reference data for MEA, CAP, CaL tail-end, and CaL EF was obtained from Voldsund et al. (2019a), who considered the application of these technologies in the cement production process. No data was available for the nuclear scenario

In Fig. 6, the *SPECCA* values of different post-combustion carbon capture processes are compared with the ones corresponding to the IHCaL scenarios, for the different energy scenarios considered in this work. The selected post-combustion CO_2 capture processes for this comparison are: (i) monoethanolamine absorption (MEA), a technologically ready process; (ii) chilled ammonia process (CAP); (iii) tail-end directly heated CaL; and (iv) entrained flow (EF) directly heated CaL. As a reference for the MEA, CAP, and CaL technologies, the *SPECCA* data from the CEMCAP project was used (Voldsund et al., 2019a). These values were calculated for cement production, which is similar to lime production, as discussed in the introductory chapter. It can be seen that the *SPECCA* of the IHCaL scenarios is considerably lower than the ones reported for the other carbon capture methods, except for the renewable scenarios. The IHCaL process allows for CO_2 capture with very low primary energy consumption, less than 2.1 $MJ_{LHV}/kg_{CO2,av}$, when using waste-derived fuel. Nevertheless, the *SPECCA* values increase drastically for the renewable scenario. Thereby, the electrical power is considered equivalent as the primary energy; thus, the additional power generation in the IHCaL process is not advantageous as in the other scenarios. Furthermore, the assumption of $\eta_{ref,el}$ = 100% associated with this scenario is unfairly high considering the type of feedstock involved.

The main challenge of the IHCaL process is the significant increase in the absolute heat required for the capture, i.e., HR_a, which is around 30% higher than for an oxy-fired CaL process[10]. Nonetheless, dynamic investment models suggest that the IHCaL technology would be superior in terms of global economic performance, compared to other post-combustion CO_2 capture processes (Junk et al., 2016). Within the ANICA Project, the concepts presented in this work are being evaluated to assess their viability in terms of CO_2 avoidance costs and environmental impact (Ströhle et al., 2021).

4 Conclusion

An innovative CO_2 post-combustion carbon capture method, the IHCaL process, was analyzed in this work. The configuration presented is suitable for retrofitting lime and cement plants. To evaluate its performance with alternative fuel firing, mass and heat balances with different fuels were performed, and the most relevant KPIs were calculated.

From the direct emissions breakdown, it was shown that the combustor influences the direct formation of CO_2 the most. The direct CO_2 formation is minimized by fuels with a lower CO_2 emissions index, $e_{CO2,fuel}$. Additionally, the utilization of dried lignite yielded an increase of approximately 100% in the total direct fossil CO_2 formation. This means that the additional generation associated with the carbon capture was approximately equal to the avoided CO_2. With this consideration, it appears more reasonable to use waste-derived fuels for the tail-end IHCaL, whereby the increase in total direct fossil CO_2 formation linked to the avoidance is relatively low (around 30%).

The results show that very low *SPECCA* values can be achieved for three of the simulated scenarios[11]: from 0.50 to 2.79 $MJ_{LHV}/kg_{CO2,av}$. In particular, *SPECCA* values between 0.50 and 1.98 $MJ_{LHV}/kg_{CO2,av}$ were achieved for the scenarios utilizing waste-derived fuels in the combustor. By reason of its low primary energy requirements[12], the IHCaL process is a very promising retrofitting technology for carbon capture from lime and cement plants. It may be deployed in scenarios, in which the associated power generation is an advantage. This is not the case for the 100% renewables scenario, which assumes the same worth for generated power and primary energy ($\eta_{ref,el}$ = 100%). For this scenario, the *SPECCA* values were higher than 4.6 $\mathrm{MJ_{LHV}/kg_{CO2,av}}$.

---

[10] Estimated by comparing the results from this work with the total heat input increase reported by De Lena et al. (2017) in the analysis of an integrated CaL-process for CO_2 capture in cement plants.

[11] State-of-the-art coal power plant, energy mix (2015), and nuclear.

[12] When comparing these *SPECCA* values with the available literature for other post-combustion carbon capture processes for lime and cement plants: De Lena et al. (2022), De Lena et al. (2019), De Lena et al. (2017), Voldsund et al. (2019a), Voldsund et al. (2019b).

Furthermore, it was demonstrated that the IHCaL process is suitable for achieving net negative CO_2 emissions; thus, carbon dioxide removal (CDR). For all the scenarios, the highest negative emissions were obtained with MSW fuel. Net negative emissions as high as −1805 $\mathrm{kg_{CO2}/t_{CaO}}$ were achieved[13]. This value represents an equivalent CO_2 avoidance of more than 230%, with respect to the reference plant without capture (1368 $\mathrm{kg_{CO2}/t_{CaO}}$).

The IHCaL process is particularly suitable for fuels with a high biogenic fraction (x_{bio}) and low specific CO_2 emissions ($e_{CO2,fuel}$). This combination of properties can be found in high caloric SRF, such as the one considered in this work (class 3 SRF, according to DIN EN ISO, 2021). The utilization of these fuels in the IHCaL combustor allows for net negative CO_2 emissions (−1019 $\mathrm{kg_{CO2}/t_{CaO}}$) with very low *SPECCA* (1.48 $\mathrm{MJ_{LHV}/kg_{CO2,av}}$)[14].

Appendix 1. Additional input data

The fuel data used for the calculations in this work are provided in Table 7.

The carbonator was modeled based on the work of Lasheras et al. (2011). The main model assumptions are reported in Table 8. The governing equations for the carbonation model were:

$$\begin{aligned} \frac{1}{K_r} &= \frac{d_p}{6 \cdot K_g} + \frac{1}{K_{ri}} \\ K_g &= \frac{D_{CO2}}{d_p \cdot Sh} \\ K_{ri} &= k_s \cdot \frac{X_{b,N} \cdot S_0 \cdot \rho_{CaO}}{M_{CaO}} \cdot (1 - X)^{2/3} \end{aligned} \tag{14}$$

K_r is the global reaction rate, K_g and K_{ri} are the diffusion-controlled rate and the chemical rate, respectively, d_p is the particle diameter, and *Sh* is the Sherwood dimensionless number. *X* is the conversion, i.e., fraction of active sorbent that has been carbonated. The rest of the constants are defined in Table 8. The active fraction of CaO ($X_{b,N}$) was calculated with the deactivation model of Abanades et al. (2005), according to Eq. (15).

$$X_{b,N} = \frac{f_m \cdot \left(1 - f_w\right) \cdot F_0}{F_0 + F_R \cdot \left(1 - f_m\right)} + f_w \tag{15}$$

---

[13] Utilizing MSW in the combustor; calculated with the state-of-the-art coal power plant energy scenario (η_e = 44.2%; $e_{ref,el}$ = 770 $\mathrm{kg_{CO2}/MWh_{el}}$).

[14] Calculated with the state-of-the-art coal power plant energy scenario (η_e = 44.2%; $e_{ref,el}$ = 770 $\mathrm{kg_{CO2}/MWh_{el}}$).

Table 7 Detailed fuel data used in this work

Property	Dried lignite	RDF pellets	SRF	MSW
Proximate analysis (%$_{\mathrm{dry}}$)				
Moisture content	10.3	8.1	19.4	25.0
Fix carbon	63.2	54.0	47.2	38.5
Volatile matter	30.7	33.9	33.7	36.4
Ash content	6.1	12.1	19.1	25.1
Ultimate analysis (%$_{\mathrm{dry}}$)				
Carbon	63.2	54.0	47.2	38.5
Hydrogen	4.8	7.0	6.5	4.3
Nitrogen	0.8	0.3	1.2	0.7
Chlorine	0.2	0.5	0.9	0.5
Sulfur	0.9	0.5	0.4	0.1
Oxygen	24.0	25.7	24.7	30.8
Ash	6.1	12.1	19.1	25.1
Higher heating value (HHV_{dry}) (MJ/kg$_{\mathrm{dry}}$)	25.3	23.1	21.5	15.1
Lower heating value (LHV_{wet}) (MJ/kg$_{\mathrm{wet}}$)	21.5	19.6	15.7	10.0

Table 8 Inputs for the carbonator reactor model

Parameter	Symbol	Unit	Value
Main inputs			
Make-up rate	Λ	$\mathrm{mol_{CaCO3}/mol_{CO2}}$	0.10
Carbonator operating temperature	T_{carb}	°C	650
Free-gas velocity	u_0	m/s	4.5
Carbonator total height	h_{total}	m	15
Carbonator pressure drop	Δp_{carb}	mbar	100
Inputs for hydrodynamic model			
Mean particle diameter	$d_{p,50}$	µm	180
Decay constant lean region	a	-	3
Volume fraction at dense region	ε_{sd}	-	0.16
Inputs for carbonation reaction model			
Effective gas diffusivity of CO_2 in air	D_{CO2}	m^2/s	$8.75 \cdot 10^{-5}$
Initial specific surface area	S_0	m^2/m^3	$1.70 \cdot 10^{7}$
Carbonation rate constant	k_s	$m^4/(s \cdot mol)$	$5.95 \cdot 10^{-10}$

Appendix 2. Detailed results

See Tables 9, 10, 11, 12, and 13.

Table 9 Results from the power calculations in MW_e

	Ref.	Dried lignite	RDF pellets	SRF	MSW
$P_{compression}$	0.0	7.6	7.4	7.2	10.2
$P_{blowers}$	0.0	3.2	3.4	3.3	4.6
P_{kiln}	0.7	0.7	0.7	0.7	0.7
$P_{in,total}$	0.7	11.5	11.5	11.2	15.6
$P_{out,total}$	0.0	43.1	42.8	42.4	62.7

Table 10 CO_2 formation in kg_{CO2}/t_{CaO}, detailed results

	Component	Fossil	Biogenic	Total
Reference facility	Lime kiln	1344	0	1344
	Calciner	0	0	0
	Combustor	0	0	0
	Total formation	*1344*	*0*	*1344*
	Total capture	*0*	*0*	*0*
Dried lignite	Lime kiln	977	0	977
	Calciner	224	0	224
	Combustor	1264	0	1264
	Total formation	*2465*	*0*	*2465*
	Total capture	*2218*	*0*	*2218*
RDF pellets	Lime kiln	980	0	980
	Calciner	220	0	220
	Combustor	596	623	1219
	Total formation	*1796*	*622*	*2418*
	Total capture	*1620*	*554*	*2174*
SRF	Lime kiln	988	0	988
	Calciner	215	0	215
	Combustor	638	522	1160
	Total formation	*1841*	*522*	*2362*
	Total capture	*1661*	*464*	*2126*
MSW	Lime kiln	885	0	885
	Calciner	274	0	274
	Combustor	741	1111	1852
	Total formation	*1900*	*1108*	*3007*
	Total capture	*1719*	*990*	*2709*

Table 11 Result from CO_2 emission calculations in kg_{CO2}/t_{CaO} considering different energy scenarios

	Ref.	Dried lignite	RDF pellets	SRF	MSW
Direct CO_2 emissions					
Fossil	1344	245	244	237	298
Biogenic	0	0	−622	−522	−1108
Total	*1344*	*245*	*−378*	*−285*	*−810*
Indirect CO_2 emissions					
Coal	24	−735	−729	−734	−995
Energy mix	8	−250	−248	−250	−339
Renewables	0	0	0	0	0
Nuclear	0	0	0	0	0
Equivalent CO_2 emissions					
Coal	1368	−488	−1107	−1019	−1805
Energy mix	1352	−3	−626	−535	−1148
Renewables	1344	247	−378	−285	−810
Nuclear	1344	247	−378	−285	−810

Table 12 Results of *SPECCA* breakdown in MJ_{LHV}/$kg_{CO2,av}$

Energy scenario	*SPECCA* breakdown	Dried lignite	RDF pellets	SRF	MSW
Coal	Fuel requirement increase	6.20	4.68	4.84	4.90
	Power requirement increase	0.38	0.31	0.31	0.30
	CPU power requirement	1.01	0.74	0.75	0.72
	Power generation	−5.71	−4.27	−4.42	−4.41
	Total	*1.88*	*1.46*	*1.48*	*1.50*
Energy mix	Fuel requirement increase	8.49	5.86	6.12	6.21
	Power requirement increase	0.51	0.37	0.38	0.36
	CPU power requirement	1.33	0.89	0.91	0.88
	Power generation	−7.53	−5.14	−5.39	−5.39
	Total	*2.79*	*1.98*	*2.03*	*2.06*
Renewables	Fuel requirement increase	10.49	6.73	7.09	7.21
	Power requirement increase	0.29	0.20	0.20	0.19
	CPU power requirement	0.75	0.47	0.49	0.47
	Power generation	−4.27	−2.71	−2.86	−2.87
	Total	*7.26*	*4.69*	*4.92*	*5.00*
Nuclear	Fuel requirement increase	10.49	6.73	7.09	7.21
	Power requirement increase	0.87	0.59	0.62	0.58
	CPU power requirement	2.28	1.42	1.47	1.42
	Power generation	−12.94	−8.21	−8.68	−8.70
	Total	*0.70*	*0.53*	*0.50*	*0.51*

Table 13 Results for the carbonator reactor model: variables from the process model and reactor model results

Parameter	Unit	Dried lignite	RDF pellets	SRF	MSW
Inputs from process model					
$y_{CO2,in}$	mol/mol	0.16	0.15	0.15	0.15
$T_{FlueGas}$	°C	269	269	269	269
F_{CO2}	mol/s	468	458	444	630
Results from reactor model					
Φ	mol_{Ca}/mol_{CO2}	5.40	5.50	5.60	5.65
X_{bN}	mol_{CaCO3}/mol_{Ca}	0.190	0.190	0.189	0.189
X_{carb}	mol_{CaCO3}/mol_{Ca}	0.167	0.161	0.161	0.161
E_{carb}	%	89	89	89	89
τ_{carb}	min	5.3	5.6	5.7	5.5
h_{bed}	m	3.3	3.3	3.3	3.3
Specific inventory	kg/m^2	1020	1020	1020	1020

Appendix 3. Calculation of heat ratio for different fuels

For the calculation of the heat requirement in the combustor, for any fuel, the heat balance of the system calciner-combustor is performed.

$$\{combustion\ \ heat\} = \{heat\ \ requirement\ \ calciner\} + \{sensible\ \ heat\ \ loss\ \ in\ \ combustor\}$$
$$\dot{Q}_{comb} = \dot{m}_{fuel} \cdot LHV_{wet} = F_{CO2} \cdot \Psi_1 + \dot{m}_{fuel} \cdot \Psi_2 \tag{16}$$

This equation can be solved using the specific heat capacities of the substances (c_p) and the operational parameters of the IHCaL facility:

$$\begin{aligned}
\Psi_1 &= \left(\Lambda + \Phi \cdot X_{carb}\right) \cdot E_{calc} \cdot \Delta H_{calc} + \left(T_{calc} - T_{sorb,calc,in}\right) \cdot \left[\left(\Lambda + \Phi \cdot X_{carb}\right) \cdot \overline{c}_{p,CaCO3} + \left(1 - X_{carb}\right) \cdot \overline{c}_{p,CaO}\right] \\
\Psi_2 &= AFR \cdot c_{p,air} \cdot \left(T_{comb} - T_{preheat}\right) + c_{p,fuel} \cdot \left(T_{comb} - T_0\right) \\
\dot{Q}_{comb} &= F_{CO2,plant} \cdot \Psi_1 \cdot \left(1 - \frac{e_{CO2,fuel}}{M_{CO2}} \cdot \Psi_1 + \frac{\Psi_2}{LHV}\right)^{-1}
\end{aligned} \tag{17}$$

The values assumed for the calculation of the curves of Fig. 3 are reported in Table 14.

Table 14 Values for the calculation of typical heat ratios for different $e_{CO2,fuel}$

Parameter	Unit	Bottom boundary	Base value	Top boundary
$F_{CO2,plant}$	kmol/h		735	
$\dot{Q}_{ref}$	MW_{th}		38.7	
E_{calc}	%		99	
E_{carb}	%		88	
Λ	mol_{CaCO3}/mol_{CO2}		0.1	
T_{calc}	°C		900	
$T_{sorb,calc,in}$	°C		810	
$T_{preheat}$	°C		800	
T_{comb}	°C		1000	
T_0	°C		20	
$c_{p,air}$	kJ/(kg·K)		1.1	
$\bar{c}_{p,CaO}$	J/(mol·K)		51.7	
$\bar{c}_{p,CaCO3}$	J/(mol·K)		131.3	
Φ	mol_{Ca}/mol_{CO2}	5.2	5.5	5.8
LHV_{wet}	MJ/kg_{wet}	22.0	15.5	9.0
Air-fuel ratio (*AFR*) [a]	kg_{air}/kg_{fuel}	9.0	9.0	4.8
$c_{p,fuel}$ [b]	kJ/(kg·K)	1.0	1.25	1.50

[a] Lignite (base and bottom) and RDF (top). Data from Liu et al. (2020), with $\lambda = 1.2$

[b] Based on data from Savage (1989) and Strezov et al. (2004)

Copyright notice References to Aspen Plus® are used with permission from Aspen Technolgy, Inc. AspenTech® and Aspen Plus® are trademarks of Aspen Technology, Inc. All rights reserved.

Author contribution Martin Greco-Coppi: conceptualization, methodology, software, visualization, and writing (original draft); Carina Hofmann: writing (review and editing); Diethelm Walter: writing (review and editing). Jochen Ströhle: writing (review and editing), supervision, project administration, and funding acquisition; Bernd Epple: supervision and funding acquisition.

Funding The work leading to these results has received funding through the ACT program (Accelerating CCS Technologies, Horizon 2020 Project N° 294766) within the ANICA project. Financial contributions were made by the German Federal Ministry for Economic Affairs and Climate Action. Open Access funding enabled and organized by Projekt DEAL.

Data availability The datasets generated and analyzed during the current study are available from the corresponding author on reasonable request.

Declarations

Competing interests The authors Martin Greco-Coppi, Carina Hofmann, Jochen Ströhle, Bernd Epple, and Diethelm Walter filed a patent application titled “Apparatus and Method for Producing Lime”, Assignees: Technical University of Darmstadt and Lhoist Germany Rheinkalk GmbH, patent pending before the German Patent and Trademark Office, Application number 10 2023 114 354.9.

Open Access This article is licensed under a Creative Commons Attribution 4.0 International License, which permits use, sharing, adaptation, distribution and reproduction in any medium or format, as long as you give appropriate credit to the original author(s) and the source, provide a link to the Creative Commons licence, and indicate if changes were made. The images or other third party material in this article are included in the article’s Creative Commons licence, unless indicated otherwise in a credit line to the material. If material is not included in the article's Creative Commons licence and your intended use is not permitted by statutory regulation or exceeds the permitted use, you will need to obtain permission directly from the copyright holder. To view a copy of this licence, visit http://creativecommons.org/licenses/by/4.0/.

References

Abanades JC, Anthony EJ, Lu DY, Salvador C, Alvarez D (2004) Capture of CO_2 from combustion gases in a fluidized bed of CaO. AICHE J 50:1614–1622. https://doi.org/10.1002/aic.10132

Abanades JC, Anthony EJ, Wang J, Oakey JE (2005) Fluidized bed combustion systems integrating CO_2 capture with CaO. Environ Sci Technol 39:2861–2866. https://doi.org/10.1021/es0496221

Anantharaman R, Berstad D, Cinti G, Gatti M (2018) D3.2 CEMCAP framework for comparative techno-economic analysis of CO_2 capture from cement plants

Arias B, Alonso M, Abanades C (2017a) CO_2 capture by calcium looping at relevant conditions for cement plants: experimental testing in a 30 kW_{th} pilot plant. Ind Eng Chem Res 56:2634–2640. https://doi.org/10.1021/acs.iecr.6b04617

Arias B, Diego ME, Abanades JC, Lorenzo M, Diaz L, Martínez D, Alvarez J, Sánchez-Biezma A (2013) Demonstration of steady state CO_2 capture in a 1.7MW_{th} calcium looping pilot. Int J Greenh Gas Control 18:237–245. https://doi.org/10.1016/j.ijggc.2013.07.014

Arias B, Diego ME, Méndez A, Abanades JC, Díaz L, Lorenzo M, Sanchez-Biezma A (2017b) Operating experience in la Pereda 1.7 MW_{th} calcium looping pilot. Energy Procedia 114:149–157. https://doi.org/10.1016/j.egypro.2017.03.1157

Astolfi M, De Lena E, Romano MC (2019) Improved flexibility and economics of calcium looping power plants by thermochemical energy storage. Int J Greenh Gas Control 83:140–155. https://doi.org/10.1016/j.ijggc.2019.01.023

Astrup T, Møller J, Fruergaard T (2009) Incineration and co-combustion of waste: accounting of greenhouse gases and global warming contributions. Waste Manag Res 27:789–799. https://doi.org/10.1177/0734242X09343774

Barker DJ, Turner SA, Napier-Moore PA, Clark M, Davison JE (2009) CO_2 capture in the cement industry. Energy Procedia 1:87–94. https://doi.org/10.1016/j.egypro.2009.01.014

Bhatt M, Chakinala AG, Joshi JB, Sharma A, Pant KK, Shah K, Sharma A (2021) Valorization of solid waste using advanced thermo-chemical process: a review. J Environ Chem Eng 9:105434. https://doi.org/10.1016/j.jece.2021.105434

Bonalumi D, Valenti G, Lillia S, Fosbøl PL, Thomsen K (2016) A layout for the carbon capture with aqueous ammonia without salt precipitation. Energy Procedia 86:134–143. https://doi.org/10.1016/j.egypro.2016.01.014

Busch P, Kendall A, Murphy CW, Miller SA (2022) Literature review on policies to mitigate GHG emissions for cement and concrete. Resour Conserv Recycl 182:106278. https://doi.org/10.1016/j.resconrec.2022.106278

Carbone C, Ferrario D, Lanzini A, Stendardo S, Agostini A (2022) Evaluating the carbon footprint of cement plants integrated with the calcium looping CO_2 capture process. Front Sustain 3:809231. https://doi.org/10.3389/frsus.2022.809231

Carrasco F, Grathwohl S, Maier J, Ruppert J, Scheffknecht G (2019) Experimental investigations of oxyfuel burner for cement production application. Fuel 236:608–614. https://doi.org/10.1016/j.fuel.2018.08.135

Carrasco-Maldonado F, Spörl R, Fleiger K, Hoenig V, Maier J, Scheffknecht G (2016) Oxy-fuel combustion technology for cement production – state of the art research and technology development. Int J Greenh Gas Control 45:189–199. https://doi.org/10.1016/j.ijggc.2015.12.014

Charitos A, Rodríguez N, Hawthorne C, Alonso M, Zieba M, Arias B, Kopanakis G, Scheffknecht G, Abanades JC (2011) Experimental validation of the calcium looping CO_2 capture process with two circulating fluidized bed carbonator reactors. Ind Eng Chem Res 50:9685–9695. https://doi.org/10.1021/ie200579f

Chen X, Jin X, Ling X, Wang Y (2020) Exergy analysis of concentrated solar power plants with thermochemical energy storage based on calcium looping. ACS Sustain Chem Eng 8:7928–7941. https://doi.org/10.1021/acssuschemeng.0c01586

Clarke L, Jiang K, Akimoto K, Babiker M, Blanford G, Fisher-Vanden K, Hourcade JC, Krey V, Kriegler E, Löschel A (2014) Assessing transformation pathways. In: Change IPoC, Edenhofer O (eds) Climate change 2014: mitigation of climate change; working group III contribution to the fifth assessment report of the intergovernmental panel on climate change. Cambridge University Press, New York, pp 413–510

De Lena E, Arias B, Romano MC, Abanades JC (2022) Integrated calcium looping system with circulating fluidized bed reactors for low CO_2 emission cement plants. Int J Greenh Gas Control 114:103555. https://doi.org/10.1016/j.ijggc.2021.103555

De Lena E, Spinelli M, Gatti M, Scaccabarozzi R, Campanari S, Consonni S, Cinti G, Romano MC (2019) Techno-economic analysis of calcium looping processes for low CO_2 emission cement plants. Int J Greenh Gas Control 82:244–260. https://doi.org/10.1016/j.ijggc.2019.01.005

De Lena E, Spinelli M, Martínez I, Gatti M, Scaccabarozzi R, Cinti G, Romano MC (2017) Process integration study of tail-end Ca-looping process for CO_2 capture in cement plants. Int J Greenh Gas Control 67:71–92. https://doi.org/10.1016/j.ijggc.2017.10.005

De Lena E, Spinelli M, Romano MC (2018) CO_2 capture in cement plants by “tail-end” calcium looping process. Energy Procedia 148:186–193. https://doi.org/10.1016/j.egypro.2018.08.049

Dean C, Hills T, Florin N, Dugwell D, Fennell PS (2013) Integrating calcium looping CO_2 capture with the manufacture of cement. Energy Procedia 37:7078–7090. https://doi.org/10.1016/j.egypro.2013.06.644

Diego ME, Arias B, Abanades JC (2016a) Analysis of a double calcium loop process configuration for CO_2 capture in cement plants. J Clean Prod 117:110–121. https://doi.org/10.1016/j.jclepro.2016.01.027

Diego ME, Arias B, Abanades JC (2020) Investigation of the dynamic evolution of the CO_2 carrying capacity of solids with time in La Pereda 1.7 MW_{th} calcium looping pilot plant. Int J Greenh Gas Control 92:102856. https://doi.org/10.1016/j.ijggc.2019.102856

Diego ME, Arias B, Méndez A, Lorenzo M, Díaz L, Sánchez-Biezma A, Abanades JC (2016b) Experimental testing of a sorbent reactivation process in La Pereda 1.7 MW_{th} calcium looping pilot plant. Int J Greenh Gas Control 50:14–22. https://doi.org/10.1016/j.ijggc.2016.04.008

Dieter H, Bidwe AR, Varela-Duelli G, Charitos A, Hawthorne C, Scheffknecht G (2014) Development of the calcium looping CO_2 capture technology from lab to pilot scale at IFK, University of Stuttgart. Fuel 127:23–37. https://doi.org/10.1016/j.fuel.2014.01.063

DIN EN (2011) Solid recovered fuels - Methods for the determination of biomass content; German version EN 15440:2011

DIN EN ISO (2021) Solid recovered fuels - Specifications and classes (ISO 21640:2021); German version EN ISO 21640:2021

Epple B (2009) Method and arrangement for separation of CO_2 from combustion flue gas (U.S. Patent No. US2010/0086456A1). U.S. Patent and Trademark Office

Erans M, Hanak D, Mir J, Anthony E, Manovic V (2016) Process modelling and techno-economic analysis of natural gas combined cycle integrated with calcium looping. Therm Sci 20:59–67. https://doi.org/10.2298/TSCI151001209E

Eriksson M, Hökfors B, Backman R (2014) Oxyfuel combustion in rotary kiln lime production. Energy Sci Eng 2:204–215. https://doi.org/10.1002/ese3.40

European Union (2015) L335/54: reviewing harmonised efficiency reference values for separate production of electricity and heat in application of Directive 2012/27/EU of the European parliament and of the council and repealing commission implementing decision 2011/877/EU. Official Journal of the European Union

Fantini M, Balocco M, Buzzi L, Canonico F, Consonni S, Cremona R, Gatti M, Hammerich J, Koehler R, Magli F, Romano MC, Spinelli M (2021) Calcium looping technology demonstration in industrial environment: status of the CLEANKER pilot plant. SSRN J. https://doi.org/10.2139/ssrn.3817346

Furimsky E (2007) Carbon dioxide emission index as a mean for assessing fuel quality. Energ Sourc Part A 30:119–131. https://doi.org/10.1080/15567030600820583

Fuss S, Canadell JG, Peters GP, Tavoni M, Andrew RM, Ciais P, Jackson RB, Jones CD, Kraxner F, Nakicenovic N, Le Quéré C, Raupach MR, Sharifi A, Smith P, Yamagata Y (2014) Betting on negative emissions. Nat Clim Chang 4:850–853. https://doi.org/10.1038/nclimate2392

Fuss S, Lamb WF, Callaghan MW, Hilaire J, Creutzig F, Amann T, Beringer T, de Oliveira Garcia W, Hartmann J, Khanna T, Luderer G, Nemet GF, Rogelj J, Smith P, Vicente JLV, Wilcox J, Del Mar Zamora Dominguez M, Minx JC (2018) Negative emissions—Part 2: costs, potentials and side effects. Environ Res Lett 13:63002. https://doi.org/10.1088/1748-9326/aabf9f

Gardarsdottir S, de Lena E, Romano M, Roussanaly S, Voldsund M, Pérez-Calvo J-F, Berstad D, Fu C, Anantharaman R, Sutter D, Gazzani M, Mazzotti M, Cinti G (2019) Comparison of technologies for CO_2 capture from cement production—part 2: cost analysis. Energies 12:542. https://doi.org/10.3390/en12030542

Garðarsdóttir SÓ, Normann F, Skagestad R, Johnsson F (2018) Investment costs and CO_2 reduction potential of carbon capture from industrial plants – a Swedish case study. Int J Greenh Gas Control 76:111–124. https://doi.org/10.1016/j.ijggc.2018.06.022

Gerassimidou S, Velis CA, Williams PT, Komilis D (2020) Characterisation and composition identification of waste-derived fuels obtained from municipal solid waste using thermogravimetry: a review. Waste Manag Res 38:942–965. https://doi.org/10.1177/0734242X20941085

Grasa GS, Abanades JC (2006) CO_2 capture capacity of CaO in long series of carbonation/calcination cycles. Ind Eng Chem Res 45:8846–8851. https://doi.org/10.1021/ie0606946

Greco-Coppi M, Hofmann C, Ströhle J, Walter D, Epple B (2021) Efficient CO_2 capture from lime production by an indirectly heated carbonate looping process. Int J Greenh Gas Control 112:103430. https://doi.org/10.1016/j.ijggc.2021.103430

Grote K-H, Feldhusen J (eds) (2007) Dubbel: Taschenbuch für den Maschinenbau, 22nd edn. Springer-Verlag, Berlin, Heidelberg, New York

Haaf M, Anantharaman R, Roussanaly S, Ströhle J, Epple B (2020a) CO_2 capture from waste-to-energy plants: techno-economic assessment of novel integration concepts of calcium looping technology. Resour Conserv Recycl 162:104973. https://doi.org/10.1016/j.resconrec.2020.104973

Haaf M, Hilz J, Peters J, Unger A, Ströhle J, Epple B (2020b) Operation of a 1 MW_{th} calcium looping pilot plant firing waste-derived fuels in the calciner. Powder Technol 372:267–274. https://doi.org/10.1016/j.powtec.2020.05.074

Haaf M, Ohlemüller P, Ströhle J, Epple B (2020c) Techno-economic assessment of alternative fuels in second-generation carbon capture and storage processes. Mitig Adapt Strateg Glob Chang 25:149–164. https://doi.org/10.1007/s11027-019-09850-z

Haaf M, Peters J, Hilz J, Unger A, Ströhle J, Epple B (2020d) Combustion of solid recovered fuels within the calcium looping process – experimental demonstration at 1 MW_{th} scale. Exp Thermal Fluid Sci 113:110023. https://doi.org/10.1016/j.expthermflusci.2019.110023

Hills TP (2016) Investigations of the use of spent sorbent from the Ca looping process in cement manufacture and investigation of long-term CO_2 uptake in cement and concrete. PhD Thesis. Imperial College London of Science, Technology and Medicine. https://doi.org/10.25560/39286

Hilz J, Helbig M, Haaf M, Daikeler A, Ströhle J, Epple B (2017) Long-term pilot testing of the carbonate looping process in 1 MW_{th} scale. Fuel 210:892–899. https://doi.org/10.1016/j.fuel.2017.08.105

Hilz J, Helbig M, Haaf M, Daikeler A, Ströhle J, Epple B (2018) Investigation of the fuel influence on the carbonate looping process in 1 MW_{th} scale. Fuel Process Technol 169:170–177. https://doi.org/10.1016/j.fuproc.2017.09.016

Hoeftberger D, Karl J (2013) Self-fluidization in an indirectly heated calciner. Chem Eng Technol 36:1533–1538. https://doi.org/10.1002/ceat.201300111

Hoeftberger D, Karl J (2016) The indirectly heated carbonate looping process for CO_2 capture—a concept with heat pipe heat exchanger. J Energy Resour Technol 138(042211):148A. https://doi.org/10.1115/1.4033302

Hofmann C, Greco-Coppi M, Ströhle J, Epple B (2022a) Operation of a 300 kW_{th} indirectly heated carbonate looping pilot plant for CO_2 capture from lime industry. Fluidized Bed Conversion Conference, 8-11 May 2022, Chalmers University of Technology (Sweden)

Hofmann C, Greco-Coppi M, Ströhle J, Epple B (2022b) Pilot testing of the indirectly heated carbonate looping process for cement and lime plants. Proceedings of the 16th Greenhouse Gas Control Technologies Conference (GHGT-16) 23-24 Oct 2022. https://doi.org/10.2139/ssrn.4278810

Hornberger M, Moreno J, Schmid M, Scheffknecht G (2020) Experimental investigation of the carbonation reactor in a tail-end calcium looping configuration for CO_2 capture from cement plants. Fuel Process Technol 210:106557. https://doi.org/10.1016/j.fuproc.2020.106557

Hornberger M, Moreno J, Schmid M, Scheffknecht G (2021) Experimental investigation of the calcination reactor in a tail-end calcium looping configuration for CO_2 capture from cement plants. Fuel 284:118927. https://doi.org/10.1016/j.fuel.2020.118927

IEA (2020a) Energy technology perspectives 2020 - special report on carbon capture utilisation and storage: CCUS in clean energy transitions. OECD; OECD Publishing, Paris

IEA (2020b) Projected Costs of Generating Electricity, Paris

IPCC (2018) Global warming of 1.5°C: an IPCC special report on the impacts of global warming of 1.5°C above pre-industrial levels and related global greenhouse gas emission pathways, in the context of strengthening the global response to the threat of climate change

IPCC (2022) Climate change 2022: mitigation of climate change. Contribution of Working Group III to the Sixth Assessment Report of the Intergovernmental Panel on Climate Change

Jackson S, Brodal E (2019) Optimization of the energy consumption of a carbon capture and sequestration related carbon dioxide compression processes. Energies 12:1603. https://doi.org/10.3390/en12091603

Jafarian M, Dally BB, Nathan GJ (2022) Hydrogen peroxide for fuel oxidation to achieve CO_2 capture from lime production. Energy Convers Manag X 15:100276. https://doi.org/10.1016/j.ecmx.2022.100276

Junk M, Reitz M, Ströhle J, Epple B (2013) Thermodynamic evaluation and cold flow model testing of an indirectly heated carbonate looping process. Chem Eng Technol 36:1479–1487. https://doi.org/10.1002/ceat.201300019

Junk M, Reitz M, Ströhle J, Epple B (2016) Technical and economical assessment of the indirectly heated carbonate looping process. J Energy Resour Technol 138:042210. https://doi.org/10.1115/1.4033142

Kremer J, Galloy A, Ströhle J, Epple B (2013) Continuous CO_2 capture in a 1-MW_{th} carbonate looping pilot plant. Chem Eng Technol 36:1518–1524. https://doi.org/10.1002/ceat.201300084

Kunii D, Levenspiel O (1991) Fluidization Engineering, 2nd edn. Butterworth-Heinemann, Boston

Lasheras A, Ströhle J, Galloy A, Epple B (2011) Carbonate looping process simulation using a 1D fluidized bed model for the carbonator. Int J Greenh Gas Control 5:686–693. https://doi.org/10.1016/j.ijggc.2011.01.005

Liu Z, Liu S, Shi R, Wang J, Xie M, Zheng S (2020) A control strategy of the air flow rate of coal-fired utility boilers based on the load demand. ACS Omega 5:31199–31208. https://doi.org/10.1021/acsomega.0c04585

Madejski P, Chmiel K, Subramanian N, Kuś T (2022) Methods and techniques for CO_2 capture: review of potential solutions and applications in modern energy technologies. Energies 15:887. https://doi.org/10.3390/en15030887

Magli F, Spinelli M, Fantini M, Romano MC, Gatti M (2022) Techno-economic optimization and off-design analysis of CO_2 purification units for cement plants with oxyfuel-based CO_2 capture. Int J Greenh Gas Control 115:103591. https://doi.org/10.1016/j.ijggc.2022.103591

Martínez I, Fernández JR, Abanades JC, Romano MC (2018) Integration of a fluidised bed Ca–Cu chemical looping process in a steel mill. Energy 163:570–584. https://doi.org/10.1016/j.energy.2018.08.123

Martínez I, Grasa G, Parkkinen J, Tynjälä T, Hyppänen T, Murillo R, Romano MC (2016) Review and research needs of Ca-looping systems modelling for post-combustion CO_2 capture applications. Int J Greenh Gas Control 50:271–304. https://doi.org/10.1016/j.ijggc.2016.04.002

Merk C, Grunau J, Riekhof M-C, Rickels W (2022) The need for local governance of global commons: the example of blue carbon ecosystems. Ecol Econ 201:107581. https://doi.org/10.1016/j.ecolecon.2022.107581

Mohn J, Szidat S, Fellner J, Rechberger H, Quartier R, Buchmann B, Emmenegger L (2008) Determination of biogenic and fossil CO_2 emitted by waste incineration based on $^{14}CO_2$ and mass balances. Bioresour Technol 99:6471–6479. https://doi.org/10.1016/j.biortech.2007.11.042

Mohn J, Szidat S, Zeyer K, Emmenegger L (2012) Fossil and biogenic CO_2 from waste incineration based on a yearlong radiocarbon study. Waste Manag 32:1516–1520. https://doi.org/10.1016/j.wasman.2012.04.002

Moora H, Roos I, Kask U, Kask L, Ounapuu K (2017) Determination of biomass content in combusted municipal waste and associated CO_2 emissions in Estonia. Energy Procedia 128:222–229. https://doi.org/10.1016/j.egypro.2017.09.059

Nhuchhen DR, Sit SP, Layzell DB (2022) Decarbonization of cement production in a hydrogen economy. Appl Energy 317:119180. https://doi.org/10.1016/j.apenergy.2022.119180

Obermoser M, Fellner J, Rechberger H (2009) Determination of reliable CO_2 emission factors for waste-to-energy plants. Waste Manag Res 27:907–913. https://doi.org/10.1177/0734242X09349763

Plaza MG, Martínez S, Rubiera F (2020) CO_2 capture, use, and storage in the cement industry: state of the art and expectations. Energies 13:5692. https://doi.org/10.3390/en13215692

Posch S, Haider M (2012) Optimization of CO_2 compression and purification units (CO_2CPU) for CCS power plants. Fuel 101:254–263. https://doi.org/10.1016/j.fuel.2011.07.039

Quader MA, Ahmed S (2017) Bioenergy with carbon capture and storage (BECCS). In: Rasul MG, Azad AK, Sharma SC (eds) Clean energy for sustainable development: comparisons and contrasts of new approaches. Academic Press, Amsterdam, Boston, Heidelberg, London, New York, Oxford, Paris, San Diego, San Francisco, Singapore, Sydney, Tokyo, pp 91–140

Reitz M, Junk M, Ströhle J, Epple B (2014) Design and erection of a 300 kW_{th} indirectly heated carbonate looping test facility. Energy Procedia 63:2170–2177. https://doi.org/10.1016/j.egypro.2014.11.236

Reitz M, Junk M, Ströhle J, Epple B (2016) Design and operation of a 300 kW_{th} indirectly heated carbonate looping pilot plant. Int J Greenh Gas Control 54:272–281. https://doi.org/10.1016/j.ijggc.2016.09.016

Rolfe A, Huang Y, Haaf M, Pita A, Rezvani S, Dave A, Hewitt NJ (2018) Technical and environmental study of calcium carbonate looping versus oxy-fuel options for low CO_2 emission cement plants. Int J Greenh Gas Control 75:85–97. https://doi.org/10.1016/j.ijggc.2018.05.020

Sarc R, Lorber KE (2013) Production, quality and quality assurance of refuse derived fuels (RDFs). Waste Manag 33:1825–1834. https://doi.org/10.1016/j.wasman.2013.05.004

Savage GM (1989) Thermal conductivity and specific heat of densified refuse derived fuel. Waste Manag Res 7:83–92. https://doi.org/10.1016/0734-242X(89)90010-4

Schorcht F, Kourti I, Scalet BM, Roudier S, Delgado Sancho L (2013) Best available techniques (BAT) reference document for the production of cement, lime and magnesium oxide: Industrial Emissions Directive 2010/75/EU (integrated pollution prevention and control). Publications Office, Luxembourg

Shimizu T, Hirama T, Hosoda H, Kitano K, Inagaki M, Tejima K (1999) A twin fluid-bed reactor for removal of CO_2 from combustion processes. Chem Eng Res Des 77:62–68. https://doi.org/10.1205/026387699525882

Spinelli M, Campanari S, Consonni S, Romano MC, Kreutz T, Ghezel-Ayagh H, Jolly S (2018) Molten carbonate fuel cells for retrofitting postcombustion CO_2 capture in coal and natural gas power plants. J Electrochem Energy Convers Storage 15:031001. https://doi.org/10.1115/1.4038601

Strezov V, Lucas JA, Evans TJ, Strezov L (2004) Effect of heating rate on the thermal properties and devolatilisation of coal. J Therm Anal Calorim 78:385–397. https://doi.org/10.1023/B:JTAN.0000046105.01273.61

Ströhle J, Hilz J, Epple B (2020) Performance of the carbonator and calciner during long-term carbonate looping tests in a 1 MW_{th} pilot plant. J Environ Chem Eng 8:103578. https://doi.org/10.1016/j.jece.2019.103578

Ströhle J, Hofmann C, Greco-Coppi M, Epple B (2021) CO_2 capture from lime and cement plants using an indirectly heated carbonate looping process - the ANICA project. In: TCCS-11: CO_2 capture, transport and storage. Short papers from the 11th International Trondheim CCS Conference, Trondheim, Norway. June 21-23. SINTEF Academic Press, Oslo, pp 529–535

Ströhle J, Junk M, Kremer J, Galloy A, Epple B (2014) Carbonate looping experiments in a $1MW_{th}$ pilot plant and model validation. Fuel 127:13–22. https://doi.org/10.1016/j.fuel.2013.12.043

Svensson E, Wiertzema H, Harvey S (2021) Potential for negative emissions by carbon capture and storage from a novel electric plasma calcination process for pulp and paper mills. Front Clim 3:705032. https://doi.org/10.3389/fclim.2021.705032

Velis CA, Longhurst PJ, Drew GH, Smith R, Pollard SJT (2010) Production and quality assurance of solid recovered fuels using mechanical—biological treatment (MBT) of waste: a comprehensive assessment. Crit Rev Environ Sci Technol 40:979–1105. https://doi.org/10.1080/10643380802586980

Voldsund M, Anantharaman R, Berstad D, De Lena E, Fu C, Gardarsdottir SO, Jamali A, Pérez-Calvo JF, Romano M, Roussanaly S, Ruppert J, Stallmann O, Sutter D (2019a) D4.6 CEMCAP comparative techno-economic analysis of CO_2 capture in cement plants

Voldsund M, Gardarsdottir S, De Lena E, Pérez-Calvo J-F, Jamali A, Berstad D, Fu C, Romano M, Roussanaly S, Anantharaman R, Hoppe H, Sutter D, Mazzotti M, Gazzani M, Cinti G, Jordal K (2019b) Comparison of technologies for CO_2 capture from cement production—part 1: technical evaluation. Energies 12:559. https://doi.org/10.3390/en12030559

Yang Y, Wang L, Xia D, Jiang Z, Jiang B, Zhang P (2020) Novel lime calcination system for CO_2 capture and its thermal-mass balance analysis. ACS Omega 5:27413–27424. https://doi.org/10.1021/acsomega.0c03850

Publisher's note Springer Nature remains neutral with regard to jurisdictional claims in published maps and institutional affiliations.

Authors and Affiliations

Martin Greco-Coppi[1] · **Carina Hofmann**[1] · **Diethelm Walter**[2] · **Jochen Ströhle**[1] · **Bernd Epple**[1]

✉ Martin Greco-Coppi
martin.greco@est.tu-darmstadt.de

Carina Hofmann
carina.hofmann@est.tu-darmstadt.de

Diethelm Walter
diethelm.walter@lhoist.com

Jochen Ströhle
jochen.stroehle@est.tu-darmstadt.de

Bernd Epple
bernd.epple@est.tu-darmstadt.de

[1] Technical University of Darmstadt, Institute for Energy Systems and Technology, Otto-Berndt-Str. 2, 64287 Darmstadt, Germany

[2] Lhoist Germany Rheinkalk GmbH, Am Kalkstein 1, 42489 Wülfrath, Germany

Research Paper III

Research Paper III

Title: Efficient CO_2 capture from lime plants: Techno-economic assessment of integrated concepts using indirectly heated carbonate looping technology

Authors: Martin Greco Coppi, Peter Seufert, Carina Hofmann, Angela Rolfe, Ye Huang, Sina Rezvani, Jochen Ströhle, Bernd Epple

Journal: Carbon Capture Science & Technology (Elsevier)

Status: Published (December 25, 2023)

Volume: 11 (June 2024)

DOI: https://doi.org/10.1016/j.ccst.2023.100187

Licensing: The authors. CC BY 4.0

Graphical abstract

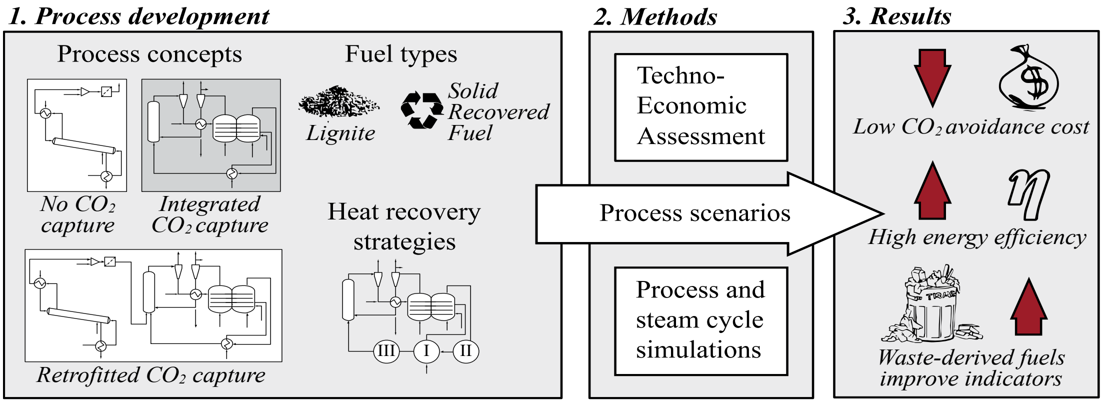
1. Process development
Process concepts
Fuel types
Lignite
Solid Recovered Fuel
No CO₂ capture
Integrated CO₂ capture
Heat recovery strategies
III
I
II
Retrofitted CO₂ capture
2. Methods
Techno-Economic Assessment
Process scenarios
Process and steam cycle simulations
3. Results
Low CO₂ avoidance cost
η
High energy efficiency
Waste-derived fuels improve indicators

Short Summary

Within this work, ten scenarios using IHCaL technology to capture CO_2 from a lime plant were simulated. Hereby, different process configurations, heat recovery strategies and fueling options were computed. The calculations for the capture facilities were performed with Aspen Plus software and EBSILON Professional was used to simulate the steam cycles. A techno-economic assessment aided by the ECLIPSE software was included as well. The results demonstrate that the fuel selection not only affects the CO_2 balance and energy performance but is also an important cost driver. There were considerable economic advantages for the computed cases with middle-caloric solid recovered fuel (SRF). The heat recovery strategy can be optimized to achieve tailored outcomes, such as reduced fuel requirement or increased power production. The specific primary energy consumption and cost for CO_2 avoided using SRF are considerably low, compared with other technologies for the same application. The sensitivity study revealed that the main parameters that impact the economics are the discount rate and the project life. The capture plants are more sensitive to parameter changes than the reference plant, and the plants using SRF are more sensitive than the lignite-fueled plants.

Carbon Capture Science & Technology 11 (2024) 100187

Contents lists available at ScienceDirect

Carbon Capture Science & Technology

journal homepage: www.elsevier.com/locate/ccst

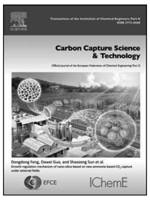

Full Length Article

Efficient CO_2 capture from lime plants: Techno-economic assessment of integrated concepts using indirectly heated carbonate looping technology

Martin Greco-Coppi[a,*], Peter Seufert[a], Carina Hofmann[a], Angela Rolfe[b], Ye Huang[b], Sina Rezvani[c], Jochen Ströhle[a], Bernd Epple[a]

[a] Technical University of Darmstadt, Department of Mechanical Engineering, Institute for Energy Systems and Technology, Otto-Berndt-Str. 2, 64287 Darmstadt, Germany
[b] Ulster University, School of the Built Environment, Centre for Sustainable Technologies, 2-24 York Street, Belfast BT15 1AP, Northern Ireland, United Kingdom
[c] ESTRA–Energy Technology Strategies Ltd., 1 Gardens Road, Clevedon BS21 7QQ, United Kingdom

ARTICLE INFO

Keywords:
Indirectly heated carbonate looping
Techno-economic assessment
Solid recovered fuel (SRF)
CO_2 capture in the lime production
Heat recovery optimization
Carbon dioxide removal (CDR)

ABSTRACT

The quest to decarbonize the lime and cement industry is challenging because of the amount and the nature of the CO_2 emissions. The process emissions from calcination are unavoidable unless carbon capture is deployed. Nevertheless, the majority of the available carbon capture technologies are expensive and energy inefficient. The indirectly heated carbonate looping (IHCaL) process is a promising technology to capture CO_2 from the lime and cement production, featuring low penalties in terms of economics and energy utilization. Previous works have highlighted the potential of the IHCaL, but the optimization of the process has not been discussed in enough detail and techno-economic implications are not yet fully understood. Within this work, ten scenarios using IHCaL technology to capture CO_2 from a lime plant were simulated. Hereby, different process configurations, heat recovery strategies and fueling options were computed. The calculations for the capture facilities were performed with Aspen Plus® software and EBSILON®*Professional* was used to simulate the steam cycles. A techno-economic assessment was included as well, aided by the ECLIPSE software.

The results demonstrate that the selection of the fuel for the combustor not only affects the CO_2 balance and energy performance but is also an important cost driver —there were considerable economic advantages for the computed cases with middle-caloric solid recovered fuel (SRF). The analysis shows how the heat recovery strategy can be optimized to achieve tailored outcomes, such as reduced fuel requirement or increased power production. The specific primary energy consumption (from −0.3 to +2.5 $MJ_{LHV}/t_{CO2,av}$) and cost for CO_2 avoided (from −11 to +25 €/$t_{CO2,av}$) using SRF are considerably low, compared with other technologies for the same application. The sensitivity study revealed that the main parameters that impact the economics are the discount rate and the project life. The capture plants are more sensitive to parameter changes than the reference plant, and the plants using SRF are more sensitive than the lignite-fueled plants. The conclusions from this work open a new pathway of experimental research to validate key assumptions and enable the industrial deployment of IHCaL technology before 2030.

1. Introduction

The production of lime and cement is responsible for around 8 % of global anthropogenic CO_2 emissions (Andrew, 2018). About 65 % of these emissions are associated with the calcination of limestone (IEA, 2020; Schorcht et al., 2013) and can only be avoided with carbon capture. There are many carbon capture technologies available —absorption, e.g., using methanolamine (MEA); adsorption; membrane separation; cryogenic capture; oxy-fuel combustion; chemical and carbonate looping; and biological CO_2 removal—, but the majority have high thermodynamic and economic penalties (Cachola et al., 2023; Hong, 2022; Krishnan et al., 2023; Voldsund et al., 2019).

One promising technology that may be used to decarbonize the lime industry is the direct separation of the Leilac-1 —low emissions intensity lime and cement— project (Hills et al., 2017), which uses an indirectly heated vertical tube for the calcination. Direct separation enables capture for all the process emissions with low cost (Driver et al., 2022), but is not able to separate the CO_2 produced by combustion. This technology has been demonstrated up to the 240 t/d raw meal scale, separating 85 t/d of CO_2. A scale-up of the technology will take place within the Leilac-2 project (European Commission, 2020). The start of construction is scheduled for the year 2023.

Among the available technologies for capturing CO_2 from lime and cement production, carbonate looping (CaL) (Shimizu et al., 1999) is one of the most promising, because it can enable synergies with the calcination process, and thus allow to capture CO_2 efficiently without incurring high costs (De Lena et al., 2022; Zhao et al., 2013). The CaL process

---

[*] Corresponding author.
E-mail address: martin.greco@est.tu-darmstadt.de (M. Greco-Coppi).

https://doi.org/10.1016/j.ccst.2023.100187
Received 21 September 2023; Received in revised form 8 December 2023; Accepted 24 December 2023

2772-6568/© 2023 The Authors. Published by Elsevier Ltd on behalf of Institution of Chemical Engineers (IChemE). This is an open access article under the CC BY license (http://creativecommons.org/licenses/by/4.0/)

Nomenclature

Latin symbols

BESP	breakeven selling price (€/t_{lime})
CAC	CO_2 avoidance cost (€/tCO_2,av)
e_{CO2}	specific CO_2 emissions (g_{CO2}/kg_{CaO})
$e_{ref,el}$	CO_2 emissions factor of the grid (g_{CO2}/ MJ)
$e_{CO2,fuel}$	fuel specific CO_2 emissions (g_{CO2}/MJ_{LHV})
E_{cc}	carbon capture efficiency (–)
f_m; f_w	fitting constants for Eq. (3) (–)
F_{CO2}	CO_2 molar flow rate (into carbonator) (mol_{CO2}/s)
F_t	fuel expenditure in year *t* (M€)
F_R	sorbent molar circulation rate (mol_{Ca}/s)
F_0	make-up molar flow rate (mol_{CaCO3}/s)
HtPR	heat-to-power ratio (–)
HR	specific heat ratio (–)
HR_a	absolute heat ratio (–)
I_t	investment expenditure (CAPEX) in year *t* (M€)
I_0	initial investment expenditure (initial CAPEX) (M€)
LHV	lower heating value (kJ/kg)
$\dot{m}_{CaO}$	product mass flow rate (t/h)
$\dot{m}_{fuel}$	fuel mass flow rate/ fuel requirement (t/h)
$\dot{m}_{CO2}$	CO_2 mass flow rate (t/h)
M_t	operation and maintenance expenditure in year *t* (M€)
n	system lifetime (year)
p	pressure (bar)
P_{el}	electric power (MW)
PR	product ratio (–)
q	specific primary energy consumption (J/kg_{CaO})
Q	heat flow rate/ heat duty (MW)
r	discount rate (%)
SPECCA	specific primary energy consumption for CO_2 avoided ($MJ_{LHV}/kg_{CO2,av}$)
T	temperature (°C)
u_0	free gas velocity (m/s)
x_{bio}	fuel carbon biogenic fraction (–)
X	degree of carbonation (mol_{CaCO3}/mol_{Ca})
$X_{ave,max}$	maximum carbonation after carbonator (sorbent activity) (mol_{CaCO3}/mol_{Ca})

Greek symbols

Δp	pressure drop through component/reactor (mbar)
$\eta_{net,SC}$	steam cycle net efficiency (–)
$\eta_{ref,el}$	reference electrical efficiency of the grid (–)
Λ	specific make-up rate (mol_{CaCO3}/mol_{CO2})
Φ	specific sorbent circulation rate (mol_{Ca}/mol_{CO2})

Abbreviations

ASU	air separation unit
BECCS	bioenergy with carbon capture and storage
bio	biogenic (fraction)
CaL	carbonate looping/ calcium looping
CAPEX	capital expenditure
CEPCI	Chemical Engineering Plant Cost Index
CCS	carbon capture and storage
CDR	CO_2 removal
ECO	economizer
EPC	engineering, procurement and construction (cost)
ES	energy scenario
EU-28	European Union (energy mix)
EVA	evaporator
IHCaL	indirectly heated carbonate looping
KPI	key performance indicator
Leilac	low emissions intensity lime and cement (project)
MEA	monoethanolamine
NGCC	natural gas combined cycle
NPV	net present value
OPEX	operating expenditure
O&M	operating and maintenance (costs)
PRK	preheated rotary kiln (reference/host facility)
RDF	refuse-derived fuel
RH	reheater
ROI	return on investment
S	process scenario
SH	superheater
SRF	solid recovered fuel
TEA	techno-economic assessment
TCC	total capital cost

Subscripts and superscripts

bio	biogenic (fraction)
calc	calciner (exit)
capt	captured CO_2
carb	carbonator (exit)
comb	combustor (exit)
foss	fossil (fraction)
FA	fluidization agent
FG	flue gas
ref	reference facility without carbon capture
SC	steam cycle
wet	wet basis

(see Fig. 1) operates with two reactors, namely, a carbonator (ca. 650 °C) and a calciner (ca. 900 °C), using solid sorbents, such as lime (mainly CaO). The high temperatures enable manifold regenerative heat integration options. The operating principle is the reversible carbonation-calcination reaction of CaO. CO_2 from flue gases is bound through carbonation of the sorbent inside the carbonator, which typically operates in the bubbling or circulating fluidized bed regime (Abanades et al., 2004; Charitos et al., 2011). The carbonated sorbent is regenerated in the calciner, also operating as a fluidized bed reactor (Wang et al., 2007). In the standard configuration, the heat for the calcination is provided via oxy-fuel combustion, directly in the combustor, using pure oxygen and fuel (see Myöhänen et al., 2009). CaL technology has been demonstrated up to the pilot scale for manifold operating conditions (Arias et al., 2017; Arias et al., 2013; Diego et al., 2016b; Dieter et al., 2014; Kremer et al., 2013; Ströhle et al., 2014), including firing with waste-derived fuels (Haaf et al., 2020c; Haaf et al., 2020b).

The drawback of standard CaL technology is the requirement of pure oxygen, which is obtained with an energy-intensive air separation unit (ASU). The installation of an ASU entails significant investment.

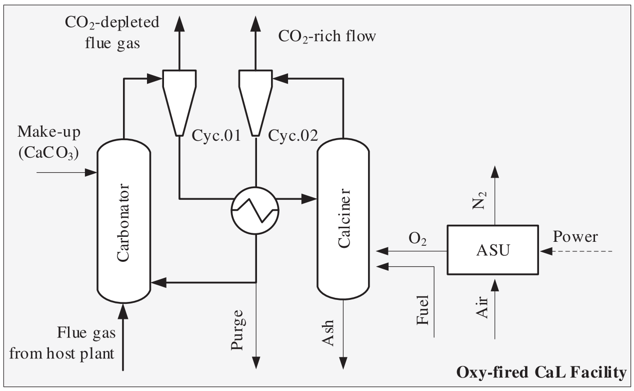

Fig. 1. Oxy-fired carbonate looping process with air separation unit (ASU).

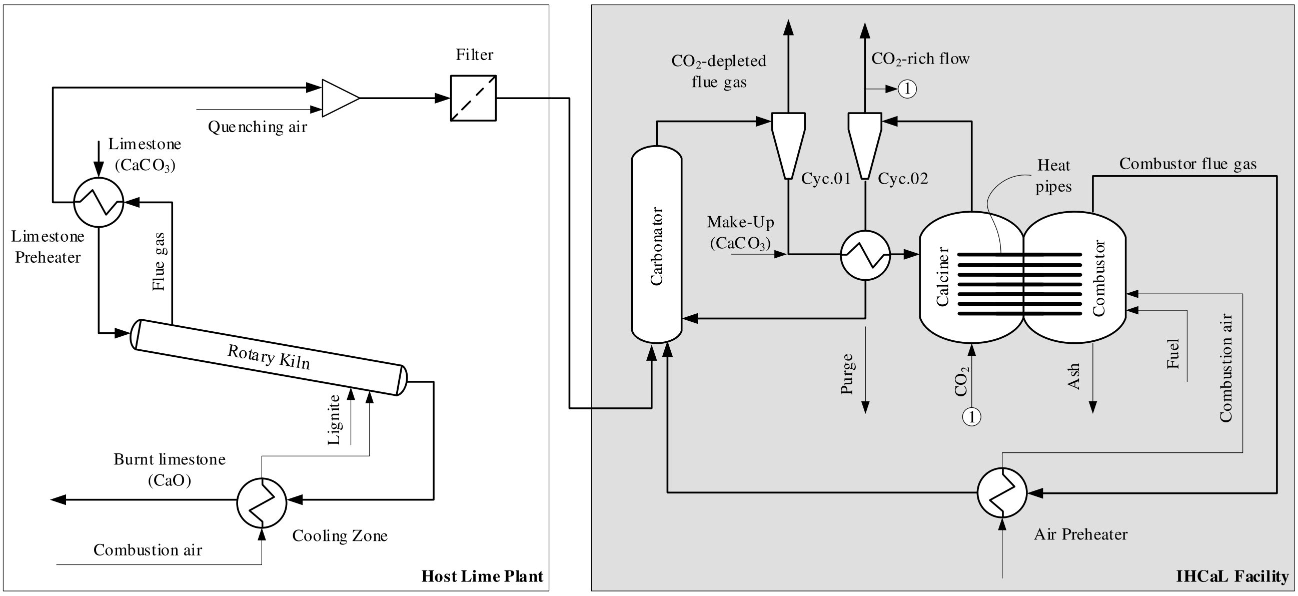

Fig. 2. Lime production facility with carbon capture using a retrofitted indirectly heated carbonate looping process (IHCaL), adapted from Greco-Coppi et al. (2021) with permission of Elsevier.

De Lena et al. (2022) calculated that the ASU accounts for around 15 % of the total plant cost for an integrated CaL system for CO_2 capture from a cement plant. A similar result was obtained by Fu et al. (2021) for the implementation of the CaL process in natural gas combined cycle plants. Additionally, the electric power required to operate the ASU can be higher than 40 % of the electricity demand of the entire CaL system (De Lena et al., 2022; Haaf et al., 2020a).

From the entire carbon capture and storage (CCS) value chain —separation, transport, and geological storage—, the capture process is the most energetically demanding and it accounts for about 70–80 % of the total costs (Vitillo et al., 2017). Santos and Hanak (2022) reviewed the available techno-economic analysis studies on carbon capture for industrial processes of the last ten years. They concluded that CaL is superior to other technologies (amine scrubbing, physical absorption, vacuum pressure swing absorption, and oxy-fuel combustion) for this kind of application. According to their estimations, CaL technology has an average CO_2 avoidance cost of 32.7 to 42.9 €/$t_{CO2,av}$ and an equivalent energy requirement between 2.0 and 3.7 $MJ_{th}/kg_{CO2,av}$. Membrane separation technology —which was not included in the review of Santos and Hanak (2022)— is sometimes regarded as a competitive alternative to decarbonize the cement industry, but it is still costly (> 80 EUR/$t_{CO2,av}$) if capture rates of more than 80 % are to be achieved (Baker et al., 2018; Ferrari et al., 2021; Gardarsdottir et al., 2019). De Lena et al. (2019) analyzed CaL technology for cement plants and obtained slightly higher costs (52–58.5 €/$t_{CO2,av}$) for the scenarios considered. Romano et al. (2013) presented an integrated concept for cement production and power generation that would be profitable even for low carbon taxes, starting at 27 €/t_{CO2}.

Gardarsdottir et al. (2019) compared different carbon capture technologies for the cement production. According to their calculations, the lowest avoidance costs, amounting to 42 €/$t_{CO2,av}$, would be achieved with oxy-fuel technology. However, they explained that retrofitability issues might negatively impact the cost performance of the oxy-fuel process. Cormos et al. (2020) evaluated capture technologies to decarbonize different industrial processes, including cement production, for which they estimated that a 90 % decarbonization rate could be achieved with a cost of 57.8 €/$t_{CO2,av}$ with CaL technology. Yang et al. (2021) carried out an extensive techno-economic analysis, in which they considered numerous carbon capture technologies and integration options. One of their most relevant findings is that the utilization of biomass with carbon capture and storage, i.e., BECCS, improves the technical and economic performance of the CO_2 capture. To date, not many works have been published analyzing the costs of capturing CO_2 from lime plants. Moreover, there are many similarities between lime and cement production; therefore, conclusions about CO_2 capture can be extrapolated from one industry to the other —see Greco-Coppi et al. (2023) for a thorough discussion on this matter.

To reduce the penalties of the CaL, the heat for the calcination can be provided indirectly, thus eliminating the need for an ASU. This technology is known as the indirectly heated carbonate looping (IHCaL) (Junk et al., 2013). Indirect heating can be achieved with different mechanisms, such as utilization of steam (Fan, 2012; Ramkumar and Fan, 2010; Wang et al., 2010), direct heat transfer through the reactor walls (Abanades et al., 2005; Grasa and Abanades, 2007), or by means of solid heat carriers (Abanades et al., 2005; Diego et al., 2016a; Martínez et al., 2011). One of the most promising approaches consists in utilizing heat pipes connecting the calciner and the combustor (Hoeftberger and Karl, 2016; Junk et al., 2013; Reitz et al., 2014). The IHCaL technology utilizing heat pipes to indirectly heat the calciner has been validated during pilot testing at the 300 kW_{th} scale test rig of the Technical University of Darmstadt (Reitz et al., 2016), including operation in relevant conditions for the lime industry (Hofmann et al., 2024, 2022a). Junk et al. (2016) estimated that the CO_2 avoidance cost for a coal power plant with IHCaL technology would be 22.6 €/$t_{CO2,av}$.

Greco-Coppi et al. (2021) developed the IHCaL process for use in lime plants and indicated the importance of heat recovery in the global process efficiency, due to the high temperatures of the process (over 650 °C). They presented two possible configurations to produce lime with low CO_2 emissions: (i) a tail-end configuration, which is useful for retrofitting an existing lime kiln (see Fig. 2); and (ii) a fully integrated solution (see Fig. 3).

The tail-end configuration consists in an IHCaL facility placed downstream of a host lime plant, as shown in Fig. 2. It permits capturing CO_2 with minimal impact on the upstream process. Additionally, it expands the production capacity of the entire facility through the utilization of spent sorbent (purge stream).

The fully integrated solution (illustrated in Fig. 3) involves the construction of a completely new facility; thus, it is not suitable for retrofitting existing lime kilns. This new facility constitutes an entire lime production plant with integrated carbon capture through carbon-

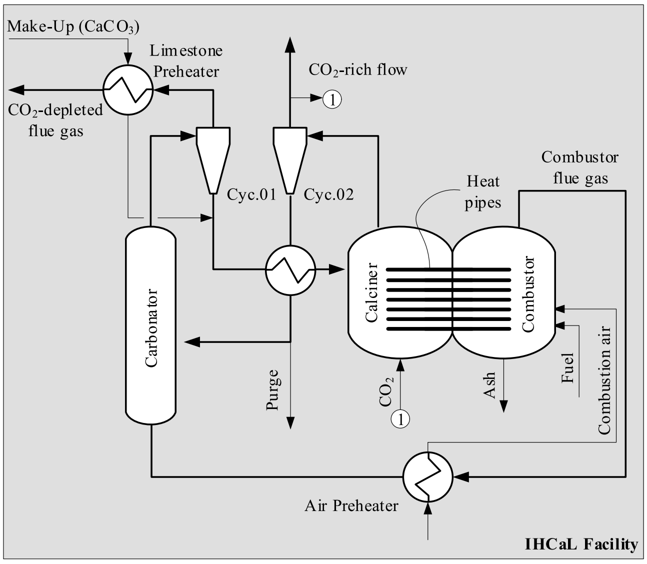

Fig. 3. Lime production facility with carbon capture using a fully integrated IHCaL facility to produce lime with low CO2 emissions, adapted from Greco-Coppi et al. (2021) with permission of Elsevier.

ate looping, where the make-up stream is the raw limestone and the purge stream is the product (lime). A detailed explanation of the two configuration concepts can be found in previous publications (Greco-Coppi et al., 2023; Greco-Coppi et al., 2021; Junk et al., 2013).

A detailed analysis and optimization of the heat recovery system —indispensable to exploit the potential of the IHCaL in the lime production— is yet to be done. Furthermore, the advantage of utilizing waste-derived fuel —such as solid recovered fuel (SRF) or refuse-derived fuel (RDF) (see Gerassimidou et al., 2020; Sarc and Lorber, 2013; Velis et al., 2010)— to produce the heat for the combustion was established (Greco-Coppi et al., 2023), but the techno-economic impact is not fully understood yet.

This work closes an important knowledge gap in the route to develop the IHCaL process by delineating the economic and technical implications of applying this technology to the lime production. To achieve this, a comprehensive process modeling of the IHCaL process is performed. Furthermore, the design of the heat recovery steam cycle is investigated and three alternative heat recovery strategies are analyzed. For the heat production in the combustor, two options are evaluated, namely, utilizing lignite or fueling SRF. Altogether, eleven process scenarios are compared with each other in terms of CO_2 formation, energy utilization, and economic performance. Finally, a sensitivity analysis is included.

2. Methods

2.1. IHCaL process and scenarios analyzed

In this work, different strategies to reduce CO_2 emissions in the lime production were analyzed. An operating lime production plant from Germany was taken as the reference facility for the study and the host plant for the retrofitting configurations. This plant utilizes a preheated rotary kiln (PRK) for the calcination of limestone. It is described in detail in the work of Greco-Coppi et al. (2021).

The different process scenarios (S) that were studied differ in terms of plant concept, fuel type for the combustor, and heat recovery concept (see Section 2.2 for this last category). In total, eleven scenarios were computed (see Table 1): the reference German lime plant as-built, without carbon capture (S-1); four retrofitting or "tail-end" configurations for lime production with carbon capture using lignite (S-2 and S-3) and SRF (S-4 and S-5); as well as six fully integrated solutions using lignite (S-6 to S-8) and SRF (S-9 to S-11).

Greco-Coppi et al. (2023) showed that fueling the IHCaL with waste-derived fuels allows for carbon dioxide removal (CDR) through negative CO_2 emissions (Kemper, 2015; Yang et al., 2021). This holds true if the biogenic fraction (bio) of CO_2 from the combustion is captured and effectively removed from the atmosphere —mainly through subsequent geological storage.

The fuels for this analysis were selected following the work from Greco-Coppi et al. (2023). The lignite properties were obtained from the fuel analysis of the lignite used in the host plant in Germany. The properties of the SRF implemented in this work are consistent with the SRF used to successfully operate the 1 MW_{th} CaL plant in Darmstadt (Haaf et al., 2020d; Haaf et al., 2020b). The composition and main properties of the fuels are presented in Table 2, where LHV is the lower heating value in wet basis, x_{bio} is the carbon biogenic fraction in the fuel (Astrup et al., 2009; Moora et al., 2017), and $e_{CO2,fuel}$ is the fuel CO_2 emissions index (Furimsky, 2007; Madejski et al., 2022), i.e., the specific CO_2 emissions for the combustion of the fuel.

Fig. 4 is a simplified IHCaL flow diagram that shows the main molar flows (F) of sorbent and CO_2, as well as the sorbent carbonation degrees (X). The sorbent molar flow rates are F_R, for the sorbent circulation between the carbonator and calciner, and F_0, for the fresh make-up and the purge streams. The make-up stream consists of pure limestone (mainly $CaCO_3$). The total CO_2 molar flow rate into the carbonator is indicated with F_{CO2}.

For the calculations and the comparisons, it is generally useful to work with dimensionless parameters; thus, the specific make-up rate

Table 1
Process scenarios (S) calculated.

Plant concept	IHCaL integration	Fuel IHCaL combustor	Heat recovery concept[a]	Process scenario (S) no.
Reference PRK	–	–	–	S-1
PRK with downstream carbon capture (see Fig. 2)	Tail-end	Lignite	I	S-2
			II	S-3
		SRF	I	S-4
			II	S-5
Lime production facility with fully integrated carbon capture (see Fig. 3)	Fully integrated	Lignite	I	S-6
			II	S-7
			III	S-8
		SRF	I	S-9
			II	S-10
			III	S-11

[a] I: only air preheater; II: heat exchanger before air preheater; III: heat exchanger after air preheater.

Table 2
Input data of the fuels, adopted from Greco-Coppi et al. (2023).

Parameter	Dried lignite	SRF	Unit
LHV	21.5	15.7	MJ/kg_{wet}
x_{bio}	0	45	%
$e_{CO2,fuel}$	96.7	88.7	g_{CO2}/MJ_{LHV}
Particle size	0–4	d_{95} < 50	mm
Composition			
C	56.7	38.0	wt.$\%_{wet}$
H	4.3	5.2	wt.$\%_{wet}$
N	0.7	1.0	wt.$\%_{wet}$
S	0.8	0.3	wt.$\%_{wet}$
O	21.5	19.9	wt.$\%_{wet}$
Cl	0.2	0.7	wt.$\%_{wet}$
H_2O	10.3	19.4	wt.$\%_{wet}$
Ash	5.5	15.4	wt.$\%_{wet}$
Reference	Greco-Coppi et al. (2021)	Haaf et al. (2020d)	

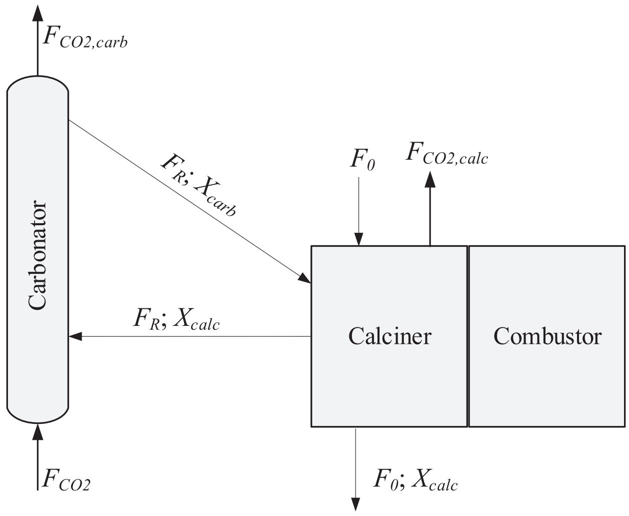

Fig. 4. Indirectly heated carbonate looping process: simple process diagram with main molar flow and carbonization degree parameters.

(Λ) and the specific sorbent circulation rate (Φ) are defined according to Eqs. (1) and (2), respectively. These parameters are varied in order to optimize the processes (Greco-Coppi et al., 2021).

$$\Lambda = \frac{F_0}{F_{CO2}} \tag{1}$$

$$\Phi = \frac{F_R}{F_{CO2}} \tag{2}$$

2.2. Heat recovery and steam cycle

Due to the high operating temperatures (> 650 °C), the IHCaL process offers the possibility of recovering heat by means of a steam cycle. The usable sources for heat recovery are:

- CO_2-depleted flue gas from the carbonator (650 °C)
- CO_2-rich flow from the calciner (900 °C)
- Flue gases from the combustor (1000 °C)
- Heat from the carbonator cooling (650 °C)

The flue gas from the external combustion chamber has a temperature of 1000 °C. This stream is used to preheat the combustion air (see Figs. 2 and 3). It is necessary to investigate how the use of the flue gas for steam generation affects the preheating temperature, which in turn has an important impact in the fuel requirement for the carbon capture (cf. Greco-Coppi et al., 2021).

Another point of integration is the utilization of the carbonator flue gases to preheat the fresh limestone before it enters the system, prior to exchanging heat with the steam cycle (see Fig. 3). It is included for all the fully integrated concepts (S-6 to S-11). This heat recovery strategy is not implemented in the tail-end configurations (S-2 to S-5), where the specific make-up rates are much lower and the energy penalty of heating the make-up is negligible.

Considering the impact of the heat recovery on the energy balance, three recovery concepts were developed (illustrated in Fig. 5). The proposed concepts are analyzed and discussed to understand the effect of the heat recovery in the IHCaL process.

In configuration (I) (Fig. 5.a), the flue gas is not used to transfer heat into the steam cycle, but only for the preheating of the combustor air. Thus, the IHCaL process is not affected by the heat recovery.

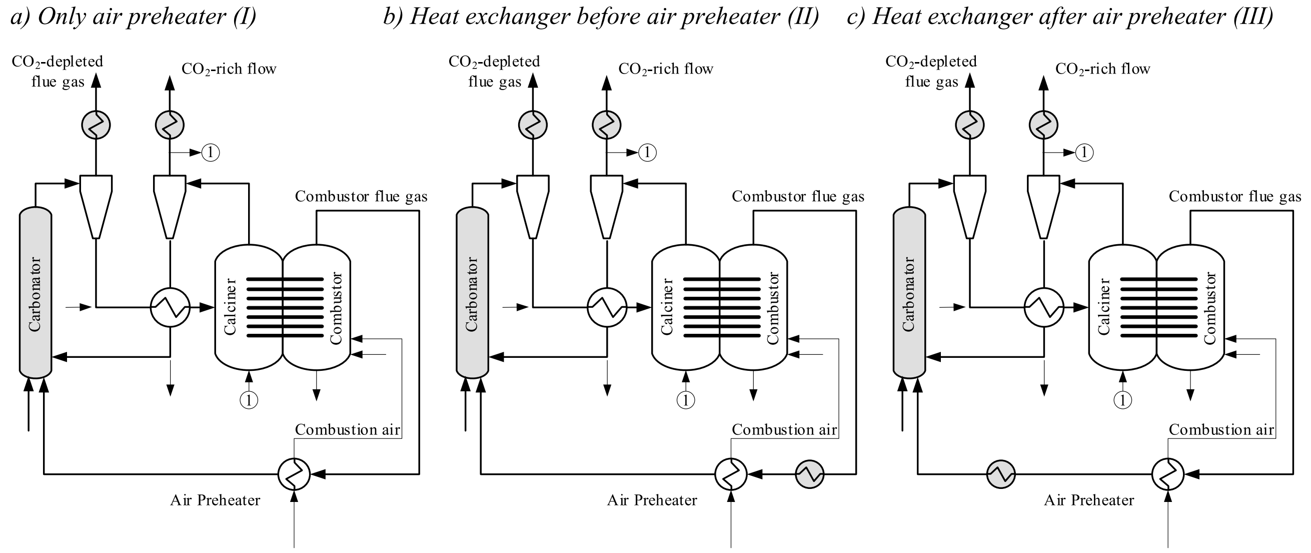
a) Only air preheater (I) *b) Heat exchanger before air preheater (II)* *c) Heat exchanger after air preheater (III)*

Fig. 5. Concepts for the recovery of heat from the IHCaL facility. The configurations differ in the utilization of the heat from the combustor flue gases: (a) only for air preheating (concept I), (b) in the steam cycle before the air preheater (concept II), and (c) in the steam cycle after the air preheating (concept III). The heat exchangers used to transfer heat to the steam cycle are indicated with a blue shading.

Table 3
Main assumptions for the steam cycles.

IHCaL integration	Tail-end		Fully integrated		
Heat recovery concept	I	II	I	II	III
Steam cycles					
Turbine efficiency					
Mechanical	99.5 %	99.5 %	99.5 %	99.5 %	99.5 %
Isentropic	85 %	85 %	82 %	82 %	82 %
Generator efficiency	98.6 %	98.6 %	98.6 %	98.6 %	98.6 %
Pump efficiency					
Mechanical	99.8 %	99.8 %	99.8 %	99.8 %	99.8 %
Isentropic	80 %	80 %	80 %	80 %	80 %
Superheater					
p (bar)	130	130	130	130	130
T (°C)	565	565	565	565	565
Reheater					
p (bar)	–	30	–	–	–
T (°C)	–	565	–	–	–
Exhaust					
p (bar)	0.07	0.07	0.07	0.07	0.07
FWPH[a]	6	6	5	6	6
Heat exchangers[b]					
Carbonator	EVA-SH1	EVA	EVA-SH1	EVA	EVA-SH1
T_{carb} (°C)	650	650	650	650	650
Carbonator flue gas	SH2-ECO	SH1-EVA-ECO	ECO	ECO	ECO2
T_{in} (°C)	650	650	420	430	430
T_{out} (°C)	286	266	276	266	266
Calciner flue gas	SH3-ECO	SH2-ECO	SH2-ECO	EVA	SH3-ECO1
T_{in} (°C)	900	900	900	900	900
T_{out} (°C)	286	266	276	344	503
Combustor flue gas	–	RH; SH3	–	SH	SH2
T_{in} (°C)	–	1000	–	1000	600
T_{out} (°C)	–	604	–	737	450

[a] FWPH: Feedwater preheating;

[b] EVA: Evaporator; ECO: Economizer; SH: Superheater; RH: Reheater.

This approach has the advantage that the complexity of the steam cycle is significantly reduced. An air preheating temperature of 800 °C can be achieved so that fuel consumption is kept as low as possible. However, this approach has the consequence that less power is generated within the steam cycle, so that some optimizations (e.g., reheating) are no longer economical.

The second approach (II) (Fig. 5.b) consists in recovering heat from the flue gas directly downstream of the combustion chamber. Thus, the flue gas is cooled before using it for air preheating. The advantage of this approach is that significantly more heat is available for the steam cycle; thus, higher power output can be achieved, which means that further optimization of the steam cycle is worth implementing. The subsequent air preheating with the flue gas heats the air to approx. 450–500 °C. These preheating temperatures are achievable with the current state-of-the-art air preheaters. The disadvantage of configuration (II) is that the preheating temperature of the combustion air is significantly lower than in the reference case (≈ 40 % lower). This leads to a higher fuel requirement to provide the necessary heat for the calciner.

To compensate for the disadvantages of configurations (I) and (II), a third concept (III) was considered (Fig. 5.c). It is analogous to approach (II), but in this case, the flue gas is used for steam generation after air preheating; thus, less energy is lost, which increases the overall energy efficiency of the system.

Energy involved in the compression of CO_2 could be partially recovered, e.g., through feed-water preheating. Hanak et al. (2014) evaluated different options to optimize the electric generation of a coal-fired steam power plant retrofitted with an integrated CO_2 capture process. He concluded that utilizing the intercooler heat for the feed-water heating is not as efficient in terms of cost, compared to, e.g., using flue gas for this purpose. Consequently, it was decided to leave the heat recovery from the CO_2 compression train out of this analysis.

The three concepts for recovery (I, II, and III) were studied for the tail-end and the fully integrated IHCaL processes utilizing lignite and SRF to fuel the combustor (see Table 1). Since the temperature of the flue gas after the air preheater was too low to justify the addition of a heat exchanger in the tail-end configuration, concept (III) in the tail-end integration was deemed unrealistic and was not pursued; thus, the results of the tail-end concept are only presented for heat recovery concepts (I) and (II). The detailed investigation of the variation of the steam cycle with the fuel was out of the scope of this work. For the calculations of the steam cycle, the results from the simulations with lignite were used. The cycle's efficiency was assumed invariant with the fuel used in the IHCaL, and the heat recovered was scaled-up with the heat input in the IHCaL process. This assumption is reasonable considering the similar CO_2 emission factor ($e_{CO2,fuel}$) of the fuels in this work, and the low variation of firing capacity with the fuels considered (see Section 3.1). Furthermore, the results of the simulations show a very small variation of heat requirement in the calciner with the fuel type (less than 3 % for all cases), which further supports the assumption. A special discussion on chloride-assisted corrosion is included in Section 3.1, since many waste-derived fuels have high chlorine content.

The main assumptions for the design of the steam cycles are presented in Table 3. To increase the steam cycle efficiency, regenerative feed-water preheating from turbine extractions was considered (Böckh, 2018). Menny (2006) recommended 6 to 10 extractions for commercial facilities. In this work, 6 extractions were assumed considering the relatively low power output of the process, except for the fully integrated scenario (II), for which 5 extractions were considered, due to the lower power output (< 10 MW_{el}). The isentropic efficiency of the turbines was specified using data from Consonni and Viganò (2012), together with preliminary estimations of heat recovery. The configuration of the heat exchangers is presented in Table 3, in the sequence order viewed from the process side. The numbering of the heat exchangers corresponds to the sequence viewed form the steam side. For parallel heat exchangers, the same numbering is used.

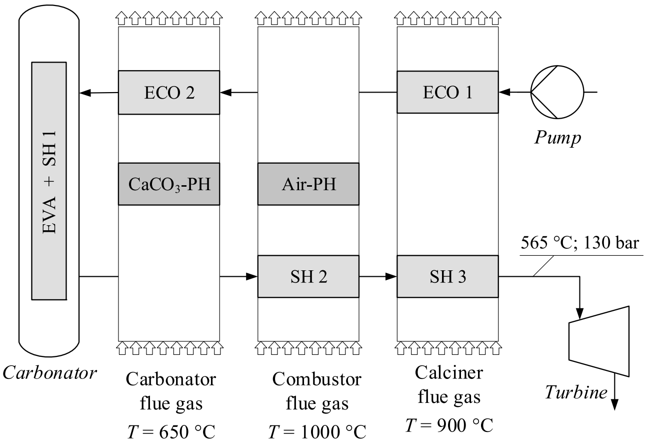

Fig. 6. Flow diagram of one steam cycle to recover heat from the IHCaL-facility, corresponding to the fully integrated (III) scenario. In this configuration, heat is recovered from the carbonator cooling system in the evaporator (EVA) and superheater (SH1), from the CO_2-depleted flue gas exiting the carbonator in the economizer (ECO2), from the combustor flue gas in the superheater (SH2), and from the high purity CO_2 stream leaving the calciner in the superheater (SH3) and the economizer (ECO1). The fresh limestone ($CaCO_3$-PH) and the combustion air (Air-PH) are preheated with the flue gases from the carbonator and the combustor, respectively.

A flow diagram of one steam cycle is included in Fig. 6 for illustration purposes. It corresponds to the fully integrated heat recovery configuration with upstream combustion air preheating (recovery concept III). Heat is recovered from the carbonator cooling system in the evaporator (EVA) and superheater (SH1), from the CO_2-depleted flue gas exiting the carbonator in the economizer (ECO2), from the combustor flue gas in the superheater (SH2), and from the high purity CO_2 stream leaving the calciner in the superheater (SH3) and the economizer (ECO1).The fresh limestone ($CaCO_3$-PH) and the combustion air (Air-PH) are preheated with the flue gases from the carbonator and the combustor, respectively. The feed-water preheating is not included in the illustration for simplicity.

2.3. Process modeling

For the calculation of heat and mass balances, and the main thermodynamic key performance indicators (KPIs), process simulation software was utilized. The lime plant and IHCaL facilities were calculated with the software Aspen Plus® (Aspen Technology, Inc., 2020). The steam cycle was simulated and optimized with the aid of EBSILON®*Professional* software (Steag Energy Services GmbH, 2022). The input data for the steam cycle model was taken from the Aspen Plus® simulations.

The Aspen Plus® simulations were performed using available material property data (ASPEN APV120 database) and property methods (Aspen Technology, Inc., 2001). The Redlich–Kwong–Soave model was used to estimate the properties of the gases (Cormos et al., 2021; Ghanbari et al., 2017; Tilak and El-Halwagi, 2018). The properties of the solids —heat capacity, enthalpy, entropy, and energy— were calculated with the Barin equations (Aspen Technology, Inc., 2001; Barin, 1995).

For the modeling of the IHCaL loop, the same approach as in the work of Greco-Coppi et al. (2023) was used. The make-up input and the purge were located at the calciner input and the calciner output, respectively. The composition of the limestone used for all the processes was assumed to be equivalent to the composition of the raw material of the lime plant, displayed in Table 4.

To achieve fluidization, CO_2 is recirculated from the calciner exit back into the inlet. The amount of fluidizing agent required ($F_{CO2,rec}$) was calculated with the assumptions presented by Greco-Coppi et al. (2023). Since $F_{CO2,rec}$ both depends on and influences the calciner heat requirement, these two quantities were calculated by solving the whole mass and energy balances iteratively until the relative variation of $F_{CO2,rec}$ was less than 10 %.

Table 4
Composition of the limestone from the host lime plant, used as raw material and as make-up for the IHCaL process. Adopted from Greco-Coppi et al. (2021).

Component	Mass fraction (wt.%)
$CaCO_3$	98.3
$MgCO_3$	0.7
SiO_2	0.7
Fe_2O_3	0.1
Al_2O_3	0.2
SO_3	< 0.1

Table 5
Main assumptions and general input parameters for the calculation of power requirements with values form Greco-Coppi et al. (2023).

	Value	Unit
CO_2 compression		
Number of stages[a]	5	–
Temperature after intercooler	25	°C
Pressure drop intercooler	100	mbar
Polytropic efficiency	80	%
Mechanical efficiency	95	%
Discharge conditions		
Temperature	25	°C
Pressure	110	bar_a
Inlet conditions		
Temperature	25	°C
Pressure	1.013	bar_a
Blowers of the IHCaL facility		
Mechanical efficiency	90	%
Isentropic efficiency	65	%
Δp_{carb}	100	mbar
Δp_{calc}	130	mbar
Δp_{comb}	150	mbar
$u_{0,calc}$	0.25	m/s
$T_{FA,carb}$	250	°C
$T_{FA,calc}$	450	°C

[a] Equal pressure ratio.

For the calcination of $CaCO_3$, a conversion of 99 % in the calciner was assumed. The deactivation of the sorbent was calculated considering the carbonator and the calciner as perfectly stirred reactors, with a model described elsewhere (Abanades et al., 2005; Abanades, 2002). The active fraction of CaO entering the carbonator ($X_{ave,max}$) was obtained with Eq. (3).

$$X_{ave,max} = \frac{f_m(1 - f_w)F_0}{F_0 + F_R(1 - f_m)} + f_w \tag{3}$$

Here, the values of the fitting constants reported by Abanades and Alvarez (2003) for natural limestone were adopted: $f_m = 0.77$ and $f_w = 0.17$. This model was programmed into a FORTRAN routine in the Aspen Plus® process model. For the computation of the CO_2 absorption, the hydrodynamics of the carbonator were simulated with models from Kunii and Levenspiel (1991) and the reaction kinetics were modeled following Abanades et al. (2004). The solid circulation (Φ) was varied until a capture efficiency (E_{cc}) of 90 % was achieved with less than 0.05 % absolute error. A detailed description of the carbonator reactor model can be found in the work of Lasheras et al. (2011). The main model assumptions were adopted from Greco-Coppi et al. (2023).

The main assumptions affecting the power requirements in the IHCaL process are displayed in Table 5. The power requirement calculations were performed with the Aspen Plus® models. The CO_2 compression represents the highest power input. The electric power consumption for circulation of the flue gases and propelling of the fluidization agents was also taken into account.

Table 6
Energy scenarios (SC) for the *SPECCA* calculations, based on data from Anantharaman et al. (2018).

Energy scenario (ES)	$\eta_{ref,el}$ (%)	$e_{ref,el}$ (kg_{CO2}/MWh)	ES no.
EU-28[a] energy mix (2015)	45.9	262	ES-1
Coal, state-of-the-art	44.2	770	ES-2
Coal, sub-critical	35.0	973	ES-3
NGCC[b]	52.5	385	ES-4
Renewables	100.0	0	ES-5
Nuclear	33.0	0	ES-6

[a] EU-28: European Union.

[b] NGCC: Natural gas combined cycle.

2.4. Process key performance indicators

The process key performance indicators (KPIs) were defined based on the work of Anantharaman et al. (2018).The capture efficiency (E_{CC}) is defined as the ratio of captured CO_2 to the total CO_2 generated, including the kiln —for the tail-end configurations—, and the IHCaL combustor and calciner. It was calculated with Eq. (4), considering the molar flow rate of CO_2 leaving the carbonator (not captured) and the molar flow rate of CO_2 leaving the calciner (captured). Herby, it was assumed that no CO_2 slip occurs.

$$E_{CC} \equiv \frac{\{Captured\ CO_2\}}{\{Generated\ CO_2\}} = \left(1+\frac{F_{CO2}^{carb}}{F_{CO2}^{calc}}\right)^{-1} \tag{4}$$

It is useful to define normalized values of the heat and the production to evaluate the performance of the capture facility. The absolute heat ratio (HR_a) is the quotient of the total heat input in the new concept,$\dot{Q}_{in}$, and the heat requirement of the reference facility, $\dot{Q}_{in}^{ref}$. The (specific) heat ratio (HR) is the ratio of specific heat requirement per ton of produced lime. The product ratio is the ratio of product mass flow in the new concepts to the production of the reference facility. These quantities are defined mathematically in Eq. (5), where $\dot{m}_{CaO}$ is the mass flow of product flow rate.

$$HR_a \equiv \frac{\dot{Q}_{in}}{\dot{Q}_{in}^{ref}};\ HR \equiv \frac{\dot{Q}_{in}/\dot{m}_{CaO}}{\dot{Q}_{in}^{ref}/\dot{m}_{CaO}^{ref}};\ PR \equiv \frac{\dot{m}_{CaO}}{\dot{m}_{CaO}^{ref}} \tag{5}$$

For the calculation of HR and HR_a, it was assumed that the purge from the IHCaL process can be sold as product. There is evidence in the literature that supports this assumption. Dean et al. (2013), Telesca et al. (2014), Telesca et al. (2015), and Hills (2016) studied the utilization of carbonate looping purged sorbent in the cement industry. Their results suggest that this kind of integration would be possible. Furthermore, the results from the sorbent analysis of the IHCaL pilot plant operation at the technical university of Darmstadt (Hofmann et al., 2022b; Ströhle et al., 2021) show that purge samples have similar properties to commercial lime, especially in terms of reactivity. These results will be reported and discussed in a later publication.

To evaluate the heat recovery with the steam cycle, a new KPI is defined, namely the heat-to-power ratio (*HtPR*). The *HtPR* is the quotient of the net generated power in the steam cycle to the heat input in the IHCaL combustor, and can be calculated with the following equation:

$$HtPR = \frac{P_{el,SC}}{\dot{m}_{fuel}^{comb} \cdot LHV} \tag{6}$$

Where, $P_{el,SC}$ is the net power of the steam cycle in MW_e —without subtracting the power requirement of the capture facility for the blowers and the compression—, $\dot{m}_{fuel}^{comb}$is the mass flow input of fuel in the combustor, and LHV is the corresponding lower heating value.

To evaluate the heat and energy utilization, the specific primary energy consumption for CO_2 avoided (*SPECCA*) was calculated according to Eq. (7).

$$SPECCA = \frac{q - q^{ref}}{e_{CO2}^{ref} - e_{CO2}} \tag{7}$$

Here, q and e_{CO2} are the specific primary energy consumption and the specific CO_2 emissions, respectively. q is obtained considering the direct primary energy consumption from the fuel input and the indirect primary energy consumption related to the net power requirement (P_{el}), according to Eq. (8).

$$q = \frac{\dot{m}_{fuel} \cdot LHV + P_{el}/\eta_{ref,el}}{\dot{m}_{CaO}} \tag{8}$$

Here, a reference electrical efficiency of the grid ($\eta_{ref,el}$) was assumed. For the computation of the specific emissions, the direct CO_2 emissions from the combustion and calcination were considered, as well as the indirect CO_2 emissions associated with the electric power. The following equation was used to calculate this parameter:

$$e_{CO2} = e_{CO2,d} + \frac{P_{el}}{\dot{m}_{CaO}} \cdot e_{ref,el} \tag{9}$$

$e_{ref,el}$ is the CO_2 emissions factor of the electricity mix considered, and $e_{CO2,d}$ are the direct fossil CO_2 emissions per unit of product. $e_{CO2,d}$ was calculated from the fossil CO_2 generation rate ($\dot{m}_{CO2,foss}$) and the CO_2 capture rate ($\dot{m}_{CO2,capt}$) with Eq. (10).

$$e_{CO2,d} = \frac{\dot{m}_{CO2,foss} - \dot{m}_{CO2,capt}}{\dot{m}_{CaO}} \tag{10}$$

For all the calculations, different energy scenarios were assumed to assess the variability of the results with the efficiency and the reference emissions factor of the energy mix. The corresponding assumptions were adopted from Anantharaman et al. (2018), and are presented in Table 6. Here, EU-28 is the European energy mix calculated for the year 2015, and NGCC means “natural gas combined cycle”.

2.5. Economic model

The economic analysis was performed with the ECLIPSE modeling and simulation software (Ulster University, 1992; Williams and McMullan, 1996). ECLIPSE is a program developed by Ulster University with the aim of seamlessly merging the process modeling and the economic assessment, thus enabling the complete techno-economic assessment (TEA) within a single software suite. It has been widely used in the last years to assess the economic performance of different technologies, including CO_2 capture processes (Dave et al., 2013; Huang et al., 2018; Rolfe et al., 2018b; Rolfe et al., 2018a). A detailed description of the ECLIPSE model and its validation is given in Williams and McMullan (1996), while an overview of ECLIPSE is included herein.

The ECLIPSE program structure is shown in Fig. 7. ECLIPSE requires user input to define and specify the process. This includes the process flow diagram and relevant technical data. Other information is read from the embedded databases. There are three databases used by ECLIPSE: compound, utilities, and cost. They are continuously updated and expanded, taking into account the specific needs of the project studied and incorporating data from industrial partners, the project itself, and the literature.

Once the process flow diagram and technical data is input into ECLIPSE, the mass and energy balance is calculated. ECLIPSE transfers the results along with user input utilities data and database information,

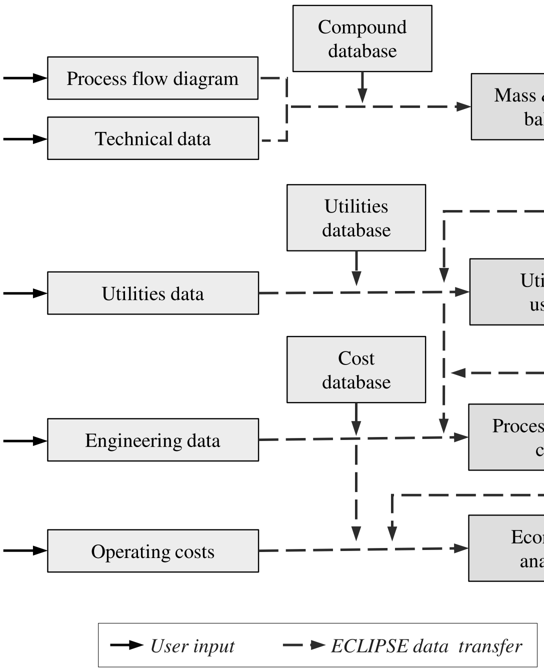
Compound database
Process flow diagram
Technical data
Mass & energy balance
Utilities database
Utilities data
Utilities usage
Cost database
Engineering data
Process capital cost
Operating costs
Economic analysis
User input
ECLIPSE data transfer

Fig. 7. ECLIPSE program structure adapted from Williams and McMullan (1996) with permission from John Wiley and Sons.

to determine the utilities usage (electricity, water, etc.,) for the process. The data on utilities usage is then applied in the capital cost estimation, incorporating user input engineering data and information from the cost database. Finally, the economic analysis is completed using the cost database and previously determined capital cost data, as well as operating costs.

The economic analysis consists of estimating the capital and operating costs, as well as giving an indication of the convenience of the investment based on the net present value (NPV) approach (Huang et al., 2013). There are three stages to the economic analysis: (i) determination of the fixed process capital costs, and process utility capital cost; (ii) determination of the operation and maintenance (O&M) costs; and (iii) economic assessment. For this work, the Chemical Engineering Plant Cost Index (CEPCI) was used to normalize the data and the results to the year 2020 (Chemical Engineering, 2023; Mignard, 2014).

The calculation of initial capital costs (initial CAPEX, i.e., I_0) is performed using the two approaches illustrated in Fig. 8. For standard equipment (i.e., market-available equipment), manufacturers' quotes, published prices in literature, and historical project data are used (see Fig. 8, right branch). If the capital cost of similar components but with a different size or capacity is known, the capital cost is scaled up or down using the correlation given in Eq. (11) (Gogulancea et al., 2023).

$$Cost = Cost_{ref}\left(\frac{Size}{Size_{ref}}\right)^{Factor} \tag{11}$$

Where $Cost_{ref}$ is the reference cost of equipment of capacity $Size_{ref}$, and $Cost$ is the approximate cost of equipment with a corresponding capacity $Size$. $Factor$ is the value of the scaling exponent, which ranges from 0.6 to 0.8 for most components (Gogulancea et al., 2023).

For non-standard equipment, a bottom-up cost approach based on the mass and energy balances within the ECLIPSE simulation is adopted. This approach is illustrated in the left branch of Fig. 8. It involves the dimensioning of the components with the results from the mass and energy balance; the estimation of the raw material, fabrication, and miscellaneous costs; and the addition of the assembly and testing costs.

After the estimation of the equipment costs, each individual cost is expanded by an allowance for installation and integration, such as piping, valves, instrumentation, and civil work (see last two blocks in Fig. 8), thus obtaining the final component costs. The absolute accuracy for an individual unit, for this type of capital cost estimation procedure, is estimated at about ± 25–30 %. Since the concepts assessed consist of similar types of equipment, the analysis maintains a consistent basis, ensuring comparability of results (cf. Wang et al., 2006).

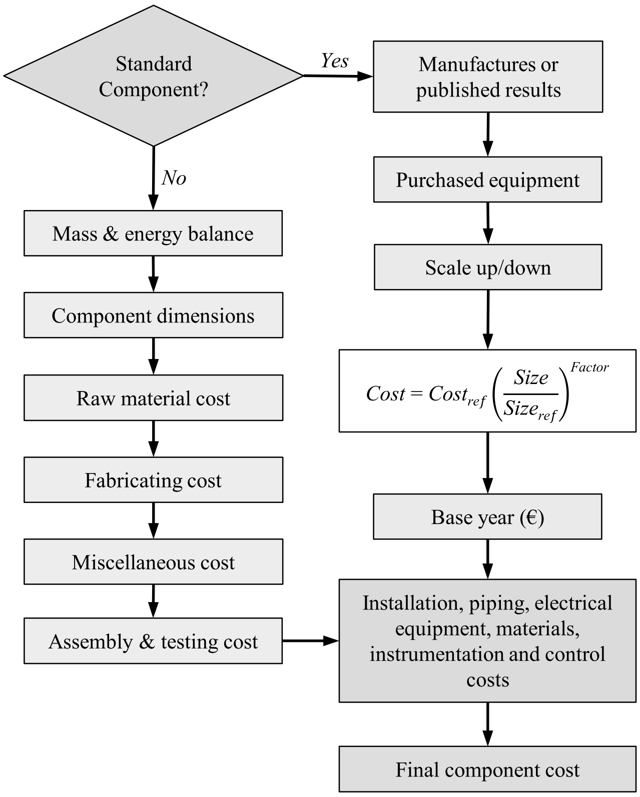
Standard Component?
Yes
No
Manufactures or published results
Purchased equipment
Scale up/down
Cost = Cost_ref (Size / Size_ref)^Factor
Base year (€)
Mass & energy balance
Component dimensions
Raw material cost
Fabricating cost
Miscellaneous cost
Assembly & testing cost
Installation, piping, electrical equipment, materials, instrumentation and control costs
Final component cost

Fig. 8. Methodology for capital cost estimation of standard and non-standard components.

Operation and maintenance (O&M) costs include (i) annual capital expenditure (CAPEX) for spares, maintenance, and plant replacement; (ii) fixed operating expenditure (OPEX) for labour, overhead, and insurance; and (iii) variable OPEX for consumables, such as fuel and limestone. These costs are based on the mass and energy balances produced within the ECLIPSE software, and the stream costs specified by the user (Williams and McMullan, 1996). While technically the electricity export is a variable OPEX, it is reported as a separate element for clarification purposes. An annual miscellaneous cost category is also included for the remaining expenses, i.e., facility supplies, building extension, power transformer upgrading, chemicals, and other regular operating costs.

The final step consists in the economic assessment, considering the overall process investment (I_0), together with the individual input streams, and the O&M costs. With all the costing results, the annual cash flow and the breakeven selling price (*BESP*) of lime (product) were calculated (see Section 2.6). Additionally, a sensitivity analysis was performed to disclose the effect of dominant parameters, such as energy cost, feedstock price, plant capacity factor, and fixed OPEX.

The main economic assumptions and relevant conditions for this work are shown in Table 7. The minimum and maximum columns were used as boundaries for the sensitivity analysis. The engineering, procurement, and construction (EPC) costs were attained via summation of the fixed process capital costs, the process utility capital costs, and the balance of plant costs. Unfortunately, due to commercial sensitivities, these values cannot be published. The initial capital expenditure (I_0) was determined by considering the owner's costs, which include work-

Table 7
Boundary conditions for the economic assessment.

Category	Parameter	Min.	Baseline	Max.	Unit
Economic parameters	Contingency	10	15	20	% of EPC
	Discount rate (r)	4	6	8	%
	Plant life	20	25	30	years
	Construction time		2		years
	Interest rate during construction period		3		%
	Plant operating hours		8000		hours
	Payment schedule				
	Year 1		40		%
	Year 2		60		%
Initial CAPEX (I_0)	EPC	Undisclosed due to commercial sensitivities			
	Fixed process CAPEX				
	Process utility CAPEX				
	Balance of plant				
	Owner's costs				
	Working capital		2		% of EPC
	Capital fees		1		% of EPC
	Commissioning costs		1		% of EPC
Annual CAPEX	Annual maintenance costs inc. labour & supplies		3.5		% of I_0
OPEX	Fixed OPEX				
	Annual insurance costs		1.5		% of I_0
	Annual operating costs inc. labour & supplies		3		% of I_0
	Variable OPEX				
	Lignite	0.96	1.2	1.44	€/GJ
	SRF	−48	−40	−32	€/t
	Limestone		4		€/t
	Electricity import[a]		120		€/MWh
	Electricity export		60		€/MWh

[a] Eurostat (2022).

ing capital, capital fees, and commissioning costs, as well as the EPC. The owners' costs were determined as a percentage of the EPC[1].

2.6. Economic key performance indicators

For the economic analysis, the key performance indicators are the break-even selling price (*BESP*) and the CO_2 avoidance cost (*CAC*). Due to commercial sensitivity, the return on investment (ROI) is not disclosed in this work.

The *BESP* is the price that the lime must sell for to cover all associated lifetime costs, i.e., the lime price that makes NPV = 0 at the end of the plant life. The *BESP* for each plant configuration and fuel type was calculated and compared to the reference plant. If the *BESP* is too high, then the plant may not be economically competitive, as the selling price required to recover costs and return a reasonable profit on the investment may be too great in comparison to the average market selling price. The *BESP* can be calculated using Eq. (12):

$$BESP = \frac{\sum_{t=1}^{n} \frac{I_t + M_t + F_t}{(1+r)^t} + I_0}{\sum_{t=1}^{n} \frac{L_t}{(1+r)^t}} \tag{12}$$

Where I_t is the investment expenditure in year t (annual CAPEX), M_t is the O&M expenditure in year t, F_t is the fuel expenditure in year *t*, L_t is the quantity of lime produced in year *t*, r is the discount rate, I_0 is the initial investment (CAPEX), and n is the system life.

For the impact of CO_2 capture on the plant economics, the CO_2 avoidance costs (*CAC*), Eq. (13), were calculated. The *CAC* is based on the reduction of CO_2 emissions per unit of the net product produced (Roussanaly, 2019; Simbeck and Beecy, 2011).

$$CAC = \frac{BESP_{capture} - BESP_{ref}}{CO_{2,emissions,ref} - CO_{2,emissions,capture}} \tag{13}$$

In general, the emissions were computed regardless of their biogenic or fossil origin throughout this work. Nevertheless, for the *CAC*, the economic benefit of CDR was also calculated by treating the captured biogenic CO_2 emissions as negative in Eq. (13) for the scenarios with SRF (see Fig. 15). Costs for CO_2 transport and storage were excluded from the calculations.

3. Results and discussion

In this chapter, the results are discussed in two separate sections. The first section corresponds to the results of the process model, including the steam cycle, and the second section reports the results of the economic analysis.

3.1. Process analysis

Three different heat recovery concepts for the high temperature (1000 °C) combustor flue gases were analyzed (see Fig. 5). These concepts consisted in recovering heat only through combustion air preheating (I), recovering heat with a steam cycle before air preheating (II), and recovering heat into the steam cycle after air preheating (III). The optimal configuration of the corresponding steam cycles includes feedwater preheating, and superheating of steam up to 565 °C and 130 bar. Apart from the heat recovery from the combustor flue gases, heat is recovered from the carbonator cooling system, the carbonator flue gases, and the calciner flue gases. Recovering heat from the combustor flue gases is detrimental to the thermodynamics of the entire process, but it may be used to decrease the operating temperature of some components (e.g.,

---

[1] This is a similar methodology to the one presented by Roussanaly et al. (2017). They use a slightly different nomenclature and grouping of the subtotals. In their work, the total plant costs (TPC) are determined by multiplying the EPC by a factor, and the EPC are calculated by multiplying the total direct costs (TDC) by another factor.

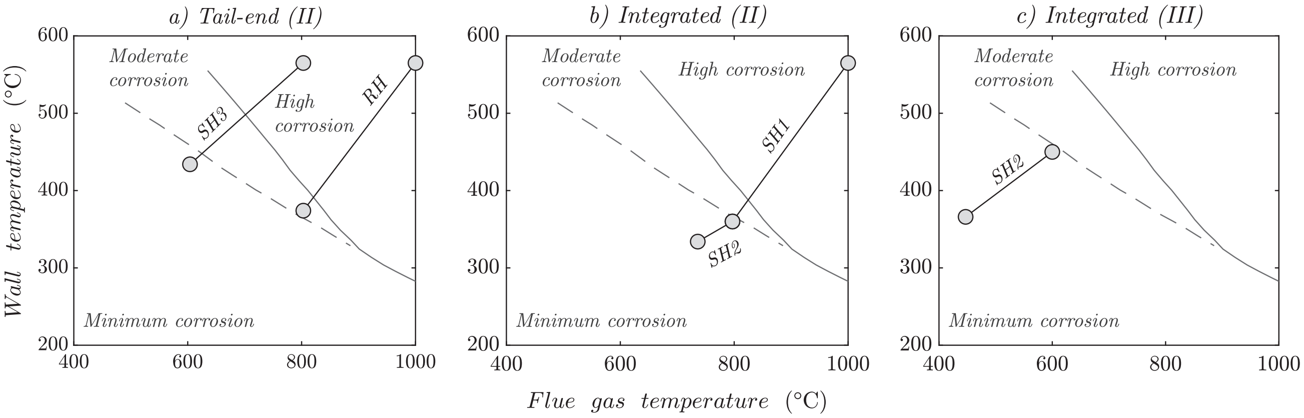

Fig. 9. Flingern diagram for the heat recovery from combustor flue gases when firing waste-derived fuels. The corrosion limits were adopted from Warnecke (2004).

filters and blowers), and thus reduce costs. From the heat input into the IHCaL process, up to ca. 80 % can be recovered in a steam cycle to produce electricity with a net electric efficiency of 41–42 %. This value is lower than values reported in the literature for power plants, due to the smaller size of the steam cycle and the capture facility. For example, Hawthorne et al. (2009) reported a net power efficiency of 45.3 % for the steam cycle associated with a 1599 MW_{th} CaL unit.

If waste-derived fuels are used in the combustor, chlorine-aided corrosion may be an issue for the system. One way to evaluate this is with the aid of the Flingern diagram (Haider et al., 2008), which takes its name from the incineration facility in Düsseldorf–Flingern. In this facility, the influence of the flue gas temperature and the superheater temperature in the corrosion was quantified during the 1970s (Haider et al., 2008). The diagram that resulted from the empirical investigations establishes limits for three operating regimes, categorized according to the probability of corrosion —namely, minimum corrosion, moderate corrosion, and high corrosion.

The analysis of the corrosion limits with the Flinger diagram is illustrated in Fig. 9 for the concepts in which combustor flue gases are cooled down by superheating or reheating steam. In the integrated concept (III), the superheater (SH2) operates below the corrosion limit because the flue gases from the combustor are cooled down by the air preheater before recovering heat through the steam cycle. Hence, the integrated concept (III) is suitable for operation with waste-derived fuels, such as SRFs, from the point of view of the low corrosion risk.

The tail-end concept (II) and the integrated concept (II) have heat exchangers operating in the high corrosion regimes. The reasons for this are the high temperature of the combustor gases at the point of heat recovery, and the configuration of the steam cycle. Corrosion problems are to be expected with these arrangements if the combustor is fueled with waste-derived fuels.

To mitigate corrosion issues, different strategies may be adopted. One option would be to use the combustor flue gases to exchange heat with an evaporator instead of (or before) a preheater or superheater. This would lower the wall temperature of the heat exchanger, displacing the operation regime toward a less problematic regime in terms of corrosion. Another strategy, which was not computed in this work but may be useful in some applications, would be to cool down the flue gases by preheating the sorbent make-up streams, thus reducing the temperature of the flue gas, while recovering heat for the capture process. Reducing the temperature of the live steam may also reduce corrosion problems, but would impact the efficiency of the steam cycle negatively. Finally, a combination of the strategies proposed could give an optimal solution in terms of achieving a compromise between minimizing the corrosion issues and maximizing the power output of the steam cycle.

Notwithstanding the foregoing, it is worth pointing out that the corrosion issues in the IHCaL process may also arise inside the combustor, where the metallic heat pipes lay for the heat transfer to the calciner. Considering the high temperature of operation (ca. 1000 °C), high concentrations of chlorine should be avoided to protect metallic components (mainly the heat pipes). Chlorine flue gas concentrations higher than 600 ppm (Qu et al., 2020) should be avoided for the combustor, which limits the selection of waste-derived fuels in terms of chlorine content.

The main results from the process modeling are shown in Table 8. In the tail-end solution, the use of SRF instead of lignite reduces the energy consumption for the configuration (I). This is due to the lower CO_2 emission factor of this fuel. For the configuration (II), the trend is reversed. This is because, in this configuration, less preheating of the combustion air is possible. Preheating is more critical for SRF, because of the higher air input requirement. This effect prevails over the reduction in heat requirement due to the lowest $e_{CO2,fuel}$.

For the integrated arrangement, the heat requirement is almost independent of the fuel type for the configurations (I) and (II). For the configuration (III), the solution with SRF is associated with a 3 % reduction in the heat requirement compared with the lignite-fired concept. This is because of the relatively high amount of flue gases from the combustion of SRF compared to lignite, which allows heating up the combustion air up to higher temperatures. The ratios of flue gas to air are 112 % and 115 % for lignite and SRF, respectively. Overall, outside of these small differences, the variation of the heating requirement with the fuel type are negligible for all the cases considered. This is mainly because the main parameters of the fuels, *LHV* and $e_{CO2,fuel}$, mutually compensate for their effects —higher *LHV* (as in lignite) and lower $e_{CO2,fuel}$ (as in SRF) reduce the heat requirements.

The circulation rate and the make-up rate have an important influence on the heat requirement of the process. For the tail-end solution, the make-up is given as an input, namely $\Lambda = 0.10$. In this configuration, higher circulation rates are required with SRF because less CO_2 from make-up is being calcined in the calciner; thus, higher capture rates in the carbonator are necessary to achieve the same overall capture efficiency. For the fully integrated concepts, the trend is reversed as the SRF generates less CO_2 and, since the mass flow rate of make-up is fixed, there is higher sorbent activity, which means that less circulation of sorbent is required.

The heat-to-power ratio (*HtPR*) is higher for the tail-end concepts (31–35 %) because more heat is required for the capture than in the integrated solutions. This heat can be recovered in a steam cycle. For the integrated configuration, less power is generated (*HtPR* between 16 and 25 %) because the heat is more efficiently used for the regeneration of the sorbent.

The formation of CO_2 is illustrated in Fig. 10. Here, only the generation of CO_2 is considered, i.e., the capture is not displayed. The CO_2 formation is classified in four categories: (i) kiln, for the process and fuel emissions from the PRK; (ii) make-up, for the CO_2 formed from the calcination of limestone in the capture facility; (iii) fuel (fossil), for the fossil

Table 8
Main results of the process modeling.

IHCaL integration	Tail-end				Fully integrated					
Fuel IHCaL combustor	Lignite		SRF		Lignite			SRF		
Heat recovery concept	I	II	I	II	I	II	III	I	II	III
E_{cc}	90 %	90 %	90 %	90 %	90 %	90 %	90 %	90 %	90 %	90 %
$Q_{in,comb}$ (MW_{th})	121	174	119	178	46	62	59	46	62	57
Φ	5.40	5.37	5.55	5.60	1.36	1.68	1.64	1.30	1.60	1.52
Λ	0.10	0.10	0.10	0.10	1.20	0.89	0.93	1.30	0.96	1.05
$\eta_{net,SC}$	42.4 %	43.4 %	42.4 %	43.4 %	41.2 %	41.3 %	42.4 %	41.2 %	41.3 %	42.4 %
HR_a	4.17	5.56	4.12	5.67	1.20	1.62	1.55	1.21	1.63	1.50
HR	3.03	3.79	3.03	3.89	1.20	1.63	1.55	1.21	1.63	1.50
PR	1.38	1.47	1.36	1.46	1.00	1.00	1.00	1.00	1.00	1.00
$HtPR$	32.9 %	38.8 %	32.9 %	38.8 %	16.8 %	17.0 %	24.8 %	16.8 %	17.0 %	24.8 %
$Q_{in,SC}$ (MW_{th})	94.0	155.7	92.7	159.5	18.7	25.5	34.6	18.8	25.7	33.5
P_{gross} (MW_e)	40.8	68.9	40.2	70.6	7.9	10.8	15.0	7.9	10.9	14.5
P_{net} (MW_e)	39.8	67.6	39.3	69.2	7.7	10.5	14.7	7.7	10.6	14.2
η_{net}	42.4 %	43.4 %	42.4 %[a]	43.4 %[a]	41.2 %	41.3 %	42.4 %	41.2 %[a]	41.3 %[a]	42.4 %[a]

[a] Assumption.

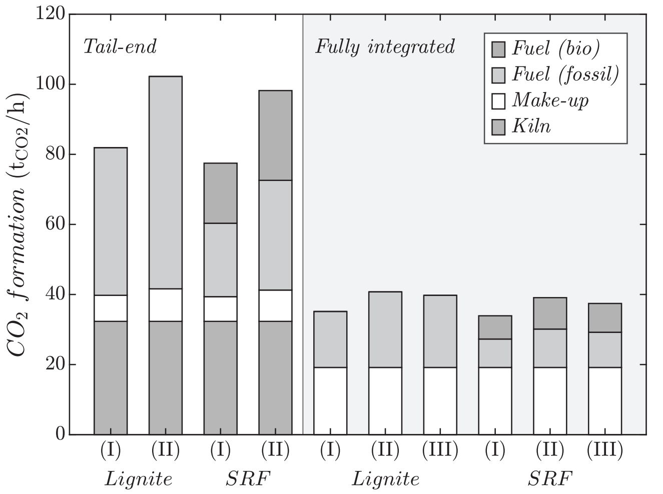

Fig. 10. CO_2 formation breakdown for all the scenarios with CO_2 capture considered in the process model

CO_2 produced in the IHCaL combustor; and (iv) fuel (bio), for the biogenic CO_2 formed by the combustion of fuel in the IHCaL plant. For the tail-end configurations, the additional CO_2 associated with the capture is higher than the original CO_2 formation. This is particularly critical for the lignite-fueled cases, where all the formation is fossil CO_2. When utilizing SRF in the IHCaL combustor, the increase of fossil CO_2 formation is less than the original CO_2 from the rotary kiln. For the fully integrated configurations, the total formation is almost equal to the emissions from the rotary kiln for all the cases, meaning that the capture facility does not significantly increase the CO_2 formation.

The specific flow of energy for the different concepts is shown in Fig. 11, broken-down according to the destination of the energy. Here, the categories are (i) calcination, for the energy used in the reaction to form CaO, (ii) power generation, for the net energy recovered in the steam cycle, and losses from the (iii) steam cycle and the (iv) capture process. The majority of the steam cycle losses are associated with the heat leaving the system through the condenser —due to thermodynamic limitations (law of entropy). For all the capture scenarios, there is an increase in the direct specific heat requirements due to the losses in the IHCaL process. The steam cycle configurations (I) are optimal from the point of view of reducing the fuel requirements but have less capacity to generate power. The integrated configurations have fewer specific requirements because of the efficient indirectly heated calcination in the calciner and the low amount of circulating sorbent.

The results of the *SPECCA* calculations for all the process configurations with carbon capture are displayed in Fig. 12. Here, the energy

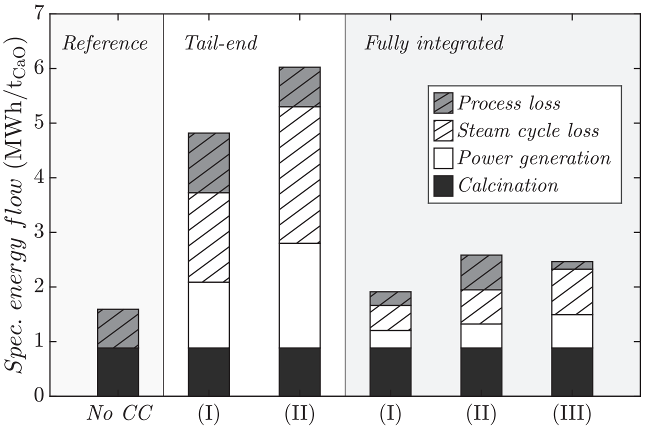

Fig. 11. Specific energy flow for the reference lime plant without CO_2 capture (no CC), and for the scenarios with CO_2 capture considered in the process modeling.

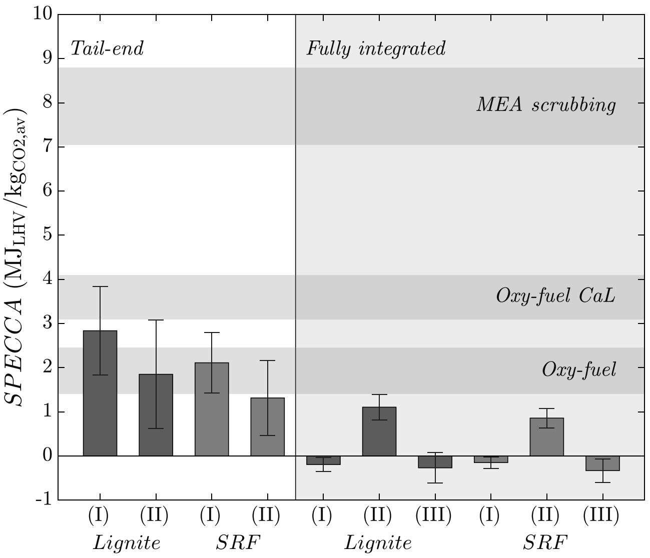

Fig. 12. *SPECCA* results using energy scenarios ES-1 to ES-4. The bars show the mean values, and the error bands show the variation of plus-minus one standard deviation. Data for blue bands was obtained from Voldsund et al. (2019) for the same energy scenarios.

Table 9
SPECCA in $MJ_{LHV}/t_{CO2,av}$, for the process scenarios with CO_2 capture (S-2 to S-11), computed for different energy scenarios (ES).

IHCaL integration	Tail-end				Fully integrated					
Fuel IHCaL combustor	Lignite		SRF		Lignite			SRF		
Heat recovery concept	I	II	I	II	I	II	III	I	II	III
ES-1	3.57	2.63	2.56	1.79	−0.15	1.26	−0.18	−0.11	0.97	−0.27
ES-2	2.53	1.50	1.95	1.15	−0.18	1.08	−0.24	−0.14	0.85	−0.30
ES-3	1.34	0.02	1.06	0.01	−0.44	0.65	−0.81	−0.36	0.51	−0.75
ES-4	3.91	3.25	2.86	2.30	−0.01	1.43	0.14	0.00	1.10	−0.01
ES-5	7.70	9.86	5.19	6.00	0.46	2.27	1.36	0.39	1.73	0.88
ES-6	1.87	−0.86	1.28	−0.53	−0.60	0.65	−1.32	−0.47	0.49	−1.12
Mean	3.49	2.73	2.49	1.79	−0.15	1.22	−0.17	−0.12	0.94	−0.26
Standard deviation	2.09	3.48	1.37	2.12	0.33	0.55	0.84	0.28	0.42	0.62

scenarios ES-1 and ES-4 were used for the calculations[2]. The height of the bars indicate the mean *SPECCA* values, while the error bands corresponds to plus-minus one standard deviation of the corresponding results. The detailed results are included in Table 9.

The calculated values are relatively low, compared to other technologies (Voldsund et al., 2019). The reason for this is the efficient energy utilization enabled by the high temperatures and the net power production. The values for the fully integrated scenarios are particularly low due to the better heat utilization associated with the indirect calcination of limestone. Among the integrated configurations, the recovery strategies (I) and (III) performed better than (II). This is mainly due to the harnessing of the process heat, which was less effective for approach (II), as can be seen in the process losses illustrated in Fig. 11.

The *SPECCA* results depend on the value assigned to the generated power; thus, since there is considerable power generation in all process configurations, there is high variability with the scenarios. Especially if the renewable (ES-5) and the nuclear (ES-6) energy scenarios are taken into account (see Table 9), extreme results are obtained, corresponding with the extreme values of the reference efficiency, $\eta_{ref,el}$. Overall, the results indicate that IHCaL technology is more attractive in energy scenarios with low renewable share and high CO_2 emissions associated with power generation. Depending on the local energy mix —considering also the expected variation during the lifetime of the capture project— a facility may be optimized for either power production (e.g., II), or reduced fuel requirement (e.g., I).

One of the main conclusions of this analysis is that the strategy for utilizing heat from the combustor flue gases is a key aspect for the integration. This is because of the high temperatures (≈1000 °C) and the high amount of sensible heat associated. One of the strategies for integration (I) consists in recovering energy only through preheating of the combustor air. This increases the thermal efficiency of the IHCaL process but requires a gas-gas heat exchanger operating at high temperatures —up to 1000 °C on the hot side, and up to 800 °C on the cold side. Another possibility is to utilize this heat in a steam cycle (e.g., III). This may be a straightforward solution if lignite is fueled, but the design of the corresponding steam cycle would have to address chlorine-aided corrosion if waste-derived fuels are used. Preheating the make-up with combustor flue gases may be advantageous, especially for the fully integrated solutions that have high make-up rates. In this case, the system should be designed to avoid calcination before the entrance into the calciner. This last option was not investigated in this work.

3.2. Techno-economic analysis

The boundary conditions for the cost calculation are shown in Table 7. The year 2020 was taken as the reference for the price indexing. Table 10 shows the change in initial CAPEX (I_0) estimated for each of the plant configurations and fuels studied, compared to the reference case. The tail-end cases tend to have larger I_0 than the fully integrated cases. This is due to the tail-end cases having greater solid circulation, as seen in Table 8, requiring larger plant sizes than the integrated cases.

Table 10
Percentage change in capital cost estimation compared to the reference case, for the scenarios with CO_2 capture (S-2 to S-11).

IHCaL integration	Fuel IHCaL combustor	Heat recovery concept	Initial CAPEX increase against the reference case (%)
Tail-end	Lignite	I	367
		II	399
	SRF	I	367
		II	399
Fully integrated	Lignite	I	105
		II	112
		III	112
	SRF	I	105
		II	112
		III	118

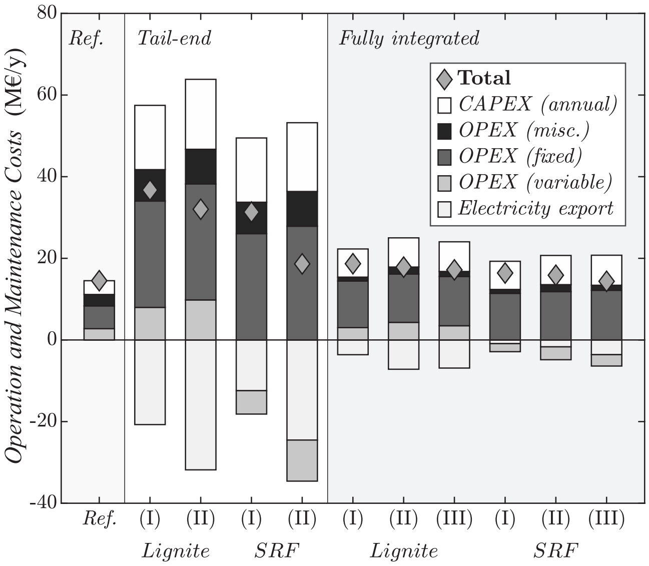

Fig. 13. Annual operation and maintenance costs, for all the scenarios (S-1 to S-11).

The breakdown of the annual operation and maintenance (O&M) costs are given in Fig. 13. These include the annual costs for fuel and raw material costs, electricity revenue, end of pipe clean-up and waste disposal, as well as insurance, maintenance, and labor costs. The O&M

---

[2] ES-5 and ES-6 were excluded from Fig. 12 as they represent extreme cases rather than realistic energy mixes. The results from ES-1 to ES-4 are more representative of the process performance. For completeness, the full dataset is provided in Table 9.

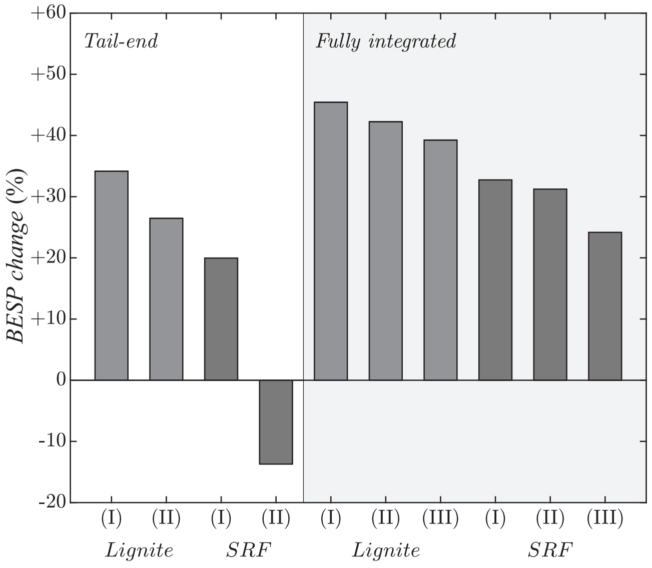

Fig. 14. Lime plant *BESP* change compared to the reference case without carbon capture, for the scenarios with CO_2 capture (S-2 to S-11).

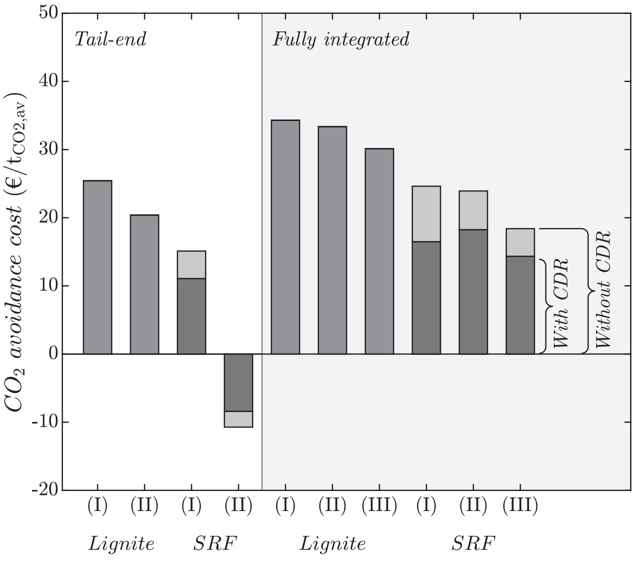

Fig. 15. CO_2 avoidance cost (*CAC*) for the scenarios with CO_2 capture (S-2 to S-11).

costs for the integrated plants, for both fuel selections, are lower than for the tail-end plants. This is due to lower OPEX and CAPEX costs compared to the tail-end cases. The lignite integrated plants also have lower fuel costs in line with the fuel requirements as per Table 8. For the lignite capture plants, the O&M costs are offset by revenue from electricity export. When lignite is replaced by the SRF, the O&M costs are offset by revenue from the electricity export and from SRF revenue —this is discussed in more detail in Section 3.2.2.

Using the I_0 estimates, O&M costs, and the economic assumptions described in Table 7, the *BESP* for the lime product were calculated using the discounted cash flowrate analysis. The corresponding results are presented in Fig. 14. Due to commercial considerations, the absolute value of the reference plant *BESP* has not been disclosed, and therefore, the *BESP* for the capture plants are presented in percentage change from the reference plant.

The techno-economic evaluation shows that for the lignite fueled plants, the fully integrated lignite (I) case has the highest *BESP*, which is a 45 % increase compared to the base case. Cross-referencing this plant with the process modeling results in Table 8, it is shown that the fully integrated lignite (I) plant has the lowest thermal input of all the plants, and hence the lowest electricity export. Conversely, the lignite plant with the highest thermal input and electricity generation is the tail-end lignite (II) plant, which is also the lignite capture case with the lowest *BESP*, with only a 26 % increase compared to the base case plant.

The same plant configurations have the highest and lowest *BESP* when the fuel is switched to SRF, however, the *BESP* is 33 % and −14 %, respectively, compared to the reference lignite plant. The tail-end SRF (II) plant is the only one with *BESP* value lower than the base case *BESP*. This is highly dependent on two revenue streams, electricity export, and SRF consumption. This plant has a large thermal input, which is fueled via the SRF, and has the greatest amount of heat recovery for electricity production and export, see Table 8.

Another point of note is that from Table 10 and Fig. 13, the capital costs and O&M costs, are higher for the tail-end plants than for the integrated plants, yet the *BESP* is lower for the tail-end plants. As previously stated in Section 2.4, purge material from the tail-end IHCaL process can be sold as product; thus, the tail-end lime plants have increased lime output, and given that the *BESP* is calculated on per ton of product produced bases, the higher capital and O&M costs are absorbed by the higher lime output.

The CO_2 avoidance costs (*CAC*) are shown in Fig. 15. For the lignite plants, the *CAC* ranges from 20.4 to 34.3 €/$t_{CO2,av,}$ with the tail-end (II) case having the lowest values and the fully integrated (I) plant having the highest. Overall, these values are lower than what was reported by Santos and Hanak (2022), and De Lena et al. (2019).

For the SRF plants, the *CAC* range is −10.7 to 24.6 €/$t_{CO2,av}$. The extreme values correspond to the tail-end SRF (I) case and the fully integrated SRF (I) case, respectively, without computing negative emissions from captured biogenic CO_2. Again, electricity export has a large influence on the avoidance costs. Further to this, as already stated, the SRF plants attain additional revenue from utilizing this kind of fuel. As the tail-end SRF (II) plant consumes the largest quantity of SRF, it receives a higher income from this revenue stream, and hence the negative *CAC*.

The influence of CDR is illustrated in Fig. 15. If negative CO_2 emissions are computed for the captured biogenic CO_2, net negative emissions are achieved in all the scenarios using SRF as fuel for the IHCaL. The *CAC* is reduced (excepting negative *CAC*) because of the higher amount of CO_2 avoided. If the economic benefit of CDR is considered, the avoidance costs are lower than 19 EUR/$t_{CO2,av}$ for all the SRF scenarios analyzed.

3.2.1. Sensitivity analysis

The influence of the main economic parameters on the *BESP* of lime produced has been investigated. The tail-end (I) and fully integrated (I) cases, fueled with lignite and SRF have been selected for the sensitivity study. The sensitivity parameters selected for the study include fuel price, project lifetime, discount rate (*r*), and contingency value. The results are shown in Fig. 16 as relative change of *BESP* when the parameters are varied between the minimum and maximum boundaries from Table 7. For all lime plants, the discount rate (*r*) and project life are the main parameters that influence the *BESP*. Fuel price and contingencies have a lower impact on the *BESP*.

For the reference plant, increasing *r* from 6 % to 8 % increases the *BESP* by 8.4 %, while decreasing *r* to 4 % reduces the *BESP* by 6.7 %. Increasing the project life to 30 years from 25 decreases the *BESP* by 2.4 %, while decreasing the project life to 20 years increases the *BESP* by 5.1 %. Increasing the contingency from 15 % to 20 % increases the *BESP* by 2.1 %, and decreasing to 10 %, decreases the *BESP* by 1.1 %. Lastly, increasing the lignite price to 1.44 from 1.2 €/GJ increases the *BESP* by 2 %, while decreasing the lignite price to 0.96 €/GJ decreases the *BESP* by 1 %.

The tail-end lignite (I) configuration is more sensitive to variations than the reference scenario, increasing the *r* from 6 % to 8 % increases the *BESP* by 12.4 %, while decreasing *r* to 4 % reduces the *BESP* by

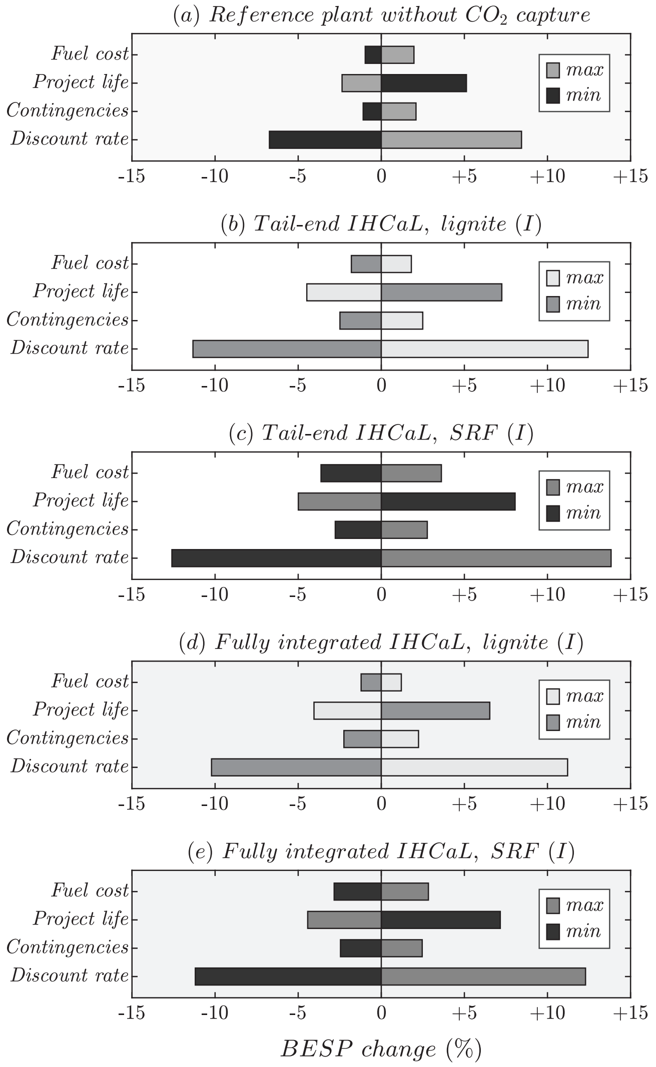

Fig. 16. Results of the economic sensitivity analysis.

11.3 %. Increasing the project life to 30 years from 25, decreases the *BESP* by 4.5 %, while decreasing the project life to 20 years increases the *BESP* by 7.3 %. Increasing the contingency from 15 % to 20 % increases the *BESP* by 2.5 %, and decreasing to 10 %, decreases the *BESP* by 2.5 %. Lastly, increasing the lignite price to 1.44 from 1.2 €/GJ increases the *BESP* by 1.8 %, while decreasing the lignite price to 0.96€/GJ decreases the *BESP* by 1.8 %.

The integrated configuration using lignite as fuel (S-6) is more sensitive to variations than the reference plant but less so than the tail-end plant. Increasing the *r* from 6 % to 8 % increases the *BESP* by 11.2 %, while decreasing *r* to 4 % reduces the *BESP* by 10.2 %. Increasing the project life to 30 years from 25, decreases the *BESP* by 4 %, while decreasing the project life to 20 years increases the *BESP* by 6.5 %. Increasing the contingency from 15 % to 20 % increases the *BESP* by 2.2 %, and decreasing to 10 %, decreases the *BESP* by 2.2 %. Lastly, increasing the lignite price to 1.44 from 1.2 €/GJ increases the *BESP* by 1.2 %, while decreasing the lignite price to 0.96 €/GJ decreases the *BESP* by 1.2 %.

The same trends in key parameters are seen in the plants fueled by SRF. The tail-end SRF (I) case is more sensitive to economic parameters' variations than the reference case and the same plant fueled by lignite. Increasing the *r* from 6 % to 8 % increases the *BESP* by 13.8 %, while decreasing *r* to 4 % reduces the *BESP* by 12.6 %. Increasing the project life to 30 years from 25, decreases the *BESP* by 5 %, while decreasing the project life to 20 years increases the *BESP* by 8.1 %. Increasing the contingency from 15 % to 20 % increases the *BESP* by 2.8 %, and decreasing to 10 %, decreases the *BESP* by 2.8 %. Lastly, increasing the SRF price to 1.44 from 1.2 €/GJ increases the *BESP* by 3.6 %, while decreasing the lignite price to 0.96 €/GJ decreases the *BESP* by 3.6 %.

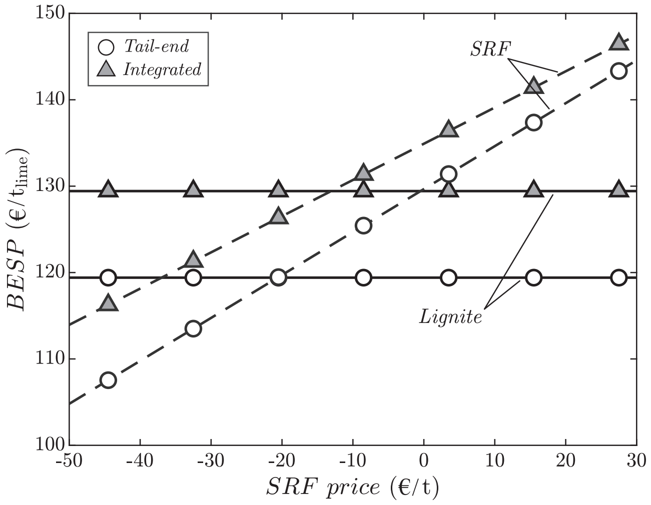

Fig. 17. Extended sensitivity study on the SRF price using heat recovery strategy (I).

The fully integrated SRF (I) case is more sensitive to economic parameters' variations than the reference scenario and the same plant fueled by lignite, but less so than the tail-end SRF (I) plant. Increasing the *r* from 6 % to 8 % increases the *BESP* by 12.3 %, while decreasing *r* to 4 % reduces the *BESP* by 11.2 %. Increasing the project life to 30 years from 25, decreases the *BESP* by 4.4 %, while decreasing the project life to 20 years increases the *BESP* by 7.2 %. Increasing the contingency from 15 % to 20 % increases the *BESP* by 2.5 %, and decreasing to 10 %, decreases the *BESP* by 2.5 %. Lastly, increasing the SRF price to 1.44 from 1.2€/GJ increases the *BESP* by 2.8 %, while decreasing the lignite price to 0.96 €/GJ decreases the *BESP* by 2.8 %.

Overall, the capture cases are more sensitive to variation than the reference case, and the tail-end cases more so than the integrated cases. The SRF fueled cases are more sensitive to variation than their counterpart fueled by lignite. The variation of the discount rate (*r*) has the greatest impact on the *BESP*, and the contingency and fuel price have similar impacts on the *BESP*.

3.2.2. Extended SRF price analysis

SRF has often a negative price; thus, the SRF producer pays the end user to utilize SRF. Normal industrial waste collection procedures require a waste company to collect waste for a fee. The SRF producer collects the waste for a fee lower than the landfill tax —currently in England and Northern Ireland, £102.10 (119.16 €) per tonne (UK Government Digital Service, 2023). The waste is sorted and processed into SRF incurring a processing cost of around 15–20 €/t, this has thus far resulted in negative SRF prices.

Currently, in the Unite Kingdom and Europe, SRF does not attract carbon tax, however, this is due to change in 2028 (Reeves et al., 2023). Furthermore, as demand for SRF increases and supply is limited by production capacity, market forces for supply and demand have the potential to increase the price of SRF.

An extended sensitivity study has been done to consider the impact on the *BESP* for both lime plant IHCaL configurations with heat recovery strategy (I). The results are displayed in Fig. 17. The SRF price ranges between −50 and +30 €/t. The results are benchmarked against the BESP of the lignite-fueled scenarios for the same heat recovery strategy. For the tail-end option, an SRF price of approx. −20 €/t gives an economic equivalence to the lignite-fueled plant. For the fully integrated plant, the lignite equivalence occurs when the SRF price is approx. −12 €/t.

The crossover values would be higher if a profit were associated with CDR for the biogenic CO_2 from the combustion of SRF (cf. Fig. 15).

4. Conclusion

Within this work, ten different integrated concepts of the indirectly heated carbonate looping (IHCaL) process for the lime production were analyzed. A tail-end and a fully integrated configuration were studied in combination with various approaches to recover heat using a steam cycle. Furthermore, the corresponding technical implications of the integration options were discussed. The heat recovery strategy for the combustor flue gases was found to be a key factor to enable the deployment of the IHCaL technology.

For the tail-end solution, recovering heat from combustion flue gases allows for high recovery rate and substantial power production in a steam cycle, but increases the fuel requirement by 44 %. An efficient option to minimize the heat input in the combustor is to utilize the combustion flue gases only for the preheating of the combustion air. For the fully integrated configurations, recovering heat from combustion flue gases, downstream from the air preheater, is a reasonable strategy to increase the power output of the steam cycle (91 % increase) with relatively low increase in the fuel demand (29 % increase).

Relatively low values of specific primary energy consumption for CO_2 avoided (*SPECCA*) are achieved compared with values from other capture technologies reported in the literature for similar applications (De Lena et al., 2022; De Lena et al., 2019; Voldsund et al., 2019). Utilizing solid recovered fuel (SRF) gives better results than firing lignite but could lead to chlorine-aided corrosion in some configurations of the steam cycle. Additionally, negative *SPECCA* values are obtained for some fully integrated arrangements, which reveals the high efficiency of this kind of integration. Because of the considerable net power generation of the IHCaL concepts, there is a relatively high dependency of the results on the energy grid scenario assumed. The best results in terms of *SPECCA* are obtained for energy mixes with high CO_2 emissions associated with power generation, where the advantage of the net power injected to the grid is more significant.

The avoidance costs of the process scenarios with CO_2 capture are lower than the ones reported for other capture technologies for comparable applications (De Lena et al., 2019; Santos and Hanak, 2022). For all the plants considered, there are three possible avenues for revenue: (i) product sale, (ii) electricity export, and (iii) SRF utilization. The tail-end configurations produce additional lime in the downstream capture plants, which can be sold as product. This lowers the breakeven selling price (*BESP)*, and the CO_2 avoidance costs.

Electricity generation, utilization, and export is key for favorable economics. Process scenarios with greater net electricity available for export have better economic results, such as lower *BESP* and CO_2 avoidance costs. However, they also entail higher heat requirements, leading to an increased fuel demand. In the tail-end SRF (II) case, the convergence of high electricity export and increased lime production leads to a lower *BESP* compared to the reference case. This, in turn, results in negative CO_2 avoidance cost (10.7 €/$t_{CO2,av}$).

Utilizing waste-derived fuels in the IHCaL process has the potential to provide twofold economic benefits. On the one hand, it is a means of waste management, corresponding to the fourth policy in the hierarchy of the European legislation (European Union, 2018, 2008), thus enabling “negative costs” of fuel, associated with the added value of the disposal. On the other hand, net negative CO_2 emissions may be achieved, which, if marketed as credits from carbon dioxide removal (CDR), can further decrease the avoidance costs. In all the SRF scenarios analyzed throughout this work, CDR reduced the CO_2 avoidance costs by around 25 % and the maximum costs were 18.2 EUR/$t_{CO2,av}$, excluding costs for transport and geological storage.

SRF is a finite resource, dependent on available waste streams and production capacity. The required specifications (e.g. impurities, heating value, and grain size distribution) may further limit the availability of suitable SRF. It is therefore reasonable to consider that the costs of this fuel may increase in the future, which would reduce the advantage of SRF over lignite.

The availability of lignite will decrease gradually in parallel to the closure of the German coal power plants until 2038. In line with this, it is necessary for lime producers to look for new fuel substitutes, such as SRFs, RDFs, and biomass-based fuels. This study presents one possible path to replace today’s fossil fuel utilization by an alternative fuel, namely SRF.

To push forward the IHCaL technology, some issues still need to be addressed. The sorbent calcination in the indirectly heated calciner of the IHCaL process requires further investigation. The IHCaL calciner did not perform as expected during the experimental pilot testing (Hofmann et al., 2024; Reitz et al., 2016), but the impact of the calciner performance in the CO_2 capture efficiency of the IHCaL system and the main factors affecting the calcination in the indirectly heated calciner are not yet fully understood.

Furthermore, there are still technical unknowns that can only be clarified with a scale-up of the IHCaL test rig. The next step towards industrial implementation of the technology by 2028 is the construction of a demonstration facility to capture CO_2 from flue gases of a cement or lime plant (Ströhle et al., 2021). This would enable the testing of a solid-solid heat exchanger to recover heat between the looped sorbent streams, and a high-temperature regenerative preheater for the combustion air. Additionally, the long-term operation of the demonstration plant would serve for the validation of the lifespan of the heat pipes heat exchanger in real operating environment, and the firing of waste-derived fuels in the combustor. Finally, the operation under low circulation rates and high make-up rates would validate the fully integrated concept.

Declaration of competing interest

The authors declare the following financial interests/personal relationships which may be considered as potential competing interests: Martin Greco-Coppi reports financial support was provided by the German Federal Ministry for Economic Affairs and Climate Action. Angela Rolfe reports financial support was provided by the Department for Business, Energy and Industrial Strategy of the United Kingdom. Martin Greco-Coppi, Carina Hofmann, Jochen Ströhle, and Bernd Epple have patent No. 10 2023 114 354.9, “Apparatus and Method for Producing Lime” (German Patent and Trademark Office), pending to Technical University of Darmstadt.

CRediT authorship contribution statement

Martin Greco-Coppi: Conceptualization, Methodology, Software (Aspen Plus®, EBSILON®Professional), Visualization, Writing – Original Draft (lead), and Writing – Review & Editing (lead). **Peter Seufert:** Writing – Original Draft (supporting), and Software (Aspen Plus®, EBSILON®Professional). **Carina Hofmann:** Writing – Review & Editing. **Angela Rolfe:** Methodology, Writing – Original Draft (economic assessment), and Writing – Review & Editing (economic assessment). **Ye Huang:** Software (ECLIPSE). **Sina Rezvani:** Writing – Review & Editing. **Jochen Ströhle:** Writing – Review & Editing, Supervision, Project Administration, and Funding Acquisition. **Bernd Epple:** Supervision and Funding Acquisition.

Acknowledgments

The work leading to these results has received funding through the ACT program (Accelerating CCS Technologies, Horizon 2020 Project No. 691712) within the ANICA project. Financial contributions were made by the German Federal Ministry for Economic Affairs and Climate Action, the Department for Business, Energy and Industrial Strategy of the United Kingdom, and the Greek General Secretariat for Research and Technology. The support from Falah Alobaid in the design of the steam cycles and the assistance of Alina Greco Coppi in proofreading the article are greatly acknowledged as well.

References

Abanades, J.C., 2002. The maximum capture efficiency of CO_2 using a carbonation/calcination cycle of $CaO/CaCO_3$. Chem. Eng. J. 90, 303–306. doi:10.1016/S1385-8947(02)00126-2.

Abanades, J.C., Alvarez, D., 2003. Conversion limits in the reaction of CO_2 with lime. Energy Fuel. 17, 308–315. doi:10.1021/ef020152a.

Abanades, J.C., Anthony, E.J., Lu, D.Y., Salvador, C., Alvarez, D., 2004. Capture of CO_2 from combustion gases in a fluidized bed of CaO. AIChE J. 50, 1614–1622. doi:10.1002/aic.10132.

Abanades, J.C., Anthony, E.J., Wang, J., Oakey, J.E., 2005. Fluidized bed combustion systems integrating CO_2 capture with CaO. Environ. Sci. Technol. 39, 2861–2866. doi:10.1021/es0496221.

Anantharaman, R., Berstad, D., Cinti, G., Gatti, M., 2018. D3.2 CEMCAP Framework for Comparative Techno-Economic Analysis of CO_2 Capture from Cement Plants doi:10.5281/zenodo.1257111.

Andrew, R.M., 2018. Global CO_2 emissions from cement production. Earth Syst. Sci. Data 10, 195–217. doi:10.5194/essd-10-195-2018.

Arias, B., Diego, M.E., Abanades, J.C., Lorenzo, M., Diaz, L., Martínez, D., Alvarez, J., Sánchez-Biezma, A., 2013. Demonstration of steady state CO_2 capture in a 1.7MW_{th} calcium looping pilot. Int. J. Greenhouse Gas Control 18, 237–245. doi:10.1016/j.ijggc.2013.07.014.

Arias, B., Diego, M.E., Méndez, A., Abanades, J.C., Díaz, L., Lorenzo, M., Sanchez-Biezma, A., 2017. Operating experience in la Pereda 1.7 MW_{th} calcium looping pilot. Energy Procedia 114, 149–157. doi:10.1016/j.egypro.2017.03.1157.

Aspen Technology, Inc, 2001. Aspen Physical Property System: Physical Property Methods and Models V11.1, p. 436 Cambridge.

Aspen Technology, Inc, 2020. Aspen Plus® V12 (38.0.0.380) [*Computer software*]. https://www.aspentech.com/en/products/engineering/aspen-plus .

Astrup, T., Møller, J., Fruergaard, T., 2009. Incineration and co-combustion of waste: accounting of greenhouse gases and global warming contributions. Waste Manage. Res. 27, 789–799. doi:10.1177/0734242X09343774.

Baker, R.W., Freeman, B., Kniep, J., Huang, Y.I., Merkel, T.C., 2018. CO_2 capture from cement plants and steel mills using membranes. Ind. Eng. Chem. Res. 57, 15963–15970. doi:10.1021/acs.iecr.8b02574.

Barin, I., 1995. Thermochemical Data of Pure Substances. VCH, Weinheim, p. 924. doi:10.1002/9783527619825.

Böckh, P.von, Stripf, M., 2018. Thermische Energiesysteme: Berechnung klassischer und regenerativer Komponenten und Anlagen. Springer Vieweg, Berlin, Heidelberg, p. 276. https://doi.org/10.1007/978-3-662-55335-0

Cachola, C.d.S, Ciotta, M., Azevedo dos Santos, A., Peyerl, D., 2023. Deploying of the carbon capture technologies for CO_2 emission mitigation in the industrial sectors. Carb. Capt. Sci. Technol. 7, 100102. doi:10.1016/j.ccst.2023.100102.

Charitos, A., Rodríguez, N., Hawthorne, C., Alonso, M., Zieba, M., Arias, B., Kopanakis, G., Scheffknecht, G., Abanades, J.C., 2011. Experimental validation of the calcium looping CO_2 capture process with two circulating fluidized bed carbonator reactors. Ind. Eng. Chem. Res. 50, 9685–9695. doi:10.1021/ie200579f.

Chemical Engineering, 2023. The Chemical Engineering Plant Cost Index. https://www.chemengonline.com/pci-home (accessed 19 November 2023).

Consonni, S., Viganò, F., 2012. Waste gasification vs. conventional Waste-to-Energy: a comparative evaluation of two commercial technologies. Waste Manage. 32, 653–666. doi:10.1016/j.wasman.2011.12.019.

Cormos, A.-M., Dragan, S., Petrescu, L., Sandu, V., Cormos, C.-C., 2020. Techno-economic and environmental evaluations of decarbonized fossil-intensive industrial processes by reactive absorption & adsorption CO_2 capture systems. Energies 13, 1268. doi:10.3390/en13051268.

Cormos, C.-C., Dragan, S., Cormos, A.-M., Petrescu, L., Dumbrava, I.-D., Sandu, V., 2021. Evaluation of calcium looping cycle as a time-flexible CO_2 capture and thermo-chemical energy storage system. Chem. Eng. Transact. 88, 19–24. doi:10.3303/CET2188003.

Dave, A., Huang, Y., Rezvani, S., McIlveen-Wright, D., Novaes, M., Hewitt, N., 2013. Techno-economic assessment of biofuel development by anaerobic digestion of European marine cold-water seaweeds. Bioresour. Technol. 135, 120–127. doi:10.1016/j.biortech.2013.01.005.

De Lena, E., Arias, B., Romano, M.C., Abanades, J.C., 2022. Integrated calcium looping system with circulating fluidized bed reactors for low CO_2 emission cement plants. Int. J. Greenhouse Gas Control 114, 103555. doi:10.1016/j.ijggc.2021.103555.

De Lena, E., Spinelli, M., Gatti, M., Scaccabarozzi, R., Campanari, S., Consonni, S., Cinti, G., Romano, M.C., 2019. Techno-economic analysis of calcium looping processes for low CO_2 emission cement plants. Int. J. Greenhouse Gas Control 82, 244–260. doi:10.1016/j.ijggc.2019.01.005.

Dean, C., Hills, T., Florin, N., Dugwell, D., Fennell, P.S., 2013. Integrating calcium looping CO_2 capture with the manufacture of cement. Energy Procedia 37, 7078–7090. doi:10.1016/j.egypro.2013.06.644.

Diego, M.E., Arias, B., Abanades, J.C., 2016a. Analysis of a double calcium loop process configuration for CO_2 capture in cement plants. J. Clean. Prod. 117, 110–121. doi:10.1016/j.jclepro.2016.01.027.

Diego, M.E., Arias, B., Méndez, A., Lorenzo, M., Díaz, L., Sánchez-Biezma, A., Abanades, J.C., 2016b. Experimental testing of a sorbent reactivation process in La Pereda 1.7 MW_{th} calcium looping pilot plant. Int. J. Greenhouse Gas Control 50, 14–22. doi:10.1016/j.ijggc.2016.04.008.

Dieter, H., Bidwe, A.R., Varela-Duelli, G., Charitos, A., Hawthorne, C., Scheffknecht, G., 2014. Development of the calcium looping CO_2 capture technology from lab to pilot scale at IFK, University of Stuttgart. Fuel 127, 23–37. doi:10.1016/j.fuel.2014.01.063.

Driver, J.G., Hills, T., Hodgson, P., Sceats, M., Fennell, P.S., 2022. Simulation of direct separation technology for carbon capture and storage in the cement industry. Chem. Eng. J. 449, 137721. doi:10.1016/j.cej.2022.137721.

European Commission, H., 2020. Low Emissions Intensity Lime and Cement 2: Demonstration Scale. Leilac2 Project doi:10.3030/884170.

European Union, 2008. Directive 2008/98/EC of the European Parliament and of the Council of 19 November 2008 on waste and repealing certain Directives. http://data.europa.eu/eli/dir/2008/98/oj (accessed 12 May 2023).

European Union, 2018. Consolidated text: Directive 2008/98/EC of the European Parliament and of the Council of 19 November 2008 on waste and repealing certain Directives. http://data.europa.eu/eli/dir/2008/98/2018-07-05 (accessed 12 May 2023).

Eurostat, 2022. Electricity price statistics. https://ec.europa.eu/eurostat/statistics-explained/index.php?title=Electricity_price_statistics (accessed 15 December 2022).

Fan, L.-S., 2012. Separation of Carbon Dioxide from Gas Mixtures by Calcium based Reaction Separation. https://patents.google.com/patent/US8226917B2.

Ferrari, M.-C., Amelio, A., Nardelli, G.M., Costi, R., 2021. Assessment on the application of facilitated transport membranes in cement plants for CO_2 capture. Energies 14, 4772. doi:10.3390/en14164772.

Fu, C., Roussanaly, S., Jordal, K., Anantharaman, R., 2021. Techno-economic analyses of the $CaO/CaCO_3$ post-combustion CO_2 capture from NGCC power plants. Front. Chem. Eng. 2, 596417. doi:10.3389/fceng.2020.596417.

Furimsky, E., 2007. Carbon dioxide emission index as a mean for assessing fuel quality. Energy Source. Part A 30, 119–131. doi:10.1080/15567030600820583.

Gardarsdottir, S., Lena, E.de, Romano, M., Roussanaly, S., Voldsund, M., Pérez-Calvo, J.-F., Berstad, D., Fu, C., Anantharaman, R., Sutter, D., Gazzani, M., Mazzotti, M., Cinti, G., 2019. Comparison of technologies for CO_2 capture from cement production—part 2: cost analysis. Energies 12, 542. doi:10.3390/en12030542.

Gerassimidou, S., Velis, C.A., Williams, P.T., Komilis, D., 2020. Characterisation and composition identification of waste-derived fuels obtained from municipal solid waste using thermogravimetry: a review. Waste management & research: the journal of the International Solid Wastes and Public Cleansing Association. ISWA 38, 942–965. doi:10.1177/0734242X20941085.

Ghanbari, M., Ahmadi, M., Lashanizadegan, A., 2017. A comparison between Peng–Robinson and Soave–Redlich–Kwong cubic equations of state from modification perspective. Cryogenics 84, 13–19. doi:10.1016/j.cryogenics.2017.04.001.

Gogulancea, V., Rolfe, A., Jaffar, M., Brandoni, C., Atsonios, K., Detsios, N., Dieringer, P., Huang, Y., 2023. Technoeconomic and environmental assessment of biomass chemical looping gasification for advanced biofuel production. Int. J. Energy Res. 2023, 1–17. doi:10.1155/2023/6101270.

Grasa, G.S., Abanades, J.C., 2007. Narrow fluidised beds arranged to exchange heat between a combustion chamber and a CO_2 sorbent regenerator. Chem. Eng. Sci. 62, 619–626. doi:10.1016/j.ces.2006.09.026.

Greco-Coppi, M., Hofmann, C., Ströhle, J., Walter, D., Epple, B., 2021. Efficient CO_2 capture from lime production by an indirectly heated carbonate looping process. Int. J. Greenhouse Gas Control 112, 103430. doi:10.1016/j.ijggc.2021.103430.

Greco-Coppi, M., Hofmann, C., Walter, D., Ströhle, J., Epple, B., 2023. Negative CO_2 emissions in the lime production using an indirectly heated carbonate looping process. Mitig. Adapt. Strateg. Glob. Change 28. doi:10.1007/s11027-023-10064-7.

Haaf, M., Anantharaman, R., Roussanaly, S., Ströhle, J., Epple, B., 2020a. CO_2 capture from waste-to-energy plants: Techno-economic assessment of novel integration concepts of calcium looping technology. Resour. Conserv. Recycl. 162, 104973. doi:10.1016/j.resconrec.2020.104973.

Haaf, M., Hilz, J., Peters, J., Unger, A., Ströhle, J., Epple, B., 2020b. Operation of a 1 MW_{th} calcium looping pilot plant firing waste-derived fuels in the calciner. Powder Technol. 372, 267–274. doi:10.1016/j.powtec.2020.05.074.

Haaf, M., Müller, A., Unger, A., Ströhle, J., Epple, B., 2020c. Combustion of solid recovered fuels in a semi-industrial circulating fluidized bed pilot plant - Implications of bed material and combustion atmosphere on gaseous emissions. VGB Power Tech. 3, 51–56.

Haaf, M., Peters, J., Hilz, J., Unger, A., Ströhle, J., Epple, B., 2020d. Combustion of solid recovered fuels within the calcium looping process – experimental demonstration at 1 MW_{th} scale. Exp. Therm Fluid Sci. 113, 110023. doi:10.1016/j.expthermflusci.2019.110023.

Haider, F., Horn, S., Waldmann, B., Warnecke, R., 2008. *Quantifizierung des Korrosionsdiagramms auf der Basdis von Messungen mit der Augsburger Korrosionssonde*. VDI-Korrosions-Tagung, 2008.06.12-13 in Oberhausen.

Hanak, D.P., Biliyok, C., Yeung, H., Białecki, R., 2014. Heat integration and exergy analysis for a supercritical high-ash coal-fired power plant integrated with a post-combustion carbon capture process. Fuel 134, 126–139. doi:10.1016/j.fuel.2014.05.036.

Hawthorne, C., Trossmann, M., Galindo Cifre, P., Schuster, A., Scheffknecht, G., 2009. Simulation of the carbonate looping power cycle. Energy Procedia 1, 1387–1394. doi:10.1016/j.egypro.2009.01.182.

Hills, T.P., 2016. Investigations of the use of spent sorbent from the Ca looping process in cement manufacture and investigation of long-term CO_2 uptake in cement and concrete. PhD Thesis. Imperial College, London. https://doi.org/10.25560/39286

Hills, T.P., Sceats, M., Rennie, D., Fennell, P., 2017. LEILAC: low cost CO_2 capture for the cement and lime industries. Energy Procedia 114, 6166–6170. doi:10.1016/j.egypro.2017.03.1753.

Hoeftberger, D., Karl, J., 2016. The indirectly heated carbonate looping process for CO_2 capture—a concept with heat pipe heat exchanger. J. Energy Res. Technol. 138, 042211. doi:10.1115/1.4033302.

Hofmann, C., Greco-Coppi, M., Ströhle, J., Epple, B., 2022a. Operation of a 300 kW_{th} indirectly heated carbonate looping pilot plant for CO_2 capture from lime industry.

Fluidized Bed Conversion Conference, 8-11th May 2022. Chalmers University of Technology (Sweden) doi:10.26083/tuprints-00026550.

Hofmann, C., Greco-Coppi, M., Ströhle, J., Epple, B., 2022b. Pilot testing of the indirectly heated carbonate looping process for cement and lime plants. In: Proceedings of the 16th Greenhouse Gas Control Technologies Conference (GHGT-16) 23-24 Oct 2022 doi:10.2139/ssrn.4278810.

Hofmann, C., Greco-Coppi, M., Ströhle, J., Epple, B., 2024. Enhancement of a 300 kW_{th} pilot plant for testing the indirectly heated carbonate looping process for CO_2 capture from lime and cement industry. Exp. Therm Fluid Sci. 151, 111091. doi:10.1016/j.expthermflusci.2023.111091.

Hong, W.Y., 2022. A techno-economic review on carbon capture, utilisation and storage systems for achieving a net-zero CO_2 emissions future. Carb. Capt. Sci. Technol. 3, 100044. doi:10.1016/j.ccst.2022.100044.

Huang, Y., Keatley, P., Chen, H.S., Zhang, X.J., Rolfe, A., Hewitt, N.J., 2018. Techno-economic study of compressed air energy storage systems for the grid integration of wind power. Int. J. Energy Res. 42, 559–569. doi:10.1002/er.3840.

Huang, Y., Wang, Y. D., Rezvani, S., McIlveen-Wright, D. R., Anderson, M., Mondol, J., Zacharopolous, A., Hewitt, N.J., 2013. A techno-economic assessment of biomass fuelled trigeneration system integrated with organic Rankine cycle. Applied Thermal Engineering 53 (2), 325–331. doi:10.1016/j.applthermaleng.2012.03.041.

IEA, 2020. Energy Technology Perspectives 2020 - Special Report on Carbon Capture Utilisation and Storage: CCUS in Clean Energy Transitions. OECD Publishing, Paris, p. 174. doi:10.1787/208b66f4-en.

Junk, M., Reitz, M., Ströhle, J., Epple, B., 2013. Thermodynamic evaluation and cold flow model testing of an indirectly heated carbonate looping process. Chem. Eng. Technol. 36, 1479–1487. doi:10.1002/ceat.201300019.

Junk, M., Reitz, M., Ströhle, J., Epple, B., 2016. Technical and economical assessment of the indirectly heated carbonate looping process. J. Energy Res. Technol. 138, 042210. doi:10.1115/1.4033142.

Kemper, J., 2015. Biomass and carbon dioxide capture and storage: a review. Int. J. Greenhouse Gas Control 40, 401–430. doi:10.1016/j.ijggc.2015.06.012.

Kremer, J., Galloy, A., Ströhle, J., Epple, B., 2013. Continuous CO_2 capture in a 1-MW_{th} carbonate looping pilot plant. Chem. Eng. Technol. 36, 1518–1524. doi:10.1002/ceat.201300084.

Krishnan, A., Nighojkar, A., Kandasubramanian, B., 2023. Emerging towards zero carbon footprint via carbon dioxide capturing and sequestration. Carb. Capt. Sci. Technol. 9, 100137. doi:10.1016/j.ccst.2023.100137.

Kunii, D., Levenspiel, O., 1991. Fluidization Engineering doi:10.1016/C2009-0-24190-0.

Lasheras, A., Ströhle, J., Galloy, A., Epple, B., 2011. Carbonate looping process simulation using a 1D fluidized bed model for the carbonator. Int. J. Greenhouse Gas Control 5, 686–693. doi:10.1016/j.ijggc.2011.01.005.

Madejski, P., Chmiel, K., Subramanian, N., Kuś, T., 2022. Methods and techniques for CO_2 capture: review of potential solutions and applications in modern energy technologies. Energies 15, 887. doi:10.3390/en15030887.

Martínez, I., Murillo, R., Grasa, G., Rodríguez, N., Abanades, J.C., 2011. Conceptual design of a three fluidised beds combustion system capturing CO_2 with CaO. Int. J. Greenhouse Gas Control 5, 498–504. doi:10.1016/j.ijggc.2010.04.017.

Menny, K., 2006. *Strömungsmaschinen: Hydraulische und thermische Kraft- und Arbeitsmaschinen*. Teubner, Wiesbaden doi:10.1007/978-3-322-96735-0.

Mignard, D., 2014. Correlating the chemical engineering plant cost index with macro-economic indicators. Chem. Eng. Res. Des. 92, 285–294. doi:10.1016/j.cherd.2013.07.022.

Moora, H., Roos, I., Kask, U., Kask, L., Ounapuu, K., 2017. Determination of biomass content in combusted municipal waste and associated CO_2 emissions in Estonia. Energy Procedia 128, 222–229. doi:10.1016/j.egypro.2017.09.059.

Myöhänen, K., Hyppänen, T., Pikkarainen, T., Eriksson, T., Hotta, A., 2009. Near zero CO_2 emissions in coal firing with oxy-fuel circulating fluidized bed boiler. Chem. Eng. Technol. 32, 355–363. doi:10.1002/ceat.200800566.

Qu, Z., Zhong, R., Wang, L., Zhao, W., Tian, X., Wang, H., 2020. Research progress on high temperature corrosion mechanism of waste incineration power generation boiler. IOP Conf. Ser.: Earth Environ. Sci. 598, 12008. doi:10.1088/1755-1315/598/1/012008.

Ramkumar, S., Fan, L.-S., 2010. Thermodynamic and experimental analyses of the three-stage calcium looping process. Ind. Eng. Chem. Res. 49, 7563–7573. doi:10.1021/ie100846u.

Reeves, E., Smith, C., Johnson, A., Stalbow, N., Antypas, I., Nierinck, J., 2023. Energy from Waste to be included in the EU Emissions Trading System. https://www.ashurst.com/en/insights/energy-from-waste-to-be-included-in-the-eu-emissions-trading-system/ (accessed 9 June 2023).

Reitz, M., Junk, M., Ströhle, J., Epple, B., 2014. Design and erection of a 300 kW_{th} indirectly heated carbonate looping test facility. Energy Procedia 63, 2170–2177. doi:10.1016/j.egypro.2014.11.236.

Reitz, M., Junk, M., Ströhle, J., Epple, B., 2016. Design and operation of a 300 kW_{th} indirectly heated carbonate looping pilot plant. Int. J. Greenhouse Gas Control 54, 272–281. doi:10.1016/j.ijggc.2016.09.016.

Rolfe, A., Huang, Y., Haaf, M., Pita, A., Rezvani, S., Dave, A., Hewitt, N.J., 2018a. Technical and environmental study of calcium carbonate looping versus oxy-fuel options for low CO_2 emission cement plants. Int. J. Greenhouse Gas Control 75, 85–97. doi:10.1016/j.ijggc.2018.05.020.

Rolfe, A., Huang, Y., Haaf, M., Rezvani, S., McIlveen-Wright, D., Hewitt, N.J., 2018b. Integration of the calcium carbonate looping process into an existing pulverized coal-fired power plant for CO2 capture: Techno-economic and environmental evaluation. Appl. Energy 222, 169–179. doi:10.1016/j.apenergy.2018.03.160.

Romano, M.C., Spinelli, M., Campanari, S., Consonni, S., Cinti, G., Marchi, M., Borgarello, E., 2013. The calcium looping process for low CO_2 emission cement and power. Energy Procedia 37, 7091–7099. doi:10.1016/j.egypro.2013.06.645.

Roussanaly, S., 2019. Calculating CO_2 avoidance costs of carbon capture and storage from industry. Carb. Manag. 10, 105–112. doi:10.1080/17583004.2018.1553435.

Roussanaly, S., Fu, C., Voldsund, M., Anantharaman, R., Spinelli, M., Romano, M., 2017. Techno-economic analysis of MEA CO_2 capture from a cement Kiln – impact of steam supply scenario. Energy Procedia 114, 6229–6239. doi:10.1016/j.egypro.2017.03.1761.

Santos, M.P.S., Hanak, D.P., 2022. Carbon capture for decarbonisation of energy-intensive industries: a comparative review of techno-economic feasibility of solid looping cycles. Front. Chem. Sci. Eng. 16, 1291–1317. doi:10.1007/s11705-022-2151-5.

Sarc, R., Lorber, K.E., 2013. In: Production, quality and quality assurance of Refuse Derived Fuels (RDFs), 33. Waste management, (New York, N.Y.), pp. 1825–1834. doi:10.1016/j.wasman.2013.05.004.

Schorcht, F., Kourti, I., Scalet, B.M., Roudier, S., Delgado Sancho, L., 2013. Best available techniques (BAT) reference document for the production of cement, lime and magnesium oxide: Industrial Emissions Directive 2010/75/EU (integrated pollution. In: prevention and control). Publications Office, Luxembourg doi:10.2788/12850.

Shimizu, T., Hirama, T., Hosoda, H., Kitano, K., Inagaki, M., Tejima, K., 1999. A twin fluid-bed reactor for removal of CO_2 from combustion processes. Chem. Eng. Res. Des. 77, 62–68. doi:10.1205/026387699525882.

Simbeck, D., Beecy, D., 2011. The CCS paradox: the much higher CO_2 avoidance costs of existing versus new fossil fuel power plants. Energy Procedia 4, 1917–1924. doi:10.1016/j.egypro.2011.02.071.

Steag Energy Services GmbH, 2022. EBSILON®*Professional* Version 16.0.0.32608 [Computer software]. https://www.ebsilon.com/de/.

Ströhle, J., Hofmann, C., Greco-Coppi, M., Epple, B., 2021. CO_2 Capture From Lime and Cement Plants Using an Indirectly Heated Carbonate Looping Process - The ANICA Project, in: TCCS-11: CO_2 capture, transport and storage, Trondheim, 22nd–23rd June 2021: Short papers from the 11th International Trondheim CCS Conference, Trondheim, Norway. SINTEF Academic Press, Oslo, pp. 529–535. https://portal.issn.org/resource/ISSN/2387-4295.

Ströhle, J., Junk, M., Kremer, J., Galloy, A., Epple, B., 2014. Carbonate looping experiments in a 1MW_{th} pilot plant and model validation. Fuel 127, 13–22. doi:10.1016/j.fuel.2013.12.043.

Telesca, A., Calabrese, D., Marroccoli, M., Tomasulo, M., Valenti, G.L., Duelli, G., Montagnaro, F., 2014. Spent limestone sorbent from calcium looping cycle as a raw material for the cement industry. Fuel 118, 202–205. doi:10.1016/j.fuel.2013.10.060.

Telesca, A., Marroccoli, M., Tomasulo, M., Valenti, G.L., Dieter, H., Montagnaro, F., 2015. Calcium looping spent sorbent as a limestone replacement in the manufacture of portland and calcium sulfoaluminate cements. Environ. Sci. Technol. 49, 6865–6871. doi:10.1021/acs.est.5b00394.

Tilak, P., El-Halwagi, M.M., 2018. Process integration of Calcium Looping with industrial plants for monetizing CO_2 into value-added products. Carbon Resources Conversion 1, 191–199. doi:10.1016/j.crcon.2018.07.004.

UK Government Digital Service, 2023. Landfill Tax Increase in Rates Policy paper.. https://www.gov.uk/government/publications/landfill-tax-rates-for-2023-to-2024/landfill-tax-increase-in-rates (accessed 5 November 2023).

Ulster University, 1992. ECLIPSE Process Simulator. Energy Research Centre, University of Ulster, Coleraine Copyright 1992 [Computer software].

Velis, C.A., Longhurst, P.J., Drew, G.H., Smith, R., Pollard, S.J.T., 2010. Production and quality assurance of solid recovered fuels using mechanical—biological treatment (MBT) of waste: a comprehensive assessment. Crit. Rev. Environ. Sci. Technol. 40, 979–1105. doi:10.1080/10643380802586980.

Vitillo, J.G., Smit, B., Gagliardi, L., 2017. Introduction: carbon capture and separation. Chem. Rev. 117, 9521–9523. doi:10.1021/acs.chemrev.7b00403.

Voldsund, M., Gardarsdottir, S., Lena, E.de, Pérez-Calvo, J.-F., Jamali, A., Berstad, D., Fu, C., Romano, M., Roussanaly, S., Anantharaman, R., Hoppe, H., Sutter, D., Mazzotti, M., Gazzani, M., Cinti, G., Jordal, K., 2019. Comparison of technologies for CO_2 capture from cement production—part 1: technical evaluation. Energies 12, 559. doi:10.3390/en12030559.

Wang, W., Ramkumar, S., Li, S., Wong, D., Iyer, M., Sakadjian, B.B., Statnick, R.M., Fan, L.-S., 2010. Subpilot demonstration of the carbonation−calcination reaction (CCR) process: high-temperature CO_2 and sulfur capture from coal-fired power plants. Ind. Eng. Chem. Res. 49, 5094–5101. doi:10.1021/ie901509k.

Wang, Y., Lin, S., Suzuki, Y., 2007. Study of limestone calcination with CO_2 capture: decomposition behavior in a CO_2 atmosphere. Energy Fuels 21, 3317–3321. doi:10.1021/ef700318c.

Wang, Y.D., Huang, Y., McIlveen-Wright, D., McMullan, J., Hewitt, N., Eames, P., Rezvani, S., 2006. A techno-economic analysis of the application of continuous staged-combustion and flameless oxidation to the combustor design in gas turbines. Fuel Process. Technol. 87, 727–736. doi:10.1016/j.fuproc.2006.02.003.

Warnecke, R., 2004. Einfluss von Strömung und chemischen Reaktionen im rauchgasseitigen Belag auf Korrosion an Überhitzer-Rohern in Müllverbrennungsanlagen. VGB PowerTech 52–59 9/2004.

Williams, B.C., McMullan, J.T., 1996. Techno-economic analysis of fuel conversion and power generation systems — the development of a portable chemical process simulator with capital cost and economic performance analysis capabilities. Int. J. Energy Res. 20, 125–142. doi:10.1002/(SICI)1099-114X(199602)20:2%3C125::AID-ER239%3E3.0.CO;2-2.

Yang, F., Meerman, J.C., Faaij, A., 2021. Carbon capture and biomass in industry: a techno-economic analysis and comparison of negative emission options. Renew. Sustain. Energy Rev. 144, 111028. doi:10.1016/j.rser.2021.111028.

Zhao, M., Minett, A.I., Harris, A.T., 2013. A review of techno-economic models for the retrofitting of conventional pulverised-coal power plants for post-combustion capture (PCC) of CO_2. Energy Environ. Sci. 6, 25–40. doi:10.1039/C2EE22890D.

Research Paper IV

Research Paper IV

Title: A carbonator model for CO_2 capture based on results from pilot tests. Part I: Hydrodynamics and reactor model

Authors: Martin Greco Coppi, Jochen Ströhle, Bernd Epple

Journal: Chemical Engineering Journal (Elsevier)

Status: Published (August 23, 2024)

Volume: 500 (November 15, 2024)

DOI: https://doi.org/10.1016/j.cej.2024.155119

Licensing: The authors. CC BY 4.0

Graphical abstract

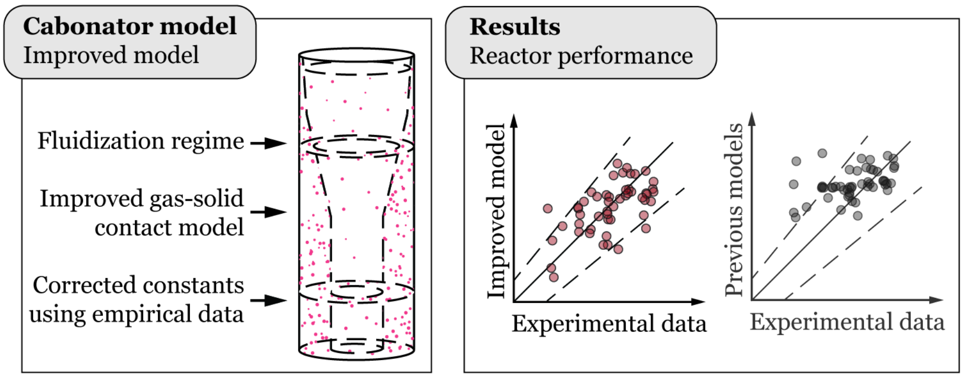
Cabonator model
Improved model
Fluidization regime
Improved gas-solid contact model
Corrected constants using empirical data
Results
Reactor performance
Improved model
Experimental data
Previous models
Experimental data

Short Summary

In this work, we present and validate a novel carbonator model for CO_2 capture using CaL technology, consisting in a reactor sub-model and a particle sub-model. Our model is based on a systematic literature review and experimental results from pilot tests. This publication deals with the reactor sub-model, dealing with the simulation of flow patterns and gas-solid contact. The particle sub-model is discussed in Research Paper V. Our study features a rigorous analysis of carbonator fluidization regimes. We highlight that modeling assumptions commonly found in the literature can result in a significant overestimation of the carbonator performance. Additionally, we offer guidelines for the appropriate selection of these assumptions.

Chemical Engineering Journal 500 (2024) 155119

Contents lists available at ScienceDirect

Chemical Engineering Journal

journal homepage: www.elsevier.com/locate/cej

A carbonator model for CO_2 capture based on results from pilot tests. Part I: Hydrodynamics and reactor model

Martin Greco-Coppi *, Jochen Ströhle, Bernd Epple

Technical University of Darmstadt, Department of Mechanical Engineering, Institute for Energy Systems and Technology, Otto-Berndt-Str. 2, 64287 Darmstadt, Germany

ARTICLE INFO

Keywords:
CO_2 capture
Carbonate looping
Indirectly heated carbonate looping
Reactor modeling
Fluidization engineering
Pilot testing

ABSTRACT

Carbonate looping (CaL) technology has the potential to efficiently capture CO_2 from power plants and carbon-intensive industries such as cement production. Its feasibility has been demonstrated in numerous pilot campaigns, including tests validating advanced features such as indirectly heating the sorbent regenerator. However, some issues, such as the role of reactor hydrodynamics, need to be discussed more thoroughly to reliably scale up CaL plants for commercial operation. In this work, we present a novel carbonator model based on a systematic literature review and experimental data from pilot tests, including a rigorous analysis of carbonator fluidization regimes. We highlight that modeling assumptions commonly found in the literature can result in a significant overestimation of carbonator performance. Additionally, we offer guidelines for the appropriate selection of these assumptions. Our carbonator model provides an effective tool for the next scale-up step of CaL technology.

1. Introduction

The *carbonate looping* (CaL) process, also known as the *calcium looping* process, uses CaO as a sorbent for capturing CO_2 from off-gases generated by industrial or power-generation processes. This promising technology, first introduced by Shimizu et al. [1] in 1991, has the potential to achieve high levels of thermodynamic efficiency and low CO_2 avoidance costs [2–6]. It is particularly suitable for the cement and lime industry because of the synergies associated with valorizing deactivated sorbent. Fig. 1 is a scheme of the CaL process, illustrating its operating principle. Off-gas with CO_2 enters the *carbonator,* a circulating fluidized bed reactor, where CO_2 reacts with solid CaO at around 650 °C, forming $CaCO_3$ and heat. The gas exiting the carbonator is nearly depleted of CO_2. The particles of $CaCO_3$ (carbonated sorbent) circulate into a *calciner*, which is either a bubbling bed or a circulating fluidized bed reactor, operating at 900 °C. Due to the high temperatures, $CaCO_3$ undergoes calcination, forming CaO and CO_2. As a result, CO_2 exits the calciner in a concentrated form. To maintain a sufficient sorbent activity, fresh material (limestone) is added into the system, either continuously or batchwise. Many tests up to the pilot scale proved the feasibility of CaL technology. The most important CaL pilot facilities are a 200-kW_{th} plant in Stuttgart (Germany) [7–9], a 1-MW_{th} plant in Darmstadt (Germany) [10,11], a 1.7-MW_{th} plant in La Pereda (Spain) [12,13], and a 1.9-MW_{th} plant in Taiwan [14,15]. A systematic review of CaL testing facilities is available elsewhere [16].

In the standard CaL process, the heat for the calcination is obtained through the in-situ combustion of fuels in the calciner. To avoid diluting the separated CO_2, pure O_2 is required for operation, which is obtained through cryogenic separation from air in an *air separation unit* (ASU). The ASU is linked to high investment costs and considerable electric power requirements [17]. Previous studies [18–20] have proposed strategies for electrifying calciners to enable CO_2 capture without an ASU, including the use of plasma burners, electrical resistance, and induction. Another alternative that also avoids the use of an ASU and does not rely on electricity to generate heat for calcination consists in the combustion of fuels in an external combustion chamber. This promising solution is known as the *indirectly heated carbonate looping* (IHCaL) [21–23]. The IHCaL using a heat-pipes heat exchanger [24] was demonstrated for the first time in 2015 through pilot tests at the Technical University of Darmstadt (TU Darmstadt) [25]. The aim was to investigate CO_2 capture from power plants. Lately, the pilot plant at TU Darmstadt was upgraded with a new flue-gas tract to enable flue gas recirculation, and a solid-fuel feeding system to fire coal and pelletized refuse-derived fuel (RDF) [26]. The plant was operated in the new configuration during the year 2022, achieving capture efficiencies higher than 90 % for operating conditions relevant to the lime and cement industry. Greco-Coppi et al. [27] presented different concepts for integrating the IHCaL process into lime plants. They identified the critical points for efficient operation and obtained preliminary results

---

* Corresponding author.
E-mail address: martin.greco@est.tu-darmstadt.de (M. Greco-Coppi).

https://doi.org/10.1016/j.cej.2024.155119
Received 25 April 2024; Received in revised form 19 August 2024; Accepted 22 August 2024

Available online 23 August 2024
1385-8947/© 2024 The Author(s). Published by Elsevier B.V. This is an open access article under the CC BY license (http://creativecommons.org/licenses/by/4.0/).

Nomenclature

Latin symbols

a	Decay constant for solid fraction in Eq. (10) (m^{-1})
b	Decay constant for gas–solid contact efficiency in Eq. (51) (m^{-1})
$a_{\text{c-w}}$	Specific core-wall area (m^2/m^3)
$A_{\text{c-w}}$	Core-wall area (m^2)
Ar	Archimedes number; Eq. (1) (–)
A_t	Internal section area of the carbonator (m^2)
$\mathfrak{C}$	CO_2 concentration driving force; Eq. (31) (mol/m^3)
$\mathfrak{C}^*$	Equivalent CO_2 concentration driving force (mol/m^3)
$\mathfrak{C}_d$	CO_2 concentration driving force on top of dense region (mol/m^3)
$\mathfrak{C}_{\text{in}}$	CO_2 concentration driving force at reactor inlet (mol/m^3)
$\mathfrak{C}_{\text{out}}$	CO_2 concentration driving force at reactor outlet (mol/m^3)
C_{CO2}	CO_2 concentration (mol/m^3)
$C_{\text{CO2,eq}}$	Equilibrium CO_2 concentration (mol/m^3)
d	Diameter (m)
d_c	Core diameter (m)
d_{p}	Particle diameter (m)
$d_{p,50}$	Mass-median particle diameter (m)
d_p^*	Dimensionless particle diameter; Eq. (2) (–)
$\left(d_p^*\right)_{AB}$	A-B Geldart classification boundary, Eq. (3) (–)
d_T	Reactor internal diameter (m)
D_g	Gas diffusion coefficient (m^2/s)
E_{carb}	Carbonator efficiency (%)
$E_{\text{carb,eq.}}$	Equilibrium carbonator efficiency (%)
E_{RM}; E_{PM}	E_{carb} from reactor sub-model; particle sub-model (%)
F_{CO2}; F_R; F_0	Molar circulation rate of CO_2; sorbent circulation; sorbent make-up (mol/s)
g	Earth gravity (9.81 m/s^2)
G_s	Specific entrainment rate ($kg/m^2/s$)
G_s^*	Saturated mass flux of solids; Eq. (13) ($kg/m^2/s$)
H_T; H_d; H_l	Reactor height: total, dense region, lean region (m)
H_{mf}	Bed height at minimum fluidizing conditions (m)
k_{Lewis}	Lewis constant for Eq. (12) (s^{-1})
$K_{\text{b-c}}$	Bubble-cloud gas exchange coefficient (s^{-1})
$K_{\text{b-e}}$	Bubble-emulsion gas exchange coefficient (s^{-1})
$K_{\text{c-e}}$	Cloud-emulsion gas exchange coefficient (s^{-1})
$k_{\text{c-w}}$	Specific core-wall gas interchange coefficient (m/s)
$K_{\text{c-w}}$	Core-wall gas interchange coefficient (s^{-1})
$K'_{\text{c-w}}$	Dimensionless core-wall gas interchange coefficient (–);
K_r	Global first-order reaction rate constant (s^{-1})
M_i	Molar mass of component *i* (kg/mol)
$M_{\text{s,a}}$	Molar mass of potentially active solids (kg/mol)
N_i	Number of moles of component *i* (mol)
p	Pressure (Pa)
p_0	Standard pressure (1.013 bar)
p_{CO2}	Partial pressure of CO_2 (Pa)
$p_{\text{CO2,eq}}$	Equilibrium pressure of CO_2 (Pa)
P_{ent}	Probability of entrainment (–)
Re_c	Particle Reynolds number based on u_c (–);$Re_c \equiv d_p u_c \rho_g / \mu$
Re_{core}	Particle Reynolds number based on d_c (–);$Re_{\text{core}} \equiv d_c u_0 \rho_g / \mu$
Re_p	Particle Reynolds number (–);$Re_p \equiv d_p u_0 \rho_g / \mu$
$Re_{\text{p,mf}}$	Particle Reynolds number at minimum fluidizing conditions (–); $Re_{\text{p,mf}} \equiv d_p\, u_{\text{mf}}\, \rho_g \,/\, \mu$
Re_{se}	Particle Reynolds number based on u_{se} (–); $Re_{\text{se}} \equiv d_p\, u_{\text{se}}\, \rho_g \,/\, \mu$
Sc	Schmidt number (–); $Sc \equiv \mu \,/\, (\rho_g\, D_g)$
T	Temperature (K)
T_0	Standard temperature (273.15 K)
u_0	Superficial gas velocity (m/s)
u_c	Superficial gas velocity at the onset of the turbulent regime (m/s)
u_{mf}	Superficial gas velocity at minimum fluidizing conditions (m/s)
u_s	Mean particle velocity (m/s)
u_{slip}	Slip velocity between the gas and the solid particles (m/s)
u_{se}	Superficial gas velocity at the onset of the fast regime (m/s)
u_t	Terminal velocity of a falling particle (m/s)
u_0^*	Dimensionless superficial gas velocity (–)
u_c^*	Dimensionless superficial gas velocity at onset of the turbulent regime (–)
u_{mf}^*	Dimensionless superficial gas velocity at minimum fluidizing conditions (–)
u_{se}^*	Dimensionless superficial gas velocity at onset of the fast regime (–)
u_t^*	Dimensionless terminal velocity of a falling particle (–)
V	Volume (m^3)
$V_{\text{s,a}}$	Particle volume (apparent) of potentially active sorbent (m^3)
W_{carb}	Carbonator total solid inventory (kg)
x_{CaSO4}	Molar fraction of $CaSO_4$ in the solid sorbent (mol%)
X	Particle conversion (carbonation) (mol_{CaCO3}/mol_{Ca})
X_{calc}	Particle conversion at carbonator inlet (mol_{CaCO3}/mol_{Ca})
X_{carb}	Particle conversion at carbonator outlet (average) (mol_{CaCO3}/mol_{Ca})
y_{CO2}	CO_2 molar concentration (mol%)
$y_{\text{CO2,eq}}$	Equilibrium CO_2 molar concentration (mol%)
$y_{\text{CO2,in}}$	CO_2 molar concentration at reactor inlet (mol%)
$y_{\text{CO2,out}}$	CO_2 molar concentration at reactor outlet (mol%)
z	Axial distance form reactor bottom (m)

Greek symbols

γ	Sorbent age (–); $\gamma \simeq F_R \,/\, F_0$
δ	Core volume fraction (m^3/m^3)
δ_d	Core volume fraction in the dense region (m^3/m^3)
$\delta_l\,(z)$	Core volume fraction in the lean region (m^3/m^3)
$\overline{\delta_l}$	Mean core volume fraction of the lean region (m^3/m^3)
δ_{out}	Core volume fraction at reactor outlet (m^3/m^3)
η	Reactor gas–solid contact efficiency (%)
η_d	Reactor gas–solid contact efficiency in the dense region (%)
$\eta_l\,(z)$	Reactor gas–solid contact efficiency in the lean region (%)
η_l^*	Equivalent gas–solid contact efficiency of the lean region (%)
$\overline{\eta_l}$	Mean gas–solid contact efficiency of the lean region (%)
ε	Voidage (–)
ε_{mf}	Voidage at minimum fluidizing conditions (–)
ε_s	Solid volume fraction (also *solid concentration* or *volume fraction of solids*) (–)
ε_s^*	Saturated solid volume fraction (–)
$\varepsilon_{s,c}$	Solid volume fraction in the core (–)
$\varepsilon_{s,d}$	Solid volume fraction in the dense region (–)
$\overline{\varepsilon_{s,l}}$	Mean solid volume fraction in the lean region (–)
$\varepsilon_{s,\text{mf}}$	Solid volume fraction at minimum fluidizing conditions (–)
$\varepsilon_{s,\text{out}}$	Solid volume fraction at reactor outlet (–)
$\varepsilon_{s,w}$	Solid volume fraction in the wall zone (annulus) (–)
Φ_s	Particle sphericity (–)
μ	Dynamic viscosity (Pa s)
ξ	Volume ratio of potentially active sorbent (CaO and $CaCO_3$) to solids (–)
ρ_i	Density of component *i* (kg/m^3)
ρ_g	Gas density (kg/m^3)

ρ_s	Solid apparent density (kg/m^3)
$\rho_{s,a}$	Apparent density of potentially active sorbent (kg/m^3)
τ_d	Characteristic time of gas–solid contact in the dense region (s)
τ_l	Characteristic time of gas–solid contact in the lean region (s)
τ_{reactor}	Characteristic time of gas–solid contact in the reactor (s)
$\tau_T{}^*$	Equivalent gas residence time (s)

Abbreviations

ASU	Air separation unit
CaL	Carbonate (or calcium) looping
CFB	Circulating fluidized bed
CFD	Computational fluid dynamics
CSTR	Continuous stirred-tank reactor
C*i*	Campaign number *i*
ID	Internal diameter (also d_T)
ID fan	Induced draft fan
IHCaL	Indirectly heated CaL
KL	Kunii and Levenspiel (model)
PM	Particle sub-model
PSD	Particle size distribution
RM	Reactor sub-model
RTD	Residence time distribution
TDH	Transport Disengaging Height
TU	Technical University (of Darmstadt)

Subscripts and superscripts

a	Potentially active solids
c	Core, coalescence
calc	Calciner (outlet)
carb	Carbonator (outlet)
d	Dense region (or immediately after dense region)
g	Gas
in	Inlet
l	Lean region
out	Outlet
p	Particle or apparent (volume/density)
s	Solid (apparent density/volume)
T	Total (diameter/ height)
w	Wall/annulus
*	Saturation or dimensionless

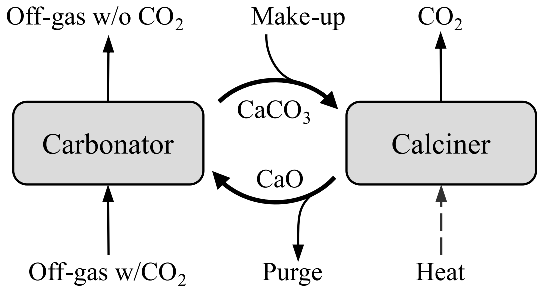

Fig. 1. Scheme of the carbonate looping (CaL) process.

from mass and energy balances. Nevertheless, their models present limitations regarding reactor assumptions.

Accurate carbonator models are necessary to assess sorbent performance, interpret experimental findings, and safely upscale CaL technology for commercial applications [28]. There are various approaches to modeling the circulating-fluidized-bed carbonator [28]. Some models are based on continuous stirred-tank reactor (CSTR) operation [29–31]. They have the advantage of being easy to calculate but do not consider the influence of reactor hydrodynamics in the capture process. Other models are based on three-dimensional CFD simulations [32–34], which can predict empirical data well, but require considerable computational resources, which makes them impractical for many applications, especially modeling of big reactors. The objective of this work was to develop a reactor model, which can be easily integrated in process models for the analysis, optimization, and scale-up of CaL systems. Therefore, the approach we follow is the so-called *Kunii and Levenspiel* (KL) reactor model for fluidized beds [35], which considers two phases (gas, solid) for the simulations and uses semi-empirical equations to model the solids distribution and the gas–solid contact behavior. KL models give good results with less computational effort than three-dimensional CFD models [28] (cf. [32]). There are many KL-type carbonator models in the literature. Lasheras et al. [36] developed a model based on semi-empirical equations from Kunii and Levenspiel [37] and particle models from previous works [38,39]. They assumed that the sorbent entering the carbonator was fully calcined. Their model overpredicted empirical data for some operating conditions of the 1-MW_{th} CaL pilot plant at TU Darmstadt [11]. Romano [40] developed a carbonator model considering a particle *residence time distribution* (RTD) for the calculation of sorbent deactivation and carbonation reaction rates. Although his results presented reasonable agreement with experimental data, he reported a systematic overestimation of the capture efficiency. Ylätalo et al. [41] used a one-dimensional model to evaluate the performance of a carbonator, considering an axial temperature gradient across the height of the reactor. The results they obtained were consistent with data obtained from a CaL laboratory test rig (30 kW) during steady-state operation. Their model relied on a *back-flow ratio*, which was not disclosed. It is uncertain whether their accurate predictions rely on a fitting process specific to the laboratory operating conditions. Recently, Tizfahm et al. [42] developed a model that considers reaction kinetics and reactor hydrodynamics. However, they only validated the kinetic sub-model with experimental data, not the KL reactor model. Most KL carbonator models lack a comprehensive discussion of their methodology. Furthermore, new models often build upon old ones without scrutinizing underlying assumptions. For instance, solids distribution profiles are usually adopted from previous works without analyzing the fluidization regimes for which they are valid. Something similar occurs with the constants for the calculation of core-wall gas interchange and the equations to obtain the reactor gas-particle contact efficiencies.

There are still issues that need to be investigated to enable the commercialization of CaL and IHCaL. One of the unanswered questions is how fluidization regimes influence carbonator behavior. Charitos et al. [29] compared two CaL test rigs and reported high CO_2 capture rates for facilities operating in different fluidization regimes. However, he pointed out that the reactors operating in the turbulent fluidization presented better gas–solid contact. Recently, Diego and Arias [43] reported experimental results from a 1.7-MW_{th} CaL pilot facility showing that the carbonator performance was better for lower gas velocities. Still, there has been no investigation of the fluidization regimes of CaL carbonators using appropriate explanatory models.

In this study, we introduce a novel carbonator model grounded on a systematic literature review. The model was developed to analyze reactor performance in a semi-industrial CO_2 capture facility and to effectively upscale the carbonator for commercial applications. Our work is presented in a two-part publication. In Part I (this work) we explain the *hydrodynamics sub-model* and the *reactor sub-model*. The model results are validated using data from pilot tests on the 300-kW_{th} scale. Furthermore, we demonstrate how incorrect assumptions can lead

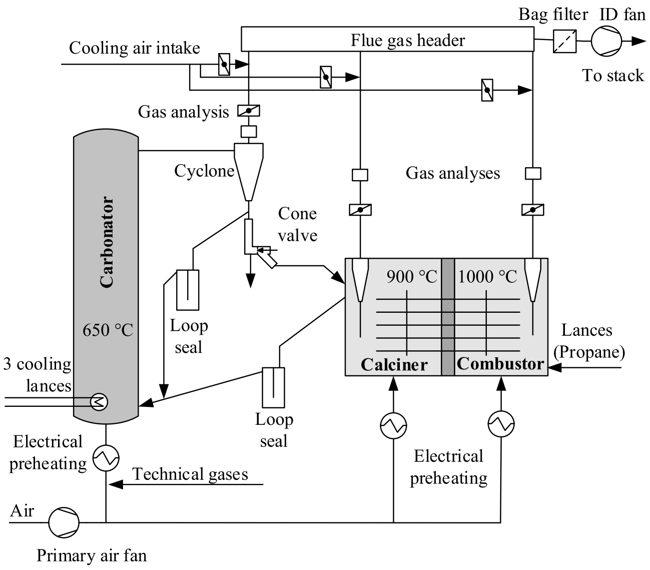

Fig. 2. Flow diagram of the pilot plant at TU Darmstadt for the investigation of the indirectly heated carbonate looping (IHCaL) process. The main reactors are shaded. The carbonator, which is the object of this study is shaded in red.

Table 1
Operating conditions for each test campaign within the pilot testing of the 300-kW$_{th}$ pilot plant, with data from Reitz [51].

Campaign no.	**Synthetic flue gas composition at carbonator inlet**				**Limestone (sorbent)**
	CO_2 (vol%$_{wb}$)	**H_2O (vol%$_{wb}$)**	**SO_2 (ppm$_{wb}$)**	**Air (vol%)**	
C1*	13–15	–	–	Rest	Messinghausen fine
C2	13–14	–	–	Rest	Messinghausen fine
C3	6–13	6–10	0–800	Rest	Messinghausen fine
C4*	11–13	4–10	0–600	Rest	Messinghausen coarse

*Not analyzed in this work.

to significant overprediction of carbonator performance and provide guidelines for selecting assumptions appropriately. Finally, we discuss the implications of our discoveries. The *particle sub-model*, including particle kinetics and sorbent deactivation, is explained in Part II [44]. Our model serves as a platform for scaling up both conventional CaL technology and new-generation CaL processes, such as IHCaL [27,45–49].

2. Experimental methods

In this work, experimental data from pilot testing at the 300-kW$_{th}$ IHCaL pilot plant of the TU Darmstadt was used as the reference for the model development. The pilot rig is illustrated in Fig. 2. It is composed of three reactors: a carbonator for CO_2 capture, a calciner for sorbent regeneration, and a combustor for heat generation. The carbonator is an eight-meter-high circulating fluidized bed (CFB) with an internal diameter (ID) of 250 mm. Heat is transferred into the calciner via heat pipes. A *cone valve* is located downstream of the carbonator to control the sorbent circulation rate. Solid sorbent can be extracted discontinuously from the cone-valve arrangement for sampling. A detailed explanation of the experimental setup can be found elsewhere [25,26,50,51].

Reitz [51] reported the results of the first four test campaigns of the IHCaL pilot plant at TU Darmstadt. In our study, we analyze the results from the second campaign (C2) and the third campaign (C3), due to the much higher availability of solid samples, compared to the other campaigns (C1 and C4). The sorbent for CO_2 capture was Messinghausen limestone, which is the same one that was utilized in previous tests of the 300-kW$_{th}$ IHCaL pilot plant and the 1-MW$_{th}$ CaL pilot facility, both at TU Darmstadt. Two grindings of Messinghausen limestone were used as sorbent for CO_2 capture: coarse (ca. 300 – 700 µ m) and fine (ca. 100 – 300 µm). For campaigns C1, C2, and C3, fine limestone was utilized. For the last campaign, the sorbent was continuously replaced by adding coarse limestone. Because of this, the PSD of the sorbent was not constant within the first half of C4 [51]. An overview of the operating conditions for each campaign is presented in Table 1.

The particle size distribution (PSD) of the fresh material and the spent sorbent are included in Fig. 3. The PSD of the used material was obtained from solid samples taken during operation from the cone valve located downstream of the carbonator (see Fig. 2). Due to attrition, the particles tend to reduce their size, and due to elutriation, smaller particles exit the system faster than bigger particles. This explains the displacement of the curves of spent sorbent in Fig. 3. For the case of fine limestone, the elutriation effect is so strong, that the particles in the system are bigger than the fresh particles. For coarse limestone, most particles under 150 µm are entrained and leave the system. Nevertheless, due to attrition, the big particles become smaller, resulting in a reduction of the mass-median particle diameter ($d_{p,50}$). Both limestone grindings (fine and coarse) had the same composition, reported in Table 2.

For the reactor modeling, the mass-median diameter ($d_{p,50} = 227$ µm) of the used sorbent was selected as the characteristic diameter, because it represents better the operating conditions inside of the reactor, compared to the fresh sorbent. The PSD is narrow (see Fig. 3, left, and cf. [52]) and exhibits a Gaussian distribution. Therefore, we do not expect a significant effect of the PSD in the determination of the fluidization regime or the gas–solid contact efficiency [53]. For wider PSDs, the transition into the turbulent regime (see Section 3.1.1) occurs earlier and the reactor performance in terms of CO_2 capture could be enhanced. Lastly, the PSD can influence the entrainment rate significantly [54].

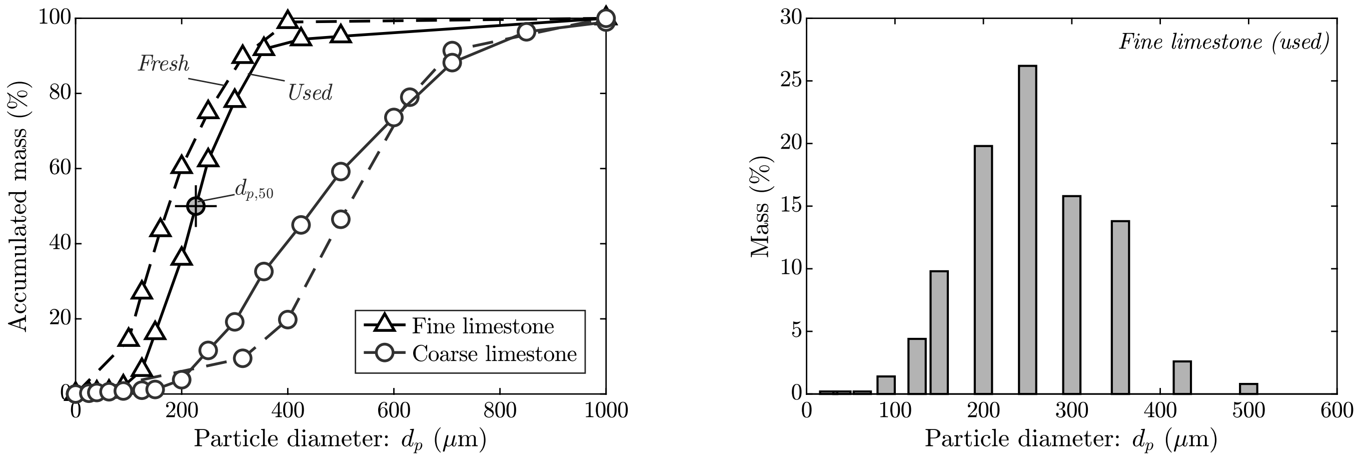

Fig. 3. Particle size distribution of the limestone used in the pilot tests. Data of fresh material provided by Lhoist [51]. Data from used sorbent collected from PSD analysis of solid samples from the pilot tests. All data is presented in terms of accumulated mass on the left. The PSD of the fine limestone from solid samples in terms of mass fraction is presented on the right.

Table 2
Composition of the Messinghausen limestone utilized as the sorbent in this work.

Component	Mass fraction (wt.%)
$CaCO_3$	98.3
$MgCO_3$	0.7
SiO_2	0.7
Al_2O_3	0.2
Fe_2O_3	0.1
SO_3	< 0.1

Adopted from [27].

To account for the actual surface area of the particles, we consider the particle sphericity in our calculations. For the kinetic model, the specific surface area is calculated according to Grasa et al. [55], as explained in Part II [44]. The particles were assumed to be isotropically shaped. Particle sphericity (Φ_s) and voidage at minimum fluidization ($\varepsilon_{\mathrm{mf}}$) were set to: $\Phi_s = 0.67$ (this coincides with [56]) and $\varepsilon_{\mathrm{mf}} = 0.54$. This assumptions are based on empirical data from Kunii and Levenspiel [37, p.69], considering brittle fracture. This last consideration should be qualified. On the one hand, brittle fracture is common for $CaCO_3$ [57], on the other, the complex attrition phenomena in a CaL system is dependent on several variables such as sulphation degree, residence time in the system, and sorbent properties after calcination (see [58,59,60]). The modeling of attrition and entrainment was out of the scope of our work. The reader interested in these topics is referred to the work of Haaf et al. [61].

3. Carbonator model

In this section, the modeling of the carbonator is described. The carbonator model is divided into the following sub-models:

a. *Hydrodynamics sub-model* to calculate the solids distribution in the reactor (Section 3.1)
b. *Reactor sub-model* to calculate the CO_2 absorption rate in the carbonator (Section 3.2)
c. *Particle sub-model* (or *reaction sub-model*) to calculate the particle carbonation degree (Part II [44])

In this work (Part I), we develop the hydrodynamics and the reactor sub-models. The particle sub-model, including considerations on reaction kinetics and sorbent deactivation, is based on the work of Romano [40]. The average conversion in the reactor is calculated considering the particle residence time distribution (RTD) and the calcination performance. The particle sub-model is discussed and validated in Part II [44].

3.1. Hydrodynamics sub-model

The main objective of the hydrodynamics sub-model is to simulate the solids distribution within the circulating-fluidized-bed carbonator for relevant operating conditions. Throughout the investigations reported in this study, it was observed that the carbonator hydrodynamics have a significant impact on the CO_2 capture capacity of the system.

3.1.1. Characterization of operating conditions

The first step in modeling a fluidized bed reactor is the characterization of the particles and the mapping of the operating regime. A first approximation to the particle characterization can be made with a *Geldart diagram* [62] (see Fig. 4).

The Geldart diagram in Fig. 4 illustrates the mapping of the particle behavior, indicating a sand-like behavior for our pilot tests. This diagram is valid for ambient operating conditions and air fluidization [37].

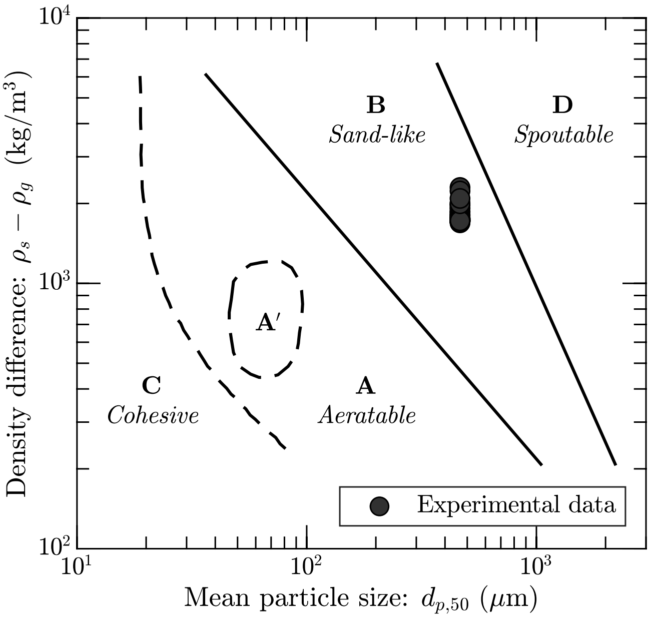

Fig. 4. Geldart diagram, adapted from [37,62]. The operating conditions corresponding to the pilot data is indicated with red dots.

For other conditions, the Geldart classification can be verified using the dimensionless particle diameter (d_p^*), which is calculated from the Archimedes number (Ar):

$$\mathrm{Ar} = \frac{d_p^3 \rho_g (\rho_s - \rho_g) g}{\mu^2} \tag{1}$$

$$d_p^* = \mathrm{Ar}^{1/3} \tag{2}$$

In Eq. (1), d_p is the particle diameter, μ is the dynamic viscosity of the gas, g is the gravitational constant, ρ_g is the gas density, and ρ_s is the apparent density of the solid particles. The gas constants (ρ_g and μ) are calculated for each balance point considering the carbonator operating conditions and the gas composition at the reactor inlet [63]. With these parameters, Eq. (2) yields $d_p^* \approx 3.8$. The boundary between A and B Geldart classification, $\left(d_p^*\right)_{AB}$, for conditions other than ambient and gases other than air can be obtained with Eq. (3) [37, p.88], which gives $\left(d_p^*\right)_{AB} \approx 2.83 < d_p^*$. Consequently, the solid sorbent presents Geldard-B-type particle behavior in the operating conditions of our pilot tests, in agreement with Fig. 4.

$$\left(d_p^*\right)_{AB} = 101 \cdot \left(\frac{\rho_g}{\rho_s - \rho_g}\right)^{0.425} \tag{3}$$

In previous publications, the carbonator of the 300-kW$_{\mathrm{th}}$ pilot plant has been described as a “circulating fluidized bed” [25,26,64]. However, the designation *circulating fluidized bed* (CFB) corresponds to a mode of operation compatible with different fluidization regimes [65–67], including pneumatic conveying, fast fluidization, turbulent fluidization, and even bubbling fluidization [67,68]. A comprehensive understanding of the fluidization regime is crucial to characterize the reactor behavior and develop accurate models. This aspect is elaborated hereunder.

The characterization of the fluidization regime of a fluidized bed reactor is generally performed with the so-called *Grace diagram* [69] (see Fig. 5). The Grace diagram allows mapping the fluidization regimes based on two dimensionless variables —namely, the dimensionless diameter from Eq. (2), and the dimensionless superficial gas velocity, calculated with Eq. (4).

$$u_0^* = \mathrm{Re_p}/d_p^* \tag{4}$$

Here the particle Reynolds number ($\mathrm{Re_p}$) is defined as:

$$\mathrm{Re_p} \equiv d_p u_0 \rho_g / \mu \tag{5}$$

In Eq. (5), u_0 is the superficial gas velocity. It is calculated using the experimental data of the volume flow rate at carbonator inlet, the ideal gas law, and the spatial average temperature and pressure of the reactor.

According to the Grace diagram in Fig. 5, the operating conditions of the data from pilot tests correspond mainly to the turbulent fluidization. In the last decades, this regime has been recognized as ranging between a transitional superficial gas velocity (u_c) and the onset of fast fluidization [72]. It is distinct from the bubbling and the fast fluidization regimes.

The Grace diagram is generated using correlations available in the open literature. For the calculation of the superficial gas velocity at minimum fluidizing conditions (u_{mf}), the general equation from Kunii and Levenspiel is considered [37, p.69]:

$$\frac{1.75}{\varepsilon_{\mathrm{mf}}^3 \Phi_s}\mathrm{Re}_{\mathrm{p,mf}}^2 + \frac{150\left(1-\varepsilon_{\mathrm{mf}}\right)}{\varepsilon_{\mathrm{mf}}^3 \Phi_s^2}\mathrm{Re}_{\mathrm{p,mf}} - \mathrm{Ar} \ = \ 0 \tag{6}$$

Here, $\mathrm{Re}_{\mathrm{p,mf}}$ is the particle Reynolds number at minimum fluidizing conditions, calculated by replacing u_0 with u_{mf} in Eq. (5). Since this equation depends on the voidage at minimum fluidizing conditions and the sphericity of the particles, the result is a surface in Fig. 5, instead of a curve. To draw the surface, we assume the following boundaries for the constants: $\varepsilon_{\mathrm{mf}} = 0.45$–$0.55$; and $\Phi_s = 0.65$–0.75. The red dashed line corresponds to the calculations with the operating conditions of this work: $\varepsilon_{\mathrm{mf}} = 0.54$; and $\Phi_s = 0.67$.

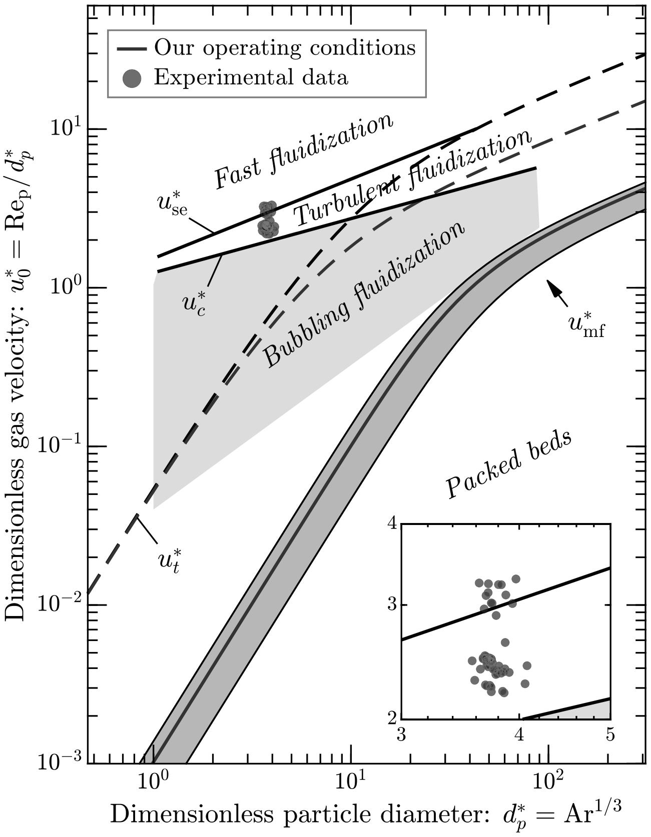

Fig. 5. Grace diagram based on [37,70,71] with fitting equations from [37,70], and data from pilot tests [51]. The red lines indicate the boundaries for the operating conditions of our work. The red dots indicate the operating conditions of the balance points from the pilot tests. A close-up view of the same diagram is included in the bottom-right corner.

The terminal velocity (u_t) is calculated with the expression from Haider and Levenspiel [73]:

$$u_t^* = \left(\frac{18}{\mathrm{Ar}^{2/3}} + \frac{2.3348 - 1.7439\,\Phi_s}{\mathrm{Ar}^{1/6}}\right)^{-1} \tag{7}$$

In Fig. 5, the terminal velocity calculated with $\Phi_s = 1$ is indicated in black. The value calculated using $\Phi_s = 0.67$, i.e., the condition assumed in our work, is displayed in red.

The turbulent regime is generally characterized for exhibiting high bubble *coalescence* [72,74]. The transition superficial gas velocity from bubbling or slugging to turbulent regime (u_c) is defined as the superficial gas velocity that maximizes the standard deviation of pressure fluctuations [72]. This definition is widely regarded as the standard for establishing the onset of turbulent regime. For the calculation of u_c, the following correlation from Bi and Grace [75] is used:

$$\mathrm{Re_c} = 1.243\ \mathrm{Ar}^{0.447} \tag{8}$$

This gives $u_c^* \approx 2$ for the operating conditions considered in this work (see Fig. 5). Cai [76] found that the transition velocity u_c depends on the reactor ID, but only for small columns (<0.2 m) (see also [77,78]). Our pilot facility has an ID of 0.25 m; thus, we do not expect such dependency in the context of this work.

There are numerous correlations for u_c^* available [72]; however, further research is needed to predict this velocity reliably [77]. The correlation of Eq. (8) is regarded as one of the most accurate in predicting empirical data [72] and is generally used to plot the Grace diagram. The postulated correlations are also dependent on the measuring techniques [75]. Results from differential pressure fluctuations, such as the ones used to obtain the correlation of Eq. (8) (see [79]), give higher values of u_c than results from absolute pressure fluctuations for the same operating conditions. Internals were found to reduce u_c because they promote the breakup of bubbles and restrict bubble size, thus facilitating the transition to turbulent fluidization [80]. There are three 1.5-m cylindrical cooling lances (see Fig. 2) installed in the bottom section of the carbonator, which may reduce the transition velocity to values lower than $u_c^* \approx 2$. Consequently, it is safe to assume that the carbonator operates above the bubbling fluidization regime (see Fig. 5).

Contrary to the transition from the bubbling regime into the turbulent regime, there is more than one criterion for the definition of the transition velocity into the fast-fluidization regime. In this work, we follow Bi et al. [72], who suggest using the critical velocity based on *solid entrainment* (u_{se}). This parameter was found to be independent of the reactor dimensions, and mainly depends on the properties of the gas and the particles (i.e., Ar) [72,79]. We use the correlation of Bi et al. [79], which gives $u_{\text{se}}^* \approx 3$ for the operating conditions of our pilot plant.

$$\text{Re}_{\text{se}} = 1.53\ \text{Ar}^{0.5} \tag{9}$$

Eq. (9) was used to correlate empirical data successfully. For large particles, when the expression gives values of u_{se}^* higher than the terminal velocity (u_t^*), the authors suggested taking these velocities as equal ($u_{\text{se}}^* = u_t^*$).

Overall, the analysis of this section reveals that the operating conditions of the plant correspond mostly to the higher boundary of the turbulent fluidization regime. Previous studies usually associate turbulent regimes with gas velocities of 1–3 m/s, and even lower [72]. This is because most of the experimental data corresponds to trials using air at ambient temperature for the fluidization. Due to the high temperatures in the carbonator of our pilot plant, the gas density is reduced, thus yielding lower Re_p, which explains the turbulent regimes in our range of operation ($u_0 \cong 4$ m/s). Notwithstanding the above, our calculations suggest that some empirical operating points are past the fast-fluidization-onset limit (see Fig. 5).

3.1.2. Solids distribution

The solids axial distribution inside of the carbonator operating as a circulating fluidized bed is sometimes computed using an exponential decay model developed by Kunii and Levenspiel [37] (e.g., [36,40,42,61,81]). The corresponding equations consider the average solid concentration within each cylinder of differential height (dz), denoted as $\varepsilon_s(z)$, representing the solid concentration value averaged over the cross section.[1] The decay model is formulated mathematically as follows:

$$\begin{cases} \varepsilon_s(z) = \varepsilon_{s,d}; & z \leqslant H_d \\ \dfrac{\varepsilon_s(z) - \varepsilon_s^*}{\varepsilon_{s,d} - \varepsilon_s^*} = \exp[-a(z - H_d)]; & z > H_d \end{cases} \tag{10}$$

This equation is valid for heights (z) lower than the *Transport Disengaging Height* (TDH). The expression for $z > H_d$ can be rewritten as:

$$-\ln\left(\frac{\varepsilon_s(z) - \varepsilon_s^*}{\varepsilon_{s,d} - \varepsilon_s^*}\right) = a(z - H_d); \quad z > H_d \tag{11}$$

Here, z is the axial coordinate increasing from zero (at the reactor inlet) to H_T (at the reactor outlet), and ε_s^* and $\varepsilon_{s,d}$ are the saturated solid concentration and the dense-region solid concentration, respectively. The value of $\varepsilon_{s,d}$ depends mainly on the fluidization regime, as well as on parameters such as the superficial velocity, the particle density, and the riser diameter [82,83]. Despite the availability of some correlations, the determination of this parameter still relies on empirical data (see Table 3 and Section 4.1.1). The decay constant a is calculated following Lewis et al. [84] (Eq. (12)), who discovered that a variates linearly with u_0.

$$k_{\text{Lewis}} \equiv a\ u_0 \tag{12}$$

At this point it is important to highlight that the authors indicated a dependency of the *Lewis constant* (k_{Lewis}) with the reactor diameter and particle type. This dependency is typically overlooked in carbonator modeling.

The exponential decay model of Eqs. (10–12) has a simple formulation that relies on the input of three parameters —namely ε_s^*, $\varepsilon_{s,d}$, and the Lewis constant (k_{Lewis}). If these parameters are selected appropriately, the model allows predicting empirical results accurately with low computational effort [32,41]. This is why it has been selected by many authors for modeling the carbonator. We also follow this approach.

The values of $\varepsilon_{s,d}$ and k_{Lewis} are usually assumed using empirical data available in the open literature. The value of ε_s^* is generally estimated from the saturated mass flux of solids (G_s^*) [37]:

$$G_s^* = \rho_s \varepsilon_s^* u_s \tag{13}$$

Eq. (13) is obtained through a mass balance at the reactor exit, where u_s is the mean velocity of the solids. This expression can be solved by approximating the slip velocity between the gas and the solid particles (u_{slip}) with u_t, and considering that $\varepsilon_s^* \ll 1$:

$$u_s \equiv \frac{u_0}{1 - \varepsilon_s^*} - u_{\text{slip}} \cong u_0 - u_t \tag{14}$$

Thus, obtaining:

$$\varepsilon_s^* \cong \frac{G_s^*}{(u_0 - u_t)\rho_s} \tag{15}$$

In previous publications, G_s^* has been calculated with the equation of Geldart et al. [85]:

$$G_s^* = 23.7 \rho_s u_0 \exp(-5.4\ u_t/u_0) \tag{16}$$

Despite the widespread of this expression within the literature on carbonator models, it is sometimes used without the required discussion. This expression was obtained in the frame of elutriation from captive fluidized beds, for particle size between 60 and 350 μ m, and two riser IDs were considered (0.076 and 0.30 m). The velocities of the experiments were 0.6–3 m/s. Kunii and Levenspiel [37, p.178] collected different expressions to estimate G_s^*, which are valid for various ranges of operating conditions. Eq. (16) was developed to estimate the elutriation from fluidized beds. A rigorous calculation would require the integration of this expression for the entire PSD of particles inside the reactor (see [37, p.174]). This is generally not done, probably because the value ε_s^* is mainly used to estimate the height of the dense region and does not appear to have a strong impact on the results of CO_2 capture. For simplicity, we use Eq. (16), assuming particles of constant size $d_{\text{p},50}$ (see Fig. 3), and compare the results of ε_s^* with empirical data for validation (see Section 4.1.1).

Eq. (10) is used to calculate the height of the dense region (H_d) and the lean region (H_l), thus obtaining the complete solids distribution across the height of the reactor. Romano[2] [40] expressed the material balance to achieve this as follows:

---

[1] The *solid concentration* is also known as the *solid volume fraction* or *volume fraction of solids*. In our work we use the first two designations interchangeably.

[2] The expression reported by Romano [40, Eq. (12)] has a minor mistake. Here, we present the corrected version.

Table 3
Empirical constants to compute solids axial and radial distribution.

	Solid concentration				Lewis constant
	Dense region $\varepsilon_{s,d}$	Saturation ε_s^*	Core‡ $\varepsilon_{s,c}$	Wall‡ $\varepsilon_{s,w}$	(see Eq. (12)) $k_{\mathrm{Lewis}} \equiv a\,u_0$ (s^{-1})
Model assumptions					
Hawthorne et al. (2008) [91,92]	0.23–0.25	–	0.01	0.037	n/a
Ströhle et al. (2009) [81]	0.16	Eq. (16)	0.01	0.15	3.0
Lasheras et al. (2011) [36]	0.16	Eq. (16)	0.01	0.15	3.0
Romano (2012) [40]	0.15	0.01	0.01	0.5	3.0
Atsonios et al. (2015) [32]	0.15	0.032 ($\overline{\varepsilon_{s,l}}$)	n/a	n/a	n/a
Cormos and Simon (2015) [93,94]	0.25 (TF†); 0.16 (FF†)	Eq. (16)	n/a	n/a	4.0
Sattari et al. (2021) [88]	0.16	Eq. (16)	0.01	0.15	3.0
Empirical data – Various test rigs					
Kunii and Levenspiel (1991) [37]	0.40–0.55 (BF†); 0.22–0.40 (TF†); 0.16–0.22 (FF†)	0.01 [95]	0.01	0.1–0.2; $\delta_{\mathrm{reactor}} = 0.6$–$0.9$	2–5 ($d_p < 70$ μm); 4–12 ($d_p > 88$ μm)
Kunii and Levenspiel (1997) [65]	0.20–0.40 (TF†); 0.06–0.20 (FF†)	≤ 0.02 (A†); ≤ 0.01 (B†)	–	–	2–4 (A†); 5 (AB†); 7 (B†)
Bi et al. (2000) [72]	0.25–0.35 (TF†)	–	–	–	–
This work					
Model assumptions	0.30	Eq. (16)	$\cong \varepsilon_s^*$	$\cong \varepsilon_{\mathrm{mf}}$	8.0
Pilot plant data (TU Darmstadt)	0.2–0.4	0.002–0.008 ($\varepsilon_{s,out}$)	–	–	4–17

†BF: bubbling fluidization; TF: turbulent fluidization; FF: fast fluidization; A, AB, B: Geldart A, AB, B particles.
‡Of the dense region

$$\frac{W_{\mathrm{carb}}}{A_t \rho_s} = H_d \varepsilon_{s,d} + \int_{H_d}^{H_T} \varepsilon_s^* + \left(\varepsilon_{s,d} - \varepsilon_s^*\right) \exp(-a(z - H_d))\, dz \tag{17}$$

Here, A_t is the internal section area of the carbonator, and W_{carb} is the inventory of the carbonator, which is calculated using the pressure drop measured across the reactor. Solving the integral gives (see Appendix A):

$$\frac{W_{\mathrm{carb}}}{A_t \rho_s} = \frac{\varepsilon_{s,d} - \varepsilon_{\mathrm{s,out}}}{a} + H_T\, \varepsilon_{s,d} - H_l\left(\varepsilon_{s,d} - \varepsilon_s^*\right) \tag{18}$$

This is exactly the same expression obtained by Lasheras et al. [36] with an approximation. Here, $\varepsilon_{\mathrm{s,out}} = \varepsilon$ ($z = H_T$) is computed with Eq. (10). Because of the exponential term, this equation should be solved numerically. We use the Newton-Raphson method for this purpose [36,86]. For high reactors —i.e., H_T higher than the *Transport Disengaging Height* (TDH) [87]— Eq. (18) can be approximated as:

$$H_d \cong \frac{W_{\mathrm{carb}}}{A_t\, \rho_s}\left(\varepsilon_{s,d} - \varepsilon_s^*\right)^{-1} - \frac{1}{a} \tag{19}$$

For our reactor, Eq. (19) approximates Eq. (18) with an absolute error of around 60 mm for the balance points, with $H_d \approx 1$ m. This may be acceptable for some applications, but we decided to use Eq. (18) for our model calculations, considering the significant influence of the solids distribution in the CO_2 capture.

Knowing the solids distribution, the specific entrainment rate (G_s) can be calculated from the solid concentration at exit, using an equation analogous to Eq. (15):

$$G_s \cong \mathrm{P}_{\mathrm{ent}}\, \varepsilon_{\mathrm{s,out}} (u_0 - u_t) \rho_s \tag{20}$$

Here, $\mathrm{P}_{\mathrm{ent}}$ is the probability of entrainment, which depends mainly on the reactor outlet geometry and the particle velocity (u_s). A thorough discussion of this matter, as well as correlations for $\mathrm{P}_{\mathrm{ent}}$, is available in the study of Dieringer et al. [54]. An accurate prediction of G_s would have to consider the influence of the entire PSD (see [37, p.174]). This is beyond the scope of our study.

The radial distribution in the fluidized bed is illustrated in Fig. 6. It is modeled as having a central zone or *core*, lean in solids, and an outer annulus or *wall* region, having a much higher solid concentration [35]. The core diameter is constant for the dense region, while it increases in the lean region following the decay of solid concentration.

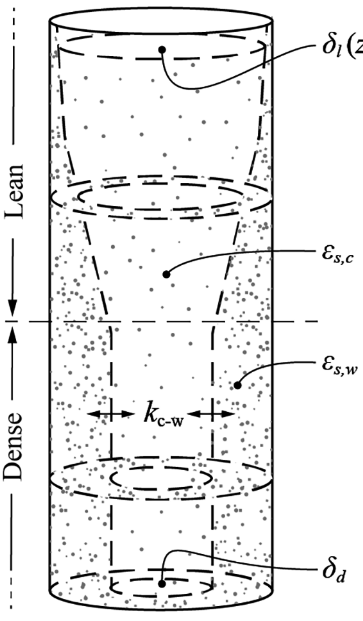

Fig. 6. Core-wall distribution of solids in our study, based on the work of Kunii and Levenspiel [35].

For the calculation of the CO_2 capture, the core volume fraction (δ) needs to be estimated. Considering the core diameter (d_c) at any height z and the reactor internal diameter (d_T), the core volume fraction at height z can be expressed as:

$$\delta(z) = \frac{(\pi/4)\; d_c^2(z)\; dz}{(\pi/4)\; d_T^2\; dz} \tag{21}$$

From Eq. (21), the relation between the core diameter and the reactor diameter can be established:

$$d_c(z) = d_T\sqrt{\delta(z)} \tag{22}$$

This expression is useful to estimate the core-wall gas interchange coefficient (see Section 3.2.4). An expression relating the core volume fraction and the solids fractions can be achieved with a mass balance of any section of the reactor [65]:

$$\delta(z) = \frac{\varepsilon_{s,w} - \varepsilon_s(z)}{\varepsilon_{s,w} - \varepsilon_{s,c}} \tag{23}$$

The constants $\varepsilon_{s,c}$ and $\varepsilon_{s,w}$ represent the solid volume fraction in the core and the wall (annulus) of the dense region, respectively. Thes constants are generally approximated with the saturation and the minimal-fluidization solid volume fractions, respectively [35,65]:

$$\varepsilon_{s,c} \cong \varepsilon_s^* \tag{24}$$

$$\varepsilon_{s,w} \cong \varepsilon_{s,\mathrm{mf}} \tag{25}$$

These two approximations are commonly used in KL models and in carbonator models (e.g., [40,88]). We are aware that axial variations in core and wall solid concentrations have been reported for circulating fluidized beds in general [89] and for a CaL carbonator [90] in particular. However, for the sake of simplicity, we follow the same approach as previous KL carbonator models (i.e., Eqs. (24) and (25)). Detailed modeling of the radial distribution in the carbonator was outside the scope of our work but could be the subject of further research.

For the dense region, the core diameter is assumed constant (see Fig. 6), thus, from Eq. (23):

$$\delta_d = \frac{\varepsilon_{s,w} - \varepsilon_{s,d}}{\varepsilon_{s,w} - \varepsilon_{s,c}} \tag{26}$$

The mean core volume fraction of the lean region ($\overline{\delta_l}$) is obtained integrating Eq. (23) over H_l:

$$\overline{\delta_l} = \frac{\varepsilon_{s,w} - \overline{\varepsilon_{s,l}}}{\varepsilon_{s,w} - \varepsilon_{s,c}} \tag{27}$$

Here, $\overline{\varepsilon_{s,l}}$ is the mean solid concentration in the lean region, which is calculated by integrating Eq. (10) over H_l:

$$\overline{\varepsilon_{s,l}} = \varepsilon_s^* + \left(\varepsilon_{s,d} - \varepsilon_s^*\right)\frac{1 - \exp(-aH_l)}{aH_l} \tag{28}$$

The constant $\varepsilon_{s,d}$ is the mean solid volume fraction in the dense region. Using our input values (Table 3), we obtain $\delta_d \approx 0.35$, which is lower than the values generally assumed for carbonator models [37].

The values of the constants used to determine the solids distribution in the models using the exponential-function approach are presented in Table 3. Other reference values from the literature are also included, as well as the values used in our model and the ones obtained from the pilot plant data.

The values assumed for $\varepsilon_{s,d}$ are generally low (0.15–0.16) and correspond to the lower boundary for the fast fluidization regime [33]. Cormos and Simon [93,94] evaluated their model for fast and turbulent fluidization, setting $\varepsilon_{s,d}$ equal to 0.16 and 0.25, respectively. Hawthorne et al. [91] used 0.23–0.25, which corresponds to the lower boundary of the values recommended for the turbulent regime [37,65,72]. From our experimental results, we assume $\varepsilon_{s,d} = 0.30$, which is considerably higher than the values used in other carbonator models. The validity of our assumption is defended in Section 4.1.1. The consequences of this assumption are discussed in Section 4.2.

Within the carbonator models using the exponential descriptions of Eq. (12), there is consensus in the assumption for the Lewis constant, k_{Lewis}. The values reported in the reviewed references are 3.0–4.0 s^{-1} (see Table 3). This consensus contrasts with the wide ranges reported in the literature —dependent on the particle size [37,65] and the reactor diameter [84]—, which appear to indicate that the values of k_{Lewis} are generally adopted from previous models without considering the specific operating conditions of the capture process. This is notable considering that prominent references on fluidizations recommend higher values for coarse particles [37,65], as the ones normally used in CaL [16,29,96–99]. In our work, we adopt $k_{\mathrm{Lewis}} = 8.0\ \mathrm{s}^{-1}$, consistent with empirical data from our pilot plant (see Section 4.1.1).

For the computation of ε_s^*, the common approach is to use Eq. (16). Romano [40] used a constant value of 0.01 for his calculations. Atsonios et al. [32] used a mean concentration of the lean region ($\overline{\varepsilon_{s,l}}$) obtained from the results of a CFD model. We use Eq. (16) in our model and obtain good predictions of empirical data (see Section 4.1.1).

3.2. Reactor sub-model

The CO_2 capture in the carbonator is based on the carbonation reaction, which is a heterogeneous reversible reaction that follows the following equation [100]:

$$\mathrm{CO_{2(g)}} + \mathrm{CaO_{(s)}} \rightleftarrows \mathrm{CaCO_{3(s)}} \tag{29}$$

The equilibrium equation for this reaction was presented by García-Labiano et al. [101], who developed an expression based on the work of Barin [102]:

$$p_{\mathrm{CO2,eq}} = 4.137\ 10^{12}\ \exp(-20474\ \mathrm{K}/T)\ [\mathrm{Pa}] \tag{30}$$

Here, $p_{\mathrm{CO2,eq}}$ is the equilibrium CO_2 pressure, and T is the temperature in K. The carbonator reactor is modeled according to the KL-model [35] (see Fig. 6), dividing it into two zones: (i) a dense zone of height H_d, and (ii) a lean zone with height H_l (see Fig. 6). We assume a core-annulus distribution for both zones. In this section, we derive the equations to calculate the reactor gas–solid contact efficiency, which determines the reactor performance along with the global reaction rate (K_r). For this study, K_r is treated as a constant. Its calculation is a complex matter, which is discussed in Part II [44].

3.2.1. Governing equations

Since the reaction rates depend on the concentration difference with respect to the equilibrium concentration, we define the driving force $\mathfrak{C}$ according to the following expression:

$$\mathfrak{C}_i \equiv C_{\mathrm{CO2},i} - C_{\mathrm{CO2,eq}} \tag{31}$$

Here, i represents any point in the reactor, including the inlet (in), the end of the dense region (d), and the outlet (out). The equilibrium concentration ($C_{\mathrm{CO2,eq}}$) is calculated using Eq. (30) and the ideal gas law. If the temperature or pressure gradients are neglected, the equilibrium concentration can be assumed constant; thus, in derivative form, the differential of the driving force is equal to the differential of concentration:

$$d\mathfrak{C}_i \equiv d\left(C_{\mathrm{CO2},i} - C_{\mathrm{CO2,eq}}\right) = dC_{\mathrm{CO2},i} \tag{32}$$

This allows us to simplify the calculations and highlight the physical meaning of the equations that follow. From the point of view of the reactor, the CO_2 conversion in the carbonator follows a fist order reaction,[3] thus [37]:

$$\frac{dN_{\mathrm{CO2}}}{dt} = -V_{\mathrm{s,a}}K_r\mathfrak{C} \tag{33}$$

Here, N_{CO2} is the number of moles of CO_2, $V_{\mathrm{s,a}}$ is the particle volume of potentially active sorbent (CaO and $CaCO_3$) and K_r is the first-order reaction coefficient. The units of K_r are $m^3_{gas}/(m^3_{particle}\ s)$. For simplicity, s^{-1} is used. The differential equation governing the concentration variation in the reactor can be expressed considering a gas–solid contact efficiency (η) for the deviation from the ideal plug-flow reactor (see Appendix C):

---

[3] This assumption is thoroughly discussed in Part II [44].

$$d\mathfrak{C}/dz = -\eta\, K_r\, \mathfrak{C}\, \xi\, \varepsilon_s/u_0 \tag{34}$$

Where z is the reactor height, ε_s is the solid volume fraction, and ξ is the volume ratio of potentially active sorbent (CaO and $CaCO_3$) to solids —to account for inert species such as ash or $CaSO_4$ (see [40]). The particle conversion (X) can be expressed as:

$$X \equiv \frac{N_{\mathrm{CaCO3}}}{N_{\mathrm{Ca}}} = \frac{N_{\mathrm{CaCO3}}}{V_{\mathrm{s,a}}\rho_{\mathrm{s,a}}/M_{\mathrm{s,a}}} \tag{35}$$

In Eq. (35), N_{Ca} is the number of moles of CaO and $CaCO_3$, and $M_{s,a}$ and $\rho_{s,a}$ are the molar mass and apparent particle density of the potentially active solids (i.e., CaO and $CaCO_3$) in the carbonator, respectively. Assuming that the density and molar mass of solids remain constant throughout the reactor:

$$dX = \frac{dN_{\mathrm{CaCO3}}}{V_{\mathrm{s,a}}\rho_{\mathrm{s,a}}/M_{\mathrm{s,a}}} \tag{36}$$

For every mol of $CaCO_3$ generated, one mol of CO_2 disappears; thus,

$$dX\ V_{\mathrm{s,a}}\rho_{\mathrm{s,a}}/M_{\mathrm{s,a}} = -dN_{\mathrm{CO2}} \tag{37}$$

Comparing Eq. (37) with Eq. (33), an expression relating the particle and reactor sub-models is found:

$$\frac{dX}{dt}\rho_{\mathrm{s,a}}/M_{\mathrm{s,a}} = K_r\mathfrak{C} \tag{38}$$

The calculation of the density and molar mass of the potentially active solids is performed with the following equations:

$$M_{\mathrm{s,a}} = X_{\mathrm{carb}}M_{\mathrm{CaCO3}} + (1 - X_{\mathrm{carb}})M_{\mathrm{CaO}} \tag{39}$$

$$\frac{1}{\rho_{\mathrm{s,a}}} = \frac{(1 - X_{\mathrm{carb}})M_{\mathrm{CaO}}/M_{\mathrm{s,a}}}{\rho_{\mathrm{CaO,p}}} + \frac{X_{\mathrm{carb}}\ M_{\mathrm{CaO}}/M_{\mathrm{s,a}}}{\rho_{\mathrm{CaCO3,p}}} \tag{40}$$

3.2.2. *Dense region*

Applying the core-annulus K-L model [37,65], the CO_2 concentration at the end of the dense zone can be calculated by solving Eq. (34):

$$\mathfrak{C}_d = \mathfrak{C}_{\mathrm{in}}\exp(-\eta_d K_r \tau_d) \tag{41}$$

Where η_d is the gas–solid contact efficiency of the dense region and τ_d is the characteristic time of gas–solid contact in the dense region, defined as:

$$\tau_d \equiv \xi\varepsilon_{s,d}H_d/u_0 \tag{42}$$

The calculation of η_d considers the added contributions of the core and the wall zones in series. The wall region is considered stagnant; thus, a gas volume exchange is required for the reaction to take place. This is computed as an additional resistance in parallel [35]:

$$\begin{aligned}(\text{reaction in dense zone}) &= (\text{reaction in core})\\ &\quad + \left[(\text{transfer to wall})^{-1} + (\text{reaction in wall})^{-1}\right]^{-1}\end{aligned} \tag{43}$$

$$\eta_d\ \varepsilon_{s,d} = \delta_d\ \varepsilon_{s,c}\ + \left[\frac{K_r}{\delta_d\ K_{\mathrm{c\text{-}w,d}}} + \frac{1}{(1-\delta_d)\varepsilon_{s,w}}\right]^{-1} \tag{44}$$

Here, $K_{c\text{-}w}$ is the coefficient of gas interchange between the core and the wall region. This is an important parameter for the reactor sub-model, which is thoroughly discussed in Section 3.2.4.

Lasheras et al. [36] and Ströhle et al. [81] used an equation from Kunii and Levenspiel [37, Eq. 12.66] to model the contact efficiency in the dense region. However, in the primary source, the volume fraction of bubbles and the core volume fraction were both named with the same symbol (i.e., δ). This led to an inadequate derivation of the gas–solid contact equations. Therefore, we do not recommend using their approach to calculate the CO_2 absorption in the dense region (i.e., [36, Eqs. (21–23)]).

3.2.3. *Lean region*

The calculation of the carbonation in the freeboard is performed considering an equivalent contact efficiency of the lean region (η_l^*):

$$\mathfrak{C}_{\mathrm{out}} = \mathfrak{C}_d\exp(-\eta_l^* K_r\tau_l) \tag{45}$$

Here, the characteristic time of the lean region (τ_l) is calculated analogously to that of the dense region. Since the solid volume fraction varies throughout the lean region, the mean value is used; thus,

$$\tau_l \equiv \xi\overline{\varepsilon_{s,l}}H_l/u_0 \tag{46}$$

We consider the approach from Kunii and Levenspiel [35] to obtain η_l^*, proceeding analogously as we do for the dense region (see Section 3.2.2 and Eq. (43)):

$$\overline{\varepsilon_{s,l}}\eta_l^* = \overline{\delta_l}\ \varepsilon_{s,c}\ + \left[\frac{K_r}{\overline{\delta_l}\ K_{\mathrm{c\text{-}w,l}}} + \frac{1}{(1-\overline{\delta_l})\varepsilon_{s,w}}\right]^{-1} \tag{47}$$

Here, $\overline{\delta_l}$ and $\overline{\varepsilon_{s,l}}$ are obtained from Eqs. (27) and (28), respectively. Using Eqs. (41) and (45), the outlet concentration is obtained:

$$\mathfrak{C}_{\mathrm{out}} = \mathfrak{C}_{\mathrm{in}}\exp(-K_r\tau_T^*) \tag{48}$$

$$\tau_T^* \equiv \eta_d\tau_d + \eta_l^*\tau_l \tag{49}$$

Here, τ_T^* is an equivalent gas residence time for the entire reactor, considering hydrodynamics. It can be used to study the influence of the inputs in the reactor performance (derivation in Appendix D):

$$1 - \mathfrak{C}_{\mathrm{out}}/\mathfrak{C}_{\mathrm{in}} = 1 - \exp(-K_r\tau_T^*) \approx E_{\mathrm{carb}}/E_{\mathrm{carb,eq}} \tag{50}$$

In this expression, E_{carb} is the carbonator efficiency defined as the ratio of the molar rate of CO_2 captured in the carbonator to the total amount of CO_2 entering the carbonator [21]. The maximum achievable carbonator efficiency due to equilibrium limitations is denoted with $E_{carb,eq}$. Another approach, used in some carbonator models [40,42], considers an exponential decay for the contact efficiency in the lean region. This approximation is based on the experiments by Furusaki et al. [103], who studied the hydrogenation of ethylene at 140 °C, with a reactor of $d_T = 53$ mm and $H_T = 0.13$ m. They used an impregnated nickel catalyst of $d_{p,50} = 62$ μm. Kunii and Levenspiel [37, p.283,65] presented the following equation based on their empirical data:

$$\eta_l(z) = 1 - (1-\eta_d)\exp(-bz) \tag{51}$$

This expression fitted the data satisfactorily for $b = 6.62\ m^{-1}$. CaL operating conditions are far from those of the experiments of Furusaki's team; thus, the application of this fitting into a carbonator model is questionable. Despite the widespread use of this fitting for carbonator models, we recommend caution when using Eq. (51) and the expressions derived. These are presented hereunder for comparison purposes. Following this approach, the equivalent efficiency throughout the lean region is obtained using Eq. (10) and integrating Eq. (51):

$$\overline{\varepsilon_{s,l}}\ \eta_l^* = \overline{\varepsilon_{s,l}}\ - \varepsilon_s^*(1-\overline{\eta_l}) - (\varepsilon_{s,d} - \varepsilon_s^*)(1-\eta_d)\frac{1-\exp(-(a+b)\ H_l)}{(a+b)H_l} \tag{52}$$

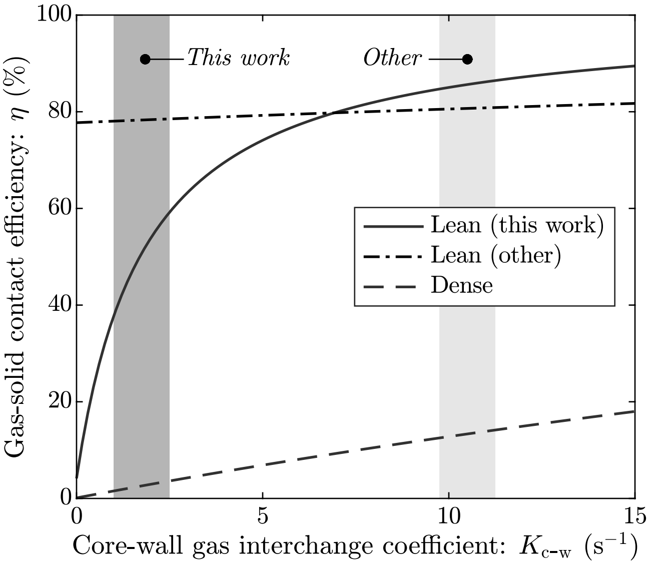

Fig. 7. Contact efficiency for the lean and dense regions with varying $K_{\text{c-w}}$. Our results for the lean region using our model, i.e., Eq. (47) are compared to those of other models, calculated with Eq. (52). The shaded areas represent the values of $K_{\text{c-w}}$ obtained with our assumptions and operating conditions (left) and those normally used in carbonator models(right).

An expression for the mean contact efficiency ($\overline{\eta_l}$) is obtained by integrating the distribution from Eq. (51) over the height of the lean region:

$$\overline{\eta_l} = 1 - (1 - \eta_d)\frac{1 - \exp(- bH_l)}{bH_l} \tag{53}$$

An equation analogous to Eq. (52) was used by Romano in his carbonator model [40]. Results using Eq. (47) are similar to those from Eq. (52) for some operating conditions. However, there are considerable differences between the models when some input parameters are changed, as illustrated in Fig. 7 for varying $K_{\text{c-w}}$.

3.2.4. *Core-wall gas interchange coefficient*

The state-of-the-art carbonator models generally assume $K_{\text{c-w}} \approx 10$ s^{-1} [36,40]. This practice appears to follow a convention rather than an assumption based on empirical data, probably from the suggestion of Kunii and Levenspiel (1991) [37, p.309] that $K_{\text{c-w}} > 11\ \text{s}^{-1}$. The authors explained that this value resulted from preliminary estimates. In the literature, lower values were reported by Kruse et al. [104], who determined that $K_{\text{c-w}} = 0.3\ \text{s}^{-1}$ for sand particles in a dilute circulating fluidized bed. This value was adopted by Kunii and Levenspiel (2000) [35] for their calculations on circulating fluidized beds using the K-L model in a more up-to-date work [65]. Levenspiel [105] admitted in 1999 that empirical values of $K_{\text{c-w}}$ were still missing and recommended estimating its order of magnitude from the bubble-cloud and cloud-emulsion exchange coefficients ($K_{\text{b-c}}$, $K_{\text{c-e}}$) of the bubbling fluidized bed, thus $K_{\text{c-w}} \sim K_{\text{b-e.}}$ However, this neglects the different nature of the fast and turbulent fluidization regimes, for which the bubble-emulsion mechanism is not valid and most of the gas bypasses as throughflow.

The coefficient $K_{\text{c-w}}$ is sometimes adopted as a constant in the literature. Nevertheless, this is disadvantageous, considering the expected dependency on the interface area, which can even change in the same facility —e.g., for varying inventory. The specific core-wall area ($a_{\text{c-w}}$) can be calculated with (see Appendix B):

$$a_{\text{c-w}} = 4\ d_c\ d_T^{\ -2} \tag{54}$$

Using this expression, $K_{\text{c-w}}$ can be calculated from the geometry of the core, assuming a cylindrical geometry for the dense zone and a conical geometry for the lean zone (see Appendix B):

$$K_{\text{c-w}}\ \equiv k_{\text{c-w}}\ a_{\text{c-w}} \tag{55}$$

$$K_{\text{c-w,d}}\ = k_{\text{ c-w}}\ 4\ \delta_d^{0.5}\ d_T^{-1} \tag{56}$$

$$K_{\text{c-w,l}}\ = k_{\text{c-w}}\ 2\left(\delta_d^{0.5} + \delta_{\text{out}}^{0.5}\right)\ d_T^{-1} \tag{57}$$

Here, $k_{\text{c-w}}$ is the specific core-wall dispersion coefficient, which is estimated from empirical data reported by Yang [106, p.521], adopting the mean value: $k_{\text{c-w}} = 0.158$ m/s. The obtained values of $K_{\text{c-w}}$ are compared with those reported in the literature, for validation. The assumed value

Table 4
Interphase gas transfer coefficient values.

	$K^{'}_{\text{c-w}}$ (−)	$K_{\text{c-w}}$ (s^{-1})	$k_{\text{c-w}}$ (m/s)
Carbonator model assumptions			
Hawthorne et al. (2008) [91,92]	0.72¥, †	$K_{\text{b-e}} \approx 4.5\ u_{\text{mf}}/d_T\ K_{\text{b-e}} = 0.45$†	–
Ströhle et al. (2009) [81]	55¥	11	–
Lasheras et al. (2011) [36]	55¥	11	–
Romano (2012) [40]	20–80¥	10	–
Atsonios et al. (2015) [32]	–	–	–
Cormos and Simon (2015) [93,94]	–	(not specified)	–
Sattari et al. (2021) [88]	55¥	11	–
Empirical data and other models			
Kunii and Levenspiel (1991) [37]	–	> 11	–
Kunii and Levenspiel (1997) [65]	–	5–20	–
Bi et al. (2000) [72]⹋ (TF*); $u_0 < 2.6$ m/s	2.9–13.0¥ ($H_T \sim 5\ H_{\text{mf}}$)	0.2–4.6	0.003–0.23¥
Kunii and Levenspiel (2000) [35,104]	1.0¥	0.3	–
Bi (2002) [107] (FF*); $1.5 < u_0 < 8$ m/s	0.02–10.5¥	0.016–8.0	0.001–0.3
Yang (2003) [106, p.521] ‡	0.01–10¥	–	0.015–0.3
This work			
Values used	2.2–4.8	1.5–2.0	0.158 (input)
With Eq. (58)	0.5–0.7	0.2–0.5	0.01–0.03
With Eq. (61), (TF*)	$\cong$ 11.7	4.9–8.0	0.3–0.5

⹋Interphase mass transfer coefficient (bubble-voids). Suggested correlations are incompatible with our operating conditions.
‡Core-to-annulus interregion mass transfer coefficient.
¥Our calculation with data reported in the reference.
†With our operating conditions.
*TF: turbulent fluidization; FF: Fast fluidization.

is plausible, as can be derived from Table 4. Still, there is some uncertainty in the prediction of this parameter, and more empirical data is required to obtain reliable values for carbonator modeling. The coefficients calculated with Eqs. (55–57) are inversely proportional to d_T, which is expected considering the linear reduction in the area-to-volume ratio with the upscaling of the reactor diameter.

For comparison purposes, a dimensionless core-annulus transfer coefficient is calculated as [106]:

$$K'_{\text{c-w}} \equiv k_{\text{c-w}}\, a_{\text{c-w}}\, H_T/u_0 = k_{\text{c-w}}\, 4\, d_c\, d_T^{-2}\, H_T/u_0 \ = K_{\text{c-w}} H_T/u_0 \tag{58}$$

When the core diameter is not available, the following approximation is used for comparison [107]:

$$K_{\text{c-w}} \approx 4\, k_{\text{c-w}}\, d_T^{-1} \tag{59}$$

Bi [107] recommends a correlation from Patience and Chaouki [108] that can be written as:

$$K_{\text{c-w}} = d_t^{-2}\, D_g\, \text{Sc}^{0.5}\, \text{Re}_{\text{core}}^{0.75} \left(\frac{G_s}{\rho_s\, u_0}\right)^{0.25} \tag{60}$$

In this expression, Sc is the Schmidt number, defined as:

$$\text{Sc} \equiv \frac{\mu}{\rho_g\, D_{\text{CO2-air}}} \tag{61}$$

Re_{core} is the Reynolds number based on the core diameter:

$$\text{Re}_{\text{core}} \equiv \rho_g u_0 d_c/\mu \tag{62}$$

For turbulent beds, Bi et al. [72] recommend the correlation from Foka et al [109]:

$$K_{\text{c-w}} = 1.631\ \text{Sc}^{0.37}\ u_0 \tag{63}$$

The gas diffusivity, $D_g = D_{\text{CO2-air}}$, is obtained with the correlation proposed by Massman [110]:

$$D_{\text{CO2-air}}(T,p) = \left(0.1381\ \text{cm}^2/s\right)\ (p_0/p)\ (T/T_0)^{1.81} \tag{64}$$

Here, the standard pressure (p_0) is 1.013 bar and the standard temperature (T_0) is 273.15 K. Our underlying assumptions are that Eq. (64) is still valid for the high operating temperatures of the carbonator —justified by comparing with experimental results, e.g., [111]— and that off-gas composition (different than air) does not have a significant influence in the diffusion coefficient. This last can be inferred from Massman's work [110]. Overall, the influence of this factor in the model is low, as long as the values assumed are within the true order of magnitude.

Other correlations to obtain $K_{\text{c-w}}$ are available in the literature [72,107], but none was found to be valid for our operating conditions. These correlations were obtained based on experiments with air at ambient temperature. However, the influence of the gas temperature on $K_{\text{c-w}}$ is uncertain. On top of this, they tend to be process-specific and lack validity outside the test environments for which they were elaborated. Our calculations with the proposed correlations give results of different orders of magnitude (see Table 4).

The interphase gas transfer coefficient values found in the literature of KL carbonator models are summarized in Table 4. Here, we also report data from experiments and empirical correlations from the literature. Lastly, the values used in our model are included in Table 4 as well.

3.3. Calculation logic

The kinetic constant for the carbonation (K_r) depends on the CO$_2$ concentration and the carbonation degree of the particles. To account for the variation of CO$_2$ concentration throughout the reactor, an equivalent driving force ($\mathfrak{C}^*$) for the particle sub-model is computed through iteration using the reactor sub-model [40]. The output from the particle sub-model is X_{carb}. Since, for the particles, the assumption of perfect mixing is reasonable due to the strong mixing of particles in the reactor [40], the particle conversion in the entire reactor can be assumed equal to the average conversion at the reactor outlet (X_{carb}). The particle sub-model is used to calculate K_r [44], which is the input for the reactor sub-model.

The outlet CO$_2$ concentration ($y_{\text{CO2,out}}$) is obtained from the reactor sub-model (RM). With known $y_{\text{CO2,out}}$, the carbonator efficiency according to the RM ($E_{\text{carb}} = E_{\text{RM}}$) [21] can be calculated:

$$E_{\text{carb}} = 1 - \left(y_{\text{CO2,out}}/y_{\text{CO2,in}}\right)\left(1 - y_{\text{CO2,in}}\right)/\left(1 - y_{\text{CO2,out}}\right) \tag{65}$$

The sorbent conversion at the reactor outlet (X_{carb}) is obtained from the particle sub-model (PM) (see Part II [44]). The carbonator efficiency ($E_{\text{carb}} = E_{\text{PM}}$) can then be calculated with a mass balance:

$$(X_{\text{carb}} - X_{\text{calc}})F_R = E_{\text{carb}}F_{\text{CO2}} \tag{66}$$

For the iterative calculations, it is useful to calculate the CO$_2$ outlet concentration and solve the model until the prediction from the particle and the reaction sub-models converge. For this, we derived the following equation from Eq. (66):

$$y_{\text{CO2,out}} = \left[1 - \frac{1 - y_{\text{CO2,in}}^{-1}}{1 - (X_{\text{carb}} - X_{\text{calc}})F_R/F_{\text{CO2}}}\right]^{-1} \tag{67}$$

The calculation logic is illustrated in Fig. 8. First, the inputs for the three sub-models are specified. For the pilot testing, these were based on empirical data from measurements and samples. For the parametric

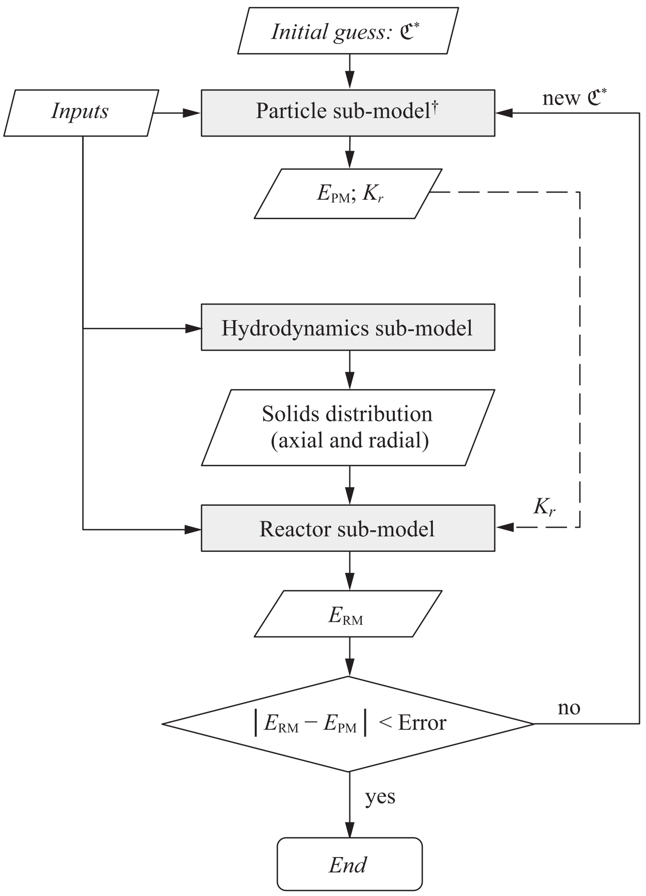

Fig. 8. Calculation logic for the carbonator model. The model includes a hydrodynamics sub-model, a reactor sub-model, and a particle sub-model. †Discussed in Part II [44].

Table 5
Inputs for the carbonator model.

Parameter	Symbol	Range	Value (ref.)	Unit
Constant values				
Reactor height	H_T	–	8	m
Reactor internal diameter	d_T	–	250	mm
Particle diameter	$d_{p,50}$	–	226.7	μm
Particle sphericity	Φ_s	–	0.67	–
Voidage at mf	ε_{mf}	–	0.54	–
Bed solid density	$\varepsilon_{s,d}$	–	0.3	–
Lewis constant	k_{Lewis}	–	8.0	s^{-1}
Core-wall gas interchange	$k_{c\text{-}w}$	–	0.158	m/s
Solids volume ratio	ξ	–	1	–
Particle density of $CaCO_3$	$\rho_{CaCO3,p}$	–	2710 [39]	kg/m^3
Particle density of CaO	$\rho_{CaO,p}$	–	1670 [44]	kg/m^3
Molar mass of $CaCO_3$	M_{CaCO3}	–	100	g/mol
Molar mass of CaO	M_{CaO}	–	56.1	g/mol
Time-dependent inputs				
Superficial gas velocity	u_0	3.4–5.5	(4)	m/s
Reactor temperature	T_{carb}	550–700	(650)	°C
Reactor pressure	p	1.0–1.1	(1.1)	bar
Reactor inventory	W_{carb}	20–60	(50)	kg
CO_2 input	F_{CO2}	0.16–0.49	(0.5)	mol/s
Inlet CO_2 concentration	$y_{CO2,in}$	6.2–13.8	(12)	$vol\%_{wb}$
Gas viscosity	μ	39–41	(40)	10^{-6} Pa s
Gas density	ρ_g	0.39–0.44	(0.5)	kg/m^3
System age [44]	γ	0–150	(50)	–
$CaSO_4$ concentration [44]	x_{CaSO4}	0.00–0.10	(0)	mol%
Sample-dependent inputs				
Solids density*	$\rho_{s,a}$	1.7–2.3	(2.0)	g/cm^3
Solids molar mass*	$M_{s,a}$	57–82	(56)	g/mol
Sorbent circulation	F_R	4–13	(10)	mol/s
Reaction rate	K_r	20–130	(80)	s^{-1}
Inlet carbonation degree	X_{calc}	0.00–0.14	(0.00)	mol_{CaCO3}/mol_{Ca}

*Of potentially active solids.

study and sensitivity analysis (Section 4), the input parameters were the mean operating conditions (reference values in Table 5), unless otherwise stated. The particle sub-model, with the input of the CO_2 concentration ($\mathfrak{C}^*$), gives the kinetic rate (K_r), which is used as an input for the reactor sub-model. The hydrodynamics sub-model gives the solids distribution that is used in the reactor sub-model to calculate the CO_2 concentration profile and the CO_2 capture efficiency. The model is solved iteratively until the predictions of the particle sub-model (E_{PM}) and the reactor sub-model (E_{RM}) coincide.

4. Results and discussion

4.1. Validation

In this section, the validation of our carbonator model is discussed. The validation was performed mainly with experimental data from the pilot tests in the 300-kW_{th} IHCaL plant in the year 2015, at the Technical University of Darmstadt [64]. The experiments corresponding to the data used for the validation were reported by Reitz et al. [2]. The IHCaL process is similar to the CaL process in terms of carbonator operation. However, due to the indirect calcination, the operating conditions in the calciner are different than for the oxy-fired CaL. This has an influence on the sorbent activity [28,112,113]; thus, it is discussed in the frame of the development and analysis of the particle sub-model (Part II [44]).

4.1.1. Hydrodynamics sub-model

To obtain the appropriate constants for our model, we analyzed the data from the pilot plant operation. The pressure (p) data was translated into solids distribution (ε_s) by balancing the forces in each height differential segment of the carbonator (dz). Here, ε_s represented the average solid concentration in a reactor disc of differential height (dz). The weight of the particles was considered equal to the drag force generated by the upward-moving gas [37]. In mathematical form, the equilibrium equation gives the following expression for ε_s:

$$\varepsilon_s = -\frac{1}{(\rho_s - \rho_g)g}\frac{dp}{dz} \tag{68}$$

The pressure data was differentiated numerically using a central-difference scheme [86]. The calculated values using stable operating points are illustrated in Fig. 9. Fig. 9 displays the pressure (left) and solids distribution (middle and right) for low-speed ($u_0^* < 2.6$) and high-speed ($u_0^* > 2.6$), corresponding to turbulent and fast fluidization, and high inventory ($W_{carb} > 45$ kg) and low-inventory ($W_{carb} < 45$ kg). For all the balance points, the bed density is higher than the values generally assumed in the literature for carbonator models (see Table 3). In our work, we assume $\varepsilon_{s,d} = 0.3$ from empirical data. This value is slightly low for turbulent fluidization and slightly high for fast fluidization considering the empirical data reported in Table 3. The complete model was computed by modifying the bed voidage ($\varepsilon_{s,d}$) according to the superficial gas velocity with the correlations in Fig. 10, but the results were similar to those obtained assuming a constant value of $\varepsilon_{s,d} = 0.3$. This last approach was preferred for simplicity.

Junk [114, p.113] also reported high values of $\varepsilon_{s,d}$ when analyzing data from a 1-MW_{th} CaL facility. He obtained an average value of $\varepsilon_{s,d} = 0.46$ using empirical data, which is much higher than the values recommended in the literature for carbonator modeling (see Table 3). Only after incorporating this input into his hydrodynamics sub-model, he achieved good agreement with experimental results. Previous studies [83] reported an increase in $\varepsilon_{s,d}$ with riser diameter (d_T), reaching asymptotic values for $d_T > 500$ mm. This explains the higher values of $\varepsilon_{s,d}$ in the 1-MW_{th} facility ($d_T = 600$ mm) [114] compared with those in the 300-kW_{th} plant ($d_T = 250$ mm, our study).

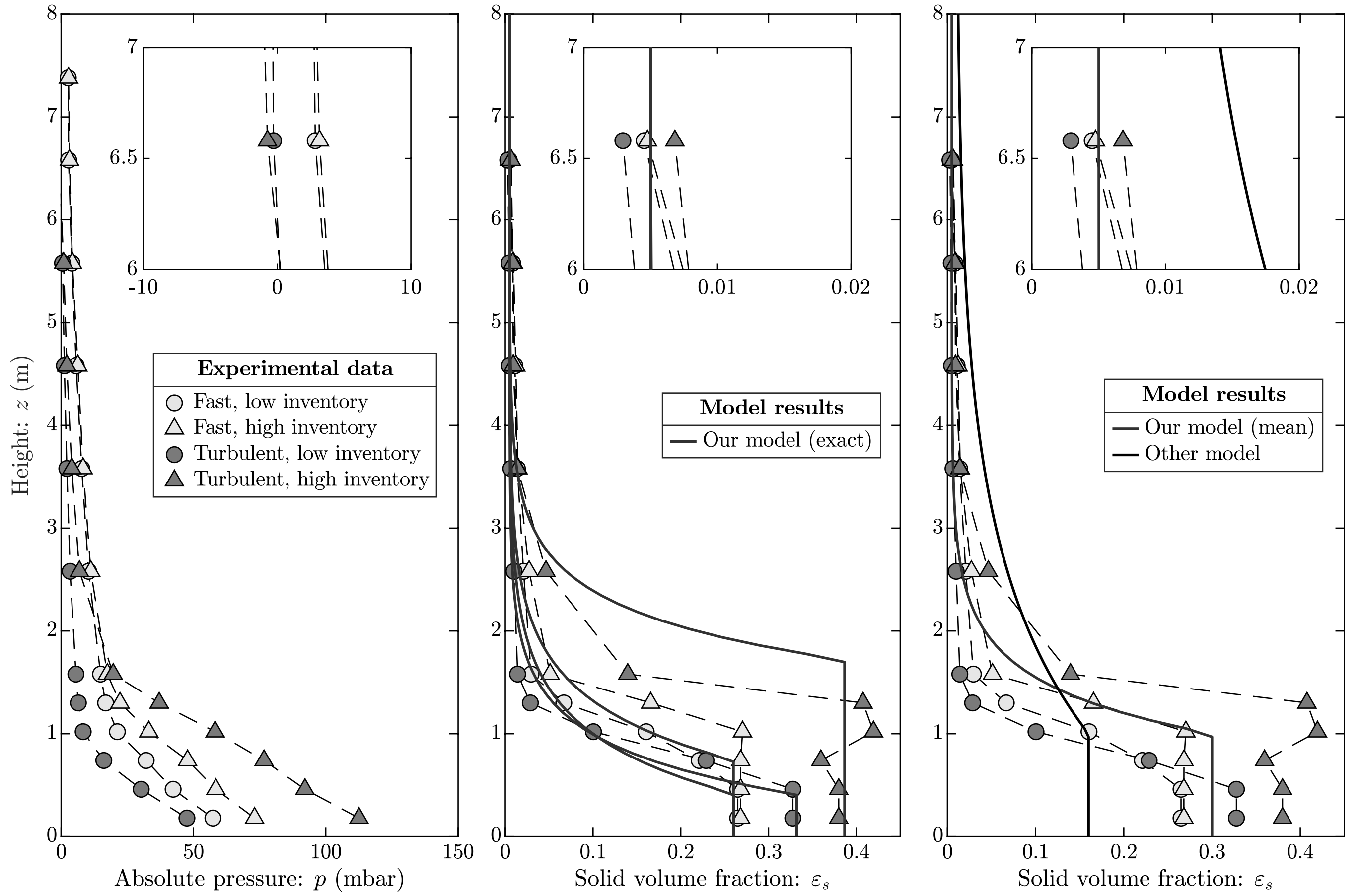

Fig. 9. Hydrodynamics of the pilot plant: pressure experimental data (left), solid volume fraction from experimental data compared with our model predictions (middle), and solid volume fraction from experimental data compared with our model (mean values) and other model based on typical assumptions from the literature (right).

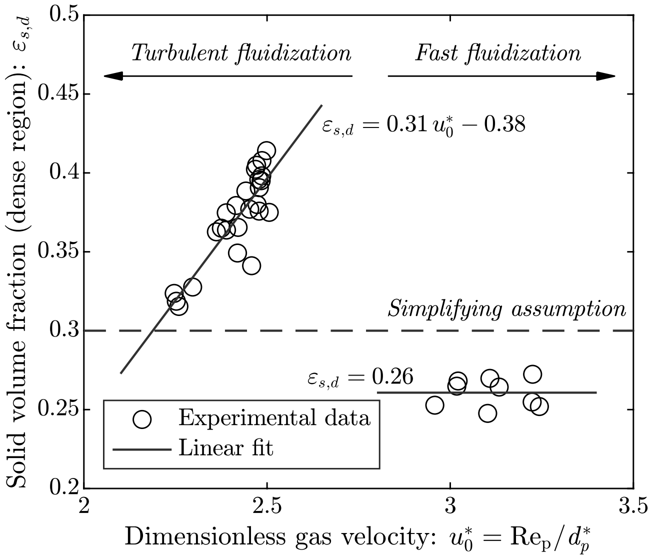

Fig. 10. Calculated solid volume fraction in the dense region using experimental data from the stable operating points during the pilot tests.

The empirical values of solid concentration at the exit ($\varepsilon_{\mathrm{s,out}}$) range between 0.002 and 0.008. The calculations using Eq. (16) gave $\varepsilon_s^* \approx 0.002$, which is coherent with the empirical data. We highlight that the application of this equation in our work was mainly to comply with previous models for comparison purposes. However, since the correlation of Eq. (16) was obtained in the frame of elutriation from captive fluidized, the application in carbonator modeling is questionable. A safer approach would be the integration over the complete particle size distribution of a correlation derived for circulating fluidized bed operation (see, e.g., [115]). The assumption $\varepsilon_s^* = 0.01$ (from [37,40]) is somewhat incompatible with our experimental values since the saturation concentration sets a minimum limit to the exit concentration. In Fig. 9, the model predictions are indicated in red for our assumptions and in black for those of Romano [40] (see Table 3). The *exact* model results (middle) include the calculation of the bed height with Eq. (18) and the utilization of the correlations of Fig. 10 and Fig. 11. For the *mean* model results (right), we consider the average bed height throughout the tests ($H_d = 1$ m) and the model constants reported in Table 3. In Fig. 9 (right), we highlight that using model constants from previous studies can lead to significant inaccuracies in predicting the solids distribution. This, in turn, affects the calculation of the carbonator performance in the reactor model.

For all the balance points in this work, a dense region can be distinguished. This corresponds to values of $H_d > 0$ obtained in the model. For beds with very low inventory —lower than the ones from our pilot-test balance points— the entire reactor becomes lean, thus establishing the *pneumatic transport regime* [35]. Mathematically, this corresponds to H_d becoming negative when calculated with Eq. (18). Throughout this work, our model predicts the pneumatic transport regime when the hydrodynamics constants (see Section 3.1.2) are inadequately chosen. The pneumatic-transport operation of a carbonator for CO_2 capture is disadvantageous, because of the low contact

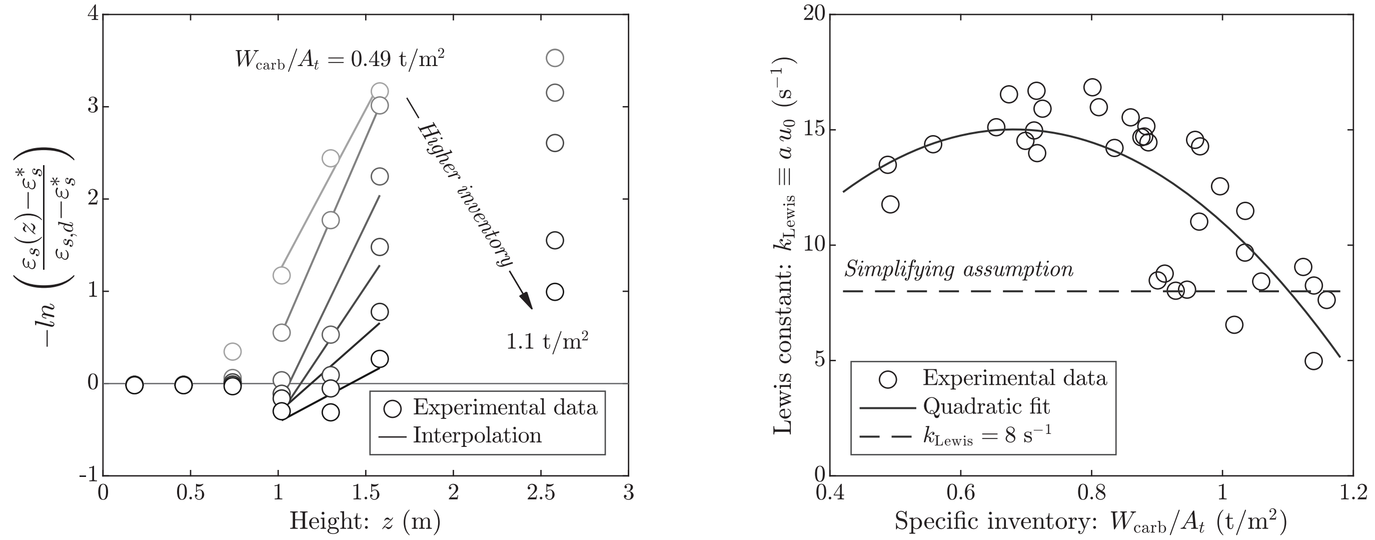

Fig. 11. Estimation of the Lewis constant for the solid distribution decay law: methodology displaying selected operating points using Eq. (11) (left), and results for all operating points (right).

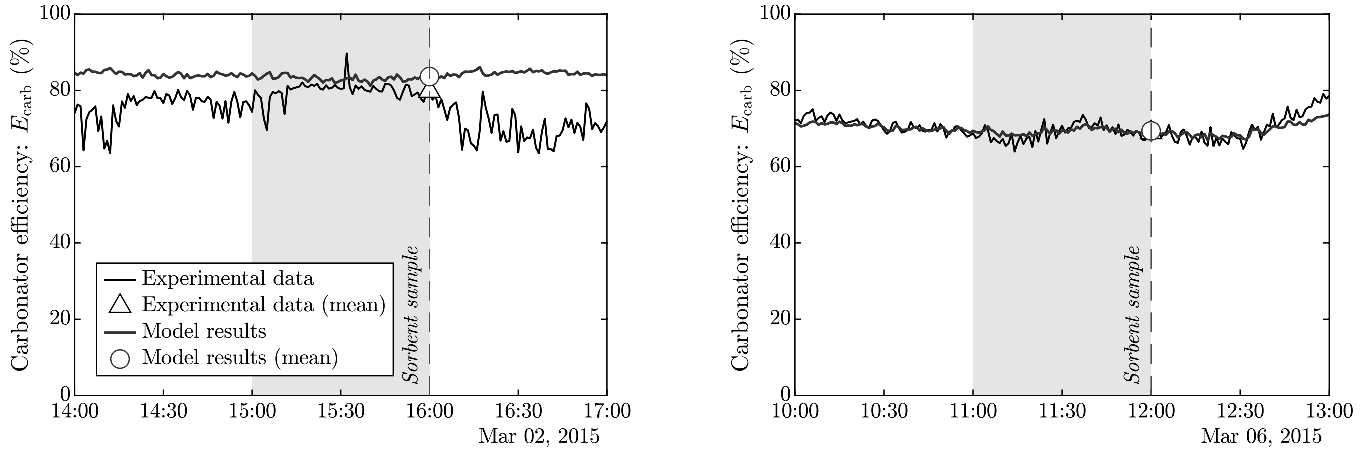

Fig. 12. Illustration of the validation methodology for the carbonator model: an unstable balance point (left) and a stable balance point (right). The gray area represents the period of time used to calculate the mean values of E_{carb}.

efficiency associated with this regime. If the hydrodynamic models predict the operation in this regime, we recommend checking the hydrodynamics constants and the empirical data.

The variation of the solid volume fraction in the dense region ($\varepsilon_{s,d}$) with the operating conditions is illustrated in Fig. 10. In the region corresponding to turbulent fluidization (left), $\varepsilon_{s,d}$ seems to increase linearly with the dimensionless superficial gas velocity (u_0*). For fast fluidization (right), $\varepsilon_{s,d}$ adopts lower values and is not affected by u_0*.

Fig. 11 indicates the methodology to estimate the Lewis constant (left), as well as the variation of this constant with the specific inventory (right). The Lewis constant was calculated using a linear interpolation in Eq. (11) and time-averaged data from pressure measurements. No meaningful correlation between the velocity and the Lewis constant (k_{Lewis}) was found. For high specific inventory (>0.6 kg/m^2), k_{Lewis} decreases with the bed height. For low inventory, the tendency appears to be reversed, probably due to the operation close to the pneumatic transport regime (i.e., the disappearance of dense bed).

4.1.2. Reactor sub-model

To validate the reactor sub-model, we consider the carbonator efficiency (E_{carb}), which is the main performance indicator for the reactor. The experimental values of E_{carb} are calculated with Eq. (65), using the data of gas analysis at carbonator exit and the volume flow rates of the gases entering the carbonator. In the model, E_{carb} depends on variables that are only known from sorbent samples. Therefore, meaningful values can only be obtained for the periods of time close to sorbent sampling. Such variables are the carbonation degree at the carbonator inlet (X_{calc}) and the sorbent molar circulation rate (F_{R}), among others. Since these variables affect mainly the particle sub-model, they are discussed in Part II [44]. The inputs for the carbonator model are listed in Table 5, including their values. For the variable parameters, the range of variation is included, as well as the reference values used for the model analyses in the following sections. Due to the low concentration of inert species in the pilot plant [51], the volume ratio of potentially active sorbent to solids was set to $\xi = 1$.

The values of E_{carb} were calculated with our model for each sorbent sample available. The calculation was performed using the time-averaged values for the time-dependent parameters (see Table 5), over a one-hour period until sampling time. This methodology assumes that only the operational history before sampling influences the state of the system at the moment of taking the sample. Since the sampling process involved removing sorbent, it sometimes induced instabilities in the

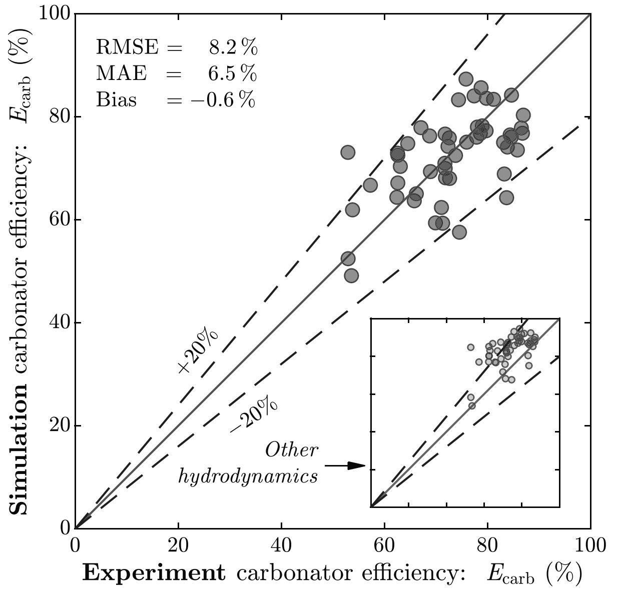

Fig. 13. Validation of the carbonator model. The capture efficiency predicted by the model is compared with the carbonator efficiency from pilot tests. The small figure in the bottom-right corner illustrates the results obtained using the set of assumptions for the hydrodynamics sub-model that is generally found in the literature of carbonator models. Number of balance points: 51.

system. In some cases, sorbent circulation was interrupted or reduced shortly after sample collection, leading to transient losses in capture efficiency (see Fig. 12, left). The experimental and model averages were computed using the same one-hour time periods.

The validation procedure is illustrated in Fig. 12. The apparent transient behavior of Fig. 12 results from the time-dependent input of the CO_2 concentration at reactor inlet. However, our model is steady-state. The moment of sorbent sampling is indicated with a broken line. A gray area indicates the time period for the time averaging, which extends to two hours before sampling. The carbonator efficiency (E_{carb}) calculated with experimental data is plotted in black and the model results are illustrated in red. The calculated values with average conditions are indicated with a triangle (experimental) and a circle (model). These last values are used for the model validation.

For the balance points exhibiting unstable operation (see Fig. 12, left), the model was not able to predict the exact values of E_{carb}. This is because of the nature of the model that does not consider transient effects such as short-time interruptions of the circulation. The mean behavior can be captured with reasonable accuracy. For stable operating points, the model predicts experimental E_{carb} with higher accuracy (see Fig. 12, right).

The mean capture efficiency calculated with the carbonator model is compared with the experimental results in Fig. 13. The simulation results agree with the time-averaged experimental data within the ± 20 % relative error for the majority of the balance points. The root-mean-square error (RMSE) and the average error (MAE) are 8.2 % and 6.5 %, respectively. The parity values are evenly distributed on both sides of the identity line and the bias modulus is less than 1 %.

The main source of error was the calculation of the deactivation, which corresponds to the particle sub-model (see Part II [44]). Additionally, the values of X_{calc} and $K_{\mathrm{c\text{-}w}}$ had a considerable influence on the model results. On the bottom-right corner of Fig. 13, we included the model predictions assuming the set of assumptions for hydrodynamics from Romano [40]. The simulation values of E_{carb} were much higher than those calculated from the empirical data, indicating that the set of hydrodynamics assumptions typically used in the literature overpredict our experimental results.

4.2. Inventory and fluidization regime

The fast fluidization regime is sometimes associated with a loss of inventory. One possible explanation for this is that the onset of the fast fluidization regime generates sudden increases in entrainment, which are not always possible to counteract, thus causing an inventory loss. For further testing and for the design of a commercial facility, this aspect should be considered. For this, we suggest predicting the fluidization regime in advance for the different operating conditions. This can be done following the methodology from Section 3.1. If regime transitions are expected in operation, control strategies should be studied and implemented effectively. For this, the design of cyclones and coupling elements is crucial.

During the different test campaigns in the 300-kW$_{\mathrm{th}}$ pilot plant, two different particle sizes were tested (see Section 2). In this work, we evaluated the operating points using the fine fraction. For this PSD, we had more entrainment issues. In general, the operation with coarser PSD

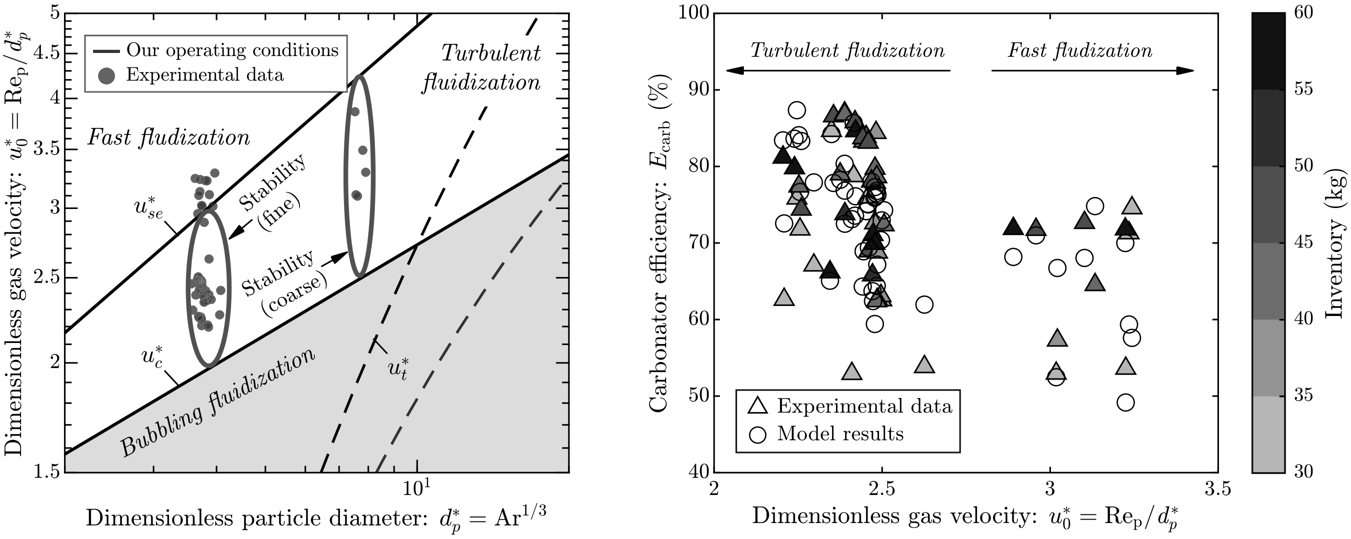

Fig. 14. Stability of the pilot plant in the turbulent fluidization regime for two limestone PSDs (left) and influence of the fluidization regime in the carbon capture efficiency and the inventory (right).

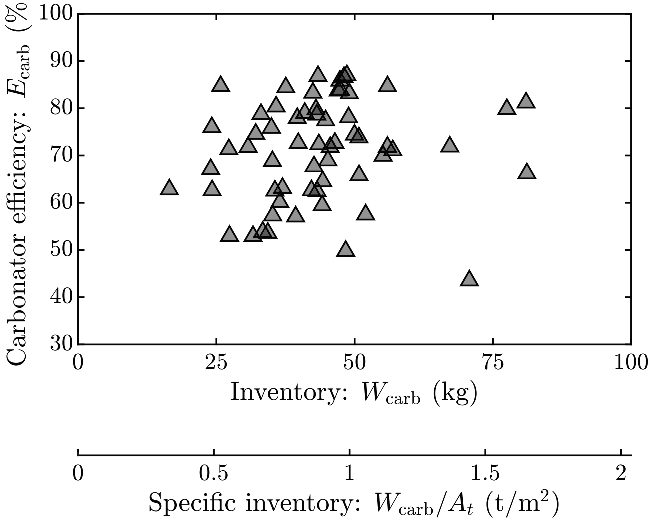

Fig. 15. Variation of the carbonator efficiency (E_{carb}) with the reactor inventory (W_{carb}) using pilot plant data from the balance points.

was characterized by higher stability. This can be explained by analyzing the operation window of the turbulent regime in the Grace diagram of Fig. 14. For the fine particles used in this work, the gas velocities corresponding to the turbulent fluidization regime were 3.4–5.1 m/s, while for the coarser particles, the operating window was 3.6–6.1 m/s. On top of the wider range of stable operation, the carbonator was designed to operate between 2.5 and 7.0 m/s [64]; thus, the system with coarser particles operates closer to the maximum design velocities, which improves the performance of the fluidization nozzles at the bottom of the reactor.

During our experimental investigations, we obtained higher capture rates operating in the turbulent fluidization regime (see Fig. 14, right). For higher velocities, beyond the onset of fast fluidization, it was not possible to achieve more than 75 % capture efficiency. Our model predicts the capture efficiency in this region with acceptable accuracy but shows a slight positive bias. This may be caused by the loss of the contact efficiency due to the transition into the fast fluidization regime that is not captured by the model, as $k_{\text{c-w}}$ is kept constant. The lower performance cannot be explained by changes in the inventory.

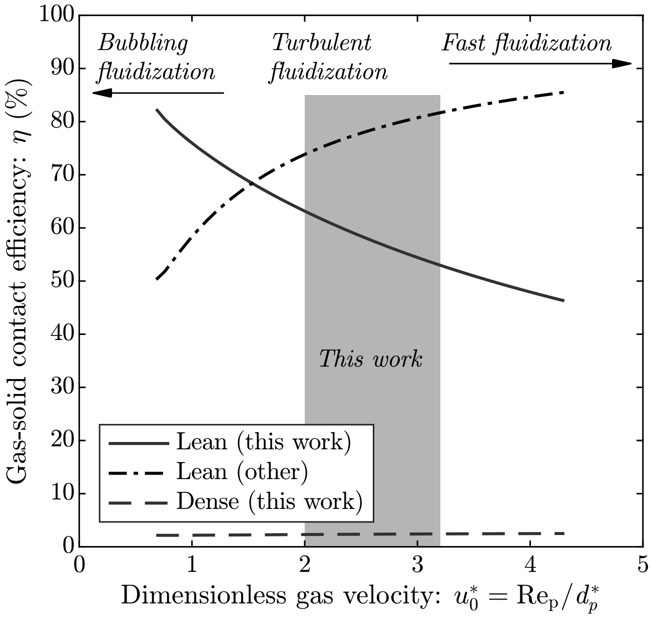

Fig. 16. Predicted variation of the gas-solid contact efficiency with the dimensionless superficial gas velocity.

Charitos et al. [29] compared two CaL test rigs. One of them was operated in the turbulent fluidization regime (INCAR-CSIC), whereas the other was operated in the fast fluidization regime (IFK). They concluded that the operation in both regimes is possible but reported that the gas–solid contact efficiency of the turbulent bed was 62 % higher than that of the fast-fluidized reactor. Our results point in the same direction.

Recently, Diego and Arias [43] reported better carbonator performance for lower gas velocities, based on experimental results from a 1.7-MW$_{\mathrm{th}}$ CaL pilot facility. They explained that the inventory reduction due to increased entrainment was the cause of performance loss at higher velocities. Nevertheless, with appropriate reactor design and coupling devices (taller reactor, efficient cyclones, etc.) the high entrainment can be compensated for. Our observation of a shift in fluidization regime gives a plausible explanation for the significant entrainment increase and the impaired reactor performance.

Regarding the influence of the inventory on the carbonator efficiency (E_{carb}), it is generally reported that high inventories increase CO_2 capture rates. We found this to be true up to a minimum threshold, after which E_{carb} is almost independent of the amount of sorbent in the reactor. This is explained by the low contact efficiency in the dense region or bed, meaning that the lean region is responsible for most of the CO_2 capture (see Fig. 7 and Fig. 16). As long as there is a minimum amount of material to maintain a dense bed at the bottom of the reactor, the lean region remains almost unaffected by the additional inventory. Our observations from the reactor sub-model match the experimental data well, which do not indicate any influence of the inventory in the reactor performance beyond $W_{\mathrm{carb}}/A_t \approx 400$ kg/m^2 (see Fig. 15). A similar behavior has been reported in previous experimental studies. Diego et al. [43] observed a sharp decrease of CO_2 capture capacity below the 400-kg/m^2 threshold based on experimental data from a 1.7-MW$_{\mathrm{th}}$ plant. Haaf et al. [97] indicated a good carbonator performance for inventories between 400 and 500 kg/m^2 in a 1-MW$_{\mathrm{th}}$ CaL pilot plant.

A higher contact efficiency in the reactor means that sufficient CO_2 capture may be achieved with lower inventories or shorter reactors.

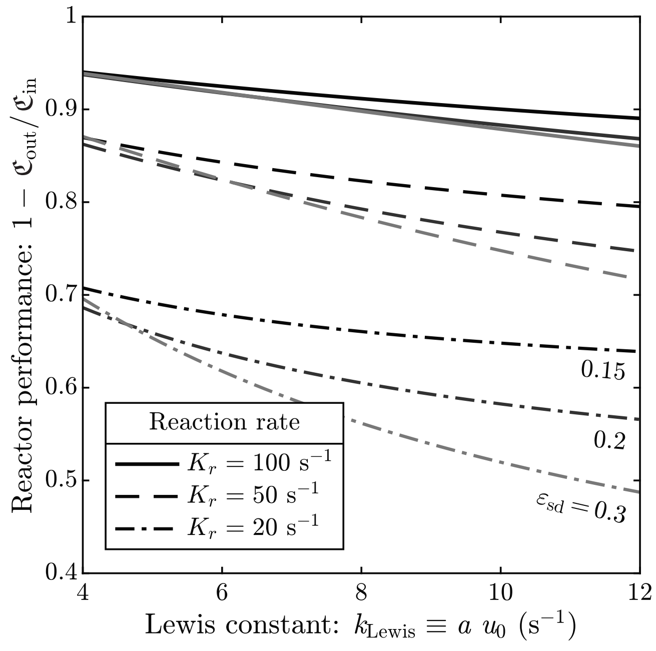

Fig. 17. Variation of the reactor performance with the Lewis constant (k_{Lewis}) and with the solid concentration in the dense region ($\varepsilon_{s,d}$), for different reaction rates (K_r). Increasing these parameters has a negative effect on the carbonation efficiency.

Lowering the reactor inventories is desirable because of the associated reduction in the pressure drop that the carbonator blower needs to overcome. Shorter reactors imply lower investment costs. One objection to operating in the turbulent fluidization regime is the lower entrainment rates that may yield the sorbent circulation insufficient. Many experimental investigations have proven the feasibility of operating CaL-carbonators in the turbulent regime [25,26,29,116], but solid circulation problems were reported in some of them [116]. If our hypotheses regarding the turbulent fluidization regime are correct, this operational regime could offer advantages for CO_2 capture in the carbonator.

The variation of the contact efficiency with the superficial gas velocity is illustrated in Fig. 16. The results of this model using Eqs. (44) and (47) are displayed in red. The range of velocities achieved during pilot operation is indicated with a red-shaded area. The model predicts a high contact efficiency for the turbulent fluidization regime that decreases with the velocity. If in the transition into the fast fluidization regime the constant $k_{\text{c-w}}$ is reduced according to empirical data (see Table 4), the contact efficiency is strongly reduced (not included in the figure). With the appropriate modification of constants, our model may be valid further into the higher regions of the fast fluidization regime. Contrary to this, the model is not compatible with bubbling fluidization. For this kind of operating regime, the reactor sub-model would have to be modified (for this, see [38,65]).

The results for the lean region using Eq. (52) (black broken line in Fig. 16) indicate an increase in the contact efficiency with the superficial gas velocity. This is contrary to our observations of the experimental data presented in Fig. 14. The equation relies on the assumption of a constant decay factor for the contact efficiency (b) in the lean region, which is independent of the velocity. This may explain the different behavior.

The calculated contact efficiency in the dense region was significantly lower than in the lean region. However, this does not necessarily imply a low reactivity in the bed, as faster kinetics can be expected due to the higher driving forces at the bottom of the reactor. The contributions of both the dense and lean regions not only depend on the contact efficiencies but also on the CO_2 concentrations and the effective residence times of gas-particle contact in each of them.

The variation of the reactor performance with the Lewis constant ($k_{\text{Lewis}} \equiv a\, u_0$) and the solid concentration in the dense region ($\varepsilon_{s,d}$) was analyzed using Eq. (50). The results are plotted in Fig. 17 for different reaction rates (K_r), which depend on the sorbent activity in the reactor. The calculations yield higher reactor performance for lower values of k_{Lewis} and $\varepsilon_{s,d}$, which correspond to the fast fluidization regime. The sensitivity to these parameters is higher as the sorbent becomes less reactive, i.e., for lower K_r. The values typically assumed for k_{Lewis} and $\varepsilon_{s,d}$ were much lower than the ones we obtained from our pilot data (see Sections 3.1 and 4.1.1). Using these typical values in our model led to an overestimation of the performance of our pilot plant.

Previous studies concluded that the carbonator performance has low sensitivity to k_{Lewis} and $\varepsilon_{s,d}$ [36,88]. This contrasts with our findings for several reasons. Firstly, those studies utilize smaller ranges than we do. We consider ranges corresponding to both fast and turbulent fluidization. Secondly, it is often overlooked that as the decay constant (k_{Lewis}) increases, the solid concentration in the bed also does. The combined effect of increasing both variables can result in a performance loss of more than 20 % in extreme cases. Lastly, the variation in sensitivity with other parameters, such as sorbent reactivity, had not been discussed before. As illustrated in Fig. 17, for lower values of K_r, the values assumed for k_{Lewis} and $\varepsilon_{s,d}$ will have a higher influence on the reactor performance. Another parameter affecting the sensitivity is the coefficient $k_{\text{c-w}}$. Higher values of $k_{c\text{-w}}$ increase the sensitivity of the carbonator performance to the parameters of the solids distribution (i.e., k_{Lewis} and $\varepsilon_{s,d}$).

4.3. Upscaling considerations

If temperature, gas composition, and particle properties are kept constant, the same gas velocities will yield the same fluidization regime in the Grace diagram (see Fig. 5). This would indicate that there would be no change in the fluidization regime from the scale-up.[4] For the following discussion, the same hydrodynamics sub-model and hydrodynamics constants as in the previous sections are considered.

Since the models are sensitive to the diameter and the height of the reactor, the influence of scaling up on the performance of the carbonator needs to be assessed. In scaling up, we considered that the radial solids distribution will change because of the dependency of the surface-area-to-volume ratio with the reactor size (d_T). When d_T increases, the wall layer becomes less important compared to the core, which is accounted for in Eqs. (54–57). This leads to a decrease in the core-wall contact area, which previous models often neglect, resulting in an overprediction of the reactor performance.

The variation of the carbonation efficiency with the plant scale, using the carbonator model developed in this work, is illustrated in Fig. 18. The reactor height (H_T) was assumed equal to 8 m up to a diameter of $d_T = 0.25$ m. Above this value, H_T increased linearly, reaching a maximum of 50 m as d_T expanded to 10 m. For larger reactors, H_T was kept constant due to practical operation restrictions [118,119]. The variation of H_T with d_T is illustrated in Fig. 18 (left). In Fig. 18 (left), we include the dimensions of operational CaL pilot plants [10,12,15,64] and commercial fluidized bed facilities [37, ch.2] [120,121] for comparison purposes, using the hydraulic diameter for rectangular-section reactors. The typical diameters for the pilot scale and commercial scale are indicated with red (darker) and gray (lighter) areas, respectively.

We considered six scenarios with different sorbent age ($\gamma \simeq F_R / F_0$) and circulation rate (F_R). The reference values in Table 5 were used as input for the calculations, except for the parameters that were variated for the upscaling study (d_T, H_T, F_R, F_{CO2}, and γ). The results are presented in terms of carbonator diameter (Fig. 18, middle) and CO_2 mass flow into the carbonator (Fig. 18, right). The results in Fig. 18 show a peculiar trend for E_{carb} with the scale-up, decreasing up to $d_T \approx 1$ m, increasing beyond that, and decreasing again for $d_T > 10$ m. The reason for this is the varying ratio of H_T to d_T. The results presented here should not be taken as general rules, since the scale-up law used for H_T may not be representative of scale-up conditions for every project. Instead, our results indicate that a variation of the carbonation efficiency with the reactor geometry is to be expected, particularly due to scale-up. For taller reactors, the carbonator efficiency is higher due to the increased residence time with reactor height (H_{T}).

The influence of additional variables is illustrated in Fig. 19. Here, five parameters were variated linearly within the boundaries reported in Table G.1. The specific circulation rate was $F_R/F_{CO2} = 10$, and the sorbent age was $\gamma = 50$. The rest of the inputs were specified from the reference values of Table 5. The parameters that most affect the reactor performance are the particle diameter ($d_{p,50}$) and the specific core-wall exchange coefficient ($k_{\text{c-w}}$). The bigger the particles, the lower the carbonator efficiency. Furthermore, a wider particle size distribution (PSD) may yield better reactor performance (see [52]). Higher values of $k_{\text{c-w}}$ yield higher values of E_{carb} (see Fig. 7). The strong influence of $k_{\text{c-w}}$ in

---

[4] Wang et al. [117] analyzed the fluidization regimes of circulating fluidized bed (CFB) combustors using empirical data from various studies. They concluded that this type of commercial boilers operates in a so-called *bubbling-entrainment bed* regime, characterized by a bubbling dense bed and a fast-fluidized freeboard. Contrary to CFB combustors, carbonators exhibit narrow particle size distributions (PSDs) and do not utilize secondary combustion air. Because of these differences, we do not expect a bubbling-entrainment bed regime in commercial carbonators. The reader is referred to the work of Kunii and Levenspiel [35] to adapt our model to bubbling-bed and pneumatic-transport operation, if necessary.

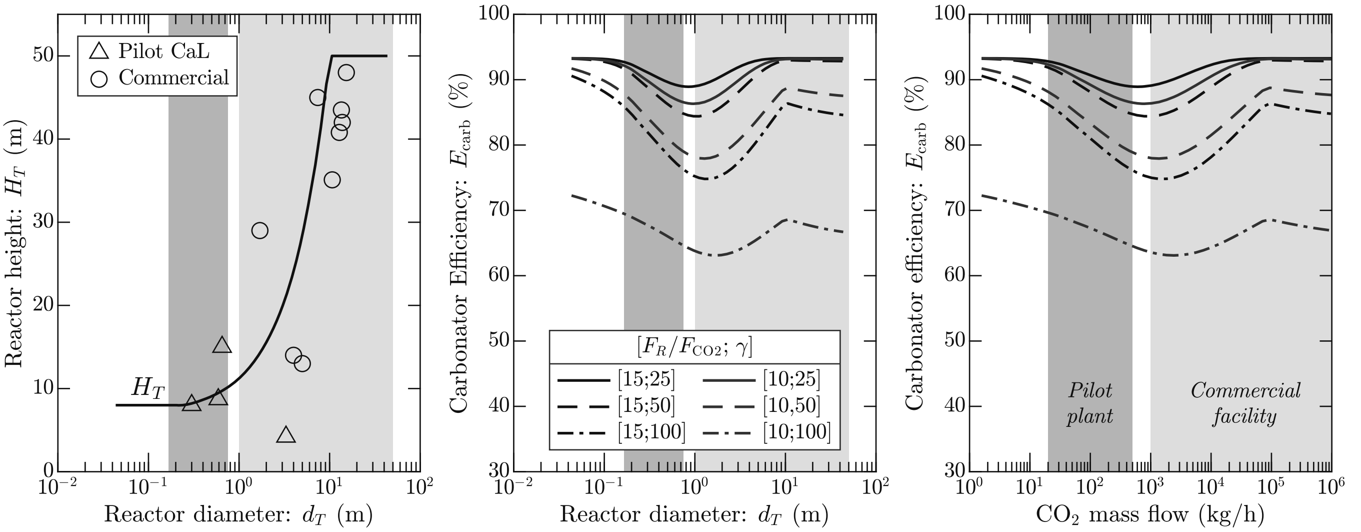

Fig. 18. Upscaling law for the reactor height (left), including data of existing pilot (CaL) and commercial plants (circulating fluidized beds), and variation of the carbonation efficiency (E_{carb}) with the plant scale in terms of carbonator diameter (middle) and CO_2 mass flow into the carbonator (right), both in logarithmic scale. The calculations were performed for different combinations of specific sorbent circulation rate (F_R / F_{CO_2}) and sorbent age ($\gamma \simeq F_R$ / F_0). The regions corresponding to pilot plants and to the commercial scale are indicated with red (darker) and gray (lighter) areas, respectively.

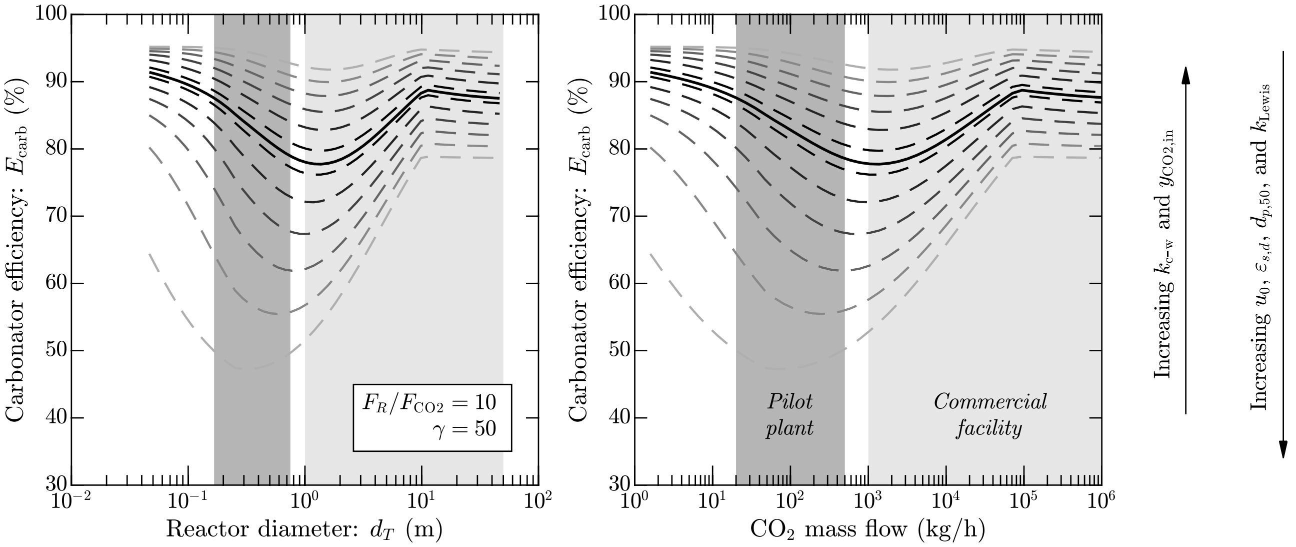

Fig. 19. Sensitivity of the upscaling results to the specific core-wall gas interchange coefficient ($k_{\text{c-w}}$), the CO_2 concentration at the carbonator inlet ($y_{\text{CO2,in}}$), the superficial gas velocity (u_0), the solid volume fraction in the dense region ($\varepsilon_{s,d}$), the mean particle size ($d_{\text{p},50}$), and the Lewis constant (k_{Lewis}). The figure illustrates the variation of the carbonation efficiency (E_{carb}) with the plant scale in terms of carbonator diameter (middle) and CO_2 mass flow into the carbonator (right), both in logarithmic scale. The boundaries are reported in Table G.1. The continuous curve corresponds to the base case. The top curve and the bottom curve correspond to the best case and the worst case, respectively.

E_{carb} indicates that the fluidization regime can be decisive in achieving high CO_2 capture rates. Carbonators operating in the turbulent fluidization regime (higher $k_{\text{c-w}}$) will perform better than those operating in the fast fluidization regime (lower $k_{\text{c-w}}$).

5. Conclusion

In this work, a carbonator model has been developed, including novel approaches to modeling hydrodynamics and reactor performance. The validation was carried out using results from test campaigns in the 300-kW$_{\text{th}}$ indirectly heated carbonate looping (IHCaL) plant at the Technical University of Darmstadt. The model was used to analyze carbonator behavior and scale-up issues for carbonate looping (CaL) technology.

Our findings regarding carbonator hydrodynamics fit the famous Aristotelian expression stating that a minor mistake in the beginning leads to a major mistake in the conclusions [122]. If reactor hydrodynamics are not properly modeled considering riser characteristics and operating conditions, the carbonator model may fail to predict the reactor behavior accurately. However, simulation studies dealing with carbonator hydrodynamics often select the model constants without enough explanation. With our experimental data, we found that an error in the constants for the axial solids distribution in the carbonator leads to a considerable overestimation of the capture efficiency. A mistake of this kind in the design of a commercial facility would have significant economic implications.

In this study, we also found that carbonators operating in the turbulent fluidization regime profit from higher gas–solid contact efficiency, meaning that sufficient capture can be achieved with more tolerant specifications, enabling potential cost reductions. Nevertheless, turbulent fluidized bed reactors exhibit lower entrainment rates than fast-fluidized beds. Many studies proved the feasibility of operating carbonators in the turbulent regime, but solid circulation problems were reported in some of them. If these problems are solved, the operation in the turbulent fluidization regime may become the preferred option for carbonator operation.

Many of the modeling assumptions found in the literature of carbonator models lead to overprediction of our pilot plant experimental data. Our study presents guidelines for accurate carbonator modeling, including a methodology for deriving model constants from empirical data, improved gas–solid contact equations, and a thorough discussion of fluidization regimes. If these guidelines are not taken into account for upscaling carbonators, the first commercial plants may underperform, even despite generous safety factors. Although we were able to validate our model, more data is required to ensure that the model predictions are still valid up to higher scales and for a wider range of operating conditions. The radial solids distribution was not modeled in detail in our study. Further work should assess whether this may affect the accuracy of our model under different operating conditions, and if so, improve the model to achieve a more detailed description of the radial solids distribution. Additionally, there is still uncertainty related to wall effects and particle attrition in larger carbonators. Therefore, further experimental research in pilot and demonstration plants is still necessary before the deployment of CaL and IHCaL technology on a commercial scale can be realized without incurring significant risks.

CRediT authorship contribution statement

Martin Greco-Coppi: Conceptualization, Methodology, Software (MATLAB), Validation, Investigation, Data curation, Visualization, Writing – original draft, Writing – review & editing. **Jochen Ströhle:** Writing – review & editing, Supervision, Project administration, Funding acquisition. **Bernd Epple:** Supervision.

Declaration of competing interest

Martin Greco-Coppi, Jochen Ströhle, and Bernd Epple have patent “Apparatus and Method for Producing Lime” (No. 10 2023 114 354.9) pending to Technical University of Darmstadt and Rheinkalk GmbH, and patent “Apparatus and Method for Producing Lime and Cement” (No. 10 2024 109 181.9) pending to Technical University of Darmstadt.

Data availability

Data will be made available on request.

Acknowledgements

The work leading to these results has received funding through the ACT program (Accelerating CCS Technologies, Horizon 2020 Project No. 691712) within the ANICA project (ACT Project No. 299653). Financial contributions were made by the German Federal Ministry for Economic Affairs and Climate Action (BMWK Project No. 03EE5025). The authors would like to thank Diethelm Walter (Lhoist Germany Rheinkalk GmbH) for providing the Messinghausen limestone samples, Paul Bickel (Technical University of Darmstadt) for assisting in the data curation of experimental results, Matteo C. Romano (Politecnico di Milano) for sharing the MATLAB code from his carbonator model, Alina M. Greco-Coppi for proof-reading this article, and the team of the University and State Library Darmstadt for their help in gaining access to primary sources. Finally, Martin Greco-Coppi extends special thanks to Juan Carlos Abanades (Spanish National Research Council) for the fruitful discussions on carbonator models.

Appendix A. Calculation of dense region height

$$\frac{W_{\mathrm{carb}}}{A_t \rho_s} = H_d \varepsilon_{s,d} + \int_{H_d}^{H_t} \varepsilon_s^* + \left(\varepsilon_{s,d} - \varepsilon_s^*\right) \exp(-a(z - H_d)) dz \tag{A.1}$$

The integral from Eq. (17) can be solved analytically:

$$\int_{H_d}^{H_l} \varepsilon_s^* + \left(\varepsilon_{s,d} - \varepsilon_s^*\right) \exp(-a(z - H_d)) dz = \frac{\varepsilon_s^* H_l + \left(\varepsilon_{s,d} - \varepsilon_s^*\right)}{a[1 - \exp(-aH_l)]} \tag{A.2}$$

Thus:

$$\frac{W_{\mathrm{carb}}}{A \rho_s} = H_d \varepsilon_{s,d} + \varepsilon_s^* H_l + \left(\varepsilon_{s,d} - \varepsilon_s^*\right) \frac{1 - \exp(-aH_l)}{a} \tag{A.3}$$

The equation can be simplified using the solid concentration at exit:

$$\frac{W_{\mathrm{carb}}}{A \rho_s} = \frac{\varepsilon_{s,d} - \varepsilon_{\mathrm{s,out}}}{a} + H_t \varepsilon_{\mathrm{s,d}} - H_l \left(\varepsilon_{s,d} - \varepsilon_s^*\right) \tag{A.4}$$

For high reactors (H_T>TDH), a simplified equation can be found setting $\varepsilon_{\mathrm{s,out}} \approx \varepsilon_s^*$:

$$\frac{W_{\mathrm{carb}}}{A \rho_s} \approx \frac{\varepsilon_{s,d} - \varepsilon_s^*}{a} + H_t \varepsilon_{s,d} - H_l \left(\varepsilon_{s,d} - \varepsilon_s^*\right) \tag{A.5}$$

Since $\varepsilon_s^* \ll \varepsilon_{\mathrm{s,d}}$:

$$H_d \cong \frac{W_{\mathrm{carb}}}{A \ \rho_s \ \left(\varepsilon_{s,d} - \varepsilon_s^*\right)} - \frac{1}{a} \tag{A.6}$$

Appendix B. Derivations of specific core-wall areas

The core-wall area in the dense region ($A_{\text{c-w,d}}$) is calculated using Eq. (22) and assuming δ is constant throughout the dense region —in this assumption, we followed [35].

$$A_{\text{c-w,d}} = \pi \, d_c \, H_d \tag{B.1}$$

$$A_{\text{c-w,d}} = \pi \, \delta_d^{0.5} \, d_T \, H_d \tag{B.2}$$

Thus, the specific core-wall area in the dense region ($a_{\text{c-w,d}}$) in $\text{m}^2_{\text{interphase}}/\text{m}^3_{\text{reactor}}$ is:

$$a_{\text{c-w,d}} = 4 \, \delta_d^{0.5} \, d_T^{-1} \tag{B.3}$$

For the lean region, since δ variates with the height of the reactor, the calculation of the area $A_{\text{c-w}}$ requires an integration:

$$A_{\text{c-w,l}} = \int_0^{H_l} \pi \, d_{\text{c,l}}(z) \, dz \tag{B.4}$$

Using Eq. (22):

$$A_{\text{c-w,l}} = \pi \, d_T \int_0^{H_l} \sqrt{\delta(z)} \, dz \tag{B.5}$$

An analytical result can be found by considering the surface of a truncated cone. With this simplifying assumption:

$$A_{\text{c-w,l}} \approx \left[\pi \left(d_{\text{c,d}} + d_{\text{c,out}}\right)/2\right] H_l$$

Here, $d_{\text{c,d}}$ and $d_{\text{c,out}}$ are the core diameter at the dense region and the reactor outlet, respectively. Using Eq. (22),

$$A_{\text{c-w,l}} \approx 0.5 \, \pi\left(\delta_d^{0.5} + \delta_{\text{out}}^{0.5}\right) d_T \, H_l \tag{B.6}$$

Dividing by the corresponding reactor volume, the specific core-wall area in the lean region can be found:

$$a_{\text{c-w,l}} \approx 2\left(\delta_d^{0.5} + \delta_{\text{out}}^{0.5}\right) d_T^{-1} \tag{B.7}$$

Appendix C. Governing differential equation of the reactor sub-model

From the point of view of the reactor (gas), the binding of CO_2 in the carbonator follows a first-order reaction, according to Eq. (33). Dividing by the volume of gas, this equation can be expressed in terms of variation of concentration driving force with Eq. (32).

$$C_{\text{CO2}} = N_{\text{CO2}}/V_{gas} \tag{C.1}$$

$$C_{\text{CO2}} - C_{\text{CO2,eq}} = N_{\text{CO2}}/V_{gas} - C_{\text{CO2,eq}} \tag{C.2}$$

$$d\left(N_{\text{CO2}}/V_{gas} - C_{\text{CO2,eq}}\right)/dt = d\left(C_{\text{CO2}} - C_{\text{CO2,eq}}\right)/dt = d\mathfrak{C}/dt \tag{C.3}$$

Assuming constant equilibrium concentration and constant gas volume, the equation simplifies to:

$$dN_{\text{CO2}}/dt = V_{gas} d\mathfrak{C}/dt \tag{C.4}$$

Using Eq. (C.4) in Eq. (33):

$$d\mathfrak{C}/dt = -\left(V_{sa}/V_{gas}\right) K_r \mathfrak{C} \tag{C.5}$$

The volume relation between the potentially active solids and the gas can be expressed as follows.

$$\frac{V_{sa}}{V_{gas}} = \frac{\xi \, V_s}{V_{gas}} = \frac{A_t \, \varepsilon_s \, \xi \, dz}{A_t \, u_0 \, dt} = \frac{\varepsilon_s \, \xi}{u_0} \frac{dz}{dt} \tag{C.6}$$

Here, the departure from the ideal plow-flow reactor is considered using a gas–solid contact efficiency (η). Finally, using Eqs.(C.6) and (C.5) gives:

$$d\mathfrak{C}/dz = -\eta \, K_r \, \mathfrak{C} \, \xi \, \varepsilon_s/u_o \tag{C.7}$$

If ε_s and η are constant throughout the height of the reactor, an analytical expression for the integral form can be found:

$$\mathfrak{C}_{\text{out}} = \mathfrak{C}_{\text{in}}\exp(-\eta\ K_r\ \tau_{\text{reactor}}) \tag{C.8}$$

Here, the characteristic time is:

$$\tau_{\text{reactor}} \equiv \xi\varepsilon_s H_T/u_o \tag{C.9}$$

Appendix D. Approximation of carbonator efficiency

$$1 - \mathfrak{C}_{\text{out}}/\mathfrak{C}_{\text{in}} = 1 - \left(y_{\text{CO2,out}} - y_{\text{CO2,eq}}\right)/\left(y_{\text{CO2,in}} - y_{\text{CO2,eq}}\right) \tag{D.1}$$

The carbonator and the equilibrium efficiencies can be approximated as:

$$E_{\text{carb,eq}} \approx 1 - \left(y_{\text{CO2,eq}}/y_{\text{CO2,in}}\right) = \left(y_{\text{CO2,in}} - y_{\text{CO2,eq}}\right)/y_{\text{CO2,in}} \tag{D.2}$$

$$E_{\text{carb}} \approx 1 - \left(y_{\text{CO2,out}}/y_{\text{CO2,in}}\right) = \left(y_{\text{CO2,in}} - y_{\text{CO2,out}}\right)/y_{\text{CO2,in}} \tag{D.3}$$

Using Eqs. (D.2) and (D.3) in Eq. (D.1), the following approximation is obtained:

$$1 - \mathfrak{C}_{\text{out}}/\mathfrak{C}_{\text{in}} \approx E_{\text{carb}}/E_{\text{carb,eq}} \tag{D.4}$$

Appendix E. Contact efficiency of the lean region in Romano's model

The final expression to calculate the contact efficiency in the lean region using Romano's approach [40] can be obtained by solving the following integral:

$$\text{Int.} = \int_0^{H_l} \left[\varepsilon_s^* + \left(\varepsilon_{s,d} - \varepsilon_s^*\right)\exp(-az)\right]\ \left[1 - (1 - \eta_d)\exp(-bz)\right]\ dz \tag{E.1}$$

Integrating Eq. (E.1) yields:

$$\text{Int.} = \frac{H_l}{\overline{\varepsilon_l}}\left[1 - \frac{\varepsilon_s^*}{\overline{\varepsilon_l}}(1 - \overline{\eta_l}) - \frac{\varepsilon_{s,d} - \varepsilon_s^*}{\overline{\varepsilon_l}}(1 - \eta_d)\frac{1 - \exp(-(a+b)H_l)}{(a+b)H_l}\right] \tag{E.2}$$

Integrating, using Eq. (10), an expression for the outlet concentration is found:

$$\mathfrak{C}_{\text{out}} = \mathfrak{C}_d\exp\left\{-K_r\tau_l\left[1 - \frac{\varepsilon_s^*}{\overline{\varepsilon_l}}(1 - \overline{\eta_l}) - \frac{\varepsilon_{s,d} - \varepsilon_s^*}{\overline{\varepsilon_l}}(1 - \eta_d)\frac{1 - \exp(-(a+b)H_l)}{(a+b)H_l}\right]\right\} \tag{E.3}$$

With

$$\tau_l \equiv \xi\overline{\varepsilon_l}H_l/u_0 \tag{E.4}$$

Appendix F. Correlations for core-wall exchange coefficient

Bi [107] recommends the following correlation from Patience and Chaouki:

$$\frac{k_{\text{c-w}}\ d_T}{D_g}4(d_c/d_T) = \text{Sc}^{0.5}\ \text{Re}_{\text{p}}^{0.75}\ \left[G_s/(\rho_s\ u_0)\right]^{0.25} \tag{F.1}$$

Using Eqs. (54–56):

$$k_{\text{c-w}}\ a_{\text{c-w,d}} = k_{\text{c-w}}\ 4\ d_c\ d_T^{-2} = d_T^{-2}\ D_g\ \text{Sc}^{0.5}\ \text{Re}_{\text{p}}^{0.75}\ \left[G_s/(\rho_s\ u_0)\right]^{0.25} \tag{F.2}$$

An expression for $K_{\text{c-w}}$ is:

$$K_{\text{c-w}} = d_T^{-2}\ D_g\ \text{Sc}^{0.5}\ \text{Re}_{\text{p}}^{0.75}\ \left[G_s/(\rho_s u_0)\right]^{0.25} \tag{F.3}$$

And for $k_{\text{c-w}}$:

$$k_{\text{c-w}} = 0.25\ d_c^{-1}\ D_g\ \text{Sc}^{0.5}\ \text{Re}_\text{p}^{0.75}\ \left[G_s/(\rho_s u_0)\right]^{0.25} \tag{F.4}$$

Appendix G. Range of variation for the upscaling parametric study

The range of variation of the parameters considered in the calculations of Fig. 19 is displayed in Table G.1.

Table G1
Range of variation of parameters for Fig. 19.

Parameter		Best case	Base case	Worst case	Unit
Specific core-wall gas interchange coefficient	$k_{\text{c-w}}$	0.3	0.158	0.015	m/s
Inlet CO_2 concentration	$y_{\text{CO2,in}}$	0.18	0.12	0.8	vol%$_\text{wb}$
Superficial gas velocity	u_0	2.5	4	5.5	m/s
Solid volume fraction in the dense region	$\varepsilon_{s,d}$	0.15	0.30	0.45	–
Mean particle size	$d_{\text{p,50}}$	127	227	327	µm
Lewis constant	k_{Lewis}	4	8	12	1/s

References

[1] T. Shimizu, T. Hirama, H. Hosoda, K. Kitano, M. Inagaki, K. Tejima, A Twin Fluid-Bed Reactor for Removal of CO_2 from Combustion Processes, Chem. Eng. Res. Des. 77 (1999) 62–68, https://doi.org/10.1205/026387699525882.

[2] S. Gardarsdottir, E. de Lena, M.C. Romano, S. Roussanaly, M. Voldsund, J.-F. Pérez-Calvo, D. Berstad, C. Fu, R. Anantharaman, D. Sutter, M. Gazzani, M. Mazzotti, G. Cinti, Comparison of Technologies for CO_2 Capture from Cement Production—Part 2: Cost Analysis, Energies 12 (2019) 542, https://doi.org/10.3390/en12030542.

[3] M. Haaf, R. Anantharaman, S. Roussanaly, J. Ströhle, B. Epple, CO_2 capture from waste-to-energy plants: Techno-economic assessment of novel integration concepts of calcium looping technology, Resour. Conserv. Recycl. 162 (2020) 104973, https://doi.org/10.1016/j.resconrec.2020.104973.

[4] M. Zhao, A.I. Minett, A.T. Harris, A review of techno-economic models for the retrofitting of conventional pulverised-coal power plants for post-combustion capture (PCC) of CO_2, Energy Environ. Sci. 6 (2013) 25–40, https://doi.org/10.1039/C2EE22890D.

[5] M. Voldsund, S. Gardarsdottir, E. de Lena, J.-F. Pérez-Calvo, A. Jamali, D. Berstad, C. Fu, M.C. Romano, S. Roussanaly, R. Anantharaman, H. Hoppe, D. Sutter, M. Mazzotti, M. Gazzani, G. Cinti, K. Jordal, Comparison of Technologies for CO_2 Capture from Cement Production—Part 1: Technical Evaluation, Energies 12 (2019) 559, https://doi.org/10.3390/en12030559.

[6] A. Rolfe, Y. Huang, M. Haaf, S. Rezvani, D. McIlveen-Wright, N.J. Hewitt, Integration of the calcium carbonate looping process into an existing pulverized coal-fired power plant for CO_2 capture: Techno-economic and environmental evaluation, Appl. Energy 222 (2018) 169–179, https://doi.org/10.1016/j.apenergy.2018.03.160.

[7] H. Dieter, A.R. Bidwe, G. Varela-Duelli, A. Charitos, C. Hawthorne, G. Scheffknecht, Development of the calcium looping CO_2 capture technology from lab to pilot scale at IFK, University of Stuttgart, Fuel 127 (2014) 23–37, https://doi.org/10.1016/j.fuel.2014.01.063.

[8] M. Hornberger, J. Moreno, M. Schmid, G. Scheffknecht, Experimental investigation of the carbonation reactor in a tail-end Calcium Looping configuration for CO_2 capture from cement plants, Fuel Process. Technol. 210 (2020) 106557, https://doi.org/10.1016/j.fuproc.2020.106557.

[9] C. Hawthorne, H. Dieter, A.R. Bidwe, A. Schuster, G. Scheffknecht, S. Unterberger, M. Käß, CO_2 capture with CaO in a 200 kW$_\text{th}$ dual fluidized bed pilot plant, Energy Procedia 4 (2011) 441–448, https://doi.org/10.1016/j.egypro.2011.01.073.

[10] J. Kremer, A. Galloy, J. Ströhle, B. Epple, Continuous CO_2 Capture in a 1-MW$_\text{th}$ Carbonate Looping Pilot Plant, Chem. Eng. Technol. 36 (2013) 1518–1524, https://doi.org/10.1002/ceat.201300084.

[11] J. Ströhle, M. Junk, J. Kremer, A. Galloy, B. Epple, Carbonate looping experiments in a 1MW$_\text{th}$ pilot plant and model validation, Fuel 127 (2014) 13–22, https://doi.org/10.1016/j.fuel.2013.12.043.

[12] B. Arias, M.E. Diego, J.C. Abanades, M. Lorenzo, L. Diaz, D. Martínez, J. Alvarez, A. Sanchez-Biezma, Demonstration of steady state CO_2 capture in a 1.7MW$_\text{th}$ calcium looping pilot, Int. J. Greenhouse Gas Control 18 (2013) 237–245, https://doi.org/10.1016/j.ijggc.2013.07.014.

[13] M.E. Diego, B. Arias, A. Méndez, M. Lorenzo, L. Díaz, A. Sanchez-Biezma, J. C. Abanades, Experimental testing of a sorbent reactivation process in La Pereda 1.7 MW$_\text{th}$ calcium looping pilot plant, Int. J. Greenhouse Gas Control 50 (2016) 14–22, https://doi.org/10.1016/j.ijggc.2016.04.008.

[14] M.-H. Chang, W.-C. Chen, C.-M. Huang, W.-H. Liu, Y.-C. Chou, W.-C. Chang, W. Chen, J.-Y. Cheng, K.-E. Huang, H.-W. Hsu, Design and Experimental Testing of a 1.9MW$_\text{th}$ Calcium Looping Pilot Plant, Energy Procedia 63 (2014) 2100–2108, https://doi.org/10.1016/j.egypro.2014.11.226.

[15] M.-H. Chang, C.-M. Huang, W.-H. Liu, W.-C. Chen, J.-Y. Cheng, W. Chen, T.-W. Wen, S. Ouyang, C.-H. Shen, H.-W. Hsu, Design and experimental investigation of calcium looping process for 3-kW$_\text{th}$ and 1.9-MW$_\text{th}$ Facilities, Chemical Engineering & Technology 36 (2013) 1525–1532, https://doi.org/10.1002/ceat.201300081.

[16] Y. Tan, W. Liu, X. Zhang, W. Wei, S. Wang, Conventional and optimized testing facilities of calcium looping process for CO_2 capture: A systematic review, Fuel 358 (2024) 130337, https://doi.org/10.1016/j.fuel.2023.130337.

[17] M. Greco-Coppi, P.M. Seufert, C. Hofmann, A. Rolfe, Y. Huang, S. Rezvani, J. Ströhle, B. Epple, Efficient CO_2 capture from lime plants: Techno-economic assessment of integrated concepts using indirectly heated carbonate looping technology, Carbon Capture Science & Technology 11 (2024) 100187, https://doi.org/10.1016/j.ccst.2023.100187.

[18] E. Svensson, H. Wiertzema, S. Harvey, Potential for Negative Emissions by Carbon Capture and Storage From a Novel Electric Plasma Calcination Process for Pulp and Paper Mills, Front. Clim. 3 (2021) 705032, https://doi.org/10.3389/fclim.2021.705032.

[19] R.M. Jacob, L.-A. Tokheim, Electrified calciner concept for CO_2 capture in pyro-processing of a dry process cement plant, Energy 268 (2023) 126673, https://doi.org/10.1016/j.energy.2023.126673.

[20] L.-A. Tokheim, A. Mathisen, L.E. Øi, C.K. Jayarathna, N.H. Eldrup, T. Gautestad, Combined calcination and CO_2 capture in cement clinker production by use of electrical energy., in: TCCS–10, in: CO2 Capture, Transport and Storage. Trondheim 17th–19th June 2019. Selected Papers from the 10th International Trondheim CCS Conference, 2019, pp. 101–109.

[21] M. Greco-Coppi, C. Hofmann, D. Walter, J. Ströhle, B. Epple, Negative CO_2 emissions in the lime production using an indirectly heated carbonate looping process, Mitig Adapt Strateg Glob Change 28 (2023), https://doi.org/10.1007/s11027-023-10064-7.

[22] M. Junk, M. Reitz, J. Ströhle, B. Epple, Technical and Economical Assessment of the Indirectly Heated Carbonate Looping Process, J. Energy Res. Technol. 138 (2016) 042210, https://doi.org/10.1115/1.4033142.

[23] J. Yin, C. Li, G. Paicu, S. Su, Techno-economic assessment of retrofitting indirect-heated calcium looping using coal and biomass as fuels into an existing cement plant for CO_2 capture, Gas Science and Engineering 123 (2024) 205236, https://doi.org/10.1016/j.jgsce.2024.205236.

[24] D. Höftberger, J. Karl, The Indirectly Heated Carbonate Looping Process for CO_2 Capture—A Concept With Heat Pipe Heat Exchanger, J. Energy Res. Technol. 138 (2016) 042211, https://doi.org/10.1115/1.4033302.

[25] M. Reitz, M. Junk, J. Ströhle, B. Epple, Design and operation of a 300 kW$_\text{th}$ indirectly heated carbonate looping pilot plant, Int. J. Greenhouse Gas Control 54 (2016) 272–281, https://doi.org/10.1016/j.ijggc.2016.09.016.

[26] C. Hofmann, M. Greco-Coppi, J. Ströhle, B. Epple, Enhancement of a 300 kW$_\text{th}$ pilot plant for testing the indirectly heated carbonate looping process for CO_2 capture from lime and cement industry, Exp. Therm Fluid Sci. 151 (2024) 111091, https://doi.org/10.1016/j.expthermflusci.2023.111091.

[27] M. Greco-Coppi, C. Hofmann, J. Ströhle, D. Walter, B. Epple, Efficient CO_2 capture from lime production by an indirectly heated carbonate looping process, Int. J. Greenhouse Gas Control 112 (2021) 103430, https://doi.org/10.1016/j.ijggc.2021.103430.

[28] I. Martínez, G. Grasa, J. Parkkinen, T. Tynjälä, T. Hyppänen, R. Murillo, M. C. Romano, Review and research needs of Ca-Looping systems modelling for post-combustion CO_2 capture applications, Int. J. Greenhouse Gas Control 50 (2016) 271–304, https://doi.org/10.1016/j.ijggc.2016.04.002.

[29] A. Charitos, N. Rodríguez, C. Hawthorne, M. Alonso, M. Zieba, B. Arias, G. Kopanakis, G. Scheffknecht, J.C. Abanades, Experimental Validation of the Calcium Looping CO_2 Capture Process with Two Circulating Fluidized Bed Carbonator Reactors, Ind. Eng. Chem. Res. 50 (2011) 9685–9695, https://doi.org/10.1021/ie200579f.

[30] C. Ortiz, R. Chacartegui, J.M. Valverde, J.A. Becerra, L.A. Perez-Maqueda, A new model of the carbonator reactor in the calcium looping technology for post-combustion CO2 capture, Fuel 160 (2015) 328–338, https://doi.org/10.1016/j.fuel.2015.07.095.

[31] M. Alonso, N. Rodríguez, G. Grasa, J.C. Abanades, Modelling of a fluidized bed carbonator reactor to capture CO_2 from a combustion flue gas, Chem. Eng. Sci. 64 (2009) 883–891, https://doi.org/10.1016/j.ces.2008.10.044.

[32] K. Atsonios, M. Zeneli, A. Nikolopoulos, N. Nikolopoulos, P. Grammelis, E. Kakaras, Calcium looping process simulation based on an advanced thermodynamic model combined with CFD analysis, Fuel 153 (2015) 370–381, https://doi.org/10.1016/j.fuel.2015.03.014.

[33] M. Zeneli, A. Nikolopoulos, N. Nikolopoulos, P. Grammelis, E. Kakaras, Application of an advanced coupled EMMS-TFM model to a pilot scale CFB carbonator, Chem. Eng. Sci. 138 (2015) 482–498, https://doi.org/10.1016/j.ces.2015.08.008.

[34] A. Stroh, F. Alobaid, J. Ströhle, J. Hilz, B. Epple, CFD simulation of 1 MW carbonator using DDPM-DEM model. In: 6th High Temperature Solid Looping Cycles Network Meeting, 2015.

[35] D. Kunii, O. Levenspiel, The K-L reactor model for circulating fluidized beds, Chem. Eng. Sci. 55 (2000) 4563–4570, https://doi.org/10.1016/S0009-2509(00)00073-7.

[36] A. Lasheras, J. Ströhle, A. Galloy, B. Epple, Carbonate looping process simulation using a 1D fluidized bed model for the carbonator, Int. J. Greenhouse Gas Control 5 (2011) 686–693, https://doi.org/10.1016/j.ijggc.2011.01.005.

[37] D. Kunii, O. Levenspiel. Fluidization Engineering, second ed., Elsevier, 1991 https://doi.org/10.1016/C2009-0-24190-0.

[38] J.C. Abanades, E.J. Anthony, D.Y. Lu, C. Salvador, D. Alvarez, Capture of CO_2 from combustion gases in a fluidized bed of CaO, AIChE J. 50 (2004) 1614–1622, https://doi.org/10.1002/aic.10132.

[39] S.K. Bhatia, D.D. Perlmutter, Effect of the product layer on the kinetics of the CO_2-lime reaction, AIChE J. 29 (1983) 79–86, https://doi.org/10.1002/aic.690290111.

[40] M.C. Romano, Modeling the carbonator of a Ca-looping process for CO_2 capture from power plant flue gas, Chem. Eng. Sci. 69 (2012) 257–269, https://doi.org/10.1016/j.ces.2011.10.041.

[41] J. Ylätalo, J. Ritvanen, B. Arias, T. Tynjälä, T. Hyppänen, 1-Dimensional modelling and simulation of the calcium looping process, Int. J. Greenhouse Gas Control 9 (2012) 130–135, https://doi.org/10.1016/j.ijggc.2012.03.008.

[42] M. Tizfahm, M. Tahmasebpoor, H.R. Behtash, M. Balsamo, F. Montagnaro, Coupled kinetic and hydrodynamic model for a carbonator reactor of calcium looping process: Sulfur dioxide effect, Process Saf. Environ. Prot. (2024), https://doi.org/10.1016/j.psep.2024.03.065.

[43] M.E. Diego, B. Arias, Impact of load changes on the carbonator reactor of a 1.7 MW_{th} calcium looping pilot plant, Fuel Processing Technology 200 (2020) 106307, https://doi.org/10.1016/j.fuproc.2019.106307.

[44] M. Greco-Coppi, J. Ströhle, B. Epple, A carbonator model for CO2 capture based on results from pilot tests. Part II: Deactivation and reaction model, SSRN preprint (2024), https://doi.org/10.2139/ssrn.4948852.

[45] M. Ramezani, P. Tremain, K. Shah, E. Doroodchi, B. Moghtaderi, Derivation of Kinetics and Design Parameters for a Carbonator Reactor in a Greenhouse Calcium Looping Process, Energy Technol. 5 (2017) 644–655, https://doi.org/10.1002/ente.201600427.

[46] J. Carlos Abanades, Y.A. Criado, R. García, Countercurrent moving bed carbonator for CO_2 capture in decoupled calcium looping systems, Chemical Engineering Journal 461 (2023) 141956, https://doi.org/10.1016/j.cej.2023.141956.

[47] I. Martínez, B. Arias, G.S. Grasa, J.C. Abanades, CO_2 capture in existing power plants using second generation Ca-Looping systems firing biomass in the calciner, J. Clean. Prod. 187 (2018) 638–649, https://doi.org/10.1016/j.jclepro.2018.03.189.

[48] M. Greco-Coppi, A. Dinkova, C. Hofmann, D. Walter, K. Böge, J. Ströhle, B. Epple, Design of a 2 MW_{th} Indirectly Heated Carbonate Looping Demonstration Facility at a Lime Plant in Germany, in: 7th Post Combustion Capture Conference, Pittsburgh, Pennsylvania, 2023, https://doi.org/10.26083/tuprints-00026537.

[49] B. Arias, Y. Alvarez Criado, A. Méndez, P. Marqués, I. Finca, J.C. Abanades, Pilot Testing of Calcium Looping at TRL7 with CO_2 Capture Efficiencies toward 99%, Energy & Fuels 38 (2024) https://doi.org/10.1021/acs.energyfuels.4c02472.

[50] C. Hofmann, M. Greco-Coppi, J. Ströhle, B. Epple, Pilot Testing of the Indirectly Heated Carbonate Looping Process for Cement and Lime Plants, in: Proceedings of the 16th Greenhouse Gas Control Technologies Conference, 2022, https://doi.org/10.2139/ssrn.4278810.

[51] M. Reitz, Experimentelle Untersuchung und Bewertung eines indirekt beheizten Carbonate-Looping-Prozesses, Dissertation, first ed., Cuvillier Verlag, Göttingen, 2017.

[52] G. Sun, J.R. Grace, Effect of particle size distribution in different fluidization regimes, AIChE J. 38 (1992) 716–722, https://doi.org/10.1002/aic.690380508.

[53] J.R. Grace, G. Sun, Influence of particle size distribution on the performance of fluidized bed reactors, Can J Chem Eng 69 (1991) 1126–1134, https://doi.org/10.1002/cjce.5450690512.

[54] P. Dieringer, F. Marx, J. Ströhle, B. Epple, System Hydrodynamics of a 1 MW_{th} Dual Circulating Fluidized Bed Chemical Looping Gasifier, Energies 16 (2023) 5630, https://doi.org/10.3390/en16155630.

[55] G.S. Grasa, J.C. Abanades, M. Alonso, B. González, Reactivity of highly cycled particles of CaO in a carbonation/calcination loop, Chem. Eng. J. 137 (2008) 561–567, https://doi.org/10.1016/j.cej.2007.05.017.

[56] F. Fang, Z.-S. Li, N.-S. Cai, Experiment and Modeling of CO_2 Capture from Flue Gases at High Temperature in a Fluidized Bed Reactor with Ca-Based Sorbents, Energy Fuels 23 (2009) 207–216, https://doi.org/10.1021/ef800474n.

[57] D. Bortzmeyer, J.C. Goimard, Mechanical properties and attrition behaviour of $CaCO_3$ powders: influence of particle shape, Powder Technol. 86 (1996) 163–169, https://doi.org/10.1016/0032-5910(95)03063-8.

[58] F. Scala, R. Chirone, P. Salatino, Attrition phenomena relevant to fluidized bed combustion and gasification systems, in: Fluidized Bed Technologies for near-Zero Emission Combustion and Gasification, Elsevier, 2013, pp. 254–315, https://doi.org/10.1533/9780857098801.1.254.

[59] A. Coppola, F. Montagnaro, P. Salatino, F. Scala, Attrition of Limestone During Fluidized Bed Calcium Looping Cycles for CO_2 Capture, Combust. Sci. Technol. 184 (2012) 929–941, https://doi.org/10.1080/00102202.2012.663986.

[60] A. Coppola, F. Scala, P. Salatino, F. Montagnaro, Fluidized bed calcium looping cycles for CO_2 capture under oxy-firing calcination conditions: Part 1, Assessment of Six Limestones, Chemical Engineering Journal 231 (2013) 537–543, https://doi.org/10.1016/j.cej.2013.07.113.

[61] M. Haaf, A. Stroh, J. Hilz, M. Helbig, J. Ströhle, B. Epple, Process Modelling of the Calcium Looping Process and Validation Against 1 MW_{th} Pilot Testing, Energy Procedia 114 (2017) 167–178, https://doi.org/10.1016/j.egypro.2017.03.1159.

[62] D. Geldart, A.R. Abrahamsen, Homogeneous fluidization of fine powders using various gases and pressures, Powder Technol. 19 (1978) 133–136, https://doi.org/10.1016/0032-5910(78)80084-9.

[63] M. Kleiber, R. Joh, D1: *Berechnungsmethoden für Stoffeigenschaften*, in: VDI-Wärmeatlas: Mit 320 Tabellen, eleventh., bearb. und erw. Aufl, Springer Vieweg, Berlin, Heidelberg, 2013, pp. 137–174.doi, https://doi.org/10.1007/978-3-642-19981-3_11.

[64] M. Reitz, M. Junk, J. Ströhle, B. Epple, Design and Erection of a 300 kW_{th} Indirectly Heated Carbonate Looping Test Facility, Energy Procedia 63 (2014) 2170–2177, https://doi.org/10.1016/j.egypro.2014.11.236.

[65] D. Kunii, O. Levenspiel, Circulating fluidized-bed reactors, Chem. Eng. Sci. 52 (1997) 2471–2482, https://doi.org/10.1016/S0009-2509(97)00066-3.

[66] J.R. Grace, High-velocity fluidized bed reactors, Chem. Eng. Sci. 45 (1990) 1953–1966, https://doi.org/10.1016/0009-2509(90)80070-U.

[67] J.R. Grace, X.T. Bi, Introduction to Circulating Fluidized Beds, in: J.R. Grace, A. A. Avidan, T.M. Knowlton (Eds.), Circulating Fluidized Beds, Springer, Netherlands, Dordrecht, 1996, pp. 1–20, https://doi.org/10.1007/978-94-009-0095-0_1.

[68] B. Leckner, Fluidization Characteristics of Circulating Fluidized Bed Boilers, Chem. Ing. Tech. 95 (2023) 32–39, https://doi.org/10.1002/cite.202200068.

[69] J.R. Grace, Contacting modes and behaviour classification of gas-solid and other two-phase suspensions, Can J Chem Eng 64 (1986) 353–363, https://doi.org/10.1002/cjce.5450640301.

[70] X.T. Bi, J.R. Grace, Flow regime diagrams for gas-solid fluidization and upward transport, Int. J. Multiph. Flow 21 (1995) 1229–1236, https://doi.org/10.1016/0301-9322(95)00037-X.

[71] K. Lim, J. Zhu, J.R. Grace, Hydrodynamics of gas-solid fluidization, Int. J. Multiph. Flow 21 (1995) 141–193, https://doi.org/10.1016/0301-9322(95)00038-Y.

[72] X.T. Bi, N. Ellis, I.A. Abba, J.R. Grace, A state-of-the-art review of gas–solid turbulent fluidization, Chem. Eng. Sci. 55 (2000) 4789–4825, https://doi.org/10.1016/S0009-2509(00)00107-X.

[73] A. Haider, O. Levenspiel, Drag coefficient and terminal velocity of spherical and nonspherical particles, Powder Technol. 58 (1989) 63–70, https://doi.org/10.1016/0032-5910(89)80008-7.

[74] X.T. Bi, J.R. Grace, K.S. Lim, Transition from Bubbling to Turbulent Fluidization, Ind. Eng. Chem. Res. 34 (1995) 4003–4008, https://doi.org/10.1021/ie00038a041.

[75] X.T. Bi, J.R. Grace, Effect of measurement method on the velocities used to demarcate the onset of turbulent fluidization, The Chemical Engineering Journal and the Biochemical Engineering Journal 57 (1995) 261–271, https://doi.org/10.1016/0923-0467(94)02875-B.

[76] P. Cai, The transition of flow regime in dense phase gas–solid fluidized bed, Tsinghua University, Beijing, China, 1989. PhD dissertation.

[77] T. Wytrwat, E.-U. Hartge, M. Yazdanpanah, S. Heinrich, Influences on the transition from bubbling to turbulent fluidization for Geldart's group B particles, Powder Technol. 375 (2020) 81–88, https://doi.org/10.1016/j.powtec.2020.07.086.

[78] X.T. Bi, A. Chen, Pressure fluctuations in gas-solids fluidized beds, China Particuology 1 (2003) 139–144, https://doi.org/10.1016/S1672-2515(07)60130-4.

[79] X.T. Bi, J.R. Grace, J. Zhu, Regime transitions affecting gas-solids suspensions and fluidized-beds, Chem. Eng. Res. Des. 73 (1995) 154–161.

[80] Y. Jin, Z.Q. Yu, Z.W. Wang, P. Cai, A criterion for transition from bubbling to turbulent fluidization, in: Fluidization V: Proceedings of the Fifth Engineering Foundation Conference on Fluidization, Elsinore, Denmark, May 18-23, 1986, Engineering Foundation, 1986.

[81] J. Ströhle, A. Lasheras, A. Galloy, B. Epple, Simulation of the Carbonate Looping Process for Post-Combustion CO_2 Capture from a Coal-Fired Power Plant, Chem. Eng. Technol. 32 (2009) 435–442, https://doi.org/10.1002/ceat.200800569.

[82] A. Mahecha-Botero, in: Catalytic Fluidized Bed Reactors, Essentials of Fluidization Technology, Wiley, 2020, pp. 333–361, https://doi.org/10.1002/9783527699483.ch15.

[83] N. Ellis, A. Mahecha-Botero, Scale-Up of Fluidized Beds, in: J. Grace, X. Bi, N. Ellis (Eds.), Essentials of Fluidization Technology, Wiley, 2020, pp. 405–429, https://doi.org/10.1002/9783527699483.ch17.

[84] W.K. Lewis, F.R. Gilliland, P. Lang, Entrainment from fluidized beds, AIChE Symp. Ser. 58 (38) (1962) 65–78.

[85] D. Geldart, J. Cullinan, S. Georghiades, D. Gilvray, D.J. Pope, Effect of fines on entrainment from gas fluidized beds, Trans. Inst. Chem. Eng 57 (1979).

[86] J.H. Mathews, K.D. Fink. Numerical methods using MATLAB, fourth ed., Prentice Hall, Upper Saddle River, N.J., London, 1999.

[87] A. Cahyadi, A.H. Neumayer, C.M. Hrenya, R.A. Cocco, J.W. Chew, Comparative study of Transport Disengaging Height (TDH) correlations in gas–solid fluidization, Powder Technol. 275 (2015) 220–238, https://doi.org/10.1016/j.powtec.2015.02.010.

[88] F. Sattari, M. Tahmasebpoor, J.M. Valverde, C. Ortiz, M. Mohammadpourfard, Modelling of a fluidized bed carbonator reactor for post-combustion CO_2 capture considering bed hydrodynamics and sorbent characteristics, Chem. Eng. J. 406 (2021) 126762, https://doi.org/10.1016/j.cej.2020.126762.

[89] C. Wang, J. Zhu, Circulating Fluidized Beds, in: J. Grace, X. Bi, N. Ellis (Eds.), Essentials of Fluidization Technology, Wiley, 2020, pp. 239–268, https://doi.org/10.1002/9783527699483.ch12.

[90] A. Daikeler, J. Ströhle, B. Epple, Experimental flow structure analysis in a 1 MW_{th} circulating fluidized bed pilot plant, Chem. Eng. Sci. 195 (2019) 921–934, https://doi.org/10.1016/j.ces.2018.10.037.

[91] C. Hawthorne, M. Trossmann, P. Galindo Cifre, A. Schuster, G. Scheffknecht, Simulation of the carbonate looping power cycle, Energy Procedia 1 (2009) 1387–1394, https://doi.org/10.1016/j.egypro.2009.01.182.

[92] C. Hawthorne, A. Charitos, C.A. Perez-Pulido, Z. Bing, G. Scheffknecht, Design of a dual fluidised bed system for the post-combustion removal of CO_2 using CaO. Part I: CFB carbonator reactor model, in: Proceedings of the 9th International Conference on Circulating Fluidized Beds, TuTech Innovation Gmbh, Hamburg, Germany, 2008.

[93] A.-M. Cormos, A. Simon, Assessment of CO_2 capture by calcium looping (CaL) process in a flexible power plant operation scenario, Appl. Therm. Eng. 80 (2015) 319–327, https://doi.org/10.1016/j.applthermaleng.2015.01.059.

[94] A.-M. Cormos, A. Simon, Dynamic modelling of CO_2 capture by calcium-looping cycle, Chem. Eng. Trans. 35 (2013) 421–426, https://doi.org/10.3303/CET1335070.

[95] L. Monceaux, M. Azzi, Y. Molodtsof, J.F. Large, Overall and Local Characterisation of Flow Regimes in a Circulating Fluidized Bed (1986) 185–191, https://doi.org/10.1016/B978-0-08-031869-1.50022-3.

[96] D.P. Hanak, E.J. Anthony, V. Manovic, A review of developments in pilot-plant testing and modelling of calcium looping process for CO_2 capture from power generation systems, Energy Environ. Sci. 8 (2015) 2199–2249, https://doi.org/10.1039/C5EE01228G.

[97] M. Haaf, J. Hilz, J. Peters, A. Unger, J. Ströhle, B. Epple, Operation of a 1 MW_{th} calcium looping pilot plant firing waste-derived fuels in the calciner, Powder Technol. 372 (2020) 267–274, https://doi.org/10.1016/j.powtec.2020.05.074.

[98] M. Hornberger, J. Moreno, M. Schmid, G. Scheffknecht, Experimental investigation of the calcination reactor in a tail-end calcium looping configuration for CO_2 capture from cement plants, Fuel 284 (2021) 118927, https://doi.org/10.1016/j.fuel.2020.118927.

[99] R.C. Toledo, G.L.A.F. Arce, J.A. Carvalho, I. Ávila, Experimental Development of Calcium Looping Carbon Capture Processes: An Overview of Opportunities and Challenges, Energies 16 (2023) 3623, https://doi.org/10.3390/en16093623.

[100] E.H. Baker, The calcium oxide–carbon dioxide system in the pressure range 1–300 atmospheres, J. Chem. Soc. (1962) 464–470, https://doi.org/10.1039/JR9620000464.

[101] F. García-Labiano, A. Abad, L.F. de Diego, P. Gayán, J. Adánez, Calcination of calcium-based sorbents at pressure in a broad range of CO_2 concentrations, Chem. Eng. Sci. 57 (2002) 2381–2393, https://doi.org/10.1016/S0009-2509(02)00137-9.

[102] I. Barin. Thermochemical data of pure substances, third, VCH, Weinheim, 1995, https://doi.org/10.1002/9783527619825.

[103] S. Furusaki, T. Kikuchi, T. Miyauchi, Axial distribution of reactivity inside a fluid-bed contactor, AIChE J. 22 (1976) 354–361, https://doi.org/10.1002/aic.690220218.

[104] M. Kruse, H. Schoenfelder, J. Werther, A two-dimensional model for gas mixing in the upper dilute zone of a circulating fluidized bed, Can J Chem Eng 73 (1995) 620–634, https://doi.org/10.1002/cjce.5450730505.

[105] O. Levenspiel, Chemical reaction engineering, third ed., John Wiley & Sons Inc, 1999.

[106] W.-C. Yang, Handbook of Fluidization and Fluid-Particle Systems, CRC Press (2003), https://doi.org/10.1201/9780203912744.

[107] X.T. Bi, Some Issues on Core-Annulus and Cluster Models of Circulating Fluidized Bed Reactors, Can J Chem Eng 80 (2002) 809–817, https://doi.org/10.1002/cjce.5450800504.

[108] G.S. Patience, J. Chaouki, Gas phase hydrodynamics in the riser of a circulating fluidized bed, Chem. Eng. Sci. 48 (1993) 3195–3205, https://doi.org/10.1016/0009-2509(93)80205-5.

[109] M. Foka, J. Chaouki, C. Guy, D. Klvana, Gas phase hydrodynamics of a gas-solid turbulent fluidized bed reactor, Chem. Eng. Sci. 51 (1996) 713–723, https://doi.org/10.1016/0009-2509(95)00326-6.

[110] W.J. Massman, A review of the molecular diffusivities of H_2O, CO_2, CH_4, CO, O_3, SO_2, NH_2, N_2O, NO, and NO_2 in air, O_2 and N_2 near STP, Atmos. Environ. 32 (1998) 1111–1127, https://doi.org/10.1016/S1352-2310(97)00391-9.

[111] C.S. Ellis, J.N. Holsen, Diffusion Coefficients for He-N_2 and N_2-CO_2 at Elevated Temperatures, Ind. Eng. Chem. Fund. 8 (1969) 787–791, https://doi.org/10.1021/i160032a030.

[112] J. Agnew, E. Hampartsoumian, J. Jones, W. Nimmo, The simultaneous calcination and sintering of calcium based sorbents under a combustion atmosphere, Fuel 79 (2000) 1515–1523, https://doi.org/10.1016/S0016-2361(99)00287-2.

[113] V. Manovic, J.-P. Charland, J. Blamey, P.S. Fennell, D.Y. Lu, E.J. Anthony, Influence of calcination conditions on carrying capacity of CaO-based sorbent in CO_2 looping cycles, Fuel 88 (2009) 1893–1900, https://doi.org/10.1016/j.fuel.2009.04.012.

[114] M. Junk, Technical and economical assessment of various carbonate looping process configurations, first ed., Cuvillier Verlag, Göttingen, 2017.

[115] R.W. Breault, J. Weber, J. Yang, Saturation carrying capacity Group B particles in a circulating fluidized bed, Powder Technol. 384 (2021) 442–451, https://doi.org/10.1016/j.powtec.2021.02.041.

[116] M. Alonso, N. Rodríguez, B. González, G. Grasa, R. Murillo, J.C. Abanades, Carbon dioxide capture from combustion flue gases with a calcium oxide chemical loop. Experimental results and process development, Int. J. Greenhouse Gas Control 4 (2010) 167–173, https://doi.org/10.1016/j.ijggc.2009.10.004.

[117] Jiaying Wang, Zeneng Sun, Yuanyuan Shao, Jesse Zhu, J. Wang, Z. Sun, Y. Shao, J. Zhu, Operating regimes in circulating fluidized bed combustors: fast fluidization or bubbling-entrained bed? Fuel 297 (2021) https://doi.org/10.1016/j.fuel.2021.120727.

[118] J.M. Matsen, Design and scale-up of CFB catalytic reactors, in: J.R. Grace, A. A. Avidan, T.M. Knowlton (Eds.), Circulating Fluidized Beds, Springer, Netherlands, Dordrecht, 1996, pp. 489–503, https://doi.org/10.1007/978-94-009-0095-0_14.

[119] T. Lockwood, Techno-economic analysis of PC versus CFB combustion technology, IEA Clean Coal Centre, Report CCC/226, London, 2013.

[120] R. Psik, Z. Slomczynski, Final stage of first supercritical 460 MW_e CFB boiler construction–project update, Orlando, Florida, Power Gen International, 2008, pp. 1–13.

[121] Q. Zhu, Developments in circulating fluidised bed combustion, IEA Clean Coal Centre 219 (2013).

[122] T. Aquinas, De ente et essentia, prologus, Brepols Publishers, Turnhout, 2014.

Research Paper V

Research Paper V

Title: A carbonator model for CO_2 capture based on results from pilot tests. Part II: Deactivation and reaction model

Authors: Martin Greco Coppi, Jochen Ströhle, Bernd Epple

Journal: Chemical Engineering Journal (Elsevier)

Status: Published (December 30, 2024)

Volume: 508 (March 15, 2025)

DOI: https://doi.org/10.1016/j.cej.2024.159041

Licensing: The authors. CC BY 4.0

Graphical abstract

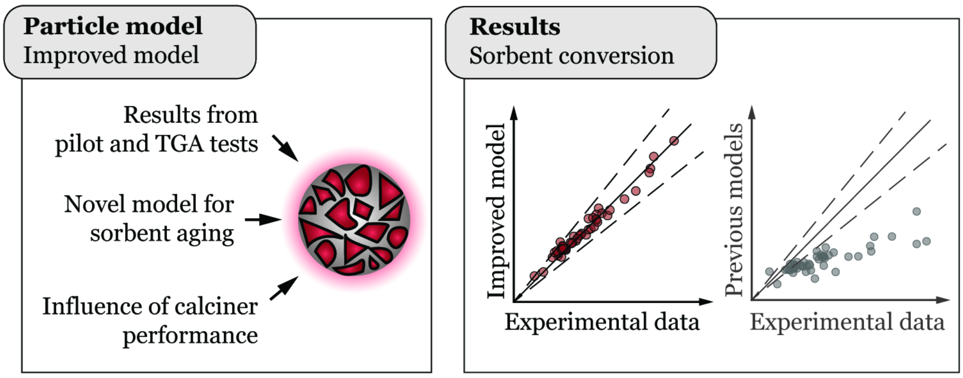
Particle model
Improved model
Results from pilot and TGA tests
Novel model for sorbent aging
Influence of calciner performance
Results
Sorbent conversion
Improved model
Experimental data
Previous models
Experimental data

Short Summary

In this work, we present a novel particle sub-model to predict the carbonation behavior of CaO for CO_2 capture in a CaL process. The sub-model deals with sorbent deactivation and reaction kinetics. We follow an original approach to non-ideal calcination and introduce a new calculation methodology for sorbent aging that considers fluctuations in sorbent circulation and make-up rates. The sub-model presented in this article is used in conjunction with the reactor model of Research Paper IV to predict the CO_2 capture efficiency of a CaL pilot plant. The results of the particle sub-model were validated with experimental data from thermogravimetric analysis (TGA) and pilot tests at the 300-kW_{th} scale. Our study provides new insights for more accurately selecting assumptions and better modeling sorbent behavior in CaL systems.

Chemical Engineering Journal 508 (2025) 159041

Contents lists available at ScienceDirect

Chemical Engineering Journal

journal homepage: www.elsevier.com/locate/cej

A carbonator model for CO_2 capture based on results from pilot tests. Part II: Deactivation and reaction model☆

Martin Greco-Coppi *, Jochen Ströhle, Bernd Epple

Technical University of Darmstadt, Department of Mechanical Engineering, Institute for Energy Systems and Technology, Otto-Berndt-Str. 2, 64287 Darmstadt, Germany

ARTICLE INFO

Keywords:
CO_2 capture
Calcium looping
Indirectly heated carbonate looping
Sorbent deactivation
Thermogravimetric analysis
Pilot testing

ABSTRACT

Carbonate looping (CaL) is a promising technology for CO_2 capture from carbon-intensive processes. The performance of CaL strongly depends on sorbent kinetics and carrying capacity. In this work, we present a novel particle sub-model to predict the carbonation behavior of CaO for CO_2 capture in a CaL process. The sub-model deals with sorbent deactivation and reaction kinetics. We follow an original approach to non-ideal calcination and introduce a new calculation methodology for sorbent aging that considers fluctuations in sorbent circulation and make-up rates. The sub-model presented in this article is used in conjunction with the reactor model of Part I [1] to predict the CO_2 capture efficiency of a CaL pilot plant. The results of the particle sub-model were validated with experimental data from thermogravimetric analysis (TGA) and pilot tests at the 300-kW_{th} scale. Our study provides new insights for more accurately selecting assumptions and better modeling sorbent behavior in CaL systems.

1. Introduction

The *carbonate looping* (CaL) or *calcium looping* process [2] has been widely investigated for over two decades. Extensive experimental and modeling results indicate the high potential of this CO_2 capture technology for decarbonizing power plants and industrial facilities [3,4]. It is widely recognized that the capture efficiency of the process is heavily influenced by sorbent kinetics and carrying capacity, both of which strongly depend on sorbent make-up and circulation rates [5–7]. Carbonator models are essential for linking these parameters to predict reactor behavior and effectively scale-up CaL plants. However, experimental and modeling results often exhibit contradictions across different studies. Furthermore, previous assumptions are generally incorporated into new models without critically assessing the studies on which they are based. This issue is not consistently addressed when incorporating particle sub-models into carbonator models.

Considering the interconnectedness of the carbonator and the calciner is crucial for developing a comprehensive CaL model. This is especially true for the indirectly heated carbonate looping (IHCaL) process, which uses an external combustor to generate the heat for calcination [8]. Indirectly heating a calciner has been proposed previously, including the use of solar energy [9], fuel combustion [10], and electricity [11]. Some indirect-heating methods involve the use of conductive walls [10,12] and solid carriers [13]. The calciner in the IHCaL plant at the Technical University of Darmstadt (TU Darmstadt) uses heat pipes, which efficiently transfer heat via evaporation and condensation of a working solid (i.e., sodium, in this application) [14]. The IHCaL with heat pipes provides the advantage of a high-purity sorbent circulation stream, which is not contaminated by in-situ combustion in the calciner, unlike in oxy-fueled CaL [15]. However, high calcination temperatures should be avoided to prevent damaging the heat pipes. Therefore, a precise model of the calciner's influence on the carbonator operation is required. Developing this model is the objective of the current study.

Despite reported challenges in achieving high calcination efficiency across various operating conditions, the impact of calcination degree on carbonator performance is not fully understood yet. Rodríguez et al. [16] identified low calcination efficiency as a possible cause for carbonator performance drop in a 30-kW_{th} CaL test facility. Haaf et al. [17] reported a reduction in calciner efficiency associated with low calcination temperatures in a 1-MW_{th} CaL pilot plant using waste-derived fuels to fire the calciner. Reitz et al. [18] disclosed difficulties in achieving high calcination efficiencies in a 300-kW_{th} indirectly heated test rig. Rodríguez et al. [19] used a simplified CaL process model to explain that lower calcination efficiencies affect carbonator performance by

---

☆ The first part of this work (Part I: Hydrodynamics and reactor model) is available at https://doi.org/10.1016/j.cej.2024.155119.

* Corresponding author.
E-mail address: martin.greco@est.tu-darmstadt.de (M. Greco-Coppi).

https://doi.org/10.1016/j.cej.2024.159041
Received 22 August 2024; Received in revised form 11 December 2024; Accepted 26 December 2024

Available online 30 December 2024
1385-8947/© 2024 The Author(s). Published by Elsevier B.V. This is an open access article under the CC BY license (http://creativecommons.org/licenses/by/4.0/).

Nomenclature

Latin symbols

A	Constant for the make-up function of Fig. 7 (mol/s)
a_g	Area-to-volume ratio of the gas diffusion layer $(\mathrm{m^2/m^3})$
c_1; c_2	Variables for analytical integration in Appendix A (1/s); (−)
$\mathfrak{C}$	CO_2 concentration driving force (see Eq. (4)) $(\mathrm{mol/m^3})$
$\mathfrak{C}^*$	Equivalent CO_2 concentration driving force $(\mathrm{mol/m^3})$
C_{CO2}; $C_{CO2,eq}$	CO_2 concentration; for equilibrium conditions $(\mathrm{mol/m^3})$
$D_{CO2\text{-}air}$	CO_2 gas diffusion coefficient in air $(\mathrm{m^2/s})$
d_p	Particle diameter (m)
$d_{p,50}$	Mass-median particle diameter (m)
$\mathbf{E}(t)$	Particle residence time distribution (1/s)
E_{carb}	Carbonator efficiency (%)
f_{calc}	Calcination efficiency (−)
f_{carb}	Degree of carbonation relative to the sorbent activity ($\overline{X}_N$) (−)
F_{CO2}; F_{SO2}	Molar input rate into the carbonator of CO_2; of SO_2(mol/s)
F_R; F_0	Molar sorbent circulation rate; make-up rate (mol/s)
h	Thickness of the $CaCO_3$ layer formed around CaO (m)
H_T	Total reactor height (m)
k	Sorbent deactivation constant for Eq. (26) (−)
k'	Sorbent deactivation constant under the presence of $CaSO_4$ (−)
k_g	Diffusion-controlled rate $(\mathrm{m^3/m^2/s})$
k_r; K_r	First-order global rate constant for the particle sub-model; reactor sub-model (1/s)
$K_{r,0}$	Zero-order global rate constant for the reactor sub-model $(\mathrm{mol/m^3/s})$
k_{ri}; $\overline{k}_{ri}$; K_{ri}; $\overline{K}_{ri}$	First-order carbonation reaction constant for the particle sub-model; average for the particle sub-model; for the reactor sub-model; average for the reactor sub-model (1/s)
k_s	First-order intrinsic kinetic constant for the carbonation in the fast stage $(\mathrm{m^4/mol/s})$
k_x	First-order kinetic constant for the carbonation in the fast stage $(\mathrm{m^3/mol/s})$
K_{ED}	First-order external diffusion constant (1/s)
M_i	Molar mass of component i (kg/mol)
$M_{s,a}$	Molar mass of the potentially active solids (kg/mol)
n^{carb}_{CaSO4}; n^{syst}_{CaSO4}	Molar inventory of $CaSO_4$ in the carbonator; in the entire system (mol)
n_s	Total sorbent inventory in the system $(\mathrm{mol_{Ca}})$
$n_{s,carb}$	Total sorbent inventory in the carbonator $(\mathrm{mol_{Ca}})$
N	Number of complete cycles or *particle age* (−)
p	Pressure (Pa)
PV; PV_0	Pore volume of used sorbent; pore volume of fresh sorbent $(\mathrm{m^3/g})$
p_{CO2}; $p_{CO2,in}$; $p_{CO2,eq}$	Partial pressure of CO_2; at carbonator inlet; for equilibrium conditions (Pa)
r_0; r'_0	Initial calcination rate (1/s); per unit of specific surface (nm/s)
$\mathbf{r}(N)$	Fraction of particles that underwent N complete cycles (particle age distribution) (−)
R^2	Coefficient of determination (−)
$\mathrm{Re}_{p,mf}$	Particle Reynolds number at minimum fluidizing conditions (−); $\mathrm{Re}_{p,mf} \equiv d_p\, u_{mf}\, \rho_g / \mu$
Sh	Sherwood number (−); $\mathrm{Sh} \equiv k_g\, d_p / D_{CO2\text{-}air}$
Sc	Schmidt number (−); $\mathrm{Sc} \equiv \nu / D_{CO2\text{-}air}$
S'; S_p; S_t	Specific surface area of aged sorbent per unit of mass $(\mathrm{m^2/g})$, apparent volume $(\mathrm{m^2/cm_p^3})$; and true volume $(\mathrm{m^2/cm_t^3})$
S'_0; $S_{0,p}$; $S_{0,t}$	Specific surface area of fresh sorbent per unit of mass $(\mathrm{m^2/g})$, apparent volume $(\mathrm{m^2/cm_p^3})$; and true volume $(\mathrm{m^2/cm_t^3})$
t	Time, residence time (s)
t_{lim}; $\hat{t}_{lim}$	Time until full carbonation (s); dimensionless (−)
T	Temperature (of the carbonator) (K)
u_0	Superficial gas velocity (m/s)
V_M	True molar volume $(\mathrm{m_t^3/mol})$
w	Angular frequency of the sine function of Fig. 7 (rad/s); $w = 2\pi/(50\tau_s)$
x_{CaSO4}; x^{carb}_{CaSO4}; x^{syst}_{CaSO4}	Molar fraction of $CaSO_4$ in the solid sorbent; in the carbonator; in the system (mol%)
X	Particle conversion $(\mathrm{mol_{CaCO3}/mol_{Ca}})$
X_{carb}	Degree of carbonation after the carbonator $(\mathrm{mol_{CaCO3}/mol_{Ca}})$
X_{calc}	Degree of carbonation before the carbonator $(\mathrm{mol_{CaCO3}/mol_{Ca}})$
X_r	Residual activity after a high amount of cycles for Eq. (26) $(\mathrm{mol_{CaCO3}/mol_{Ca}})$
X'_r	Residual activity constant under the presence of $CaSO_4$ $(\mathrm{mol_{CaCO3}/mol_{Ca}})$
X_N	Activity of the sorbent after N complete cycles $(\mathrm{mol_{CaCO3}/mol_{Ca}})$
$\overline{X}_N$	Average activity of the sorbent in the carbonate loop $(\mathrm{mol_{CaCO3}/mol_{Ca}})$
$\overline{X}_{N+1}$	Average activity of the sorbent using TGA analysis of solid samples from pilot tests $(\mathrm{mol_{CaCO3}/mol_{Ca}})$
y_i	Volume concentration of gas i $(\mathrm{vol\%_{wet}})$

Greek symbols

γ	Overall system age number (−); $\gamma \simeq F_R/F_0$
η	Reactor gas–solid contact efficiency (%)
ε; ε_{mf}	Voidage; voidage at minimum fluidizing conditions (−)
ε_s	Solid volume fraction (also *solid concentration* or *volume fraction of solids*) (−)
ϵ; ϵ_0	Particle porosity of aged CaO $(\mathrm{m^3/m_p^3})$; fresh CaO $(\mathrm{m^3/m_p^3})$
μ	Dynamic viscosity (Pa s)
ν	Kinematic viscosity $(\mathrm{m^2/s})$
ξ	Volume ratio of potentially active sorbent (CaO and $CaCO_3$) to solids (−)
$\rho_{p,i}$; $\rho_{t,i}$	Particle density of i $(\mathrm{kg/m_p^3})$; true density of i $(\mathrm{kg/m_t^3})$
$\rho_{s,a}$	Particle density of the potentially active solids $(\mathrm{kg/m_p^3})$
τ_s	Mean system circulation time (s)
$\tau_{s,carb}$; $\hat{\tau}$	Mean residence time of the potentially active solids in the carbonator (s); dimensionless (−)
$\tau_{reactor}$	Reactor gas residence time (s)
τ_0	Mean residence time of the particles in the system (s)

Abbreviations

BET	Brunauer-Emmet-Teller (analysis)
BJH	Barret-Joyner-Halenda (analysis)
CaL	Carbonate (or calcium) looping
CFD	Computational fluid dynamics
ED	External diffusion
ID	Induced draft (fan)
IHCaL	Indirectly heated CaL
PM	Particle sub-model
PSD	Particle size distribution
RM	Reactor sub-model
RTD	Residence time distribution
TGA	Thermogravimetric analysis
TU	Technical University (of Darmstadt)

Subscripts and superscripts

a	Potentially active solids
calc	Calciner (outlet)
carb	Carbonator (outlet)
g	Gas

in	Inlet	s	Solid (apparent density/volume)
mf	Minimum fluidizing conditions	syst	System
out	Outlet	t	True density/ volume
p	Particle or apparent (volume/density)		

reducing the amount of CaO available for CO_2 capture. Martínez et al. [20] integrated Rodríguez et al.'s model into a CaL process model in Aspen Hysys® and adjusted operating conditions to achieve 95 % calcination efficiency. The deviation from ideal calcination resulted in a slight improvement in sorbent activity, which seems to contradict the system behavior observed during pilot tests. Atsonios et al. [21] investigated the influence of calcination efficiency on the carbonator under a specific set of operating conditions. For this, they used a CFD model coupled with an Aspen Plus® routine. They observed a significant decline in the CO_2 capture rate when the $CaCO_3$ content upstream from the carbonator exceeded 4 mol%. However, they did not discuss how varying the operating parameters, such as the sorbent circulation rate, affects the carbonator's sensitivity to calciner performance.

Sorbent deactivation increases the required make-up and circulation rates, which affects fuel requirements and component dimensions [22–24]. Sorbent activity decreases rapidly throughout the first calcination-carbonation cycles and stabilizes slowly towards a residual value that is normally smaller than 0.1. The cause of the deactivation is thought to be the sintering of the sorbents and the associated loss of porosity, which is enhanced by high calcination temperatures [23,25–29]. Consequently, it is desired to operate the calciner at low temperatures, which typically yield lower calcination efficiencies. The overwhelming majority of sorbent deactivation models applied to CaL systems rely on the assumption of stable operation over long periods of time (e.g., [19]). However, this is usually not the case in pilot plant operation, which poses challenges for the application and validation of these models.

The objective of this work is to develop an improved particle submodel that can be integrated into system models of the CaL process, alongside a reactor sub-model, for system analysis and upscaling. In this study, our particle sub-model is coupled with the reactor sub-model from Part I [1], which is compatible with circulating fluidized bed (CFB) operation. Additionally, we provide guidelines for integrating it with reactor sub-models suitable for other reactor types. For the development of the sub-model and its validation, the results from pilot tests in an IHCaL plant at TU Darmstadt are used. Our sub-model includes a new methodology to consider the influence of calcination performance on the carbonator efficiency. Furthermore, we introduce a novel approach to modeling sorbent deactivation that predicts sorbent activity under fluctuating operating conditions. In this study, we validate our model using experimental data and discuss our main findings regarding sorbent particle modeling.

2. Experimental

2.1. Pilot tests

Experimental data and results from pilot tests at the IHCaL plant of the Technical University of Darmstadt [2] were used to develop and validate the carbonator model. The pilot plant has a nominal scale of 300 kW_{th}, which corresponds to the amount of flue gas entering the carbonator for CO_2 capture [30].

Fig. 1 is a flow diagram of the pilot plant. The carbonator is the reactor where the CO_2 capture occurs through the carbonation of CaO (sorbent). It has an internal diameter of 250 mm and an internal height of 8 m. In Fig. 1, the carbonator with its internal circulation path is outlined in red. The carbonated sorbent flows into the calciner through a cone valve, where the CO_2 is released as the temperature increases to approximately 900 °C. The sorbent exits the calciner with a high content of CaO and flows back into the carbonator closing the solid loop. A sorbent sampling port is located at the cone valve. This enables the determination of the carbonation rate of the sorbent downstream of the carbonator using solid samples. Over 60 samples were taken throughout the pilot tests in 2015. The time corresponding to each sample is

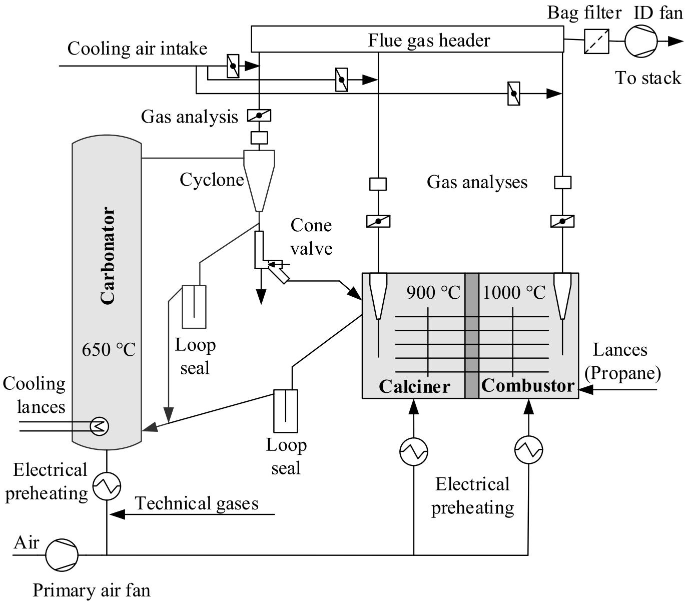

Fig. 1. The pilot plant at the Technical University of Darmstadt for testing the indirectly heated carbonate looping (IHCaL) process at the 300-kW_{th} scale. Adapted from [1]. The main reactors are shaded in gray. The carbonator with the internal circulation is indicated with red borders.

considered a *balance point* for the analysis and the validation within our study. A detailed description of the pilot plant is available elsewhere [18,31–33].

Pilot plant data and results relevant to this study are reported in Fig. 2. The CO_2 partial pressure at the carbonator inlet varied between 10 and 15 kPa throughout the test campaigns (see Fig. 2.a). To investigate the deactivation of the sorbent through sulfation, SO_2 was injected into the carbonator. The molar flow rate of injected SO_2 and the calculated concentration of $CaSO_4$ in the solid streams is reported in Fig. 2.b. These values, calculated using a molar balance (see Section 3.2.2), were validated against the composition of solid samples obtained from the sampling point located at the cone valve.

The limestone used for the investigations came from a query in Messinghausen, Germany. The mean particle size of the fresh material was ca. 180 μm. This sorbent has been used in other pilot tests of our research group [17,34,35]. The PSD of the fresh material and the spent sorbent are reported in Part I [1], including a discussion on particle size and attrition (see also Section 3). Information on the composition and other properties of the Messinghausen limestone is available in previous publications [1,15,31].

2.2. Sorbent deactivation

Thermogravimetric analysis (TGA) was used to characterize the sorbent deactivation. The studied sorbent was the finely ground Messinghausen limestone that had been used in the pilot tests (see Section 2.1). The analyses were performed using an STA 449 *F3 Jupiter* apparatus from the company Netzsch [36]. It is a TGA device with two oven systems. The oven system utilized in this work comprises an isolated chamber that can be heated. The sample carrier is located within this chamber, where a crucible with the sample to be tested is housed. The temperature can be controlled by means of electrical heating elements and a temperature sensor up to 1100 °C. In this oven, the input gases flow from the bottom to the top and can be controlled with mass flow controllers to set the desired atmosphere for the experimental tests. The crucible and the sample are weighed to quantify the phase changes and the heterogeneous reactions occurring in the sample. Before each test, a correction measurement was run with the same operating parameters as the actual test with the exception that the crucible was empty. The results of the correction runs were subtracted from the raw data of the actual tests to obtain the weight change caused only by the reacting material in the crucibles.

The testing process to characterize the sorbent deactivation is illustrated in Fig. 3. It consisted in the cyclic calcination and carbonation of limestone samples up to 50 cycles. This was achieved through successive variations of the temperature and gas composition of the oven chamber, where 20 mg of sample were located inside of a ceramic crucible.

The temperature and CO_2 concentration were set to 650 °C and 10 vol% for carbonation, and 900 °C and 0 vol% for calcination. The CO_2 concentrations correspond to the inlet concentrations of the carbonator and the calciner (air fluidization) of the pilot plant, respectively. The concentrations were chosen to match the operating conditions of the pilot plant. Commercial calciners may operate with much higher CO_2 concentrations [37], potentially leading to slightly different deactivation profiles for real operating conditions (cf. [28,38]). However, previous studies have shown that the CO_2 concentration during calcination and the calcination times have a very modest impact on the cyclic deactivation of limestone [39].

The carbonation time was 10 min. To prevent early calcination, the CO_2 concentration was increased to 90 vol% during heating. The calcination occurred very fast; thus, it was not necessary to maintain the temperature. To reduce the test time, the calcination and the cooling phase were made simultaneously. This phase had a duration of 17 min. The total run time for each test was 46 h. The tests were performed twice and compared for control purposes.

2.3. Sorbent kinetics

The same materials and apparatus of the deactivation tests (see Section 2.2) were also used to evaluate the kinetic behavior of the sorbent. Each sample for these tests consisted of 3 mg of fresh Messinghausen limestone. The total volume flow of gas was set to 190 mL/min to avoid external diffusion effects. The tests were performed with the fraction of fine limestone with particle size 106–200 μm.

We performed preliminary kinetic tests with different sample masses and particle sizes to confirm that external diffusion and pore diffusion were not influencing the reaction rate (see Section S1 of the supplementary material). This allowed us to obtain the information of the

(a) Gas composition at carbonator inlet

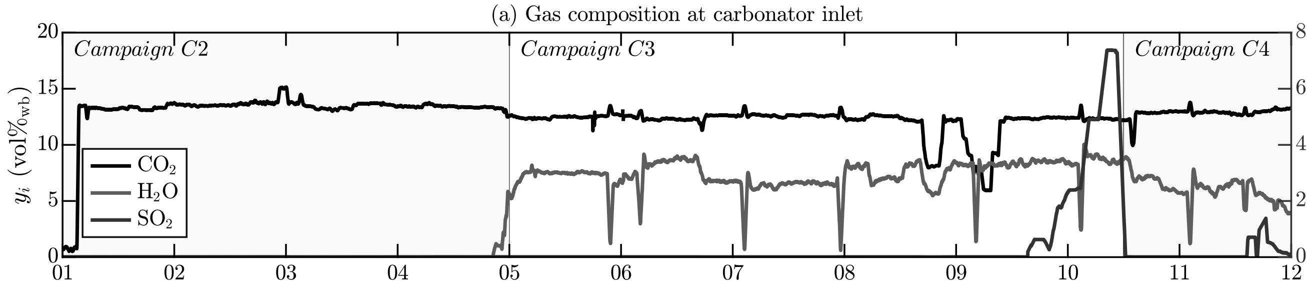

(b) Molar flow rate of SO_2 into the carbonator (F_{SO2}) and $CaSO_4$ concentration (x_{CaSO4})

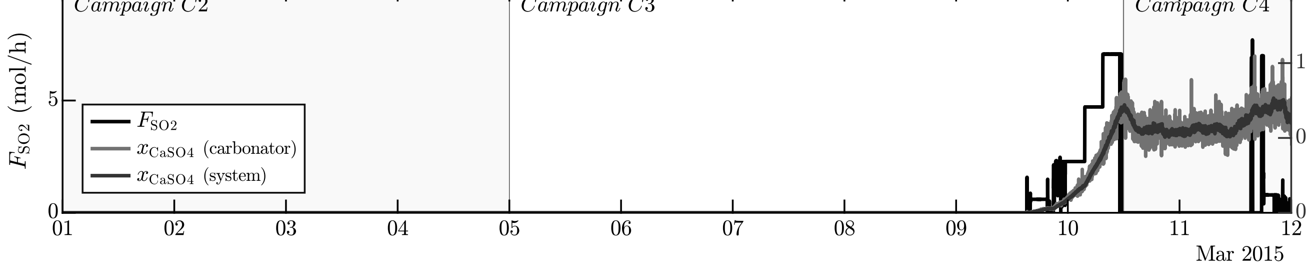

Fig. 2. Pilot tests at the 300-kW$_{\mathrm{th}}$ IHCaL plant: (a) gas composition at the carbonator inlet, and (b) molar flow rate of SO_2 into the carbonator (F_{SO2}) and $CaSO_4$ concentration (x_{CaSO4}) in the carbonator and the entire system.

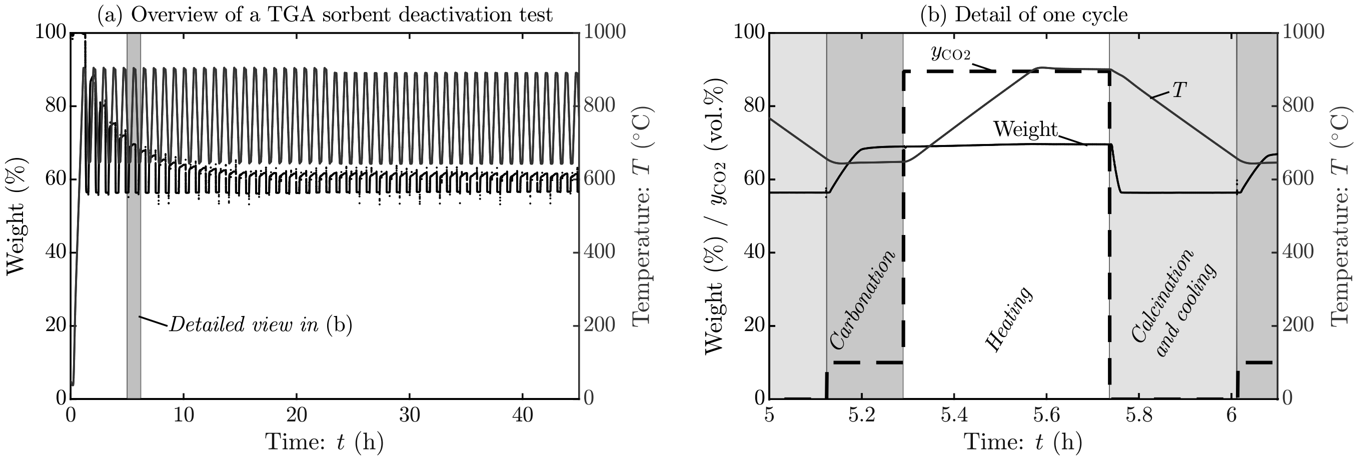

Fig. 3. Cycle test to determine the deactivation behavior of the sorbents. The displayed results correspond to the Messinghausen limestone: (a) overview of the entire test, (b) detail of one cycle. The region corresponding to the detail is indicated with a shade in Figure (a).

carbonation kinetics depending only on the chemical rate and the product diffusion (cf. [40]). The results of the preliminary tests are reported in the supplementary material (Fig. S1). Section 3.1.1 includes the consideration of diffusion phenomena and reaction mechanisms in the fluidized bed, which is relevant for applying the TGA results to the CFB carbonator model.

CO_2 concentrations from 6 to 15 % were tested, with carbonation temperatures of 650 °C and 700 °C. The carbonation and calcination testing conditions were selected considering the operating conditions of the pilot plant (Section 2.1). The input parameters of each TGA test are reported in Table S1. The results of the kinetic tests were used for the validation of the kinetic model (see Section 4.1.1).

3. Modeling

The carbonator model comprises three sub-models: the hydrodynamic sub-model, the reactor sub-model, and the particle sub-model. The particle sub-model is used to determine the global reaction rate (K_r), which is necessary to calculate the CO_2 capture efficiency in the carbonator. In this section, the development of this sub-model is presented. The complete structure of the carbonator model, along with the other sub-models, is explained in Part I [1].

In this study, we consider the particle size distribution (PSD) of the used material because it is representative of the sorbent inside of the carbonator during operation. The underlying assumption is that after several hours of operation, during which attrition, fragmentation, and entrainment occur, the particle size distribution (PSD) stabilizes and remains relatively constant for the remainder of the pilot tests, which lasted several days. This assumption is supported by observations from previous pilot tests [41]. The PSD is obtained from solid samples collected during the pilot tests (see Section 2.1), which were extracted from the sampling port located at the cone valve (see Fig. 1). This aspect is explained and discussed in Part I [1]. Considering the narrow Gaussian PSD, we neglect the effects of the distribution, thus considering all particles as having the same diameter ($d_{p,50} = 227$). Modeling or analyzing the attrition and entrainment in the pilot plant is beyond the scope of this article. A more detailed discussion of this aspect can be found in Part I [1]. The reader is referred to the work of Haaf et al. [42] to incorporate an attrition model to the carbonator model. An assessment of attrition and entrainment in our pilot plant (see Section 2.1), including PSD data and results from attrition tests, has been performed by Reitz [33]. General considerations regarding attrition and fragmentation of sorbents in CaL systems are available in the literature [41,43–46].

3.1. The carbonation reaction

3.1.1. Reaction mechanism

The CO_2 capture from flue gases occurs through the carbonation reaction, which is a heterogeneous reversible reaction that follows this expression [47]:

$$CO_{2(g)} + CaO_{(s)} \rightleftarrows CaCO_{3(s)} \tag{1}$$

An equilibrium correlation for this reaction (Eq. (2)) was obtained by García-Labiano [48] using data from Barin [49].

$$p_{CO2,eq} = 4.137\ 10^{12}\ \exp(-20474\ \mathrm{K}/T)\ [\mathrm{Pa}] \tag{2}$$

This expression is commonly used for modeling the carbonation-calcination equilibrium in CaL applications [37]. We followed this approach as well. For the carbonation to take place, the following in-series steps need to occur (see [50,51,52]): (i) CO_2 mass transfer through the gas film that surrounds the sorbent particle (*external mass transfer*), (ii) internal diffusion of CO_2 inside the pores of the solid (*pore diffusion*), (iii) CO_2 penetration and diffusion through the solid layer of $CaCO_3$ that was formed by previous reaction events (*product diffusion*), and (iv) CO_2 reaction with CaO according to Eq. (1) (*chemical reaction*). The first step is modeled using a gas–gas diffusion approach, but it is generally irrelevant to the carbonation kinetics in CaL systems (see Section 3.1.3). The second step can be neglected for typical operating conditions of CFB carbonators for particle sizes of 70–400 μm [53]. This is because of the large pores present in the deactivated sorbent, as demonstrated by Grasa and Abanades [54]. To account for the third step, we consider only the reaction kinetics on the chemically controlled *fast stage*, in which the product diffusion is irrelevant. It is well known that beyond this stage the kinetics are considerably slower (*slow stage*) due to limiting product diffusion [40,55]. We assume that no further reaction occurs beyond the fast stage, which is a reasonable assumption under industrial operating conditions in CFB carbonators [7,56]. The end of the chemically controlled fast stage is marked by a specific carbonation degree, known as *sorbent activity* (X_N), beyond which the product layer becomes thick enough to limit the reaction kinetics [57]. The value of X_N depends on the number of complete calcination-carbonation cycles the sorbent has undergone. For a thorough discussion on the effect of partial calcination or carbonation on sorbent activity, the reader is referred to the study from Rodríguez et al. [19]. The calculation of the sorbent activity is discussed in Section 3.2. The fourth step (chemical reaction) is modeled in Section 3.1.4.

3.1.2. Reaction order

The carbonation reaction is considered first-order with the CO_2 driving force up to at least 10 kPa [40,58,59]. However, there is no consensus on whether or not there is a shift to zero-order kinetics beyond this pressure level [5,60]. Grasa et al. [54] suggested that the first-order dependency is maintained up to 100 kPa. Recently, Scaltsoyiannes et al. [61] provided a considerable amount of data from TGA analysis that points in the direction of a first-order reaction at least up to 101 kPa. They used different CaO-based sorbents and reported the same behavior for all of them when adjusting their model to consider the presence of inert compounds.

Contrary to the intuition of Grasa et al. [54], Sun et al. [58] suggested a shift to zero-order for CO_2 partial pressures starting at $\sim$ 10 kPa. They supported their assumptions with a dataset of around 15 pressure points from 5 to 100 kPa, for two temperature levels (600 and 850 °C), and two types of sorbent (Strassburg limestone and Artic dolomite) —totaling more than 60 relevant runs. Results from Kyaw et al. [62] suggest zero-order dependency for 20–101 kPa. Bhatia and Perlmutter [40] reported first-order dependency with CO_2 concentrations up to 1.5 $mol/m^3 \sim 10$ kPa. On top of this, they presented a significant number of data points showing that the conversion over time exhibited the same behavior when only the CO_2 concentration was changed from 10 to 42 %, with all other parameters remaining constant.

For the above reasons, we believe that a reaction order shift at pressures higher than 10 kPa in the carbonation of lime cannot be excluded. More experimental data and comparative analyses are required to clarify the explained disagreement in the literature. In the case of our operating conditions, the CO_2 partial pressure of the gas entering the carbonator was $\approx$ 10 kPa, meaning that a major part of the reaction happens at pressures lower than the limit of reaction shift. Because of this, we adopted a first-order model without shifting to zero-order kinetics. The first-order conversion is described mathematically with the following differential equation:

$$\frac{dX}{dt} \equiv k_r\, \mathfrak{C} \tag{3}$$

Here, X is the particle conversion (carbonation), k_r is the global reaction rate for the particle sub-model, and $\mathfrak{C}$ is the driving force. The driving force ($\mathfrak{C}$) depends on the CO_2 concentration (C_{CO2}) and the equilibrium CO_2 concentration ($C_{CO2,eq}$) according to the following expression [1]:

$$\mathfrak{C} \equiv C_{CO2} - C_{CO2,eq} \tag{4}$$

Some previous studies (e.g., [63]) model the order shift in the reaction for the particle sub-model but assume constant first-order dependency in the reactor sub-model. This inconsistency leads to mistakes in the calculations, such as mismatched units. For the modeling of the order shift, both the governing equations for the particle sub-model and the reactor sub-model should be modified. A method for including the order shift in the reactor sub-model is indicated in Appendix A.1.

3.1.3. External diffusion

External diffusion (ED) effects in carbonators are commonly modeled following Abanades et al. [64]. A diffusion constant (K_{ED}) is calculated from the area-to-volume ratio of the gas diffusion layer (a_g) and the diffusion rate (k_g) [23]:

$$K_{ED} = k_g\, a_g \tag{5}$$

Where, for a spherical particle,

$$a_g = 6/d_p \tag{6}$$

Here, d_p is the particle diameter. Note that the units of K_{ED} are $m_g^3/(m_p^3\, s)$, which is compatible with the reactor sub-model [1]. In our work, we utilize the mean particle diameter of the samples of the pilot tests ($d_{p,50}$) —this is not the same as the mean particle diameter of the fresh material—, which was $d_{p,50} = 227$ µm [1]. The Sherwood[1] (Sh) and Schmidt (Sc) numbers, which are defined in Eqs. (7) and (8) [65, p.702], are used to obtain k_g.

$$\mathrm{Sh} \equiv k_g\, d_p / D_{CO2\text{-}air} \tag{7}$$

$$\mathrm{Sc} \equiv \nu / D_{CO2\text{-}air} \tag{8}$$

Here, $D_{CO2\text{-}air}$ represents the effective gas diffusivity of CO_2 in air. Abanades et al. [64] calculated Sh with a correlation introduced by Turnbull and Davidson [66] for combustion of char and volatiles in fluidized beds, based on the Frössling correlation [67]:

$$\mathrm{Sh} = 2\varepsilon_{mf} + 0.95\, \left(\mathrm{Re}_{p,mf}/\varepsilon_{mf}\right)^{0.5}\, \mathrm{Sc}^{0.3} \tag{9}$$

This equation is sometimes wrongly reported in the literature, omitting the voidage at minimum fluidization velocity (ε_{mf}) dividing the Reynolds number. Eq. (9) was developed by fitting data from fluidized combustion and considers the diffusion of isolated particles. A detailed analysis of the applicability of this equation to the carbonator operating conditions is yet to be done. However, due to the relatively high Re ($\sim$ 1), it is reasonable to assume that the concentration boundary layer surrounding the particles is considerably thinner than the typical distance between neighboring particles. Consequently, the influence of the particles on each other is neglected, as required for the application of Eq. (9). A detailed study of external mass transfer in multiparticle systems, including useful equations for obtaining Sh, was conducted by Scala [68].

The overall rate constant (K_r) for the reactor sub-model [1] can be calculated considering the three in-series steps necessary for the carbonation to take place [64,69] (see Section 3.1.1):

$$K_r = \left((1/K_{ED}) + (1/K_{ri})\right)^{-1} \tag{10}$$

Here, K_{ED} is the external diffusion constant, which is obtained from the external diffusion model, and K_{ri} is the reaction constant for the carbonation, which is calculated from the particle sub-model, with Eq. (49). Note that in the case of an order shift for the reaction, the diffusion remains first-order with the CO_2 concentration, thus Eq. (10) is no longer valid.

Using Eqs. (5)–(9), we find that the values of K_{ED} are more than two orders of magnitude higher than those of K_{ri} for all our balance points. This indicates that external diffusion effects do not significantly impact the carbonation of the sorbent. This has been observed previously by Lasheras et al. [69]. If external diffusion effects become relevant (e.g., for much bigger particles), Eq. (9) may be used.

3.1.4. Particle conversion

It is well known that the CaO-carbonation kinetics are characterized by an initial fast stage and a second, much slower, stage [40]. There is general agreement that the shift in the reaction rate is due to the transition from a reaction-controlled regime to a regime controlled by the diffusion in the product ($CaCO_3$) layer [7,47]. For engineering applications, the first stage is relevant, while the second, slower stage is usually neglected for the purpose of CO_2 capture in the carbonator [56]. For this reason, we considered only the fast stage in our model.

The many definitions of density

---

[1] Note that previous works on carbonator modeling wrongly define the Sherwood number. The correct definition is given in Eq. (7).

For studies with porous reactants, there are two density definitions to consider [65,70–72]. The (i) *true density* (ρ) —also real density, skeletal density,[2] crystal density, or absolute density— is the “ratio of particle mass to particle volume excluding all pores, closed or open, and surface fissures” [72]. It can be measured through helium displacement; thus, it is sometimes called “helium density”. The (ii) *particle density* (ρ_p) —also envelope density, buoyant density, or apparent density— is calculated by dividing the mass of solid particles by the volume including particle porosity and excluding the interstitial volume, i.e., the volume between the particles. Normally, the displacement of mercury or a fine powder is used to calculate the particle density. Throughout this work, the *true density* is intended, except when noted explicitly. In case of ambiguity, we use the subscripts ‘t’ for true density (and volume) and ‘p’ for particle density (and volume).

Model for the kinetically controlled fast stage

There are many particle models used for carbonation in the fast stage. A systematic review on the subject was performed by Fedunik-Hofman et al. [60]. Further information about different models can be found in the work of Martínez et al.[5]. In our work, we use the grain particle model from Nitsch [73], with the rate constant calculated according to Grasa et al. [54] to account for the deactivation. This approach is widely used for carbonator modeling [56,74–76]. With these considerations, the differential equation for the conversion up until the maximum carrying capacity has the following form:

$$\frac{dX}{dt} = k_x(1-X)^{2/3}\mathfrak{C} \tag{11}$$

Here, k_x is the first-order kinetic constant for the carbonation in the fast-reaction stage in $\mathrm{m_g^3/mol_g/s}$, which depends on the specific active surface area of the particle (S_t):

$$k_x \equiv k_s\, S_\mathrm{t} \tag{12}$$

Where S_t is calculated with the following equation:

$$S_t = X_N\,(1/h)\left(V_\mathrm{M,CaCO3}/V_\mathrm{M,CaO}\right) \tag{13}$$

Here, S_t is expressed in $\mathrm{m_{active}^2/m_t^3}$; X_N is the maximum achievable conversion, dependent on the number of complete calcination-carbonation cycles (N); k_s is the intrinsic kinetic constant in the fast-reaction stage; and h is the thickness of $CaCO_3$ formed around CaO. The intrinsic kinetic constant was found to be $k_s \approx 5.95\;10^{-10}\;\mathrm{m^4/(s\;mol)}$ [40,54,58]. The parameter h is approximately equal to 50 nm, according to the measurements of Alvarez and Abanades [57]. The true molar volumes (V_M) of $CaCO_3$ and CaO are 36.9 $\mathrm{cm_t^3/mol}$ and 16.9 $\mathrm{cm_t^3/mol}$, respectively [40]. With numerical values:

$$S_\mathrm{t} = X_N\left(43.7\;10^6\;\mathrm{m^2/m^3}\right) \tag{14}$$

The specific surface area can also be expressed per unit of mass (S') and in terms of particle volume (S_p). The equivalences between these parameters are given by:

$$S' = S_\mathrm{t}/\rho_\mathrm{CaO,t} \tag{15}$$

$$S_p = S_t(1-\epsilon) \tag{16}$$

Here, ϵ is the particle porosity of CaO, in $\mathrm{m^3/m_p^3}$, which establishes the relation between the true and the particle density:

$$\rho_\mathrm{CaO,p} = \rho_\mathrm{CaO,t}(1-\epsilon) \tag{17}$$

Other models in the literature propose different ways of obtaining k_x. Abanades et al. [64] used the following expression [40], which was followed by others [69,77]:

$$S_t = X_N\;S_\mathrm{0,t} = X_N\;S_\mathrm{0,p}/(1-\epsilon_0) \tag{18}$$

Here, $S_\mathrm{0,p}$ is the initial specific surface area in $\mathrm{m_{active}^2/m_p^3}$ of fresh CaO, and ϵ_0 is the initial particle porosity of fresh CaO, which is generally assumed ≈ 0.5. In numbers, using $S_\mathrm{0,p} = 17\;\mathrm{m_{active}^2/cm_p^3}$ [40,69], this gives:

$$k_x = k_s\,X_N\left(34\;10^6\;\mathrm{m^2/m^3}\right) \tag{19}$$

The models are equivalent (see Eq. (14)). If there is no data of sorbent active surface, we recommend setting $\mathrm{S_{0,p}} = 17\;\mathrm{m^2/cm_p^3}$ (conservative value) or applying Eq. (14) when a particle model of the form presented in Eq. (11) is used. In our model, we follow this last approach because it better predicts our TGA data and the data available in the open literature (see Section 4.1.1). In summary, the expression we use to calculate k_x is:

$$k_x = k_s\,X_N\,(1/h)\left(V_\mathrm{M,CaCO3}/V_\mathrm{M,CaO}\right) \tag{20}$$

The conversion progress with time can be found by integrating Eq. (11). In our work, we consider the influence of partial calcination by setting the starting conversion equal to the average conversion of the particles exiting the calciner (X_calc). Thus, the lower boundary for integration is $X(t=0) = X_\mathrm{calc}$, yielding:

$$\begin{cases} X(t) = 1 - \left[(1-X_\mathrm{calc})^{1/3} - (k_x\mathfrak{C}/3)t\right]^3; & t < t_\mathrm{lim} \\ X(t) = X_N; & t \geq t_\mathrm{lim} \end{cases} \tag{21}$$

Where t_lim, the time required to achieve the maximum conversion (X_N), is given by:

$$\begin{cases} t_\mathrm{lim} = (3/k_x\mathfrak{C})\left[(1-X_\mathrm{calc})^{1/3} - (1-X_N)^{1/3}\right]; & X_\mathrm{calc} < X_N \\ t_\mathrm{lim} = 0; & X_\mathrm{calc} \geq X_N \end{cases} \tag{22}$$

For X_calc values higher or equal to the maximum conversion, t_lim becomes zero and no CO_2 can be captured. If X_calc is zero, Eqs. (21) and (22) become analogous to those found by Romano [56] assuming complete calcination in the calciner.

Fitting constants

Despite intense study of CaL systems, there are only a few publications providing kinetic constants based on experimental data. Historically, the work of Bhatia and Perlmutter [40] has been one of the most important references in this regard. They fitted a random pore model using data from TGA, with particles having $S_\mathrm{0,p} = 14\text{–}25\;\mathrm{m^2/cm_p^3}$.

Sun et al. [58] used CaO with an active surface area twice as large as that analyzed by Bhatia and Perlmutter—but similar total pore volume—, as shown in Table 2. Under the same operating conditions, the carbonation rates were very similar because the higher specific surface of CaO in [58] compensated the slower rates per unit of surface area (r) (see Appendix A.6).

In a recently published work, Scaltsoyiannes et al. [27] analyzed four different CaO-based sorbents using a lab-scale fixed bed reactor. They achieved good agreement between simulations and experiments using a modified random pore model with the same kinetic parameters for the different sorbents, thus demonstrating that the kinetic behavior is independent of the inert materials. Interestingly, their results match those obtained by Grasa et al. [54] with a very different experimental set-up, based mainly on TGA measurements. This confirmation, along with the substantial experimental data reported in their work, establishes Scaltsoyiannes et al.’s model as one of the most reliable for carbonation reaction modeling in the fast stage.

---

[2] The skeletal density is the “ratio of the mass of discrete pieces of solid material to the sum of the volumes of the solid material in the pieces and closed (or blind) pores within the pieces” [72]. Strictly, this, and not the true particle density, can be measured by penetration, since the gas cannot penetrate inside of the blind pores.

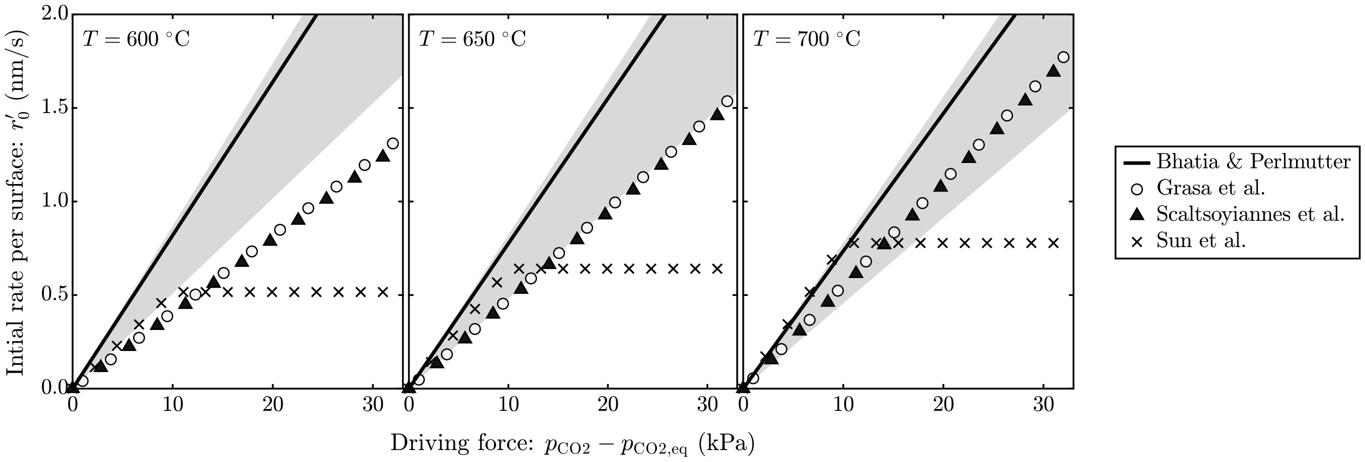

Fig. 4. Comparison of the initial reaction rate predicted by different models: Bhatia & Perlmutter [40], Scaltsoyiannes et al. [27], Grasa et al. [78], and Sun et al. [58]. The shaded red area represents the complete range reported by Bhatia & Perlmutter [40].

In terms of industrial applications, the initial reaction rate (r_0) is of utmost importance in the characterization of the kinetic regime. Mathematically, r_0 is (see Eq. (11)):

$$r_0 \equiv dX/dt|_{t=0} \tag{23}$$

If r_0 is known, a simple kinetic model can be used to predict carbonation accurately in operating times and conditions relevant for CaL applications. Since it is generally accepted that r_0 is first-order dependent on the specific active surface area, we studied the initial rate per surface r'_0, defined as:

$$r'_0 \equiv r_0/S_t \tag{24}$$

The results of r'_0 obtained using the main particle models from the open literature are presented in Fig. 4. Here, the work from Bhatia and Perlmutter [40], indicated with a solid black line, is taken as the reference model —mainly due to historical reasons and considering its utilization in many carbonation models. The engineers from the University of Pennsylvania fit carbonation data using pressures of 2 and 10 kPa. They indicated a mean value of $k_s = 5.95\ 10^{-10}$ m^4/(mol s), which is the standard value for this constant, despite the considerable variation throughout their experiments. To illustrate this variation, we included a gray-shaded area representing the entire range reported by Bhatia and Perlmutter.

For the range 600–700 °C, which is of interest for CaL applications, the values from Scaltsoyiannes et al. [27] and Grasa et al. [78] are lower than for the other models. As noted above, there is strong agreement among them. Especially for higher temperatures, their kinetic rates are close to the lower boundary of those measured by Bhatia and Perlmutter [40]. The work from Sun et al. [58] presents reasonable agreement with the other models for pressures lower than 15 kPa, but indicates much slower values for higher pressures due to the reaction-order shift. The main operating parameters and the experimental methods of the models used in Fig. 4 are summarized in Table 1.

For the reasons presented above, we believe that the values from Scaltsoyiannes et al. [27] are reliable within the range of their experiments and may be used to obtain the constant k_s. The corresponding Arrhenius equation to obtain k_s with this method is Eq. (25).

$$k_s = 6.08\ 10^{-9}\ \left(\mathrm{m^4 mol^{-1}\ s^{-1}}\right)\ \times\ \exp[-22.1\ (\mathrm{kJ/mol})/(RT)] \tag{25}$$

Since Bhatia and Perlmutter [40] fitted their data using pressures that are more representative of the conditions inside our pilot carbonator, we decided to use their model for our calculations and set $k_s = 5.95\ 10^{-10}$ m^4/(mol s) independently of temperature variations. This assumes zero activation energy. Using this constant, the particle submodel agrees with empirical values from TGA tests (see Section 4.1.1) conducted on the same limestone that was used in the pilot plant (see Section 2.1).

Specific surface area

The values of specific surface area and porosity of lime depend on the calcination method and the properties of the limestone. Values for these parameters corresponding to publications dealing with carbonation of CaO are presented in Table 2. Higher values of surface area of more than 50 m^2/g can be achieved. However, the calcination conditions necessary for this are not feasible in CaL industrial applications. Borgwardt [79] obtained calcines with $S'_0 \approx 104$ m^2/g. For this, he calcined high-purity $CaCO_3$ at 700 °C. He indicated that active surface reduction is strongly dependent on the calcination temperature and the amount of impurities. In addition, the presence of CO_2 and H_2O was found to catalyze the sintering that reduces the active surface area of CaO [80,81].

Throughout the literature, surface areas per unit of volume are reported either in terms of true volume or in terms of particle volume. In some cases, it is not clearly stated which convention is used, leading to mistakes in carbonator models due to confusion between S_p and S_t. We hope that our work, especially the information in Table 2, will help prevent inaccuracies in the future.

Surface areas of used-sorbent samples from our pilot tests (see Section 2.1) were obtained through Brunauer-Emmett-Teller analysis (BET) [82]. Values of $S' \approx 2$ m^2/g were measured for samples with activities of ≈ 0.1 [33]. With equation Eq. (13), using the mean value of X_N, we

Table 1
Main kinetic models: operating parameters and experimental methods.

Reference	T (°C)	p_{CO2} (kPa)	d_p (μm)	Sample size (mg)	Experimental method
Bhatia and Perlmutter [40]	550–725	2; 10*	74–8; 125–149	< 1.3	TGA
Sun et al. [58]	500–845	3–100	38–45	< 2.9	TGA
Grasa et al. [78]	550–750	10–100	50–75	2	TGA
Scaltsoyiannes et al. [27]	670–820	10–120	45–75	100	Fixed bed reactor

TGA: Conversion calculated through particle weight change.

Fixed bed reactor: Conversion calculated from the off-gas concentration and the known trace gas (Ar) mass flow.

* For fitting of k_s. Runs with $p_{\mathrm{CO2}} > 10$ kPa, up to 42 kPa, were reported but were not utilized to estimate k_s.

Table 2
Specific surface area and porosity of lime. Experimental values and model assumptions.

Sources [limestone name] (conditions)	Surface Area S' (m^2/g)	S_p (m^2/cm^3_p)	S_t (m^2/cm^3_t)	Porosity ϵ (m^3/m^3_p)	PV (cm^3/g)	Method (equipment)
Fresh sorbent ($N = 0$)						
Bhatia and Perlmutter (1983) [40]						Hg porosimetry (Micrometrics 910)
(0 % CO_2)	16[¥]	25	52[¥]	0.52	0.30–0.35	
(10 % CO_2)	12[¥]	19	40[¥]	0.53	0.30–0.35	
(20 % CO_2)	9[¥]	14	29[¥]	0.51	0.30–0.35	
García-Labiano et al. (2002) [48]						(not specified)
[Blanca]	19.0	27.9[¥]	63.5[¥]	0.56	–	
[Mequinenza]	19.4	20.7[¥]	64.8[¥]	0.68	–	
Abanades et al. (2004) [64]	12	19.2[¥]	40[†]	0.5	–	From [40]
Fennell et al. (2007) [83] (Laboratory fluidized bed)						BET, BJH. Samples sieved to separate from sand.
[Purbeck]	19–24	32–40[¥]	64–80[¥]	–	0.19	
[Cadomin]	38	63[¥]	127[¥]	–	0.20	
[Penirth]	39	65[¥]	130[¥]	–	0.23	
[Glen Morrison]	22	37[¥]	74[¥]	–	0.22	
[Havelock]	32	53[¥]	107[¥]	–	0.20	
Sun et al. (2008) [58] [Strassburg]	29	48[¥]	97[¥]	–	0.35	N_2 adsorption (S); Hg porosimetry (PV_0)
Bouquet et al. (2008), $N = 1$ [84]	15	25[¥]	50[¥]	–	0.14	BET-N_2 at 77 K (Micrometrics ASAP 2010); Hg porosimetry
Grasa et al. (2009) [78]						
[Imeco]	19[¥]	35	65[¥]	0.46	–	
[Katowice]	24[¥]	42	75[¥]	0.47	–	
Lasheras et al. (2011) [85]	10[¥]	17	34[¥]	–	–	From [40]
Martínez (2012) [86]						Hg porosimetry (PV_0) (Quantachrome Pore Master);
[Limestone A]	21	37[¥]	70[¥]	0.478	–	BET-N_2 at 77 K (Micrometrics ASAP 2010)
[Limestone B]	19	34[¥]	63[¥]	0.468	–	
Scaltsoyiannes et al. (2021) [61]	17.0	35.9	56.7[¥]	–	–	BET-N_2 at 77 K; BJH (Autosorb-1 Quantachrome)
Used sorbent ($N > 0$)						
Alvarez and Abanades (2005) [87] ($N = 100$)	0.6	1	2	–	0.15	Hg porosimetry. S estimated from PV.
Grasa et al. (2008) [54,56] ($N > 100$)	1.0	1.6[‡]	3.3[¥]	–	–	Eq. (13); X = 0.075
Bouquet et al. (2008) [84] ($N = 40$)	8–10	13–17[¥]	27–33[¥]	–	0.05	BET-N_2 at 77 K (Micrometrics ASAP 2010)
Pilot data [33] [Messinghausen]	1.4–2.3	2.3–3.8	4.7–7.7	0.5[*]	0.002–0.004	BET, BJH; $0.03 < X_N < 0.21$
This work	1.7	2.8	5.7	0.5[*]	–	Eq. (13); $X_N = 0.13$

BET: Brunauer-Emmett-Teller analysis [82] for S; BJH: Barrett-Joyner-Halenda analysis [89] for PV.

[†] They reported 40 m^2/m^3, but they meant 40 m^2/cm^3.

[¥] Our calculation with data reported in the reference using $\rho_{CaO,t} = 3.34$ g/cm^3; $\epsilon_0 = 0.52$[40].

[*] Assumption.

[‡] They reported 1–2 m^2/cm^3 for S_t, but in reality this range corresponds to $S_{N,p}$ (cf. [88]).

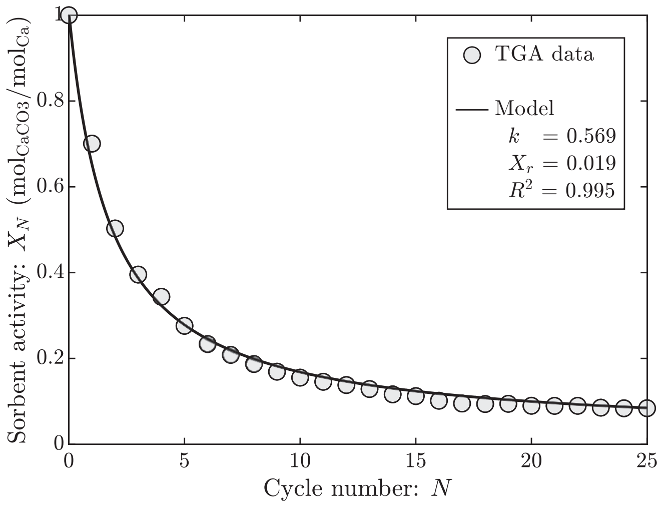

Fig. 5. Sorbent deactivation for a batch of particles with the same number of cycles (N).

obtained surface areas close to the ones measured through BET, namely $S' = 1.7$ m^2/g (see Table 2). This supports the validity of the kinetic model of Eq. (13) in terms of the reactivity of cycled particles.

3.2. Sorbent deactivation

Sorbent deactivation [55] is among the most influential parameters affecting the carbonator efficiency [6,26,90]. Consequently, reliable deactivation models are crucial for commercial deployment of CaL technology. There are various models available in the literature [5,7,91] to incorporate the effects of calcination-carbonation cycles in the maximum achievable carbonation within the fast stage (X_N). We followed the work of Romano [56] to model the deactivation, as its balance between accuracy and complexity is suitable for our application.

3.2.1. Deactivation with cycles

The first step in simulating deactivation is to model the activity decay of a batch of particles that have undergone the same number of complete calcination-carbonation cycles, designated as *particle age* (N). Grasa and Abanades [38] proposed a fitting function to obtain the sorbent activity (X_N), which is expressed in Eq. (26).

$$X_N = \frac{1}{(1 - X_r)^{-1} + k\,N} + X_r \tag{26}$$

Here, k is a deactivation constant, and X_r is the residual activity after a high amount of cycles (> 300). We obtained X_r considering it equal to the minimum activity from the sorbent samples obtained in the pilot plant before the addition of SO_2 (see Fig. 2.b). To obtain k, we fitted TGA experimental data of cyclic tests (see Section 2.2) with Eq. (26). The model results, compared with the data from TGA analysis for the first 25 cycles, are presented in Fig. 5. The values obtained for the fitting constants are within the range of those reported in the open literature [38,92], considering the variation in the carbonation temperature between 550 and 700 °C.

Some previous studies reported higher levels of residual activity X_r. Diego et al. [93] fitted a model using $X_r \sim 0.10$ $\mathrm{mol_{CaCO3}/mol_{Ca}}$ with empirical data from CaL pilot tests. Charitos et al. [94] indicated residual values of $X_r \sim 0.07$ and $X_r \sim 0.10$ for two pilot plants operating with different types of limestone. On the other hand, Hilz et al. [95] reported a carbonate content of 0.03–0.10 $\mathrm{mol_{CaCO3}/mol_{Ca}}$ in samples taken from the carbonator outlet of a CaL pilot plant, which is consistent with very low residual activities ($X_r < 0.03$). The data from cyclic calcination-carbonation of limestone from Barker [55] was fit with $X_r = 0.035$ [24]. Our low X_r may be explained by the carbonation conditions in the pilot plant (see [24]).

3.2.2. Sulfation

The carbonator can be used to separate both SOx and CO_2 from the flue gases, simultaneously [21]. This has the advantage of avoiding the investment costs associated with a desulfurization unit for the removal of SOx. The operating conditions of both the carbonator and the calciner are favorable for the reaction of SOx with $CaCO_3$ (direct sulfation) and CaO (indirect sulfation) [56]. However, SOx reacts with the active sorbent (CaO) and forms a stable compound ($CaSO_4$) [96], thus reducing the sorbent's capacity to capture CO_2 (sorbent deactivation). The deactivation not only occurs due to the consumption of CaO, but also due to the blockage of pores caused by the formation of $CaSO_4$, which has a higher molar volume than CaO and $CaCO_3$. Consequently, the actual deactivation is considerably higher than the deactivation that would be expected only from stoichiometry [97–99].

To investigate this issue, SO_2 was injected into the carbonator during the last part of the pilot tests (see Section 2.1). To calculate the concentration of $CaSO_4$ in the sorbent inventory, we performed the molar balance for both the carbonator and the entire system. We assumed complete conversion of SO_2 into $CaSO_4$ in the carbonator. The system balance for the S species, neglecting material loss, is:

$$d\left(n_{\mathrm{CaSO4}}^{\mathrm{syst}}\right)/dt = F_{\mathrm{SO2}} \tag{27}$$

The carbonator balance gives:

$$d\left(n_{\mathrm{CaSO4}}^{\mathrm{carb}}\right)/dt = F_{\mathrm{SO2}} - (F_R + F_{\mathrm{SO2}})x_{\mathrm{CaSO4}}^{\mathrm{carb}} + F_R x_{\mathrm{CaSO4}}^{\mathrm{syst}} \tag{28}$$

Here, $x_{\mathrm{CaSO4}}^{\mathrm{carb}}$ and $x_{\mathrm{CaSO4}}^{\mathrm{syst}}$ are the molar fraction of $CaSO_4$ in the carbonator and the system, respectively. The balance was solved numerically, using a left rule and a time step of one second, corresponding to the interval between data logs. The concentration values obtained are displayed in Fig. 2.b.

We adopted the simple model from Romano [56] with data from Grasa et al. [99] for the enhancement of the deactivation due to the presence of SO_2 (see also [76]). The model quantifies the deactivation due to the blockage of the pores caused by the formation of $CaSO_4$. The new deactivation constant (k') as a function of the mass fraction of $CaSO_4$ in the carbonator (x_{CaSO4}) is calculated with the following equation:

$$k' = k(1 + 29.6\, x_{\mathrm{CaSO4}}) \tag{29}$$

The new the residual activity (X_{r}') is calculated with the following piecewise function:

$$\begin{cases} X_{\mathrm{r}}' = X_r(1 - 115\, x_{\mathrm{CaSO4}}); & x_{\mathrm{CaSO4}} \leq 0.5\% \\ X_{\mathrm{r}}' = X_r(0.577 - 30.8\, x_{\mathrm{CaSO4}}); & x_{\mathrm{CaSO4}} > 0.5\% \end{cases} \tag{30}$$

These equations are illustrated in Fig. 6. The values of the constants in the presence of $CaSO_4$ are normalized using the corresponding values without sulfation (i.e., $x_{\mathrm{CaSO4}} = 0$). The equations were obtained through linear interpolation of the experimental data for x_{CaSO4} equal to 0.5 % and 1.0 %. The experimental data is indicated with markers (circles and triangles). The values obtained with Eqs. (29) and (30) are illustrated with lines.

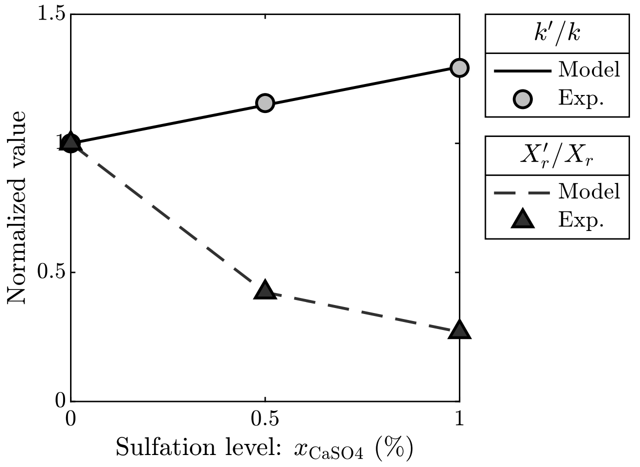

Fig. 6. Deactivation enhancement through sulfation according to [56]. The new deactivation constant (k') and the new residual activity (X_r') are normalized with the values without $CaSO_4$, i.e., k and K_r, respectively. The lines represent the calculated values using Eqs. (29) and (30), which were implemented in our carbonator model. The markers (circles and triangles) indicate the experimental data (exp.) from [99].

3.3. Overall system age

Previous deactivation models assume constant circulation and make-up rates [91,100]. This may be sensible for the design of new facilities but does not represent the real operating conditions in our pilot plant. Furthermore, in an industrial facility, it may be useful to modify these parameters to achieve different outcomes. For these reasons, it is necessary to develop a model of the sorbent deactivation of the CaL system with varying circulation and make-up molar rates. For the modeling of the sorbent deactivation, we consider all the components of the CaL system in which there is circulating sorbent: the carbonator, the calciner, and the connecting elements (return legs, loop seals, and cone valve).

To obtain the sorbent activity in non-steady-state CaL systems, we use an *overall system age number* γ —from the Greek word *γῆρας*, i.e., old age— that represents the overall deactivation history of the CaL system. The variable $\gamma(t)$ represents the equivalent steady-state F_R/F_0 ratio for a non-steady-state system with time-varying $F_R(t)$ and $F_0(t)$. It is defined as the constant F_R/F_0 ratio that yields the same average sorbent activity ($\overline{X}_N(t)$) in a steady-state CaL system, assuming all other operating parameters remain unchanged. Over long-term operation with constant operating parameters, $\gamma(t)$ converges to the actual F_R/F_0 ratio. Mathematically,

$$\frac{dF_R}{dt} = \frac{dF_0}{dt} = 0 \Rightarrow \lim_{t\to\infty}\gamma = F_R/F_0 \tag{31}$$

In other words, γ is asymptotically equal to the molar ratio of sorbent circulation to make-up, as the operation times become very large, i.e., $\gamma \simeq F_R/F_0$. This parameter γ must fulfill additional requirements. Firstly, the aging should be proportional to the circulation when no make-up is present, i.e., $d\gamma/dt \propto F_R$. Secondly, when there is make-up and circulation, the system age number (γ) tends to the quotient of the circulation and the make-up, i.e., F_R/F_0. Additionally, the molar inventory of the system (n_s) functions as the inertia for both the aging and the renewal of sorbent. An expression of γ that satisfies these requirements is:

$$\frac{d\gamma(t)}{dt} = \frac{F_R(t)}{n_s(t)} - \frac{F_0(t)\ \gamma(t)}{n_s(t)} \tag{32}$$

The rate of variation $d\gamma/dt$ depends on the circulation rate (F_R) and the make-up rate (F_0), as well as the inventory (n_s) that acts as a buffer, dampening the variations of γ. The presence of γ multiplying F_0 modifies the equation so that the system age number is only reduced if $F_R(t)/F_0(t) < \gamma(t)$. If $F_R(t)/F_0(t) > \gamma(t)$, the system age number increases. Lastly, for $F_R(t)/F_0(t) = \gamma(t)$, the system age number remains constant.

In our study, we adopt Eq. (32) to calculate γ. We assume that our system behaves like a steady-state system with $F_R/F_0 = \gamma$, in terms of the activity of the sorbent (see Section 3.4). In the validation section (Section 4.1.2), we show that Eq. (32) allows us to correctly represent the deactivation behavior of our pilot plant, thus validating the assumption.

If the molar flow rates and the molar inventory are constant and $\gamma(0\ \text{s}) = 0$, an analytical expression for the integrated form of Eq. (32) can be found:

$$\gamma(t) = (F_R/F_0)[1 - \exp(-t\,F_0/n_s)] \tag{33}$$

This expression, which is compatible with Eqs. (31) and (32), was used to analyze the behavior of the overall system age. For validation, Eq. (32) was implemented using numerical integration, based on empirical data for the time-varying F_R, F_0, and n_s. The calculated γ was used as an input for the deactivation model to obtain the mean maximum carbonation at the carbonator outlet at each time, i.e., $\overline{X}_N(t)$.

The average circulation time of a particle in the system (τ_s) is calculated with Eq. (34):

$$\tau_s = n_s/F_R \tag{34}$$

During stable pilot-test operation, the molar inventory varied between 7 and 10 kmol, and the circulation rate was 4–11 mol/s. This yields $\tau_s \approx 19$ min.

Fig. 7 illustrates the variation of γ over time for different make-up and circulation conditions. The time scale is normalized with τ_s. Fig. 7.a represents the start-up, during which, the system age number increases until it stabilizes at the value corresponding to the F_R/F_0 rate. The reaction of the system to a sudden make-up reduction of 50 % is illustrated in Fig. 7.b. Due to the reduced make-up rate, the system age number gradually increases until it doubles its original value. The behavior of the system for discontinuous make-up, simulated using a sine function (red continuous line), is similar to the reference case with continuous make-up (black continuous line), except for mild oscillations. The asymptotic value of $F_R/F_0 = 100$ corresponds to typical operating condition.

The results from Fig. 7 show that it would take up to several days to stabilize the system in terms of sorbent activity after start-up (Fig. 7.a) or significant make-up variation (Fig. 7.b). Using the definition of τ_s, Eq. (33) gives:

$$\gamma(t) = (F_R/F_0)\{1 - \exp[-(t/\tau_s)\ (F_0/F_R)]\} \tag{35}$$

In this exponential equation, the mean lifetime is the average residence time of a particle in the system (τ_0), which corresponds to the average time between its entry as make-up and its exit as purged or entrained material. Mathematically,

$$\tau_0 = n_s/F_0 \tag{36}$$

$$\gamma(t) = (F_R/F_0)[1 - \exp(-t/\tau_0)] \tag{37}$$

In other words, the time for the application of the changes in sorbent activity (τ_0) is about two orders of magnitude higher than the system's characteristic time (τ_s), which indicates a slow response. Even though the time required for stabilization is high, there is not much stability penalty if the make-up is given discontinuously (see Fig. 7, red lines). In the example, the period of the sine function representing the discontinuous addition of make-up is 50 $\tau_s \approx 12$ h. Yet, the corresponding system age number shows very mild oscillations. This suggests that the method of feeding make-up into the system does not significantly affect stability, as long as, on average, the same amount of make-up is provided over a period, such as a day or more. In a commercial facility, one would expect a slow response of the activity to make-up variations. On the one hand, this facilitates the control of the system, e.g., by allowing for intermittent make-up feeding. On the other, the slow response may be disadvantageous if fast changes are required, e.g., to adjust for partial-load operation.

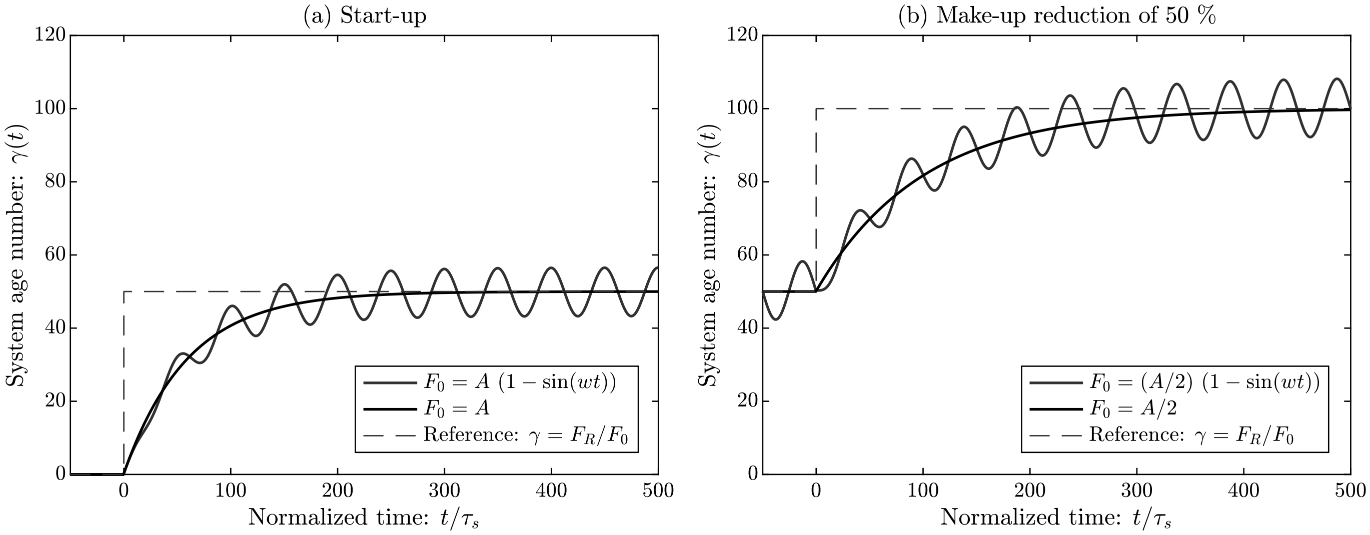

Fig. 7. Variation of the system age number (γ) with the dimensionless time (t/τ_s) (a) after start-up at t = 0 s, and (b) after a sudden 50 % make-up reduction at $t = 0$ s. The red lines represent the behavior of a system with discontinuous or variable make up, computed as a sine function with a period of 50 τ_s, whereas the black curves represent a system with constant make up. For the sine functions, the results were generated by solving Eq. (32) numerically. The curves with constant make-up were obtained using Eq. (33).

The model presented here fits the empirical data from sorbent samples well (see Fig. 12). During the pilot testing, the slow response of the sorbent to make-up was not accounted for in the dosage strategy. This resulted in strong variations of the mean system age number, as discussed in Section 4.1.2. In oxy-fired CaL facilities, the specific inventories are normally lower than those in IHCaL plants [40,75,76]. For these lower inventories, the response to make-up variation would require several hours (calculated with Eq. (36)).

3.4. *Residence time and particle age distributions*

To obtain the particle residence time distribution (RTD) in the carbonator, we assume complete mixing of the solids in the carbonator, including the return leg (internal recirculation, see Fig. 1). This assumption is justified by the strong particle mixing and high rates of solid recirculation typical of circulating fluidized beds [56]. Based on the assumption of perfect mixing of particles, we obtain the RTD [50, p.338] of Eq. (38), which provides the probability distribution of particles for each residence time in the carbonator.

$$\mathbf{E}(t) = \tau_{\mathrm{s,carb}}^{-1}\exp\left(-t/\tau_{\mathrm{s,carb}}\right) \tag{38}$$

Where $\tau_{\mathrm{s,carb}}$ is the mean residence time of the potentially active solids in the carbonator, calculated as:

$$\tau_{\mathrm{s,carb}} = n_{\mathrm{s,carb}}/F_R \tag{39}$$

Here $n_{\mathrm{s,carb}}$ is the number of moles of CaO and $CaCO_3$ in the carbonator and F_R is the molar flow rate of sorbent considering the internal circulation as part of the carbonator.

In continuous operation, particles will undergo varying numbers of calcination-carbonation cycles in the system and, consequently, will have different carrying capacities. It is of interest to calculate the average activity of the particles in the system and to estimate the system's behavior based on the contribution of each particle. Some models use an average number of cycles for the calculations. A more accurate approach is to include the probability distribution of the *particle age*, $\mathbf{r}(N)$, in the calculations. Rodríguez et al. [19] derived the following expression for this distribution, accounting for a reduction in the total amount of *complete* cycles due to incomplete calcination and carbonation:

$$\mathbf{r}(N) = \left[\frac{F_0(1-f_{\mathrm{calc}})}{F_0+F_R\,f_{\mathrm{calc}}}+\frac{F_0}{F_R}\right]\frac{f_{\mathrm{carb}}^{N-1}f_{\mathrm{calc}}^{N}}{\left(f_{\mathrm{carb}}\,f_{\mathrm{calc}}+F_0/F_R\right)^N} \tag{40}$$

Here, N is the number of complete calcination-carbonation cycles or *particle age*, and f_{carb} and f_{calc} are the extent of carbonation and calcination per cycle, calculated with the following equations:

$$f_{\mathrm{carb}} = (X_{\mathrm{carb}} - X_{\mathrm{calc}})/(\overline{X}_N - X_{\mathrm{calc}}) \tag{41}$$

$$f_{\mathrm{calc}} = (X_{\mathrm{carb}} - X_{\mathrm{calc}})/X_{\mathrm{carb}} \tag{42}$$

The expression in Eq. (40) is only valid if the make-up and circulation rates are kept constant throughout the entire operation of the plant. During our pilot tests, however, these parameters showed considerable variation (see Fig. 12.a); therefore, Eq. (40) cannot be applied using the values of F_R/F_0. Instead, we use the definition of the system age number, which implies that the system's sorbent activity is equivalent to that of a steady-state system with $F_R/F_0 = \gamma$. This gives the following particle age distribution:

$$\mathbf{r}(N) = \left(\frac{1-f_{\mathrm{calc}}}{1+\gamma f_{\mathrm{calc}}}+\gamma^{-1}\right)\frac{f_{\mathrm{carb}}^{N-1}f_{\mathrm{calc}}^{N}}{\left(f_{\mathrm{carb}}\,f_{\mathrm{calc}}+\gamma^{-1}\right)^N} \tag{43}$$

The variation of γ is very slow compared to the particle and gas residence times in the carbonator (see Section 3.3). This allows us to neglect the time-dependence of $\mathbf{r}(N)$ and implement Eq. (43) in our steady-state carbonator model. Considering that the solid samples from the pilot tests (see Section 2.1) where almost fully carbonated up to the maximum capacity (see Fig. 8), the value of f_{carb} was set equal to 0.95. The calciner efficiency was set considering an average performance of $f_{\mathrm{calc}} = 0.8$.

Using the particle age distribution, the mean parameters for the reaction model can be obtained by adding the contributions of each particle group. The average activity is [7]:

$$\overline{X}_N = \sum_{N=1}^{\infty}\mathbf{r}(N)\,X_N \tag{44}$$

Here, X_N is given by Eq. (26). To calculate the average conversion at the carbonator outlet and the average kinetic constant, both, the residence-time and the particle age distribution are used [56]:

$$X_{\mathrm{carb}} = \overline{X} = \sum_{N=1}^{\infty}\mathbf{r}(N)\int_0^{\infty}\mathbf{E}(t)X(t,N,\mathfrak{C}^*)\,dt \tag{45}$$

Here, $X(t)$ is computed with Eq. (21), using an equivalent driving force ($\mathfrak{C}^*$) that depends on the CO_2 concentration in the carbonator. An alternative expression for Eq. (45), suitable for numerical calculations is presented in Appendix A.3. The expression to calculate the average reaction rate is:

$$\overline{k}_{\mathrm{ri}} = \sum_{N=1}^{\infty}\mathbf{r}(N)\int_0^{\infty}\mathbf{E}(t)\,k_r(t,N,\mathfrak{C}^*)\,dt \tag{46}$$

In Part I [1], the following first-order expression for the carbonation was obtained:

$$\frac{dX}{dt}\rho_{\mathrm{s,a}}/M_{\mathrm{s,a}} = K_r\mathfrak{C} \tag{47}$$

Here, K_r is the global reaction rate of the particle model, $\rho_{\mathrm{s,a}}$ is the density of the potentially active particles (CaO and $CaCO_3$), and $M_{\mathrm{s,a}}$ is the molar mass of the potentially active particles. The reaction rates of the particle (k_{ri}) and the reactor (K_{ri}) sub-models can be related using Eq. (47) and Eq. (3):

$$K_{\mathrm{ri}} = k_{\mathrm{ri}}\;\rho_{\mathrm{s,a}}/M_{\mathrm{s,a}} \tag{48}$$

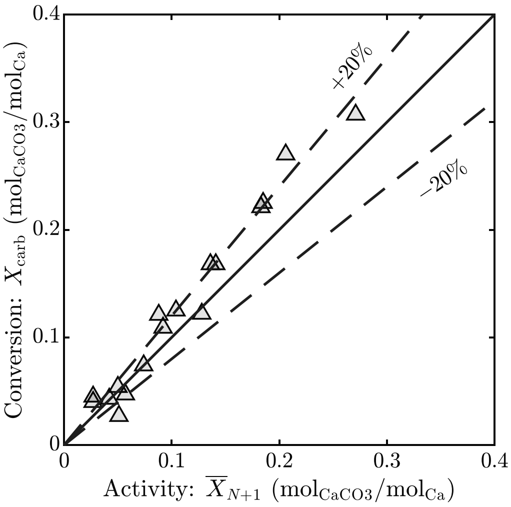

Fig. 8. Comparison between the conversion (X_{carb}) and the activity ($\overline{X}_{N+1}$) from pilot plant samples. The meaning and calculation of $\overline{X}_{N+1}$ are discussed in Section 4.1.2. Data from [33].

An expression for the average reaction rate for the reactor sub-model, consistent with [56], can be obtained using Eqs. (46) and (48):

$$\overline{K}_{\mathrm{ri}} = \frac{\rho_{\mathrm{s,a}}}{M_{\mathrm{s,a}}} \sum_{N=1}^{\infty} \mathbf{r}(N) \int_0^{\infty} \mathbf{E}(t)\, k_x \left(1 - X(t, N, \mathfrak{C}^*)\right)^{2/3} dt \tag{49}$$

Eq. (49) can be integrated to obtain an expression that can be solved numerically. The steps to do this, as well as the final expression, are presented in Appendix A.4. To incorporate external diffusion effects, see Section 3.1.3 (mainly Eq. (10)).

Some models use the average conversion to calculate the reaction constant for the reactor model (K_r):

$$\overline{K}_{ri} = \left(\rho_{\mathrm{s,a}}/M_{\mathrm{s,a}}\right) k_x (1 - \overline{X})^{2/3} \tag{50}$$

Replacing k_x for the expressions in Eqs. (12) and (18):

$$\overline{K}_{ri} = k_s \frac{\overline{X}_N S_{0,\mathrm{p}} \rho_{\mathrm{s,a}}/(1 - \epsilon_0)}{M_{\mathrm{s,a}}} (1 - \overline{X})^{2/3} \tag{51}$$

Here, $\overline{X}_N$ is the mean activity of the particles, usually calculated with a simplified expression from Abanades et al. [101, Eq.4]. Generally, Eq. (51) is computed assuming that the sorbent properties correspond to pure CaO, thus:

$$\overline{K}_{ri} = k_s \frac{\overline{X}_N S_{0,\mathrm{p}} \rho_{\mathrm{CaO,t}}}{M_{\mathrm{CaO}}} (1 - \overline{X})^{2/3} \tag{52}$$

Many models [63,64,69,85,102] use Eq. (52), but the underlying assumptions are not always indicated. For comparison purposes, we computed the maximum conversion using this calculation method, which resulted in a considerable overprediction of the sorbent activity compared to the values measured from pilot-test samples. For this reason, we used Eqs. (44), (45), (46), and (49) for our model calculations.

3.5. Calculation logic

The calculation logic of a carbonator model using the particle sub-model developed in this study is illustrated in Fig. 9.a. The calculation starts with an initial guess for the equivalent CO_2 concentration driving force ($\mathfrak{C}^*$) and the inputs from Table B.1. The inputs for the deactivation correlation (k, X_r) may need to be adjusted based on the type of sorbent and the operating conditions.

With the required inputs, the particle sub-model is used to simulate the system and particle deactivation, as well as the carbonation reaction (see Fig. 9.b). The main results from the deactivation model are the system age number (γ) and the particle activity ($\overline{X}_N$), with the latter depending on N. The main outputs from the reaction model are the particle kinetic rate (k_x), the global reaction rate (K_r), and the particle conversion (X_{carb}). The value of X_{carb} is used to compute the carbonation efficiency of the particle sub-model (E_{PM}) based on a molar balance, as explained in Part I [1]. The reaction rate is an input for the reactor sub-model (see, e.g., Part I [1]). The reactor sub-model gives a corresponding carbonation efficiency (E_{RM}). If the prediction of both sub-models coincides within a tolerable error (Err), the calculation can be terminated. Otherwise, a new value of $\mathfrak{C}^*$ is computed, and a new iteration begins. The model is solved iteratively using the bisection method of Bolzano [103, p.53–59].

For the assessment of experimental tests using our model, f_{carb} and f_{calc} are inputs that can be estimated from empirical data. For the design of carbonators, f_{carb} and f_{calc} are obtained iteratively from Eqs. (41) and (42), where X_{calc} is an input from a calciner model (e.g., [37]).

4. Results and discussion

4.1. Model validation

In this section, the validation of the particle sub-model developed in this work is presented. Relevant information on the validation procedure of the entire carbonator model (see [1]) is also reported here. The validation was performed using experimental data from pilot tests at the 300-$\mathrm{kW_{th}}$ scale (see Section 2.1) and TGA analysis from our experiments (see Section 2.2 and Section 2.3) and from the open literature [40,54]. We considered three aspects for the validation: (i) validation of the reaction kinetics using TGA data (Section 4.1.1); (ii) validation of the

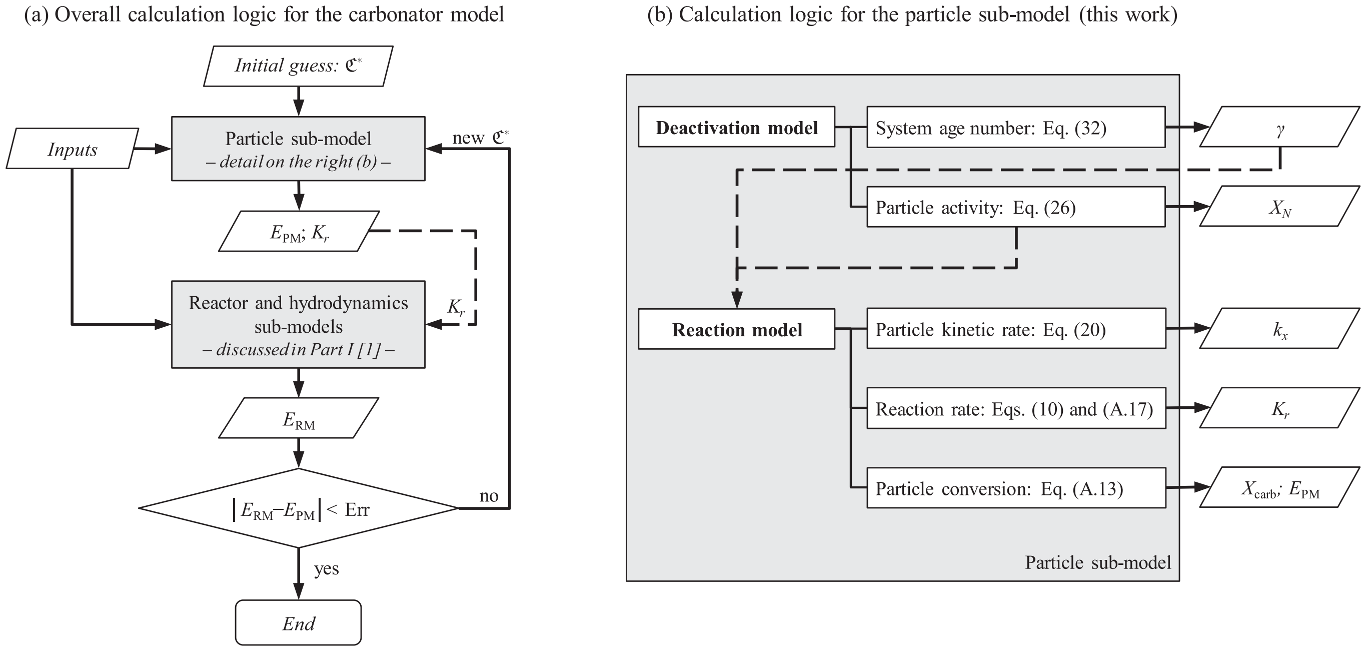
(a) Overall calculation logic for the carbonator model
Initial guess: $\mathfrak{C}^*$
Inputs
Particle sub-model
– detail on the right (b) –
new $\mathfrak{C}^*$
E_{PM}; K_r
Reactor and hydrodynamics sub-models
– discussed in Part I [1] –
K_r
E_{RM}
$|E_{\mathrm{RM}} - E_{\mathrm{PM}}| <$ Err
no
yes
End
(b) Calculation logic for the particle sub-model (this work)
Deactivation model
System age number: Eq. (32)
γ
Particle activity: Eq. (26)
X_N
Reaction model
Particle kinetic rate: Eq. (20)
k_x
Reaction rate: Eqs. (10) and (A.17)
K_r
Particle conversion: Eq. (A.13)
X_{carb}; E_{PM}
Particle sub-model

Fig. 9. Calculation logic of a carbonator model: (a) overall calculation logic, adapted from [1]; and (b) detail of the particle sub-model developed in this work. The reactor and hydrodynamics sub-models are explained in Part I [1]. The system age number (γ) is calculated using Eq. (32) and the particle activity (X_N) using Eq. (26). The particle kinetic rate (k_x) is obtained with Eq. (20), the reaction rate (K_r) with Eqs. (10) and (A.17), and the particle conversion (X_{carb}) with Eq. (A.13).

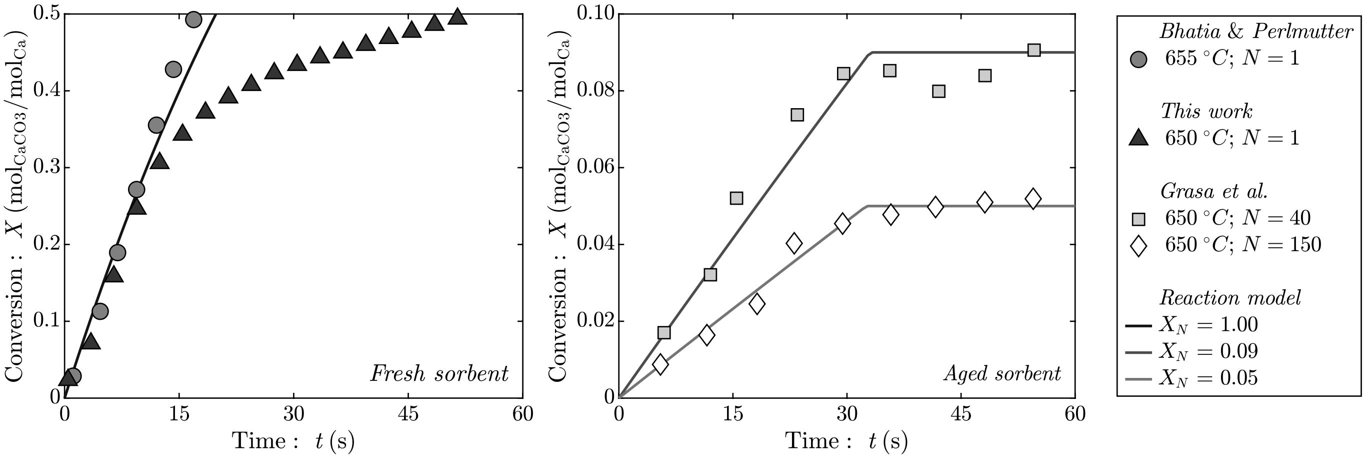

Fig. 10. Validation of the reaction model using data from TGA analysis obtained using the sorbent from the pilot tests (Messinghausen), and data from the open literature [40,54]. The results are compared for fresh sorbent (left) and aged sorbent (right). For all the runs, the CO_2 partial pressure was 10 kPa.

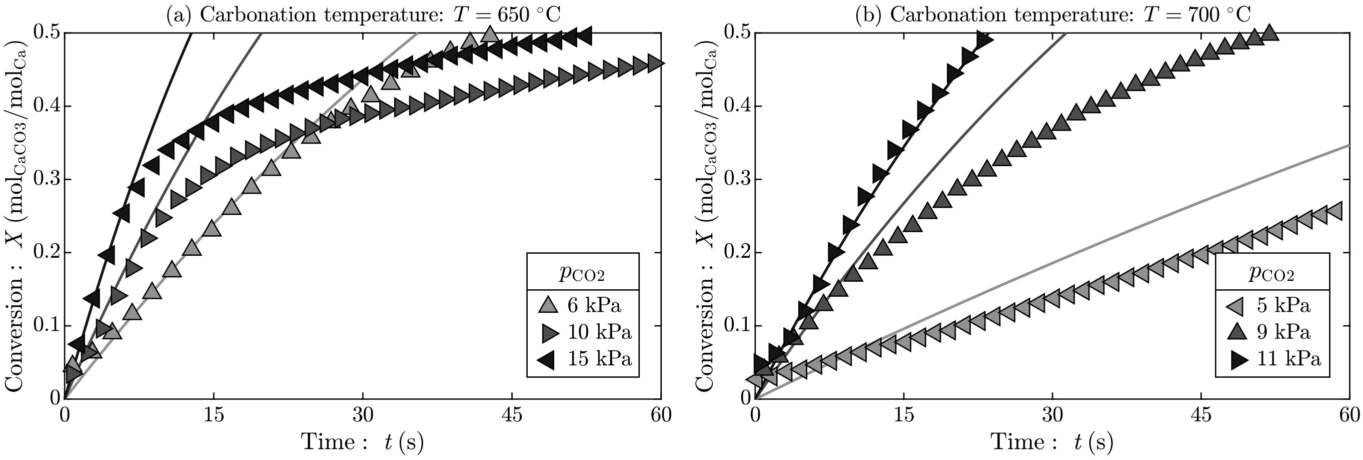

Fig. 11. Validation of the reaction model using data from TGA analysis obtained using fresh Messinghausen limestone. Test results for different carbonation temperatures and CO_2 partial pressures (p_{CO2}). The model results are illustrated with continuous lines and the experimental data is indicated with the markers (triangles).

sorbent deactivation using results from pilot plant operation, which is independent of the reactor sub-model (Section 4.1.2); and (iii) validation of the entire model using pilot test results (Section 4.1.3). For the last aspect (iii), the overall model including the particle sub-model (this work) and the reactor sub-model (Part I [1]) are validated using the particle carbonation degree after the carbonator (X_{carb}).

4.1.1. Reaction kinetics

The reaction model was validated using data available in the open literature [40,54] and our data from TGA performed on the Messinghausen limestone (see Section 2.3). Fig. 10 compares the model results with the experimental data. The model calculations were performed using Eqs. (20), (21), and (22). For the fresh sorbent, X_N was set equal to one, which gives an initial specific surface area of $S_{0,t} = 43.7$ m^2/cm_t^3. For the aged sorbent, X_N was adjusted to correspond with the end of the chemically controlled fast stage.

To validate the fresh-sorbent kinetics, we used data from Bhatia and Perlmutter [40] (see Fig. 10, left). It is not surprising that the model correctly predicts their data, as we utilized the kinetic constant $k_s = 5.95\ 10^{-10}$ $m^4/(mol\ s)$ suggested by them. There is a good correlation between our TGA data and the model for the fresh sorbent in the kinetic range for different conditions (see Fig. 11), especially for the tests at 650 °C. The differences in the maximum conversions are probably due to the different calcination conditions (see Section 2.3 and Table S1).

We used the data reported by Grasa et al. [54] for the validation of the kinetic behavior of the aged sorbent. The model represents the experimental results accurately, as illustrated in Fig. 10 (right). Although no kinetic data were available for our aged sorbent, the accurate prediction of the surface areas (see Table 2) supports the validity of this kinetic model for highly cycled particles. The validation of the reactor model (see Section 4.1.2) further supports the assumptions made for the simulations of the particle reaction.

4.1.2. Sorbent deactivation

In this section, the validation of the sorbent deactivation model is discussed. Experimental data from pilot tests (see Section 2.1) were used for the validation.

The sorbent carbonation rate after the carbonator (X_{carb}) in the pilot tests was obtained from sorbent samples using either TGA or weight-loss measurements. Each sample corresponds to a balance point used to

(a) Molar circulation rate (F_R) and molar make-up rate (F_0) throughout the pilot tests

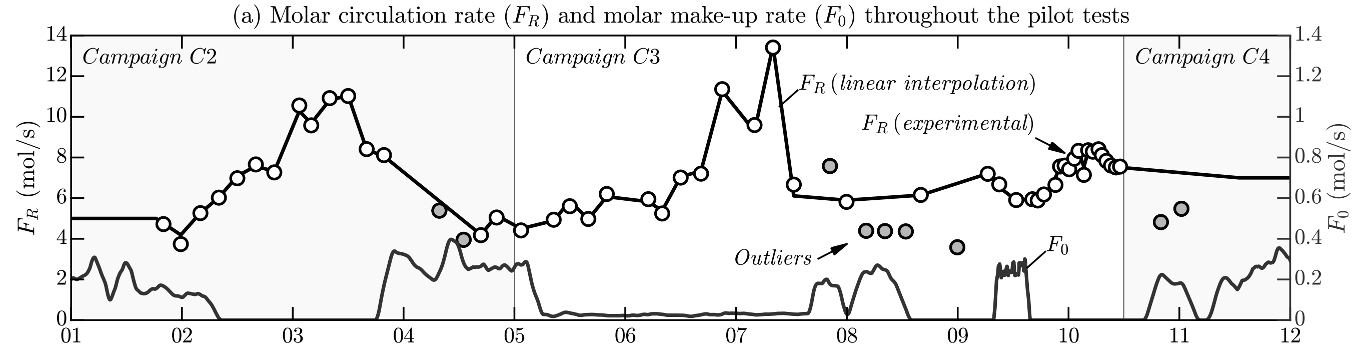

(b) Sorbent age throughout the pilot tests

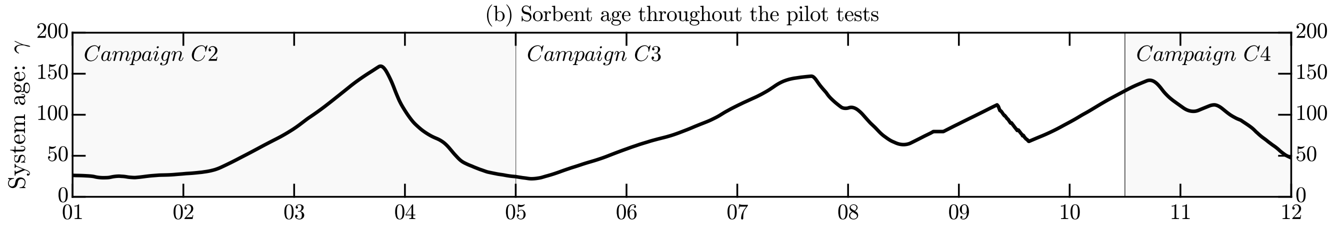

(c) Carbonator efficiency throughout the pilot tests

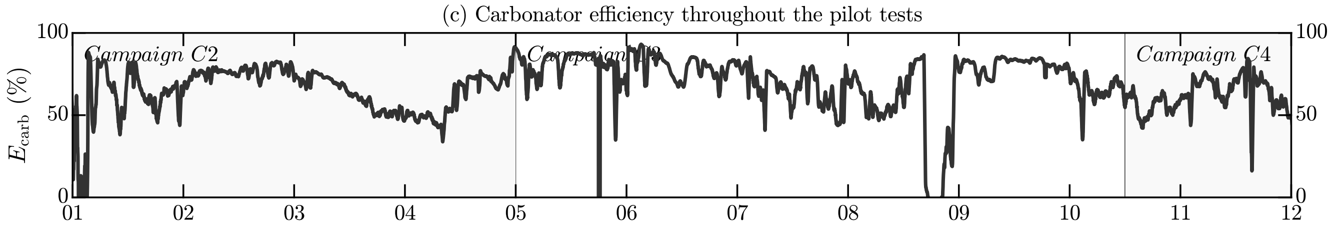

(d) Sorbent activity throughout the pilot tests and validation of the deactivation model

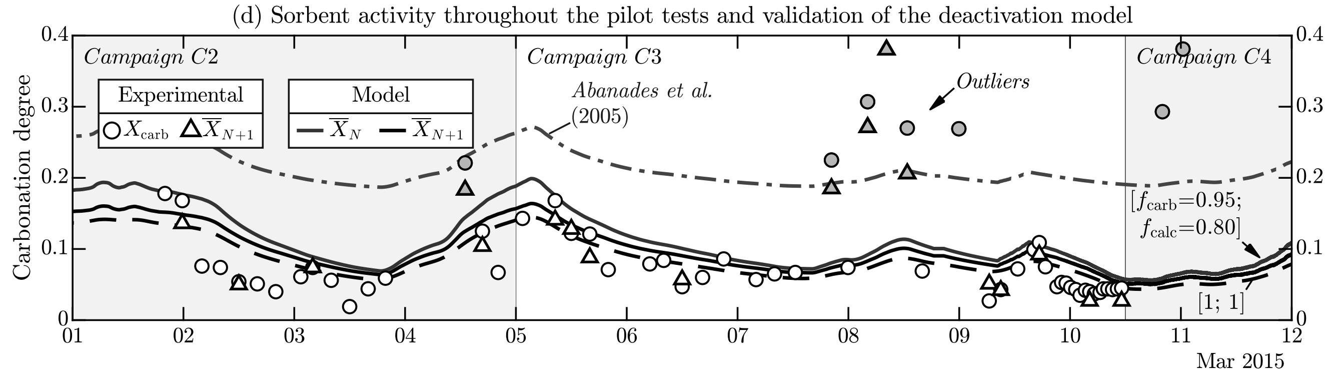

Fig. 12. Sorbent behavior throughout the pilot tests: (a) molar circulation rate and make-up rate, (b) system age number, (c) carbonator efficiency, and (d) sorbent activity and validation of deactivation model. The markers represent discrete data from sorbent samples taken during the pilot tests. The gray markers correspond to outliers.

validate our model. To obtain the average activity ($\overline{X}_N$) of the sorbent samples, the maximum carbonation degree was calculated through calcination and carbonation in a TGA. Since the method added one complete calcination-carbonation cycle to the sample, the acquired data was $\overline{X}_{N+1}$. There is less data for $\overline{X}_{N+1}$ than for X_{carb} because the former could only be calculated with TGA, which is more complex than the weight-loss procedure. A detailed description of the methods used to obtain these data, as well as the complete dataset for the sorbent particles, is available elsewhere [33]. The data of X_{carb} and $\overline{X}_{N+1}$ from solid samples is illustrated in Fig. 12.d with circles and triangles, respectively.

The molar make-up rate (F_0) and circulation rate (F_R) of the solid sorbent are two significant operational parameters for CaL systems. Fig. 12.a illustrates the variation of these parameters throughout the pilot tests. The make-up rates (F_0) were calculated from loss-in-weight measurements of the make-up feeding systems. Fresh material was fed intermittently, partly in batches. Apart from the addition of fresh material, sometimes, old material was fed back into the system to compensate for the high material loss. This *spurious* make-up was considered as $F_0 = 0$ since it did not increase the activity of the system. The high material loss was caused by high entrainment and low cyclone efficiency. In the following tests campaigns, coarser particles were used, thus reducing the entrainment and material loss considerably [104,105]. On March 9, low-cycled particles were fed back into the system. Since these particles were subjected to fewer calcination-carbonation cycles than the average particles of the system, they were computed as fresh make-up with a correction factor of 0.5 on F_0, assuming CaO material properties. Some samples exhibit considerably higher concentrations of $CaCO_3$ than the rest of the samples (*outliers* in Fig. 12, illustrated with gray markers). These samples were taken while make-up was being fed directly into the carbonator. Presumably, a high amount of the sampled material consisted of fresh make-up. Since these samples are not representative of the average sorbent properties in the system at the sampling time, they were excluded from the validation.

The solid circulation rates (F_R) were obtained through mass and

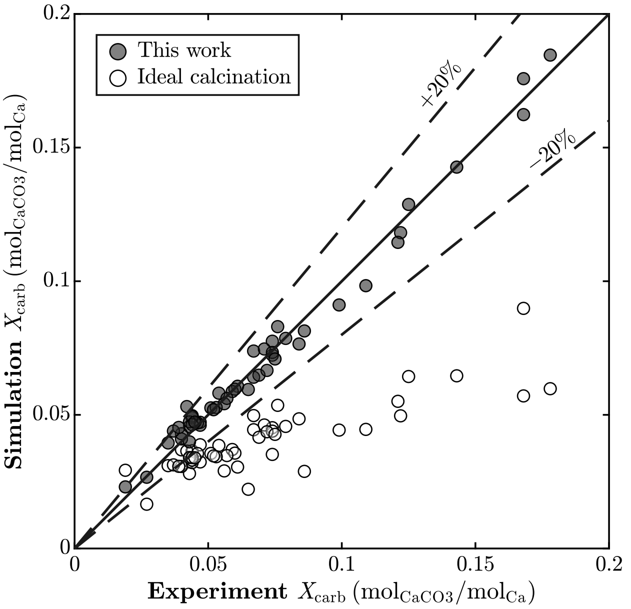

Fig. 13. Validation of the carbonator model using the carbonation rate at the carbonator outlet (X_{carb}). The model results are compared with the data from solid samples from the pilot tests (this work). Neglecting the incomplete calcination significantly reduces the accuracy of the model (ideal calcination).

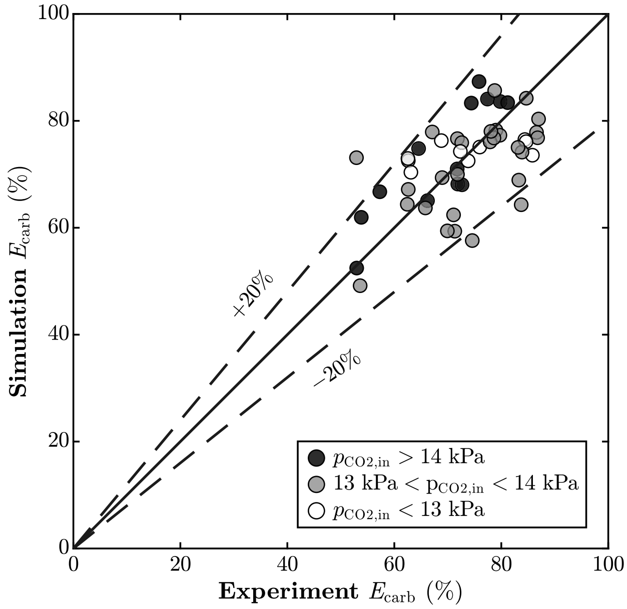

Fig. 14. Parity diagram comparing the carbonation efficiency calculated with experimental data and computed with the reactor model. There is a slight systematic overprediction of the carbonation efficiency for high CO_2 concentrations ($p_{\mathrm{CO2,in}} > 14$ kPa).

energy balances of the carbonator, using the values of X_{carb} from the solid samples. The average carbonation rate of the solids entering the carbonator (X_{calc}), which is an input for our carbonator model, was calculated from the mass and energy balances as well. A detailed explanation of this balancing method, including a validation using measurements of pressure drop in a loop seal, is available in the work of Reitz [33]. The values of F_R for each balance point are indicated with circles in Fig. 12.a. The continuous data set of F_R throughout the pilot tests was obtained by linear interpolation of these values, as illustrated in Fig. 10.a with a solid black line.

The system age number (γ) at each time during the pilot tests was obtained by solving Eq. (32) numerically. The inputs for the calculation were the data of F_0 and F_R from Fig. 12.a. The calculated values of γ are reported in Fig. 12.b. Evidently, γ increases during periods of low make-up and high circulation and decreases during periods of high make-up and low circulation. The value of γ variates between 20 and 160 throughout the tests, indicating instability in sorbent activity. Periods of high input of fresh material (F_0) occur immediately after the sorbent in the system has undergone significant deactivation. However, it takes more than one day to restore the system's activity, as seen in Fig. 12.b and discussed in Section 3.3. This is an inefficient strategy to control sorbent activity leading to underperformance, and energetic and economic penalties in commercial facilities. If the activity of the CaL system is predicted using the model developed in this work, particularly with γ, stable sorbent activities can be achieved, thus enhancing performance and efficiency. This is especially relevant for IHCaL systems that have high solid inventories and correspondingly slow responses to make-up variations.

The validation of the deactivation model is illustrated in Fig. 12.d. The mean sorbent activity ($\overline{X}_N$) of the model was obtained by solving Eq. (44) numerically. Hereby, the calculated values of γ (see Fig. 12.b) were the main inputs for the calculation. The model results are indicated with a red continuous line in Fig. 12.d. The same calculation was performed by starting the series of Eq. (44) at $N = 2$ (corresponding to $N + 1$), yielding the model values of $\overline{X}_{N+1}$. These values of $\overline{X}_{N+1}$ are displayed using a black continuous line in Fig. 12.d. The calculated $\overline{X}_N$ is slightly higher than the values of X_{carb} determined from solid samples (indicated with circles). This indicates that the prediction is accurate because $\overline{X}_N$ is the maximum threshold of X_{carb}. The model results of $\overline{X}_{N+1}$ fit the empirical data (triangles in Fig. 12.d) reasonably well. The deviations can be explained by the uncertainties in calculating the circulation and make-up rates, as well as the variability in performance of the carbonator and the calciner (f_{carb} and f_{calc}). Overall, our deactivation model predicts the empirical data with reasonable accuracy, despite significant variations in make-up and circulation rates.

Two alternative calculations of $\overline{X}_{N+1}$ were performed for comparison.

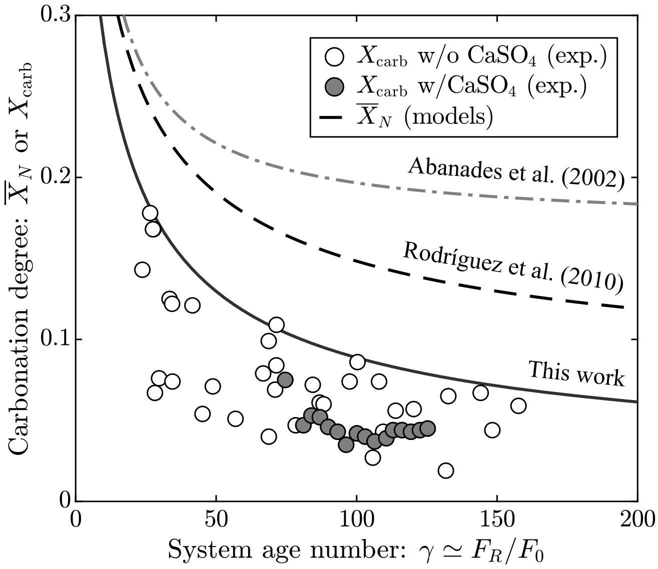

Fig. 15. Prediction of the sorbent deactivation model for variating sorbent age. The lines indicate the maximum activity predicted by our model, and the models from Abanades et al. [7] and Rodríguez et al. [19]. We assumed $f_{\mathrm{carb}} = 0.95$ and $f_{\mathrm{calc}} = 0.8$ for all of them. The results are compared with the carbonation degree at carbonator exit (X_{carb}) obtained from sorbent samples during our pilot tests, displayed with circles. The gray circles correspond to balance points with more than 100 $\mathrm{ppm_{mol}}$ of $CaSO_4$ in the solid stream.

The first one was based on our deactivation model, but complete carbonation and calcination were assumed for every cycle (i.e., $f_{\mathrm{carb}} = f_{\mathrm{calc}} = 1$). The corresponding results, plotted with a broken line in Fig. 12.d, are slightly lower than the ones from the original calculation. The second alternative calculation, illustrated with a dash-dotted line in Fig. 12.d, was performed using the model from Abanades et al. [101]. It resulted in a considerable overprediction of the activity. This indicates that it is necessary to implement the particle age distribution (**r**) (see Section 3.4) and the appropriate deactivation constants (see Section 3.2.1) to obtain accurate results.

At the end of March 9, SO_2 was added to the gas entering the carbonator to evaluate the influence of this contaminant in the capture capacity (see Fig. 2.b). Around this time, many sorbent samples were taken (see Fig. 12.d). There is some overprediction of the sorbent activity, which may indicate that the deactivation due to formation of $CaSO_4$ was higher than the one calculated with Eqs. (29) and (30).

Overall, the carbonation degree of the particles at the carbonator outlet was relatively low. This may be due to prolonged periods with little or no make-up material added. Another possible reason is that the calciner was operated near equilibrium, which likely caused multiple recarbonation and calcination cycles within the reactor, accelerating particle deactivation. During some periods of low X_{carb}, high carbonation efficiency (E_{carb}) could still be achieved due to the high circulation rates (see Fig. 12.c).

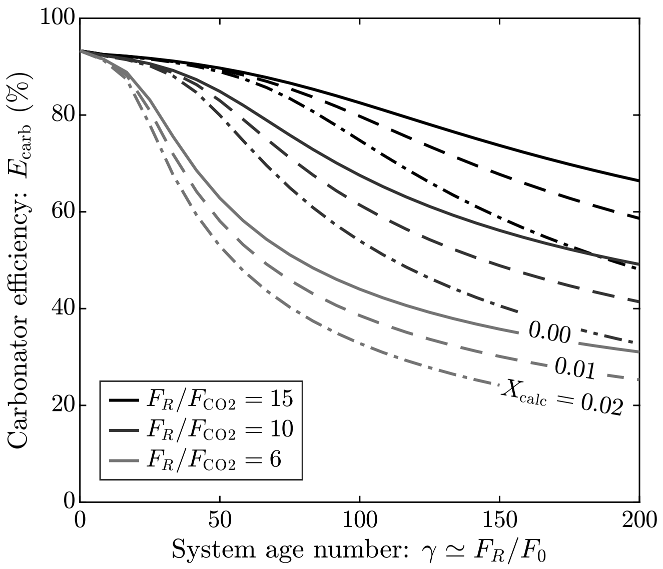

Fig. 16. Influence of the sorbent age in the carbonator efficiency (E_{carb}). The different colors indicate different circulation rates, and the line type indicate the calciner performance in terms of X_{calc}. Other input parameters are included in Table B1.

4.1.3. *Overall model*

The validation in terms of sorbent carbonation rate at the carbonator outlet (X_{carb}) is illustrated in a parity plot (Fig. 13). Here, the values of X_{carb} from the model (simulation) are compared with those obtained from solid samples from the pilot tests (experimental). Each circle represents one balance point. The solid line indicates the perfect agreement, and the broken lines indicate the 20 % deviation boundaries. The model values were calculated using the particle sub-model developed in this study and the reactor sub-model of Part I [1]. For comparison, the same calculations were performed neglecting partial calcination by forcing $X_{\mathrm{calc}} = 0$ (ideal calcination, white circles).

The predictions of our model agree with experimental data. For most of the balance points, the simulation results are within the 20-% error bounds. On the other hand, if the calcination degree of the sorbent entering the carbonator is neglected (ideal calcination), X_{carb} cannot be predicted accurately.

4.2. *Influence of CO_2 partial pressure*

The influence of the CO_2 concentration in our reactor model is analyzed with a parity plot in Fig. 14. Here, the carbonator efficiency (E_{carb}) of the pilot tests is compared with our model predictions. E_{carb} is the ratio of CO_2 captured in the carbonator to the total CO_2 entering the carbonator [106]. The data is categorized according to the inlet CO_2 partial pressures ($p_{\mathrm{CO2,in}}$) of each balance point. For $p_{\mathrm{CO2,in}}$ higher than 14 kPa, there is a slight systematic error of overprediction in the model. This may be the result of assuming first-order kinetics with CO_2 concentration (see Section 3.1.2). Sun et al. [58] reported that the reaction kinetics is zero-order for partial pressures of $p_{\mathrm{CO2}} < 10$ kPa. Considering that the mean reactor concentrations are still well below this limit, it is reasonable that the influence of an order shift at 10 kPa would be relatively low. One option to improve the accuracy of the simulations could be to include the reaction shift in the reactor KL model. This was beyond the scope of this work since the accuracy penalty of the assumption of a constant reaction rate is relatively low. Nevertheless, it may be relevant for the application of CaL and IHCaL carbon capture from industrial sources with higher CO_2 concentrations in the flue gases, such as cement and lime plants [31,107].

The equations for the zero-order model are included in Appendix A.1. The expression we found is only valid if external diffusion

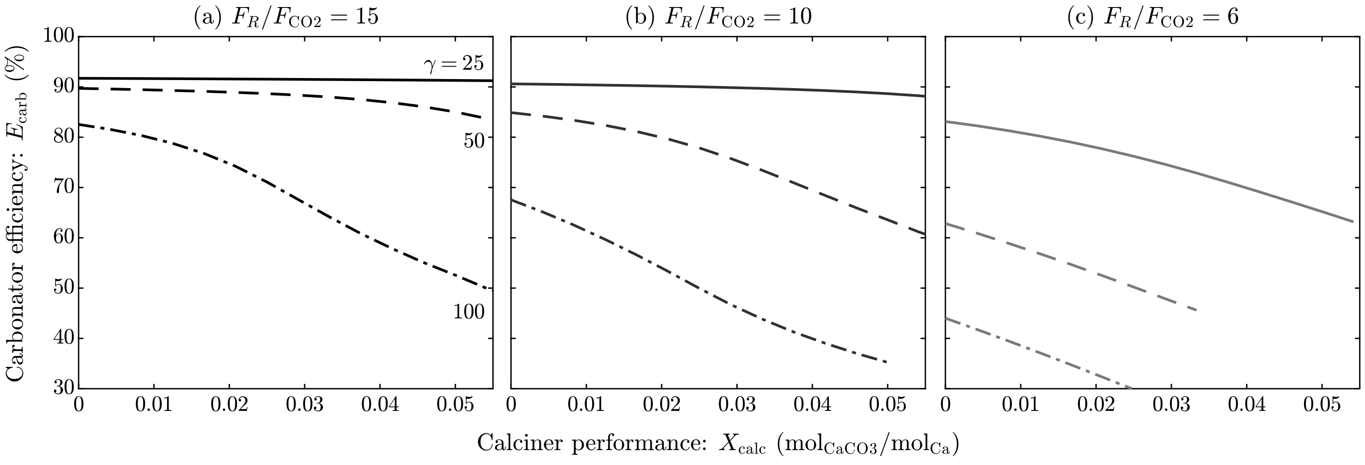

Fig. 17. Variation of the carbonator efficiency (E_{carb}) with the calcination performance (characterized by X_{calc}). Results are displayed for different specific circulation rates (a–c) and different sorbent ages (γ). Other input parameters are listed in Table B1.

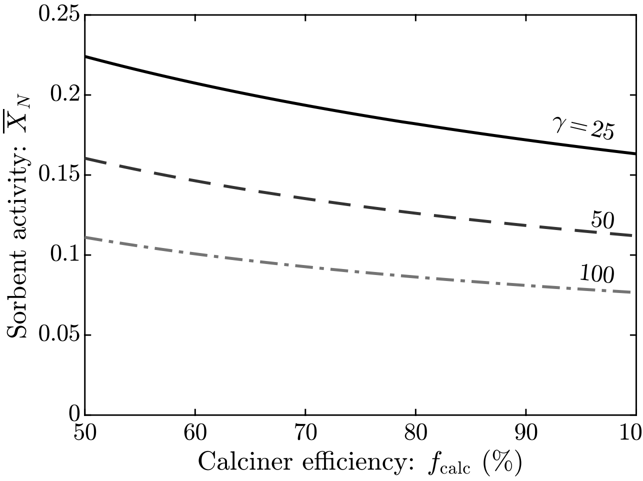

Fig. 18. Variation of sorbent activity with the calciner efficiency for different particle ages. Here, the circulation rates are kept constant, thus allowing a reduction in carbonation efficiency. The improvement in activity with low f_{calc} is spurious since the CO_2 capture efficiency decreases with lower f_{calc}. Other input parameters are available in Table B1.

effects are neglected, which is generally acceptable, as discussed in Section 3.1.3. An appropriate model would have to consider that a transition of the reaction order occurs inside the reactor, which requires discretizing the reactor height, thus increasing the computational complexity.

4.3. Modeling sorbent deactivation

Modeling sorbent deactivation accurately is crucial for obtaining reliable predictions of carbonator performance. In Fig. 15, we compare our model with two other models widely used in carbonator calculations (e.g., [20,85,108]). The results of maximum activity ($\overline{X}_N$) are plotted against the system age number (γ) calculated with Eq. (32). The sorbent-sample data of carbonation degree at the reactor outlet (X_{carb}) is included for validation.

The predictions of our model, illustrated in Fig. 15, constitute a maximum limit for all the X_{carb} points —only one point was slightly over the predicted value of $\overline{X}_N$. Considering that the carbonation degree of the samples was very close to the maximum conversion calculated with our model, it appears that our model accurately describes cyclic sorbent deactivation. It should be noted that some balance points presented less activity due to sulfurization. These points are shown in Fig. 15 (gray circles), but the model predictions are not included.

The activity predicted by the other two models is significantly higher and does not accurately represent the experimental results. This disparity can be attributed to these models being fit using laboratory operating conditions, which differ from those of our pilot plant. Our model, on the other hand, was calibrated using data specific to the conditions of this study. Therefore, the fitting constants should be adjusted before applying the model to different operating environments (e.g., with TGA data, see Section 3.2.1).

There have been many efforts to describe the influence of material properties and operating conditions in the sorbent activity and deactivation. However, no deactivation model currently exists that can incorporate variations in operating conditions —such as calcination temperature or carbonation degree— over long-term operating periods for realistic full-scale applications. (cf. [5, p.283]). One possible way to do this would be to modify Eq. (32), making γ dependent on those parameters known to accelerate deactivation [24,27,92]. This should be the subject of further investigation.

The influence of the system age on the carbonator efficiency (E_{carb}) is illustrated in Fig. 16, using the inputs from Table B1. As expected, fresh sorbent (low γ) gives much higher values of E_{carb}. For low sorbent circulation rates (F_R), fresher sorbent is required to maintain high E_{carb}. The calciner performance has a significant influence on the CO_2 capture. This is discussed in Section 4.4.

Despite the mild calcination conditions in the IHCaL calciner, the sorbent exhibited low CO_2 carrying capacity (see Fig. 12.d) compared to previous studies [35,94,109,110]. We used data from the solid sorbent samples to fit the residual activity (X_r) (see Section 3.2.1), which allowed us to accurately predict the sorbent activity throughout the pilot tests. The low value of this constant ($X_r = 0.019$) can be explained by the low carbonation temperatures and the operation of the calciner close to equilibrium conditions (low T and high p_{CO2}) [18]. Criado et al. [92] found that low carbonation temperatures (T) enhance the cyclic deactivation of the sorbent. In our pilot tests, T varied between 550 and 700 °C during operation. Furthermore, Diego et al. [100] indicated that particles undergo additional calcination-carbonation cycles inside of the calciner if the operating CO_2 partial pressure is close to the equilibrium, e.g., due to low calcination temperatures. This effect accelerates sorbent deactivation. Another explanation for the low activity could be the higher particle residence times in the calciner, compared to oxy-fired CaL (cf. [79]). The issue of sorbent deactivation, especially in IHCaL systems, needs to be further investigated with pilot experiments focusing on the effect of calciner and carbonator operating conditions.

4.4. Influence of calciner performance

The influence of the calciner on the CO_2 capture efficiency (E_{carb}) is illustrated in Fig. 17, using the input values of Table B1. Here, the carbonation ratio at the carbonator inlet (X_{calc}), which coincides with the carbonation ratio at the calciner outlet (see Fig. 1), is used as the indicator of the calciner performance. For high circulation rates (Fig. 17.a), incomplete calcination only affects the carbonator efficiency for highly aged sorbent ($\gamma > 50$). For medium circulation rates (Fig. 17.b), the effect of the calciner performance is appreciable starting at $\gamma \approx 25$. For very low circulation rates (Fig. 17.c), high calcination efficiencies ($X_{\mathrm{calc}} < 0.01$) are critical for achieving suitable values of E_{carb}. In a nutshell, the sensitivity of the CaL process to the calciner performance increases with the aging of the particles and with lower circulation rates.

Atsonios et al. [21] used an Aspen Plus Gibbs reactor to take the calcination into account for their CaL CFD simulations. Assuming $F_{\mathrm{R}}/F_{\mathrm{CO2}} = 14$, they observed a drop in CO_2 capture efficiency for $X_{\mathrm{calc}} > 0.04$. Our results confirm their observations for the case $\gamma = 50$ (see Fig. 17.a).

If the sorbent circulation rate is kept constant, there is an improvement in the sorbent activity ($\overline{X}_N$) for lower calciner efficiency (f_{calc}, Eq. (42)) due to a reduction in the number of effective calcination-carbonation cycles of the particles (see Fig. 18). This improvement is spurious since it comes with a reduction in E_{carb}. Rodríguez et al. [19] observed that, if E_{carb} is maintained constant by adjusting F_{R}, the value of $\overline{X}_N$ is reduced for lower f_{calc}. They indicated that this effect is stronger for higher sorbent make-up rates. Nevertheless, as shown in Fig. 17, systems with more aged sorbent are more sensitive to f_{calc}; thus, higher make-up rates reduce the sensitivity to loss in calcination efficiency. In summary, CaL systems experiencing calcination issues will benefit from additional make-up.

Apart from the penalty in E_{carb}, the destination of the spent sorbent is to be considered for the design of the calciner. If the spent sorbent is to be used as quicklime or as material for the production of cement clinker, high calcination rates with mild operating conditions (e.g., low temperature) are desirable [105]. In some scenarios, the specifications of the spent sorbent may be stricter than the process constraints.

5. Conclusion

In this study, a deactivation and particle-sub model for CaL systems has been developed. The model incorporates a new methodology to account for fluctuations in sorbent make-up and circulation rates. The influence of the calcination in the capture capacity and the reactivity of the sorbent is considered through a novel calculation procedure. The model has been validated using results from TGA analysis and pilot tests in a 300-kW$_{th}$ IHCaL plant.

Our carbonation reaction model is based on previous studies. It accurately predicts results from pilot tests with low CO_2 partial pressures ($p_{CO2} \sim 5$ kPa) and operating temperatures of around 650 °C in the carbonator. However, there is still no consensus on the kinetic behavior of the carbonation reaction for higher p_{CO2}. While some authors suggest that the reaction becomes zero-order after 10 kPa, others report first-order behavior up to at least 100 kPa. Although this is not a problem for low CO_2 flue gas concentrations, it becomes relevant for industrial applications such as carbon capture in the cement or lime industry, where CO_2 partial pressures of 20 kPa or higher can be expected at the carbonator inlet. The issue of the reaction order shift requires clarification through experimental investigations. The methodology for adapting our carbonator model for zero-order carbonation is included in Appendix A.1. Further studies should compare our model predictions with results from pilot tests using flue gas with higher p_{CO2}, e.g., [31,111].

Sorbent deactivation was modeled using a novel calculation methodology to predict the sorbent aging in long operational periods with varying sorbent circulation and make-up rates. The deactivation constants were adjusted to account for the operating conditions, the sorbent properties, and the presence of $CaSO_4$. Our model satisfactorily predicts empirical results from pilot tests despite strong variations in make-up and circulation rates. Furthermore, it is useful for optimizing the input of fresh sorbent in CaL systems during operation, thereby ensuring consistently high CO_2 capture rates without incurring increased costs and efficiency penalties from excessive make-up.

This study could serve as a foundation for developing a more generalized deactivation model capable of predicting sorbent activity across different operating conditions and for various sorbents. To achieve this, our deactivation model should be advanced using more experimental data from TGA and pilot tests. These tests should cover a wide range of operating conditions, including various temperatures, CO_2 partial pressures, and residence times in both the calciner and the carbonator.

Our model has been used to evaluate the influence of the calciner's performance on the carbonator efficiency. We found that calcination issues in CaL systems can be compensated for with higher sorbent make-up and circulation rates, thus maintaining high CO_2 capture efficiency. This is particularly relevant for IHCaL facilities, where attaining high calcination rates is challenging.

Despite having been developed and validated with data from the IHCaL process, our model is applicable to other operating conditions, including the better-known oxy-fired CaL. We propose the following considerations to advance and adapt our model to a wide range of applications:

- Current experimental efforts in pilot plants are focused on assessing the influence of real flue gases —containing SOx, NOx, Cl, and solid particles— in the long-term operation of CaL systems. The findings from ongoing projects should be used to update our model to different operating conditions, including CO_2 capture from cement plants, waste to energy (WtE) facilities, and steel mills.
- For larger particles (> 500 μm), diffusion effects may become more relevant. Some insights on modeling external diffusion are provided in Section 3.1.3. A recent study [112] dealing with centimeter-scale sorbent particles may be useful to adapt our model for operation with large particles.
- Our model relies on the assumption that the mixing of particles in the reactor is good enough to consider it perfectly mixed. This is a reasonable assumption for CFB carbonators, but not for other types of reactors, such as fixed-bed, slow-moving (cf. [113]), or entrained-bed (see [114]) carbonators.
- We considered that only the chemically controlled rate is driving the carbonation kinetics, which is valid for CFB carbonators. However, for higher residence times (e.g., fixed bed), carbonation in the product-diffusion phase would occur, thus allowing for even higher carbonation rates. A model describing this phenomenon has been developed by Grasa et al. [115].
- To incorporate the effect of attrition, the reader is referred to the work of Haaf et al. [42].
- It may be challenging to achieve high calciner efficiency under realistic operating conditions for the IHCaL process, particularly regarding the operating temperature limit to avoid damaging the heat pipes (ca. 950 °C for our pilot plant, cf. [105,116]). This issue is addressed in a recent study on calciner modeling [37] that considers the particular case of the IHCaL calciner with a heat-pipes heat exchanger.

CRediT authorship contribution statement

Martin Greco-Coppi: Conceptualization, Methodology, Software (MATLAB), Validation, Investigation, Data curation, Visualization, Writing – original draft, Writing – review & editing. **Jochen Ströhle:** Writing – review & editing, Supervision, Project administration, Funding acquisition. **Bernd Epple:** Supervision.

Declaration of competing interest

Martin Greco-Coppi, Jochen Ströhle, and Bernd Epple have patent "Apparatus and Method for Producing Lime" (No. 10 2023 114 354.9) pending to Technical University of Darmstadt and Rheinkalk GmbH, and patent "Apparatus and Method for Producing Lime and Cement" (No. 10 2024 109 181.9) pending to Technical University of Darmstadt.

Acknowledgements

The work leading to these results has received funding through the ACT program (Accelerating CCS Technologies, Horizon 2020 Project No. 691712) within the ANICA project (ACT Project No. 299653). Financial contributions were made by the German Federal Ministry for Economic Affairs and Climate Action (BMWK Project No. 03EE5025). The authors would like to thank Diethelm Walter (Lhoist Germany Rheinkalk GmbH) for providing the Messinghausen limestone samples and Paul Bickel (Technical University of Darmstadt) for assisting in the data curation of experimental results. Furthermore, the support of Yassin Azbairi (Technical University of Darmstadt) in conducting TGA experiments under the supervision of Martin Greco-Coppi is greatly acknowledged. Additionally, Martin Greco-Coppi would like to thank Mateo C. Romano (Politecnico di Milano) for sharing the MATLAB code from his carbonator model [56], Isabel Martínez (Spanish National Research Council) for her explanations on her article of 2018 [20], Gemma Grasa (Spanish National Research Council) for the clarifications on her work of 2008 [54], Alina M. Greco Coppi for proof-reading this article, and the team of the University and State Library Darmstadt for their help in gaining access to primary sources. Finally, Martin Greco-Coppi extends special thanks to Juan Carlos Abanades (Spanish National Research Council) for the fruitful discussions on CaO active surface.

Appendix A. Demonstrations and derivation of equations

A.1. Governing equations for zero-order carbonation

For zero-order carbonation, the reaction can be described with the following differential equation:

$$\frac{dN_{\mathrm{CO2}}}{dt} = -V_{\mathrm{s,a}}K_{r,0} \tag{A.1}$$

Note that here the units of $K_{r,0}$ are (mol/m^3)/s, which is different than for first-order carbonation. Considering the deviation from the ideal plug-flow-reactor behavior, as in Part I [1], the following expression is obtained:

$$\frac{d\mathfrak{C}}{dz} = -\eta K_{r,0}\xi\varepsilon_s/u_o \tag{A.2}$$

Eq. (A.2) can be solved by integration throughout the height of the reactor. If ε_s and η are invariant with the reactor height, an analytical expression for the integral form can be found:

$$\mathfrak{C}_{\mathrm{out}} = \mathfrak{C}_{\mathrm{in}} - \eta K_{r,0}\tau_{\mathrm{reactor}} \tag{A.3}$$

Here, the characteristic time (τ_{reactor}) is:

$$\tau_{\mathrm{reactor}} \equiv \xi\varepsilon_s H_T/u_o \tag{A.4}$$

Since the same reaction order applies to both the particle and the reactor sub-models, the equations derived to relate both sub-models, particularly Eq. (48), are still valid. This is true since we neglect the diffusion, which is justified by the high CO_2 concentration associated with the zero-order carbonation. Without this assumption, the model would have to assume a zero-order dependency for the reaction and a first-order dependency for the diffusion, making the analytical integration more challenging.

A.2. Verification of the aging function

To verify the aging function $\gamma(t)$, we first integrate Eq. (32) with t ranging from zero to $+\infty$. For this, we consider that, at $t = 0$, $\gamma = 0$; and that, for $t \to \infty$, the system age number reaches an asymptotic value of γ.

$$\lim_{t\to\infty}\int_0^{\gamma}(F_R - F_0\,\gamma)^{-1}d\gamma = \int_0^{+\infty}\frac{dt}{n_s(t)} \tag{A.5}$$

Now, we consider that F_{R} and F_0 do not variate with time. Solving the integral and considering that the molar inventory (n_{s}) is positive and does not tend to zero:

$$\lim_{t\to\infty}[-\ln(F_R/F_0 - \gamma) + \ln(F_R/F_0 - 0)] = +\infty \tag{A.6}$$

Finally, solving for γ gives:

$$\lim_{t\to\infty}\gamma = F_R/F_0 \tag{A.7}$$

This is what had to be shown (see Eq. (31)).

A.3. Particle model – Calculation of average conversion ($\overline{X}$)

To make the calculations simpler, we define the variables c_1 and c_2 and rewrite $X(t)$ (Eq. (21)) as:

$$X\left(t,N,C_{CO2}^{*}\right) = 1-(c_2 - c_1t)^3; \quad \textit{for } t \le t_{\mathrm{lim}} \tag{A.8}$$

$$c_1 \equiv k_S S_N \mathfrak{C}^{*}/3 \tag{A.9}$$

$$c_2 \equiv (1 - X_{\mathrm{calc}})^{1/3} \tag{A.10}$$

Furthermore, we define a dimensionless carbonator residence time ($\widehat{\tau}$) and a dimensionless t_{lim} ($\widehat{t}_{\mathrm{lim}}$) for the calculations as follows:

$$\widehat{\tau} \equiv \tau_{\mathrm{s,carb}}\; c_1 \tag{A.11}$$

$$\widehat{t}_{\mathrm{lim}} \equiv t_{\mathrm{lim}}\; c_1 \tag{A.12}$$

$X_{\mathrm{carb}} = \overline{X}$ can be calculated using Eq. (45). Hereby, we consider that for $t > t_{\mathrm{lim}}$ the maximum conversion, X_{N}, is achieved:

$$\overline{X} = \sum_N^{+\infty}\mathbf{r}(N)\int_0^{t_{\mathrm{lim}}}\frac{1-(c_2-c_1t)^3}{\tau_{\mathrm{s,carb}}}\exp\left(-\frac{t}{\tau_{\mathrm{s,carb}}}\right)\,dt + \sum_N^{+\infty}\mathbf{r}(N)X_N\exp\left(\frac{-t_{\mathrm{lim}}}{\tau_{\mathrm{s,carb}}}\right) \tag{A.13}$$

To solve this expression, t_{lim} is obtained with Eq. (22). The analytical solution to the integral is:

$$\begin{aligned}&\int_0^{t_{\mathrm{lim}}}\frac{1-(c_2-c_1t)^3}{\tau_{\mathrm{s,carb}}}\exp\left(-\frac{t}{\tau_{\mathrm{s,carb}}}\right)\,dt = \\ &= \exp\left(-\frac{\widehat{t}_{\mathrm{lim}}}{\widehat{\tau}}\right)\left(-6\widehat{\tau}^3 - 6\widehat{t}_{\mathrm{lim}}\widehat{\tau}^2 + 6c_2\widehat{\tau}^2 - 3\widehat{t}_{\mathrm{lim}}^2\widehat{\tau} + 6c_2\widehat{t}_{\mathrm{lim}}\widehat{\tau} - 3c_2^2\widehat{\tau} - \widehat{t}_{\mathrm{lim}}^3 + 3c_2\widehat{t}_{\mathrm{lim}}^2 - 3c_2^2\widehat{t}_{\mathrm{lim}} + c_2^3 - 1\right) + 6\widehat{\tau}^3 - 6c_2\widehat{\tau}^2 + 3c_2^2\widehat{\tau} - c_2^3 + 1\end{aligned} \tag{A.14}$$

If $X_{\text{calc}} = 0$, then $c_2 = 1$, which gives:

$$= \exp\left(-\frac{\widehat{t}_{\text{lim}}}{\widehat{\tau}}\right)\left(-6\widehat{\tau}^3 - 6\widehat{t}_{\text{lim}}\widehat{\tau}^2 + 6\widehat{\tau}^2 - 3\widehat{t}_{\text{lim}}^2\widehat{\tau} + 6\widehat{t}_{\text{lim}}\widehat{\tau} - 3\widehat{\tau} - \widehat{t}_{\text{lim}}^3 + 3\widehat{t}_{\text{lim}}^2 - 3\widehat{t}_{\text{lim}}\right) + 6\widehat{\tau}^3 - 6\widehat{\tau}^2 + 3\widehat{\tau} \tag{A.15}$$

A.4. Particle model – Calculation of average reaction rate ($\overline{K}_{ri}$)

The average global rate is calculated by integrating Eq. (49). The reaction stops at full conversion, which occurs at t_{lim}. With this consideration, the integral can be simplified:

$$\overline{K}_{\text{ri}} = \frac{\rho_{\text{s,a}}}{M_{\text{s,a}}} \sum_{N=1}^{\infty} \mathbf{r}(N) \int_0^{t_{\text{lim}}} \mathbf{E}(t)\, k_x (1 - X(t, N, \mathfrak{C}^*))^{2/3}\, dt \tag{A.16}$$

Replacing the residence time distribution $\mathbf{E}(t)$ (Eq. (38)), and the conversion function $X(t)$ (Eq. (21)) gives:

$$\overline{K}_{ri} = \frac{\rho_{\text{s,a}}}{M_{\text{s,a}}} \sum_{N=1}^{+\infty} \mathbf{r}(N) k_s\, S_N \int_0^{t_{\text{lim}}} \frac{(c_2 - c_1\, t)^2}{\tau_{\text{s,carb}}} \exp\left(-\frac{t}{\tau_{\text{s,carb}}}\right)\, dt \tag{A.17}$$

Where the constants c_1 and c_2 are given by Eq. (A.9) and (A.10). The definite integral can be solved analytically:

$$\int_0^{t_{\text{lim}}} \frac{(c_2 - c_1\, t)^2}{\tau_{\text{s,carb}}} \exp\left(-\frac{t}{\tau_{\text{s,carb}}}\right)\, dt = -\exp\left(-\frac{\widehat{t}_{\text{lim}}}{\widehat{\tau}}\right)\left[2\widehat{\tau}^2 + (2\widehat{t}_{\text{lim}} - 2c_2)\widehat{\tau} + \widehat{t}_{\text{lim}}^2 - 2c_2\widehat{t}_{\text{lim}} + c_2^2\right] + 2\widehat{\tau}^2 - 2c_2\widehat{\tau} + c_2^2 \tag{A.18}$$

If $X_{\text{calc}} = 0$, then $c_2 = 1$, which gives:

$$= -\exp\left(-\frac{\widehat{t}_{\text{lim}}}{\widehat{\tau}}\right)\left[2\widehat{\tau}^2 + (2\widehat{t}_{\text{lim}} - 2)\widehat{\tau} + \widehat{t}_{\text{lim}}^2 - 2\widehat{t}_{\text{lim}} + 1\right] + 2\widehat{\tau}^2 - 2\widehat{\tau} + 1 \tag{A.19}$$

A.5. Calculation of initial reaction rates

Model of Bhatia and Perlmutter

The general equation for the reaction from Bhatia and Perlmutter [40] is:

$$\frac{1}{\Psi}\left[\sqrt{1 - \Psi \ln(1 - X)} - 1\right] = \frac{k_s\, S_0\, \left(C_{\text{CO2}} - C_{\text{CO2},eq}\right)\, t}{2(1 - \epsilon_0)} \tag{A.19}$$

In explicit form:

$$X = 1 - \exp\left\{\frac{1}{\Psi}\left[1 - \left(1 + \frac{k_s\, S_0\, \left(C_{\text{CO2}} - C_{\text{CO2},eq}\right)\, \Psi}{2(1 - \epsilon_0)} t\right)^2\right]\right\} \tag{A.20}$$

To obtain the initial reaction rate, we differentiate Eq. (A.20) and set $X = 0$, which yields:

$$\left.\frac{dX}{dt}\right|_{X=0} = \frac{S_{0,p}}{(1 - \epsilon_0)} k_s \mathfrak{C} \tag{A.21}$$

Model of Scaltsoyiannes et al.

The reaction progress with the model of Scaltsoyiannes et al. [61] is described by the following equation:

$$\frac{dX}{d\tau} = \frac{3}{\sigma}\left(1 - \frac{\tau}{\sigma}\right)^2 \exp\left[-\tau\left(1 + \frac{\Psi\tau}{4}\right)\right] + \left(1 - \frac{\tau}{\sigma}\right)^3\left(1 + \frac{\Psi\tau}{4}\right)\exp\left[-\tau\left(1 + \frac{\Psi\tau}{4}\right)\right] \tag{A.22}$$

Here, σ, τ, and Ψ are dimensionless numbers. If the time is zero ($t = 0$), the dimensionless time τ also becomes zero. Consequently,

$$\left.\frac{dX}{d\tau}\right|_{\tau=0} = \frac{3}{\sigma} + 1 \tag{A.23}$$

To obtain an expression in terms of known variables, we use the definition of τ from [61], namely

$$\tau \equiv \frac{r\, S_0\, t}{1 - \epsilon_0} \tag{A.24}$$

Using a variable change based on Eq. (A.24) and the definition of σ from [61], Eq. (A.23) can be rewritten:

$$\left.\frac{dX}{dt}\right|_{t=0} = \left(\frac{6(1 - \epsilon_0)}{d_p\, S_{0,p}} + 1\right)\frac{S_{0,p}}{1 - \epsilon_0} k_s \mathfrak{C} \tag{A.25}$$

In general, since $d_p\, S_{0,\text{p}} \gg 100$, we can approximate Eq. (A.25) with the following expression:

$$\left.\frac{dX}{dt}\right|_{t=0} \approx \frac{S_{0,p}}{1 - \epsilon_0} k_s \mathfrak{C} \tag{A.26}$$

A.6. Comparison of reaction rates between two studies

In this section, exemplary results from two important studies on carbonation kinetics are compared to show that they are both in the same order of magnitude. Bhatia and Perlmutter [40] use the equation from the Gavalas' model [117] to obtain S_0:

$$S_0 = 2(1-\epsilon_0)\int_0^\infty \frac{dv_0}{r(1-v_0)} \tag{A.27}$$

The factor including the voidage indicates that S_0 must be expressed in m^2/m_p^3, thus being $S_{0,p}$. With Bhatia and Perlmutter's model for $T = 650\ ^\circ C$, $p_{CO2} - p_{CO2,eq} = 10$ kPa, and the surface corresponding to calcination with pure N_2 reported by them (see Table 2):

$$dX/dt = k_{s,BP}\ S_{0,t}\left(C_{CO2} - C_{CO2,eq}\right) = k_{s,BP}\ \ S_{0,t}\left(p_{CO2} - p_{CO2,eq}\right)\Big/(R\ T) \tag{A.28}$$

$$dX/dt = \frac{5.9510^{-10}\left(m^4 s^{-1} mol^{-1}\right)\ \times\ 52.1\ \left(10^6\right)\ \left(m^2/m_t^3\right)\ \times\ 10,000\ Pa}{8.314\ \left(m^3\ Pa\ K^{-1} mol^{-1}\right)\ \times\ 923.15\ K} = 0.0404\ s^{-1} \tag{A.29}$$

With Sun et al.'s model [58], for $T = 650\ ^\circ C$, $p_{CO2} - p_{CO2,eq} = 10$ kPa, and $X = 0$:

$$dX/dt = M_{CaO} k_s S_0'\left(p_{CO2} - p_{CO2,eq}\right) \tag{A.30}$$

$$dX/dt = 56\left(g\ mol^{-1}\right)\ \times\ 29\left(m^2/g\right)\ \times\ 1.664\ 10^{-3}\left(mol\ m^{-2} s^{-1}\right) = 0.062\ s^{-1} \tag{A.31}$$

Appendix B. Base case for carbonator modeling

The input parameters for the calculations of the carbonator model are included in Table B1. The values reported here were used for the sensitivity analyses and model calculations of Section 3.5, unless otherwise stated. These values are based on the operating conditions of the pilot tests (see Section 2.1). For the validation, the time-dependent inputs and sample-dependent inputs were adjusted with empirical data of the corresponding balance points.

Table B1
Inputs for the calculation of the carbonator model, with data from [1], including the reference values and ranges corresponding to our pilot tests.

Parameter	Symbol	Range	Value	Unit
General inputs				
Molar mass of $CaCO_3$	M_{CaCO3}	–	100	g/mol
Molar mass of CaO	M_{CaO}	–	56.1	g/mol
Particle density of $CaCO_3$	$\rho_{p,CaCO3}$	–	2710 [40]	kg/m^3
Particle density of CaO	$\rho_{p,CaO}$	–	1670	kg/m^3
Gas density	ρ_g	0.39–0.44	0.5	kg/m^3
Solids density*	$\rho_{s,a}$	1.7–2.3	2.0	g/cm^3
Solids molar mass*	$M_{s,a}$	57–82	56	g/mol
Sorbent circulation	F_R	4–13	10	mol/s
Sorbent make-up	F_0	0–0.4	0.2	mol/s
CO_2 input	F_{CO2}	0.16–0.49	0.5	mol/s
Reactor temperature	T_{carb}	550–700	650	°C
Superficial gas velocity	u_0	3.4–5.5	4	m/s
Reactor pressure	p_{carb}	1.0–1.1	1.1	bar
Reactor inventory	W_{carb}	20–60	50	kg
Inlet CO_2 concentration	y_{CO2}	6.2–13.8	12	$vol\%_{wb}$
Gas viscosity	μ	39–41	$40\ 10^{-6}$	Pa s
Gas density	ρ_g	0.39–0.44	0.5	kg/m^3
Equilibrium CO_2 partial pressure	$p_{CO2,eq}$	–	Eq. (2)	kPa
Inputs for the particle sub-model (this work)				
Deactivation model				
$CaSO_4$ concentration	x_{CaSO4}	0.00–0.10	0	mol%
Calcination efficiency	f_{calc}	–	0.80	–
Degree of carbonation	f_{carb}	–	0.95	–
Deactivation constant	k	–	0.569	–
Residual activity	X_r	–	0.019	–
Reaction model				
Inlet carbonation degree	X_{calc}	0.00–0.14	0.00	mol_{CaCO3}/mol_{Ca}
True molar volume of $CaCO_3$	$V_{M,CaCO3}$	–	36.9	cm_t^3/mol
True molar volume of CaO	$V_{M,CaO}$	–	16.9	cm_t^3/mol
Thickness of $CaCO_3$ layer	h	–	50 [57]	nm
Intrinsic kinetic constant	k_s	–	$5.95\ 10^{-10}$	$m^4/(mol\ s)$
Equivalent CO_2 concentration driving force	$\mathfrak{C}^*$	–	(iteration variable)	mol/m^3

(*continued on next page*)

Table B1 (*continued*)

Parameter	Symbol	Range	Value	Unit
Inputs for the reactor sub-model (Part I [1])				
Reactor height	H_T	–	8	m
Reactor internal diameter	d_T	–	250	mm
Particle diameter	$d_{p,50}$	–	226.7	μm
Particle sphericity	Φ_s	–	0.67	–
Voidage at minimum fluidizing conditions	ε_{mf}	–	0.54	–
Bed solid density	$\varepsilon_{s,d}$	–	0.3	–
Lewis constant	k_{Lewis}	–	8.0	s^{-1}
Core-wall gas interchange coefficient (specific)	$k_{c\text{-}w}$	–	0.158	m/s
Volume ratio of potentially active sorbent to solids	ξ	–	1	–
Reaction coefficient (from particle sub-model)	K_r	20–130	80	s^{-1}

* Of potentially active solids.

Appendix C. Supplementary data

Supplementary data to this article can be found online at https://doi.org/10.1016/j.cej.2024.159041.

Data availability

Data will be made available on request.

References

[1] M. Greco-Coppi, J. Ströhle, B. Epple, A carbonator model for CO_2 capture based on results from pilot tests. Part I: Hydrodynamics and reactor model, Chem. Eng. J. 500 (2024) 155119, https://doi.org/10.1016/j.cej.2024.155119.

[2] T. Shimizu, T. Hirama, H. Hosoda, K. Kitano, M. Inagaki, K. Tejima, A Twin Fluid-Bed Reactor for Removal of CO_2 from Combustion Processes, Chem. Eng. Res. Des. 77 (1999) 62–68, https://doi.org/10.1205/026387699525882.

[3] C. Wu, Q. Huang, Z. Xu, A.T. Sipra, N. Gao, L.P.d.S. Vandenberghe, S. Vieira, C.R. Soccol, R. Zhao, S. Deng, S.K. Boetcher, S. Lu, H. Shi, D. Zhao, Y. Xing, Y. Chen, J. Zhu, D. Feng, Y. Zhang, L. Deng, G. Hu, P.A. Webley, D. Liang, Z. Ba, A. Mlonka-Mędrala, A. Magdziarz, N. Miskolczi, S. Tomasek, S.S. Lam, S.Y. Foong, H.S. Ng, L. Jiang, X. Yan, Y. Liu, Y. Ji, H. Sun, H. Yang, X. Zhang, M. Sun, D.C. Tsang, J. Shang, C. Muller, M. Rekhtina, M. Krödel, A.H. Bork, F. Donat, L. Liu, X. Jin, W. Liu, S. Saqline, X. Wu, Y. Xu, A.L. Khan, Z. Ali, H. Lin, L. Hu, J. Huang, R. Singh, K. Wang, X. He, Z. Dai, S. Yi, A. Konist, M.H.S. Baqain, Y. Zhao, S. Sun, G. Chen, X. Tu, A. Weidenkaff, S. Kawi, K.H. Lim, C. Song, Q. Yang, Z. Zhao, X. Gao, X. Jiang, H. Ji, T.E. Akinola, A. Lawal, O.S. Otitoju, M. Wang, G. Zhang, L. Ma, B.C. Sempuga, X. Liu, E. Oko, M. Daramola, Z. Yu, S. Chen, G. Kang, Q. Li, L. Gao, L. Liu, H. Zhou, A comprehensive review of carbon capture science and technologies, Carbon Capture Science & Technology 11 (2024) 100178. https://doi.org/10.1016/j.ccst.2023.100178.

[4] Y. Tan, W. Liu, X. Zhang, W. Wei, S. Wang, Conventional and optimized testing facilities of calcium looping process for CO_2 capture: A systematic review, Fuel 358 (2024) 130337, https://doi.org/10.1016/j.fuel.2023.130337.

[5] I. Martínez, G. Grasa, J. Parkkinen, T. Tynjälä, T. Hyppänen, R. Murillo, M. C. Romano, Review and research needs of Ca-Looping systems modelling for post-combustion CO_2 capture applications, Int. J. Greenhouse Gas Control 50 (2016) 271–304, https://doi.org/10.1016/j.ijggc.2016.04.002.

[6] N. Afandi, M. Satgunam, S. Mahalingam, A. Manap, F. Nagi, W. Liu, R.B. Johan, A. Turan, A. Wei-Yee Tan, S. Yunus, Review on the modifications of natural and industrial waste CaO based sorbent of calcium looping with enhanced CO_2 capture capacity, Heliyon 10 (2024) e27119, https://doi.org/10.1016/j.heliyon.2024.e27119.

[7] J.C. Abanades, The maximum capture efficiency of CO_2 using a carbonation/calcination cycle of $CaO/CaCO_3$, Chem. Eng. J. 90 (2002) 303–306, https://doi.org/10.1016/S1385-8947(02)00126-2.

[8] M. Junk, M. Reitz, J. Ströhle, B. Epple, Thermodynamic evaluation and cold flow model testing of an indirectly heated carbonate looping process, Chem. Eng. Technol. 36 (2013) 1479–1487, https://doi.org/10.1002/ceat.201300019.

[9] S.G. Spyroglou, A.A. Skaltsogiannis, S.G. Yiantsios, A.A. Lemonidou, Multiscale modeling of an entrained flow solar calciner for thermochemical energy storage via calcium looping, Chem. Eng. J. 486 (2024) 150171, https://doi.org/10.1016/j.cej.2024.150171.

[10] T. Hills, M. Sceats, D. Rennie, P. Fennell, LEILAC: Low cost CO_2 capture for the cement and lime industries, Energy Procedia 114 (2017) 6166–6170, https://doi.org/10.1016/j.egypro.2017.03.1753.

[11] R.M. Jacob, L.-A. Tokheim, Electrified calciner concept for CO_2 capture in pyro-processing of a dry process cement plant, Energy 268 (2023) 126673, https://doi.org/10.1016/j.energy.2023.126673.

[12] P. Hodgson, M. Sceats, A. Vincent, D. Rennie, P. Fennell, T. Hills, Direct separation calcination technology for carbon capture: Demonstrating a low cost solution for the lime and cement industries in the LEILAC project, SSRN Electron. J. (2019), https://doi.org/10.2139/ssrn.3365844.

[13] M.E. Diego, B. Arias, J.C. Abanades, Analysis of a double calcium loop process configuration for CO_2 capture in cement plants, J. Clean. Prod. 117 (2016) 110–121, https://doi.org/10.1016/j.jclepro.2016.01.027.

[14] D. Höftberger, J. Karl, The indirectly heated carbonate looping process for CO_2 capture—A concept with heat pipe heat exchanger, J. Energy Res. Technol. 138 (2016) 042211, https://doi.org/10.1115/1.4033302.

[15] M. Greco-Coppi, C. Hofmann, J. Ströhle, D. Walter, B. Epple, Efficient CO_2 capture from lime production by an indirectly heated carbonate looping process, Int. J. Greenhouse Gas Control 112 (2021) 103430, https://doi.org/10.1016/j.ijggc.2021.103430.

[16] N. Rodríguez, M. Alonso, J.C. Abanades, Experimental investigation of a circulating fluidized-bed reactor to capture CO_2 with CaO, AIChE J. 57 (2011) 1356–1366, https://doi.org/10.1002/aic.12337.

[17] M. Haaf, J. Peters, J. Hilz, A. Unger, J. Ströhle, B. Epple, Combustion of solid recovered fuels within the calcium looping process – Experimental demonstration at 1 MW_{th} scale, Exp. Therm Fluid Sci. 113 (2020) 110023, https://doi.org/10.1016/j.expthermflusci.2019.110023.

[18] M. Reitz, M. Junk, J. Ströhle, B. Epple, Design and operation of a 300 kW_{th} indirectly heated carbonate looping pilot plant, Int. J. Greenhouse Gas Control 54 (2016) 272–281, https://doi.org/10.1016/j.ijggc.2016.09.016.

[19] N. Rodríguez, M. Alonso, J.C. Abanades, Average activity of CaO particles in a calcium looping system, Chem. Eng. J. 156 (2010) 388–394, https://doi.org/10.1016/j.cej.2009.10.055.

[20] I. Martínez, B. Arias, G.S. Grasa, J.C. Abanades, CO_2 capture in existing power plants using second generation Ca-Looping systems firing biomass in the calciner, J. Clean. Prod. 187 (2018) 638–649, https://doi.org/10.1016/j.jclepro.2018.03.189.

[21] K. Atsonios, M. Zeneli, A. Nikolopoulos, N. Nikolopoulos, P. Grammelis, E. Kakaras, Calcium looping process simulation based on an advanced thermodynamic model combined with CFD analysis, Fuel 153 (2015) 370–381, https://doi.org/10.1016/j.fuel.2015.03.014.

[22] C. Zhang, Absorption principle and techno-economic analysis of CO_2 absorption technologies: A review, IOP Conf. Ser.: Earth Environ. Sci. 657 (2021) 12045, https://doi.org/10.1088/1755-1315/657/1/012045.

[23] J.C. Abanades, D. Alvarez, Conversion limits in the reaction of CO_2 with lime, Energy Fuels 17 (2003) 308–315, https://doi.org/10.1021/ef020152a.

[24] B. Arias, J.C. Abanades, G.S. Grasa, An analysis of the effect of carbonation conditions on CaO deactivation curves, Chem. Eng. J. 167 (2011) 255–261, https://doi.org/10.1016/j.cej.2010.12.052.

[25] J. Blamey, E.J. Anthony, J. Wang, P.S. Fennell, The calcium looping cycle for large-scale CO_2 capture, Prog. Energy Combust. Sci. 36 (2010) 260–279, https://doi.org/10.1016/j.pecs.2009.10.001.

[26] A.I. Lysikov, A.N. Salanov, A.G. Okunev, Change of CO_2 carrying capacity of CaO in isothermal recarbonation−decomposition cycles, Ind. Eng. Chem. Res. 46 (2007) 4633–4638, https://doi.org/10.1021/ie0702328.

[27] A.A. Scaltsoyiannes, A.A. Lemonidou, On the factors affecting the deactivation of limestone under calcium looping conditions: A new comprehensive model, Chem. Eng. Sci. 243 (2021) 116797, https://doi.org/10.1016/j.ces.2021.116797.

[28] V. Manovic, J.-P. Charland, J. Blamey, P.S. Fennell, D.Y. Lu, E.J. Anthony, Influence of calcination conditions on carrying capacity of CaO-based sorbent in CO_2 looping cycles, Fuel 88 (2009) 1893–1900, https://doi.org/10.1016/j.fuel.2009.04.012.

[29] J. Agnew, E. Hampartsoumian, J. Jones, W. Nimmo, The simultaneous calcination and sintering of calcium based sorbents under a combustion atmosphere, Fuel 79 (2000) 1515–1523, https://doi.org/10.1016/S0016-2361(99)00287-2.

[30] M. Reitz, M. Junk, J. Ströhle, B. Epple, Design and Erection of a 300 kW_{th} Indirectly Heated Carbonate Looping Test Facility, Energy Procedia 63 (2014) 2170–2177, https://doi.org/10.1016/j.egypro.2014.11.236.

[31] C. Hofmann, M. Greco-Coppi, J. Ströhle, B. Epple, Enhancement of a 300 kW_{th} pilot plant for testing the indirectly heated carbonate looping process for CO_2

capture from lime and cement industry, Exp. Therm Fluid Sci. 151 (2024) 111091, https://doi.org/10.1016/j.expthermflusci.2023.111091.

[32] C. Hofmann, M. Greco-Coppi, J. Ströhle, B. Epple, Pilot testing of the indirectly heated carbonate looping process for cement and lime plants, in: Proceedings of the 16th International Conference on Greenhouse Gas Control Technologies, 23–24 Oct, 2022. https://doi.org/10.2139/ssrn.4278810.

[33] M. Reitz, *Experimentelle Untersuchung und Bewertung eines indirekt beheizten Carbonate-Looping-Prozesses*, Cuvillier Verlag, Göttingen, 2017. Doctoral dissertation, first ed.

[34] M. Helbig, J. Hilz, M. Haaf, A. Daikeler, J. Ströhle, B. Epple, Long-term Carbonate Looping Testing in a 1 MWth Pilot Plant with Hard Coal and Lignite, Energy Procedia 114 (2017) 179–190, https://doi.org/10.1016/j.egypro.2017.03.1160.

[35] J. Ströhle, J. Hilz, B. Epple, Performance of the carbonator and calciner during long-term carbonate looping tests in a 1 MW$_{th}$ pilot plant, J. Environ. Chem. Eng. 8 (2020) 103578, https://doi.org/10.1016/j.jece.2019.103578.

[36] Erich Netzsch GmbH & Co. Holding KG, STA 449 F3 Jupiter, 2023. https://analyzing-testing.netzsch.com/_Resources/Persistent/4/c/b/e/4cbe0375352415b080dab9d281329c613a551c10/STA_449_F3_Jupiter_de_web.pdf (accessed 8 August 2023).

[37] M. Greco-Coppi, J. Ströhle, B. Epple, Modeling and design of a calciner for commercial-scale CO$_2$ capture using stochastic methods and results from pilot tests, Fuel 388 (2025) 133931, https://doi.org/10.1016/j.fuel.2024.133931.

[38] G.S. Grasa, J.C. Abanades, CO$_2$ Capture Capacity of CaO in Long Series of Carbonation/Calcination Cycles, Ind. Eng. Chem. Res. 45 (2006) 8846–8851, https://doi.org/10.1021/ie0606946.

[39] M. Alonso, Y.A. Criado, J.C. Abanades, G. Grasa, Undesired effects in the determination of CO$_2$ carrying capacities of CaO during TG testing, Fuel 127 (2014) 52–61, https://doi.org/10.1016/j.fuel.2013.08.005.

[40] S.K. Bhatia, D.D. Perlmutter, Effect of the product layer on the kinetics of the CO$_2$-lime reaction, AIChE J. 29 (1983) 79–86, https://doi.org/10.1002/aic.690290111.

[41] B. González, M. Alonso, J.C. Abanades, Sorbent attrition in a carbonation/calcination pilot plant for capturing CO$_2$ from flue gases, Fuel 89 (2010) 2918–2924, https://doi.org/10.1016/j.fuel.2010.01.019.

[42] M. Haaf, A. Stroh, J. Hilz, M. Helbig, J. Ströhle, B. Epple, Process modelling of the calcium looping process and validation against 1 MW$_{th}$ pilot testing, Energy Procedia 114 (2017) 167–178, https://doi.org/10.1016/j.egypro.2017.03.1159.

[43] A. Coppola, F. Montagnaro, P. Salatino, F. Scala, Fluidized bed calcium looping: The effect of SO$_2$ on sorbent attrition and CO$_2$ capture capacity, Chem. Eng. J. 207–208 (2012) 445–449, https://doi.org/10.1016/j.cej.2012.06.149.

[44] A. Coppola, F. Montagnaro, P. Salatino, F. Scala, Attrition of limestone during fluidized bed calcium looping cycles for CO$_2$ capture, Combust. Sci. Technol. 184 (2012) 929–941, https://doi.org/10.1080/00102202.2012.663986.

[45] A. Coppola, A. Esposito, F. Montagnaro, G. de Tommaso, F. Scala, P. Salatino, Effect of exposure to SO$_2$ and H$_2$O during the carbonation stage of fluidised bed calcium looping on the performance of sorbents of different nature, Chem. Eng. J. 377 (2019) 120626, https://doi.org/10.1016/j.cej.2018.12.086.

[46] M. Alonso, B. Arias, J.R. Fernández, O. Bughin, C. Abanades, Measuring attrition properties of calcium looping materials in a 30 kW pilot plant, Powder Technol. 336 (2018) 273–281, https://doi.org/10.1016/j.powtec.2018.06.011.

[47] E.H. Baker, The calcium oxide–carbon dioxide system in the pressure range 1—300 atmospheres, J. Chem. Soc. (1962) 464–470, https://doi.org/10.1039/JR9620000464.

[48] F. García-Labiano, A. Abad, L.F. de Diego, P. Gayán, J. Adánez, Calcination of calcium-based sorbents at pressure in a broad range of CO$_2$ concentrations, Chemical Engineering Science 57 (2002) 2381–2393. https://doi.org/10.1016/S0009-2509(02)00137-9.

[49] I. Barin, Thermochemical data of pure substances, third. ed., VCH, Weinheim, 1995. https://doi.org/10.1002/9783527619825.

[50] D. Kunii, O. Levenspiel, Fluidization Engineering, second ed., Elsevier, 1991. https://doi.org/10.1016/C2009-0-24190-0.

[51] J. Szekely, J.W. Evans, H.Y. Sohn, Gas-solid reactions, first ed., Academic Press, New York, 1976.

[52] Z. Li, H. Sun, N. Cai, Rate equation theory for the carbonation reaction of CaO with CO$_2$, Energy Fuels 26 (2012) 4607–4616, https://doi.org/10.1021/ef300607z.

[53] M. Alonso, N. Rodríguez, G. Grasa, J.C. Abanades, Modelling of a fluidized bed carbonator reactor to capture CO$_2$ from a combustion flue gas, Chem. Eng. Sci. 64 (2009) 883–891, https://doi.org/10.1016/j.ces.2008.10.044.

[54] G.S. Grasa, J.C. Abanades, M. Alonso, B. González, Reactivity of highly cycled particles of CaO in a carbonation/calcination loop, Chem. Eng. J. 137 (2008) 561–567, https://doi.org/10.1016/j.cej.2007.05.017.

[55] R. Barker, The reversibility of the reaction $CaCO_3 \rightleftarrows CaO + CO_2$, J. Appl. Chem. 23 (1973) 733–742, https://doi.org/10.1002/jctb.5020231005.

[56] M.C. Romano, Modeling the carbonator of a Ca-looping process for CO$_2$ capture from power plant flue gas, Chem. Eng. Sci. 69 (2012) 257–269, https://doi.org/10.1016/j.ces.2011.10.041.

[57] D. Alvarez, J.C. Abanades, Determination of the critical product layer thickness in the reaction of CaO with CO$_2$, Ind. Eng. Chem. Res. 44 (2005) 5608–5615, https://doi.org/10.1021/ie050305s.

[58] P. Sun, J.R. Grace, C.J. Lim, E.J. Anthony, Determination of intrinsic rate constants of the CaO–CO$_2$ reaction, Chem. Eng. Sci. 63 (2008) 47–56, https://doi.org/10.1016/j.ces.2007.08.055.

[59] A. Silaban, D.P. Harrison, High temperature capture of carbon dioxide: Characteristics of the reversible reaction between CaO(s) and CO$_2$(g), Chem. Eng. Commun. 137 (1995) 177–190, https://doi.org/10.1080/00986449508936375.

[60] L. Fedunik-Hofman, A. Bayon, S.W. Donne, Kinetics of solid-gas reactions and their application to carbonate looping systems, Energies 12 (2019) 2981, https://doi.org/10.3390/en12152981.

[61] A.A. Scaltsoyiannes, A. Antzaras, G. Koilaridis, A. Lemonidou, Towards a generalized carbonation kinetic model for CaO-based materials using a modified random pore model, Chem. Eng. J. 407 (2021) 127207, https://doi.org/10.1016/j.cej.2020.127207.

[62] K. Kyaw, M. Kanamori, H. Matsuda, M. Hasatani, Study of carbonation reactions of Ca-Mg oxides for high temperature energy storage and heat transformation, J. Chem. Eng. Japan / JCEJ 29 (1996) 112–118, https://doi.org/10.1252/jcej.29.112.

[63] J. Ströhle, M. Junk, J. Kremer, A. Galloy, B. Epple, Carbonate looping experiments in a 1MW$_{th}$ pilot plant and model validation, Fuel 127 (2014) 13–22, https://doi.org/10.1016/j.fuel.2013.12.043.

[64] J.C. Abanades, E.J. Anthony, D.Y. Lu, C. Salvador, D. Alvarez, Capture of CO$_2$ from combustion gases in a fluidized bed of CaO, AIChE J. 50 (2004) 1614–1622, https://doi.org/10.1002/aic.10132.

[65] H.S. Fogler, Elements of chemical reaction engineering, third. ed., Prentice Hall PTR, Upper Saddle River, NJ, 2002.

[66] E. Turnbull, J.F. Davidson, Fluidized combustion of char and volatiles from coal, AIChE J. 30 (1984) 881–889, https://doi.org/10.1002/aic.690300602.

[67] N. Frössling, Über die Verdunstung fallender Tropfen, Gerlands Beitr. Geophys. 52 (1938) 170–216.

[68] F. Scala, Particle-fluid mass transfer in multiparticle systems at low Reynolds numbers, Chem. Eng. Sci. 91 (2013) 90–101, https://doi.org/10.1016/j.ces.2013.01.012.

[69] J. Ströhle, A. Lasheras, A. Galloy, B. Epple, Simulation of the Carbonate Looping Process for Post-Combustion CO$_2$ Capture from a Coal-Fired Power Plant, Chem. Eng. Technol. 32 (2009) 435–442, https://doi.org/10.1002/ceat.200800569.

[70] R.R. Hudgins, B. Kadlec, P.L. Silverston, Optimum catalyst pellet densities allowing for density-dependent specific surface, J. Catal. 32 (1974) 237–246, https://doi.org/10.1016/0021-9517(74)90072-4.

[71] B.D. Soane, The role of organic matter in soil compactibility: A review of some practical aspects, Soil Tillage Res. 16 (1990) 179–201, https://doi.org/10.1016/0167-1987(90)90029-D.

[72] ISO, International Standard no. 18747-1:2018 – Determination of particle density by sedimentation methods: Part 1: Isopycnic interpolation approach, 2018.

[73] W. Nitsch, *Über die Druckabhängigkeit der CaCO$_3$-Bildung aus dem Oxyd*, Zeitschrift für Elektrochemie, Berichte der Bunsengesellschaft für physikalische Chemie 66 (1962) 703–708. https://doi.org/10.1002/bbpc.19620660821.

[74] A.-M. Cormos, A. Simon, Assessment of CO$_2$ capture by calcium looping (CaL) process in a flexible power plant operation scenario, Appl. Therm. Eng. 80 (2015) 319–327, https://doi.org/10.1016/j.applthermaleng.2015.01.059.

[75] A.-M. Cormos, A. Simon, Dynamic modelling of CO$_2$ capture by calcium-looping cycle, Chemical, Eng. Trans. 35 (2013) 421–426, https://doi.org/10.3303/CET1335070.

[76] M. Junk, Technical and economical assessment of various carbonate looping process configurations, first ed., Cuvillier Verlag, Göttingen, 2017.

[77] C. Hawthorne, A. Charitos, C.A. Perez-Pulido, Z. Bing, G. Scheffknecht, Design of a Dual Fluidised Bed System for the Post-Combustion Removal of CO$_2$ Using CaO. Part I: CFB Carbonator Reactor Model, TuTech Innovation Gmbh, Hamburg, Germany, 2008.

[78] G. Grasa, R. Murillo, M. Alonso, J.C. Abanades, Application of the random pore model to the carbonation cyclic reaction, AIChE J. 55 (2009) 1246–1255, https://doi.org/10.1002/aic.11746.

[79] R.H. Borgwardt, Sintering of nascent calcium oxide, Chem. Eng. Sci. 44 (1989) 53–60, https://doi.org/10.1016/0009-2509(89)85232-7.

[80] R.H. Borgwardt, Calcium oxide sintering in atmospheres containing water and carbon dioxide, Ind. Eng. Chem. Res. 28 (1989) 493–500, https://doi.org/10.1021/ie00088a019.

[81] Y. Liu, Y. Yang, Evolution of the Surface Area of Limestone during Calcination and Sintering, JPEE 03 (2015) 56–62, https://doi.org/10.4236/jpee.2015.34009.

[82] S. Brunauer, P.H. Emmett, E. Teller, Adsorption of Gases in Multimolecular Layers, J. Am. Chem. Soc. 60 (1938) 309–319, https://doi.org/10.1021/ja01269a023.

[83] P.S. Fennell, R. Pacciani, J.S. Dennis, J.F. Davidson, A.N. Hayhurst, The Effects of Repeated Cycles of Calcination and Carbonation on a Variety of Different Limestones, as Measured in a Hot Fluidized Bed of Sand, Energy Fuels 21 (2007) 2072–2081, https://doi.org/10.1021/ef060506o.

[84] E. Bouquet, G. Leyssens, C. Schönnenbeck, P. Gilot, The decrease of carbonation efficiency of CaO along calcination–carbonation cycles: Experiments and modelling, Chem. Eng. Sci. 64 (2009) 2136–2146, https://doi.org/10.1016/j.ces.2009.01.045.

[85] A. Lasheras, J. Ströhle, A. Galloy, B. Epple, Carbonate looping process simulation using a 1D fluidized bed model for the carbonator, Int. J. Greenhouse Gas Control 5 (2011) 686–693, https://doi.org/10.1016/j.ijggc.2011.01.005.

[86] I. Martínez, G. Grasa, R. Murillo, B. Arias, J.C. Abanades, Kinetics of calcination of partially carbonated particles in a Ca-looping system for CO$_2$ capture, Energy Fuels 26 (2012) 1432–1440, https://doi.org/10.1021/ef201525k.

[87] D. Alvarez, J.C. Abanades, Pore-size and shape effects on the recarbonation performance of calcium oxide submitted to repeated calcination/recarbonation cycles, Energy Fuels 19 (2005) 270–278, https://doi.org/10.1021/ef049864m.

[88] G. Grasa, J.C. Abanades, The kinetics of carbonation of CaO particles cycling in a CO$_2$ capture loop, in: 8th International Conference on Greenhouse Gas Control Technologies 2006, Curran, Red Hook, NY, 2006.

[89] E.P. Barrett, L.G. Joyner, P.P. Halenda, The Determination of pore volume and area distributions in porous substances. I. Computations from nitrogen isotherms, J. Am. Chem. Soc. 73 (1951) 373–380, https://doi.org/10.1021/ja01145a126.

[90] M.C. Romano, I. Martínez, R. Murillo, B. Arstad, R. Blom, D.C. Ozcan, H. Ahn, S. Brandani, Process simulation of Ca-looping processes: review and guidelines, Energy Procedia 37 (2013) 142–150, https://doi.org/10.1016/j.egypro.2013.05.095.

[91] M. Abreu, P. Teixeira, R.M. Filipe, L. Domingues, C.I. Pinheiro, H.A. Matos, Modeling the deactivation of CaO-based sorbents during multiple Ca-looping cycles for CO_2 post-combustion capture, Comput. Chem. Eng. 134 (2020) 106679, https://doi.org/10.1016/j.compchemeng.2019.106679.

[92] Y.A. Criado, B. Arias, J.C. Abanades, Effect of the Carbonation Temperature on the CO_2 Carrying Capacity of CaO, Ind. Eng. Chem. Res. 57 (2018) 12595–12599, https://doi.org/10.1021/acs.iecr.8b02111.

[93] M.E. Diego, B. Arias, J.C. Abanades, Investigation of the dynamic evolution of the CO_2 carrying capacity of solids with time in La Pereda 1.7 MW_{th} calcium looping pilot plant, Int. J. Greenhouse Gas Control 92 (2020) 102856, https://doi.org/10.1016/j.ijggc.2019.102856.

[94] A. Charitos, N. Rodríguez, C. Hawthorne, M. Alonso, M. Zieba, B. Arias, G. Kopanakis, G. Scheffknecht, J.C. Abanades, Experimental validation of the calcium looping CO_2 capture process with two circulating fluidized bed carbonator reactors, Ind. Eng. Chem. Res. 50 (2011) 9685–9695, https://doi.org/10.1021/ie200579f.

[95] J. Hilz, M. Helbig, M. Haaf, A. Daikeler, J. Ströhle, B. Epple, Investigation of the fuel influence on the carbonate looping process in 1 MW_{th} scale, Fuel Process. Technol. 169 (2018) 170–177, https://doi.org/10.1016/j.fuproc.2017.09.016.

[96] S. Chen, C. Qin, T. Deng, J. Yin, J. Ran, Particle-scale modeling of the simultaneous carbonation and sulfation in calcium looping for CO_2 capture, Sep. Purif. Technol. 252 (2020) 117439, https://doi.org/10.1016/j.seppur.2020.117439.

[97] H.-J. Ryu, J.R. Grace, C.J. Lim, Simultaneous CO_2 /SO_2 capture characteristics of three limestones in a fluidized-bed reactor, Energy Fuels 20 (2006) 1621–1628, https://doi.org/10.1021/ef050277q.

[98] P. Sun, J.R. Grace, C.J. Lim, E.J. Anthony, Removal of CO_2 by calcium-based sorbents in the presence of SO_2, Energy Fuels 21 (2007) 163–170, https://doi.org/10.1021/ef060329r.

[99] G.S. Grasa, M. Alonso, J.C. Abanades, Sulfation of CaO particles in a carbonation/calcination loop to capture CO_2, Ind. Eng. Chem. Res. 47 (2008) 1630–1635, https://doi.org/10.1021/ie070937.

[100] M.E. Diego, B. Arias, J.C. Abanades, Evolution of the CO_2 carrying capacity of CaO particles in a large calcium looping pilot plant, Int. J. Greenhouse Gas Control 62 (2017) 69–75, https://doi.org/10.1016/j.ijggc.2017.04.005.

[101] J.C. Abanades, E.J. Anthony, J. Wang, J.E. Oakey, Fluidized bed combustion systems integrating CO_2 capture with CaO, Environ. Sci. Technol. 39 (2005) 2861–2866, https://doi.org/10.1021/es0496221.

[102] F. Sattari, M. Tahmasebpoor, J.M. Valverde, C. Ortiz, M. Mohammadpourfard, Modelling of a fluidized bed carbonator reactor for post-combustion CO_2 capture considering bed hydrodynamics and sorbent characteristics, Chem. Eng. J. 406 (2021) 126762, https://doi.org/10.1016/j.cej.2020.126762.

[103] J.H. Mathews, K.D. Fink, Numerical methods using MATLAB, third. ed., Prentice Hall, Upper Saddle River, N.J., London, 1999.

[104] B. Epple, M. Junk, J. Ströhle, M. Reitz, J. Karl, D. Höftberger, Carbon capture by means of indirectly heated carbonate looping process (CARINA): Final report, Publications Office of the European Union, Luxembourg (2016), https://doi.org/10.2777/708428.

[105] M. Greco-Coppi, C. Hofmann, J. Ströhle, Advanced indirectly heated carbonate looping process (ANICA) – Final report, Accelerating CCS Technologies (ACT) (2024). https://doi.org/10.26083/tuprints-00026729.

[106] M. Greco-Coppi, C. Hofmann, D. Walter, J. Ströhle, B. Epple, Negative CO_2 emissions in the lime production using an indirectly heated carbonate looping process, Mitig Adapt Strateg Glob Change 28 (2023), https://doi.org/10.1007/s11027-023-10064-7.

[107] M. Greco-Coppi, P.M. Seufert, C. Hofmann, A. Rolfe, Y. Huang, S. Rezvani, J. Ströhle, B. Epple, Efficient CO_2 capture from lime plants: Techno-economic assessment of integrated concepts using indirectly heated carbonate looping technology, Carbon Capture Sci. Technol. 11 (2024) 100187, https://doi.org/10.1016/j.ccst.2023.100187.

[108] I. Martínez, R. Murillo, G. Grasa, J.C. Abanades, Integration of a Ca-looping system for CO_2 capture in an existing power plant, Energy Procedia 4 (2011) 1699–1706, https://doi.org/10.1016/j.egypro.2011.02.043.

[109] B. Arias, M.E. Diego, J.C. Abanades, M. Lorenzo, L. Diaz, D. Martínez, J. Alvarez, A. Sanchez-Biezma, Demonstration of steady state CO_2 capture in a 1.7MW_{th} calcium looping pilot, Int. J. Greenhouse Gas Control 18 (2013) 237–245, https://doi.org/10.1016/j.ijggc.2013.07.014.

[110] M. Hornberger, J. Moreno, M. Schmid, G. Scheffknecht, Experimental investigation of the carbonation reactor in a tail-end Calcium Looping configuration for CO_2 capture from cement plants, Fuel Process. Technol. 210 (2020) 106557, https://doi.org/10.1016/j.fuproc.2020.106557.

[111] M. Fantini, M. Balocco, L. Buzzi, F. Canonico, S. Consonni, R. Cremona, M. Gatti, J. Hammerich, R. Koehler, F. Magli, M.C. Romano, M. Spinelli, Calcium looping technology demonstration in industrial environment: Status of the CLEANKER pilot plant, in: Proceedings of the 15th International Conference on Greenhouse Gas Control Technologies, 25–18 Mar, 2021. https://dx.doi.org/10.2139/ssrn.3817346.

[112] R. García, Y.A. Criado, Carbonation kinetics of calcium-based solids at the centimeter scale for moving bed applications, Chem. Eng. Sci. (2024) 119750, https://doi.org/10.1016/j.ces.2024.119750.

[113] J. Carlos Abanades, Y.A. Criado, R. García, Countercurrent moving bed carbonator for CO_2 capture in decoupled calcium looping systems, Chemical Engineering Journal 461 (2023) 141956, https://doi.org/10.1016/j.cej.2023.141956.

[114] M. Spinelli, I. Martínez, M.C. Romano, One-dimensional model of entrained-flow carbonator for CO_2 capture in cement kilns by Calcium looping process, Chem. Eng. Sci. 191 (2018) 100–114, https://doi.org/10.1016/j.ces.2018.06.051.

[115] G. Grasa, I. Martínez, M.E. Diego, J.C. Abanades, Determination of CaO carbonation kinetics under recarbonation conditions, Energy Fuels 28 (2014) 4033–4042, https://doi.org/10.1021/ef500331t.

[116] D. Höftberger. *Design und Dimensionierung eines indirekt beheizten Carbonate Looping Prozesses*, Dissertation, Nuremberg, 2016.

[117] G.R. Gavalas, A random capillary model with application to char gasification at chemically controlled rates, AIChE J. 26 (1980) 577–585, https://doi.org/10.1002/aic.690260408.

A carbonator model for CO_2 capture based on results from pilot tests. Part II: Deactivation and reaction model

Supplementary material

Martin Greco-Coppi[a,*], Jochen Ströhle[a], Bernd Epple[a]

[a] *Technical University of Darmstadt, Department of Mechanical Engineering, Institute for Energy Systems and Technology, Otto-Berndt-Str. 2, 64287 Darmstadt, Germany*

[*] *Corresponding author: martin.greco@est.tu-darmstadt.de*

S1. Thermogravimetric analysis

The results of the tests used to assess the influence of diffusion effects in the thermogravimetric analysis (TGA) are reported in Figure S.1. Here, the bars indicate the mean reaction rates, and the error bands indicate plus/minus one standard deviation. Each test point was run three times. The runs used to assess the influence of the sample mass (Figure S.1.a) had 190 NmL/min of gas and the original sample particle size distribution. For the runs corresponding to the influence of the particle size (Figure S.1.b), the mass was 3 mg, and the flow rate of gas was 190 NmL/min.

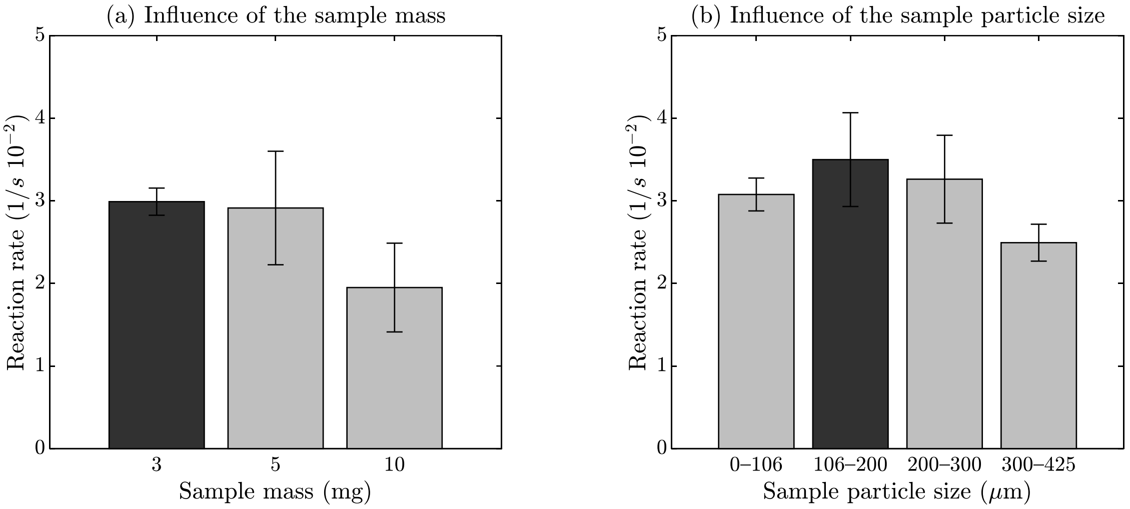

Figure S.1. Study of the influence of the sample mass and the sample particle size in the reaction rate for thermogravimetric tests. The bars indicate the mean values obtained from three runs. The error bands represent the standard deviation (± 1 SD). The red bands indicate the values of sample mass and particle size used for the kinetic runs.

The TGA test conditions are reported in Table S.1.

Table S.1. TGA test conditions

Calcination		**Carbonation**	
Temperature (°C)	CO_2 partial pressure (kPa)	Temperature (°C)	CO_2 partial pressure (kPa)
850	10	650	6
850	13	650	10
850	16	650	15
875	18	700	5
875	25	700	9
875	30	700	11

Research Paper VI

Research Paper VI

Title: Modeling and design of a calciner for commercial-scale CO_2 capture using stochastic methods and results from pilot tests

Authors: Martin Greco Coppi, Jochen Ströhle, Bernd Epple

Journal: Fuel (Elsevier)

Status: Published (January 27, 2025)

Volume: 388 (May 15, 2025)

DOI: https://doi.org/10.1016/j.fuel.2024.133931

Licensing: The authors. CC BY 4.0

Graphical abstract

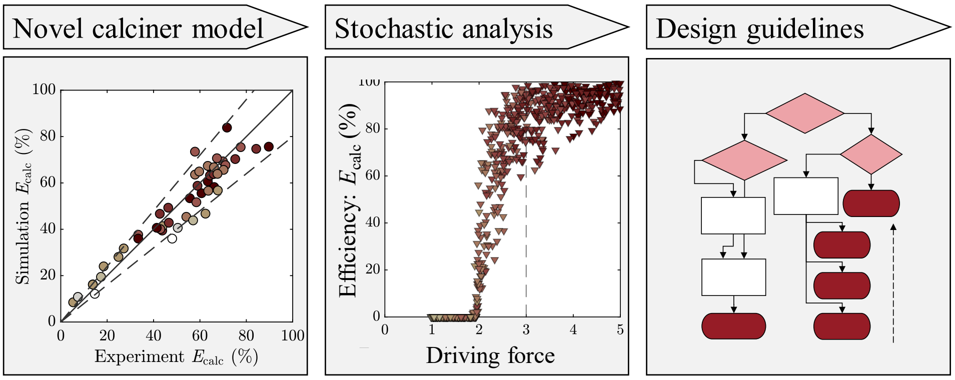

Short Summary

In this work, we develop a novel calciner model for CaL processes by combining a particle sub-model with a one-dimensional reactor sub-model. The model is validated with results from experiments in two different pilot plants in the 300-kW_{th} and 1-MW_{th} scales. The predictions of the model are interpreted using stochastic methods and dimensionless numbers. Furthermore, we introduce a three-step approach to designing calciners for CO_2 capture. Calciners with oxy-fuel combustion should be operated at 930–965 °C to achieve sufficient sorbent regeneration. Indirectly heated calciners should operate at 950 °C to achieve high performance. Lower temperatures (e.g., 900 °C) are also possible if steam is used for fluidization. Considerations regarding particle residence time are also discussed. Our guidelines are straightforward and enable the design of a calciner with simple calculations.

Fuel 388 (2025) 133931

Contents lists available at ScienceDirect

Fuel

journal homepage: www.elsevier.com/locate/fuel

Full Length Article

Modeling and design of a calciner for commercial-scale CO_2 capture using stochastic methods and results from pilot tests

Martin Greco-Coppi *, Jochen Ströhle, Bernd Epple

Technical University of Darmstadt, Department of Mechanical Engineering, Institute for Energy Systems and Technology, Otto-Berndt-Str. 2, 64287 Darmstadt, Germany

ARTICLE INFO

Keywords:
CO_2 capture
Calcium looping
Indirectly heated carbonate lopping
Reactor modeling
Fluidization engineering
Scale-up

ABSTRACT

Carbonate looping (CaL) is a CO_2 capture technology with the potential to efficiently decarbonize power plants and carbon-intensive industries, such as cement and lime production. Many pilot tests have demonstrated the feasibility of operating CaL in oxy-fuel and indirect-heating (IHCaL) modes. Still, there is no commercial facility in operation or planning. To support the scale-up of the technology, reliable reactor models are required. However, little progress has been made in calciner modeling in recent years. The available models are either too demanding in terms of computation complexity or lack support from empirical data. In this work, we develop a novel calciner model by combining a particle sub-model with a one-dimensional reactor sub-model. The model is validated with results from experiments in two different pilot plants in the 300-kW_{th} and 1-MW_{th} scales. The predictions of the model are interpreted using stochastic methods and dimensionless numbers. Furthermore, we introduce a three-step approach to designing calciners for CO_2 capture. Calciners with oxy-fuel combustion should be operated at 930–965 °C to achieve sufficient sorbent regeneration. For indirectly heated calciners, an operating temperature of 950 °C is necessary for high performance, but lower temperatures (e.g., 900 °C) are also possible using steam for fluidization. Considerations regarding particle residence time are also discussed. Our guidelines are straightforward and enable the design of a calciner with simple calculations.

1. Introduction

Concern over rising atmospheric CO_2 concentration has driven many researchers and engineers to develop processes for capturing anthropogenic CO_2 [1,2]. Amine-based absorption is regarded as the most mature CO_2-capture technology [3,4]. However, it presents serious challenges in terms of energy requirements (currently, ~ 4 GJ/t_{CO2}), solvent degradation, and solvent emissions [5]. This is why different sorbents and alternative CO_2 capture methods, with the potential to lower capture costs and energy penalties, are currently being widely investigated [3,6].

The *carbonate looping* process is an emerging technology for CO_2 capture based on the reversible gas–solid reaction between CO_2 and solid particles (i.e., *carbonation* reaction) [6]. It has been studied for a quarter of a century since its first proposal by Shimizu et al. [7]. The sorbents suggested for the carbonate looping process include CaO (from limestone), MgO (from dolomite), and synthetic materials such as doped CaO [8,9]. The *calcium looping* (CaL) process is the carbonate looping technology that uses *calcium* oxide (CaO) as the main sorbent for capturing CO_2. It is the most prominent carbonate looping technology due to its ability to achieve the highest CO_2 uptake per unit mass and favorable kinetics [8]. As a result, the terms "carbonate looping" and "calcium looping" are widely regarded as synonyms (cf. [8,10]). The carbonation of CaO is a fast reaction that occurs at high temperatures (~ 650 °C), enabling efficient CaL integration schemes through heat recovery and power generation [11–14].

The operating principle of the CaL process is illustrated in Fig. 1. The off-gas enters the carbonator (left) where the CO_2 is captured via carbonation of CaO. The decarbonized gas stream leaves the carbonator toward the stack, where it is released to the atmosphere after recovering heat (e.g., to produce steam) and conditioning (e.g., filtering). The carbonated sorbent then flows into the calciner for regeneration (right). Here, the $CaCO_3$ generated by carbonation and the fresh sorbent are calcined to obtain active, lean sorbent (CaO). The standard CaL uses an oxy-fired calciner (top-right), which requires O_2 and fuel for operation. One advantage of the CaL process is its flexibility in terms of feed-stock options (biomass, waste-derived fuels, coal) [15–17], as well as its response to load changes [18]. Indirectly heating the calciner (bottom-right) makes it possible to burn the fuels with air in an external *combustor*, which has advantages in terms of energy-efficiency and operating costs [19]. For indirect heating, the use of a heat-pipes heat

---

* Corresponding author.
E-mail address: martin.greco@est.tu-darmstadt.de (M. Greco-Coppi).

https://doi.org/10.1016/j.fuel.2024.133931
Received 23 August 2024; Received in revised form 19 November 2024; Accepted 26 November 2024
Available online 27 January 2025
0016-2361/© 2024 The Author(s). Published by Elsevier Ltd. This is an open access article under the CC BY license (http://creativecommons.org/licenses/by/4.0/).

Nomenclature

Latin symbols

A_t	Internal section area of the calciner (m^2)
c_0	Preexponential factor for the adsorption rate (Pa$^{-0.5}$)
C_{CO2}	Concentration of CO_2 (mol/m^3)
d_p	Particle diameter (m)
DF	Dimensionless driving force (−)
E_a	Activation energy for the adsorption rate (J/mol)
E_c	Activation energy for the kinetic rate (J/mol)
E_{calc}	Calciner efficiency (%)
$\mathbf{E}(t)$	Residence time distribution (s^{-1})
$\mathbf{f}$	Form function (particle kinetics) (−)
f_a	Fraction of particles that exit the reactor before complete calcination (−)
F_{CO2}	Molar flow rate of CO_2 (mol/s)
F_0	Molar flow rate of make-up $CaCO_3$ (mol/s)
$F^*_{CO2,out}$	Maximum outlet molar flow of CO_2 (for full calcination) (mol/s)
F_R; F_{R+0}	Molar circulation rate of calcium species w/o make-up; w/ make-up (mol/s)
F_{inlet}; F_{inert}; F^{fresh}_{steam}	Molar flow rate of gas into the calciner: total; gases other than CO_2; fresh steam (mol/s)
G_s	Specific solid circulation (kg/(m^2 s))
$\mathbf{h}$	Influence of CO_2 concentration on the reaction rate (−)
H_T; H_d	Reactor height (internal); reactor bed height (dense region) (m)
k_c; k	Particle kinetic rate; apparent kinetic rate ($k = k_c\,\mathbf{h}$) (1/s)
k_r; $\overline{k}_r$	Global reaction rate; mean k_r (1/s)
k_0	Preexponential factor for the kinetic rate (1/s)
K_r	Reactor global reaction rate (mol/(m^3 s))
M_i	Molar mass of "i" (kg/mol)
n	Number of active sites (L) occupied by each molecule of CO_2 chemisorbed (−)
n_o	Reaction order (−)
N_{Ca}	Calciner molar inventory of calcium species (mol)
N_{CO2}; N_{CaO}	Moles of CO_2; of CaO (mol)
p	Reactor pressure (Pa)
p_{CO2}; $p_{CO2,in}$; p^*_{CO2}	CO_2 partial pressure; inlet; equivalent (Pa)
$p_{CO2,eq}$	Equilibrium CO_2 partial pressure (Pa)
$p^*_{CO2,out}$	Outlet CO_2 partial pressure for full calcination (Pa)
R_u	Universal gas constant; $R_u = 8.314$ J/(mol K)
SR	Steam ratio (kg$_{H2O}$/kg$_{CO2}$)
t; t_c	Time (in the reactor); calcination time (s)
T	Temperature (°C)
u_0; $u_{0,out}$	Superficial gas velocity; at the reactor outlet (m/s)
$V_{s,a}$; V_{gas}	Volume of potentially active solids; of gas (m^3)
X	Molar fraction of $CaCO_3$ in calcium species (CaO and $CaCO_3$) (mol$_{CaCO3}$/mol$_{Ca}$)
X_{carb}	Fraction of $CaCO_3$ in the solids stream leaving the carbonator (mean) (mol$_{CaCO3}$/mol$_{Ca}$)
$\overline{X}_{carb}$	Fraction of $CaCO_3$ in the solids stream entering the calciner (mean) (mol$_{CaCO3}$/mol$_{Ca}$)
X_{calc}	Mean fraction of $CaCO_3$ in the calciner/leaving the calciner (mol$_{CaCO3}$/mol$_{Ca}$)
z	Distance to reactor bottom (m)

Greek symbols

α	Reaction progress (−)
ΔF^*_{CO2}	Maximum CO_2 formation in the calciner (for full calcination) (mol/s)
ε_s	Mean solid volume fraction (−)
η	Mean gas–solid contact efficiency (%)
θ	Fraction of active sites occupied by CO_2 (−)
ξ	Volume ratio of potentially active solids (m^3/m^3)
$\rho_{s,a}$	Apparent density of potentially active solids (kg/m^3)
σ	Standard deviation (normal distribution) (−)
τ	Mean (particle) residence time (s)
τ_{act}	Active (mean particle residence) time (s)
τ^*_{act}	Dimensionless active (mean particle residence) time (−)

Subscripts and superscripts

calc	Calciner
carb	Carbonator
eq	Equilibrium
inert	Inert gas (H_2O, N_2, etc.)
in	Inlet
out	Outlet
s,a	Potentially active solids
BFB	Bubbling fluidized bed
CaL	Carbonate looping (also *calcium looping*)
CFB	Circulating fluidized bed
EGR	Exhaust gas recirculation
IHCaL	Indirectly heated carbonate looping
RTD	Residence time distribution
TU	Technical University (of Darmstadt)

exchanger is the only concept that has been successfully demonstrated in pilot tests [20]. Since no oxygen is required for the calciner, fluidization can be achieved through exhaust gas recirculation (EGR), steam utilization, or a combination of both (see also [21]). The flue gas generated in the combustor is transferred to the carbonator for CO_2 capture. There are different concepts for integrating IHCaL technology into different industrial processes [11,22,23].

CaL technology has the potential to decarbonize industrial processes with minimal penalties. This is especially true when synergies involving spent-sorbent utilization and heat recovery are effectively leveraged. In recent years, the application of CaL in the lime and cement industries has been intensively studied due to the high CO_2 emissions from the calcination of $CaCO_3$, which can only be avoided with carbon capture [24]. Previous studies on oxy-fired CaL have reported CO_2 avoidance costs[1] in the range of 30–39 €/t$_{CO2,av}$ for power plants [27,28], and 53–84 €/t$_{CO2,av}$ for cement production facilities [29,30]. These numbers are low compared to the avoidance costs associated with MEA scrubbing (approximately 100 €/t$_{CO2,av}$ for cement plants) [29]. CaL has also been proposed for industrial processes beyond cement production [31]. The *indirectly heated carbonate looping* (IHCaL) uses an external combustor to generate the heat for sorbent regeneration, thus eliminating the requirement for pure O_2. The IHCaL has the potential to further decrease the cost of CO_2 capture to approximately 30 €/t$_{CO2,av}$ for power plants [27] and less than 50 €/t$_{CO2,av}$ for lime and cement production [19,32].

Since the beginning of the last decade, extensive experimental work

---

[1] These and the following costs have been adjusted to the prices of March 2024 with the Chemical Engineering Plant Cost Index [25,26]. Where the reference year was not available, the date of manuscript submission was used for indexing.

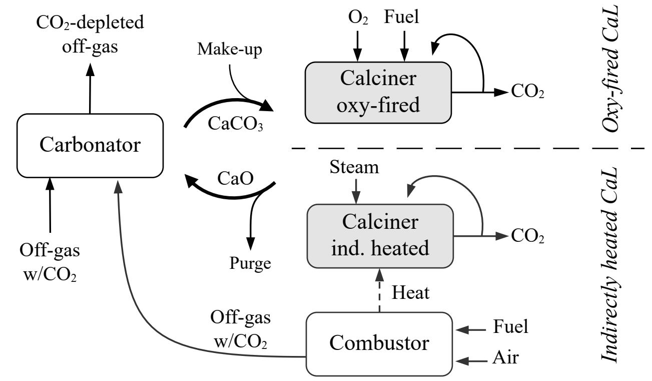

Fig. 1. Scheme of the carbonate looping (CaL) displaying two variations of calciner operation: oxy-fired (top) and indirectly heated (bottom).

has been conducted in semi-industrial facilities [33]. The oxy-fired CaL process has been demonstrated in many pilot tests. The major test facilities are located in Stuttgart (200 kW$_{th}$) [34–36] and Darmstadt (1 MW$_{th}$) [16,37], Germany; La Pereda, Spain (1.7 MW$_{th}$) [38,39]; and Heping, Taiwan (1.9 MW$_{th}$) [40]. Firing various types of fuels in the calciner was successfully demonstrated, including hard coal and lignite [41], solid recovered fuels [42], and biomass pellets [17]. The achievement of CO_2 capture rates higher than 99 % in a CaL pilot plant has been recently reported by Arias et al. [17]. Recently, Magli et al. [43] conducted tests at a pilot facility built *in situ* at a cement plant in Vernasca, Italy, which features a 105-m entrained-flow carbonator [44]. To date, the only pilot tests of the IHCaL process using a heat-pipes heat exchanger [45] were performed at a 300-kW$_{th}$ pilot facility at the Technical University of Darmstadt, Germany [46]. These tests included operating conditions relevant to power plants [20], and lime and cement plants [47]. Recently, Hofmann et al. [48] operated the IHCaL facility by co-firing propane with both dried lignite and refuse-derived fuel. Apart from empirical data from semi-industrial facilities, reliable reactor models are essential for interpreting experimental results and scaling up CaL and IHCaL technology for commercial operation.

The carbonator is one of the main reactors in the CaL process. It has been the object of considerable modeling work [49–55]. On the other hand, only a few calciner models for CaL are available in the open literature [56]. Ylätalo [57] studied a 1.7-MW$_{th}$ oxy-fired pilot calciner. They used a steady-state, three-dimensional (3-D) calciner model and a steady-state, one-dimensional (1-D) process model. Their 3-D model solves the fundamental balance equations of fluidized bed operation using the control volume method. They also included semi-empirical equations to describe solid entrainment, chemical reactions, and heat transfer, thus reducing computational effort. Both the 1-D and 3-D approaches yielded similar results. However, they did not validate their models with experimental data. Kanellis et al. [58,59] developed two 3-D CFD models capable of predicting empirical results from a single operating point of the IHCaL pilot plant at TU Darmstadt [20], namely the pressure profile, the CO_2 concentration at the calciner exit, and the CO_2 production rate. They used two different modeling strategies, obtaining similar results: their first model uses an Eulerian-Eulerian approach (Two Fluid Model [60], TFM), and their second model uses an Eulerian-Lagrangian framework (Dense Discrete Phase Model [61], DDPM). In both models, the drag coefficient is calculated with a sub-grid energy minimization multiscale (EMMS) scheme, and the calcination kinetics are described with the changing grain size model (CGSM) developed by García-Labiano et al. [62]. Höftberger et al. [45] modeled the heat transfer with heat pipes in a bench test rig using semi-empirical equations for heat transfer between fluidized beds and immersed heating surfaces [63]. Martínez et al. [64] developed a simple calciner model based on a basic description of the fluid dynamics and a grain model for the calcination [65]. This model is useful for preliminary calculations but does not include the effect of CO_2 concentration gradients in the calciner.

Despite commendable efforts in calciner modeling, the available numerical studies are not sufficiently supported by empirical data from relevant pilot tests. Moreover, existing detailed models are often too complex, allowing for the computation of only a limited number of operating points within a reasonable timeframe. Recently, Greco-Coppi et al. [55] highlighted that poor calciner performance may limit CO_2 removal efficiency by reducing the sorbent's capacity to capture CO_2 (see also [66,67]). This observation was based on a one-dimensional carbonator model and the results of pilot tests. The commercialization of carbonate looping technology requires simple yet precise design guidelines for calciners, which still need to be developed.

The objective of this study is to establish a method to efficiently analyze and design calciners for CO_2 capture with carbonate looping technology. For this, a new calciner model is developed based on data from thermogravimetric analysis and observations from pilot-plant operations. The model consists of two sub-models, which are connected through a mass balance and are solved iteratively until convergence. The results of the models are validated using empirical data from two different pilot plants: a 300-kW$_{th}$ IHCaL plant, and a 1-MW$_{th}$ oxy-fired CaL plant. Lastly, the model is processed using a stochastic methodology and dimensionless numbers to generate guidelines for calciner design without requiring complex calculations.

2. Experimental methods

In this section, the experimental tests used to obtain the empirical data for the model development and validation are reported. The tests were: (i) thermogravimetric analysis, (ii) pilot tests of the IHCaL process with heat pipes (300-kW$_{th}$ scale), and (iii) pilot tests of the oxy-fired CaL process (1-MW$_{th}$ scale).

2.1. Thermogravimetric analysis

To obtain the main kinetic parameters for the models, thermogravimetric analyses (TGA) were performed at the Technical University of Darmstadt using an STA 449 *F3 Jupiter* TGA from the company Netzsch [68]. The analyzed samples consisted of 3 mg of the sorbent used in the pilot tests, specifically Messinghausen limestone (98.3 wt% CaO; see Table S.1). For the TGA tests, the particle size of the samples was 106–200 μm. The temperatures were varied between 850 °C and 875 °C, and the CO_2 partial pressure was in the range 10–70 kPa. A more detail description of the methodology of the tests is available in a previous publication [55]. The main TGA results are included in Fig. 3 along with the corresponding results from the particle sub-model. The results from all TGA test points are available in the Supplementary Material (Figure S.4).

2.2. Indirectly heated CaL pilot tests

The 300-kW$_{th}$ IHCaL pilot plant at TU Darmstadt [46] was commissioned in 2015. It is the largest IHCaL plant ever operated. Recently, this plant has been expanded with a gas tract to feed the combustor's flue gas into the carbonator [48]. The calciner of this pilot plant is a bubbling bed fluidized with air. The height of the bed is determined by the solid outlet, which is located 1.9 m from the bottom of the reactor. The mean particle residence time was ca. 20 min throughout the pilot tests. For the validation, the pilot plant tests reported by Reitz et al. [46] were considered. The balancing of the system to obtain the circulation rates and the carbonation rates after the calciner (X_{calc}) was performed according to Reitz [69]. The inputs for the calciner model were obtained from one-hour averages of the operating parameters, according to measurements from pilot tests (see [55]). The calcination efficiency was computed from the X_{carb} values obtained from solid samples and the X_{calc} values were calculated from mass and energy balances [69]. The temperature input for the reactor model was taken from the temperature measurements in the reactor (see Supplementary material, Figure S.1).

2.3. Oxy-fired CaL pilot tests

The 1-MW$_{th}$ plant at TU Darmstadt was commissioned in the year 2011 [70]. The plant's calciner is an 11-meter-high circulating fluidized bed (CFB). The heat for the calcination is obtained through oxy-fuel combustion in the calciner. A detailed description of the components and capabilities of this plant can be found elsewhere [41,71]. The relevant specifications of both pilot plants are summarized in Table 1.

3. Theory and calculation

3.1. The calcination reaction

The regeneration of the sorbent and the release of CO_2 in a high-purity stream (>95 vol–%$_{db}$) are carried out in the calciner. This occurs through the calcination reaction (see Eq. (1)), which takes place due to the increase in the equilibrium CO_2 partial pressure ($p_{CO2,eq}$) caused by the temperature rise. The energy for the reaction is obtained through the combustion of fuels, either in an external combustion chamber (IHCaL) or *in situ* using pure oxygen (oxy-fired CaL).

$$CaCO_3(s) \leftrightarrows CaO\,(s) + CO_2(g) \tag{1}$$

The direction in which this reversible reaction takes place depends on the operating temperature (T) and CO_2 partial pressure. In this study, the equilibrium CO_2 partial pressure ($p_{CO2,eq.}$) is calculated with the expression from García Labiano et al. [62], based on thermochemical data from [73]:

$$p_{CO2,eq} = 4.137\ 10^{12}\ \exp\frac{-20474}{T + 273.15}\ [\mathrm{Pa}] \tag{2}$$

In Fig. 2, this expression is compared with others from the literature. The range of operation is displayed for the IHCaL pilot calciner, oxy-fired calciners, and commercial CaL calciners (including IHCaL) as well. The expression used by Silcox et al. [74], originally derived from [75], gives equilibrium partial pressures approximately 3 % lower than those obtained with Eq. (2). Historical correlations have been discussed by Steiner [76], the most prominent of which are included in Fig. 2, using their reported ranges of validity. Sometimes, correlations from Baker's data [77] are used in calciner studies. However, Baker's tests were conducted at high pressures (1–300 atm), which are not representative of typical CaL operation.

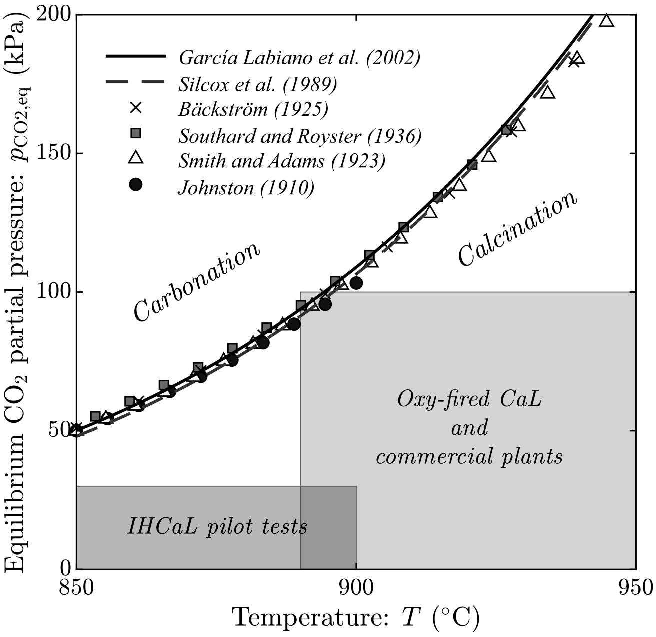

Fig. 2. Equilibrium CO_2 partial pressure for carbonation-calcination calculated using the correlations from García Labiano et al. [62], and Silcox et al. [74]. Historical correlations [76] derived from empirical data are plotted with markers only for their range of validity.

3.2. Main operating parameters

In the present section, the main operating parameters and key performance indicators (KPIs) of the IHCaL process are presented. The sorbent carbonation degree (X) is defined in Eq. (3). The main molar flows (F) of sorbent and CO_2 in a CaL plant are illustrated in Figure S.2.

$$X \equiv \frac{\text{moles of } CaCO_3}{\text{moles of Ca}} \tag{3}$$

The sorbent molar flow rates are F_R, for the sorbent circulation between the carbonator and calciner, and F_0 for the fresh make-up. We assume that all solids exit the system in a single purge stream, located downstream of the calciner, with a molar flow rate of F_0. The make-up stream consists of pure $CaCO_3$ unless otherwise stated. The total CO_2 molar flow rate into the carbonator is denoted with F_{CO2}.

The molar flow rates of sorbent determine how many times, on average, a particle cycles between the calciner and the carbonator. High make-up rates (F_0) ensure high sorbent activity. Sufficiently high

Table 1
Plant specifications and operating conditions of the pilot facilities used to validate the calciner model.

Parameter		IHCaL pilot tests [20]	CaL pilot tests [72]	Unit
Plant specifications (calciner)				
Nominal thermal power	–	300	1000	kW$_{th}$
Calciner operating mode	–	BFB	CFB	–
Calciner heat input	–	Indirect (heat-pipes HX)	Oxy-fuel combustion	–
Fluidization type	–	Air	O_2 + flue gas recirculation	–
Calciner cross section (internal)	–	1.05 × 0.3	Ø 0.4	m
Calciner height (internal)	H_t	1.91	11	m
Operating conditions (calciner)				
Temperature	T	840–860 (average at outlet)	820–920 (average)	°C
Solid circulation	G_s	0.8–2.7	1.9–4.2	kg/(m^{2}s)
Specific make-up	F_0/A_t	0–1.3	0.1–1.0	mol/(m^{2}s)
Superficial gas velocity	$u_{0,out}$	0.25–0.34	4.5–6.0	m/s
Carbonation at reactor inlet	X_{carb}	0.02–0.20	0.04–0.06	mol$_{CaCO3}$/mol$_{Ca}$
Active time	τ_{act}	120–480	4–18	min
Inlet CO_2 partial pressure	$p_{CO2,in}$	0	30–40	kPa

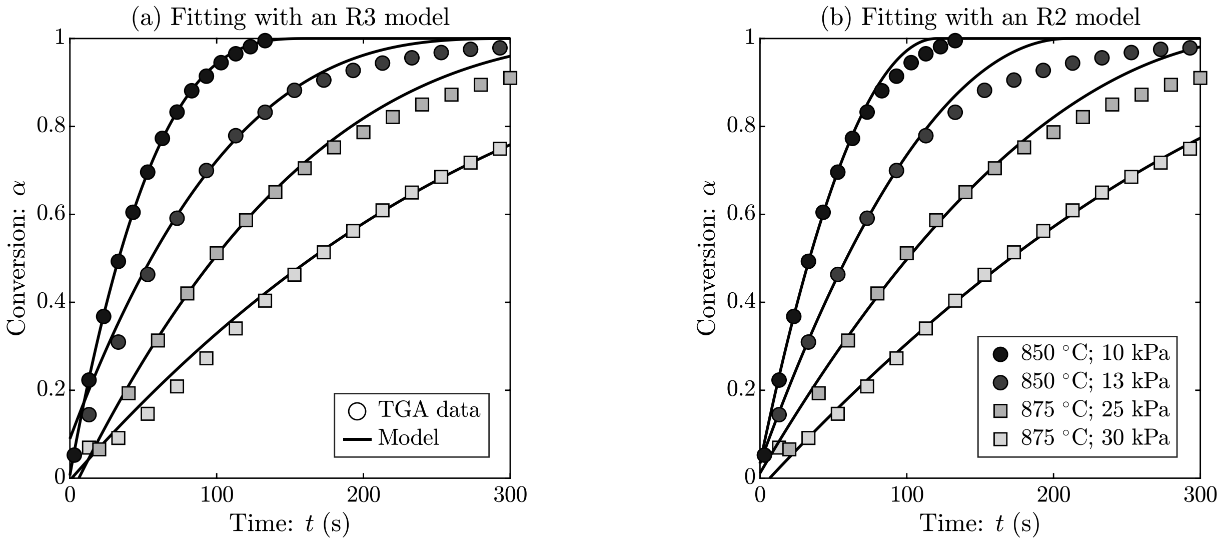

Fig. 3. Results from TGA fitted with (a) a volumetric shrinking model (R3), and (b) a surface shrinking model (R2); for different temperature and CO_2 partial pressures.

circulation rates (F_R) are one of the requirements for capturing CO_2 with a high capture efficiency (> 90 %) in the carbonator. Since high molar flow rates of sorbent are associated with increased energy requirements and costs, a compromise is necessary [11]. Furthermore, high calciner performance is required to ensure that sufficient lean sorbent enters the carbonator to capture CO_2 [54].

Apart from the flow rates and carbonation degrees, the calciner geometry, operating temperature (T), operating pressure (p), and CO_2 partial pressure (p_{CO2}) are necessary to simulate the reactor performance. We use experimental data and results from the pilot tests for the validation of our model. The instrumentation of the pilot plant, as well as the methodology to obtain empirical results, are explained elsewhere [20,54,55,69].

3.3. Key parameters and performance indicators

The calciner efficiency (E_{calc}) is an indicator of calciner performance. It is defined as the ratio of moles of $CaCO_3$ calcined to the total moles of $CaCO_3$ entering the calciner [64]. It is generally calculated using the carbonation degree (X) upstream and downstream of the calciner, $\overline{X}_{carb}$ and X_{calc}, respectively (see Figure S.2). Mathematically:

$$E_{calc} = \frac{\text{moles of } CaCO_3 \text{ calcined}}{\text{moles of } CaCO_3 \text{ introduced}} = \frac{\overline{X}_{carb} - X_{calc}}{\overline{X}_{carb}} \tag{4}$$

For the calculations in the calciner, it is advantageous to consider the mean conditions of the sorbent at the calciner inlet. For this, the average carbonation rate at the inlet of the calciner, $\overline{X}_{carb}$ is defined:

$$\overline{X}_{carb} \equiv (X_{carb}\, F_R + F_0)/(F_R + F_0) \tag{5}$$

To simplify equations, it is convenient to define the total active flow into the calciner (F_{R+0}) as:

$$F_{R+0} \equiv F_R + F_0 \tag{6}$$

Another useful parameter for the reactor model is the *mean particle residence time* (τ). It can be calculated considering the reactor molar inventory (N_{Ca}) and the molar flow:

$$\tau = N_{Ca}/F_{R+0} \tag{7}$$

Previous works proposed an *active mean particle residence time* (τ_{act}) or *active time* of the calciner to interpret results from pilot plant operation (see [20] and cf. [78]). This parameter is defined as:

$$\tau_{act} \equiv \tau/\overline{X}_{carb} \tag{8}$$

However, τ_{act} alone is not a good explanatory variable of calciner performance because it does not incorporate the effects of p_{CO2} and T, which are the main drivers of calcination. To address this issue, we develop two dimensionless parameters for assessing the calciner operation, as detailed below.

Dividing τ_{act} to remove the influence of the solid inventory gives: $\tau_{act}/N_{Ca} = (\overline{X}_{carb}\, F_{R+0})^{-1}$.This value can be related to the CO_2 formation. A theoretical maximum CO_2 formation in the calciner (ΔF^*_{CO2}) corresponds to full calcination, according to: $\Delta F^*_{CO2} = F_{R+0}\, \overline{X}_{carb} = (\tau_{act}/N_{Ca})^{-1}$. The maximum outlet molar flow of CO_2 (F^*_{CO2}) can be calculated by balancing the calciner:

$$F^*_{CO2,out} = F_{CO2,in} + \Delta F^*_{CO2} \tag{9}$$

Using the inlet partial pressure of CO_2 ($p_{CO2,in}$) and the reactor pressure (p), an expression for the maximum p_{CO2} at the outlet ($p^*_{CO2,out}$), corresponding to full calcination, is obtained:

$$p^*_{CO2,out} = p \Bigg/ \left\{ 1 + \left[\overline{X}_{carb} F_{R+0} \Big/ F_{inert} - \left(1 - p/p_{CO2,in}\right)^{-1} \right]^{-1} \right\} \tag{10}$$

Here, F_{inert} is the molar flow rate of gas other than CO_2 entering the calciner. The driving force for the calciner performance (DF) is defined as:

$$\mathrm{DF} \equiv p_{CO2,eq} \Big/ p^*_{CO2,out} \tag{11}$$

In explicit form, from input variables:

$$\mathrm{DF} = \frac{p_{CO2,eq}}{p} \left[1 + \frac{1}{\overline{X}_{carb} F_{R+0}/F_{inert} - \left(1 - p/p_{CO2,in}\right)^{-1}} \right] \tag{12}$$

The driving force (DF) determines the CO_2 formation at the calciner outlet (see Eq. (11)). DF is a better fitting parameter than τ_{act} for several reasons. Firstly, it considers the input from X_{carb} and F_{R+0}. Secondly, it incorporates the influence of gases other than CO_2, such as air or steam (F_{inert}). Thirdly, it depends on the calcination temperature (T), which is a key parameter for calciner operation. This influence is not always clear in the pilot operation because of the relatively constant time-averaged value of T at the calciner outlet throughout the pilot tests.

Finally, we introduce a *dimensionless active mean particle residence time* (τ^*_{act}), or *dimensionless active time*, to assess the influence of the particle residence time on the calciner efficiency. This parameter is based on the ratio of mean residence time (τ) to calcination time (t_c), which drives the calciner performance (see Eq. (27) and Figure S.4). Using our particle model (see Section 4.1 and Eq. (19)), we define τ^*_{act} as follows:

$$\tau^*_{\text{act}} = \frac{\tau}{3X_{\text{carb}}/k_c} = \frac{\tau_{\text{act}}}{3/k_c} \tag{13}$$

Here, $3\,X_{\text{carb}}/k_c$ represents the calcination time (t_c) without the function $\mathbf{h}$ that accounts for the influence of the CO_2 partial pressure, as this effect is already incorporated with DF. The factor 3 depends on the form function $\mathbf{f}$ (Eq. (18)) and should be adjusted if a different function $\mathbf{f}$ is used. We recommend only using τ^*_{act} in conjunction with DF, as explained in Section 5.4.2.

4. Modeling

In this Section, the development of the calciner model is discussed. The model is composed of two main sub-models:

i. a *particle sub-model*, which considers the particle conversion and reaction kinetics, and
ii. a *reactor sub-model* for the calculation of the CO_2 concentration throughout the reactor height.

For all calculations, the reactor pressure is determined as the average of pressure measurements. In cases where no pressure measurements are available, we assumed $p = 101.3$ kPa. The temperature gradients are neglected, meaning that a unique reactor temperature is considered for the calculations. In the bubbling bed calciner, the coldest areas of the reactor—approximately 50 °C lower than the mean reactor temperature (see Figure S.1, middle)—can be considered inactive regions where no calcination occurs. These regions effectively decrease the particle residence times. Since the mean particle residence times are much longer than the calcination times for IHCaL operation, it is reasonable to neglect the influence of the low temperatures in the coldest areas, which are located far from the lean-sorbent outlet (see Fig. 14 for the influence of the particle residence time). For the circulating fluidized bed (CFB) calciner, this assumption is justified by the moderate temperature gradients that primarily occur at the bottom of the reactor [72]. For the bubbling bed calciner, the temperature at the sorbent outlet is used. For the circulating fluidized bed, the maximum reactor temperature corresponding to the temperature of the major part of the reactor (excluding the bottom) is used.

There are good reasons to expect strong CO_2 partial pressure (p_{CO2}) gradients in the vertical direction. Even though there were no in-bed measurements during the pilot campaigns, the directionality of the gas flow (upwards) let us expect a rapid increase of the CO_2 concentration close to the inlet, as is typical of catalytic first-order reactors. Furthermore, results from three-dimensional modeling indicate exponential-like CO_2 concentration profiles along the reactor height for IHCaL [58,59] and oxy-fired CaL [57] calciners, with lower CO_2 concentrations at the bottom and higher at the top. To include the effects of pressure gradients in our model, we introduce an equivalent CO_2 partial pressure (p^*_{CO2}) that gives the same average conversion as the exact solution. The value of p^*_{CO2} is calculated by introducing a one-dimensional reactor sub-model (see Section 4.3) that allows for CO_2 concentration gradients in the vertical axis. Lastly, p^*_{CO2} is obtained by computing the reactor and particle models iteratively, and by balancing the mass of the reactor system.

The ranges of operating T and p_{CO2} for the calciner during the pilot tests and for the commercial plants are illustrated in Fig. 2. For the IHCaL pilot tests [20], the operation temperatures were lower than 900 °C, and good calciner performance was achieved for some balance points. The relatively low temperatures were sufficient for the calcination because the fluidization was carried out with air; and, thus, the CO_2 partial pressure was limited to approximately 30 kPa at the reactor outlet. For industrial facilities, the calciner will be fluidized with CO_2 and steam. From a thermodynamic and economic point of view, it is desired to minimize the amount of steam. However, using steam lowers the required calcination temperature, which is advantageous to avoid failure of components (e.g., heat pipes) and agglomeration problems. The optimization of the amount of steam and the operating temperature is discussed in Section 5.4.2.

4.1. Particle sub-model

Different mechanisms limit the reaction rate of the calcination, but there is no consensus on which are relevant for the modeling [79]. These mechanisms include the heat transfer between the particle and the reaction boundary layer, the internal and external mass transfer of CO_2, and the chemical reaction [80].

Khinast et al. [81] performed limestone calcination experiments with low partial pressures (0–6.5 kPa) and small particles of limestone (7.5–90 μm). They observed that particle size only limits the calcination rate for fast kinetics corresponding to very low CO_2 partial pressures relative to the equilibrium CO_2 partial pressure. Since high CO_2 partial pressures are typical in calciners for CaL applications, the effect of mass transfer related to particle size may be neglected. This is further supported by other studies that use much larger particle sizes up to ca. 2 mm [62,65,82]. A more thorough discussion on reaction mechanisms is available elsewhere [56,79]. The calcination kinetics of fine sorbent particles ($d_p \approx 100$–300 μm) can be reasonably modeled with the following differential equation [79]:

$$d(X_{\text{carb}} - X_{\text{calc}}(t))/dt = k\ \mathbf{f}(X_{\text{calc}}(t)); \quad k = k_c(T)\ \mathbf{h}(p_{\text{CO2}}; T) \tag{14}$$

Here, k is the apparent kinetic rate; k_c is the kinetic reaction rate constant, which depends on the reaction temperature; $\mathbf{f}$ is the form function that describes how the reaction rate variates with the reaction progress; and $\mathbf{h}$ is the function describing the dependency on p_{CO2} and $p_{\text{CO2,eq}}$. Using the reaction progress (α), Eq. (14) can be rewritten as:

$$d\alpha/dt = X_{\text{carb}}^{-1}\ k_c\ \mathbf{f}\ \mathbf{h}; \quad \alpha \equiv (X_{\text{carb}} - X_{\text{calc}}(t))/X_{\text{carb}} \tag{15}$$

It is assumed that T is constant throughout the entire reactor; thus, $p_{\text{CO2,eq}}$, which depends on T, is also constant and is calculated using Eq. (2) (see Fig. 2). The reaction rate, $k_c(T)$, is modeled with the Arrhenius equation:

$$k_c(T) = k_0 \exp(-E_c/R_u T) \tag{16}$$

Here, E_c is the activation energy, k_0 is the pre-exponential factor, and R_u is the universal gas constant. The function $\mathbf{f}(X_{\text{calc}})$ is the mathematical expression of the reaction mechanism, which is usually determined with TGA analysis. This is achieved by keeping T and p_{CO2} constant while measuring the evolution of X with time and obtaining k (1/s) for the best-fitting $\mathbf{f}$. Different mechanisms have been proposed [79], but, until now, the best procedure to select the appropriate one is to fit experimental data.

The experimental TGA data (see Section 2.1) for the Messinghausen limestone, which was the sorbent in the pilot tests (see Sections 2.2 and 2.3), is illustrated in Fig. 3. The best fit was achieved with a phase boundary reaction mechanism with shrinking volume (R3, Fig. 3.a, Eq. (17)); thus, it was adopted in our model. The shrinking surface mechanism (R2, see Fig. 3.b) also provided a good fit. The complete dataset, including quantitative data of the fit, is available in the Supplementary Material (Figure S.3). The R2 and R3 mechanisms also fit the data from limestone calcination in previous studies (e.g., [83], and [84] respectively). The differential equation for the calcination with an R3 mechanism is:

$$d\alpha/dt = X_{\mathrm{carb}}^{-1}\, k_c\, (1-\alpha)^{2/3}\, \mathbf{h} \tag{17}$$

Thus,

$$\mathbf{f} = (1-\alpha)^{2/3} \tag{18}$$

If the reactor temperature (T) and CO_2 partial pressure are constant, Eq. (17) can be solved analytically. Considering a generic particle in a reactor and integrating from 0 s to any time t, the following expression is obtained:

$$\alpha(t) = 1 - \left(1 - \frac{t}{t_c}\right)^3; \quad \mathrm{t_c} = \frac{3\,\mathrm{X_{carb}}}{\mathbf{h}\,\mathrm{k_c}} \tag{19}$$

During the TGA tests (see Fig. 4), the calcination rate falls rapidly with partial pressures close to the equilibrium ($p_{CO2}/p_{CO2,eq} \approx 0.5$), and near equilibrium ($p_{CO2}/p_{CO2,eq} \approx 0.8$) there is no calcination. The points with no calcination in the TGA tests are indicated with $k_c = 0$ in Fig. 4. A similar behavior has already been described in the literature. Khinast et al. [81] reported that the calcination rate decays exponentially with increasing CO_2 partial pressure. Wang et al. [85] operated a fluidized bed reactor in a 100 % CO_2 atmosphere at various temperatures and observed a strong influence of the equilibrium CO_2 partial pressure ($p_{CO2,eq}$). Valverde [86] saw that for pressures close to the equilibrium, the reaction rates are slower than what lineal models predict. He attributed this to an exothermicity related to a crystallographic structural transformation of CaO and proposed a model that allows for negative deactivation energies. Dennis and Hayhurst [82] observed that the calcination rates were lower at higher total pressures. They fitted their TGA calcination data assuming the existence of a spurious $p_{CO2,eq}$, lower than the $p_{CO2,eq}$ obtained from thermodynamic data. Only after introducing the spurious $p_{CO2,eq}$, they achieved a good fit, but they could not explain the physical significance of this assumption. Fernández et al. [87] observed a similar behavior in the calcination of cement raw meal. In their work, they saw that the minimum temperature required to start the calcination, for the same CO_2 partial pressure, varied from one raw meal type to another. García-Labiano et al. [62] performed calcination TGA tests with limestone and dolomite under varying conditions of total pressure and CO_2 partial pressure. They reported that a linear dependency with $p_{CO2} - p_{CO2,eq}$ underestimated the limiting effect of p_{CO2} for high CO_2 concentrations. They proposed to model this effect with a Langmuir-Hinshelwood kinetic-type model along with a Freundlich adsorption isotherm. This model considers that available active sites on the $CaCO_3$ surface are required for the calcination to take place, due to an adsorption–desorption process:

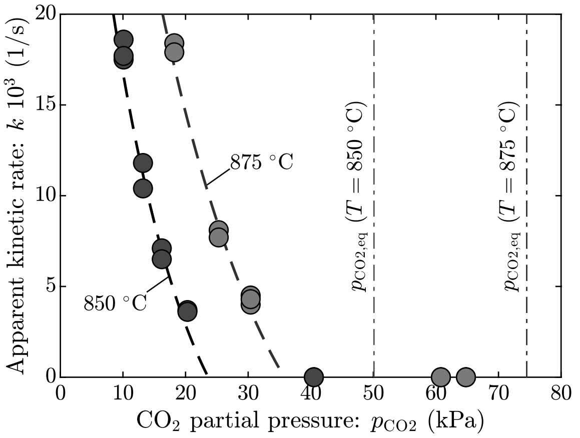

Fig. 4. Calcination apparent kinetic rate ($k = k_c\, \mathbf{h}$) for different temperatures and CO_2 partial pressures (p_{CO2}). The circles represent the data from TGA-analysis. The broken lines correspond to the fitted model. The corresponding equilibrium temperatures are displayed for reference. It is noteworthy that much lower p_{CO2} than the equilibrium CO_2 partial pressure is required to start the calcination. The color of the markers and the lines indicate the temperature: gray (darker) for 850 °C, and red (lighter) for 875 °C.

$$CaCO_3 + nL \leftrightarrows CaO + nL(CO_2) \tag{20}$$

Here, n represents the number of active sites L occupied by each molecule of CO_2 chemisorbed, $nL(CO_2)$. Generally, n varies between 0 and 2 in the adsorption processes. García-Labiano et al. [62] reported agreement with their experimental data using $n = 2$. The same approach is followed in this work.

The mathematical expression for **h** with the correction factor of the Freundlich adsorption isotherm and $n = 2$ [62] is:

$$\mathbf{h} = (1-\theta)\left(1 - p_{CO2}(t)\Big/p_{CO2,eq}\right); \quad \theta \equiv c\, p_{CO2}(t)^{1/2} \tag{21}$$

Here, c is an empirical constant that depends on T, according to an Arrhenius-type model:

$$c = c_0 \exp(-E_a/R_u T) \tag{22}$$

An alternative expression for **h**, used in a previous calciner model [64], is included in the Supplementary Material (Eq. (S.1)). The data was successfully fit with Eq. (21) (see Fig. 3). Our fitting constants, reported in Table 2, are consistent with values found in the literature, e.g. [62,88].

The expression in Eq. (21) along with a shrinking core model (Eq. (19)) fit our TGA results ($d_p \sim 200$ µm) and those from García-Labiano et al. [62], who tested limestone with particle sizes up to 2 mm, which indicates that this model is applicable to a wide range of particle sizes. The complete explicit equation of the reaction rate used in our model is included in the Supplementary Material (Eq. (S.3)).

4.2. Residence time distribution

The total calcination at the exit of the calciner is calculated considering the contributions of each particle, weighed with a residence time distribution (RTD) $\mathbf{E}(t)$:

$$E_{\mathrm{calc}} = \frac{\overline{X}_{\mathrm{carb}} - X_{\mathrm{calc}}}{\overline{X}_{\mathrm{carb}}} = \int_0^\infty \alpha(t)\, \mathbf{E}(t)\, dt \tag{23}$$

Here, t is the residence time of a particle, i.e., the time until the particle exits the reactor, and $\overline{X}_{\mathrm{carb}}$ is the average X value at the entrance of the calciner, which can be calculated with Eq. (5). The conversion of a particle after a residence time t can be calculated with Eq. (19).

Eq. (23) is solved assuming perfect mixing of the particles in the calciner, which is an accepted assumption for modeling fluidized beds at this level of detail, including calciners [7,49,64,89]. With this assumption, the residence time distribution is:

$$\mathbf{E}(t) = \tau^{-1} \exp(-t/\tau) \tag{24}$$

Here τ is the mean residence time of the particles in the reactor (Eq. (7)).

Table 2
Model constants obtained with experimental data from TGA analysis of Messinghausen limestone (p_{CO2} = 10–65 kPa; T = 850–875 °C).

Chemical reaction	
E_c (kJ/mol)	118
k_0 (1/s)	$1.84 \cdot 10^4$
Adsorption mechanism	
E_a (kJ/mol)	– 89
c_0 (Pa $^{-0.5}$)	$4.72 \cdot 10^{-7}$

4.2.1. Calcination efficiency

The calcination efficiency is calculated using Eqs. (23) and (24):

$$E_{\mathrm{calc}} = \int_0^{t_c} \alpha(t) \frac{\exp(-t/\tau)}{\tau}\, dt + (1 - f_a) \tag{25}$$

Here, f_a is the fraction of particles that exit the reactor before t_c and are therefore not fully calcined. Assuming perfect mixing of particles, f_a is calculated with Eq. (26) [64].

$$f_a = 1 - \exp(-t_c/\tau) \tag{26}$$

Lastly, replacing with Eq. (19) and integrating gives:

$$E_{\mathrm{calc}} = 6\, f_a (\tau/t_c)^3 - 6(\tau/t_c)^2 + 3(\tau/t_c) \tag{27}$$

The calcination time (t_c) is obtained from Eq. (19). Since this parameter depends on the CO_2 partial pressure, which variates throughout the reactor, the calculation of t_c is performed using the value of p^*_{CO2} from the iteration with the reactor sub-model (see Section 4.4). Previous studies used a simplification, which is compared to our model in Sections 4.2 and 4.6 of the Supplementary Material. The predictions of our model and the simplified approach are illustrated in Figure S.3 and Figure S.5. To achieve an efficiency of 90 % in the calciner, a mean residence time of $\tau \approx 2\, t_c$ is required.

The CO_2 formation rate during calcination is largely constant and independent of the carbonation rate of the particles entering the calciner [65]. Particles leaving the carbonator with a low $CaCO_3$ content calcine in a shorter time than fresh limestone particles fed as make-up (see Eq. (19)). We use the average $CaCO_3$ content of the molar flow at the entrance of the calciner ($\overline{X}_{\mathrm{carb}}$) in our calculations, which results from the mixture of the make-up flow (F_0) and the sorbent recirculation (F_R) according to Eq. (5).

4.2.2. Particle global reaction rate

For the reactor sub-model (see Section 4.3), we need to calculate the global reaction rate k_{r}, defined as:

$$k_{\mathrm{r}} \equiv k_c (1 - \alpha(t))^{2/3} \tag{28}$$

This definition considers the kinetic constant (k_c) and the shape function but omits the dependence on p_{CO2}, $\mathbf{h}$ (see Eq. (21)). Since k_{r} depends on the particle residence time, an average reaction rate $\overline{k}_{\mathrm{r}}$ needs to be computed. This is done by weighting k_{r} with the particle residence time distribution:

$$\overline{k}_{\mathrm{r}} = \int_0^{\infty} k_{\mathrm{r}}\, \mathbf{E}(t)\, dt \tag{29}$$

Using Eqs. (24) and (28), and considering that there is no reaction after t_c:

$$\overline{k}_{\mathrm{r}} = \int_0^{t_c} k_c(T) \left(1 - \alpha\left(t, p^*_{\mathrm{CO2}}\right)\right)^{2/3} \frac{\exp(-t/\tau)}{\tau}\, dt \tag{30}$$

Replacing the reaction progress and solving the integral gives:

$$\overline{k}_{\mathrm{r}} = k_c(T) \left[2 f_a (\tau/t_c)^2 - 2(\tau/t_c) + 1\right] \tag{31}$$

The underlying assumption is that the kinetic rate determined with the TGA tests is valid for the fluidized bed calciner. Dai et al. [90] observed that the calcination of limestone particles of ~ 0.8 mm was chemically controlled in a bubbling fluidized bed operating at 825–925 °C. It is reasonable to expect that for smaller particles, the kinetic rate will be chemically controlled, which supports the validity of applying Eq. (28) in the reactor model.

4.3. Reactor sub-model

The gas conversion is modeled considering the conversion rate of a solid-catalyzed reactor. For this, we follow Kunii and Levenspiel [91, p.277]. The molar rate of formation of CO_2 (dN_{CO2}/dt) is linearly dependent on $\mathbf{h}$, consistent with the particle sub-model (Section 4.1). Mathematically, the CO_2 production in the calciner is:

$$dN_{\mathrm{CO2}} \Big/ dt = V_{\mathrm{s,a}}\, K_r\, \mathbf{h}; \quad [K_r] = \mathrm{mol} \Big/ (\mathrm{m}^3_{\mathrm{particle}}\ \mathrm{s}) \tag{32}$$

Here, K_r is a global reaction rate for the reactor sub-model, and $V_{\mathrm{s,a}}$ is the apparent volume of the potentially active sorbent (i.e., $CaCO_3$ and CaO) [53]. For each mole of CO_2 generated, one mole of $CaCO_3$ is transformed into CaO. Thus, considering the density and molar mass of the potentially active sorbent (i.e., CaO and $CaCO_3$),

$$dN_{\mathrm{CO2}}/dt = dN_{\mathrm{CaO}}/dt = -V_{\mathrm{s,a}}\, \left(\rho_{\mathrm{s,a}}/M_{\mathrm{s,a}}\right)\, dX_{\mathrm{calc}}/dt \tag{33}$$

Using the definition of reaction progress α (see Eq. (15)) in this equation yields:

$$dN_{\mathrm{CO2}}/dt = V_{\mathrm{s,a}}\, \left(\rho_{\mathrm{s,a}}/M_{\mathrm{s,a}}\right)\, X_{\mathrm{carb}} \quad d\alpha/dt \tag{34}$$

Lastly, comparing Eq. (32) and Eq. (34) with Eq. (17) gives an expression that relates the reactor sub-model with the particle sub-model:

$$K_r = \left(\rho_{\mathrm{s,a}}/M_{\mathrm{s,a}}\right) k_c\, (1 - \alpha)^{2/3} \tag{35}$$

Using Eq. (28), K_r can be expressed in terms of the global reaction rate of the particle model:

$$K_r = \left(\rho_{\mathrm{s,a}}/M_{\mathrm{s,a}}\right) \overline{k}_{\mathrm{r}} \tag{36}$$

For the reactor sub-model calculations, we need the average global reaction rate $\overline{k}_{\mathrm{r}}$, which is obtained from the particle sub-model using Eq. (31). The CO_2 partial concentration profile is calculated based on the rate of formation of N_{CO2}. The formula of Eq. (32) can be rewritten in terms of CO_2 concentration by considering the gas volume (V_{gas}):

$$dC_{\mathrm{CO2}}/dt = \left(V_{\mathrm{s,a}}/V_{\mathrm{gas}}\right)\, K_r\, \mathbf{h} \tag{37}$$

To obtain an expression suitable for integration over the height of the reactor, we neglect radial gradients and consider only the concentration variation in the vertical axis. With this consideration, the relation between the volumes of the potentially active solids and the gas can be written as [54]:

$$V_{\mathrm{s,a}} \big/ V_{\mathrm{gas}} = (\varepsilon_s\, \xi/u_0)\, dz/dt \tag{38}$$

Here, ε_s is the solid volume fraction in the bed, while ξ denotes the fraction of potentially active solids to total solids in the reactor, accounting for the presence of inert solids in the bed (e.g., ash, unburnt fuel, sulfated sorbent) [53]. The free gas velocity (u_0) increases throughout the reactor. The value of u_0 corresponding to the outlet volume flow rate is used for the calculations since most of the CO_2 generation (through calcination) occurs in the lowest part of the reactor. Using Eqs. (37) and (38), and introducing a gas–solid contact efficiency (η) to account for the departure from the ideal plow-flow reactor [92], the following differential equation is obtained:

$$dC_{\mathrm{CO2}}/dz = K_r\, \mathbf{h}(p_{\mathrm{CO2}}; T)\, \eta \varepsilon_s \xi / u_0 \tag{39}$$

We could not find a sensible analytical solution for this equation using the function $\mathbf{h}$ of Eq. (21). Instead, Eq. (39) was solved numerically by dividing the bubbling bed into 10^4 cells of equal height, achieving convergence with low computational effort (≈ 1 ms).

4.4. Model closure and programming

The model was implemented in MATLAB R2023b. For the computation of the entire model, we follow a similar approach to previous works on reactor modeling (mainly [53,54]). This approach consists in solving the particle and reactor sub-models iteratively until an equivalent CO_2 partial pressure (p^*_{CO2}) that satisfies the mass balance is obtained. This is achieved using the bisection method of Bolzano [93, p. 53–55]. The input for the particle sub-model is p^*_{CO2}. The input for the reactor sub-model is K_r, which is obtained from the particle sub-model (Eqs. (31) and (36)).

The convergence criterion is the minimization of the relative error in the calculation of the CO_2 partial pressure at the reactor outlet ($p_{CO2,out}$). With the reactor sub-model (RM), $p_{CO2,out}$ is obtained using the universal gas constant (R_u) and the CO_2 concentration at $z = H_d$:

$$p^{RM}_{CO2,out} = C_{CO2}(z = H_d)\ R_u\ T \tag{40}$$

With the particle sub-model (PM), $p_{CO2,out}$ is calculated using a gas molar balance:

$$p^{PM}_{CO2,out} = \frac{p}{1 + F_{inert}/\left(F_{CO2,in} + F_{R+0}\overline{X}_{carb} - X_{calc}\right)} \tag{41}$$

Here, X_{calc} is obtained from the calcination efficiency (E_{calc}, see Eq. (27)):

$$X_{calc} = \overline{X}_{carb}(1 - E_{calc}) \tag{42}$$

5. Results and discussion

5.1. Reactor sub-model

Fig. 5 illustrates the CO_2 partial pressure (p_{CO2}) across the carbonator, obtained with the reactor sub-model for varying temperatures (T) and reaction rates (K_r). For these calculations, the reactor pressure (p) is not an input; thus, the partial pressure is not limited by the total pressure p. In the complete model, p is considered in the molar balance, limiting the CO_2 partial pressure to p (corresponding to 100 % CO_2 atmosphere). The gas–solid contact efficiency (η) is set to 10 %. This is a conservative assumption (cf. [94]) that eliminates the complexity associated with the estimation of η. Such estimation would require the use of models based on empirical constants, which vary considerably with the operating conditions (e.g., [95]). The impact of η on the calciner performance is considered in the analysis of results (see Sections 5.3.2 and 5.4). Fig. 5.a shows that the inlet p_{CO2} is zero, which is consistent with air fluidization and corresponds to the IHCaL pilot tests (see Section 2.2 and Table 1). The behavior under partial steam fluidization is illustrated in Fig. 5.b. The partial pressure profiles indicate an asymptotic behavior toward maximum values p_{CO2}. These values correspond to the saturation CO_2 partial pressures that make $\theta = 1$, which are lower than the corresponding equilibrium CO_2 partial pressures for each T. As expected, higher temperatures allow for higher p_{CO2} at the reactor outlet. The reaction constant (K_r) has a significant effect in the partial pressure profile. Although we use a constant η in Fig. 5, we vary the value of K_r. Since both η and K_r are products of the same term in the governing equation (Eq. (39)), the influence of η can also be inferred from this figure. The influence of the different parameters of the reactor model, including η, on the global reactor performance is discussed in Section 5.

As the efficiency in the calciner increases, the CO_2 partial pressure profile becomes less pronounced because almost all the $CaCO_3$ inside of the reactor has already been converted, thus having very slow kinetics (low K_r). In this way, the in-bed measurement of the concentration in the calciner can be used to evaluate the performance of the reactor during operation. In-bed concentrations close to the outlet concentrations may indicate poor performance. On the other hand, lower CO_2 concentrations in the bed are characteristic of higher calciner efficiencies. This behavior is case-dependent and should be assessed by considering whether combustion occurs, the inlet and outlet CO_2 partial pressures, and, ultimately, the empirical values of the specific calciner being evaluated.

5.2. Correlation of empirical data

In previous works, the calciner efficiency (E_{calc}) has been correlated with the active time (τ_{act}) (see Eq. (8)). This may be useful for reactors with very low inventories, in which the mean particle residence time is in the order of magnitude of the calcination time (< 100 s). In the case of the indirectly heated carbonate looping (IHCaL), the size of the calciner is determined by the amount of heat pipes [22]. The reactor inventory (N_{Ca}) does not influence E_{calc} for the operating conditions of the IHCaL BFB calciner (see Fig. 6). The mean residence times (≈ 10 min) are much larger than typical calcination times; therefore, the active time (τ_{act}) is not a suitable explanatory variable for analyzing these systems. For the same reason, the calciner performance is independent of the parameters of the reactor sub-model, i.e., the reaction rates are generally high enough for the typical gas residence times. The observations from the pilot plant data are confirmed from the study of the model developed in this work. Fig. 6 (right) shows the variation of the E_{calc} with the mean residence time (τ). The value of τ only influences the model in high-performance scenarios, where the rest of the parameters (e.g., F_{inert}) are highly optimized for enhanced calcination. However, even in those

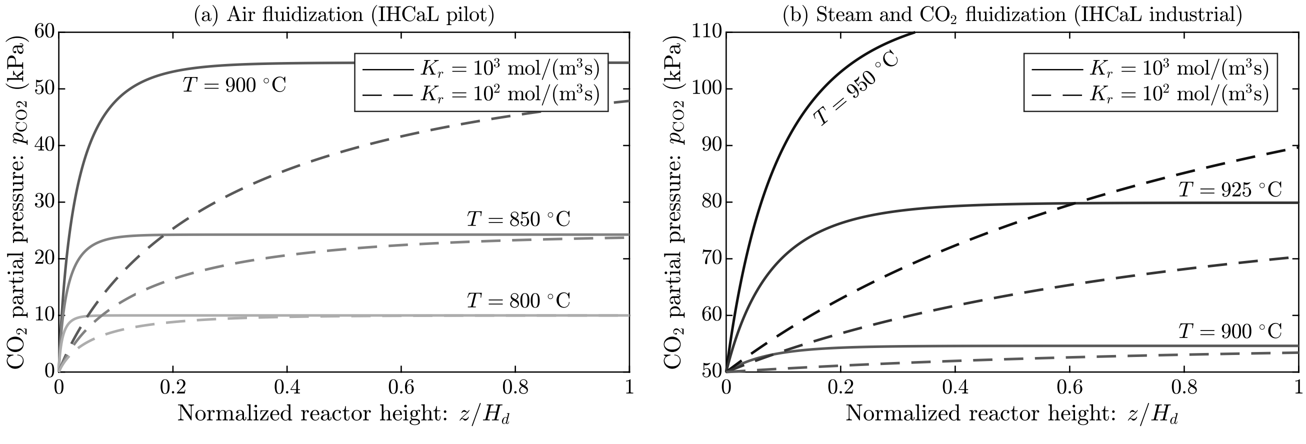

Fig. 5. CO_2 partial pressure distribution across the reactor height using the reactor sub-model developed in this work. The results are displayed for (a) air fluidization corresponding to pilot plant operation ($p_{CO2,in} = 0$ kPa) and (b) industrial operation with CO_2 recirculation and partial steam fluidization ($p_{CO2,in} = 50$ kPa). The following values were assumed for the calculations: $\xi = 1$; $u_0 = 0.2$ m/s; $H_d = 1.91$ m; $\eta = 0.1$, and $\varepsilon_s = 0.3$.

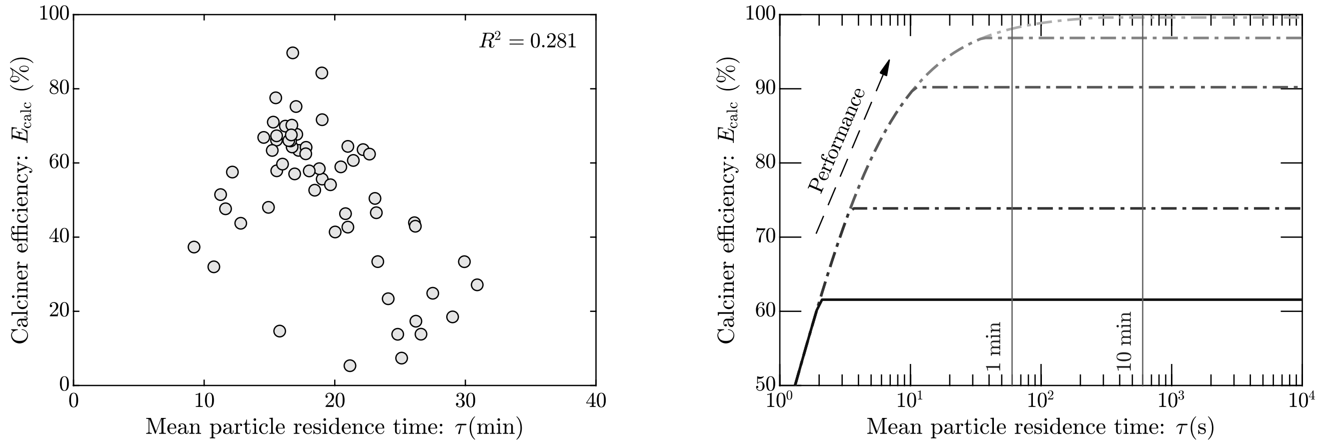

Fig. 6. Influence of the mean particle residence time in the calciner efficiency using pilot data (left) and the model developed in this work (right). The reactor temperature for the model calculations was $T = 860$ °C. The broken lines indicate different operating conditions to enhance performance. The lighter the color of the curve, the more efficient the operation (lower F_R).

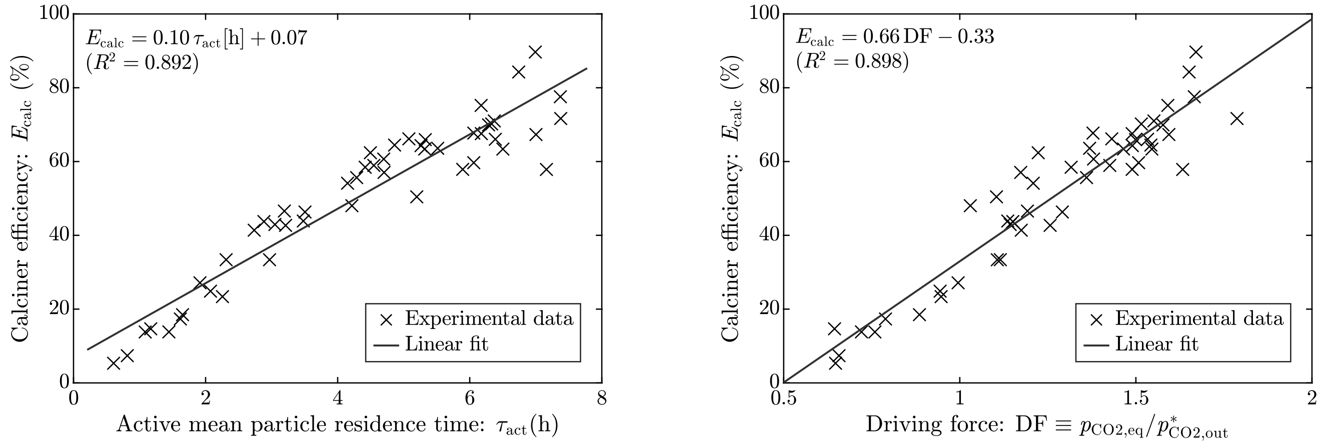

Fig. 7. Fitting the pilot-plant data of calciner efficiency with the calciner active time (τ_{act}) (left) and the specific driving force (DF) (right).

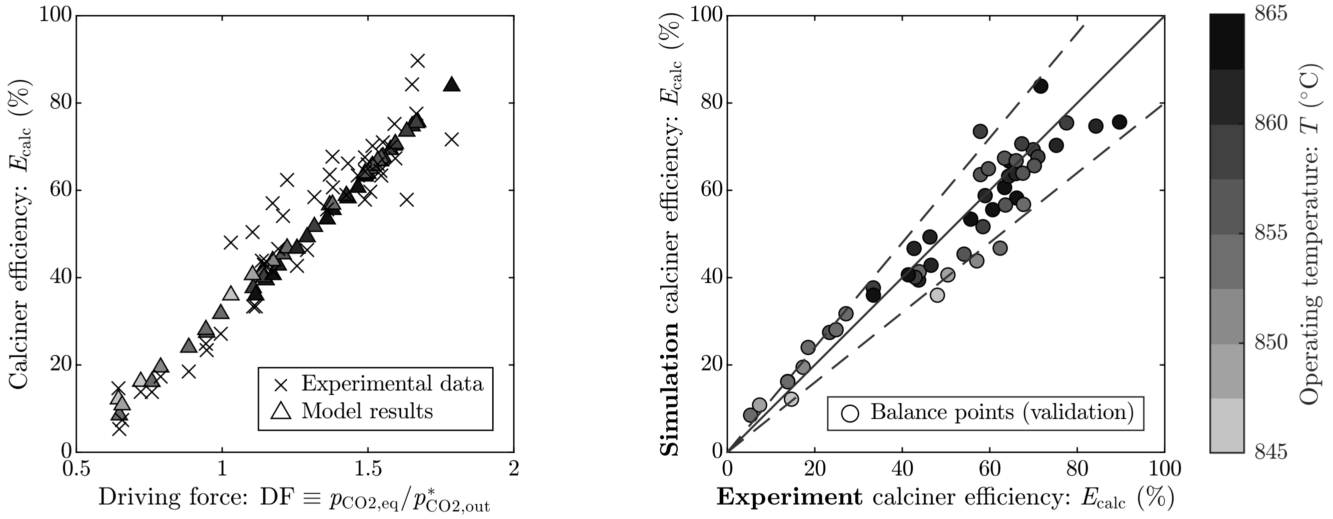

Fig. 8. Model validation using results from pilot tests at the 300-kW$_{\mathrm{th}}$ pilot plant at TU Darmstadt. The dependence of the calciner efficiency (E_{calc}) on DF (left) and the parity plot (right) show agreement between the model and the empirical results. The broken lines in the party plot (right) indicate a 20 % deviation from the experimental values.

scenarios, τ becomes a limiting factor at about $\tau \approx 1$ min, where the calcination efficiency is already higher than 95 %. Consequently, this parameter can be safely ignored for $\tau > 60$ s. The influence of τ on E_{calc} is further discussed in Section 5.4.

Previous studies [20] fit the calcination efficiency of pilot tests with τ_{act}. However, as discussed in Section 3.3, DF is a more appropriate parameter to derive correlations. The data from the IHCaL pilot tests (see Section 2.2) was fit for τ_{act} (Fig. 7, left) and DF (Fig. 7, right). The correlation in Fig. 7 (left) is only valid for our pilot plant operation at the operating temperature of the campaign. In contrast, the correlation of Fig. 7 (right) is more general and applicable for different operating conditions and different plant sizes. The model developed in this work allows to obtain more precise correlations for different operating temperatures.

5.3. Validation

Validating our model across various operating parameters is essential to assess its applicability. Consequently, we compared the model predictions with the results from two pilot plants.

5.3.1. 300-kW$_{th}$ IHCaL pilot plant

The first validation, using data from the IHCaL pilot plant (see Section 2.2), is illustrated in Fig. 8. Fig. 8 (left) illustrates the variation of the calciner efficiency (E_{calc}) with the driving force (DF). Here, the predictions of the calciner model are compared with the values obtained from experimental data. Fig. 8 (right) is a parity plot of E_{calc} comparing the simulation results with those from experimental data. The model predictions agree with the empirical values.

5.3.2. 1-MW$_{th}$ oxy-fired CaL pilot plant

The second validation using data from the oxy-fired pilot plant (see Section 2.3) is discussed in this section. Ströhle et al. [72] analyzed the performance of a calciner during long-term CO_2 capture from flue gases obtained through the combustion of pulverized coal. Compared to the experiments used in Section 5.3.1, their operating conditions included higher temperatures and much lower particle residence times. Due to the higher dispersion of the empirical values, another approach was used for the validation. This approach consisted in comparing the experimental values with the results obtained from many runs of the model with randomly generated input variables considering the reported operating ranges (see Table 1). For the independent variables (T and τ_{act}), a uniform distribution was used. The rest of the inputs were generated with a normal distribution trimmed at the extremes to limit the values to those of the operating ranges.

The results of the validation with the experimental results from the 1-MW$_{th}$ CFB plant are reported in Fig. 9. The values of τ_{act} are ca. 10 times smaller than those of the indirectly heated plant (cf. Fig. 7, left). However, there is a similar tendency, indicating the inaccuracy of using τ_{act} as the main correlation parameter for E_{calc}. Furthermore, increasing only the residence time (e.g., 100 times, see Figure S.6) does not change the model's predictions.

In Fig. 9, the results from the model runs are plotted alongside the pilot results reported by Ströhle et al. [72]. The model predictions align reasonably well with empirical values. Due to the random inputs used in the simulations, the model results exhibit dispersion, with most points aligning in an exponential-like form similar to the experimental results values.

5.4. Assessment and optimization

In this section, we assess the calciner performance for different operating conditions and discuss calciner optimization. For this purpose, we use the calciner model that has been developed and validated in this study. Since there are several variables involved in our model, we use a stochastic approach including only the ranges of variation which are relevant for the different modes of operation. Four scenarios are considered for the assessment: (I) pilot-scale (300 kW$_{th}$) indirectly heated calciner (IHCaL), (II) pilot-scale (1 MW$_{th}$) oxy-fired calciner (CaL), (III) commercial-scale indirectly heated calciner (IHCaL), and (iv) commercial-scale oxy-fired calciner (CaL). The reactor types are bubbling fluidized bed (BFB) for the IHCaL scenarios (I and III) and circulating fluidized bed (CFB) for the oxy-fired CaL scenarios (II and IV). For the stochastic analysis, the inputs are variated randomly using a uniform distribution. The distribution boundaries and the main features of the scenarios are reported in Table 3. The operating boundaries are set according to the operating conditions and the geometries of the pilot plants [15,72]. For the oxy-fired CaL plants, the volume ratio of active particles (ξ) is in the range of 0.8–1.0 to account for inerts in the solid sorbent loop [96]. In contrast, for IHCaL, we set $\xi = 1$, corresponding to the high purity of the sorbent due to the absence of combustion in the calciner [11]. The height of the commercial BFB facilities is assumed to be the same as that of the IHCaL pilot plant (see Section 2.2) to avoid excessive pressure drops. The height of the oxy-fired commercial calciner is 30–50 m, according to typical CFB reactor heights for industrial facilities [54]. For the reactor cross-sections we assume an equivalent reactor diameter of 2–20 m for the CFB, and a depth of 5–100 m for the BFB, with a width of 3 m corresponding to 6-meter-long heat pipes [22]. The CO_2 inlet partial pressures ($p_{\mathrm{CO2,in}}$) of the commercial facilities are 50–100 kPa and 0–100 kPa for scenarios III and IV, corresponding to exhaust gas recirculation (EGR) with oxy-fuel combustion, and EGR with addition of steam, respectively. The

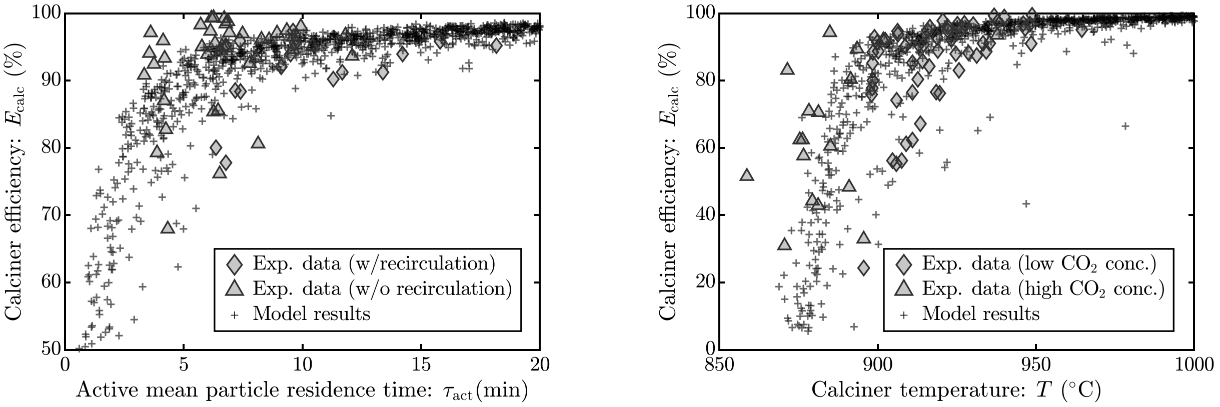

Fig. 9. Model validation with results from the 1-MW$_{th}$ oxy-fired pilot plant at TU Darmstadt: variation of the calciner efficiency with the active time (τ_{act}) for operating points with and without sorbent circulation (left), and for low CO_2 concentration ($y_{\mathrm{CO2,out}} = 43$ vol%) and high CO_2 concentration ($y_{\mathrm{CO2,out}} = 66$ vol%) (right). Experimental values from [72]. No. of model runs: 1000. Standard deviation for the normal distribution: $\sigma = 0.1$.

Table 3
Features and boundaries for the scenarios considered in the stochastic assessment.

		Scenario				
		I	II	III	IV	Unit
Main features						
Reactor type		BFB	CFB	BFB	CFB	–
Calciner heat input		Indirect	Oxy-fuel	Indirect	Oxy-fuel	–
Fluidization		Air	O_2 + EGR	H_2O + EGR	O_2 + EGR	–
Scale		300 kW_{th} (pilot)	1 MW_{th} (pilot)	Commercial	Commercial	–
Parameters						
Section area	A_t	0.315	0.126	15–300	3.1–310	m^2
Reactor height*	H	1.91	11	1.91	30–50	m
Reactor temperature	T	775–960	850–960	845–975	845–1000	°C
CO_2 inlet partial pressure	$p_{CO2,in}$	0	20–30	0–100	50–100	kPa
Volume ratio of active particles	ξ	1.0	0.8–1.0	1.0	0.8–1.0	–
Gas-solid contact efficiency	η	0.05–0.20	0.25–0.75	0.05–0.20	0.25–0.75	–
Mean solid volume fraction	ε_s	0.4–0.6	0.1–0.3	0.4–0.6	0.1–0.3	–
Inlet superficial gas velocity	$u_{0,in}$	0.02–0.10	4.0–7.0	0.02–0.10	4.0–7.0	m/s
Mean residence time	τ	120–1200	12–50	120–1200	12–50	s

*H_d for BFB, H_T for CFB.

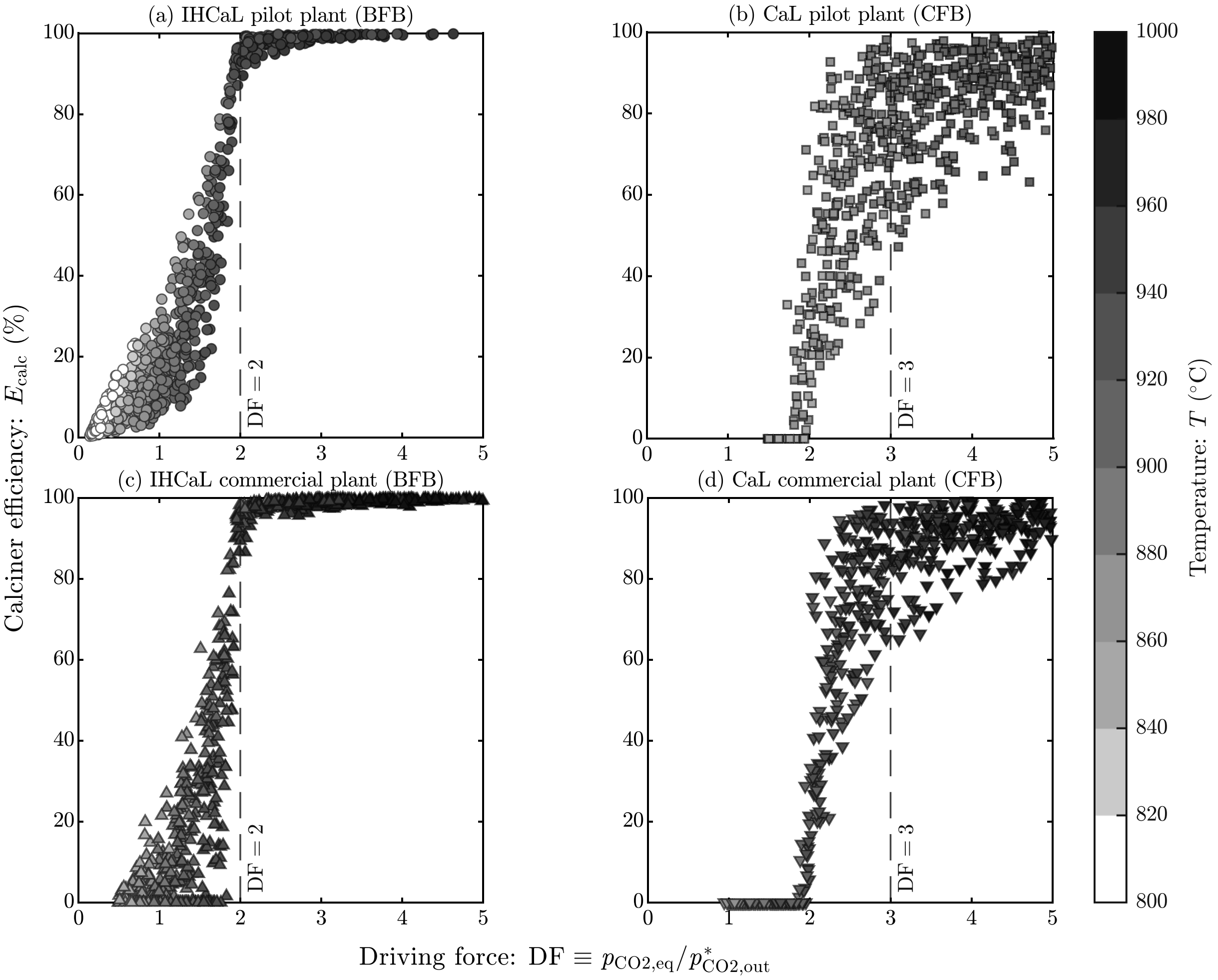

Fig. 10. Stochastic analysis of four scenarios of carbonate looping operation. The calciner performance in terms of E_{calc} is plotted against the driving force (DF), which is the main parameter determining the calcination efficiency. The color of the markers indicates the reactor temperature. No. of model runs per scenario: 1000.

temperature (T) range for commercial operation is extended and accommodated for higher temperatures to exclude irrelevant results —too low T yields $E_{calc} = 0$. Lastly, the solid volume fractions (ε_s) and gas–solid contact efficiencies (η) correspond to typical values of BFB and CFB reactors [92,97].

5.4.1. Assessment of the calciner performance

The results of the stochastic analysis are reported in Fig. 10. The model results are displayed for each scenario, for a total of 1000 runs per scenario, using randomly generated inputs within relevant operating conditions (see Table 3). Each sub-figure corresponds to one of the four scenarios. The plots illustrate the variation of the calciner efficiency

(E_{calc}) with the driving force (DF). Each marker represents one model run. The color of the markers indicates the operating temperature according to the color bar on the right. Due to the lower CO_2 concentration in pilot plant operation (Fig. 10.a–b), higher calcination efficiencies can be achieved at lower temperatures. This explains the lower operating temperatures for the pilot plants (see also Table 3).

Fig. 10.a and Fig. 10.c correspond to the pilot plant and the commercial-scale IHCaL scenarios. Due to the high residence time of the bubbling fluidized bed (BFB), the dispersion of the results is relatively low. This is particularly true for the cases that yield high performance ($E_{calc} > 90$ %). A distinct threshold for the driving force is observed at approximately DF = 2, beyond which the calciner exhibits high E_{calc} across all potential inputs for the IHCaL facilities. The notable correspondence between the model runs of Fig. 10.a and the experimental results in Fig. 7 (right) constitutes additional evidence for the existence of the threshold at DF = 2. Lastly, there is a connection between the threshold and the observations from TGA tests (see Fig. 4).

The oxy-fired CaL facilities exhibit high dispersion in the region of good performance (see Fig. 10.b and Fig. 10.d). This dispersion arises because particle residence times (τ) are short enough to reduce the calciner efficiency. For commercial oxy-fired CaL facilities, DF is insufficient as a design criterion; the active time (τ_{act}) should also be considered, as discussed in Section 5.4.2.

5.4.2. *Optimal design of a commercial calciner*

In this section, we present a three-step guideline to design a calciner. The design steps are: (i) select the type of reactor (oxy-fired CFB or indirectly heated BFB), (ii) adjust the mean residence time (for oxy-fired CFB) or the steam ratio (for indirectly heated BFB), and (iii) obtain the optimum design temperature (*T*).

Greco-Coppi et al. [55] evaluated the influence of the calciner on the carbonator efficiency for different operating conditions. From their work, it can be concluded that X_{calc} should be limited to 0.01 to achieve sufficient CO_2 capture. Assuming $X_{carb} \approx 0.1$ yields a calcination performance requirement of $E_{calc} \approx 90$ %. We assume this optimization target for the calciner design.

Indirectly heated BFB calciner (IHCaL)

The performance of a commercial IHCaL calciner for relevant operating conditions is illustrated in Fig. 10.c. As explained before, a high-performance design should aim for DF $\geq$ 2. Higher DF implies higher operating temperatures, which increase heat losses through sorbent heating and create tougher conditions for the heat-pipes heat exchanger. Therefore, it is desirable to minimize DF. Thus, the optimal design satisfies DF = 2.

The variation of the driving force (DF) with the reactor temperature (*T*) is illustrated in Fig. 11, depicting 400 model runs using pilot and commercial IHCaL input boundaries (see Table 3). The values are distributed to the left of a limit that corresponds with 100 %–CO_2 fluidization. This limit is calculated by increasing $p_{CO2,in}$ to the total pressure *p*. Taking the limit in Eq. (12) yields a driving force that only depends on *T* and *p*:

$$\lim_{p_{CO2,in} \to p} \mathrm{DF} = p_{CO2,eq} \Big/ p \qquad (43)$$

The continuous line of Fig. 11 (left) corresponds to the limit defined by Eq. (43). By intersecting this curve with the optimization target DF = 2, the optimal temperature for the calciner operation under pure-CO_2 conditions is determined: $T = 947$ °C. In the absence of steam and with only recirculated CO_2 for the fluidization, this temperature optimizes the calciner's performance.

To lower operating temperatures, it is necessary to use steam for the fluidization of the calciner. The steam requirement in terms of steam ratio (SR) for different operating temperatures is illustrated in Fig. 11 (right). Here, DF = 2 for all the calculated points. To generate Fig. 11 (right), the calciner model was run 1000 times for each partial pressure. The fresh steam input is calculated considering exhaust gas recirculation (EGR). The following equation, derived from a molar flow balance, is used for this purpose:

$$F_{steam}^{fresh} = F_{inlet}\left(1 - p_{CO2}^{in} / p_{CO2}^{out}\right) \qquad (44)$$

The rest of the input parameters are varied randomly within the boundaries of Table 3, scenario III. The steam requirement is independent of the amount of CO_2 recirculated (EGR). The amount of EGR depends on the free gas velocity (u_0) throughout the reactor to establish the fluidized bed. The design point can be selected using Fig. 11 (right).

In summary, the following simple rules should be followed when designing a commercial IHCaL BFB calciner. If fluidization is achieved only with CO_2 recirculation (no steam), set $T = 950$ °C. To lower the operating temperature, use steam with the steam ratio (SR) from Fig. 11 (right). Exhaust gas recirculation (EGR) can be used to increase the fluidization velocity (u_0). Some possible set points are $T = 900$ °C with SR = 0.4 kg_{H2O}/kg_{CO2}, and $T = 925$ °C with SR = 0.2 kg_{H2O}/kg_{CO2}. The optimization rule (DF = 2) can be checked with Eq. (12). The design process of an IHCaL calciner is summarized in Fig. 13 (right).

Oxy-fired CFB calciner (CaL)

Contrary to the IHCaL commercial facilities, the oxy-fired commercial plants exhibit high dispersion of calciner performance for high

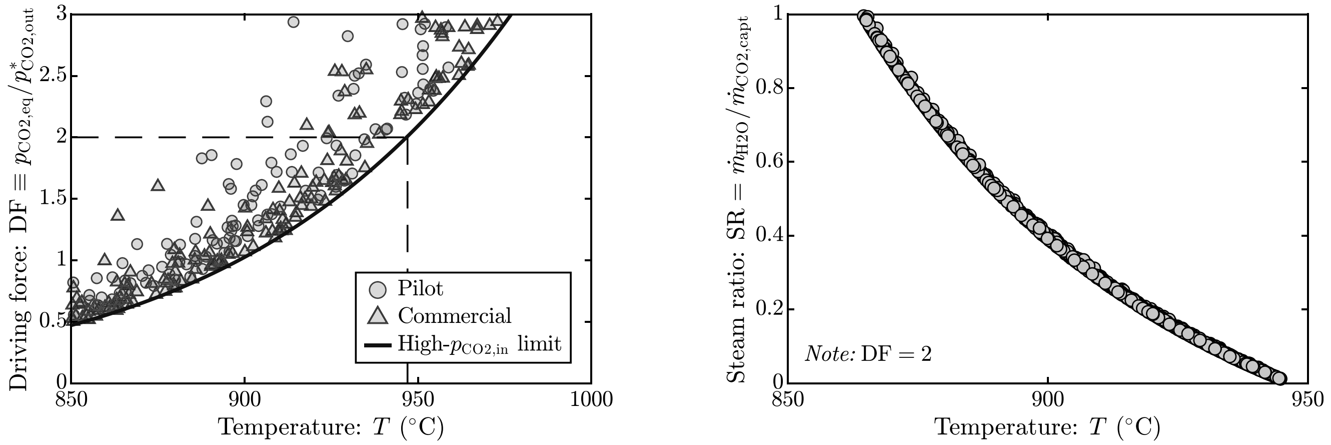

Fig. 11. Influence of the operating temperature (T) in the performance of the IHCaL BFB calciner. The results on the left correspond to the influence on the driving force (DF) based on 400 stochastic runs of the model using the pilot-scale and commercial-scale boundaries of Table 3. The high-$p_{CO2,in}$ limit is calculated with Eq. (43). The steam requirement per CO_2 captured at different operating temperatures to achieve high performance (DF = 2) is illustrated on the right, using random inputs within the boundaries of Table 3 (scenario III) (5000 model runs).

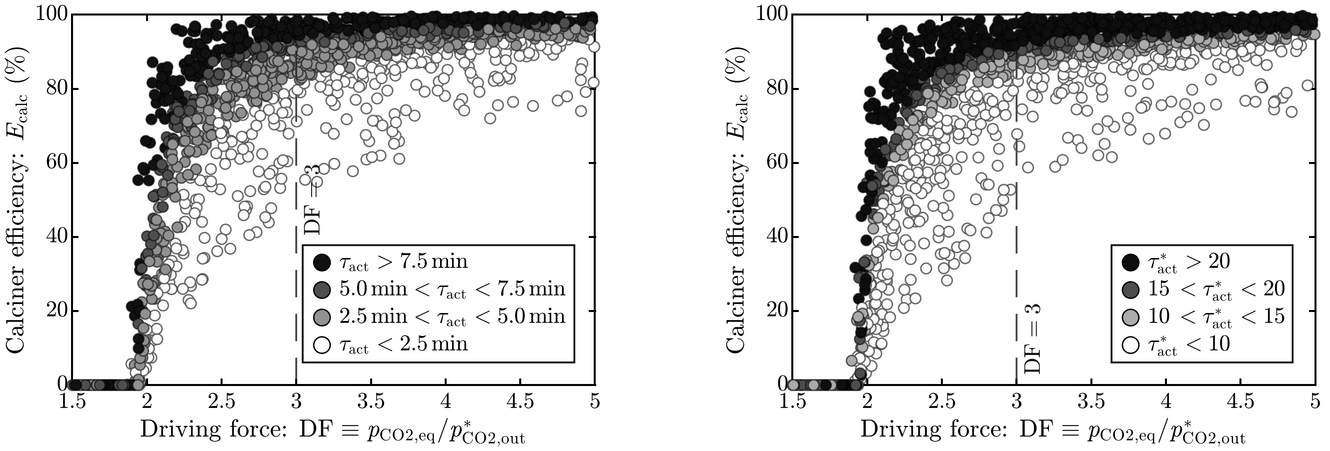

Fig. 12. Calciner efficiency for (a) variable driving force and active time (τ_{act}), and (b) variable driving force and dimensionless active time (τ^*_{act}). The results are categorized into groups of different τ_{act}. For $\tau_{\mathrm{act}} > 5$ and $\tau^*_{\mathrm{act}} > 15$, a driving force threshold becomes clear. The results were obtained using our calciner model with randomly generated inputs in the boundaries of Table 3 (scenario IV). No. of model runs: 5000.

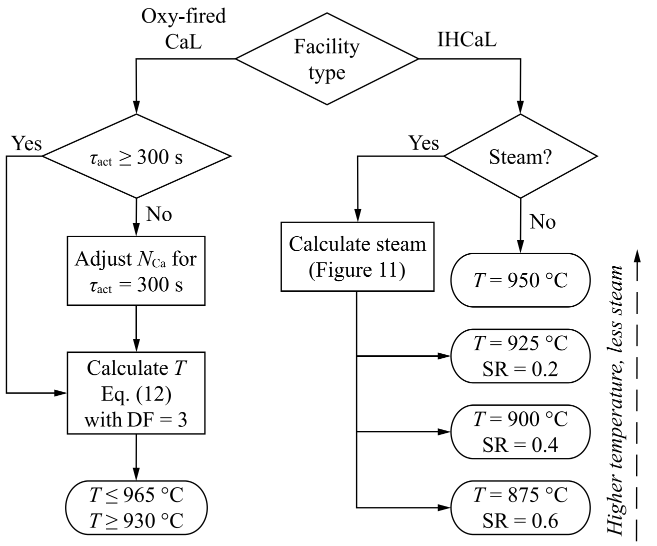
Oxy-fired CaL
Facility type
IHCaL
Yes
$\tau_{\mathrm{act}} \geq 300$ s
No
Adjust N_{Ca} for $\tau_{\mathrm{act}} = 300$ s
Calculate T Eq. (12) with DF = 3
$T \leq 965$ °C $T \geq 930$ °C
Yes
Steam?
No
Calculate steam (Figure 11)
$T = 950$ °C
$T = 925$ °C SR = 0.2
$T = 900$ °C SR = 0.4
$T = 875$ °C SR = 0.6
Higher temperature, less steam

Fig. 13. Flow chart for the design of a calciner for CO_2 capture using carbonate looping (CaL) technology.

values of DF. This difficulty can be solved by reintroducing the active time (τ_{act}) or the dimensionless active time (τ^*_{act}).

Fig. 12.a illustrates the variation of E_{calc} with DF, categorizing the active time (τ_{act}) of each set of inputs in four groups. From this diagram, it becomes clear that τ_{act} is causing the dispersion of the data. Once τ_{act} becomes higher than 5 min, a driving force threshold appears. Something similar had already been anticipated by Ströhle et al. [72], who concluded that a minimum τ_{act} of 6 min was required in pilot plant operations to obtain calciner efficiencies of 90 % or more. The threshold that marks the onset of high-performance calciner operation ($E_{\mathrm{calc}} > 90$ %) is DF = 3. For the relevant operating conditions, this is achieved with T in the range of 930–965 °C. The exact value of T for any specific set of inputs can be calculated by setting DF = 3 in Eq. (12). Fig. 12.b illustrates the variation of the calciner efficiency with the dimensionless active time (τ^*_{act}). Our results in terms of τ_{act} depend on the type of sorbent, but the conclusions regarding τ^*_{act} are valid for sorbents with different calcination kinetics.

From the above discussion, the pathway for the design of an oxy-fired CFB calciner can be established (see Fig. 13, left). Firstly, the *sine qua non* condition of $\tau_{\mathrm{act}} \geq 5$ min (or more generally, $\tau^*_{\mathrm{act}} > 15$) should be verified. Otherwise, the inventory (N_{Ca}) should be increased to achieve a minimum τ_{act} of 5 min. Secondly, calculate T by setting DF = 3 in Eq. (12). For realistic operating conditions, T will be in the range 930–965 °C.

Generalized approach

We use the dimensionless active time (τ^*_{act}, see Eq. (13)) to achieve a more generalized prediction of calciner performance. The dimensionless parameter τ^*_{act} accounts for the mean particle residence time relative to the sorbent kinetics, making our results applicable across a broader range of operating conditions, including various sorbents. Fig. 14 illustrates the influence of DF and τ^*_{act} on the calciner efficiency (E_{calc}). For calciners with a high specific inventory ($\tau^*_{\mathrm{act}} > 100$), DF = 2 provides optimal performance. For lower specific inventories, $\tau^*_{\mathrm{act}} = 15$ is effective with DF = 3. However, additional optimal combinations are possible (see Fig. 14, right). In general, the lower the τ^*_{act}, the higher the DF required to achieve high calciner efficiency.

5.5. Model scope and further design considerations

In this study, we neglected the influence of the particle size in the particle model. This implies assuming that external diffusion effects and heat transfer are not rate limiting, which is supported by sufficient empirical data, as previously discussed (e.g., [62,82]). However, for larger particles (> 2 mm), such effects may become significant and should be considered before applying our model and conclusions. To address this, our model should be extended to account for mass and heat transfer effects in particle kinetics.

The kinetic model constants (see Table 2) were obtained for a specific limestone type (Messinghausen) over a narrow temperature range (850–875 °C), corresponding to our pilot tests. Given the variability in reaction rates due to limestone composition reported in previous studies [62,65], we recommend adjusting the kinetic constants to match the sorbent used in each specific process when applying our model in calciner design. Similarly, it is advisable to vary the TGA test temperatures within a range relevant to the design.

We assumed that steam has no effect on calcination other than reducing the CO_2 partial pressure. However, previous studies suggest that steam has a catalytic effect on the calcination of $CaCO_3$ [98,99]. Further research should evaluate whether this catalytic effect significantly impacts the design temperature of CaL calciners by adapting our particle sub-model to incorporate the influence of steam on the kinetic parameters. Similarly, other proposed strategies for decreasing the calciner's operating temperature may also be integrated in our model [66].

In Section 4, we explain that our reactor sub-model model neglects

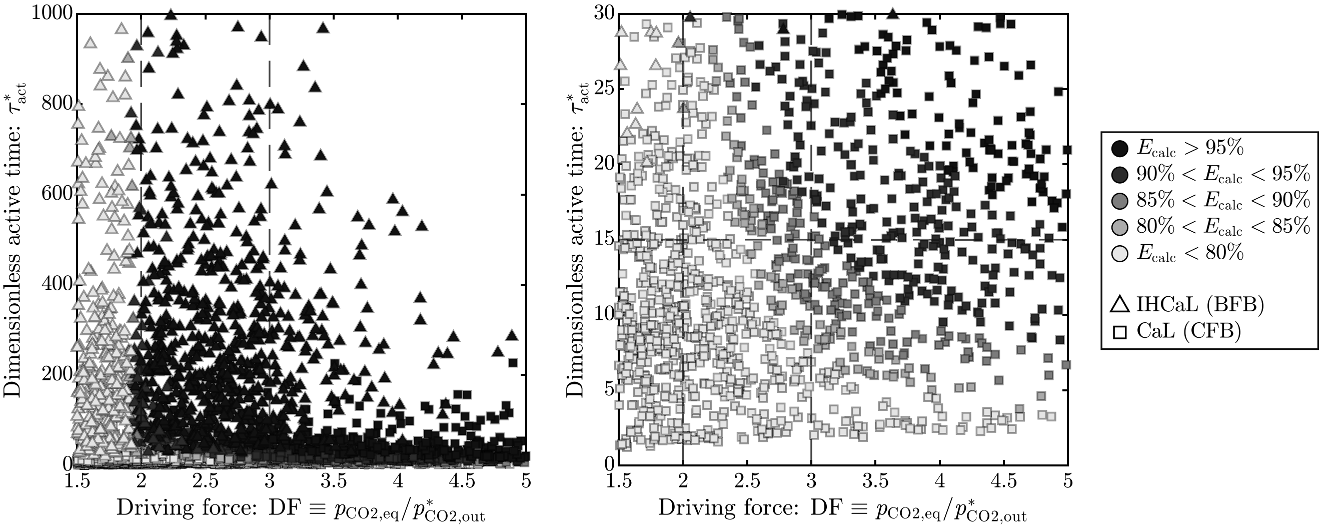

Fig. 14. Calciner performance (E_{calc}) for varying DF and τ^*_{act}, using our calciner model and the scenarios III and IV of Table 3. The two sub-figures show the same results but use different scales for τ^*_{act}. No. of model runs: 5000.

temperature gradients. This assumption is justified by the good particle mixing in CFB operating, and the high inventory of the BFB. However, strong gradients may lead to increased deactivation of the sorbent due to the recarbonation occurring in the calciner at low temperatures (cf. [55,100]). The calciner design and operation should avoid local conditions of p_{CO2} and T corresponding to the carbonation region in the equilibrium diagram (see Fig. 2). Furthermore, circulating fluidized beds, which have lower specific inventories, may experience performance issues due to lower temperatures in certain sections of the reactor. In that case, the extension of our model to consider the influence of the temperature profile inside of the reactor may be useful. One approach to achieve this is presented in the work of Ylätalo et al. [57].

In our study, we used an *indirectly heated calciner* and an *oxy-fired calciner* as the basis for the case analysis. We assumed the former operates as a BFB and the latter as a CFB, based on the most relevant pilot plants [20,37,38]. To evaluate alternative configurations, the boundaries of Table 3 should be tuned accordingly, and the model rerun. Depending on the reactor type, the reactor sub-model in Section 4.3 may also need adjustment.

6. Conclusions

Within this work, a novel model of a carbonate looping (CaL) calciner has been developed and validated. This model is composed of a particle sub-model and a reactor sub-model. The particle reaction modeling is based on the results of thermogravimetric analysis (TGA) on relevant operating conditions for CO_2 capture. A shrinking-volume-type mechanism fits the calcination rate of the solid sorbents. The dependency on CO_2 partial pressure is first-order, with a correction factor modeled with a Freundlich adsorption isotherm. The kinetic and adsorption constants follow an Arrhenius-type dependency with temperature. The particle sub-model fits the TGA data accurately and the fitting constants are consistent with the literature values. A particle residence time distribution (RTD) is used to account for the different residence times of the particles in the reactor. For the reactor sub-model, a one-dimensional discretization of the reactor in the vertical direction is performed to include variations of CO_2 concentration throughout the height of the reactor. Our calciner model has been validated with experimental results from two pilot plants with different operating conditions.

The *dimensionless driving force* (DF) introduced in this study provides a better fit for empirical results than other previously proposed parameters. For the indirectly heated calciner, the main results are predicted by a simple fitting of DF. For the oxy-fired CaL, the performance of the reactor is determined by DF and the mean particle residence time.

An important outcome of this work is a three-step guideline to design CaL calciners for commercial operation, which has been developed using stochastic methods. This guideline is suitable for a wide range of operating conditions and does not require iterative or complex calculations. For indirectly heated calciners, the operating temperature should be set to 950 °C to obtain sufficient sorbent regeneration under pure CO_2 fluidization. The temperatures can be reduced using steam as fluidization agent by more than 50 °C. For oxy-fired calciners, a minimum active time (τ_{act}) of five minutes should be guaranteed, and the optimal operating temperature is found by setting $\text{DF} = 3$.

A more generalized design approach has been introduced, which involves utilizing the *dimensionless driving force* (DF) and the *dimensionless active time* (τ^*_{act}). This approach enables calciner design for CaL systems without the need to run the full model. Furthermore, these dimensionless numbers are useful for assessing experimental data. The scope of our general guidelines is supported by validation performed using results from pilot tests in two different facilities. Further research should examine whether our conclusions are also applicable to different sorbents and operating conditions.

Our results support the technical feasibility of commercial IHCaL plants utilizing heat pipes. The next step in developing CaL technology requires scaling up the technology. For the specific case of the indirectly heated calciner, a demonstrator operating under industrially relevant conditions (steam and/or CO_2 fluidization) is a necessary step before commercialization. The model developed in this work could serve as the basis for the design of such a demonstrator.

Funding sources

The work leading to these results have received funding through the ACT program (Accelerating CCS Technologies, Horizon 2020 Project No. 691712) within the ANICA project (ACT Project No. 299653). Financial contributions were made from the German Federal Ministry of Economic Affairs and Climate Action (BMWK Project No. 03EE5025).

CRediT authorship contribution statement

Martin Greco-Coppi: Conceptualization, Methodology, Data curation, Software (MATLAB), Validation, Formal analysis, Investigation, Visualization, Writing – original draft, Writing – review & editing.

Jochen Ströhle: Writing – review & editing, Supervision, Project administration, Funding acquisition. **Bernd Epple:** Supervision.

Declaration of competing interest

Martin Greco-Coppi, Jochen Ströhle, and Bernd Epple report financial support was provided by the German Federal Ministry for Economic Affairs and Climate Action. Martin Greco-Coppi reports limestone samples were provided by Lhoist Germany Rheinkalk GmbH. Martin Greco-Coppi, Jochen Ströhle, and Bernd Epple have patent "Apparatus and Method for Producing Lime" (No. 10 2023 114 354.9) pending to Technical University of Darmstadt and Rheinkalk GmbH. Martin Greco-Coppi, Jochen Ströhle, and Bernd Epple have patent "Apparatus and Method for Producing Lime and Cement" (No. 10 2024 109 181.9) pending to Technical University of Darmstadt.

Acknowledgements

The authors wish to acknowledge Yassin Azbairi for assisting with the TGA analysis, Alina Greco-Coppi for polishing the language of this paper, and Diethelm Walter for providing the Messinghausen limestone samples.

Appendix A. Supplementary material

Supplementary data to this article can be found online at https://doi.org/10.1016/j.fuel.2024.133931.

Data availability

Data will be made available on request.

References

[1] Lackner KS, Brennan S, Matter JM, Park A-HA, Wright A, van der Zwaan B. The urgency of the development of CO_2 capture from ambient air. Proc Natl Acad Sci USA 2012;109(33):13156–62. https://doi.org/10.1073/pnas.1108765109.

[2] Wu C, Huang Q, Xu Z, Sipra AT, Gao N, Vandenberghe LPS, et al. A comprehensive review of carbon capture science and technologies. 100178 Carbon Capture Sci Technol 2024;11. https://doi.org/10.1016/j.ccst.2023.100178.

[3] Fernández JR. An overview of advances in CO_2 capture technologies. Energies 2023;16(3):1413. https://doi.org/10.3390/en16031413.

[4] IEA. CCUS in Clean Energy Transitions; 2020.

[5] Liang Z, Rongwong W, Liu H, Fu K, Gao H, Cao F, et al. Recent progress and new developments in post-combustion carbon-capture technology with amine based solvents. Int J Greenhouse Gas Control 2015;40:26–54. https://doi.org/10.1016/j.ijggc.2015.06.017.

[6] Abanades JC, Arias B, Lyngfelt A, Mattisson T, Wiley DE, Li H, et al. Emerging CO_2 capture systems. Int J Greenhouse Gas Control 2015;40:126–66. https://doi.org/10.1016/j.ijggc.2015.04.018.

[7] Shimizu T, Hirama T, Hosoda H, Kitano K, Inagaki M, Tejima K. A twin fluid-bed reactor for removal of CO_2 from combustion processes. Chem Eng Res Des 1999; 77(1):62–8. https://doi.org/10.1205/026387699525882.

[8] Blamey J, Anthony EJ, Wang J, Fennell PS. The calcium looping cycle for large-scale CO_2 capture. Prog Energy Combust Sci 2010;36(2):260–79. https://doi.org/10.1016/j.pecs.2009.10.001.

[9] Lu H, Smirniotis PG. Calcium oxide doped sorbents for CO_2 uptake in the presence of SO_2 at high temperatures. Ind Eng Chem Res 2009;48(11):5454–9. https://doi.org/10.1021/ie900162k.

[10] Ströhle J, Galloy A, Epple B. Feasibility study on the carbonate looping process for post-combustion CO_2 capture from coal-fired power plants. Energy Procedia 2009;1(1):1313–20. https://doi.org/10.1016/j.egypro.2009.01.172.

[11] Greco-Coppi M, Hofmann C, Ströhle J, Walter D, Epple B. Efficient CO_2 capture from lime production by an indirectly heated carbonate looping process. Int J Greenhouse Gas Control 2021;112:103430. https://doi.org/10.1016/j.ijggc.2021.103430.

[12] De Lena E, Arias B, Romano MC, Abanades JC. Integrated calcium looping system with circulating fluidized bed reactors for low CO_2 emission cement plants. Int J Greenhouse Gas Control 2022;114:103555. https://doi.org/10.1016/j.ijggc.2021.103555.

[13] Dean C, Hills T, Florin N, Dugwell D, Fennell PS. Integrating calcium looping CO_2 capture with the manufacture of cement. Energy Procedia 2013;37(6):7078–90. https://doi.org/10.1016/j.egypro.2013.06.644.

[14] Martínez I, Murillo R, Grasa G, Abanades JC. Integration of a Ca-looping system for CO_2 capture in an existing power plant. Energy Procedia 2011;4:1699–706. https://doi.org/10.1016/j.egypro.2011.02.043.

[15] Haaf M, Hilz J, Peters J, Unger A, Ströhle J, Epple B. Operation of a 1 MW_{th} calcium looping pilot plant firing waste-derived fuels in the calciner. Powder Technol 2020;372:267–74. https://doi.org/10.1016/j.powtec.2020.05.074.

[16] Ströhle J, Junk M, Kremer J, Galloy A, Epple B. Carbonate looping experiments in a 1MW_{th} pilot plant and model validation. Fuel 2014;127:13–22. https://doi.org/10.1016/j.fuel.2013.12.043.

[17] Arias B, Alvarez Criado Y, Méndez A, Marqués P, Finca I, Abanades JC. Pilot testing of calcium looping at TRL7 with CO_2 capture efficiencies toward 99%. Energy Fuels 2024;38(15):14757–64. https://doi.org/10.1021/acs.energyfuels.4c02472.

[18] Diego ME, Arias B. Impact of load changes on the carbonator reactor of a 1.7 MW_{th} calcium looping pilot plant. 106307 Fuel Process Technol 2020;200. https://doi.org/10.1016/j.fuproc.2019.106307.

[19] Greco-Coppi M, Seufert PM, Hofmann C, Rolfe A, Huang Y, Rezvani S, et al. Efficient CO_2 capture from lime plants: techno-economic assessment of integrated concepts using indirectly heated carbonate looping technology. Carbon Capt. Sci. Technol. 2024;11. https://doi.org/10.1016/j.ccst.2023.100187.

[20] Reitz M, Junk M, Ströhle J, Epple B. Design and operation of a 300 kW_{th} indirectly heated carbonate looping pilot plant. Int J Greenhouse Gas Control 2016;54: 272–81. https://doi.org/10.1016/j.ijggc.2016.09.016.

[21] Höftberger D, Karl J. Self-fluidization in an indirectly heated calciner. Chem Eng Technol 2013;36(9):1533–8. https://doi.org/10.1002/ceat.201300111.

[22] Greco-Coppi M, Hofmann C, Walter D, Ströhle J, Epple B. Negative CO_2 emissions in the lime production using an indirectly heated carbonate looping process. Mitig Adapt Strateg Glob Change 2023;28(6). https://doi.org/10.1007/s11027-023-10064-7.

[23] Junk M, Reitz M, Ströhle J, Epple B. Thermodynamic evaluation and cold flow model testing of an indirectly heated carbonate looping process. Chem Eng Technol 2013;36(9):1479–87. https://doi.org/10.1002/ceat.201300019.

[24] IEA. Energy Technology Perspectives 2020 - Special Report on Carbon Capture Utilisation and Storage: CCUS in clean energy transitions. Paris: OECD; OECD Publishing; 2020.

[25] Chemical Engineering. The Chemical Engineering Plant Cost Index. [accessed July 12, 2024]; Available from: https://www.chemengonline.com/pci-home.

[26] Mignard D. Correlating the chemical engineering plant cost index with macro-economic indicators. Chem Eng Res Des 2014;92(2):285–94. https://doi.org/10.1016/j.cherd.2013.07.022.

[27] Junk M, Reitz M, Ströhle J, Epple B. Technical and economical assessment of the indirectly heated carbonate looping process. J Energy Res Technol 2016;138(4). https://doi.org/10.1115/1.4033142.

[28] Rolfe A, Huang Y, Haaf M, Rezvani S, McIlveen-Wright D, Hewitt NJ. Integration of the calcium carbonate looping process into an existing pulverized coal-fired power plant for CO2 capture: techno-economic and environmental evaluation. Appl Energy 2018;222:169–79. https://doi.org/10.1016/j.apenergy.2018.03.160.

[29] Gardarsdottir S, de Lena E, Romano MC, Roussanaly S, Voldsund M, Pérez-Calvo J-F, et al. Comparison of technologies for CO_2 capture from cement production—Part 2: Cost analysis. Energies 2019;12(3):542. https://doi.org/10.3390/en12030542.

[30] De Lena E, Spinelli M, Gatti M, Scaccabarozzi R, Campanari S, Consonni S, et al. Techno-economic analysis of calcium looping processes for low CO_2 emission cement plants. Int J Greenhouse Gas Control 2019;82:244–60. https://doi.org/10.1016/j.ijggc.2019.01.005.

[31] Bazooyar B, Nabavi A, Clough P, Anthony EJ, Manovic V. Towards decarbonisation of sugar refineries by calcium looping: process integration, energy optimisation and technoeconomic assessment. 118597 Energ Conver Manage 2024;314. https://doi.org/10.1016/j.enconman.2024.118597.

[32] Yin J, Li C, Paicu G, Su S. Techno-economic assessment of retrofitting indirect-heated calcium looping using coal and biomass as fuels into an existing cement plant for CO_2 capture. 205236 Gas Sci Eng 2024;123. https://doi.org/10.1016/j.jgsce.2024.205236.

[33] Tan Y, Liu W, Zhang X, Wei W, Wang S. Conventional and optimized testing facilities of calcium looping process for CO_2 capture: a systematic review. 130337 Fuel 2024;358. https://doi.org/10.1016/j.fuel.2023.130337.

[34] Hornberger M, Moreno J, Schmid M, Scheffknecht G. Experimental investigation of the carbonation reactor in a tail-end calcium looping configuration for CO_2 capture from cement plants. 106557 Fuel Process Technol 2020;210. https://doi.org/10.1016/j.fuproc.2020.106557.

[35] Hawthorne C, Dieter H, Bidwe AR, Schuster A, Scheffknecht G, Unterberger S, et al. CO_2 capture with CaO in a 200 kW_{th} dual fluidized bed pilot plant. Energy Procedia 2011;4:441–8. https://doi.org/10.1016/j.egypro.2011.01.073.

[36] Dieter H, Bidwe AR, Varela-Duelli G, Charitos A, Hawthorne C, Scheffknecht G. Development of the calcium looping CO_2 capture technology from lab to pilot scale at IFK. University of Stuttgart Fuel 2014;127:23–37. https://doi.org/10.1016/j.fuel.2014.01.063.

[37] Kremer J, Galloy A, Ströhle J, Epple B. Continuous CO_2 capture in a 1-MW_{th} carbonate looping pilot plant. Chem Eng Technol 2013;36(9):1518–24. https://doi.org/10.1002/ceat.201300084.

[38] Arias B, Diego ME, Abanades JC, Lorenzo M, Diaz L, Martínez D, et al. Demonstration of steady state CO_2 capture in a 1.7MW_{th} calcium looping pilot. Int J Greenhouse Gas Control 2013;18:237–45. https://doi.org/10.1016/j.ijggc.2013.07.014.

[39] Arias B, Diego ME, Méndez A, Abanades JC, Díaz L, Lorenzo M, et al. Operating experience in la Pereda 1.7 MW_{th} calcium looping pilot. Energy Procedia 2017; 114:149–57. https://doi.org/10.1016/j.egypro.2017.03.1157.

[40] Chang M-H, Chen W-C, Huang C-M, Liu W-H, Chou Y-C, Chang W-C, et al. Design and experimental testing of a $1.9MW_{th}$ calcium looping pilot plant. Energy Procedia 2014;63:2100–8. https://doi.org/10.1016/j.egypro.2014.11.226.

[41] Hilz J, Helbig M, Haaf M, Daikeler A, Ströhle J, Epple B. Investigation of the fuel influence on the carbonate looping process in 1 MW_{th} scale. Fuel Process Technol 2018;169:170–7. https://doi.org/10.1016/j.fuproc.2017.09.016.

[42] Haaf M, Peters J, Hilz J, Unger A, Ströhle J, Epple B. Combustion of solid recovered fuels within the calcium looping process – experimental demonstration at 1 MW_{th} scale. Exp Therm Fluid Sci 2020;113:110023. https://doi.org/10.1016/j.expthermflusci.2019.110023.

[43] Magli F, De Lena E, Cremona R, Spinelli M, Alonso M, Mader N et al. Cleanker pilot test results. Cleanker Conference, March 15, 2023. 2023.

[44] Fantini M, Balocco M, Buzzi L, Canonico F, Consonni S, Cremona R, et al. Calcium looping technology demonstration in industrial environment: status of the CLEANKER pilot plant. SSRN J 2021. https://doi.org/10.2139/ssrn.3817346.

[45] Höftberger D, Karl J. The indirectly heated carbonate looping process for CO_2 capture—a concept with heat pipe heat exchanger. J Energy Res Technol 2016; 138(4). https://doi.org/10.1115/1.4033302.

[46] Reitz M, Junk M, Ströhle J, Epple B. Design and erection of a 300 kW_{th} indirectly heated carbonate looping test facility. Energy Procedia 2014;63:2170–7. https://doi.org/10.1016/j.egypro.2014.11.236.

[47] Hofmann C, Greco-Coppi M, Ströhle J, Epple B. Pilot testing of the indirectly heated carbonate looping process for cement and lime plants. In: Proceedings of the 16th Greenhouse Gas Control Technologies Conference (GHGT-16) 23-24 Oct 2022 2022. https://doi.org/10.2139/ssrn.4278810.

[48] Hofmann C, Greco-Coppi M, Ströhle J, Epple B. Enhancement of a 300 kW_{th} pilot plant for testing the indirectly heated carbonate looping process for CO_2 capture from lime and cement industry. Exp Therm Fluid Sci 2024;151:111091. https://doi.org/10.1016/j.expthermflusci.2023.111091.

[49] Abanades JC. The maximum capture efficiency of CO_2 using a carbonation/calcination cycle of CaO/$CaCO_3$. Chem Eng J 2002;90(3):303–6. https://doi.org/10.1016/S1385-8947(02)00126-2.

[50] Lasheras A. Simulation of the Carbonate Looping process using a 1D fluidized bed model for the carbonator [Diplomarbeit]; 2008.

[51] Hawthorne C, Trossmann M, Galindo Cifre P, Schuster A, Scheffknecht G. Simulation of the carbonate looping power cycle. Energy Procedia 2009;1(1): 1387–94. https://doi.org/10.1016/j.egypro.2009.01.182.

[52] Alonso M, Rodríguez N, Grasa G, Abanades JC. Modelling of a fluidized bed carbonator reactor to capture CO_2 from a combustion flue gas. Chem Eng Sci 2009;64(5):883–91. https://doi.org/10.1016/j.ces.2008.10.044.

[53] Romano MC. Modeling the carbonator of a Ca-looping process for CO_2 capture from power plant flue gas. Chem Eng Sci 2012;69(1):257–69. https://doi.org/10.1016/j.ces.2011.10.041.

[54] Greco-Coppi M, Ströhle J, Epple B. A carbonator model for CO_2 capture based on results from pilot tests. Part I: Hydrodynamics and reactor model. Chem Eng J 2024;500. https://doi.org/10.1016/j.cej.2024.155119.

[55] Greco-Coppi M, Ströhle J, Epple B. A carbonator model for CO_2 capture based on results from pilot tests. Part II: Deactivation and reaction model. Chem Eng J 2024. https://doi.org/10.1016/j.cej.2024.159041.

[56] Martínez I, Grasa G, Parkkinen J, Tynjälä T, Hyppänen T, Murillo R, et al. Review and research needs of Ca-Looping systems modelling for post-combustion CO_2 capture applications. Int J Greenhouse Gas Control 2016;50:271–304. https://doi.org/10.1016/j.ijggc.2016.04.002.

[57] Ylätalo J, Parkkinen J, Ritvanen J, Tynjälä T, Hyppänen T. Modeling of the oxy-combustion calciner in the post-combustion calcium looping process. Fuel 2013; 113:770–9. https://doi.org/10.1016/j.fuel.2012.11.041.

[58] Kanellis G, Zeneli M, Nikolopoulos N, Hofmann C, Ströhle J, Karellas S, et al. CFD modelling of an indirectly heated calciner reactor, utilized for CO_2 capture, in an Eulerian framework. Fuel 2023;346:128251. https://doi.org/10.1016/j.fuel.2023.128251.

[59] Kanellis G, Stefanitsis D, Zeneli M, Nikolopoulos N, Konttinen J. Development and numerical investigation of a DDPM-KTGF model for modelling flow hydrodynamics and heat transfer phenomena in a bubbling calciner reactor. Fuel 2023;352:128960. https://doi.org/10.1016/j.fuel.2023.128960.

[60] Ding J, Gidaspow D. A bubbling fluidization model using kinetic theory of granular flow. AIChE J 1990;36(4):523–38. https://doi.org/10.1002/aic.690360404.

[61] Adnan M, Sun J, Ahmad N, Wei JJ. Verification and validation of the DDPM-EMMS model for numerical simulations of bubbling, turbulent and circulating fluidized beds. Powder Technol 2021;379:69–88. https://doi.org/10.1016/j.powtec.2020.10.041.

[62] García-Labiano F, Abad A, Diego LF de, Gayán P, Adánez J. Calcination of calcium-based sorbents at pressure in a broad range of CO_2 concentrations. Chem Eng Sci 2002;57:2381–93. https://doi.org/10.1016/S0009-2509(02)00137-9.

[63] Michel W, editor. *Wirbelschichttechnik in der Energiewirtschaft: Mit 16 Tabellen*. 1st ed. Leipzig: Dt. Verl. für Grundstoffindustrie; 1992.

[64] Martínez I, Grasa G, Murillo R, Arias B, Abanades JC. Modelling the continuous calcination of $CaCO_3$ in a Ca-looping system. Chem Eng J 2013;215–216:174–81. https://doi.org/10.1016/j.cej.2012.09.134.

[65] Martínez I, Grasa G, Murillo R, Arias B, Abanades JC. Kinetics of calcination of partially carbonated particles in a Ca-looping system for CO_2 capture. Energy Fuels 2012;26(2):1432–40. https://doi.org/10.1021/ef201525k.

[66] Han R, Wang Y, Xing S, Pang C, Hao Y, Song C, et al. Progress in reducing calcination reaction temperature of calcium-looping CO_2 capture technology: a critical review. Chem Eng J 2022;450:137952. https://doi.org/10.1016/j.cej.2022.137952.

[67] Rodríguez N, Alonso M, Abanades JC. Average activity of CaO particles in a calcium looping system. Chem Eng J 2010;156(2):388–94. https://doi.org/10.1016/j.cej.2009.10.055.

[68] Erich Netzsch GmbH & Co. Holding KG. STA 449 F3 Jupiter. [Accessed August 08, 2023]; Available from: https://analyzing-testing.netzsch.com/_Resources/Persistent/4/c/b/e/4cbe0375352415b080dab9d281329c613a551c10/STA_449_F3_Jupiter_de_web.pdf.

[69] Reitz M. *Experimentelle Untersuchung und Bewertung eines indirekt beheizten Carbonate-Looping-Prozesses*. Doctoral dissertation. 1st ed. Göttingen: Cuvillier Verlag; 2017.

[70] Galloy A, Ströhle J, Epple B. Design and operation of a 1 MW_{th} carbonate and chemical looping CCS test rig. VGB Power Tech 2011;6:64–8.

[71] Hilz J, Helbig M, Haaf M, Daikeler A, Ströhle J, Epple B. Long-term pilot testing of the carbonate looping process in 1 MW_{th} scale. Fuel 2017;210:892–9. https://doi.org/10.1016/j.fuel.2017.08.105.

[72] Ströhle J, Hilz J, Epple B. Performance of the carbonator and calciner during long-term carbonate looping tests in a 1 MW_{th} pilot plant. J Environ Chem Eng 2020;8(1):103578. https://doi.org/10.1016/j.jece.2019.103578.

[73] Barin I. Thermochemical data of pure substances. 3rd ed. Weinheim: VCH; 1995.

[74] Silcox GD, Kramlich JC, Pershing DW. A mathematical model for the flash calcination of dispersed calcium carbonate and calcium hydroxide particles. Ind Eng Chem Res 1989;28(2):155–60. https://doi.org/10.1021/ie00086a005.

[75] Weast RC. CRC Handbook of Chemistry and Physics. 66th ed. Cleveland, OH: CRC Press; 1975.

[76] Steiner LE. Introduction to chemical thermodynamics. 2nd ed. Mcgraw-hill Book Company Inc; 1948.

[77] Baker EH. The calcium oxide–carbon dioxide system in the pressure range 1—300 atmospheres. J Chem Soc 1962:464–70. https://doi.org/10.1039/JR9620000464.

[78] Duelli G, Charitos A, Diego ME, Stavroulakis E, Dieter H, Scheffknecht G. Investigations at a 10 kW_{th} calcium looping dual fluidized bed facility: Limestone calcination and CO_2 capture under high CO_2 and water vapor atmosphere. Int J Greenhouse Gas Control 2015;33:103–12. https://doi.org/10.1016/j.ijggc.2014.12.006.

[79] Fedunik-Hofman L, Bayon A, Donne SW. Kinetics of solid-gas reactions and their application to carbonate looping systems. Energies 2019;12(15):2981. https://doi.org/10.3390/en12152981.

[80] Li Z, Sun H, Cai N. Rate equation theory for the carbonation reaction of CaO with CO_2. Energy Fuels 2012;26(7):4607–16. https://doi.org/10.1021/ef300607z.

[81] Khinast J, Krammer GF, Brunner C, Staudinger G. Decomposition of limestone: the influence of CO_2 and particle size on the reaction rate. Chem Eng Sci 1996;51(4):623–34. https://doi.org/10.1016/0009-2509(95)00302-9.

[82] Dennis JS, Hayhurst AN. the effect of CO_2 on the kinetics and extent of calcination of limestone and dolomite particles in fluidised beds. Chem Eng Sci 1987;42(10): 2361–72. https://doi.org/10.1016/0009-2509(87)80110-0.

[83] Ninan KN, Krishnan K, Krishnamurthy VN. Kinetics and mechanism of thermal decomposition of insitu generated calcium carbonate. J Therm Anal 1991;37(7): 1533–43. https://doi.org/10.1007/BF01913486.

[84] Yue L, shui M, Xu Z. The decomposition kinetics of nanocrystalline calcite. Thermochim Acta 1999;335(1–2):121–6. https://doi.org/10.1016/S0040-6031(99)00174-4.

[85] Wang Y, Lin S, Suzuki Y. Study of limestone calcination with CO_2 capture: decomposition behavior in a CO_2 atmosphere. Energy Fuels 2007;21(6):3317–21. https://doi.org/10.1021/ef700318c.

[86] Valverde JM. On the negative activation energy for limestone calcination at high temperatures nearby equilibrium. Chem Eng Sci 2015;132:169–77. https://doi.org/10.1016/j.ces.2015.04.027.

[87] Fernández JR, Turrado S, Abanades JC. Calcination kinetics of cement raw meals under various CO_2 concentrations. React Chem Eng 2019;4(12):2129–40. https://doi.org/10.1039/C9RE00361D.

[88] Calvo E, Arranz MA, Letón P. Effects of impurities in the kinetics of calcite decomposition. Thermochim Acta 1990;170:7–11. https://doi.org/10.1016/0040-6031(90)80519-5.

[89] Curran GP, Fink CE, Gorin E. CO_2 acceptor gasification process. studies of acceptor properties. In: Schora FC, editor. Fuel Gasification. Washington, D.C: American Chemical Society; 1967. p. 141–65.

[90] Dai P, González B, Dennis JS. Using an experimentally-determined model of the evolution of pore structure for the calcination of cycled limestones. Chem Eng J 2016;304:175–85. https://doi.org/10.1016/j.cej.2016.06.068.

[91] Kunii D, Levenspiel O. Fluidization Engineering. 2nd ed. Elsevier; 1991. https://doi.org/10.1016/C2009-0-24190-0.

[92] Kunii D, Levenspiel O. Circulating fluidized-bed reactors. Chem Eng Sci 1997;52(15):2471–82. https://doi.org/10.1016/S0009-2509(97)00066-3.

[93] Mathews JH, Fink KD. Numerical methods using MATLAB. 3rd ed. Upper Saddle River, N.J., London: Prentice Hall; 1999.

[94] Kunii D, Levenspiel O. Fluidized reactor models.: 1. For bubbling beds of fine, intermediate, and large particles. 2. For the lean phase: freeboard and fast fluidization. Ind Eng Chem Res 1990;29(7):1226–34. https://doi.org/10.1021/ie00103a022.

[95] Kunii D, Levenspiel O. The K-L reactor model for circulating fluidized beds. Chem Eng Sci 2000;55(20):4563–70. https://doi.org/10.1016/S0009-2509(00)00073-7.

[96] Haaf M, Stroh A, Hilz J, Helbig M, Ströhle J, Epple B. Process modelling of the calcium looping process and validation against 1 MW_{th} pilot testing. Energy Procedia 2017;114:167–178. https://doi.org/10.1016/j.egypro.2017.03.1159.

[97] Bi XT, Grace JR. Flow regime diagrams for gas-solid fluidization and upward transport. Int J Multiph Flow 1995;21(6):1229–36. https://doi.org/10.1016/0301-9322(95)00037-X.

[98] Silakhori M, Jafarian M, Chinnici A, Saw W, Venkataraman M, Lipiński W, et al. Effects of steam on the kinetics of calcium carbonate calcination. Chem Eng Sci 2021;246:116987. https://doi.org/10.1016/j.ces.2021.116987.

[99] Deng Y, Liu J, Li S, Dewil R, Zhang H, Baeyens J, et al. The steam-assisted calcination of limestone and dolomite for energy savings and to foster solar calcination processes. J Clean Prod 2022;363:132640. https://doi.org/10.1016/j.jclepro.2022.132640.

[100] Diego ME, Arias B, Abanades JC. Evolution of the CO_2 carrying capacity of CaO particles in a large calcium looping pilot plant. Int J Greenhouse Gas Control 2017;62:69–75. https://doi.org/10.1016/j.ijggc.2017.04.005.

Modeling and design of a calciner for commercial-scale CO_2 capture using stochastic methods and results from pilot tests

Supplementary material

Martin Greco-Coppi[a,*], Jochen Ströhle[a], Bernd Epple[a]

[a] *Technical University of Darmstadt, Department of Mechanical Engineering, Institute for Energy Systems and Technology, Otto-Berndt-Str. 2, 64287 Darmstadt, Germany*

[*] *Corresponding author: martin.greco@est.tu-darmstadt.de*

1. Temperatures in the calciner during IHCaL pilot tests

The temperature input for the reactor model of the IHCaL pilot plant (see Section 2.2) was derived from the temperature measurements in the calciner. The nearest sensor to the solid outlet was considered in the calculations (outside, top sensor). To eliminate the influence of transient events, a smoothed temperature curve was used, which was calculated using a moving average function. The temperature progression during the pilot tests is displayed in Figure S.1, including the time-averaged temperature at the reactor outlet, which was the input for the calciner model. The transient behavior is caused by load changes, interruptions of solid circulation flow, and discrete make-up feeding. The temperature in the middle section, situated far from the reactor outlet, was lower because the cold make-up input (approximately 20 °C) and the carbonated material (approximately 650 °C) entered at this point.

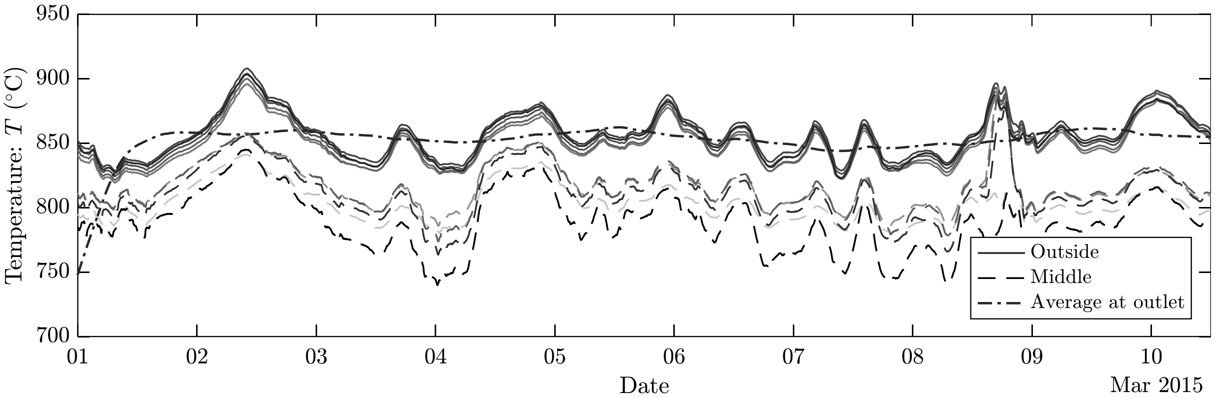

Figure S.1 Temperature variation in the calciner during the pilot tests at the 300-kW_{th} IHCaL facility [1]. Darker curves indicate higher locations in the reactor.

2. Sorbent composition

The sorbent utilized in the pilot tests and the TGA tests was Messinghausen limestone, with the composition reported in Table S.1.

Table S.1. Composition of the Messinghausen limestone. Adopted from [2,3].

Component	Mass fraction (wt.%)
$CaCO_3$	98.3
$MgCO_3$	0.7
SiO_2	0.7
Al_2O_3	0.2
Fe_2O_3	0.1
SO_3	< 0.1

3. Scheme of the carbonate looping process

Figure S.2 is a simplified process diagram of the carbonate looping process featuring the molar flows and carbonation degrees used throughout our study.

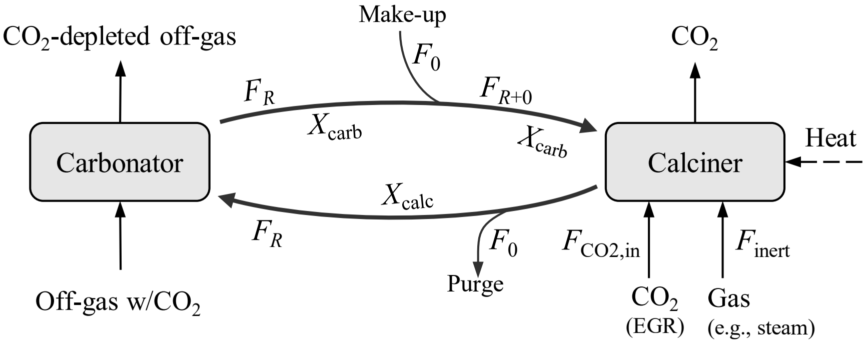
CO2-depleted off-gas
Make-up
F_0
CO2
F_R
F_{R+0}
X_{carb}
X_{carb}
Heat
Carbonator
Calciner
X_{calc}
F_R
F_0
$F_{CO2,in}$
F_{inert}
Purge
Off-gas w/CO2
CO2 (EGR)
Gas (e.g., steam)

Figure S.2 Simplified process diagram of the CaL process with main molar flows (*F*) and carbonation degrees (*X*).

4. Particle sub-model

4.1. Alternative **h** function

The influence of the concentration (**h**) is sometimes modeled as a monomial function with exponent n_o [4]:

$$\mathbf{h} = \left(C_{\mathrm{CO2,eq}} - C_{\mathrm{CO2}}(t)\right)^{n_o} \tag{S.1}$$

The exponent n_o is usually equal to 1 [4–6]. This is a simpler approach, which was applied in the calciner model of Martínez et al. [7].

4.2. Reaction progress

The reaction progress with an R3 model, an R2 model, and a linear approximation is illustrated in Figure S.3.

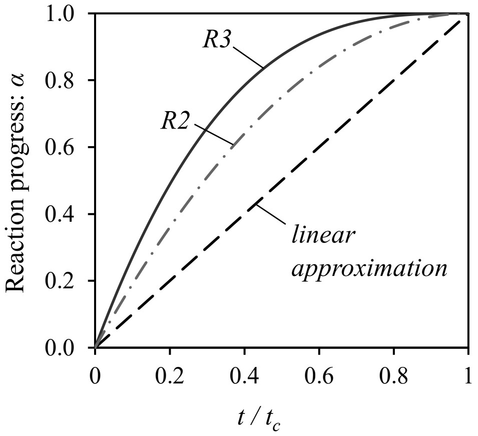

Figure S.3 Total calcination of a particle with residence time $t < t_c$ of the exact solution of the models R2 and R3, and the linear approximation.

4.3. Fitting of the form function

The complete fitting results for the form function (**f**) using results from TGA tests are reported in Figure S.4. The quality of the fit was assessed with the root mean square error (RMSE). The values of RMSE for each fit are included in the legend of Figure S.4.

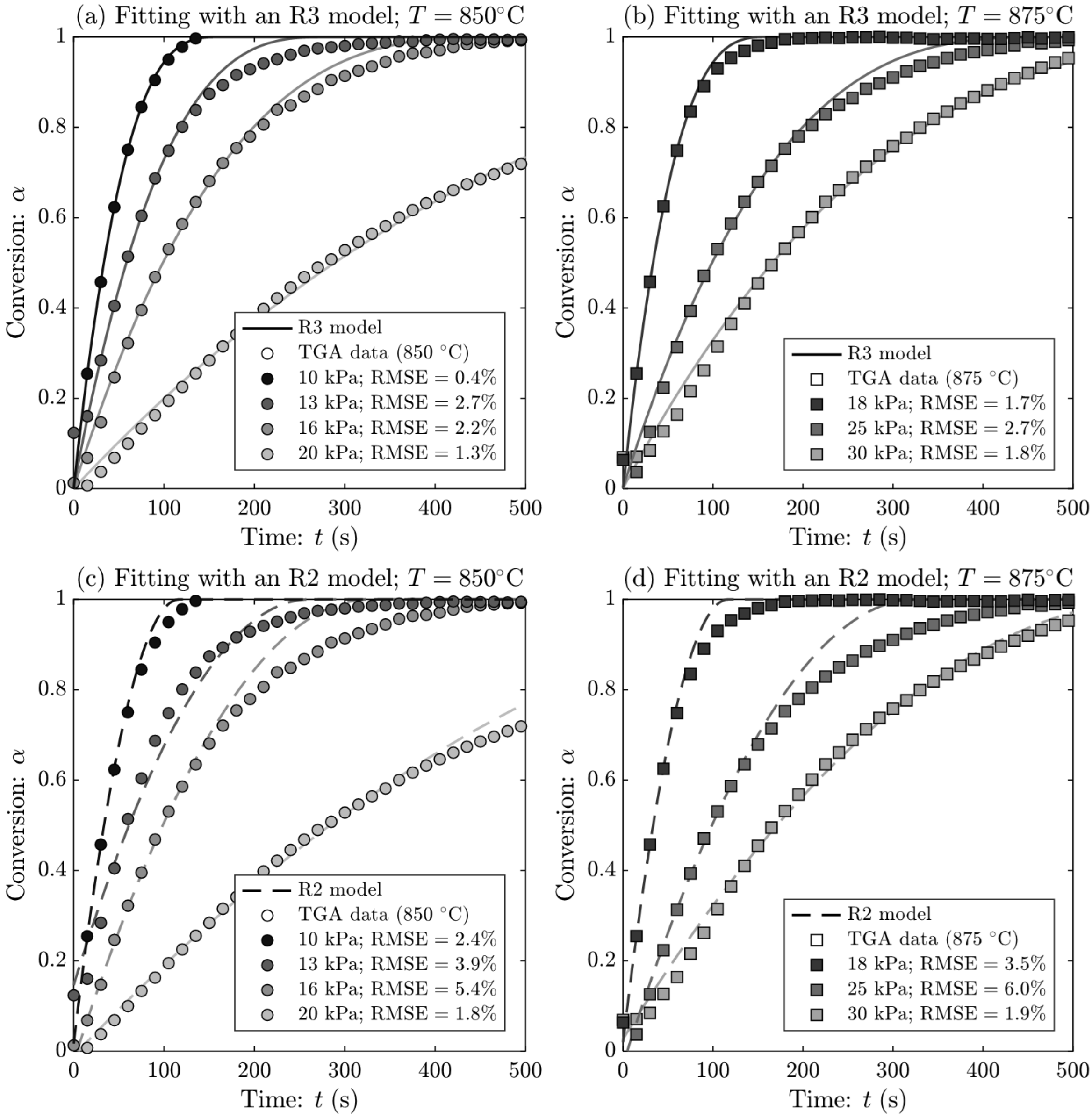

Figure S.4. Complete fitting results for the form function using results from TGA tests.

4.4. Fitting of the kinetic constants

The following equation was used to fit the TGA data and obtain the constants k_c and c:

$$k = k_c \left(1 - p_{\mathrm{CO2}} / p_{\mathrm{CO2,eq}} - c\, p_{\mathrm{CO2}}^{1/2} + c\, p_{\mathrm{CO2}}^{3/2} / p_{\mathrm{CO2,eq}}\right) \tag{S.2}$$

The TGA data and the fitting results are illustrated in Figure 4.

4.5. Complete equation for reaction kinetics

The final equation to model the reaction kinetics in our study is:

$$d\alpha / dt = X_{\mathrm{carb}}^{-1}\, k_c\, (1-\alpha)^{2/3} \left(1 - c\, p_{\mathrm{CO2}}(t)^{1/2}\right)\left(1 - p_{\mathrm{CO2}}(t) / p_{\mathrm{CO2,eq}}\right) \tag{S.3}$$

The parameters k_c and c are obtained from the Arrhenius equations Eq. (16) and Eq. (22), respectively, using the constants from Table 2.

4.6. Calciner efficiency

4.6.1. Simplified calculation

Previous studies simplify the calculation of E_{calc} by assuming a linear dependence of X_{calc} with t for the cases of partial calcination ($t < t_c$), according to Eq. (S.4) [7].

$$\overline{X}_{\text{carb}} - X_{\text{calc}}(t)\Big|_{t<t_c} = \overline{X}_{\text{carb}}\ t/t_c \tag{S.4}$$

This is a conservative assumption, illustrated in Figure S.3. The corresponding error is illustrated in Figure S.5. Replacing Eq. (S.4) into Eq. (23), gives:

$$E_{\text{calc}} = f_a\left(\tau/t_c\right) \tag{S.5}$$

4.6.2. Illustration of the model results

The calculation of the calciner efficiency by integration of the particle residence time distribution (RTD, **E**) and the particle conversion is illustrated in Figure S.5.a. The results of the calculations are illustrated in Figure S.5.b. The linear approximation gives a lower E_{calc} than the exact solution.

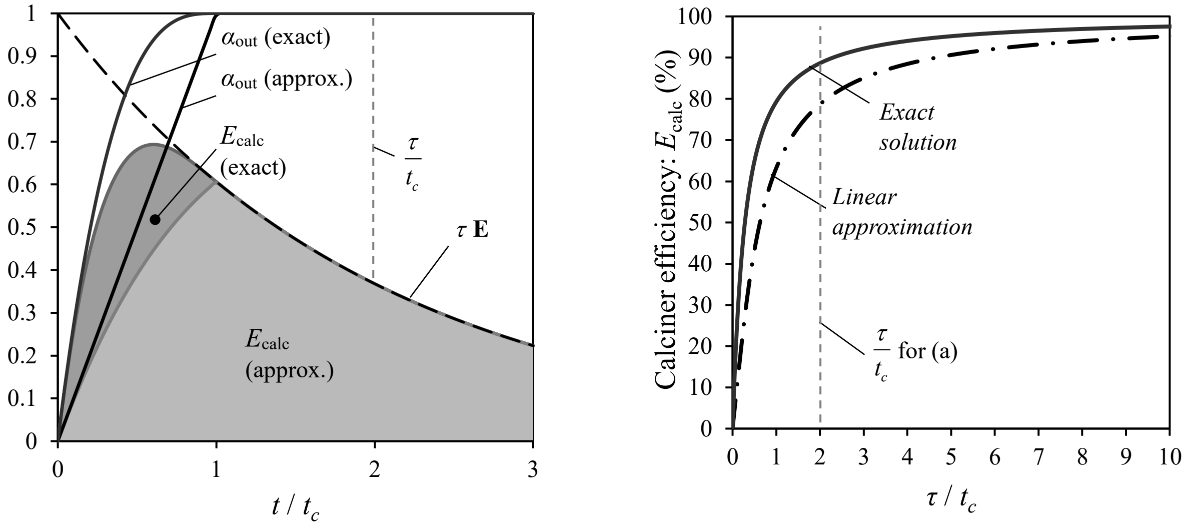
(a) Graphic summary for the calculation of E_{calc}

(b) Results from the calcination model

Figure S.5 Results of the reactor model for $\tau = 2\ t_c$. The calciner efficiency (E_{calc}) is only dependent on the calcination time (t_c) and the mean residence time (τ).

5. Validation

The validation results of Figure 9 are replicated in Figure S.6 with higher residence times to assess the influence of this parameter in the model. The results with higher residence times are similar to the original results.

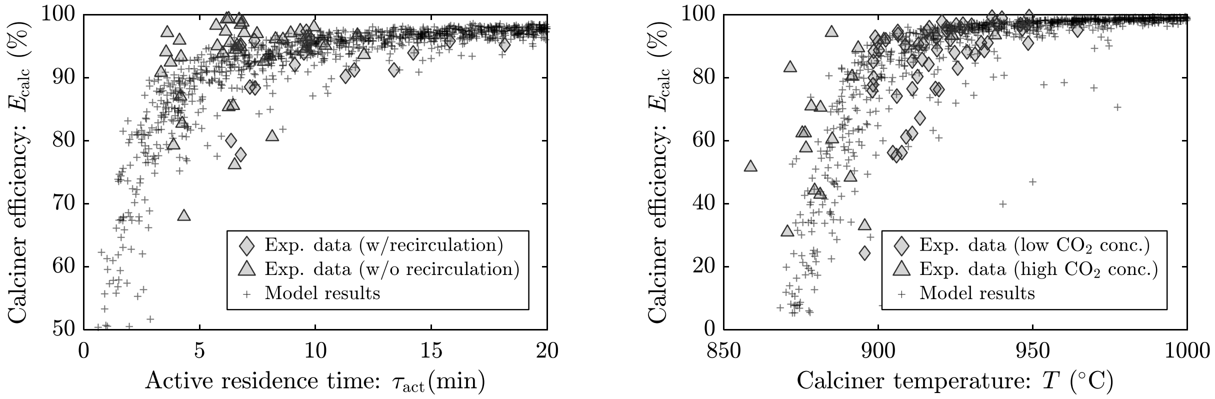

Figure S.6. Figures analogous to Figure 9 except for the particle residence time (τ), which was increased 100 times.

6. Optimization of IHCaL commercial plants

In this section, the auxiliary calculations for the optimization of IHCaL commercial plants are included. The optimization consists in setting the driving force (DF) equal to 2. Using this condition in the definition of DF, the following expression for $F_{\mathrm{R+0}}$ is obtained:

$$F_{R+0} = F_{\mathrm{inert}} \left(\frac{1}{1 - p/p_{\mathrm{CO2,in}}} - \frac{1}{1 - 2\,p/p_{\mathrm{CO2,eq}}} \right) \frac{1}{\overline{X}_{\mathrm{carb}}} \tag{S.6}$$

The methodology to obtain the optimized points consists in using Eq. (S.6) to calculate the circulation ($F_{\mathrm{R+0}}$) that makes DF = 2. To keep only the plausible values, the results that do not comply with $0.1 < F_{\mathrm{R+0}}/A_t < 20$ are discarded.

7. References

[1] Reitz M, Junk M, Ströhle J, Epple B. Design and operation of a 300 kW$_{\mathrm{th}}$ indirectly heated carbonate looping pilot plant. International Journal of Greenhouse Gas Control 2016;54:272–81. https://doi.org/10.1016/j.ijggc.2016.09.016.

[2] Greco-Coppi M, Hofmann C, Ströhle J, Walter D, Epple B. Efficient CO_2 capture from lime production by an indirectly heated carbonate looping process. International Journal of Greenhouse Gas Control 2021;112:103430. https://doi.org/10.1016/j.ijggc.2021.103430.

[3] Greco-Coppi M, Ströhle J, Epple B. A carbonator model for CO_2 capture based on results from pilot tests. Part I: Hydrodynamics and reactor model. Chemical Engineering Journal 2024;500. https://doi.org/10.1016/j.cej.2024.155119.

[4] Martínez I, Grasa G, Murillo R, Arias B, Abanades JC. Kinetics of Calcination of Partially Carbonated Particles in a Ca-Looping System for CO_2 Capture. Energy Fuels 2012;26(2):1432–40. https://doi.org/10.1021/ef201525k.

[5] Dennis JS, Hayhurst AN. the effect of CO_2 on the kinetics and extent of calcination of limestone and dolomite particles in fluidised beds. Chemical Engineering Science 1987;42(10):2361–72. https://doi.org/10.1016/0009-2509(87)80110-0.

[6] Lee J-T, Keener TC, Knoderer M, Khang S-J. Thermal decomposition of limestone in a large scale thermogravimetric analyzer. Thermochimica Acta 1993;213:223–40. https://doi.org/10.1016/0040-6031(93)80018-6.

[7] Martínez I, Grasa G, Murillo R, Arias B, Abanades JC. Modelling the continuous calcination of $CaCO_3$ in a Ca-looping system. Chemical Engineering Journal 2013;215-216:174–81. https://doi.org/10.1016/j.cej.2012.09.134.

Lime plays a crucial role in modern industry—essential in steelmaking, construction, agriculture, and chemical manufacturing. However, its production is inherently carbon intensive. To drastically reduce CO_2 emissions, efficient carbon capture solutions are needed.

The **Indirectly Heated Carbonate Looping (IHCaL) process** offers a groundbreaking approach to capturing CO_2 from lime and cement production. By leveraging synergies with existing industrial processes, IHCaL technology minimizes energy penalties and economic costs. Yet, until now, key integration challenges and modeling gaps have remained unaddressed.

This doctoral dissertation provides essential tools for effectively implementing the IHCaL process in lime production, from conceptual integration to detailed process simulations and reactor modeling.

The author presents:
- Innovative process integration approaches for efficient CO_2 capture.
- Advanced reactor models based on experimental data.
- Strategies for heat recovery, power generation, and fuel optimization.
- Insights on CO_2 capture and economics based on process simulations.
- Practical design guidelines for scaling up IHCaL technology.

Who should read this dissertation?
- Researchers and engineers working on industrial decarbonization.
- Professionals in the lime and cement industries seeking sustainable solutions.
- Policymakers and experts shaping the future of low-carbon manufacturing.
- Students in engineering, natural sciences, and energy sciences.
- Anyone interested in the challenges and innovations driving the transition to a low-carbon economy.

This dissertation is a key reference for advancing IHCaL technology toward commercialization and accelerating the decarbonization of lime production.

From the Foreword by Prof. Dr.-Ing Bernd Epple, Head of the Institute for Energy Systems and Technology at the Technical University of Darmstadt.

ISBN 978-3-68952-845-4

9 783689 528454